

**Investigation of influences of air mass transport
and chemical processes on the trace substance
distribution in the lower atmosphere
using chemical ionization mass spectrometry and
a self-developed measurement drone**

Dissertation
for the award of the degree
„Doctor of Natural Sciences“
Doctorate in Chemistry

at the Faculty of Chemistry, Pharmaceutical Sciences,
Geography and Geosciences of the
Johannes Gutenberg University Mainz

Lasse Moormann
born in Bad Soden am Taunus

Mainz (2025)



JOHANNES GUTENBERG
UNIVERSITÄT MAINZ



MAX-PLANCK-INSTITUT
FÜR CHEMIE

License and copyright agreement

All publications in this within work, i.e., chapters 3 to 6 and 8, and the thesis as well are available via the Creative Commons Attribution 4.0 License (CC-BY-4.0).

1st Supervisor:

2nd Supervisor:

Day of the oral examination: 09.12.2025

Declaration of independence

I, Moormann, Lasse hereby declare

that I have written this thesis entitled:

“Investigation of influences of air mass transport and chemical processes on the trace substance distribution in the lower atmosphere using chemical ionization mass spectrometry and a self-developed measurement drone”

independently and have not used any sources or aids (including AI-based applications or tools*) other than those specified. All verbatim or analogous citations and quotations are labelled and referenced (this also applies to texts generated by generative AI, such as Chat GPT). I confirm that I have not used any aids whose use has been explicitly excluded by the examiner. I have documented the AI tools used in the appendix "Use of AI tools". By submitting this work, I take responsibility for the overall product submitted. I am therefore also responsible for any AI-generated content that I have included in my work. I have checked the accuracy of the (AI-generated) statements and content to the best of my knowledge and belief. I am aware that a violation of the above points has consequences under examination law and may in particular result in the doctoral performance being assessed as "failed". Enrolment can be revoked for up to two years if students cheat twice or more in examinations (Section 69 (4) and (5) HochSchG):

Mainz, 27.10.2025,



Place, date and signature

* Further information on AI-based applications or tools can be found at: <https://digitale-lehre.uni-mainz.de/lehren-pruefen/ki-in-der-hochschulbildung/>

Table of Content

Abstract	9
Zusammenfassung.....	10
1 Introduction.....	11
2 Theoretical and Methodical Background	13
2.1 Atmospheric Structure	13
2.1.1 Planetary boundary layer	13
2.1.2 Air mass transport in the troposphere.....	15
2.1.3 Synoptic-scale transport.....	15
2.2 Composition of the Atmosphere	17
2.2.1 Gas phase	17
2.2.2 Particle phase	18
2.3 Measurements of Atmospheric Matter	19
2.3.1 Optical measurement techniques	20
2.3.2 Mass spectrometry.....	21
2.4 Measurement Platforms	24
2.4.1 Ground-based measurements – Mobile Laboratory.....	25
2.4.2 Drone-based measurements.....	25
2.5 Measurement Sites	26
2.5.1 Mainz, Rhineland-Palatinate: Cooking experiment and drone characterization.....	26
2.5.2 Gau-Algesheim, Rhineland-Palatinate: Drone In-flight Characterization.....	27
2.5.3 Tailfingen (Albstadt), Baden-Württemberg: BISTUM23.....	27
2.5.4 Spielberg (Brachttal), Hesse: BISTUM24	27
3 Gas and Aerosol Particle Composition from a Local Emission Source	29
3.1 Abstract	30
3.2 Introduction.....	30
3.3 Design and Operation of the AERTRACC Sampling System.....	32
3.3.1 The mobile aerosol research laboratory (MoLa).....	32
3.3.2 Setup of the AERTRACC sampling system	33
3.3.3 Control software and sampler operation	35
3.3.4 Sampling media	37
3.3.5 Analysis method	38
3.4 Characterization of the Sampling System	38
3.4.1 Particle transport efficiency	38
3.4.2 Time delay between aerosol measurement and sampling	39
3.5 In-field validation of the AERTRACC using a single point source in a semi-urban environment.....	40

3.5.1	Measurement setup	40
3.5.2	Data preparation and analysis.....	40
3.5.3	Results and discussion.....	41
3.6	Summary	49
4	Influence of Synoptic Air Mass Transport on Chlorine Chemistry	51
4.1	Abstract	52
4.2	Introduction.....	52
4.3	Methods: CIMS Operation and Calibration	55
4.3.1	VUV lamp as reagent ion source in CIMS	56
4.3.2	Calibration of chlorine-containing species	56
4.3.3	BISTUM24 field campaign: measurement site and instrumentation.....	57
4.4	Chlorine-containing Compounds and Air Mass Origin	58
4.5	The Diel Cycle of Cl ₂ , HOCl, ClNO ₂ and ClONO ₂	60
4.5.1	ClNO ₂	62
4.5.2	ClONO ₂	63
4.5.3	Formation and diel cycle of Cl ₂ and HOCl.....	66
4.6	Daytime Cl-atom Production Rates	67
4.7	Photolysis of HOCl as Source of OH.....	69
4.8	Conclusion	71
5	Development and Application of the Measurement Drone FLab	73
5.1	Abstract	74
5.2	Introduction.....	74
5.3	The Flying Laboratory FLab	76
5.3.1	Description of the FLab platform	76
5.3.2	Instrumentation	77
5.4	Characterization of FLab Performance.....	82
5.4.1	Instrumental time resolution and uncertainty.....	83
5.4.2	Influence of horizontal motion.....	85
5.4.3	Influence of vertical motion	88
5.4.4	Development of an optimized vertical profiling flight pattern	90
5.5	Applications of FLab	91
5.5.1	Evolution of the stratification of the lower troposphere	91
5.5.2	Bridging the gap between ground-based and aircraft-based measurements	94
5.6	Summary	95
6	Vertically-resolved Diurnal Variation of Organic Aerosol Particles.....	97
6.1	Abstract	98
6.2	Introduction.....	98
6.3	Experimental Procedures	99

6.3.1	Sampling system	99
6.3.2	Sampling procedure	100
6.3.3	Analysis.....	100
6.4	Results and Discussion	101
6.4.1	Sampler characteristics	101
6.4.2	Influence of the sampling UAV on the measured concentrations	103
6.4.3	Vertical profiles of biogenic, biomass burning and anthropogenic marker compounds.....	104
6.4.4	Height dependent van Krevelen diagrams	106
6.5	Conclusions.....	108
7	Influence of Irradiance and Mixing Layers on the Representativity of Ground-based Measurements	111
7.1	Abstract	112
7.2	Introduction.....	112
7.3	Methodology.....	114
7.3.1	Measurement sites.....	114
7.3.2	Experimental data	114
7.3.3	Data evaluation	115
7.4	Nocturnal Boundary Layer: Height Criteria and Fine-scale Structure	116
7.5	Influence of Solar Irradiance on Trace Matter Distribution	118
7.5.1	Classification of “clear-sky” and “cloudy” days.....	118
7.5.2	Representativity of diurnal ground-based measurements	119
7.5.3	Representativity of Ground-based Measurements in a Mixed PBL	124
7.6	Summary	127
8	Influence of Synoptic Rain Fronts on the Local Boundary Layer Dynamics	129
8.1	Abstract	130
8.2	Introduction.....	130
8.3	Methodology.....	131
8.3.1	Measurement sites.....	132
8.3.2	Experimental data	132
8.3.3	Model data	133
8.4	Case study I:	
	Delayed Breakup of NBL during Warm Front Rain in High-pressure System.....	134
8.4.1	Synoptic situation and local meteorology.....	134
8.4.2	Driving forces of air mass mixing.....	134
8.4.3	Characterization of different air masses	135
8.5	Case Study II:	
	Impact of a Cold Front and a Convergence Line on the Lowermost Troposphere	139
8.5.1	Synoptic situation and local meteorology.....	139

8.5.2	Reconstruction of air mass exchange by cold fronts and a convergence line	139
8.5.3	Impact of rain events on pollutant distribution	142
8.5.4	Influence of cold pool formation on model MLH	143
8.5.5	Convergence zone advection and measurement limitations.....	144
8.6	Summary	144
9	Conclusion and Outlook	147
	References.....	153
	Appendix.....	189
	Acronyms.....	189
	Symbols	191
	Use of AI Tools.....	192
	Supplementary Information for Chapter 3.....	193
	Supplementary Information for Chapter 4.....	204
	Supplementary Information for Chapter 5.....	210
	Supplementary Information for Chapter 6.....	222
	Supplementary Information for Chapter 7.....	228
	Supplementary Information for Chapter 8.....	234
	Acknowledgments.....	243
	Personal List of Publications.....	245
	Curriculum Vitae.....	248

Abstract

The distribution of trace substances in aerosol and gas phase varies with sources, transport mechanisms, and sinks, and influences air quality, and Earth's climate. A deeper understanding of meteorological influences on chemical processes is crucial to establish policies preventing hazards caused by humans and affecting them.

In this work, measurement devices and methods were developed to investigate chemical and microphysical processes affecting trace substances and their distribution. A thermo desorption technique for gases and aerosol particles for chemical analysis was developed as a complementary offline analysis method for an aerosol sampler that can collect aerosol and gas phase samples separately, differentiating depending on composition of the advected air. It was applied in-field near a wood-fired pizza oven to investigate cooking emissions. The separated aerosol phases were analyzed by chemical ionization mass spectrometry to identify characteristic cooking and biomass-burning markers. The second developed device is the research measurement drone FLab ("Flying Laboratory") to extend ground-based in-situ measurements into the vertical dimension to investigate transport of air masses in the planetary boundary layer (PBL). FLab was designed to measure the key variables relevant to tropospheric microphysical and chemical processes: wind, temperature and humidity, O₃, CO₂ and aerosol particle number concentration, size distribution, and black carbon concentrations. FLab was deployed in two 2.5-week long field campaigns in continental Germany (BISTUM23 and BISTUM24). A case study demonstrates successful bridging of ground-based and airborne-based measurements. During BISTUM23, particle-phase samples were collected at multiple heights throughout the day, while FLab continuously profiled the vertical 500 m-range. Combining FLab data with external targeted and non-targeted analyses of the particle phase's chemical composition revealed oxidation and transport processes of biogenic and anthropogenic compounds and the general aerosol composition, respectively.

Across both campaigns, near-hourly diurnal vertical profiling with FLab allowed detection of mixing layers in the lower troposphere. During nighttime, on average pollutant markers were more sensitive mixing layer height (MLH) tracers than meteorological variables; notably, specifically O₃ and the potential temperature were overall the most effective markers. The dataset from 383 flights to 500 m above ground was used to evaluate how representative ground-based measurements are for the whole mixing layer. Meteorological variables are most reliably estimated with ground-based stations, while the distribution of pollutant markers was more affected by irradiance or local air mass advection, requiring vertical measurement to better characterize pollutant distribution and estimate representative pollutant concentrations. The influence of two synoptic frontal events on the local pollutant distribution in the PBL was analyzed by combining model analysis, drone-borne and ground-based measurements. Frontal events strongly influence air mass dynamics and the MLH which turns out to simultaneously influence local chemical processes due to oxidant depletion and entrainment in different altitudes. Synoptic air mass transport also altered the chemical composition of air at the BISTUM24 measurement site as "marine-anthropogenic" influenced air led to significantly enhanced amounts of chlorine-containing species. Here, first-time reported tropospheric diel cycle of ClONO₂ indicate high amounts of nighttime ClO radicals. Enhanced concentrations of ClONO₂ and Cl₂ after dawn suggest vertical mixing in the PBL, while high HOCl levels show significant contribution to primary OH radical production, especially in the morning.

Zusammenfassung

Die Verteilung von Spurenstoffen wie Aerosolpartikel und Gase in der Atmosphäre variiert je nach Quellen, Transportmechanismen und Senken. Sie beeinflusst dabei die Luftqualität und das Klima der Erde. Ein tieferes Verständnis für meteorologische Einflüsse auf chemische Prozesse ist notwendig, um Maßnahmen zur Prävention menschengemachter Gefahren einzuführen.

In dieser Arbeit wurden mehrere Messgeräte und -methoden entwickelt, um chemische und mikrophysikalische Prozesse zu untersuchen, die das Auftreten und die Verteilung von Spurenstoffen beeinflussen. Zunächst wurde eine offline-Analysemethode zur chemischen Analyse von Gas- und Aerosolproben entwickelt, die auf Proben eines Aerosolsammlers angewandt wurde. Dieser kann zwischen verschiedenen Luftmassen unterscheiden und wurde in der Nähe eines Pizzaofens eingesetzt um Emissionen von Kochprozessen zu untersuchen. Mittels dieser Thermodesorption-Methode für chemische Ionisations-Massenspektrometrie wurden charakteristische Marker für Kochprozesse und die Verbrennung von Biomasse des gesammelten Aerosols identifiziert. Die Forschungsdrohne FLab („Flying Laboratory“) wurde entwickelt um bodengestützte durch vertikale Messungen in die planetare Grenzschicht (PBL) zu erweitern und um die für troposphärische mikrophysikalische und chemische Prozesse relevanten Größen zu messen: Wind, Temperatur und Feuchte, O₃, CO₂ und Aerosolpartikelanzahlkonzentration, -Größenverteilung und Rußkonzentrationen. FLab wurde in zwei 2,5-wöchigen Feldmesskampagnen in Süd- und Mitteldeutschland (BISTUM23 und BISTUM24) eingesetzt. Ein Fallbeispiel zeigt ein erfolgreiches Verknüpfen von bodengestützte und Flugzeugmessungen. Um die chemische Zusammensetzung von Aerosolpartikeln in der PBL zu messen, wurde ein extern entwickelter Aerosolsammler eingesetzt und auf weiteren Drohnen montiert. Während BISTUM23 wurden tagesüber Partikelproben in verschiedenen Höhen gesammelt, während FLab kontinuierlich vertikale Messflüge bis in 500 m Höhe durchführte. Die Kombination dieser Messmethoden zeigt Tagesgänge der Oxidations- und Transportprozesse biogener und anthropogener Partikelbestandteile.

Nahezu stündliche Vertikalprofile mit FLab ermöglichten die Identifikation von Mischschichten in der unteren Troposphäre. Während der Nacht waren Schadstoffmarker zuverlässigere Indikatoren für die Mischschichthöhe (MLH) als meteorologische Messgrößen, wobei insbesondere O₃ und die potentielle Temperatur am verlässlichsten im Erfassen von Grenzschichten waren. Der Datensatz von 383 Flügen bis zu 500 m Höhe wurde verwendet, um zu untersuchen, wie repräsentativ bodengestützte Messungen für die gesamte Mischschicht sind. Meteorologische Messgrößen konnten mit bodengestützten Stationen am zuverlässigsten bestimmt werden, während die Verteilungen von Schadstoffen stärker von der Sonneneinstrahlung oder der lokalen Luftmassenadvektion beeinflusst wurden. Der Einfluss zweier synoptischer Fronten auf die lokale Schadstoffverteilung in der PBL wurde durch die Kombination von Modellanalysen, drohnengestützten und bodengestützten Messungen analysiert. Fronten beeinflussen die Luftmassendynamik und die MLH stark, was sich gleichzeitig auf lokale chemische Prozesse durch den Abbau von O₃ sowie dessen Eintrag in verschiedenen Höhen auswirkt. Der synoptische Luftmassentransport veränderte auch die chemische Zusammensetzung der Luft während BISTUM24, als „maritim-anthropogen“ beeinflusste Luft zu deutlich erhöhten Konzentrationen an chlorhaltigen Spezies führte, wobei erstmalig in der Troposphäre gemessenes ClONO₂ auf hohe ClO-Radikalkonzentrationen während der Nacht hindeutet. Erhöhte ClNO₂- und Cl₂-Konzentrationen nach dem Sonnenaufgang implizieren eine vertikale Durchmischung der PBL, während zeitgleich die Photolyse von HOCl einen signifikanten Beitrag zur primären Produktion von OH-Radikalen zeigt.

1 Introduction

Atmospheric trace substances as aerosols and gases effect the Earth's climate, air quality and consequently the human's health (WHO, 2021; IPCC, 2023). The distribution of trace substances depends on their sources and sinks, but also on transport of matter from local up to synoptic scale distances. Oceans and forested regions are natural emitters of aerosols, whereas anthropogenic aerosol is particularly important in densely populated urban areas and can influence their surroundings. These anthropogenic emissions often originate from discrete point sources; their aggregated contribution is substantial and amenable to control through policy. As natural and anthropogenic emissions are transported and mixed by atmospheric flows, they interact chemically and microphysically to generate secondary pollutants and new particles, thereby either alleviating or worsening impacts on air quality and climate. To keep track of pollution levels and climate change indicators, measurement networks have been established in urban hot spot regions (Krzyzanowski et al., 2014; ICL, 2025), on federal scale (EPA, 2025; UBA, 2025), up to worldwide joint projects (Pastorello et al., 2020; ACTRIS, 2025).

The number of measurement stations is increasing worldwide, and measurement setups are becoming accessible to citizens (Commodore et al., 2017). This provides more data for assessing air quality, however, high uncertainties occur from instruments especially near local sources (Van Brussel and Huyse, 2019), that cannot distinguish between sampling from an emission source or background information. If the various air mass origins are not differentiated, the composition of air masses can change significantly (Struckmeier et al., 2016; Celik et al., 2020), leading to biased measurements and misinterpreted data. This is especially crucial in terms of chemical analysis of trace matter, where the number of ambient measurements is relatively limited and high-quality samples are desired. In chapter 3, an externally developed aerosol sampler was used to collect gases and aerosol particles on separate substrates, while differencing sampled air masses depending on online measured variables to intentionally avoid emission source contamination on background samples. For this sampler an offline-technique for chemical analysis of gases and aerosol particles was developed to validate the efficiency and effectivity of the aerosol sampler. The composition of gas and aerosol particle samples from background and an emission source were characterized with thermal desorption chemical ionization mass spectrometry (CIMS).

Chemical characterization of trace substances in air masses is needed for source apportionment studies (Drewnick et al., 2007; Phillips et al., 2012). Emissions that were emitted from specific local sources, like cooking emission, vehicle plumes, etc. (Zhu et al., 2002; Pikmann et al., 2024) or from broader source types like seaside, forests, or urban regions often carry specific molecular markers (Williams et al., 2010; Kourtchev et al., 2013; Struckmeier et al., 2016). While some of these marker substances are short living and degrade such that they become unidentifiable from the background compositions, others require precursors as sea salt and reactive gases to form characteristic markers. Such heterogeneously formed molecules can be found far away from the source and reveal complex atmospheric processes, which have a synoptic scale influence (Oum et al., 1998; Lelieveld et al., 2004). Therefore, in chapter 4, air masses with chlorine-containing compounds were identified with CIMS in rural Central Germany and analyzed with respect to their influence by "marine-anthropogenic" or "continental-unpolluted" conditions. Different air mass histories are analyzed regarding the abundance of various chlorinated species, their potential impact on radical formation as well as vertical air mass mixing in the morning hours was indicated by measurements of various chlorine-species at ground.

Incomplete vertical mixing and stratification formation are processes that usually constitute major limitations to ground-based measurements. While such measurements are often well-equipped to study the surface layer in detail, the vertical dimension of the planetary boundary layer (PBL) is often left to theoretical turbulent-based descriptions, but experimentally neglected. The accessibility is complicated by the high costs of aircraft measurements that are restricted to a minimum height above the surface, the short residence time in the PBL of radio sondes (Helbig et al., 2021), and the height and location limitations of measurement towers (Andreae et al., 2015). Nowadays, drones are typically used to provide in situ data up to a few kilometers above ground (Jacob et al., 2018; Hervo et al., 2023), however they usually monitor only a few, mostly meteorological, variables. Therefore, to characterize the PBL in situ, a new measurement drone “Flying Laboratory” (FLab) was developed that provides online measurements of meteorological data (wind, temperature, humidity), aerosol particles (particle number concentrations, size distribution, particulate matter and black carbon mass concentration) and trace gases (CO₂, O₃). Measurements with FLab are characterized in chapter 5 and were used to extend ground-based measurements of a highly-equipped research van up to 300 m above ground. Further it was applied to bridge the gap between ground-based measurements and aircraft measurement, while validating data from balloon-borne radio sonde ascents.

FLab was deployed during two 2.5-week long summer field campaigns in Central and Southern Germany, with the goal to investigate

- a) vertical transport of trace matter from ground to 500 m (chapter 6):
Besides the hourly vertical profiling with FLab, two other research drones operating in 120 m and 500 m above ground and a ground-station were equipped with novel low-cost aerosol samplers that each sampled 3,000 L during a flight. By comparing the aerosol composition at different altitudes with the FLab data, altitude-resolved diurnal trends were investigated applying a target analysis on biogenic and anthropogenic markers and a non-target analysis.
- b) the representativity of ground-based measurements in a hilly terrain (chapter 7):
As the vertical representativity of ground-based measurements is rarely considered and taken for granted, vertical profiling with FLab during the field campaigns helps to identify “unexpected stratification” and to examine local and irradiance-driven influences. Nighttime flights up to 120 m above ground were used to test the sensitivity of various markers to detect fine-scale layers in the atmosphere. Furthermore, vertical profiles up to 500 m were used to examine the limited representativity of ground-based measurements with respect to the diel PBL height cycle and the variability of gradients due to irradiance-driven mixing.
- c) the influence of synoptic events on the local trace matter distribution (chapter 8):
As atmospheric stratification has shown to affect the pollutant distribution in the stable continental PBL (Platis et al., 2016; Pohorsky et al., 2025), the effect of synoptic rain fronts in the mid-latitudes on stratification, pollutant distribution and chemical processes has not been studied yet. For a weak warm front in a high-pressure system and a cold front with a convergence zone, the ICON forecast model data, FLab and ground-based measurement data were combined, linking local experiments with model observation to reconstruct the lower tropospheric stability, stratification and precipitation effects on chemical processes after the rain events.

2 Theoretical and Methodical Background

This chapter provides background information to understand topics, theories and methods applied in this work. As results from field work in the lowermost atmosphere are included, meteorological concepts are explained. The composition and properties of aerosols is discussed along with measurement techniques that were applied to detecting trace matter. Finally, background information of applied measurement platforms and the respective measurement site are presented.

2.1 Atmospheric Structure

The Earth's atmosphere is formed from influences as irradiance, energy fluxes, air currents due to the Earth's rotation and the time of the year. The atmosphere consists of various layers extending from the Earth's surface into space. The layers differentiate due to different pressure regimes and temperature profiles that facilitate different air mass transport processes, interactions between layers, and define specific chemical regimes. The troposphere is the lowest layer of the atmosphere, where most weather events occur. It contains 80% of the atmosphere's total mass and extends up to approximately 8 km at the poles and up to 12 km at the equator. The troposphere is capped by the tropopause, an atmospheric boundary to the stratosphere above.

Within the troposphere, there is a capping inversion that separates it into two sub-layers: the free troposphere (FT) and the planetary boundary layer (PBL). The FT is primarily influenced by large-scale synoptic processes, while the PBL is formed due to interactions between the Earth's surface and atmosphere, such as the exchange of moisture, latent heat, momentum flux, and radiation (Stull, 1988).

2.1.1 Planetary boundary layer

The structure of the PBL is influenced by boundary layer dynamics, which are determined by surface properties and the daily variation in radiation. The Earth's surface is the lower boundary of the atmosphere and introduces friction to moving air masses. Different topographies, such as seas, grassland, forests, cities and mountain ridges with increasing surface friction, can lead to different turbulence regimes, with weak turbulence over calm oceans and strong turbulence over mountainous regions. As a result, topography causes local variations in dynamics, particularly in the surface layer, the lowest 5% of the PBL. In the surface layer, wind profiles increase logarithmically with height. The PBL is strongly influenced by local conditions such as emission sources or heat reservoirs due to absorption of irradiance.

In addition to local surface effects, solar radiation also influences the PBL. During the day, solar irradiance increases the height of the PBL (PBLH), while at night, the absence of irradiance reduces its height. This daily cycle results in the formation and dissipation of several layers, each ranging from one meter to several hundred meters in height.

During daytime, when irradiance warms the ground, i.e., the surface layer, convective uplift of air masses (see Sect. 2.1.3.1) can mix aerosol emissions and disperse them from their sources by turbulent eddies within the PBL. Therefore, the daytime PBL is referred to as the convective boundary layer (CBL), which is separated from the free troposphere (FT) by a capping inversion that prevents further mixing, but still allows entrainment under severe weather conditions (see Sect. 2.1.3). The height of the capping inversion is given by the PBLH that can increase as radiative-convective intensifies.

In the evening, as solar convective heating decreases, the intensity of turbulent mixing diminishes and cooling of the surface layer begins. The cooling leads to a natural separation of the CBL into two parts: the lower, ground-near nocturnal boundary layer (NBL) and the elevated residual layer (RL). The NBL remains turbulent due to local winds and surface friction, even though the component driven by solar irradiance is absent. Compared to daytime, thermodynamic fluxes are reversed, as temperature from warmer air above the surface layer, which is still heated from daytime, is transferred towards the cooler ground (Stull, 1988; Kotthaus et al., 2023). As air in proximity to the ground cools down, and the RL remains relatively warm, a shallow inversion layer is formed.

The RL is a remnant from the previous day's CBL and separated from the NBL by the capping inversion. As the capping inversion separates the RL from the NBL, the RL it is no longer influenced by surface friction and geostrophic winds can create a low-level jet (LLJ) above the NBL. A LLJ is a fast air stream that can range a few hundreds of meters up into the RL and transports air masses and trace substances over long distances, similar to synoptic winds. However, the LLJ only lasts for a few hours and weakens as the night progresses due to merging into the boundary layer and redistributing its momentum or reduced mesoscale pressure gradients that initially drive the LLJ (Blackadar, 1957; Luiz and Fiedler, 2024).

The diurnal cycle completes at sunrise when solar heating of the ground increases radiative-uplift of surface layer air, causing the NBL to extend into the RL and form a new CBL. The entrainment zone between RL and CBL, where this mixing occurs, can last for several hours, depending on the stability of the capping inversion and the solar heating of the lowest layer. The diurnal structure of the planetary boundary layer (PBL) is almost valid globally, varying mainly due to convective heating and local topography.

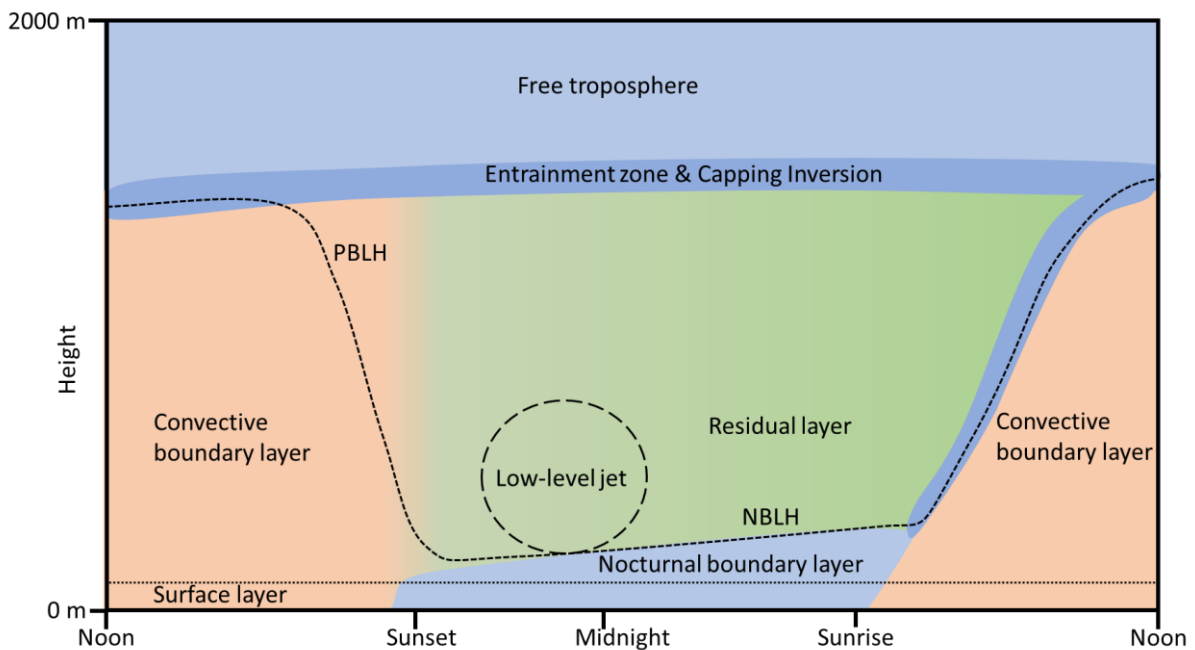


Fig. 2.1: Schematic representation of the diurnal variation of the PBL structure.

2.1.2 Air mass transport in the troposphere

Similar to the structure of the PBL, air mass transport in the troposphere is driven by solar radiation. Solar radiation heats the Earth's surface, which warms the ground-near layer through conduction and radiation. As the air temperature increases, the air expands, reducing its density relative to the surrounding cooler air. This now buoyant, less dense air rises and transfers heat to higher atmospheric layers through convection. As it ascends from the heated surface, it cools adiabatically.

The influence of radiative-heated buoyant air differs between the synoptic and local scale and time scale. The following sections describe transport processes that depend on synoptical situation and affect the free troposphere and PBL, while local transport processes that are only apparent in the PBL and occur on a daily basis are present separately.

2.1.3 Synoptic-scale transport

The influence of the synoptic weather situation on the PBL in the mid-latitudes can be explained by interaction of high-and low-pressure systems, and warm and cold air masses.

The vertical cycle of subsiding air in high-, and uplifted air in low-pressure systems can also introduce free tropospheric air into the PBL, while slowly dispersing air from the PBL in the free troposphere. In between these systems, pressure gradients drive winds that transport air masses and trace constituents over hundreds to thousands of kilometers within the lower troposphere, including the PBL.

When different air masses encounter each other, fronts as narrow transition zones between air masses of contrasting temperature and humidity can form. In a warm front, warm air slides gradually over a colder air mass, producing widespread, long-lasting precipitation. In a cold front, denser cold air undercuts warm air and forces rapid ascent of the warmer air, yielding shorter-lived but more intense, often convective precipitation (Stull, 1988). Such frontal lifting can ventilate the PBL and inject PBL air into the free troposphere, particularly in association with cold-frontal convection (Andreae et al., 2001; Wang et al., 2011).

2.1.3.1 Local-scale transport

Local-scale air mass transport differs from synoptic-scale transport because land–atmosphere interactions generate local circulations, shear, and vertical fluxes within the PBL. Synoptic-scale winds arise from pressure gradients between low- and high-pressure systems, with associated vertical circulations that can influence the PBL. By contrast, additional transport driven by surface heterogeneity is limited to local scales.

Near the surface within the PBL, differential heating and cooling among surfaces act as heat sources and sinks that create and steer local winds. Such thermally driven circulations develop between, e.g., heated cities or wildfires and their cooler surroundings (Guo et al., 2011), and between surfaces with contrasting heat capacity, as in the diurnal sea–land breeze (Vickers and Mahrt, 1999). Higher in the PBL, the influence of surface roughness decreases and the Coriolis force increasingly deflects the flow, turning it to the right in the Northern Hemisphere and to the left in the Southern Hemisphere (Ekman, 1905).

Vertical air mass motion in the PBL is primarily driven by radiative heating of the surface and the resulting sensible heat flux to the air aloft (see Sect. 2.1.2). In contrast to synoptic-scale ascent associated with low-pressure systems, local-scale vertical fluxes arise from small-scale turbulent eddies. The turbulent behavior of air is commonly explained using the air parcel concept. An air parcel is a bubble of

air with undefined size but specific characteristics like temperature, humidity, and composition. These parcels maintain their net heat budget through various processes such as advection, radiation, turbulence, and latent heat, which can transform into one another. External forcing as solar radiation or entrained air masses, continuously change the air parcel's environment; buoyant parcels accelerate upward while negatively buoyant parcels descend. The ensemble of these motions constitutes turbulence, which is intensified by surface heating. Stronger turbulence promotes rapid mixing, producing a more homogeneous layer within the PBL (Stull, 1988).

2.1.3.2 Metrics for Atmospheric Stability

The turbulence state within an atmospheric layer is commonly described as atmospheric stability. A highly stable atmospheric layer indicates weak turbulent mixing, in contrast to instable conditions. As the term "atmospheric stability" is versatile, various metrics have been developed to quantify the turbulent state of a mixing layer. Metrics used in this work are presented in the following.

Two fundamentally different perspectives are used to describe mixing-layer dynamics: Lagrangian and Eulerian. Lagrangian (parcel-based) approaches compare properties of an air parcel to those of its environment and consider parcel motion within the layer; this requires knowledge of the vertical structure.

Two commonly used Lagrangian stability markers are the gradient of the potential temperature ($d\theta/dz$) and the bulk Richardson number (Ri). $d\theta/dz$ describes how temperature changes with altitude z . The potential temperature is used instead of the air temperature to consider adiabatic cooling of the air. If warmer air overlies colder air, vertical motion is unlikely and $d\theta/dz > 0$; $d\theta/dz < 0$ indicates warmer air below colder air which leads to convective mixing (unstable).

Ri accounts for the fact that shear can generate turbulence even under stable stratification. Ri considers changes of horizontal winds with heights (Δu and Δv) and the adiabatic cooling rate like $d\theta/dz$:

$$Ri = \frac{\left(\frac{g}{T_v}\right) \frac{\Delta\theta_v}{\Delta z}}{(\Delta u)^2 + (\Delta v)^2}. \quad (2.1)$$

The definition of Ri includes latent heat, i.e., energy that is stored in the phase transition of moisture. Therefore, the gradient of the virtual potential temperature $d\theta_v/dz$ and the virtual temperature T_v are used. Dynamically unstable conditions occur when $Ri < 0$ (due to negative $d\theta_v/dz$, comparable to negative $d\theta/dz$). Shear-driven turbulence can exist for $0 < Ri < Ri_c$; a commonly used critical value is $Ri_c \approx 0.25$. For $Ri > Ri_c$, dynamically stable conditions suppress turbulent mixing across the layer. Eulerian measures describe conditions at a fixed point in space (e.g., at a given height). Eulerian metrics only require stationary measurements but do not necessarily represent the conditions throughout the entire atmospheric layer. Both Eulerian measures used in this study were derived from continuous ground-based measurements: the turbulent kinetic energy (TKE) and the heat flux (Q_H).

TKE quantifies the intensity of turbulent wind velocity fluctuations via the variances of the wind components (u' , v' , w'):

$$TKE = \frac{1}{2} \sqrt{u'^2 + v'^2 + w'^2}. \quad (2.2)$$

Larger *TKE* generally accompanies stronger turbulent mixing by larger eddies and convective instability, but *TKE* does not provide an explicit threshold for stability classification. Because *TKE* is often measured near the surface, it is strongly influenced by radiative heating of the ground.

While *TKE* only considers wind fluxes, Q_H describes the vertical turbulent sensible heat transfer and is estimated from the covariance of temperature T and vertical wind w , the specific heat of air C_p , and its density ρ :

$$Q_H = \rho C_p \overline{w'T'}. \quad (2.3)$$

The magnitude $|Q_H|$ reflects the strength of turbulent heat exchange: small $|Q_H|$ typically indicates weak mixing (often under stable or near-neutral conditions), whereas large $|Q_H|$ indicates stronger turbulent transfer. The sign of Q_H indicates direction: $Q_H > 0$ when the surface warms the overlying air (commonly daytime), and $Q_H < 0$ when the surface cools the overlying air (commonly nighttime). Unlike purely kinematic instability markers as *TKE*, Q_H is sensitive to precipitation and surface wetness: evaporation converts sensible to latent heat, reducing $|Q_H|$ or making it negative, a process not captured by other stability markers (Stull, 1988).

2.2 Composition of the Atmosphere

The atmosphere consists mostly of air, i.e., the gas phase, whose composition is described in the following section. Additionally, particles are dispersed in the gas phase, forming an aerosol. The physical and chemical properties and its composition of the aerosol vary, depending on the emission source and the history of the aerosol.

2.2.1 Gas phase

The atmospheric gas phase mainly consists of nitrogen, oxygen, argon, and CO_2 , which are present in similar proportions worldwide. A smaller portion includes a diverse range of volatile organic compounds and inorganic trace gases, which can be released from their sources through evaporation, vaporization or chemical reactions. Biogenic emissions come from sources like plants (Yatavelli et al., 2014), soil (Rossabi et al., 2018), living organisms or burning biomass (Hegg et al., 1990; Koppmann et al., 2005), while anthropogenic emissions result from, e.g., incomplete (fossil) fuel combustion, cooking (Huang et al., 2011), agricultural or industrial processes (Moomaw, 1996; Chataut et al., 2023). Gas mixtures often contain markers that are specific for their emission source, but their chemical composition is complex. Their mixture can contain hazardous components making them important for assessing health risks, especially concerning anthropogenic emissions (Hegg et al., 1990; Huang et al., 2011).

Gaseous matter typically has a limited lifetime in the atmosphere due to three loss processes: photolysis, aging, and condensation. Photolysis, the main fragmentation pathway, occurs when short-wave solar radiation breaks chemical bonds. The efficiency of photolysis depends on the available radiation (e.g., wavelengths, intensity), and the absorption cross-section of molecules that all can vary significantly (Keller-Rudek et al., 2013). Photolysis produces radicals, which reach their maximum abundance after noon and are largely absent at night, transforming into reservoir species that release radicals when photolysis resumes in the morning (Wayne et al., 1995; Young et al., 2012). These reactive, short-

lived radicals can initiate chain reactions, such as hydrogen abstraction from organic molecules, forming new reactive radicals (Droege and Tully, 1987; Hoffmann, 1998). These radicals can recombine with other organic radicals to form larger molecules or react with inorganic radicals like OH, O₂, O₃, nitroxides, or Cl. This chemical transformation with oxidants is known as aging. As molecules oxidize, they become more polar, form larger clusters with increasing interactions (e.g., chemical bonds) which reduces their volatility so that these molecules eventually form condensed matter through gas-to-particle conversion. Further condensation on already existing particles lets them grow (Hoffmann, 1998; Fry et al., 2011). Changes in the gas phase's chemical composition, influenced by surrounding conditions, directly affect the particle phase's chemical composition.

2.2.2 Particle phase

The chemical composition of aerosol particles is determined by their formation process and influenced by their history. Primary aerosol particles are directly emitted from natural sources such as wave-breaking, raising of dust, or fungi (Koulouri et al., 2008; Després et al., 2012). Anthropogenic sources are tire wear or soot emission by incomplete combustion (Farley et al., 2023; Müller et al., 2025). In contrast, secondary aerosol particles form through aging processes in the atmosphere (Pandis et al., 1992). Despite differences in chemical composition, the physicochemical properties of particles are strongly dependent on their individual sizes.

Nucleation mode particles are the smallest, ranging from small clusters of a few molecules to diameters of up to 25 nm. These particles dominate the particle number concentration but not the mass. They form from low volatile gases through stabilizing intermolecular interactions, leading to cluster formation, known as new particle formation. As low volatile gases condense on these freshly nucleated particles, they grow. Coagulation occurs when particles collide and form larger particles, reducing their number. This process, along with condensation causes particle growth up to the Aitken mode (~25 nm to ~100 nm) and the accumulation mode (~100 nm to 1 µm). Collectively, particles in these size ranges are referred to as fine particles (Hinds, 1999).

Coarse mode particles are larger than 1 µm in diameter are primary aerosols and originate from mechanical influences. Although primary aerosols are mainly inorganic, the condensation of organic matter on particles increases their average organic content.

Particle size affects properties such as transport and atmospheric lifetime. Ultra-fine mode particles (smaller than 100 nm), follow the gas phase flow and are transported by small turbulent eddies until they grow larger and their inertia reduces dynamic movement. Larger particles are influenced more by air currents or larger eddies than by small-scale transport processes.

A lack of uplifting air currents can lead to dry particle removal when particles settle to the ground or impact other surfaces due to high inertia. This process limits the lifetime of coarse mode particles, while diffusion limits the lifetime of very small, e.g., nucleation and Aitken mode particles. Accumulation mode particles, being intermediate in size, are less affected by impaction, sedimentation, and diffusion, allowing them to remain in the atmosphere longer and be transported over larger distances (Hinds, 1999; Cherrier et al., 2017). Humid conditions or rain can remove aerosols through washout, which involves uptake or droplet formation based on particle solubility, leading to quick sedimentation (Pandis et al., 1995). In summary, accumulation mode particles are the most persistent in the atmosphere, although washout can limit their lifetime as well as that of particles of other sizes. The optical properties of aerosol particles of different sizes are discussed in the next section.

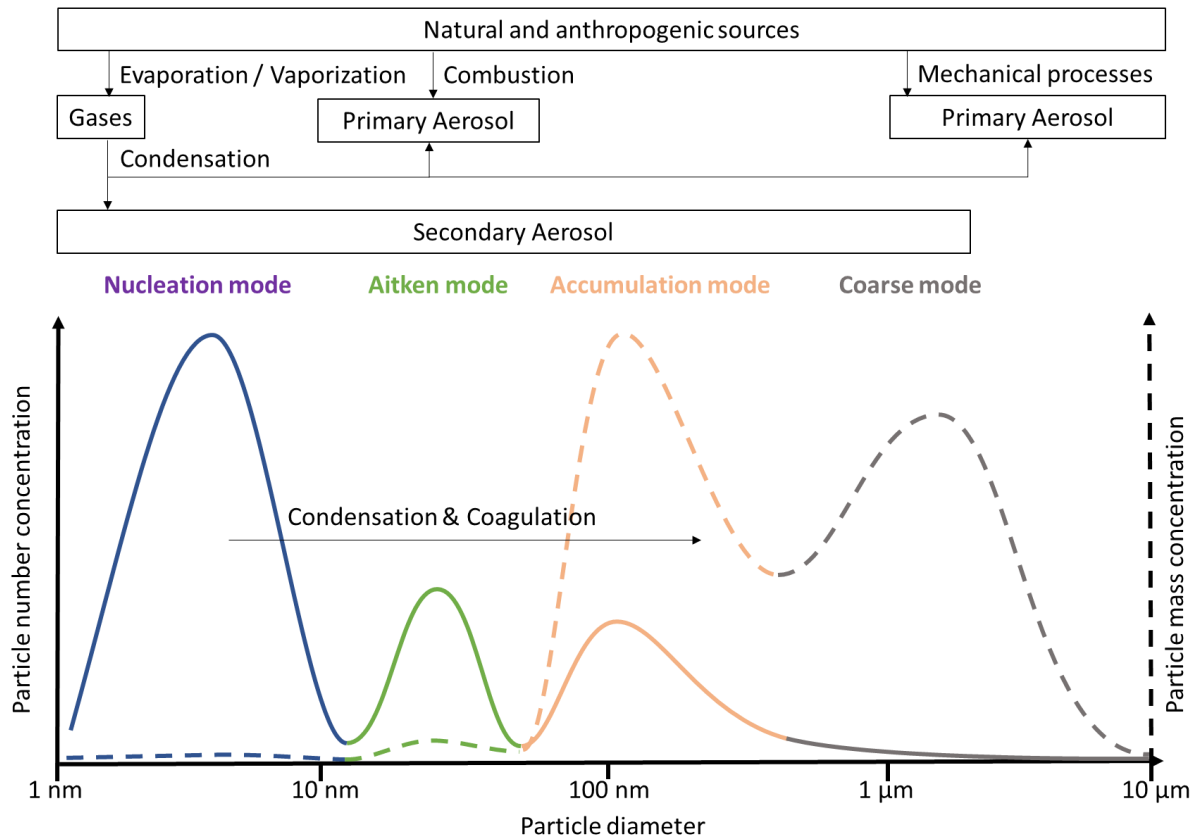


Fig. 2.2: Schematic representation of the pathway and underlying processes from emission source to particles in different modes (adapted from Pikkmann, 2023).

2.3 Measurements of Atmospheric Matter

Gases and aerosol particles have a variety of diverse chemical and physical properties, that require specific characterization methods. Measurements can be performed in real-time (online) or after sample collection (offline). Online measurements are typically employed in field studies where high temporal resolution is essential, eliminating the need for storage or complex sample preparation, thereby reducing contamination risks.

Online measurements are categorized into in-situ and remote methods. In-situ methods involve direct sampling of the target matter, such as in plumes, at specific locations, e.g., altitudes above ground, or within clouds (Altstädter et al., 2018; Galle et al., 2021), while for remote methods, instruments are positioned distant to the point of interest. These methods, including Lidars, sonars, radar, or differential optical absorption spectroscopy, can detect tracer matter without physical contact over large distances. However, they often lack high spatial resolution, have near-field dead zones close to the instrument, and face signal penetration challenges under adverse atmospheric conditions (Kotthaus et al., 2023). In contrast, in-situ measurements, while requiring more sampling effort and covering only very limited areas, offer high spatial resolution, avoid signal penetration issues, and allow for simultaneous measurement of multiple variables or sample storage for later offline analysis (Kellner et al., 2006).

Offline methods are advantageous when samples require laboratory-based instrumentation or need pre-concentration or modifications due to insufficient detection levels or complex sample matrices that hinder direct analysis. Common pre-concentration devices for gases include desorption tubes,

while filters are frequently used for aerosol particles. Desorption tubes contain a sorbent that chemically adsorbs molecules with certain properties and releases them upon heating (Dettmer and Engewald, 2002). In contrast, particles impact on the filter, allowing the gas phase to pass through and separate the aerosol phase. Particles collected on a filter can be directly analyzed microscopically, thermally desorbed into a gaseous phase, or dissolved for liquid phase analysis (Chow et al., 1994). Although offline samples enable a wide range of analysis methods, preserving the sampled material is challenging due to thermodynamic instability and unwanted reactions between the analyte and reactive surfaces or gases (Clement and Karasek, 1979; Dettmer and Engewald, 2002). Therefore, online measurements are beneficial for chemically sensitive, thermodynamically unstable, and difficult-to-isolate, but highly-abundant substances, while offline analysis is suitable for complex matrices and when analysis must continue elsewhere (Kellner et al., 2006).

Selecting the appropriate instrument or analysis method depends on the properties of interest. In this work, mainly optical measurement techniques have been used to determine mixing ratios of trace gases and physical properties of particles, while mass spectrometry was employed to analyze complex chemical compositions in both online and offline analyses.

2.3.1 Optical measurement techniques

Spectroscopy is frequently employed as a non-destructive technique to examine the chemical composition of the sample or morphology using electromagnetic radiation. A spectroscopic instrument typically includes a light source, whose light passes through an optical cell. The light source has a known intensity distribution accordingly to the wavelengths, allowing for the measurement of transmission or extinction before and after the optical cell. Within the optical cell, the light source intensity can be reduced by aerosol particles through scattering, diffraction, or absorption. In contrast, gaseous molecules reduce the laser intensity solely through absorption (Hinds, 1999; Kellner et al., 2006). The configuration of the detector varies depending on the light-matter interaction of interest. For absorption spectroscopy, the detector is positioned in line with the light source beam, while for emission spectroscopy or light scattering measurements a detector location distant, e.g., orthogonal to the primary light source beam is chosen. Further details are provided for absorption spectroscopy on gases and light scattering by particles.

2.3.1.1 Gas phase spectroscopy

Light interacts with electrons and atoms depending on its frequency. It can excite molecules into specific vibrational, rotational and electronic states. Light absorbing analytes decrease irradiance transmission according to the Lambert-Beer law. Estimating concentrations requires knowledge of the optical cell depth, the light intensity before and after absorption, and the absorption (or extinction) coefficient at the specific wavelength (Kellner et al., 2006). The absorption coefficient is a characteristic property of molecules that can be determined from a pure substance and is well-documented in databases for common atmospheric molecules (Keller-Rudek et al., 2013).

The wavelength of the incident light corresponds to a large absorption cross-section for the target molecule and a small absorption cross-section for potentially interfering molecules. This enables quasi-selective in situ measurements in complex or unknown matrices such as CO₂ or O₃ in atmospheric air. However, correction methods are often necessary to account for changes in ambient conditions, such as pressure changes in the optical cell or humidity, because H₂O absorbs and interferes across a wide range of the electromagnetic spectrum (Vaisala, 2013).

2.3.1.2 Light Scattering of Aerosols

When radiation hits a particle, the radiation is scattered in various directions. This elastic interaction is known as Mie scattering. The intensity of Mie scattering is influenced non-linearly by the particle's shape and size, the refractive index (which depends on the particle's composition), the laser frequency, and the angle relative to the laser beam. The intensity of scattered light is minimal for particles smaller than 50 nm, which limits the detectability of small particles. Mie scattering significantly increases for larger particles (ranging from 50 nm to 1 μm), thus, detecting larger particles through light scattering is an effective method for quantifying aerosol particles. However, instruments using Mie theory need to be calibrated for the laser's wavelength, the expected refractive index of the observed aerosol and most importantly for the scattering angle, which is a subject to the geometry of the optical cell.

Condensation particle counters (CPCs) are used to count ultra-fine particles (with diameters less than 100 nm) that typically cannot be measured due to low Mie scattering. In CPCs, a working fluid is evaporated at elevated temperature and condenses on ultra-fine particles in a cooled chamber, causing them to grow rapidly and enhancing their light-scattering capability. In a subsequent optical cell, a laser beam is scattered by the grown particles, so that scattered light pulses are measured for particle-poor conditions and reduced scattered light intensity in particle-rich conditions. This enables individual particle counting regardless of size or composition.

Conversely, optical particle spectrometers (OPS) determine the size distribution of particles with diameters larger than typically 250 nm from the intensity of the scattered light without condensation or artificial growth of the particles. OPS devices have detectors in the optical cell that measure signal intensity at specific angles. Since scattering angle and intensity are size-dependent, optical particle counters can determine particle size and count. In well-characterized systems, light scattering allows for sensitive and instantaneous measurements without affecting the sampled volume. However, uncertainties in particle-sizing are related to the refractive index and particle shape, due to mixed compositions, are disadvantages that must be considered (Hinds, 1999).

2.3.2 Mass spectrometry

Mass spectrometers (MS) work by transferring the analyte into the gas phase, ionizing the analyte's molecules and then separating the ions based on their mass-to-charge (m/z) ratio before detection. This fundamental principle of MS has remained consistent over the years, although advancements in analyzers and detectors have enhanced the ability to separate m/z finer and increased the number of detected ions within a given time frame. Traditional MS utilized strong magnets and coils to direct ions of a specific m/z towards a detector. In contrast, modern systems use multipoles with constant and alternating voltages to select desired ions of a single m/z more rapidly, enabling the scanning of multiple m/z values, albeit with limited resolution. ToF analyzers are the state of art technology for real-time measurements, as they can measure an entire mass spectrum directly without scanning.

In the following, the working principle of the time-of-flight (ToF) MS is described for the ToF-MS that have been used in this work. The basic structure of a ToF-MS is illustrated in Fig. 2.3. These instruments feature an inlet that transfers the sample into the gas phase, allowing ionization of the molecules. Once ionized, the molecules or clusters are guided into a high vacuum area using electrostatic lenses. These ion optics primarily focus the ion beam and remove neutrally charged particles, but they can also cut off the upper and lower limit of the m/z range that is analyzed further. In this method, an ion packet (containing different m/z) is pulsed orthogonally from the ion beam towards a reflector (a stack of electrostatic lenses). The reflector balances the kinetic energy distribution from the extractor. Ions

penetrate into the electromagnetic field according to their acceleration voltage. In the mass analyzer, the ions are expelled with the same equal kinetic energy (E_{kin}) and different flight velocities (v) based on their mass (m_i) and charge (z), into an electric field (E_{el}) with a voltage (U) and elemental particle charge (e):

$$E_{el} = ezU = \frac{1}{2}m_i v^2 = E_{kin} \quad (2.4)$$

$$v_i = \sqrt{\frac{2ezU}{m_i}} \quad (2.5)$$

The transformation from Eq. (2.4) to Eq. (2.5) shows the dependency of velocity of ions (v_i) on m/z in an electric field that enables separation based on mass and charge. The mass is a defining characteristic of the ion, which can be positively or negatively charged depending on the ionization process. Ions of the same m/z penetrate deeper into electric field, when they have experienced a higher voltage from the extractor, but arrive at the same time at the detector. Ions of different m/z separate due to different inertia due to energy conservation (Eq. (2.4)), i.e., while lighter ions are reflected sooner towards a detector plate, heavier ions have a longer flight time.

When ions hit a detector plate, they release secondary electrons which propagate into a primary current and can be converted into an electronic signal using a data acquisition system. The different arrival times of the ions, i.e., different flight times of the ions due to different m/z in the electric field, with changes in the primary current allow the representation of a mass spectrum (Gross, 2012). Although this method is computationally more complex than previous techniques, it is particularly beneficial for non-target analysis, such as determining the composition of an unknown sample.

Recent advancements in various inlet systems and ionization techniques have broadened the application range of mass spectrometers, allowing for selective analysis not only of gaseous samples but also of condensed matter in complex matrices. Aerosol and chemical ionization mass spectrometry are two widely used systems in environmental research for the chemical analysis of aerosols and gases, employing time-of-flight analyzers, and were utilized in this work.

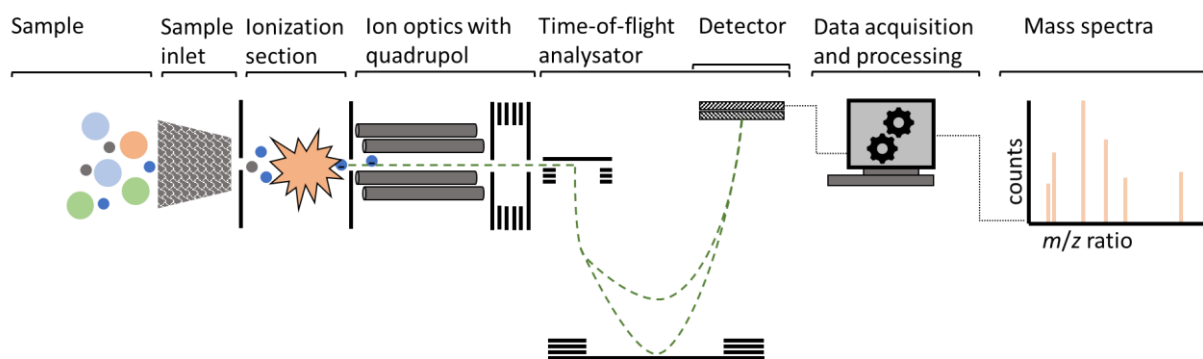


Fig. 2.3: Schematic representation of a time-of-flight mass spectrometer.

2.3.2.1 Inlet systems

The choice of inlet systems determines the kind of sample that can enter the mass spectrometer and which phase will be discarded. In this work, different approaches are applied for online- and offline-measurements and depending on the phase of interest.

For online-measurements filters can easily remove the particle phase from the sample flow, while the analysis of the particle phase in absence of reactive gases requires a denuder and a vaporization inlet for aerosols (Zhao et al., 2024). Thermal effects on aerosol particles and gases can cause molecular reactions, such as intramolecular rearrangements or fragmentation, which can bias or prohibit chemical identification (Yang et al., 2021).

For offline measurements, the selection of the inlet depends on the used sampling device and it must be able to separate adsorbed gases or collected particles from their collection substrate. In both scenarios, a heated flow of an inert carrier gas desorbs the sample into the gas phase (Dettmer and Engewald, 2002; Lopez-Hilfiker et al., 2014). The gas-phase sample can then be either preconcentrated in a cooled reservoir (commonly used in gas chromatography) or directly introduced into the ionization section. Thermal degradation of the sample molecules must be considered, however, temperature ramps can minimize these effects and even allow for the separation of individual components in a thermographic manner (Moormann, 2021).

2.3.2.2 Aerosol Mass Spectrometry

The aerosol mass spectrometer (AMS; Drewnick et al., 2005) used in this study measures the non-refractory fraction of bulk aerosol composition in real-time. As aerosol particles enter the inlet, they are aerodynamically focused to a particle beam to measure the particle size distribution and finally flash-vaporize the particles to a gas. A 70 eV-electron beam then ionizes the sample (electron ionization) so that a fraction of the ions can subsequently be directed into the analyzer-detector section of the MS using electrostatic lenses. AMS can analyze aerosol particles online, providing information of both organic and inorganic fractions. However, the characterization of species is restricted to those that can be vaporized at its respective temperature and the hard ionization process. Black carbon (non-refractory), and mineral dust cannot be vaporized and are undetectable with AMS, while sea salts vaporize slowly leading to a strong underestimation of its components. Additionally, the size range of detectable aerosol particles is limited from ~50 nm to ~900 nm, thus, coarse mode particles are not measured. Organic molecules, during vaporization and ionization, gain excess energy, causing them to fragment into smaller ions and lose neutral fragments (Jayne et al., 2000; Canagaratna et al., 2007). Due to the hard ionization, AMS typically identifies fractions of chlorine, sulfate, nitrate, and organics easily, while apportioning the organic fraction is only partially possible and requires extensive computational clustering methods (Ulbrich et al., 2009; Roth et al., 2016).

2.3.2.3 Chemical Ionization Mass Spectrometry

The choice of the ionization method for mass spectrometry depends on the type of sample and the desired information. Traditionally, electron ionization (see above) was used as it ionizes almost all substances, however, the excess energy can cause strong fragmentation of molecules into smaller ions and neutral particles, which are lost in the system. Despite this loss of molecular information, the variety of fragments can aid in reconstructing the structure of the ionized molecule, which is beneficial for pure samples (Gross, 2012).

Table 2.1: Reaction schemes of iodide-ions with target molecules in Iodide-CIMS.

Nucleophile addition:	$I^- + HX \rightarrow IHX^-$
Deprotonation:	$I^- + HX \rightarrow HI + X^-$
Ligand substitution:	$I(Y)_n^- + HX \rightarrow I(Y)_{n-1}HX^- + Y$
Fragmentation:	$IHX^- + E_{kin} \rightarrow I + HX^-$

As a new technique, chemical ionization mass spectrometry (CIMS) was developed as a gentler ionization technique that transfers less energy to the analyte, resulting in less fragmentation and conserving the molecular structure of the ions. Once the ions are generated, they are transferred and analyzed in the MS as described above. As the ionization process is complex, it is explained in the following.

Initially, primary ions are produced from an appropriate substance in an inert carrier gas using high-energy radiation such as UV, X-rays, or α -particles (Rissanen et al., 2019; Riva et al., 2019). These primary ions mix with the gaseous sample flow in an ion-molecular reactor and interact with the sample. The selectivity and sensitivity of this ionization process depend on the bonding strength between the primary ions and the sample molecules, which varies based on their nature.

Positively charged primary ions like H_3O^+ and $C_6H_6^+$ transfer protons according to the proton affinities of the sample molecules, enabling the detection of a wide range of volatile organic compounds. Conversely, highly oxidized or polar molecules can be detected using negatively charged ions such as I^- or NO_3^- . These ions bind to the analyte molecule due to sufficient polarizability or intermolecular interaction as formation of hydrogen bonds and constitute an even softer ionization method than proton transfer mechanisms. Negative reagent ions can either form a cluster with the analyte or deprotonate it. There are four potential reaction pathways for negative ions like I^- with a target molecule HX and additives Y (Table 2.1), which are highly dependent on the binding enthalpies of the target molecules and their stabilization by additives (Riva et al., 2019; Aggarwal et al., 2025). Note, that the absence of acidic hydrogen atoms rules out deprotonation, while other reactions are still possible and can occur simultaneously.

2.4 Measurement Platforms

Atmospheric measurement platforms or stations are built to house instruments which collect atmospheric data. The specific requirements for these platforms are primarily determined by the research or measurement objectives, though some generalizations can be made. The research goal dictates whether a stationary or mobile platform is necessary and how resilient it must be to withstand harsh environmental conditions, such as significant changes in temperature, humidity, or weather events like gusts, storms, or precipitation.

When building measurement platforms, the expected measurement data need justify costs and operational work. This involves considering the quality and costs of instruments and the infrastructure needed for calibration, maintenance, power supply, and data transmission. The entire setup affects the data's accessibility, accuracy, and precision. This is particularly important if the station design must comply with standards for measurement networks (Crenn et al., 2015; Hoerger et al., 2015) or if multiple platforms need to be compared with each other (Jacob et al., 2018; Poraicu et al., 2025).

2.4.1 Ground-based measurements – Mobile Laboratory

The mobile laboratory "MoLa" was developed as a ground-based measurement platform, enabling both stationary and mobile measurements (Drewnick et al., 2012). MoLa's purpose is to provide a comprehensive dataset for investigating the physical and chemical processes of aerosols in the atmosphere. It is designed to simultaneously measure the physical and chemical properties of aerosol particles, quantify trace gases, and collect meteorological data. With a high temporal resolution ranging from 1 s to 1 min, MoLa can analyze the horizontal distribution of pollutants (Fachinger et al., 2021), quasi-Lagrangian dilution and transformation of air parcels (von der Weiden-Reinmüller et al., 2014), or enable stationary characterization of emission sources (Diesch et al., 2013; Faber et al., 2015; Pikmann et al., 2024).

MoLa is a modified Ford Transit delivery vehicle, compact enough for flexible field deployment, yet spacious enough to house power generation and essential instruments for recording high-quality data in real-time. The aerosol and gas inlets for stationary use are mounted 3 – 3.5 m above MoLa (or 6 – 6.5 m above ground), facilitating sample transport into the air-conditioned interior. A meteorological weather station on top of the inlet measures horizontal wind, temperature, humidity, pressure, and precipitation. Inside MoLa, the particle phase can be investigated in terms of number or mass concentration as PM_{10} , $PM_{2.5}$, PM_{10} , or as a particle size distribution. High-grade instruments measure the concentrations of chemical constituents in PM_{10} , such as black carbon, chloride, nitrate, sulfate, and organic mass concentration. Gas phase instruments provide mixing ratios of atmospheric trace gases like CO , CO_2 , H_2O , O_3 , NO , NO_2 , and NO_x . In addition to the description by Drewnick et al. (2012), MoLa is equipped with a pyranometer for measuring solar irradiance and a ceilometer for analysis of the backscatter signal from aerosols and cloud droplets up to 10 km above ground, transforming MoLa from a pure in-situ measurement station to a remote measuring platform as well.

2.4.2 Drone-based measurements

Most individual measurement platforms, including MoLa, and monitoring networks primarily provide detailed data collected in the surface layer. These ground-based measurement stations often overlook the vertical structure and three-dimensional dynamics of the troposphere. A characterization of the troposphere's vertical structure is achievable through remote sensing or in situ methods. Remote sensing measurement techniques face challenges such as signal penetration issues under certain conditions, a limited number of observable variables, and coarse resolution, as discussed in Section 2.3.

Traditionally, in-situ measurements above the surface layer were conducted with research aircraft and balloon-borne radio sondes. Aircraft-based measurements are cost-extensive and typically legally restricted to a minimum flight level, which limits studying of the lowermost troposphere (Mirza et al., 2016). Radio sondes in contrast, ascend through the entire PBL, but are limited to a light payload, i.e., few or low-grade instruments, low spatiotemporal resolution. Additionally, material such as gas and the balloon, its one-way use, and the potential loss of the payload are costly (Sawyer and Li, 2013).

Unmanned drones equipped with instrumentations have proved to potentially close the gap between ground-based measurements and the aircraft-probed zone (down to 500 m), and showed the potential to compliment ground-based measurements into the vertical dimension. Drones are affordable, precisely maneuverable, and can access difficult-to-reach areas or follow customized flight patterns (Villa et al., 2016; Jacob et al., 2018).

Depending on the research objective, either fixed-wing or rotary-wing drones are used. Fixed-wing drones are ideal for horizontal mapping and for covering large distances, with flight durations lasting several hours at altitudes up to a few kilometers. Operating fixed-wing drones requires experienced pilots (Roberts et al., 2008; Reuder et al., 2012). Rotary-wing drones, which require less experienced personnel, allow precise flight maneuvers, including hovering and vertical profiling without changing horizontal position. However, their flight duration is very limited due to limited battery capacity and high-power consumption (Jacob et al., 2018; Hervo et al., 2023). Despite this, rotary-wing drones have become increasingly established in tropospheric research over the past 10 years (Whitehead and Hugenholtz, 2014; Jacob et al., 2018).

Research drones equipped with meteorological sensors have been used to investigate tropospheric dynamics for fundamental research or commercially motivated wind park measurements (Adkins and Sescu, 2017; Li et al., 2022). Drones with aerosol particle and trace gas sensors have studied natural emission sources, such as volcanoes or wave breaking (Galle et al., 2021; Radtke et al., 2024), and anthropogenic emission sources as agricultural farms, landfills or other industrial sites (Castro Gamez et al., 2019; Andersen et al., 2023; Bonne et al., 2024).

The number of measurable variables on-board drones is usually limited by the very limited payload. The payload is the maximum additional weight that can be carried with the drone and determines the flight duration. Consequently, most drones are equipped with either a small number of high-grade instruments (Womack et al., 2022) or a larger number of low-cost instruments that may lack precision, accuracy, and adaptability to rapidly changing ambient conditions, reducing the reliability of measurements (Brus et al., 2021b; Schuldt et al., 2023). A first approach combining meteorological measurements with gas and aerosol particle-phase analysis on-board unmanned flying platforms has been demonstrated with a modular drone (Brus et al., 2021a) and a helikite (Pohorsky et al., 2024). It was shown that simultaneous meteorological and trace substance measurements can be beneficial to understanding and explain microphysical processes, especially in the lowermost troposphere (Platis et al., 2016; Pohorsky et al., 2025).

2.5 Measurement Sites

During this work, a four measurements sites, air masses were probed and their data analyzed. An overview of the measurement sites, collected data and the respective research goals is presented in the following.

2.5.1 Mainz, Rhineland-Palatinate: Cooking experiment and drone characterization

In the summer of 2021, a pizza oven was installed at the backyard of the Max Planck Institute for Chemistry (MPIC), and emissions were measured using MoLa, positioned 10 m from the source. An automated sampling device was employed to distinguish between air masses originating from the emission source and those from the urban background. This real-time analysis enabled the separate collecting of aerosols from an emission source and the background on filters and desorption tubes for offline analysis with the CIMS in winter 2021/2022 (see chapter 3).

From 2022 to 2023, the same location was utilized for developing and characterizing the wind measurements on-board a drone under controlled conditions. For this purpose, MoLa was placed 4 m from

FLab to ensure that the similar wind speed measurements, with FLab hovering near the MoLa inlet (see chapter 5).

2.5.2 Gau-Algesheim, Rhineland-Palatinate: Drone In-flight Characterization

From 2022 to 2024, initial test flights and in-flight characterization of the research drone were carried out on a grassland between vineyards near the city of Gau-Algesheim. The permissions, granted by the authorities, allowed for vertical flights up to 300 m above ground and horizontal flights of ~700 m. At the measurement site, MoLa was used as a reference station for comparison and cross-calibration, while the drone ground station was employed to study data transmission for online monitoring (refer to chapter 5).

2.5.3 Tailfingen (Albstadt), Baden-Württemberg: BISTUM23

The main goal of the BISTUM23 (Bridging Surface emissions, Transport and UTLS Matter) campaign was to study how aerosols are distributed and lifted from the surface layer into the higher troposphere under rural convective conditions. The BISTUM23 campaign took place at a farm near Tailfingen (Albstadt) on the slopes of the rural Swabian Alp. This campaign lasted for 2.5 weeks in August 2023 and involved near-hourly drone ascents up to 500 m above ground level to observe diurnal changes of the pollutant distribution and atmospheric dynamics in the lowermost troposphere. Drone-based measurements were complemented by continuous ground-level measurements with MoLa and irregular atmospheric profiling using balloon-borne radiosondes (see chapters 7 and 8).

As a closure experiment between four individual measurement platforms, the research aircraft HALO (High Altitude-Long range) flew over the measurement site to extend detailed air mass characterization beyond the maximum permitted drone range into the free troposphere (see chapter 0). Alongside the self-developed drone FLab, two other research drones and a ground station sampled aerosol particles using low-cost samplers at 1 m, 120 m, and 500 m above ground. The corresponding chemical analysis was conducted offline (see chapter 6).

2.5.4 Spielberg (Brachtal), Hesse: BISTUM24

The measurement setup for BISTUM24 was equal to BISTUM23, with the research aim of analyzing the vertical distribution of aerosols and trace gases under more strongly anthropogenically affected conditions. A hilly location in the Vogelsberg area free from local emission sources, located about 45 km from Frankfurt was selected, where diurnal ascents up to 500 m were allowed. A distinctive feature of BISTUM24 was the performance of 30 consecutive hourly vertical profiling flights up to 120 m altitude throughout one night (see chapters 7 and 8).

While the instrumental setup of FLab remained unchanged after the characterization and BISTUM23 measurements, a CIMS was additionally included in MoLa during BISTUM24 to monitor chlorine-containing and organic trace gases at the measurement site (see chapter 4).

3 Gas and Aerosol Particle Composition from a Local Emission Source

This chapter contains a paper that has been published as

Pikmann, J., Moormann, L., Drewnick, F., Borrmann, S.: *The AERosol and TRACe gas Collector (AER-TRACC): an online-measurement-controlled sampler for source-resolved emission analysis*, *Atmos. Meas. Tech.*, 16, 1323–1341, <https://doi.org/10.5194/amt-16-1323-2023>, 2023

Contribution to this manuscript by Lasse Moormann:

As the second author of this work, I prepared the filter substrates and thermo-desorption tubes (TDTs) prior to probing in the AERTRACC. The method for analyzing filter samples using Iodide-CIMS was described in detail in Moormann (2021) and was further developed and extended by myself for TDTs. In order to analyze adsorbed gases, I developed a heating unit for the TDTs with an inlet system that was coupled to the Iodide-CIMS, which allowed the use of temperature gradients. After in-field deployment, I analyzed the molecular composition of the aerosol collected on the filters and the TDTs. I focused on identifying markers from emissions (such as cooking, biomass burning, traffic and aged aerosol) to validate the working principle of the AERTRACC. I contributed to discussions about the manuscript, created two figures and supported the writing process.

3.1 Abstract

Probing sources of atmospheric pollution in complex environments often leads to the measurement and sampling of a mixture of different aerosol types due to fluctuations of the emissions or the atmospheric transport situation. Here, we present the AERosol and TRACe gas Collector (AERTRACC), a system for sampling various aerosol types independently on separate sampling media, controlled by parallel online measurements of particle, trace gas, and meteorological variables, like particle number or mass concentration, particle composition, trace gas concentration as well as wind direction and speed. AERTRACC is incorporated into our mobile laboratory (MoLa) which houses online instruments measuring various physical and chemical aerosol properties as well as trace gas concentrations. Based on preparatory online measurements with the whole MoLa setup, suitable parameters measured by these instruments are used to define individual sampling conditions for each targeted aerosol type using a dedicated software interface. Through evaluation of continuously online measured data with regard to the sampling conditions, the sampler automatically switches between sampling and non-sampling for each of up to four samples, which can be collected in parallel. Particle and gas phase of each aerosol type, e.g., source emissions and background, are sampled onto separate filters with PM_1 and PM_{10} cut-offs, respectively, and thermal desorption tubes, respectively. Information on chemical compounds in the sampled aerosol is accomplished by thermal desorption chemical ionization mass spectrometry (TD-CIMS) as analysis method. The design, operation, and characterization of the sampler are presented. For in-field validation, wood-fired pizza oven emissions were sampled as targeted emissions separately from ambient background. Results show that the combination of well-chosen sampling conditions allows more efficient and effective separation of source-related aerosols from the background, as seen by increases of particle number and mass concentration and concentration of organic aerosol types, with minimized loss of sampling time, compared to alternative sampling strategies.

3.2 Introduction

Atmospheric aerosol changes radiative forcing, alters cloud formation and precipitation, and affects human health. Various chemical and physical processes lead to changes of the aerosol properties, like the particle size and composition (Fuzzi et al., 2015; Shrivastava et al., 2017; Johnston and Kerecman, 2019). Still the impact of these effects on climate and health are not sufficiently well understood as aerosol sources, composition, properties, and transformations are poorly characterized (Parshintsev and Hyötyläinen, 2015).

Atmospheric aerosol can originate from diverse sources, natural as well as anthropogenic ones. Primary particles can be related to anthropogenic sources like combustion processes of fossil fuel and biomass as well as natural sources emitting, e.g., sea salt and dust. Furthermore, secondary aerosol forms through gas-to-particle conversion by oxidation processes in the atmosphere (Fuzzi et al., 2015; Struckmeier et al., 2016; Gordon et al., 2017; Celik et al., 2020). Depending on the surroundings, different types of emissions and the background aerosol can blend into complex mixtures, complicating the identification of the contribution by the original emissions sources.

Atmospheric aerosol are generally classified into two major chemical fractions, the inorganic one with substances like ammonium, nitrate, sulfate, metal oxides, mineral dust, and sea salt, while the organic aerosol, the other fraction, constitutes the more complex part (Fuzzi et al., 2015). Especially fine particulate matter, which has a relevant effect on climate and health, contains usually a large organic

fraction (Zheng et al., 2020). These particles consist of many individual components but only a small fraction of them are identified by state-of-the-art instruments (Fuzzi et al., 2015; Johnston and Kerecman, 2019; Zhou et al., 2020). The analysis and identification of these organic components is necessary for better understanding of chemical processes, transport, sources, and particle formation in the atmosphere. This knowledge is crucial to improve existing models and facilitate prediction of climate effects (Johnston and Kerecman, 2019; Zhou et al., 2020).

Characterization of organic aerosol is demanding due to the broad variety of species and therefore numerous techniques for aerosol analysis have been developed (Johnston and Kerecman, 2019; Forbes, 2020). Techniques for analysis and characterization of aerosols are classified into two main categories, online and offline techniques. Offline measuring techniques frequently provide detailed information about different aerosol properties based on separate sampling and analysis (Parshintsev and Hyötyläinen, 2015). For chemical analysis, this approach offers the possibility to use all available analysis techniques to get detailed information at the expense of low time and particle size resolution (Heard, 2006; Hallquist et al., 2009). A broad variety of techniques are available for chemical analysis. Techniques like ICP-MS (inductively coupled plasma mass spectrometry) and XRF (x-ray fluorescence) provide information about the elemental composition of the sample (Ebert et al., 2016; Bhowmik et al., 2022), while FTIR (Fourier-transform infrared spectroscopy) and NMR (nuclear magnetic resonance spectroscopy) are used to determine organic functional groups in aerosols (Faber et al., 2017; Gilardoni, 2017). Techniques with separation prior to detection are applied for identification of individual species. Widely used for this purpose are GC-MS (gas chromatography mass spectrometry) and HPLC-MS (high performance liquid chromatography mass spectrometry); however they are typically only able to identify a relatively small fraction of the whole organic aerosol (Forbes, 2020). Single particle techniques like SIMS (secondary ion mass spectrometry) and SEM (scanning electron microscope) provide information about the elemental composition and its distribution as well as information about the particle morphology (Bai et al., 2018; Laskin et al., 2018).

Online and semi-online techniques are used to obtain data with high time resolution. With these techniques, samples are analyzed continuously or semi-continuously without the need of additional a-posteriori laboratory work as for offline techniques. One of the most widely used methods for aerosol online analysis is aerosol mass spectrometry (AMS) measuring the single particle or particle ensemble chemical composition of submicron particles. While offering real-time data due to short acquisition intervals it lacks detailed chemical information, lost through fragmentation during vaporization and ionization (Canagaratna et al., 2007). Consequently, identification of individual organic components is rarely possible (Hallquist et al., 2009). A semi-continuous online bulk analysis can be performed with the thermal-optical EC/OC analyzer measuring the hourly concentrations of elemental carbon (EC) and organic carbon (OC) (Zhou et al., 2015). Other semi-continuous systems like PILS (particle into liquid sampler) and MARGA (monitor for aerosols and gases in ambient air) sample the water-soluble aerosol fraction followed by subsequent analysis with, e.g., ion chromatography (Zhou et al., 2015; Stavroulas et al., 2019). More comprehensive analysis is achieved with TAG (thermal desorption aerosol gas chromatography) (Williams et al., 2006) and FIGAERO-CIMS (filter inlet for gas and aerosols chemical ionization mass spectrometry) (Lopez-Hilfiker et al., 2014), which sample aerosol for several tens of minutes and analyze the samples after automated thermal desorption. These semi-continuous techniques offer rather detailed information on the organic aerosol fraction due to low fragmentation. However, with time resolutions of tens of minutes up to an hour, characterization of transient emissions or disentanglement of aerosol blends in environments affected by several sources is not feasible

A few instruments with high time resolution in the order of seconds, sufficient for the analysis of transient aerosol occurrences, combined with detailed analysis were developed in recent years, such as the EESI-ToF (electrospray ionization time-of-flight mass spectrometer) (Lopez-Hilfiker et al., 2019; Pagonis et al., 2021) and the CHARON-PTR-MS (chemical analysis of aerosol online proton-transfer-reaction mass spectrometer) (Eichler et al., 2015; Piel et al., 2019).

To comprehensively analyze and characterize individual sources in complex environments like cities or industrial areas, where fluctuating meteorological and atmospheric transport conditions result in mixing of emissions from different sources, or transient source emissions like from ships, aircrafts or short-term processes, identification of individual species on short time scales is necessary. Offline and semi-online methods offering highly resolved speciation data do not provide the required temporal resolution and high-time resolution online methods typically do not provide in-depth chemical analysis capability. Therefore, we developed the AERosol and TRACe gas Collector (AERTRACC), which combines the advantages of both approaches. AERTRACC collects samples of different aerosol types for subsequent in-depth analysis on separate sampling media which can be quickly and simply exchanged. Separation of aerosol types is hereby achieved by controlling the sampling process with high-time resolution online measurements. AERTRACC is integrated in our mobile aerosol research laboratory (MoLa), a vehicle equipped with online measuring instruments (Drewnick et al., 2012), serving as control unit for the sampler via a tailor-made software interface. There the user can define sampling conditions based on measured parameters like particle number concentration or wind direction to separately collect the different aerosol types. While online instruments for in-depth chemical analysis with high temporal resolution are limited to the respective analysis methods, the AERTRACC sampler enables the use of the full potential of analytical chemistry and microscopic analysis for the investigation of such aerosols beyond these specific approaches. For this work, TD-HR-ToF-CIMS (thermal desorption high resolution time-of-flight chemical ionization mass spectrometry) was chosen as analysis method offering high resolution mass spectra combined with high sensitivity and low sample fragmentation as well as minimized sample preparation effort (Mercier et al., 2012; Yatavelli et al., 2012; Aljawhary et al., 2013). Here, we present the design and characteristics of AERTRACC and demonstrate its capabilities in a field experiment, probing the emissions of a pizza oven in a semi-urban environment.

3.3 Design and Operation of the AERTRACC Sampling System

3.3.1 The mobile aerosol research laboratory (MoLa)

The mobile laboratory MoLa houses the newly developed AERTRACC sampling system and serves as data-providing basis for its control unit. MoLa is designed for mobile and stationary measurements of ambient air composition and is mainly used for characterization of source specific emissions (Drewnick et al., 2012; Fachinger et al., 2021). A variety of online instruments measures different aerosol and meteorological properties providing high time resolution data of seconds until one-minute averaging intervals. This includes physical particle properties, e.g., particle number size distributions, as well as chemical characterization like the non-refractory chemical composition of submicron particles, and trace gas concentrations of various gases as NO_x , O_3 , and CO_2 . An overview of the MoLa instruments and measured variables, which are used to control the AERTRACC system, is provided in Table 3.1; for further description see Drewnick et al. (2012). Stationary measurements can be performed with the sampling inlet at different heights (3-10 m above ground level) using an inlet setup on MoLa's roof.

Table 3.1: MoLa instruments used for control of the AERTRACC sampler.

Instrument	Measured variables	Particle diameter range	Time resolution
Aethalometer ^a	Black and brown carbon mass concentration	< 1.0 μm	1 s
PAS ^b	Polyaromatic hydrocarbon mass concentration on particle surface	10 nm - 1 μm	12 s
EDM ^c	PM ₁ , PM _{2.5} , PM ₁₀ mass concentration based on optical measured size distribution	0.25 - 10 μm	6 s
CPC ^d	Particle number concentration	5 nm - 3 μm	1 s
OPC ^e	Particle size distribution based on optical diameter	0.25 - 32 μm	6 s
Airpointer ^f	Mixing ratio of CO, SO ₂ , O ₃ , NO _x	-	4 s
NO ₂ /NO/NO _x Monitor ^g	Mixing ratio of NO ₂ , NO, NO _x	-	5 s
LICOR ^h	Mixing ratio of CO ₂ , H ₂ O	-	1 s
Meteorological Station ⁱ	Wind direction, wind speed, relative humidity, temperature, rain intensity, pressure	-	1 s
GPS ^j	Location	-	1s
HR-ToF-AMS ^k	Size-dependent non-refractory chemical composition	40 nm - 1 μm	15 s

^aMagee Scientific Aethalometer[®] Model AE33, Magee Scientific, USA. ^bPhotoelectric Aerosol Sensor PAS2000, EcoChem Analytics, USA. ^cEnvironmental Dust Monitor EDM180, Grimm Aerosoltechnik, Germany. ^dCondensation Particle Counter Model 3786, TSI, Inc., USA. ^eOptical Particle Counter Model 1.109, Grimm Aerosoltechnik, Germany. ^fAirPointer, Recordum Messtechnik GmbH, Austria. ^gNO₂/NO/NO_x Monitor Model 405 nm, 2B Technologies, Inc., USA. ^hLI840, LI-COR, Inc., USA. ⁱWXT520, Vaisala, Finland. ^jNavilock NL-8022MU, Navilock, Germany. ^kHigh-resolution Time-of-Flight Aerosol Mass Spectrometer, Aerodyne Research, Inc., USA, (currently not used for AERTRACC control, but might be implemented for future studies, was used for theoretical sampling scenarios).

3.3.2 Setup of the AERTRACC sampling system

AERTRACC is designed to sample different aerosol types separately on individual sample carriers. The system is incorporated in MoLa with its own inlet and a flow path designed for minimal particle losses, minimizing non-vertical tubes and bends. With four available sampling paths up to four different aerosol types can be sampled separately. It is possible to sample particles with two different size cuts on quartz fiber or PTFE filters as well as volatile compounds onto thermal desorption tubes (TDT) filled with adsorbent material (further details in Sect. 3.3.4). A control software for the AERTRACC sampler was programmed to accomplish separate sampling of different aerosol types based on the MoLa online data (see Sect. 3.3.3).

A schematic overview and a photograph of the sampling system installed in MoLa are shown in Fig. 3.1. The AERTRACC sampler has its own inlet line (ID = 48 mm), equipped with a PM₁₀ inlet head (Digital, Switzerland, inlet flow rate 30 L min⁻¹) for sampling nominal PM₁₀, which is mounted on the roof of MoLa. The inlet is located 0.5 m apart from the MoLa online instrument inlet and their heights are adjusted to each other to assure sampling of the same aerosol.

Inside MoLa the inlet tube is split into two main paths, which are both split again, in total into four sampling paths. Main path 1 (see Fig. 3.1b) contains a PM_{10} cyclone (URG, USA, flow rate 16.7 L min^{-1}) and is connected to main path 2 with a cross tube downstream of the PM_{10} cyclone. With two ball valves, one installed in main path 2 and the other one in the cross tube between the main paths, the user can sample in two different sampling modes. Either two sampling paths are used for PM_{10} and the other two for PM_{10} (Fig. 3.1b; cross tube not used) or all four sampling paths are used for PM_{10} sampling (Fig. 3.1c; cross tube used to feed also main path 2 through the cyclone).

Each of the four sampling paths contains a custom-made filter holder made of gold-coated aluminum for filters of 25 mm diameter and a TDT. The sampling area on the filters equals the thermal desorption area for the subsequent analysis. The operation flow rate for filter sampling is limited to 4.2 or 7.5 L min^{-1} ($\frac{1}{4}$ of 16.7 or 30 L min^{-1}) due to the required flow rates for the PM_{10} cyclone or the PM_{10} inlet, depending on the chosen sampling mode (see above). The sampling line splits again behind each filter holder into a path with TDT and a TDT bypass path. This split is necessary, as the flow rate through the TDT has to be smaller (typically limited to 0.2 L min^{-1}) than the one through the filter to avoid a loss of the retention volume for the gaseous species. The described active sampling paths are shown in Fig. 3.1b as green paths. The flows through the filter holders are the sum of the flows through the respective TDT and TDT bypass lines. Simple and quick change of filter holders and TDTs is achieved with Ultra-Torr vacuum fittings (Swagelok Company, USA) before and behind each device.

To assure a permanent air flow through the whole system, independent whether a certain sample line is active or not, a non-sampling path around the sampling media is added in parallel to each sampling line (grey paths in Fig. 3.1b are the active non-sampling paths). Further, for non-sampling conditions, diffusion of volatiles from one sampling path to another is avoided as the volatiles would have to diffuse a short distance upstream the flow persisting through the non-sampling path. The flow through the sampling system is switched between sampling and non-sampling path using magnetic three-way valves (SMC, VT307, Japan) and maintained by a rotary vane pump (V-VTE 10, Gardner Denver, Inc.,

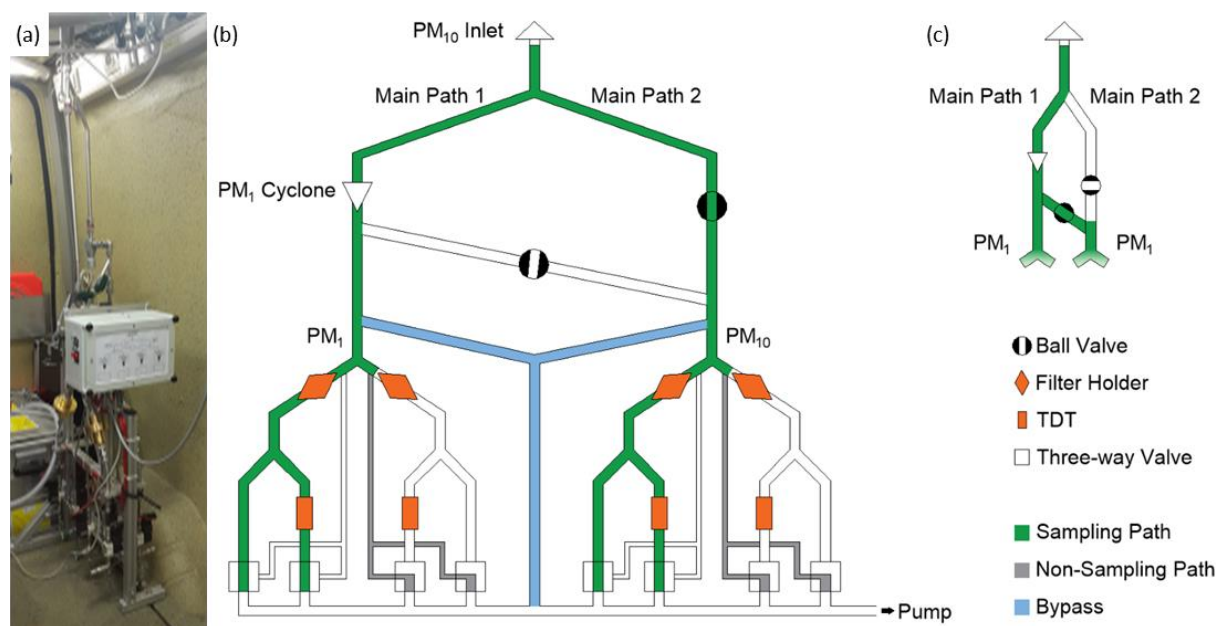


Fig. 3.1: Photo (a) and scheme (b+c) of the AERTRACC sampler with active flow paths marked in green for sampling flows, in grey for non-sampling flows, and in blue for bypass flows (b: sampling mode $PM_{10}+PM_{10}$, c: sampling mode PM_{10} only). Needle and dosing valves are located in each path directly upstream of the pump and are not shown in the scheme.

USA). This permanent air flow through the system keeps the cut-offs of the size selectors and the transport losses constant and allows the targeted aerosol to be sampled almost immediately as soon as the respective three-way valve is switched when the evaluation of the online data shows that the sampling conditions are fulfilled. The adjustment of flow rates for the sampling paths is achieved with precision dosing valves (HF-1300-SS-L-1/4-S, Hamlet, Germany) for the TDT flow rates and with needle valves (Nupro SS-4HS V51, Swagelok, USA) for the additional flow through the filters before each experiment. No change of flow rates was observed during test measurements. Replacing the needle valves by mass flow controllers for future studies is planned to ensure constant flow rates and to simplify flow settings.

Independent of the individual sample line flow rates, an additional bypass line is split from each main path (blue paths in Fig. 3.1b) to adjust the flows through the two main paths to match the specified flow rates through the inlet head and the cyclone. These bypass lines are directly connected to the pump via additional needle valves. The sampling line and bypass tubing are made of stainless steel with tube diameters of 1/2" upstream the filter holders and 1/4" after the filter holders.

The AERTRACC electronics including the control of the magnetic valves via a custom-made relay card and relays is housed in an electronic box attached to the sampler (white box in Fig. 3.1a). The front of the box contains an LED status display showing which sampling path is active. The relay card is connected via RS232 to the MoLa data acquisition computer, which collects the online instruments data.

3.3.3 Control software and sampler operation

The AERTRACC control software (ACS) is the interface between the MoLa online measurements and the sampling system and is integrated into the MoLa data acquisition software for simple and direct access to the data. It was developed in Igor Pro (Version 6.3, WaveMetrics, Inc., USA) and is available from the authors upon request. In the ACS, the user defines criteria for sampling up to four different aerosol types separately, based on measured MoLa online data. The software continuously evaluates the incoming online data whether the criteria for sampling are fulfilled and controls the flow through the individual sampling paths accordingly. A graphical user interface (Fig. 3.2) was programmed for effective and user-friendly operation where the user selects the sampling conditions for the targeted aerosol types and obtains real-time information on the sampling process, such as the accumulated sampling time and estimated collected mass on the filters. In the upper part of the main ACS window, the user chooses the operation and sampling mode. The lower part is divided into four boxes, one for each sampling path, where the user can set sampling conditions individually for each path.

Two sampling modes are available, PM_1 and PM_1+PM_{10} . For the PM_1+PM_{10} sampling mode, the same sampling conditions are used for each PM_1 / PM_{10} sampling path pair. The user can choose between two operation modes. The sampler can either be operated in *automatic mode* with user defined sampling conditions (Fig. 3.2a), which are based on variables, measured by the MoLa online instruments, or in *manual mode* (Fig. S9.4), where the user can directly start and stop sampling with the additional possibility to pre-select the collection time or collected mass on the filters. The total collected mass on the filters is calculated based on the EDM online mass concentration data, measured during the actual sampling intervals, and the respective filter flow rate.

In the *automatic mode* the user defines individual sampling conditions for each sampling path (Fig. 3.2a). Each sampling condition consists of up to four criteria, which can be logically combined using the Boolean operators AND, NOT, and OR. Individual criteria are fulfilled if the value of the selected parameter, e.g., a particle or trace gas concentration, but also time, GPS location, meteorological condition, or total collected mass, is between the user-selected minimum and maximum values. This

allows complex definitions of sampling conditions for each of the targeted aerosol types. A possible scenario, based on recent MoLa measurements (Fachinger et al., 2021), could be measuring with MoLa at a place where traffic and biomass burning emissions can be measured depending on the wind direction. Both types of emissions could be sampled separately using suitable sampling conditions. For the biomass burning aerosol the sampling condition could be “suitable wind direction range AND high black carbon concentration AND high PM₁ concentration”; while for the traffic aerosol the sampling condition could be “suitable wind direction range AND high particle number concentration AND NOT high PM₁ concentration”. For background aerosol sampling the mentioned variables should be accordingly set to low concentrations and the remaining wind direction sections.

During measurements when air masses containing different aerosol types reach the inlet, the sampler switches automatically between the according sampling paths based on the evaluation of the sampling conditions. The evaluation is performed each second based on the highest available time resolution of the instruments, hence the valves can be switched on a 1 s-base as well. While frequent switching of the valves introduces frequent flow and pressure disruptions in the sampler, these are not expected to produce enhanced sampling artefacts by e.g., re-volatilization of material from the tube surface or the filters, compared to less frequent switching scenarios. Therefore, switching between different sampling paths typically occurs multiple times within an experiment of hours of duration, which is in contrast to conventional continuous sampling. Although the AERTRACC is primarily designed for stationary measurements, it is also possible to sample during mobile measurements if the air mass segments are large enough to differentiate between them on a few seconds time scale. The *flowrate* sub-window contains information on the flow setup of the AERTRACC sampler (Fig. 3.2b). Here, the user enters the flow rates, which are adjusted with the individual needle valves. The graphical user interface automatically provides the combined flow rates at critical devices, such as the inlet cyclone, and thus supports the correct selection of the individual flow rates in order to match their required flow conditions. Furthermore, in this window the MoLa inlet height is entered. This information is used to select the correct delay times between registration of the sampling status, i.e., sampling or non-sampling, and the activation or de-activation of flows through the individual sampling paths (see Sect. 3.4.2).

When the sampling path is activated, the software continuously compares the chosen sampling conditions with the actual measured online data. For visual support a colored indicator shows for each sampling path whether sampling (green) or no sampling (red) takes place or the sampling path is inactive (grey). Depending on whether the sampling conditions for a certain sampling path are fulfilled, the respective three-way valves are switched accordingly between sampling path and non-sampling path via the relay card. Two displays in the ACS for each sampling path show the current accumulated collection time and sampled aerosol mass. A data logger automatically keeps track of all activities performed by the user on the interface and of all sampling periods, which are logged with the time stamp, type of activity and respective sampling conditions.

The chemical analysis of aerosol samples (like, e.g., when using FIGAERO-CIMS measurements of organic compounds) typically requires sampled mass in the order of 1 µg in order to exceed instrumental detection limits, depending on the specific analysis method. In urban conditions with organic mass concentrations of 5-10 µg m⁻³ (Chen et al., 2022), with a sample flow rate of 7.5 L min⁻¹ and with approximately 10 % of the time sampling source emissions (like in our validation experiment, see Section 4), a total sampling time in the order of 1-2 hours would be needed to collect enough material for analysis. Therefore, the probed source must emit over sufficiently long times to allow a successful

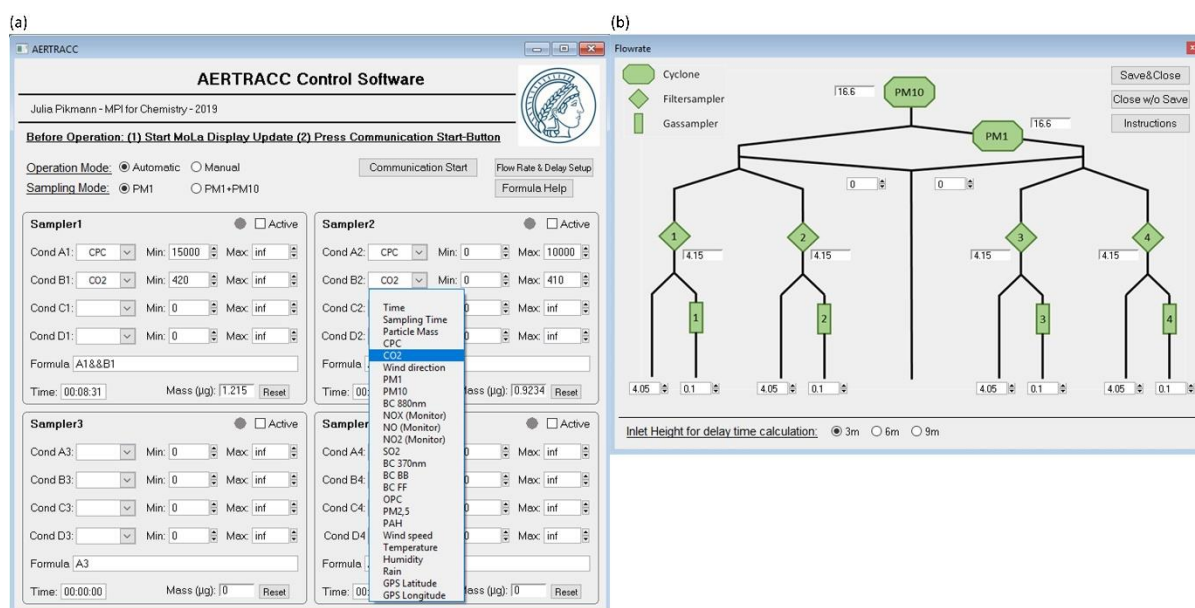


Fig. 3.2: User interface of the AERTRACC software with main window (a) and flowrate sub-window (b).

chemical characterization of their emissions. Higher emission concentrations, more stable transport conditions, and lower detection limits of the applied analysis method can reduce sampling times significantly. Especially when using microscopic and single particle techniques, which might need extremely low amounts of sample, sampling times could be reduced further and also single transient emission events might provide sufficient material for successful analysis.

3.3.4 Sampling media

Generally, the sampling media used are dependent on the subsequent offline analysis method. The choice of the sampling media for this study was based on the selection of thermal desorption as sample introduction method for the subsequent analysis using TD-CIMS, which reduces the chances of potential contamination through sample preparation. For gas phase sampling, TDTs were used, made of stainless steel (1/4" OD, 89 mm length) and packed with Tenax TA (MS Wil, Netherlands) and Carbograp 5TD (Markes International Ltd., United Kingdom), each 150 mg. Together, these adsorbents are applicable to compounds with a broad volatility range (mainly $C_4 - C_{32}$) to investigate different kinds of emissions. They were also chosen as they are hydrophobic, inert and temperature stable up to 350 °C, necessary for the high temperature during thermal desorption (Harper, 2000; Dettmer and Engewald, 2002, 2003; Woolfenden, 2010). TDTs were conditioned in a TC-20 conditioner (Markes International Ltd., United Kingdom) at 300 °C for 4 hours with nitrogen (purity 99.9999%, 0.09 L min⁻¹) before sampling.

For particle sampling, PTFE filters with 25 mm diameter (Type 11803, Sartorius, Germany) were used, which were pre-baked at 200 °C under vacuum (50 hPa) for 24 h before sampling.

Typical sampling flow rates are usually between 1 and 8 L min⁻¹ for the filter samples, with mass loadings not exceeding 2 µg to avoid overloading the CIMS, while for the TDTs flow rates between 0.02 and 0.2 L min⁻¹ are recommended with a total sampling volume up to 4 L. These limits can be included as sampling conditions to stop sampling automatically when the limits are reached. Afterwards the sampling media need to be changed manually. In our experiment, sampling media were changed after typically 1-1.5 h.

After sampling, TDTs are sealed with brass screw caps with PTFE ferrules and filters were kept between precleaned aluminium foil in separate sealed petri dishes. Both are stored at -18 °C in airtight containers until analysis.

3.3.5 Analysis method

The AERTRACC sampling can be used with various kinds of sampling media and consequently can be used in combination with a broad variety of offline analysis methods. For analysis of the samples for this study the TD-HR-ToF-CIMS method was used with the HR-ToF-CIMS (Aerodyne Research Inc., USA) coupled to the FIGAERO inlet for filters and a custom-built inlet for TDT. Iodide served as the chemical ionization reagent which is selective for polar and oxidized organic compounds (Lee et al., 2014). The CIMS allows identification of individual compounds due to soft ionization as well as high-resolution mass spectra. The high sensitivity enables the analysis of small amounts of analyte, minimizing the necessary sample collection times (Yatavelli et al., 2012; Aljawhary et al., 2013).

For ionization, methyl-iodide from custom-made permeation tubes (permeation rate 450 ng/min at 30 °C) is diluted into dry nitrogen (purity 99.9999%), subsequently ionized by an alpha-polonium source (NRD Static Control, USA) to form iodide as reagent ion and inserted into the ion-molecular reaction chamber (IMR) at a flow rate of 2.2 L min⁻¹. The filters were thermally desorbed into the IMR with heated dry nitrogen as carrier gas (purity 99.9999%, 1.9 L min⁻¹) using the FIGAERO-inlet (Lopez-Hilfiker et al., 2014); TDTs were desorbed with a flow rate of 0,120 L min⁻¹ using a custom-built desorption unit. The temperature program for the carrier gas starts at 25 °C for 3 min, heating up to 200 °C with a rate of 17.5 °C min⁻¹ and finally holding the temperature for 20 min. Tuning of the ion optics was performed before the first analysis with formic acid and triiodide for signal intensity, mass resolution, and peak shape using the software Thuner (Tofwerk AG, Switzerland). The IMR conditions were kept constant at 130 mbar and 60 °C.

The reproducibility of the integrated ion signal intensity of different calibration compounds, determined through laboratory experiments, was found to be 10% for filter and 62% for TDT samples (details see Text S9.4). Oligomerization during analysis with CIMS might occur (Lopez-Hilfiker et al., 2015) but appeared minor in our testing.

3.4 Characterization of the Sampling System

3.4.1 Particle transport efficiency

The aerosol transport losses within the AERTRACC inlet and transport system were estimated with calculations using the Particle Loss Calculator (von der Weiden-Reinmüller et al., 2014). The size-dependent transport losses were calculated based on the geometry of the tubing system considering bends and non-vertical flows as well as volumetric flow rates (Fig. S9.5). Estimated losses are below 10% for particles between 10 nm and 7 µm in diameter. For particles in the size-range 35 nm up to 3.5 µm, where most of the collected particle mass is typically found, losses are below 2%. Applying the size-dependent losses to a typical urban particle number size distribution, the overall calculated mass losses are below 1 %, both for PM₁ and PM₁₀. Therefore, we conclude that particle transport losses within the sampling system are generally negligible for the mass-based analysis methods and no correction for losses is needed.

3.4.2 Time delay between aerosol measurement and sampling

In *automatic operation mode*, the AERTRACC sampler is controlled based on the comparison of the specified sampling conditions with the online-measured MoLa data. The difference of the volumetric flow rates between the online instrument and the AERTRACC sampling inlets, which both have the same length and cross section, leads to different aerosol transport times to the instruments and the sampling media, respectively. Due to the higher flow rate through the online instrument inlet of 80 L min^{-1} , compared to 30 L min^{-1} (in *PM₁/PM₁₀ sampling mode*) or 16.7 L min^{-1} (in *PM₁-only sampling mode*) through the AERTRACC inlet, the ambient aerosol reaches the online instruments before it reaches the sampling media. This provides the opportunity of knowing in advance whether the aerosol reaching the sampling media should be sampled or not and to switch the sampling valves accordingly. It is necessary to know the time delay between the online measurement of the aerosol and the aerosol reaching the sampling media to assure timely sampling of the targeted aerosols. The time delay for each instrument is the time difference between the times it takes for the aerosol from the moment it enters the inlet heads until the reporting by the online measurements, and the aerosol reaching the sampling media, respectively.

Self-generated short spikes of elevated aerosol or trace gas concentrations were used to determine the time intervals between the aerosol entering the inlet and the same aerosol being reported by each online instrument for different inlet heights (i.e., 3 m, 6 m, 9 m). These measurements showed that these time intervals can be separated into a transport-related residence time in the inlet tubing and an instrument-specific measurement and reporting delay. The transport-related residence time was extracted from the measurements with different inlet heights, since the instrument-specific measurement and reporting delay is a constant for each instrument and independent of the inlet height. These measured transport times agree well with the calculated transport times of the aerosol, based on tube cross sections and volumetric flow rates. This allows calculating the respective transport times also for the sampling through the AERTRACC inlet without directly measuring it.

In the *PM₁/PM₁₀ sampling mode* (i.e., with high sampling flow rate) in combination with short inlets of 3 m to 5 m above ground level, for most instruments no delay time must be applied. For instruments with long measurement and reporting time, also no delay needs to be applied even for larger inlet heights.

The time delays for all instruments are implemented in the ACS software for the different inlet heights, which were specified in the *flowrate* sub-window (Fig. 3.2b). For measurement variables, which are not associated with aerosol transport, like meteorological data or GPS position, the respective instrument time delays are equal to the aerosol transport time through the AERTRACC inlet. As example, the time delays for the 6 m inlet are 5-17 s for *PM₁ sampling mode* and 4-9 s for *PM₁/PM₁₀ sampling mode*, excluding instruments with no time delay needed.

For comparison, sampling periods during the in-field validation (see Section 4) were in the order of 2-10 s. Especially under such conditions, where the sampling periods are in the same order of magnitude as the time delays, it is crucial to consider the time delays for sampling. Otherwise, a significant fraction of the aerosol which does not fulfil the various sampling criteria would nevertheless be sampled and the separation of different aerosol types would not be given anymore.

3.5 In-field validation of the AERTRACC using a single point source in a semi-urban environment

3.5.1 Measurement setup

The AERTRACC sampler was tested and validated in the field by probing emissions from a wood-fired pizza oven, operated in a semi-urban environment. The goal was to sample the biomass burning emissions separately from the semi-urban background aerosol using the wind direction and further MoLa variables as sampling conditions. The test setup was located on the premises of the institute (Mainz, Germany), which is located at the outer edge of the city center, on the 21th July 2021. A site map with the measurement location with respect to the city and to the micro-environment including a wind rose plot showing the predominant wind direction can be found in the supplementary information (Fig. S9.1). The oven was heated with logs of European beech and had a small chimney up to 4 m height above ground level. Larger roads were at a distance of 100 to 150 m, separated by a narrow row of trees and bushes from the measurement site. The main wind direction was northeast to east-northeast with one of the major roads and a fraction of the city upstream of the measurement site. MoLa with the installed AERTRACC sampler was located 13 m away from the pizza oven, in a direction that was frequently downwind of the source. Measurement and sampling inlets were at 4 m height above ground level. Wind was very unstable during the measurement with air arriving temporarily from all directions at the measurement location. Regarding other meteorological parameters, it was a sunny day with few clouds; over the course of the measurement, the temperature was slightly rising from 21 °C to 24 °C while relative humidity decreased from 42% to 35%.

The pizza oven was heated up to 400 °C before pizza baking started. The whole measurement lasted for 3.5 h including 30 min of preparatory measurements to define sampling conditions for separate collection of source emissions and background aerosol.

All MoLa instruments listed in Table 3.1, including the HR-ToF-AMS with 15 s time resolution, in V-mode for maximum sensitivity (Decarlo et al., 2006), were operated during the measurements. The flow rates for filter and TDT sampling were set to 5 L min⁻¹ and 0.12 L min⁻¹, respectively. Filter mass loading was limited to 2 µg and sampling time to 25 min to avoid overloading the filters and exceeding the breakthrough volume of the TDTs. As sampling conditions for the pizza oven emissions, the wind sector 45-90° AND OPC particle number concentrations (PNC) >250 # cm⁻³ were chosen, while for background measurements the conditions were the wind sector 135-360° AND OPC PNC <200 # cm⁻³. Two PM₁₀ and two PM₁ filters and four TDTs were sampled with pizza oven emissions, and two filters, one for PM₁₀ and PM₁ respectively, and two TDTs were sampled with background aerosol. For sampling media blank correction, two filters and TDTs each without sampling were taken as field blanks.

3.5.2 Data preparation and analysis

The online data was quality checked, corrected for sampling delays and inspected for invalid data, e.g., data affected by internal calibration procedures, on a 1 s time base. Data with highest available time resolution were used for further data analysis to be able to account for fast wind changes. PM₁ mass concentrations were calculated from combined FMPS and OPC size distribution data (details see Text S9.1). The high-resolution AMS data were analyzed with the software SQUIRREL 1.63I and PIKA 1.23I. Furthermore, positive matrix factorization (PMF; Paatero and Tapper, 1994) was applied on the organic particle fraction below m/z 116, measured with the AMS, using the PMF Evaluation Tool (PET) v3.07C

(Ulbrich et al., 2009) to identify different aerosol types. Further details about AMS data processing and PMF are provided in the supplement Text S9.2.

For analysis of the CIMS data, the software Tofware 3.2.3 (Aerodyne Inc., USA) and custom data procedures were used (details see Text S9.3). Signal intensity was normalized to the iodide-signal and sampled volumes. Afterwards, the ions signal intensities were averaged over all available samples with pizza oven emissions and background, respectively, both for TDT and filter samples. Data for PM₁ and PM₁₀ filter samples were handled and analyzed separately. The molecular formula of identified ions was determined for individual peaks; and individual species were identified through the molecular formula, detectability by Iodide-CIMS and previous mention in the literature (further details see Table S9.2). Signal intensities for individual compounds were determined semi-quantitatively in terms of detected ions as a calibration for each compound was not feasible. This allows determination of relative concentrations in separate samples as well as supporting PMF analysis for quantitative determination of aerosol type concentrations (similar to the approach by Tong et al., 2022). Independently of the sampling media, the ion signal intensities during desorption of the samples exceeded the limit of detection (three times the standard deviation of the molecular background) for all reported samples and ions, with the majority of samples and ions showing an excess by at least an order of magnitude.

3.5.3 Results and discussion

3.5.3.1 Online measurements – characteristics of the measured aerosol

During the field measurement period the AMS provided quantitative data on chemical composition of the non-refractory sub-micron particle fraction. For in-depth analysis of the organic fraction, a PMF analysis was performed for source apportionment. The identified aerosol types were biomass burning organic aerosol (BBOA), cooking organic aerosol (COA) and oxygenated organic aerosol (OOA). This was the most reasonable PMF solution based on the individual PMF factor mass spectra and time series (see Fig. S9.2). Correlation of the obtained mass spectra with reference mass spectra resulted in average Pearson's *r* values of 0.86 for BBOA, 0.90 for COA and 0.92 for OOA (Fig. S9.3). The BBOA mass spectrum shows the typical peaks at *m/z* 60 and 73, related to levoglucosan as typical biomass burning marker (Schneider et al., 2006). The OOA mass spectrum shows a strong peak for the key marker *m/z* 44 (CO₂⁺) from thermal decarboxylation without any further distinct peaks at higher *m/z* (Ng et al., 2010). For COA no distinct markers exist, except for a high *m/z* 55 signal (Sun et al., 2011) and the identification was based on comparison with reference mass spectra from the HR-AMS Spectral Database (Ulbrich, 2022). The time series of BBOA and COA frequently showed similar temporal variations indicating that they originate from the same source location while the OOA factor was mostly constant over the whole measurement interval and is representing the background aerosol. Further important time series, like PM₁ mass concentration and OPC particle number concentration, are shown in Fig. S9.6. Time intervals for sampling of source emissions and background are highlighted. Depending on the evaluation of the data, the sampling was frequently (often after only a few seconds or at most minutes) switched between source and background aerosol paths.

Because of the short measurement time and the close vicinity to the source, the temporal variations of aerosol and trace gas concentrations were mainly due to changes in wind directions and variations in emission strength of the targeted source rather than to those of other sources or of atmospheric dilution. In Fig. 3.3a the concentrations of the three organic aerosol types, i.e., PMF factors, are shown as a function of the wind direction, averaged over 15° wind sectors. Further aerosol concentrations, which are assumed to be associated with the background and source emissions, are shown in Fig. 3.3b

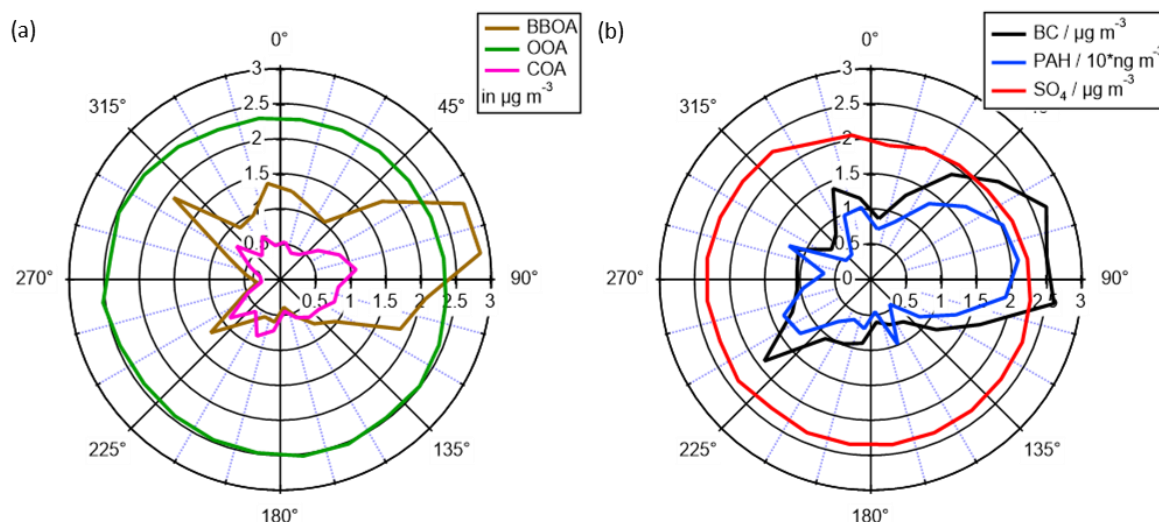


Fig. 3.3: Concentrations of the organic aerosol types (a) as well as BC, PAH and SO_4 (b) dependent on local wind direction averaged over 15° sectors. The Pizza oven was located in the direction of 70° relative to MoLa.

with suitable scaling factors to plot them together in a single polar graph. A strong dependence of mass concentration for BBOA and COA on wind direction with a maximum for wind from the sector 60° to 90° was observed (Fig. 3.3a). A similar dependence on wind direction was found for black carbon (BC) and polycyclic aromatic hydrocarbons (PAH) (Fig. 3.3b), which are also likely associated with emissions from the pizza oven as well as BBOA and COA (Fachinger et al., 2017). OOA, as an indicator of background aerosol, is almost constant for all wind directions as well as sulfate (SO_4) which is often an indicator for secondary oxidized aerosol (Sun et al., 2011). These results show a clear enhancement of concentrations of aerosol components, which are related to the pizza oven emissions, when the wind was arriving from the direction of the source, which was located in the direction of 70° with respect to the sampling location.

3.5.3.2 Filter and TDT analysis

Source and background aerosol were separately sampled on filters and TDTs with sampling conditions based on preparatory measurements (see Sect. 3.5.1). The comparison of averaged signal intensities for identified ions from PM_{10} and PM_{10} filter samples showed only negligible differences (Fig. S9.7), suggesting that most of the related aerosol mass is in the PM_{10} particle size range. Therefore, the results are discussed for the PM_{10} filters only.

The ratio of the ion signal intensity for selected identified species from the pizza oven and the background samples was calculated for the filter and the TDT samples (Fig. 3.4), respectively, to show which of the species mainly originate from background and which ones are associated with the source emissions. Additionally, the average ratio for all species assigned to only background (*aged/traffic*) and oven emissions (*biomass burning/cooking – BB/C*) as well as both groups (*mixed*) were calculated for comparison. The assignment to the sources must be regarded as a rather preliminary one, as the apportionment is only based on a literature search. The list of identified species and used acronyms is shown in Table 3.2 and 3.3 for the filter and TDT samples, respectively. Substances found on the filters and TDTs differ mainly due to gas-particle partitioning and the selectivity of the TDT adsorbents. Volatilization of material from the filters and subsequent sampling in the TDTs could lead to biased

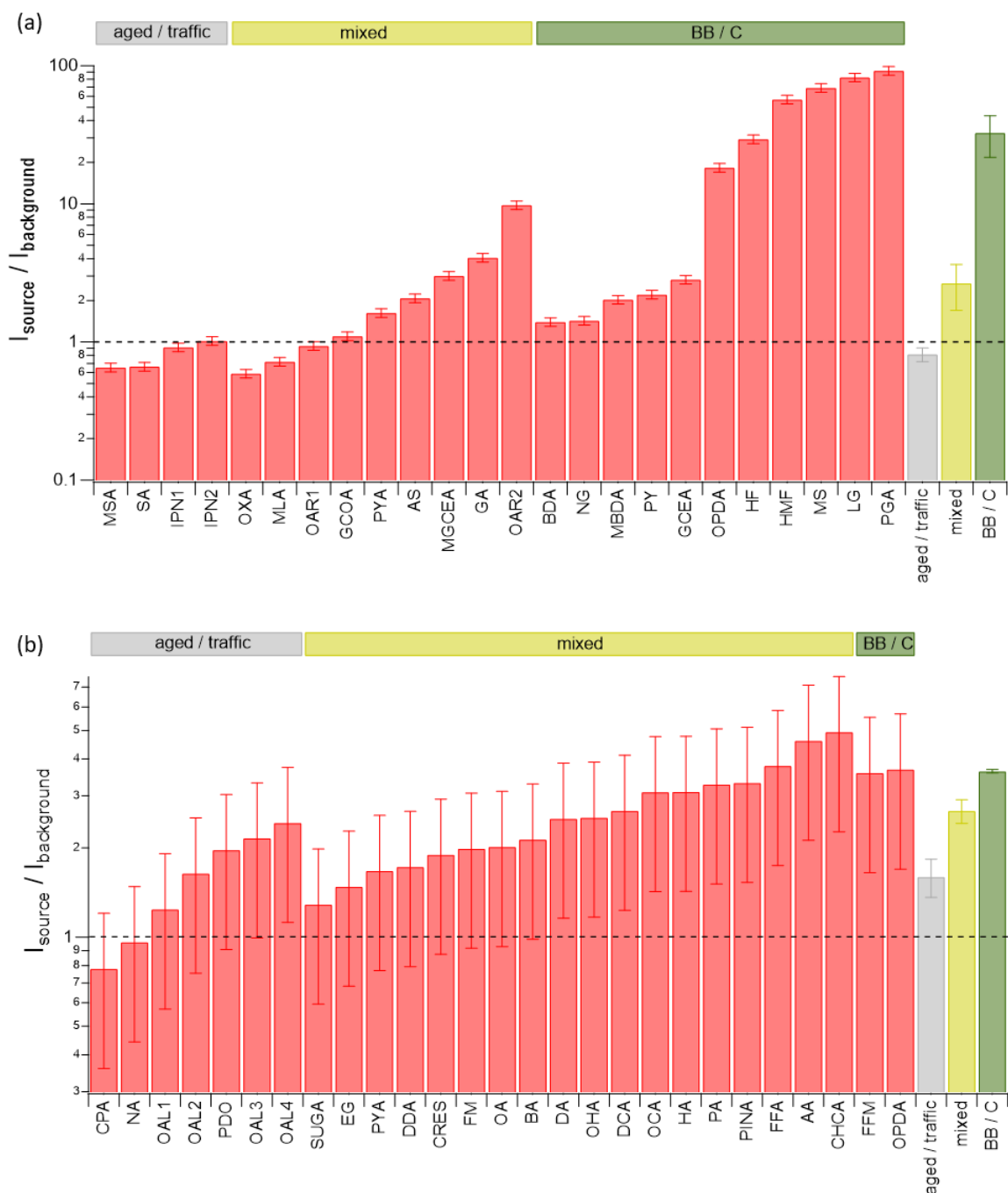


Fig. 3.4: Ion signal intensity ratios of identified compounds from pizza oven and background for filter (a) and TDT (b) samples with source apportionment based on references (see Table S9.2 and Table S9.3). The dashed line represents a ratio of one, i.e., similar intensities found on pizza oven and background samples. The abbreviations *BB* and *C* stand for biomass burning and cooking. The errors bars are based on the standard deviation of the ion signal intensity, reproducibility, and the error obtained from the blank measurements (for details see Text S9.4).

information on the partitioning of substances, however, within the uncertainties of the analysis, this effect is presumably not significant.

For some ions, based on the molecular formula, several substances are possible which are listed as well. Details like the exact m/z of the ions and references for source apportionment of the species are summarized in Table S9.2 and Table S9.3. The ratio is expected to be on the order of one for species,

which originate from background aerosol only. They are typically associated with aged, oxidized aerosol or traffic emissions and should be found on the background and source samples in roughly equal amounts, after correcting for sampled volumes, since their origins are well distributed over all wind directions (see also Fig. 3.3, OOA aerosol). This is the case for the species found on the filter samples (Fig. 3.4a) that were assigned to traffic emissions or aged aerosol.

In contrast, identified compounds from the filter samples with source-to-background intensity ratios significantly larger than one are mostly known to be associated with biomass burning and cooking emissions, which is in good agreement with their higher abundance on the pizza oven-related filters. Compounds like levoglucosan (LG) and pyroglutaminic acid (PGA) which are markers for biomass burning and cooking, respectively, show more than 85 times higher intensities on the source-related filters compared to the background filters.

Based on a literature search, some of those species, associated with cooking and biomass burning, can also originate from various other emission sources and were therefore assigned to the *mixed* group. They have a variety of different ratios between 0.6 and 10, showing that probably some of them predominantly originate from the background aerosol while others mainly from the pizza oven emissions. The large average source-to-background ratio for compounds attributed to biomass burning and cooking shows that the targeted source emissions from the pizza oven were sampled predominantly on the source-related filters and not or only to a small degree on the background filters. Compared to that the average ratios for the aged and traffic related compounds as well as the *mixed* aerosol are considerably smaller indicating a clear separation of source-related emissions from background-only aerosol using the selected AERTRACC sampling criteria.

Only two identified compounds from the TDT analysis were attributed solely to source-related emissions, i.e., cooking and biomass burning, and both substances have ratios well above one as they probably originate from the pizza oven emissions (Fig. 3.4b). The compounds assigned to traffic and aged aerosol have partially ratios on the order of one but also partially significantly above one, i.e., they are present on source-related TDTs in larger amounts than on background-related TDTs. Either these compounds are emitted by a close unknown source located in the same wind direction as the pizza oven or they are emitted by the pizza oven as well and thus would belong to the mixed group. Most of the identified compounds from the TDT samples can be assigned to different sources (*mixed*) having ratios which can be related to background aerosol and also to source related emissions.

Compared to the filter analysis the difference between average ratios of all source- and background-related compounds from the TDT analysis is smaller suggesting a weaker separation of source and background emissions. However, it must be taken into account that few compounds were assigned to only one of the aerosol types. As most of the compounds can originate from background as well as source-related emissions the enrichment of source-related compounds is smaller if these compounds are already present in the background aerosol. Thus, no specific markers were identified for the gas phase of the pizza oven emissions, which would clearly show a very strong difference between background and source-related TDTs, in contrast to e.g., levoglucosan and pyroglutaminic acid on the filter samples.

In conclusion, for the filter samples the chosen sampling conditions for the background and source emissions proved to be suitable to sample the source emissions separately while the background emissions are found in approximately equal concentrations on the source and background filters at least based on the identified compounds. A gravimetric analysis of the samples could be performed in addition to the chemical analysis to extend the general information on the sampled aerosols. For the TDT

samples the shown ratios indicate a weaker separation of source and background emissions, likely because most of the identified compounds can originate from both, background and source emissions, and no distinct markers were found for the source emissions.

Table 3.2: Selected identified compounds, measured as iodide cluster, from filter analysis and acronyms used for Fig. 3.4a. For further details see Table S9.2.

Acronym	Assigned compound	Acronym	Assigned compound
AS	ascorbic acid, hydroxyfurans	MLA	malic acid
BDA	butenedioic acid	MS	monosaccharide
GA	glutaric acid	MSA	methanesulfonic acid
GCEA	glyceric acid	NG	nitroguaiacol
GCOA	glycolic acid	OAR1	oxidized aromats, 3-acetylpentanedioic acid
HF/FA	hydroxy furfural, furoic acid	OAR2	oxidized aromats
HMF	hydroxymethyl furfural	ODPA	2-oxopropanedial, oxoacrylic acid
IPN1	oxidized isoprene nitrate	OXA	oxalic acid
IPN2	oxidized isoprene nitrate	PGA	pyroglutamic acid
LG	levoglucosan, galactosan, mannosan	PY	pyranose
MBDA	methylbutendioic acid	PYA	pyruvic acid
MGCEA	methylglyceric acid	SA	sulfuric acid

Table 3.3: Selected identified compounds, measured as iodide cluster, from TDT analysis and acronyms used for Fig. 3.4b. For further details see Table S9.3.

Acro- nym	Assigned compound	Acro- nym	Assigned compound
AA	acetic acid	OA	octanoic acid
BA	butyric acid, methyl propanoate	OAL1	oxidized alkyl
CHCA	cyclohexenecarboxylic acid	OAL2	oxidized alkyl
CPA	β -caryophyllene-aldehyde	OAL3	alkyldiole
CRES	cresol	OAL4	oxidized alkyl
DA	decanoic acid	OCA	oxocarboxylic acid
DCA	decenoic acid, pinanediol, linalool oxide	ODPA	oxopropanedial, oxoacrylic acid
DDA	dodecanoic acid, methylundecanoic acid	OHA	oxohexanoic acid, ethyl acetoacetate, methyloxopentanoic acid
EG	ethylene glycol	PA	propanoic acid
FFA	furfuryl alcohol, 2-furanmethanol	PDO	propandiol, hydroxyacetone
FFM	N-formylformamide, nitroethen	PINA	pinalic-3-acid
FM	formamide	PYA	pyruvic acid
HA	hexanoic acid, cyclopentanoic acid	SUGA	sugar acid
NA	nonenoic acid		

3.5.3.3 Evaluation of sampling conditions

The highly time-resolved MoLa online data provide the opportunity to post-evaluate the chosen AERTRACC sampling conditions. This is done by comparing average source-related and background aerosol concentrations as well as total source-related sampling time for the chosen and other potential sampling conditions and by evaluating, whether a better separation between source emissions and background could herewith have been achieved. The selected separation for the pizza oven measurement was based on a combination of PNC measured by OPC and wind direction (*Wind+OPC*), see Table S9.5 for details. For comparison, simpler conditions using only the wind direction (*Wind*) and stable wind conditions (*Wind stable*) were evaluated. Stable wind conditions are fulfilled when wind from the source sector was observed at least for the previous 8 s, the transport time from the source to the MoLa inlet, which was calculated from the distance between the measurement inlet and the pizza oven, and the average wind speed during the measurements. The combination of PNC measured by CPC and wind direction was evaluated as additional sampling scenario (*Wind+CPC*). Further sampling conditions were defined based on the AMS data using fractions of the organic signals at single m/z , e.g., at m/z 55 as f_{55} , to test whether a potential use of the AMS for AERTRACC control could improve aerosol separation. The selection of a combination of wind direction and f_{55} (*Wind + f_{55}*) as well as f_{55} and the ratio f_{55}/f_{57} (*Wind + $f_{55} + f_{55}/f_{57}$*) was based on known markers for COA while the combination of wind direction and f_{60} (*Wind + f_{60}*) was based on the known marker for BBOA. The limit values in the sampling condition definitions were chosen from literature values for these aerosol types (Mohr et al., 2009; Cubison et al., 2011; Sun et al., 2011; Saarikoski et al., 2012; Elser et al., 2016; Xu et al., 2020). The mass concentrations of black carbon (BC), polyaromatic hydrocarbons (PAH), organics measured by AMS, the AMS PMF factors BBOA, COA, and OOA, PM_1 as well as PNC measured by CPC and OPC were used to compare how well different sampling scenarios separate between source emissions and background. These parameters were chosen as they showed to be strongly affected by the source emissions during the measurement, according to the online data analysis (Sect. 3.5.3.1).

For assessment of source and background aerosol separation based on the various sampling scenarios, the ratios of averaged concentrations for “source” and “background” intervals, i.e., when the respective conditions were fulfilled, were calculated for each variable and each scenario (Fig. 3.5a).

Table 3.4: Sampling conditions for compared sampling scenarios for source and background sampling.

Sampling scenario	Source	Background
Wind	Wind direction 45-90°	Wind direction 135-360°
Wind stable	Wind direction 45-90° for 8 s	Wind direction 135-360° for 8 s
Wind + CPC	Wind direction 45-90° AND CPC PNC > 20,000 # cm ⁻³	Wind direction 135-360° AND CPC PNC < 15,000 # cm ⁻³
Wind + OPC	Wind direction 45-90° AND OPC PNC > 250 # cm ⁻³	Wind direction 135-360° AND OPC PNC < 200 # cm ⁻³
Wind + f_{55}	Wind direction 45-90° AND $f_{55} > 0.07$	Wind direction 135-360° AND $f_{55} < 0.05$
Wind + $f_{55} + f_{55}/f_{57}$	Wind direction 45-90° AND $f_{55} > 0.07$ AND $f_{55}/f_{57} > 2$	Wind direction 135-360° AND $f_{55} < 0.05$ AND $f_{55}/f_{57} < 1.5$
Wind + f_{60}	Wind direction 45-90° AND $f_{60} > 0.01$	Wind direction 135-360° AND $f_{60} < 0.005$

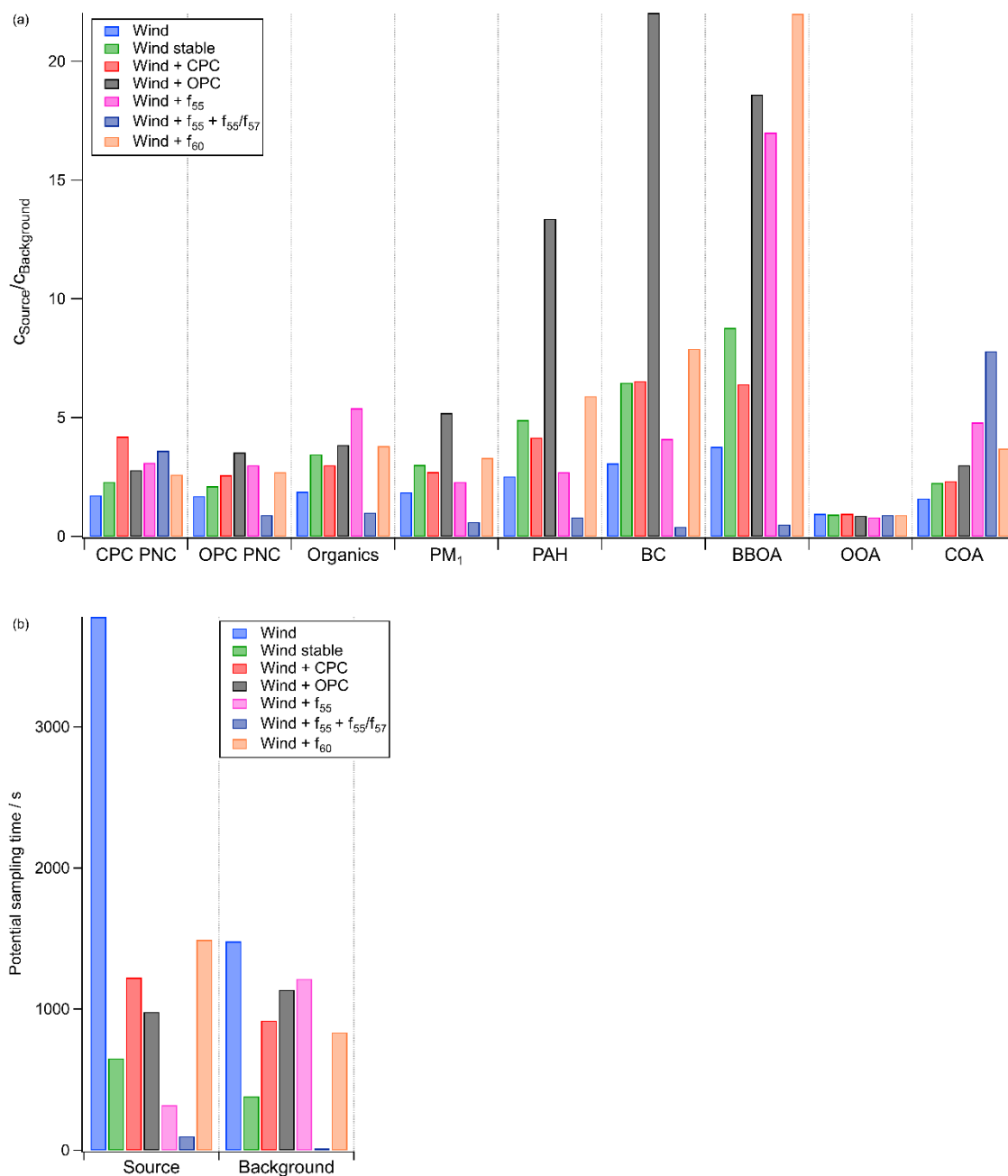


Fig. 3.5: Ratio of averaged mass concentration and PNC of “source” and “background” aerosols, according to the seven different sampling scenarios (a), and related potential source emission and background aerosol sampling times (b).

In addition, the potential sampling times that would have been spent to sample the source emissions and background aerosol for the various sampling scenarios, are shown in Fig. 3.5b.

Using only wind direction as separation criterion leads to the longest sampling times, especially for the source-related sampling. However, this approach also results in the smallest ratios of source versus background concentrations, i.e., the least effective separation of source emissions and background. Both effects are the result of the unspecific definition of the sampling condition. It is possible that source emissions miss the sampling inlet due to fast wind changes, which then samples background or mixed aerosols, even though the “source” sampling criterion is fulfilled. Using stable wind conditions

as sampling scenario improves the separation substantially, but at the expense of sampling time, which is by far the lowest for all four sampling scenarios.

The combination of elevated CPC PNC and the wind direction as sampling condition leads to higher ratios for measured CPC PNC and PM_{10} compared to the *Wind stable* sampling scenario, but similar or smaller ratios for the other parameters. The sampling time is longer than for *Wind stable*, however still much lower than for the *Wind* sampling condition.

The largest ratios for almost all variables besides the AMS-based ones, and consequently the most effective separation of source-related and background aerosol, were achieved when elevated PNC measured by OPC additional to the right wind direction were used as sampling condition (*Wind+OPC*). This sampling scenario resulted in similar sampling time as the other “complex” sampling scenario *Wind+CPC* and strongly improved sampling time, compared to the *Wind stable* scenario. Improved measurement of particle mass-related variables like PM_{10} or PAH mass concentration in this sampling scenario occurs, since the OPC counts the larger particles ($d_p = 0.25 \mu\text{m} - 32 \mu\text{m}$) and therefore the OPC PNC represents the emitted mass concentration quite well. The CPC, on the other hand, counts smaller particles ($d_p = 5 \text{ nm} - 3 \mu\text{m}$); therefore, it captures better the total emitted PNC with the very small particles contributing little to the emitted mass. Since for analysis of the sampling media, sampled particle mass is the more relevant variable, compared to particle number, the *Wind+OPC* sampling scenario is better suited to control the AERTRACC, compared to the *Wind+CPC* scenario. Contrary, in case of new particle formation events, the freshly formed aerosol could be targeted using high CPC PNC and low PM_{10} concentrations or low OPC PNC as sampling conditions.

Inclusion of the AMS data in the AERTRACC control using the fractional signal intensity of known marker m/z could improve specific sampling for certain aerosol types. This is especially the case if the AMS is operated with shorter averaging intervals to capture short-time variations of air masses containing different aerosol types. For COA, higher source/background ratios were achieved with the *Wind + f_{55}* sampling scenario, compared to the other scenarios, and even higher ones with the *Wind + $f_{55} + f_{55}/f_{57}$* scenario as it is more specific for COA. Regarding the potential sampling times especially within the latter scenario, the times are quite limited due to the very specific conditions and possibly due to shorter COA emission periods compared to the more dominant BBOA. The *Wind + f_{60}* scenario enables the most effective separation for BBOA combined with potential sampling times comparable to the *Wind+OPC* scenario. Long potential sampling times are desirable in order to quickly collect the necessary mass or sampling volume for analysis. Therefore, for scenarios like *Wind stable* and *Wind + $f_{55} + f_{55}/f_{57}$* , longer overall measurement periods in the vicinity of the source are necessary to reach sufficient sampled aerosol mass.

The choice of smaller wind sectors within the originally chosen wind sector 45-90° was evaluated in an additional analysis to investigate whether this could improve (i.e., enhance) the ratio between average source and background concentrations, compared to the *Wind+OPC* scenario. The calculated ratios for all variables for the splitting of the original wind sectors into three, five and seven sectors are shown in Table S9.4 and S9.6. The split into three sectors improves the separation of source and background emissions for the middle sector in comparison to the *Wind* scenario by at maximum 13 %. Further splitting leads to partially improved ratios between source and background emissions by at maximum 20 % for five sectors and by at maximum 22 % for seven sectors. However, the maximum values of ratios for different measured parameters spread over several wind sectors and therefore does not point towards a “better” potential selection of the source wind sector. This spread is probably due to indirect transport of the aerosol to the inlet due to frequently changing wind directions as well as due

to different time resolutions of the instruments. Additionally, with decreasing width of the wind sectors, the potential sampling time per sector decreases for all sections leading to longer overall measurement times necessary to sample sufficient amounts for subsequent analysis. Despite the improvement through smaller wind sectors, the ratios of the *Wind+OPC* scenario were by far not reached, and the source-related sampling times were shorter for the 5- and 7-sector splitting, compared to the *Wind+OPC* scenario. Consequently, using narrower wind sectors does not improve the separation of source and background emissions as effectively and as efficiently as choosing additional parameters to define the sampling conditions. In addition, using only narrow wind sectors for separation of source-related and background aerosol requires very good knowledge about the wind direction for which the emission source is probed. This is not the case when wind direction is used in combination with other emission source-related features of the aerosol as sampling criterion. Therefore, in general, source-specific markers are needed, which are known and can be measured by MoLa, to define source-specific sampling conditions and to achieve the separate sampling of these emissions.

3.6 Summary

We developed the sampling system AERTRACC (AERosol and TRACe gas Collector) to separately sample the particulate and gas phase of source emissions and background aerosol in complex environments. It is incorporated in our mobile laboratory (MoLa) with its own inlet. Up to four samples can be taken in parallel; in this study, each sample was taken onto a filter and a thermal desorption tube (TDT) for the particle and gas phase, respectively. Separation of different aerosol types is achieved through external control of the sampler based on online measurements of MoLa by setting suitable sampling conditions for the individual aerosol types, which are compared with the online data. An in-house developed software is implemented in the MoLa data acquisition software for direct data access. For each of the four sampling paths up to four measured variables can be combined to create sampling conditions for the targeted aerosol type, which are continuously compared with the current measured data. Besides the automatic sampling, the sampler can also be controlled manually.

The inlet and transport system was designed for minimal particle losses with typical estimated mass losses below 1 % for particles in the size-range 35 nm up to 3.5 μm . Due to shorter residence time of the aerosol in the MoLa online measurement inlet, compared to the sampling inlet, it can be analyzed with the online instruments and the sampling conditions are evaluated before the aerosol reaches the sampling media. These time delays were experimentally determined for all instruments and are considered in the AERTRACC control software.

For proof of concept and in-field validation, pizza oven emissions were probed in a semi-urban environment. The CIMS analysis of the hereby collected filters showed the successful separate sampling of source emissions from the background aerosol. Compounds known to be related to biomass burning and cooking were predominantly found on the source emissions filters while compounds associated with aged aerosol or traffic emissions were found in similar amounts on the background filters and the source emission filters. For gaseous species, the analysis of the TDTs indicate only a weak separation of source and background emissions mainly because most of the identified species can originate from aged and traffic aerosol as well as from biomass burning and cooking emissions and no distinct markers were identified for the pizza oven emissions. Hence, these compounds can already be present in the background aerosol leading to a smaller increase in their concentrations due to source emissions.

The comparison of different potential sampling scenarios demonstrated the advantage of combining different measured variables to achieve targeted sampling of desired emissions. The separation using solely wind direction as sampling criterion was weak due to varying wind conditions leading to non-linear aerosol transport. Adding source specific criteria like elevated particle number concentrations measured by the OPC improved the separation. As a consequence of this more effective separation of the emissions, the source apportionment of identified compounds is improved. A future addition of AMS for AERTRACC control would offer the possibility to define specific sampling conditions for certain aerosol types, like BBOA and COA, derived from AMS measurements, using known markers.

An important requirement for AERTRACC to sample targeted aerosol types is the knowledge about the source aerosol properties, which can be determined in preparatory measurements to define suitable sampling conditions for the different aerosol types. Under such conditions, AERTRACC is capable to separate emissions of individual sources from those of other sources or from the aerosol background for improved chemical analysis of source-related emissions even in complex environments. Possible complex situations could be an industrial facility, like a steel plant, with different but closely located emission sources, e.g., coke oven, blast furnace, sinter plant, and traffic; or urban environments with emissions from traffic, wood combustion, and restaurants. Apart from TD-CIMS, a broad variety of chemical, physical, and microscopical analysis methods could be used in combination with AERTRACC to acquire the desired kinds of information from the samples.

Author contribution: JP and FD conceptualized the sampling system and field measurement. JP carried out the experiment, analyzed the MoLa data and prepared the paper with contributions from FD, LM und SB. LM developed the CIMS method and analyzed the samples using the developed method.

Acknowledgements: We thank Thomas Böttger, Philipp Schuhmann, Antonis Dragoneas and the mechanical workshop for great support in the technical realization of the sampler. We also thank David Troglauer and Carsten Pallien for support during the in-field validation. Furthermore, we acknowledge the Max Planck Institute for Chemistry for funding of this work.

Financial support: The article processing charges for this open-access publication were covered by the Max Planck Society.

4 Influence of Synoptic Air Mass Transport on Chlorine Chemistry

This chapter contains a first complete manuscript draft. After further coauthor exchange and optimization, it will be submitted to a peer-review journal as

Moormann, L., Crowley, J. N., Fachinger, F., Drewnick, F.: *Quantification, Diel Variation and Photochemistry of Inorganic Chlorine Trace Gases in Continental Germany*

Contribution to this manuscript by Lasse Moormann:

As the first author of this work, I conducted all CIMS measurements of chlorine-containing compounds at the BISTUM24 campaign and analyzed the data. Following the campaign, I calibrated the CIMS for Cl₂, ClNO₂, ClONO₂ and HOCl, investigated the humidity dependency of these compounds, and performed experiments to estimate the influence of O₃ on the secondary ion chemistry of chlorinated species. I calculated and analyzed the backward trajectories to explain Cl-rich and Cl-poor periods. I also prepared the figures and wrote the manuscript, which was revised with input from all the co-authors.

4.1 Abstract

Understanding the sources, distribution, and lifetime of inorganic chlorine-containing trace gases is crucial to assessing their tropospheric impacts. We report in situ measurements of Cl_2 , HOCl, ClNO_2 , and ClONO_2 using iodide chemical ionization mass spectrometry during a 2.5-week campaign in June 2024 at a rural continental site in central Germany. Air masses that had passed over “marine-anthropogenic” regions (≈ 400 km distant) showed significantly higher mixing ratios of chlorine-containing gases than “continental-unpolluted” air masses. From the marine-anthropogenic period, we provide the first tropospheric observations of ClONO_2 (up to 59.8 pptv during daytime). Persistent nonzero ClONO_2 implies a non-photochemical source of ClONO_2 or its precursor ClO, and/or that heterogeneous loss is slower than laboratory uptake coefficients suggest. ClNO_2 levels were consistent with production via N_2O_5 uptake on chloride-containing particles; both ClNO_2 and Cl_2 were enhanced when O_3 -/ N_2O_5 -rich air entrained into the nocturnal boundary layer. Photolysis of ClNO_2 , Cl_2 , and HOCl yielded mean maximum Cl atom production rates of $1.0 \times 10^6 \text{ cm}^{-3} \text{ s}^{-1}$ under marine-anthropogenic influenced air and $1.6 \times 10^5 \text{ cm}^{-3} \text{ s}^{-1}$ under continental-unpolluted conditions. In the early morning, Cl production (due to ClNO_2 photolysis) exceeded primary-OH production from O_3 photolysis, while after noon HOCl photolysis was the dominant Cl source. At low solar zenith angles, HOCl photolysis contributed up to 40% of primary OH. These measurements indicate that Cl atoms can strongly influence hydrocarbon oxidation in similar rural regions, with potential regional and global implications (of up to 15%) for the methane lifetime.

4.2 Introduction

The role of inorganic chlorine trace-gases in atmospheric science is well established for the stratosphere, where molecules such as ClONO_2 , HOCl, HCl and thermally unstable Cl_2O_2 play a central role in ozone depletion, most noticeably in polar regions where the catalytic recycling of Cl atoms through a mixture of heterogeneous and photochemical processes leads to the formation of the “ozone-hole” (Molina and Rowland, 1974; Rowland, 1988; Solomon, 1999). In the stratosphere, the source of reactive chlorine trace gases is the photolysis of organic chlorine-containing species such as CH_3Cl and CCl_2F_2 , which were emitted into the lower atmosphere in large quantities prior to their ban in the Montreal Protocol in 1989 (Elkins et al., 1993; Engel et al., 1998; Prinn et al., 2000; Engel et al., 2002). Chlorine species are highly reactive when in radical forms such as Cl or ClO, resulting in a short lifetime (seconds) and significant chemical effects on their immediate environment. The lifetime of the inorganic radical reservoirs, including photolabile Cl_2 , ClNO_2 , ClONO_2 , and HOCl depends on the actinic flux (Ko and Sze, 1984; Von Clarmann and Johansson, 2018), while the lifetime of HCl depends on its reaction with OH and deposition. While there are several observations of ClNO_2 , HOCl, and Cl_2 in the troposphere (e.g., Thornton et al., 2010; Lawler et al., 2011; Mielke et al., 2011; Phillips et al., 2012; Bannan et al., 2015), ClONO_2 is considered as a stratospheric trace gas, which is only present in the upper troposphere as a result of intrusion from stratospheric air masses (Marcy et al., 2005; Von Hobe et al., 2005; Atkinson et al., 2007).

The presence of chlorine radicals derived from inorganic reservoirs such as ClNO_2 and HOCl enhances the rate of oxidation of hydrocarbons (forming HCl and organic peroxy radicals), which influences air composition and especially photochemical ozone production (Faxon et al., 2015; Bhattacharyya et al., 2023; Li et al., 2023a). Understanding the sources, distribution and lifetime of inorganic chlorine trace-gases is thus crucial for evaluating their impact on chemical processes in the troposphere.

The presence of inorganic chlorine in the troposphere is attributed to various sources, including sea salt aerosols, biomass burning, waste disposal, and fossil fuel extraction (Cahill et al., 1992; Oum et al., 1998; Lobert et al., 1999; Bannan et al., 2019; Masoud et al., 2023). ClNO₂ and Cl₂, HOCl and HCl (in both gas and particle phases) are generally believed to be the most abundant, inorganic chlorine-containing gas phase species in the troposphere (Wang et al., 2019). The various routes to their formation in the atmosphere are illustrated in Fig. 4.1 and described below.

The main source of gaseous inorganic chlorine in the troposphere is the release in the form of HCl, e.g., via acid displacement of chloride from sea-salt (mainly NaCl) (Keene et al., 1990; Keene et al., 1998; Volpe et al., 1998). Additionally, HCl can be formed through H-abstraction from volatile organic compounds (VOCs) by Cl atoms that originate from the mechanisms discussed below (Wang et al., 2019). In a continental atmosphere, NH₃ and HCl react to form NH₄Cl, which partially partitions into the particle phase. The heterogenous uptake of N₂O₅ on chlorinated particles, liberates chloride as ClNO₂ into the gas phase (IUPAC, 2025).



N₂O₅ is formed in the reaction between NO₂ and NO₃ (the latter formed in the oxidation of NO₂ by O₃) and, due to its thermal equilibrium with photolabile NO₃ (R2), is only present at night (Brown and Stutz, 2012):



The abundance of N₂O₅ (and thus ClNO₂) is closely tied to the availability of NO_x and the lifetime of NO₃ and is therefore maximized in nocturnal air masses that are either impacted by anthropogenic emissions with high levels of NO_x or in which the NO₃ reactivity towards unsaturated hydrocarbons is low. NO₃ and thus N₂O₅ lifetimes in forested regions are often very short (Liebmann et al., 2018; Dewald et al., 2024) as the abundance of terpenoids, which react rapidly with NO₃, is high. In this case activation of reactive chlorine from its particle reservoirs is inefficient and the formation of ClNO₂ is suppressed. High levels of ClNO₂ are typically found at night in polluted marine areas such as Asian megacities and industrial metropolitan areas (Wang et al., 2017; Priestley et al., 2018; Haskins et al., 2019; Chen et al., 2025b). ClNO₂ has also been observed in air masses which have been transported long distances from polluted and marine source regions to continental sites (Thornton et al., 2010; Phillips et al., 2012; Bannan et al., 2015).

Once formed in the multiphase reaction between N₂O₅ and particle-chloride, most of the ClNO₂, which has a low solubility (Schweitzer et al., 1998), is released into the gas phase where it is photolyzed to Cl and NO₂ (R3; Finlayson-Pitts et al., 1989; Leu et al., 1995; Phillips et al., 2016). Other loss processes, such as reaction with OH are negligible by comparison (Ganske et al., 1991).



ClNO₂ can also react with acidified (pH < 2), chloride-containing particles to generate gas-phase Cl₂:



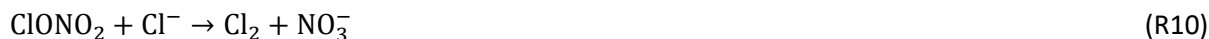
Cl₂ is also formed through the uptake of O₃ onto acidic, chloride-containing particles (Oum et al., 1998) and (as shown below) through other heterogeneous processes (Peng et al., 2022). During daytime, Cl₂ is rapidly photolyzed in the troposphere (lifetime ~10 min) to form two Cl atoms:



The ClO radical is formed when Cl atoms react with O₃ (R6; IUPAC, 2025). ClO radicals then react with HO₂ and NO₂ to form HOCl and ClONO₂, respectively (R7, R8).



As HO_x radicals are ubiquitous in the atmosphere, the ClO radical is the limiting trace gas for formation of HOCl. Consequently, larger mixing ratios of the latter have been measured near source regions with high chloride load such as marine sites or industrial facilities (Lawler et al., 2011; Chen et al., 2025a). The formation of ClONO₂ requires the presence of NO₂ and is thus formed at largest rates in regions with both anthropogenic influence and particulate chloride as precursor for Cl-atoms and thus ClO. HOCl and ClONO₂ are lost in both gas- and multiphase processes. Similar to ClNO₂, the uptake of HOCl or ClONO₂ to chloride-containing, acidic particles results in the generation of Cl₂ (R9 and R10; Eigen and Kustin, 1962; Deiber et al., 2004), while heterogenous hydrolysis of ClONO₂ forms HOCl (R11; Tolbert et al., 1987). The photolysis of HOCl leads to the production of Cl atoms and OH radicals (R12), whereas the photolysis of ClONO₂ leads mainly to Cl atoms (R13a) with a minor contribution to ClO formation (R13b, IUPAC (2025)).



Measurements of chlorine-containing trace-gases in the troposphere date back to the mid-1980s, whereby chromatographic methods were used to monitor e.g., HCl and HOCl (Cicerone, 1981; Keene et al., 1990). Recent developments in mass spectrometry have enabled sensitive and selective detection of several chlorinated trace gases with chemical-ionization mass spectrometry (CIMS) using iodide as the reagent ion for a wide variety of inorganic chlorine species (Caldwell et al., 1999; Kercher et al., 2009; Lawler et al., 2011; Bhattacharyya et al., 2023). The recent development of high-resolution (e.g., Time-of-Flight, ToF) analysers allows identification of non-fragmented chlorine species and therefore offers high selectivity as well as excellent sensitivity. However, the number of studies using such devices to examine tropospheric chlorine chemistry is still limited.

In this study we present the quantitative measurement of Cl₂, HOCl, ClNO₂ and ClONO₂ using VUV-Iodide-ToF-CIMS during field measurements in central Germany. The formation and loss of inorganic chlorine-containing species throughout the diel cycle are discussed, including the first quantitative

Table 4.1: Calibrated chlorine species with detection limit (LoD, as $3 \times \sigma$ for an averaging period of 5 min) as found in the laboratory (LoD lab) and in the field (LoD campaign), calibration method and associated uncertainty. Thermal decomposition and non-destructive cavity ring-down spectroscopy (TD-CRDS and CRDS) were used as reference instruments.

Species	I-cluster / m/z	LoD lab / pptv	LoD campaign / pptv	Calibration method	Uncertainty* / %
HOCl	178.877	3.50	2.21	Indirect (HOCl-to-Cl ₂ conversion)	13 ^a (from Cl ₂ calib.)
Cl ₂	196.843	0.05	0.03	Direct (Cl ₂ gas), CRDS	13 ^{a,d}
ClNO ₂	207.867	0.19	0.10	Indirect (N ₂ O ₅ -to-ClNO ₂ conversion), TD-CRDS	28 ^b
ClONO ₂	223.862	0.20	0.36	Direct (synthesis), FT-IR	10 ^{c,e}
N ₂ O ₅	234.886	0.12	0.03	Direct (synthesis), TD-CRDS	28 ^b

*Instrument uncertainty: ^aCRDS: <10% (Thieser et al., 2016), ^bTD-CRDS: 28% (Sobanski et al., 2016), ^cFT-IR: 3% derived from Oberto et al. (2017), Absorption cross section: ^d5% (Maric et al., 1993), ^e10% (Davidson et al., 1987), and for all calibrations: mass flow controller: 0.6% and the linear regression of the calibration curve depending on data (Fig. S9.10).

4.3.1 VUV lamp as reagent ion source in CIMS

Iodide reagent ions in the CIMS were generated using a VUV lamp mounted in front of the IMR. The VUV lamp (10.6 eV photon energy, PKR 106, Heraeus, Germany) was powered with a current of 2 mA at 1500 V DC. An electronic pre-filter was used to flatten interference from the switching power supply (Fig. S9.8).

Two major changes were implemented in our setup in contrast to the VUV lamp assembly described by Ji et al. (2020). First, an acceleration voltage of 5 V was used for the ions to guide them into the IMR, which doubled the reagent ion yield. Second, the reagent ion flow was directed towards the VUV lamp before leaving the photo-ionization region. This has the advantage of maximizing the irradiance of the reagent gas shortly before the ions enter the IMR and requires less accurate alignment of the VUV lamp in its stainless-steel tube. A detailed overview of the differences between the VUV lamp and ²¹⁰Po ion sources with regard to the characteristics of Iodide-CIMS spectra can be found in Ji et al. (2020).

4.3.2 Calibration of chlorine-containing species

Relative humidity dependent calibrations of Cl₂, ClNO₂, ClONO₂, HOCl and N₂O₅ were conducted post-campaign. In addition, we examined the effect of adding O₃ to flows of ClNO₂ and HOCl to assess potential secondary ion chemistry including the formation of IClONO₂⁻ and HO₂Cl⁻ (presented in SI). A summary of the relative humidity dependent calibration curves for ClNO₂, ClONO₂, Cl₂ and HOCl can be found in Fig. S9.9 and Fig. S9.10. Uncertainties associated with the calibrations and the detection limits during the campaign and laboratory calibration are presented in Table 4.1.

4.3.2.1 Cl₂

A canister of Cl₂ in N₂ was prepared by diluting a 5%, commercially obtained mixture in N₂ to 6 ppm. A small flow from the canister was dynamically diluted prior to simultaneous detection with the CIMS and a cavity ring-down spectrometer (Thieser et al., 2016) operating at 405 nm where Cl₂ has a well-known absorption cross-section.

4.3.2.2 N₂O₅

N₂O₅ was synthesized by flowing a mixture of NO and a large excess of O₃ into a 2 L glass reaction chamber where they reacted for ≈ 1 min (Davidson et al., 1978). The exhaust, containing N₂O₅ and O₃, passed through a glass tube at -78 °C (dry ice/acetone bath) to trap the N₂O₅ as pure crystals. For calibration of the CIMS, the head-space above the N₂O₅ crystals (at -60 °C) was flushed with N₂ carrier gas to generate a dilute N₂O₅ gas mixture, which was simultaneously sampled by the CIMS and a thermal dissociation cavity ring down spectrometer designed for measurement of N₂O₅ and NO₃ (Sobanski et al., 2016).

4.3.2.3 ClNO₂

The CIMS was calibrated for ClNO₂ by converting a known amount of N₂O₅ (from a prior N₂O₅ calibration) to ClNO₂. This was achieved flowing the N₂O₅ flow through a glass reactor internally coated with dried NaCl at room temperature. The ClNO₂ generated this way was assumed to be equivalent in concentration to the N₂O₅ lost as shown in laboratory experiments investigating the heterogeneous uptake of N₂O₅ to dry sea-salt (Kercher et al., 2009; Roberts et al., 2009).

4.3.2.4 ClONO₂

ClONO₂ was synthesized by allowing Cl₂O to react with N₂O₅ for several hours at -10 °C. Cl₂O was prepared by passing a flow of gaseous Cl₂ through a sample of HgO dispersed in glass-beads at -10 °C (Davidson et al., 1987). The ClONO₂ sample was used to generate a diluted sample in N₂ in a glass-bulb. The contents of the bulb were analyzed using a FTIR-spectrometer (Bruker Vector 22, Bruker Corporation, USA) at 0.5 cm⁻¹ resolution. The absorption features of ClONO₂ were consistent with those reported by Davidson et al. (1987), whose integrated band-strengths were used to quantify the ClONO₂ mixing ratio in the glass-bulb to be 200 ppmv. The CIMS was calibrated by sampling ClONO₂ from the storage bulb with known dilutions in N₂.

4.3.2.5 HOCl

HOCl was generated by bubbling 30 sccm N₂ through a NaOCl solution (11-14% active chlorine) and diluting this flow with 10 sLpm N₂. The gaseous mixture was then directed through a glass U-tube at -40 °C to condense moisture prior to sampling by the CIMS. To quantify the HOCl content, the HOCl flow was alternatively directed through a U-tube containing a frozen, diluted HCl solution at -40 °C, which converts HOCl to Cl₂. The amount of HOCl was determined by measuring the depletion of HOCl and the generation of Cl₂ (for which the CIMS was already calibrated) according to Lawler et al. (2011). It was crucial to remove moisture before directing the HOCl gas to the iced HCl surface, to prevent Cl₂ depletion due to uptake on moist surfaces.

4.3.3 BISTUM24 field campaign: measurement site and instrumentation

The BISTUM24 field campaign took place from June 6 to 22, 2024 in Spielberg, central Germany (50°19'N, 9°15'E, Fig. S9.11). The rural measurement site, which is located 391 m above mean sea level on top of a hill in a treeless clearing, was selected because air masses encountered at the site originate mainly from rural regions and are rarely influenced by urban pollution despite the proximity to the

Frankfurt metropolitan area (~45 km). With a distance of ~400 km to the next coastline, the North and Baltic Seas, the site may be described as continental with no direct marine influence (Fig. 4.2a and b). The instruments used in this study sampled from inlets at a height of 6 m (Fig. S9.12) and were housed in the “Mobile Laboratory” (Drewnick et al., 2012). These included the Iodide-ToF-CIMS and an Aerosol Mass Spectrometer (AMS, Aerodyne Research Inc., USA), as well as an O₃ monitor (TB205, Monitor 205 Dual Beam Ozone Monitor, 2B Technologies, Inc., USA) and a pyranometer (CMP3 Pyranometer Sensor, Campbell Scientific Inc., UK). The surface area and volume of aerosol particles were calculated from a merged size distribution from different particle sizers (Fast Mobility Particle Sizer Model 3091, TSI, Inc., USA and Optical Particle Counter Model 1.109, Grimm Aerosoltechnik GmbH, Germany, (Pikmann et al., 2024)). Local meteorological information was provided by a meteorological station (WXT520, Vaisala Oyj, Finland).

The CIMS was connected to the inlet via 6 m of PTFE tubing for which the residence time was ~1 s (corresponding to a total flow of 32 L min⁻¹). The CIMS sub-sampled 2 L min⁻¹ from this flow. The inlet line also included a PTFE-particle filter, which was changed after every 20,000 liters of sampled air (Fig. S9.12). Zero measurements were performed every 8 h for 20 min during the campaign using humidified N₂. The CIMS data were zero-corrected, and the signal at each mass analyzed was normalized to the sum of the most abundant reagent ions, I⁻ and IH₂O⁻. Calibration factors were applied, determined as described in Sect. 4.3.2 (Fig. S9.9).

4.4 Chlorine-containing Compounds and Air Mass Origin

Fig. 4.2 provides a time series of the chlorine-containing trace gases ClNO₂, ClONO₂, HOCl, Cl₂ and N₂O₅, measured by the CIMS, as well as particulate chloride (pCl⁻) as measured by the AMS. Although the AMS does not efficiently detect pCl⁻ from sea salt, it can detect pCl⁻ from, e.g., ammonium chloride. For this reason, pCl⁻ does not necessarily represent the total amount of particulate chloride present in the particle phase. Information on air mass origin was gained using HySplit (Stein et al., 2015; Rolph et al., 2017) with which 48-h backward trajectories ending 30 m above ground level at the measurement site were calculated.

In the first phase (June 6 to 14), back-trajectories showed that the air passed over the English Channel and industrialized regions in Belgium and the Netherlands, as well as the German Ruhr metropolitan area before reaching the measurement site. The transport times were 12 to 36 h for UK and Benelux and 4 to 6 h for the Ruhr region, respectively. During transport, trajectories rarely exceeded altitudes of 500 m above mean sea level, indicating that the air was transported within the boundary layer. We refer to the air masses in this period as having a “marine-anthropogenic” influence as evidenced by the enhanced levels of pCl⁻ and N₂O₅ (Fig. 4.2d).

In contrast, backward trajectories for the period June 16 to 21 indicate that the air sampled during this period travelled at altitudes > 1000 m above mean sea level for several days before descending close to the measurement site. The vast majority of these trajectories passed over the relatively sparsely populated, non-industrialized center of France and rural south-west Germany (Fig. 4.2b and Fig. S9.13b). We designate these air masses as “continental-unpolluted”. In these air masses, N₂O₅ was generally below the detection limit and concentrations of pCl⁻ were much lower than those of the other air masses.

As expected, the mixing ratios of Cl₂ and ClNO₂ were largest during the “marine-anthropogenic” period, with ClNO₂ exceeding 70 pptv every night and Cl₂ exceeding 0.5 pptv every day (Fig. 4.2e). HOCl and

ClONO₂ were less abundant than ClNO₂, with mixing ratios of up to 60 pptv (Fig. 4.2f). During this period, mean mixing ratios of 56.2 pptv ClNO₂, 0.64 pptv Cl₂, 41.3 pptv HOCl and 4.8 pptv ClONO₂ were observed, whereas during the “continental-unpolluted” period, 2.25 pptv ClNO₂, 0.17 pptv Cl₂ and 11.1 pptv HOCl were measured and ClONO₂ levels were below the detection limit.

Worldwide, the mixing ratios of inorganic chlorine species vary considerably depending on the air masses sampled and the geographical location. Our ClNO₂ mixing ratios are consistent with those observed at continental sites with similar (indirect) marine-influenced air masses, which show peak ClNO₂ concentrations of 300–700 pptv (Phillips et al., 2012; Bannan et al., 2015). These mixing ratios are higher than those measured in maritime air (Faxon et al., 2015; Chen et al., 2025a), which results from a longer residence time over landmasses with a greater anthropogenic influence, which is crucial for the formation of ClNO₂ (see Sect. 4.2). Consequently, for highly polluted sites up to 3.5 ppbv of ClNO₂ have been reported (Tham et al., 2014; Riedel et al., 2014).

During both periods of the BISTUM24 campaign, the Cl₂ levels were generally low compared to those reported in other studies, especially those influenced by highly polluted urban regions (Finley and Saltzman, 2006; Chen et al., 2025a). Measurements of Cl₂ in the marine boundary layer indicate mixing ratios varying from ~2 to ~500 pptv, depending heavily on the region (Pszenny et al., 1993; Spicer et al., 1998; Lawler et al., 2011; Riedel et al., 2014; Chen et al., 2025a). There are no previous reports of Cl₂ measurements in lower tropospheric air at rural continental sites with which to compare our data, and no previous studies reporting lower-tropospheric ClONO₂ mixing ratios.

Results from our HOCl measurements are broadly consistent with the 2 – 120 pptv HOCl range reported for continental and marine air masses (Lawler et al., 2011; Chen et al., 2025a). The large variability is related to air mass history, even when only marine regions are considered.

Fig. 4.2 reveals substantial differences in the diel profiles of the trace gases measured. N₂O₅ and ClNO₂ were observed predominantly at nighttime whereas HOCl and Cl₂ were observed predominantly during the day. The absence of N₂O₅ during the day is expected (R2, Sect. 4.2) and, as N₂O₅ is the precursor of ClNO₂, the nighttime dominance of the latter is also consistent with present knowledge of its production and loss terms (Sect. 4.2). pCl⁻ has a less clear day-night variation which is related to the presence of multiphase equilibria, whereby chloride is present as a dissolved ion in the particle phase or degassed from aerosols as HCl. For the mixing ratios of ClONO₂, the two strongest features were observed after midnight on the nights of 13th and 14th June with strong co-variance with ClNO₂. This was unexpected, as ClONO₂ is believed to be formed exclusively in the reaction of ClO with NO₂, with the ClO-radical being present at significant levels only during the daytime when photochemically generated Cl atoms react with O₃.

While many studies have reported ClNO₂ and Cl₂ in coastal regions (Osthoff et al., 2008; Kercher et al., 2009; Priestley et al., 2018; Chen et al., 2025a) or in highly polluted regions where non-marine chloride sources exist (Mielke et al., 2011; Le Breton et al., 2018; Bannan et al., 2019; Masoud et al., 2023), only few (Thornton et al., 2010; Phillips et al., 2012; Faxon et al., 2015) have identified reactive chlorine trace-gases in air masses that may be described both as non-marine (i.e., several hundred km from coastal regions) and also not impacted by local pollution. Of these, only Phillips et al. (2012) investigated chlorine chemistry in mainland Europe. They argued that, as coarse mode sea-salt particles are not efficiently transported hundreds of km, the source of particle chloride was HCl that was released from coarse-mode sea-salt particles close to coastal regions (by, e.g., acid displacement) and subsequently transported as gas phase HCl or particulate ammonium chloride. As Phillips et al. (2012) did not measure other chlorine-containing trace-gases apart from ClNO₂, they did not consider the potential role of HOCl, Cl₂ or ClONO₂ in, e.g., the production rate of Cl atoms or OH radicals.

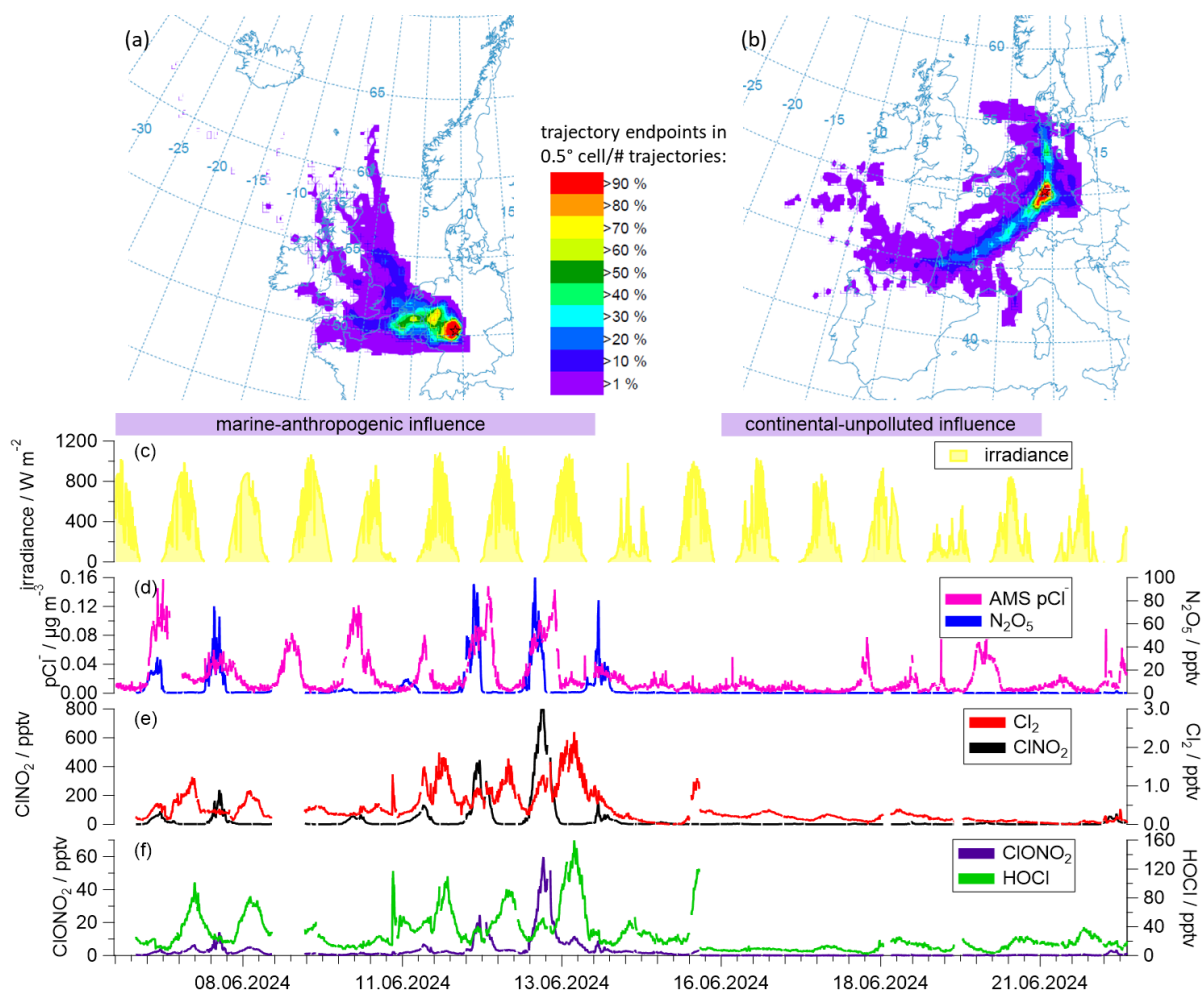


Fig. 4.2: Upper panels: 48 h-backward trajectories indicate that air masses in the period June 6 to 14, 2024 passed over marine and industrialized source regions (a). Between June 16 to 21, 2024 the air passed over rural, continental regions (b). Lower panel: Time series of irradiance (c), chlorine trace gas precursor compounds (particulate chloride (pCl^-) and N_2O_5 , d) and gaseous chlorine-containing species (e and f) measured during BISTUM24.

4.5 The Diel Cycle of Cl_2 , HOCl , ClONO_2 and ClONO_2

Fig. 4.3 displays the mean, fractional contribution of each individual chlorine-containing trace gas to the total inorganic chloride mixing ratios during BISTUM24. For the “marine-anthropogenic” influenced phase (a), ClONO_2 is dominant during the night (max. $\sim 70\%$), with HOCl being dominant during the day (max. $\sim 90\%$) and ClONO_2 and Cl_2 representing only a few percent of overall chlorine-containing species throughout the diel cycle. During the “continental-unpolluted” phase (b), HOCl is the dominant chlorine-containing trace gas both day and night, accounting for $> 60\%$ during the night and $> 80\%$ during the day. Both ClONO_2 and Cl_2 are minor contributors with $\sim 1\%$ each, while the nocturnal ClONO_2 contribution is relatively low due to N_2O_5 -poor conditions ($\sim 30\%$). The diel profile of ClONO_2 is understood in terms of its generation through multiphase chemistry involving N_2O_5 during the night, followed by its daytime photolysis to release Cl atoms that (via reactions of HO_2 and ClO) lead to daytime HOCl . The significant nighttime contribution of HOCl is likely related to incomplete loss from the previous day rather than nocturnal formation, for which a non-radical mechanism is unknown. The

heterogeneous loss rate coefficient (k_{het}) for HOCl with respect to uptake on aerosol particles was calculated with Eq. (4.1):

$$k_{\text{het}} = 0.25 \times \gamma \times A \times c_{\text{HOCl}} \quad (4.1)$$

with the mean molecular velocity $c_{\text{HOCl}} = 34700 \text{ cm s}^{-1}$, derived from the molecular weight of the gas species for 298 K, the mean aerosol particle surface during the campaign $A = 130 \mu\text{m}^2 \text{ cm}^{-3}$ and the uptake coefficient $\gamma < 2 \times 10^{-4}$ that is available for particles with $\text{pH} = 1$ (IUPAC, 2025).

The calculated lifetime of HOCl due to uptake on acidic particles ($k_{\text{het}}^{-1} \approx 5 \text{ days}$) is much longer than the lifetime with respect to photolysis ($\sim 1 \text{ h}$, Table 4.2). Hence, the observed nighttime HOCl was most likely generated photochemically the previous day.

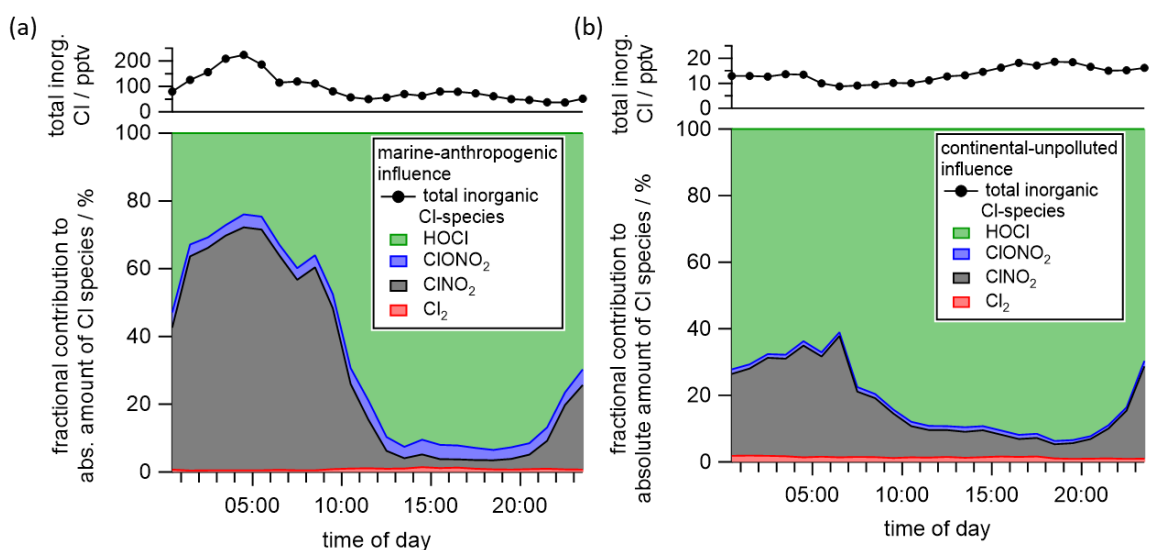


Fig. 4.3: Diel cycle of the fractional contribution of inorganic chlorine species to the total mixing ratio of the measured inorganic chlorine (excluding HCl). The data are separated into air masses designated “marine-anthropogenic” (a) and “continental-unpolluted” (b).

Table 4.2: Photolysis rate J and lifetime of photolabile species at noon from (UCAR, 2025).

Species	J / s^{-1}	Lifetime / min
$\text{O}_3(^1\text{D})$	3.52×10^{-5}	473
ClNO_2	4.97×10^{-4}	33.5
ClONO_2	4.97×10^{-5}	335
Cl_2	2.43×10^{-3}	6.9
HOCl	2.86×10^{-4}	58.3
NO_3	2.37×10^{-2}	0.7
N_2O_5	4.78×10^{-5}	349*

*Thermolabile N_2O_5 forms NO_3 during daytime in an equilibrium. Fast photolysis of NO_3 significantly decreases the N_2O_5 -lifetime.

4.5.1 ClNO₂

In the following, we investigate the formation and loss of ClNO₂ through the diel cycle during the “marine-anthropogenic” period and highlight the influence of air mass history and vertical mixing on the ClNO₂ abundance during two individual night-day transitions.

In Fig. 4.4 we present the median, diel cycles of the mixing ratios of ClNO₂, ClONO₂ and N₂O₅ over the entire “marine-anthropogenic” time period. The diel cycle is divided into three phases which represent (I) nighttime, when N₂O₅ is present, (II) the period just after sunrise when N₂O₅ is rapidly depleted and the mixing ratios of ClNO₂ and ClONO₂ are either constant or increasing, and phase III when irradiance is stronger and ClNO₂ mixing ratios decrease monotonically to zero.

The formation of ClNO₂ depends on the presence of N₂O₅ and pCl⁻ (R1) and thus we expect net-production only when N₂O₅ and pCl⁻ are present. The data in phase I and II from June 10 and 12, 2024 show that this is not always reflected in the ClNO₂ mixing ratios which remain constant or sometimes even increase during the early morning when N₂O₅ is absent, although the photolytic loss of ClNO₂ increases with intensifying irradiance. Note that, subsequent to a post-dawn peak, the ClNO₂ mixing ratios decrease with a decay constant of $5 \times 10^{-4} \text{ s}^{-1}$ in accord with J_{ClNO_2} (Table 4.2).

At the beginning of the night from June 12, from 21:00 to 01:30 (Fig. 4.5a), an approximately linear increase in ClNO₂ of $(19 \pm 1) \text{ pptv h}^{-1}$ was observed. The ClNO₂ production rate can be calculated from k_{het} , the N₂O₅ mixing ratio and the fraction α of N₂O₅ that forms ClNO₂:

$$P(\text{ClNO}_2) = [\text{N}_2\text{O}_5] \times \alpha \times k_{\text{het}} \quad (4.2)$$

where k_{het} was calculated from the uptake coefficient for N₂O₅ to an aqueous surface ($\gamma = 0.02$; IUPAC, 2025), the aerosol surface area in this period $A = 104 \mu\text{m}^2 \text{ cm}^{-3}$ and the mean molecular velocity of N₂O₅ $c_{\text{N}_2\text{O}_5} = 27800 \text{ cm s}^{-1}$. Considering a mean $[\text{N}_2\text{O}_5] = 18 \text{ pptv}$, and $\alpha = 0.8$ (given for a 0.22 M chloride in particles Roberts et al., 2009), a ClNO₂ production rate of 7.7 pptv h^{-1} is obtained. Given the factor 3 uncertainty in γ (Bertram and Thornton, 2009; IUPAC, 2025) and the AMS uncertainty in pCl⁻ (and thus; Zorn et al., 2008), the calculated $P(\text{ClNO}_2)$ is consistent with the observed, net ClNO₂ formation rates. After 01:30 the ClNO₂-to-N₂O₅ ratio switches from ~ 2 to ~ 6 , and the high ClNO₂ levels in the next 4 h cannot be explained by local production from N₂O₅. This trend continues in phase II in Fig. 4.5a, where an increase in pCl⁻ (up to 1 M Cl⁻) was accompanied by an increase in ClNO₂ levels although N₂O₅ levels were close to zero. A similar picture emerges from the data in Fig. 4.5b, in which post-dawn peaks in ClNO₂ ($\sim 55 \text{ pptv}$ between 05:00 and 06:00 and $\sim 69 \text{ pptv}$ between 08:20 and 09:20) are observed despite the production term (in the absence of N₂O₅) being zero. In both cases, the in-situ production of ClNO₂ from N₂O₅ reaction with pCl⁻ can be ruled out and the increase in ClNO₂ after dawn is attributed to the sampling of air masses in which N₂O₅ had been previously converted to ClNO₂. This simply reflects the fact that ClNO₂ is substantially longer-lived during the day than N₂O₅ as J_{ClNO_2} is much lower than J_{NO_3} (which controls the N₂O₅ lifetime due to its equilibrium with N₂O₅).

The phase II, post-dawn peaks in ClNO₂ were found to be enhanced for days when backward trajectories showed subsiding air masses 1-3 h before the air reached the measurement site (see interquartile range in Fig. 4.4). The air from higher altitudes entrains O₃-rich residual layer air into the nocturnal boundary layer (Moormann et al., 2025a), which results in enhanced formation of N₂O₅ and thus of ClNO₂. Additionally, at dawn when the nocturnal boundary layer dissipates through radiative heating and convective mixing of air from the residual layer, O₃-rich air may be transported to the surface. The daily development and breakdown of the nocturnal boundary layer can also cause variability in ClNO₂ levels due to vertical mixing.

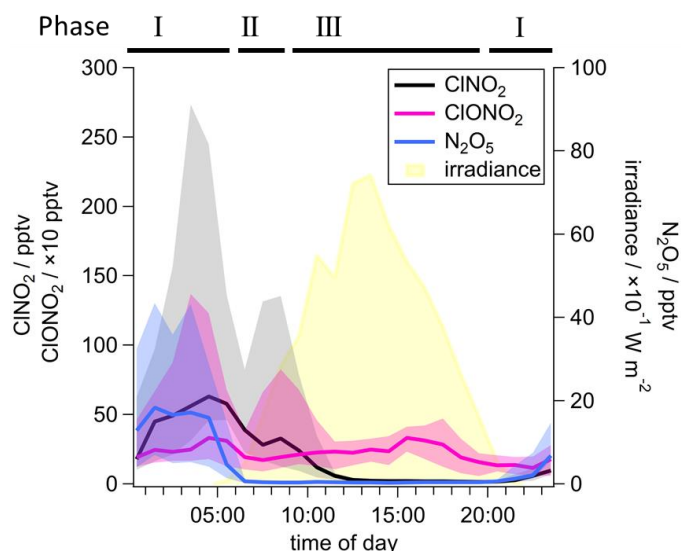


Fig. 4.4: Diel cycle of ClONO_2 (grey) and ClONO_2 (pink), N_2O_5 (blue) and irradiance (yellow) during the “marine-anthropogenic” period of the BISTUM24 campaign in local time. Lines represent the median and the interquartile ranges is given as shaded area.

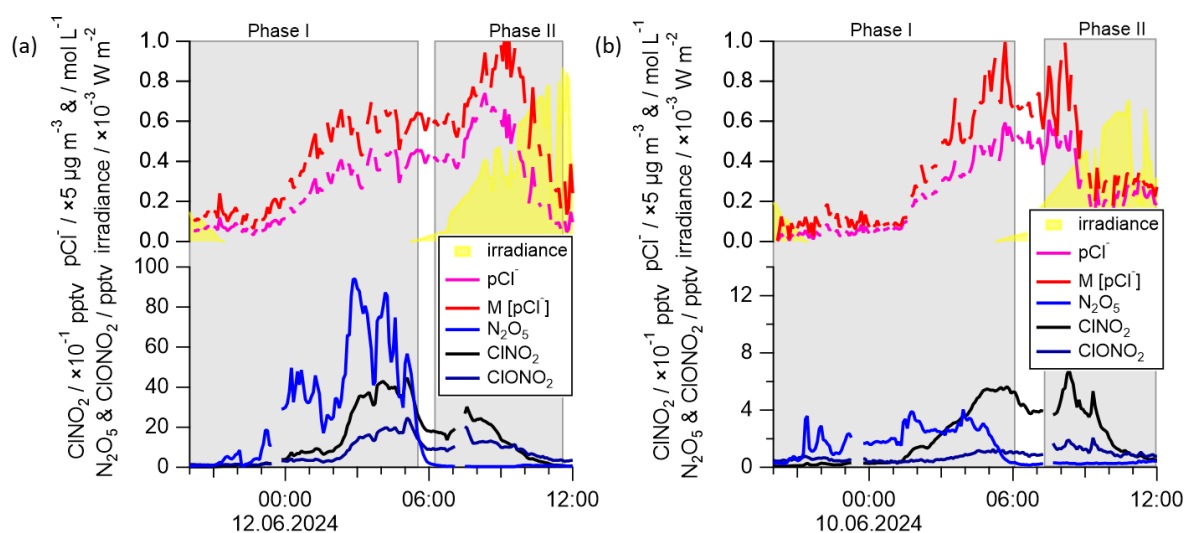


Fig. 4.5: Mixing ratios of ClONO_2 (black) and ClONO_2 (dark blue) and pCl^- (as mass (pink) and molar (red) concentration) through the diel cycle on June 10 (a) and 12 (b), 2025.

4.5.2 ClONO_2

While ClONO_2 , has been measured in the lowermost troposphere on many occasions (e.g., Thornton et al., 2010; Mielke et al., 2011; Phillips et al., 2012; Bannan et al., 2015) the detection of ClONO_2 during BISTUM24 was unexpected. Previous studies have demonstrated the potential of using CIMS methods with SF_6^- and I^- to measure ClONO_2 as FCINO_3^- and ICINO_3^- (Marcy et al., 2005; Le Breton et al., 2018) and airborne SF_6^- -CIMS measurements have quantified ClONO_2 in the upper troposphere where its presence (at levels up to 10 pptv) was explained by the entrainment of stratospheric air (Marcy et al., 2005).

Our study presents the first quantitative ambient ground-level ClONO_2 measurements using Iodide-CIMS. As already mentioned, the accepted mechanism for formation of atmospheric ClONO_2 is R8,

which requires the presence of ClO and NO₂. ClO is a radical that is formed as a result of photochemical processes and expected to be present predominantly during daytime; we therefore expect reaction R8 to be responsible for the net increase in ClONO₂ observed during the day (Phase III in Fig. 4.5). However, following this line of reasoning ClONO₂ is not expected to be formed in significant rates during the night, which we nonetheless observe (Phase I in Fig. 4.5). In the following, we first calculate the ClONO₂ lifetime and then estimate the production rate that would be required to maintain the observed levels. The photolysis frequency of ClONO₂ is $4.97 \times 10^{-5} \text{ s}^{-1}$, resulting in a lifetime of ~5-6 h with respect to this loss process (R13, Table 4.2). The heterogeneous loss frequency of ClONO₂ was calculated from Eq. (4.1) with the uptake coefficient on aqueous particles $\gamma = 0.027$ (IUPAC, 2025) and $c_{\text{ClONO}_2} = 25590 \text{ cm s}^{-1}$. Using a campaign mean particle surface area density A of $130 \mu\text{m}^2 \text{ cm}^{-3}$ results in a loss rate constant of $k_{\text{het}} = 2.25 \times 10^{-4} \text{ s}^{-1}$, or a lifetime of ~75 mins. Given this short lifetime with respect to heterogeneous uptake, ClONO₂ cannot survive from the previous day and, in the absence of sources, its mixing ratios should tend to zero in the first hours during the night. In order to explain the observed mean ClONO₂ mixing ratio of 4.3 pptv at 05:00 during the night, we require a nocturnal production rate of $\sim 2.4 \times 10^4 \text{ molecules cm}^{-3} \text{ s}^{-1}$, which can be equated to $P(\text{ClONO}_2) = k_{\text{NO}_2+\text{ClO}} \times [\text{ClO}] \times [\text{NO}_2]$. Assuming an NO₂ mixing ratio of 1 - 2 ppbv during the “marine-anthropogenic” period as measured at a similar site with similar prevailing wind direction (Crowley et al., 2010) and that the sole source of ClONO₂ is the reaction between ClO and NO₂ (with a rate coefficient, $k_{\text{NO}_2+\text{ClO}}$, at 298 K and 1 bar of $2.4 \times 10^{-12} \text{ cm}^3 \text{ molecule}^{-1} \text{ s}^{-1}$, IUPAC) we calculate that the ClO concentration necessary to maintain this level of ClONO₂ is $[\text{ClO}] = (2 - 4) \times 10^5 \text{ molecules cm}^{-3}$, where the spread in values results from the range of NO₂ mixing ratios assumed for the calculation.

A well-known source of gas phase ClO is the reaction between Cl atoms and O₃ (R6). Thus, the presence of nighttime ClONO₂ would require a reaction that generates either Cl atoms or ClO directly, both in the absence of sunlight. The conversion of Cl to ClO is directly influenced by O₃ levels and competing Cl reactions with, e.g., hydrocarbons and NO_x trace gases. The loss rate constant of Cl through its reaction with O₃ is given as $k_{\text{Cl}+\text{O}_3} \times [\text{O}_3] = 11.8 \text{ s}^{-1}$ (calculated from the mean average O₃ concentration (40 ppbv) and the rate coefficient $k_{\text{Cl}+\text{O}_3} = 1.2 \times 10^{-11} \text{ cm}^3 \text{ molecule}^{-1} \text{ s}^{-1}$ (IUPAC, 2025)).

The first-order loss rate constant of Cl atoms reacting with the most abundant alkanes can be calculated from $k_{\text{Cl}+\text{CH}_4} \times [\text{CH}_4] + k_{\text{Cl}+\text{C}_2\text{H}_6} \times [\text{C}_2\text{H}_6] + k_{\text{Cl}+\text{C}_3\text{H}_8} \times [\text{C}_3\text{H}_8]$. As concentrations of these hydrocarbons were not measured during the campaign, we use reference mixing ratios of 1.9 ppm CH₄, 0.8 ppbv C₂H₆, and 0.3 ppbv C₃H₈ that are typical for rural continental conditions and the corresponding rate coefficients with Cl (Ge et al., 2024; IUPAC, 2025). The calculated total loss rate constant for reaction with these hydrocarbons is $\sim 6.8 \text{ s}^{-1}$, with the largest single contributions from methane (4.6 s^{-1} , i.e., ~25% of Cl). We acknowledge that loss of Cl atoms due to terpenoids can be significant, however, their concentration is highly variable (even in rural continental regions) and their contribution is highly uncertain (considering 1 ppbv terpenoids with $k_{\text{Cl}+\text{isoprene}} = 4.6 \times 10^{-10} \text{ molecules cm}^{-3} \text{ s}^{-1}$ would result in a loss rate to terpenoids of $\sim 11.2 \text{ s}^{-1}$ (Ragains and Finlayson-Pitts, 1997), i.e., the same as the loss rate to O₃ adding a uncertainty factor of 2 to the calculation). Cl atoms react with NO₂ with a rate coefficient of $6.7 \times 10^{-12} \text{ cm}^3 \text{ molecule}^{-1} \text{ s}^{-1}$ (campaign conditions; Burkholder et al., 2020). Assuming (as above) that NO₂ mixing ratios were between 1 and 2 ppbv at night results in a Cl atom loss rate constant of $\sim 0.3 \text{ s}^{-1}$.

Taking together the formation rate of ClO from Cl (11.8 s^{-1}) and the loss rates of Cl through other pathways (6.8 s^{-1} and 0.3 s^{-1}), we therefore conclude that approximately 60% of the Cl atoms generated react to form ClO. We can estimate the production rate of ClO by assuming that its concentration is in steady state with respect to its gas phase formation and loss processes at night. In the absence of NO,

the dominant loss process for ClO at night is its reaction with NO₂, with a loss rate of 2.4×10^4 molecules cm⁻³ s⁻¹. Using the 60% ClO yield from Cl, this in turn can be converted into a Cl atom production rate $P(\text{Cl}) = k_{\text{NO}_2+\text{ClO}} \times [\text{ClO}] \times [\text{NO}_2] / 0.6 = (2.0 - 3.9) \times 10^4$ atoms cm⁻³ s⁻¹.

We now examine potential reactions that, at nighttime, could lead to Cl atom production rates of this magnitude. The dominant radical at nighttime is often considered to be NO₃, which initiates the oxidation of many biogenic hydrocarbons. However, reactions of NO₃ radicals with sufficiently abundant (non-radical) chlorine species to generate ClO or Cl atoms are either unknown or expected to be too slow to contribute significantly. For example, the rate coefficient for the reaction between NO₃ and HCl (R14) is $< 5 \times 10^{-17}$ cm³ molecule⁻¹ s⁻¹ (IUPAC, 2025), which would result in a maximal Cl atom production rate of 1.2×10^2 atoms cm⁻³ s⁻¹, if we assume typical mixing ratios of 100 pptv HCl (Haskins et al., 2018; Angelucci et al., 2021) and 10 to 40 pptv NO₃ (Crowley et al., 2010), which is a factor ~350 lower than that required.



As the reaction between NO₃ and HCl cannot explain the nighttime production of Cl atoms, we consider the potential role of OH radicals, which react much more rapidly with HCl (R15, $k_{\text{OH}+\text{HCl}} = 7.8 \times 10^{-13}$ cm³ molecule⁻¹ s⁻¹, IUPAC (2025)).



OH radicals are present at night owing to their formation in the ozonolysis of unsaturated hydrocarbons (Atkinson et al., 1992; Cox et al., 2020), and their abundance has been the subject of much research, with concentrations found to be varying between 9.1×10^4 and 7×10^6 molecules cm⁻³ at night time (Bey et al., 1997; Faloon et al., 2001; Ren et al., 2003; Khan et al., 2008). Due to the absence of OH measurements during BISTUM24, we assume a nighttime concentration of 1×10^5 molecules cm⁻³ that was determined in a similar agricultural rural environment (Bey et al., 1997). For the HCl mixing ratio, we again assume a value of 100 pptv HCl (derived from continental concentrations) and calculate a Cl production rate of 1.9×10^2 atoms cm⁻³ s⁻¹, which is a factor 100 - 200 smaller than the value of $(2.0 - 3.9) \times 10^4$ atoms cm⁻³ s⁻¹ derived above.

The nocturnal ozonolysis of unsaturated hydrocarbons also leads to the formation of Crige-intermediates (Cox et al., 2020; Caravan et al., 2021). Studies of the reaction of HCl with Crige-intermediates appears however not to form Cl or ClO but R₁R₂OOCI compounds, where R₁ and R₂ are organic groups (Wang and Lee, 2024).

In addition, we also consider the direct formation of ClO through the reaction of OH with HOCl (R16):



for which the rate coefficient at 298 K is $k_{\text{OH}+\text{HOCl}} = 5.0 \times 10^{-13}$ cm³ molecule⁻¹ s⁻¹ (IUPAC, 2025). Assuming again an OH concentration of 1.0×10^5 molecules cm⁻³ during night (Bey et al., 1997) and nocturnal campaign mean mixing ratio of 50 pptv for HOCl we derive a ClO production rate of 1.2×10^3 ClO cm⁻³ s⁻¹ which is a ten-fold time larger than the rate of formation of Cl from OH + HCl but falls well short of the value required to explain the observations of nighttime ClONO₂.

We thus conclude that the presence of ClONO₂ at nighttime, despite its rapid heterogeneous loss to particles, cannot be explained by the OH-induced conversion of HCl and HOCl to Cl and ClO, even within

the major uncertainties related to the estimations of the HCl and OH levels for which measurements were not available. We note however, that nighttime Cl levels of 2.0×10^4 atoms cm^{-3} have been reported in the urban UK (Khan et al., 2008), although the authors were not able to name a Cl source. Such levels of Cl result in a ClO production rate of 2.4×10^5 molecules $\text{cm}^{-3} \text{s}^{-1}$ which is a factor 10 larger than at required to explain our observations.

At this point, we examine the possibility that ClONO₂ is actually significantly longer lived at night than so far calculated based on an uptake coefficient of $\gamma = 0.027$ (IUPAC, 2025), which is the result of laboratory experiments performed on inorganic aqueous solutions containing sulphate, halides etc. We now draw analogy to the heterogeneous uptake to aqueous particles of another di-acid anhydride, N₂O₅ for which γ from laboratory studies is also very similar (~ 0.02 , (IUPAC, 2025)). In contrast to ClONO₂, the tropospheric, multiphase chemistry of N₂O₅ has been the subject of many studies and the rate of uptake to “real” atmospheric particles that are internal mixtures of organics, sulphates, nitrates etc. is a strong function of composition, where the presence of organic has been observed to reduce γ significantly (Bertram et al., 2009). As the mechanism of uptake of N₂O₅ and ClONO₂ to aqueous particles is expected to be similar (both hydrolyze/ionize on/at the surface) it is very possible that γ and the rate of uptake of ClONO₂ is greatly reduced compared to the values calculated above, and that the source term required to generate the observed mixing ratios of ClONO₂ is actually lower. In the absence of laboratory studies investigating the dependence of γ (ClONO₂) on e.g., particle organic content, this remains speculative. In addition, while no appropriate mechanism is known to us, we cannot rule out alternative (potentially multiphase) routes to ClONO₂ formation at nighttime may be more important than the gas phase reaction between ClO and NO₂.

However, to illustrate the potential importance of nocturnal Cl production we calculate its effect on the methane lifetime. Based on the measurement of ClONO₂, we derived a nocturnal Cl production rate of $(2.0 - 3.9) \times 10^4$ atoms $\text{cm}^{-3} \text{s}^{-1}$ (see above). We can combine this with the fact that $\sim 25\%$ of the Cl atoms formed will react with CH₄ (see above) to calculate a CH₄ lifetime of ~ 45 years with respect to nocturnal loss via reaction with Cl atoms. Given that the lifetime (i.e., the inverse reaction rate) of the important climate gas methane is of the order of 10 years (predominantly through reaction with OH) this translates to a $\sim 15\%$ fractional contribution to the reaction rates, which can be considered significant. We note that this calculation is based on the assumption that ClONO₂ is formed solely via gas phase reaction of ClO and NO₂. A heterogeneous process forming ClONO₂ that does not require the formation of Cl atoms would have no effect on hydrocarbon oxidation rates. A more rigorous assessment of the global impact of regional chlorine activation, for example regarding the methane lifetime, requires further related observations, inclusion of realistic chlorine activation scenarios and chlorine photochemistry in global models.

4.5.3 Formation and diel cycle of Cl₂ and HOCl

Median diel cycles of HOCl and Cl₂ are depicted in Fig. 4.6 and show that both have maxima of 60 - 70 pptv in the afternoon, implying that both are largely of photochemical origin. Strong correlations of Cl₂ ($r^2 = 0.88$) and HOCl ($r^2 = 0.85$) with O₃ indicate a photochemical source.

Cl₂ is known to be formed in the reaction between gaseous chlorine species such as ClNO₂, ClONO₂ and HOCl with pCl⁻ in acidified aerosol, which may help to explain the timing of the peak Cl₂ mixing ratio in the afternoon (phase III) after maximum irradiance (R4, R9, R10, and Oum et al. (1998)). In addition to the daytime peak, a slight increase in Cl₂ levels was monitored between 04:00 to 07:00, i.e., between

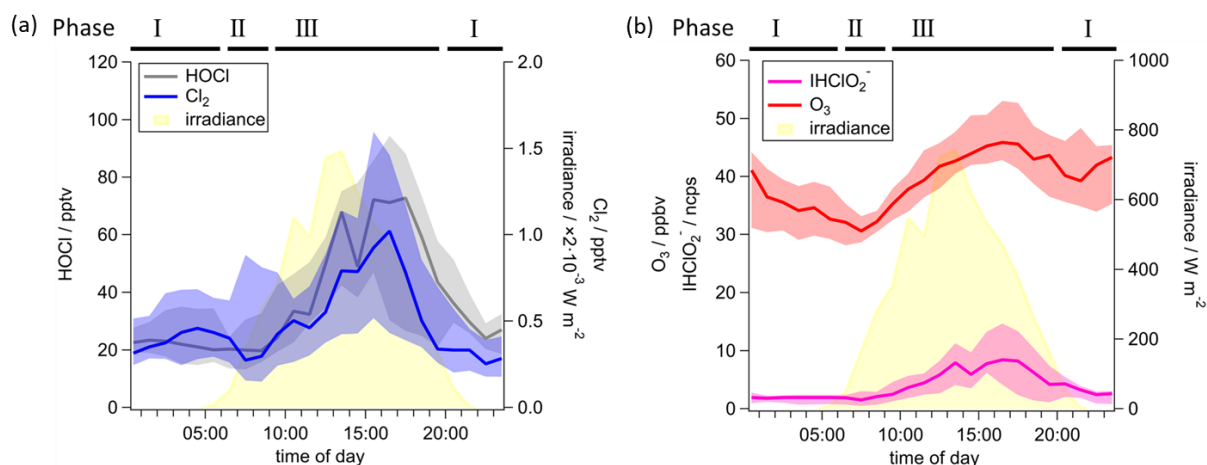


Fig. 4.6: The diel cycle shows an increase of HOCl (grey) and Cl₂ (blue) mixing ratios with higher irradiance (yellow) (a). IHO₂Cl⁻ (pink) is measured during daytime, when O₃ mixing ratios (red) are enhanced (b). Lines represent the median and the interquartile ranges are given as shaded area. The diel cycles only consider data from the “marine-anthropogenic” period of the BISTUM24 campaign in local time.

phase I and II. This observation may also be linked to the entrainment of O₃/N₂O₅-rich air from the residual layer into the nocturnal boundary layer (Sect. 4.5.1) in agreement with Xia et al. (2020), so that particle chloride can be converted into chlorine-containing gases such as Cl₂ and ClONO₂. Cl₂ is also formed in other multiphase processes involving chloride and the intermediary of NO₃⁻, O(³P), Fe(III) and TiO₂ (Li et al., 2020b; Peng et al., 2022; Dalton et al., 2023; Chen et al., 2024; Dai et al., 2025). For HOCl, the recognized and only atmospherically relevant route to its generation in the gas phase is through the reaction between two radical species, ClO and HO₂ (R7) which takes place predominantly during the daytime when active photochemistry leads to high radical concentrations. The particle phase hydrolysis of ClONO₂ (R11) also leads to the formation of HOCl, which can either degas from the particles or react with particle chloride to form Cl₂. As Cl₂ is weakly soluble, this will likely transfer to the gas phase where it is rapidly photolyzed (Table 4.2) to reform Cl atoms that, in turn, reform HCl and the HOCl precursor ClO. As HOCl is also photolabile, its gas phase mixing ratios are determined by chemical cycles that are strongly dependent on actinic flux and the availability of, e.g., O₃.

4.6 Daytime Cl-atom Production Rates

While the OH radical is the primary driver of oxidation of the vast majority of atmospheric trace gases, the oxidation rates of certain trace gases can be augmented by the presence of Cl atoms. In this section, we examine Cl-atom production rates $P(\text{Cl})$ from the photolysis of ClNO₂, ClONO₂, HOCl and Cl₂ (R3, R5, R12, R13) over the diel cycle:

$$P(\text{Cl}) = J_{\text{ClNO}_2} [\text{ClNO}_2] + J_{\text{ClONO}_2} [\text{ClONO}_2] + 2J_{\text{Cl}_2} [\text{Cl}_2] + J_{\text{HOCl}} [\text{HOCl}] \quad (4.3)$$

The photolysis frequencies J of ClNO₂, ClONO₂, HOCl and Cl₂ were derived for each trace gas through the diel cycle (data provided by the TUV calculator for cloudless conditions for the BISTUM24 location (UCAR, 2025)), corrected for reduced irradiance, measured using a local on-site pyranometer. We recognize that clouds do not impact irradiance in the same way for all wavelengths; however, considering cloudiness provides a more accurate estimate of real photolysis rates.

The results of the calculations are summarized in Fig. 4.7 which shows that Cl production follows the actinic flux, reaching a maximum of $(1.0 \pm 0.47) \times 10^6$ atoms $\text{cm}^{-3} \text{s}^{-1}$ in the period where we sampled “marine-anthropogenic” air. The maximum for “continental-unpolluted” air is a factor ~ 6 lower ($1.6 \pm 0.7) \times 10^5$ atoms $\text{cm}^{-3} \text{s}^{-1}$. The daytime maximum Cl production rates are broadly consistent with summertime observations from Los Angeles (6.2×10^5 atoms $\text{cm}^{-3} \text{s}^{-1}$), Houston (4.7×10^5 atoms $\text{cm}^{-3} \text{s}^{-1}$), Beijing (1.6×10^5 atoms $\text{cm}^{-3} \text{s}^{-1}$) and wintertime Manchester-UK (3.0×10^5 atoms $\text{cm}^{-3} \text{s}^{-1}$). Note however, that the values for Houston considered only Cl_2 and ClONO_2 as Cl sources (Faxon et al., 2015), while additionally, for Los Angeles $\text{HCl} + \text{OH}$ contributes significantly (Riedel et al., 2012). In the Beijing-study a minor role was attributed to HOCl and ClONO_2 (not quantified and considered in Le Breton et al. (2018)) and ClONO_2 was considered to be the only Cl sources in marine urban Manchester (Priestley et al., 2018). The fact that Cl production rates were observed in polluted and marine influenced regions, as well as in rural continental areas (this work) indicates the role of Cl chemistry could be more widespread than currently assumed.

The fractional contribution of each chlorine-containing trace gas to Cl atom production rates is highlighted in Fig. 4.8. HOCl is the major contributor to Cl production from photolysis, accounting in the morning for 10% for “marine-anthropogenic” air masses and 49% for air masses from “continental-unpolluted” source regions. After $\sim 12:00$, the HOCl contribution is in both cases between 70% and 80% (see Fig. 4.8a and b).

Contrary to HOCl , the contribution of ClONO_2 to Cl production decreases from 85% at sunrise (07:00) to 3% after 13:00 if the air masses were transported from the “marine-anthropogenic” source region. The contribution of ClONO_2 in continental unpolluted air, meanwhile, is significantly lower, ranging from 6% to 33%. This observation emphasizes the importance of ClONO_2 as a nighttime reservoir species, particularly for air masses affected by polluted areas.

For air masses with marine-anthropogenic signature, Cl_2 contributes approximately 5% to Cl production rate in the morning hours, increasing to 20% from 13:00 on. Despite its much lower mixing ratios, after 11:00 the contribution of Cl_2 is larger than that of ClONO_2 , which is related to the absorption cross section of Cl_2 which overlaps much more with the actinic flux (Fig. S9.15). The contribution of Cl_2 to Cl production rates from continental unpolluted air remains around 20% throughout the day.

Low daytime concentrations of maximum 3.3 pptv, coupled with low absorption cross-sections at the wavelengths of the actinic flux, mean that ClONO_2 plays a minor role in Cl production. Fig. 4.8a indicates that ClONO_2 contributes only 0.5% to Cl production, independent of the time of day, which is consistent with conclusions of Le Breton et al. (2018).

The impact of a summed, maximum daytime Cl production rate of $\sim 1 \times 10^6$ atoms $\text{cm}^{-3} \text{s}^{-1}$ (at $\sim 14:00$ local time) can also be illustrated by estimating its impact on CH_4 oxidation. As discussed in Sect. 4.5.2, $\sim 25\%$ of the Cl atoms generated under these conditions will react with CH_4 . The CH_4 loss due to Cl during one hour at noon is ~ 40 pptv. This can be compared to the CH_4 loss in the same period owing to reaction with OH, which is ~ 400 pptv, assuming OH concentrations of 1×10^7 molecules cm^{-3} using 1.9 ppmv CH_4 . While these estimations highlight the potential of Cl compared to OH regarding CH_4 oxidation, rigorous assessment of the impact of chlorine chemistry on a long-lived climate gas such as CH_4 requires implementing appropriate chemistry into global chemistry-transport models, which is beyond the scope of this manuscript.

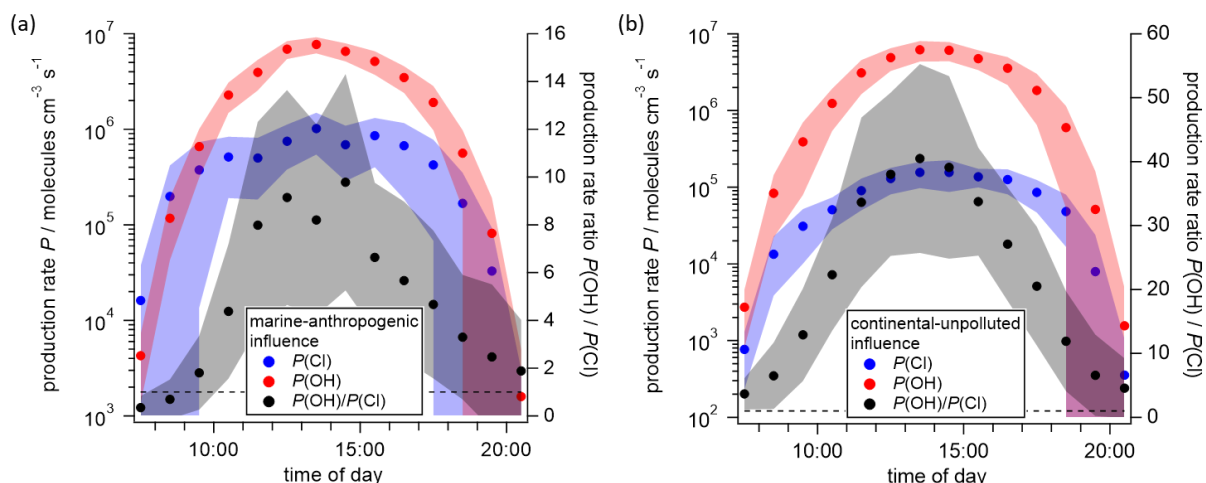


Fig. 4.7: Median production rates of Cl ($P(\text{Cl})$, blue) and OH ($P(\text{OH})$, red) from photolysis and OH-reaction reach a maximum at noon as well as the ratio of the production rates ($P(\text{OH})/P(\text{Cl})$, black) for the air masses with marine-anthropogenic (a) and with continental-unpolluted influence (b). The shaded areas represent interquartile ranges, while the dotted line indicates an equal production of Cl and OH.

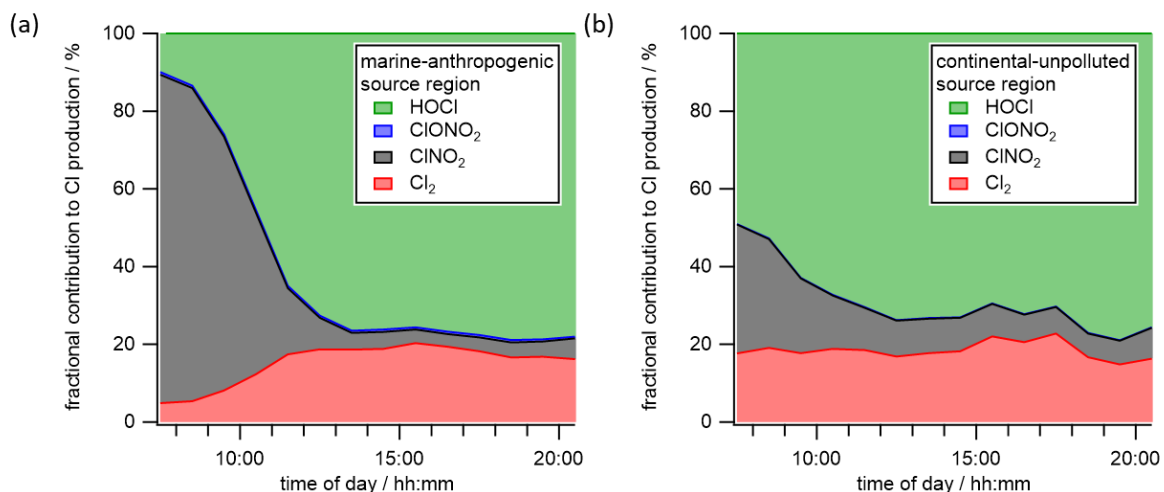


Fig. 4.8: Fractional contribution of various inorganic chlorine species to the diurnal total chlorine production rate is displayed for the air masses with marine-anthropogenic (a) and with continental-unpolluted influence (b).

4.7 Photolysis of HOCl as Source of OH

As shown in Reaction R12, the photolysis of HOCl generates both a Cl atom and an OH radical. In the following, we compare the rates of formation of OH through the diel cycle arising from HOCl photolysis with the rate of OH formation from the photolysis of O₃ in the presence of water-vapor (R19), traditionally considered the major primary source of atmospheric OH.



The primary photochemical production rate of OH from O_3 , $P_{O_3(OH)}$ was calculated from the O_3 photolysis frequency $J_{O_3(^1D)}$ modified using the rate coefficients for the $O(^1D)$ reaction with H_2O or quenching by N_2 and O_2 in Eq. (4.3). Rate coefficients k were taken from the IUPAC evaluation (IUPAC, 2025).

$$P_{O_3(OH)} = J_{O_3(^1D)} [O_3] \times 2k_{O(^1D)+H_2O} [H_2O] / (k_{O(^1D)+H_2O} [H_2O] + k_{O(^1D)+N_2} [N_2] + k_{O(^1D)+O_2} [O_2]) \quad (4.4)$$

The diurnal cycle of the Cl and OH production rates during the “marine-anthropogenic” and “continental-unpolluted” periods (Fig. 4.7) show that for both periods the OH production from O_3 reaches a maximum of $\sim 7 \times 10^6$ molecules $cm^{-3} s^{-1}$ around 13:00. For comparison, the maximum Cl (and thus OH from photolysis of HOCl) production rate is a factor of seven lower for the “marine-anthropogenic” case (Fig. 4.7a) and a factor 40 smaller for the “continental-unpolluted” case (Fig. 4.7b). However, in the early morning, in marine-anthropogenically influenced air the Cl production rate is more rapid than that of OH, which results from the red-shifted absorption spectra of Cl_2 , HOCl and $ClNO_2$ compared to O_3 and thus better overlap with the early morning actinic flux (Fig. 4.7a). This is entirely consistent with the findings of Phillips et al. (2012) at a measurement site 40 km away from our site when marine-influenced air was encountered. In this early morning period, the generation of Cl atoms results in the oxidation of hydrocarbons and thus increases the rate of formation of organic peroxy radicals that play an important role in daytime, photochemical ozone formation.

Tropospheric OH formation occurs via primary formation from O_3 photolysis as well as by recycling through reaction of HO_2 with NO and (generally less importantly) the photolysis of peroxides and HONO (Lelieveld et al., 2004; Chua et al., 2023). HOCl is generally not considered as a potential contributor to OH production due to a lack of HOCl data. However, Fig. 4.9a shows that while OH formation from photolysis of O_3 is dominant, OH formation from HOCl (compare Eq. (4.3)) is still significant at some times of the day when the actinic flux at the shorter wavelengths needed to photolyze O_3 is relatively weak (see Fig. 4.9b). For marine-anthropogenically influenced air masses, the contribution of HOCl photolysis to OH formation approaches 40% at sunrise and sunset, compared to 8% at noon. For the “continental-unpolluted” air masses, the contribution of HOCl to OH ranges from 2% at noon to 17% at sunrise and sunset. This analysis shows that HOCl should be considered as a source of primary OH formation, especially during the morning and the evening hours.

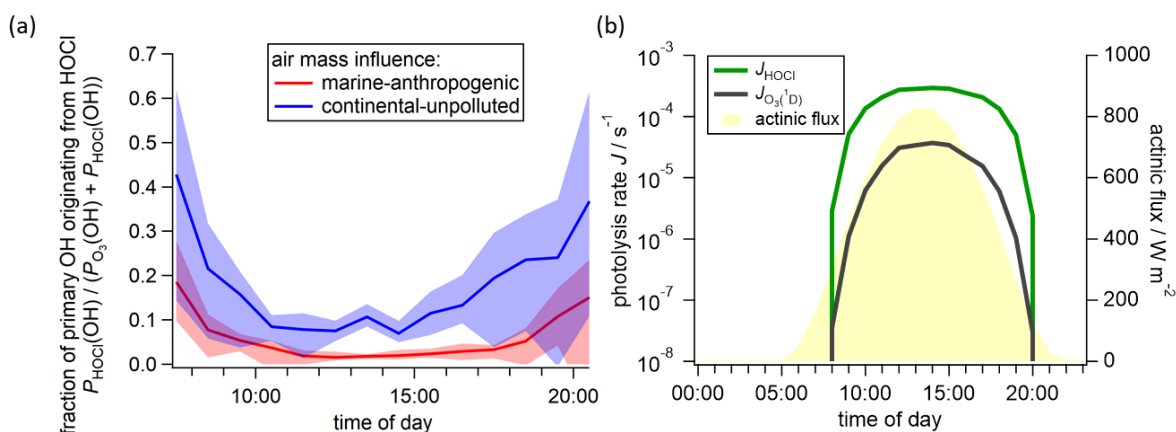


Fig. 4.9: The median fraction of primary OH originating from HOCl for both source regions (a). The actinic flux (yellow), photolysis rates of HOCl (J_{HOCl} , green) and O_3 ($J_{O_3(^1D)}$, grey) were calculated for the diurnal cycle, using the TUV calculator (UCAR, 2025), and show enhanced HOCl photolysis in the early morning (b).

4.8 Conclusion

Several inorganic chlorine species (Cl_2 , HOCl, ClNO_2 and ClONO_2) were measured with an Iodide-CIMS at a continental measurement site in rural central Germany, ~ 400 km from the nearest coastline. The largest mixing ratios were detected when 48 h-backward trajectories indicated that the air mass had passed over marine and polluted regions. The dominant chlorine-containing trace gases were ClNO_2 during the night and early-morning and HOCl throughout the day. A consistent feature of the ClNO_2 diel profile was an early morning peak, which was associated with vertical mixing. In unpolluted air, only HOCl and Cl_2 in reduced amounts were observed.

In air masses with marine-anthropogenic influence we observed not only ClNO_2 but also ClONO_2 along with enhanced particulate chlorine during the nighttime. ClONO_2 was thus observed for the first time in tropospheric air masses, albeit at low mixing ratios of 2 – 3 pptv. Laboratory experiments helped rule out that this observation was not an artefact resulting, e.g., from reaction of ClNO_2 with IO_x^- in the IMR of the instrument. Calculations of the total chlorine production rate from the photolysis of the observed species reveal values of 1.0×10^6 atoms $\text{cm}^{-3} \text{s}^{-1}$ for air masses with marine polluted source regions, and 1.6×10^5 atoms $\text{cm}^{-3} \text{s}^{-1}$ for continental clean ones. Depending on the air mass source region, ClNO_2 contributed 30-90% to Cl atom production up to three hours after sunrise and 5-10% throughout the rest of the day. Additionally, throughout the day, HOCl contributed 10-85% to Cl production, while Cl_2 was responsible for 5–20%.

Cl formation contributed significantly to radical generation (and thus oxidation rates) in the early morning implying significant peroxy radical and ClO formation rates. The formation of OH radicals from photolysis of HOCl was compared to that by photolysis of O_3 and shown to make a significant contribution for air masses that had passed over maritime and polluted regions before reaching the site with a maximum contribution of 40% of the total primary OH formation at sunrise and sunset.

Consequentially, we show that N_2O_5 -induced activation of chlorine from its particle reservoir into photolabile, gas phase forms has repercussions for the lifetimes of many hydrocarbons, highlighting methane in remote continental areas distant to source regions where it affects local chemical processes.

Author contributions: LM performed CIMS measurements, trajectory calculation, analyzed the data and drafted the manuscript. FF and FD performed ground-based measurements with the MoLa and data post-processing. JNC performed CRDS, TD-CRDS and FT-IR measurements, synthesized the ClONO_2 and helped with calibration. All authors discussed the data and the presented results. All co-authors commented on the manuscript.

Acknowledgements: The authors thank Thomas Böttger and Philipp Schuhmann for support during the BISTUM24 campaign, and Laura Wüst for preparation of N_2O_5 crystals (all Max-Planck-Institute for Chemistry). Additionally, the authors thank Yijing Chen (Tsinghua University), Lewis Marden and Jake Willow (both from University of York), Cheng Wu (University of Gothenburg) and Cora Young (York University) for discussions about secondary ion chemistry.

Financial support: This work was supported by internal funding from the Max Planck Society. LM is funded by the Deutsche Forschungsgemeinschaft (DFG, German Research Foundation) – TRR 301 “TPChange” (Project-ID 428312742).

5 Development and Application of the Measurement Drone FLab

This chapter contains a paper that has been published as

Moormann, L., Böttger, T., Schuhmann, P., Valero, L., Fachinger, F., Drewnick, F.: The Flying Laboratory FLab: development and application of a UAS to measure aerosol particles and trace gases in the lower troposphere, *Atmos. Meas. Tech.*, 18, 1441–1459, <https://doi.org/10.5194/amt-18-1441-2025>, 2025

Contribution to this manuscript by Lasse Moormann:

As the first author of this work, I conceptualized the FLab setup together with the co-authors. Prior to installation, I calibrated the FLab instruments and conducted all long-term measurements with the instruments in the FLab, in order to estimate their statistical uncertainty. I then analyzed the data. I wrote the permission proposal for the aerial deployment of FLab (for the measurement sites in sections 2.5.2 and 2.5.3). I programmed software to receive and convert data transmitted online to the FLab ground station, as well as software tools to display measured data online and convert data from multiple storage locations into a uniform format. I also added several drone-specific diagnostic functions to the PANDA analysis tool (Fachinger and Moormann, 2025), which help to analyze vertical profiles. During field experiments, I designed flight patterns, organized flights and served as pilot or co-pilot. I also analyzed all the data from this study, prepared all the figures, and wrote the manuscript, which was revised with input from all the co-authors.

5.1 Abstract

Unmanned aircraft systems (UAS) are gradually being established in environmental research to study boundary layer conditions and phenomena *in situ*; however, due to payload limitations, UAS can typically measure only a limited number of atmospheric variables simultaneously. Here we present the Flying Laboratory (FLab), a hexacopter equipped with six instruments to measure aerosol particles (particle number concentration and size distribution; $PM_{1/2.5}$ and black carbon mass concentration), trace gases (CO_2 , O_3), and meteorological variables (temperature, relative humidity, pressure, wind) in the lower troposphere in real time and with high temporal resolution. The instrumentation has been selected to provide an overview of relevant variables in urban and semi-urban environments and especially in the vicinity of aerosol sources. This paper describes the development of the technical setup of the Flying Laboratory, the characterization of the measurements with respect to horizontal and vertical motion of the UAS, and the optimization of measurement flight patterns. During two field experiments, FLab was applied to bridge the gap between ground-based and aircraft-based profiling measurements and to perform hourly vertical profiling flights up to 300 m above a ground-based reference station for eight hours. These applications demonstrate the capability of FLab to capture the evolution of the lower convective boundary layer during the day and the vertical particle transport in the afternoon up to 200 m above ground.

5.2 Introduction

Atmospheric aerosol particles have a profound impact on air quality, human health, and global climate (Li et al., 2017). However, the tropospheric distribution of aerosol particles is far from being homogeneous, with strong gradients in aerosol and trace gas concentrations, especially in the vicinity of sources. The situation is further complicated by the dynamics of the planetary boundary layer (PBL), which affects the transport of aerosol particles and trace gases and thus their distribution and concentrations (Stull, 1988). Therefore, to fully capture and characterize an emission plume, it must be analyzed in all three spatial dimensions, especially also vertically. However, even in the absence of strong sources, PBL dynamics can lead to strong inhomogeneities of pollutant distributions, requiring a comprehensive, more than one-dimensional approach for their characterization.

For a detailed characterization of the aerosol and trace gas concentrations within the PBL, remote and *in situ* methods can be used. Remote sensing methods include the use of lidar and radar, which are capable of providing vertically resolved information on, for example, aerosol backscatter. However, these methods are limited by near-field dead zones close to the instrument, leaving the lowermost part of the atmosphere uncovered. They can be deployed both stationary (ground-based) and on mobile platforms such as aircraft or satellites. While stationary deployment provides detailed information with high time resolution for a single location, the latter allows a broader view of the troposphere by capturing larger scale atmospheric phenomena (Hindman et al., 1984; Kotthaus et al., 2023), at the cost of a more limited temporal resolution. However, all of these remote sensing methods rely on the propagation of electromagnetic waves, which limits the observable variables to properties related to the scattering and absorption of these waves (Si et al., 2021).

In contrast, *in situ* methods involve direct measurements at the location of interest. Ground-based stationary measurements with high quality instrumentation can provide detailed information about the temporal evolution of, e.g., pollutant concentrations (Drewnick et al., 2012; Schrod et al., 2020) with few legal and instrumental restrictions, but only at a single location and without information

about the horizontal or especially the vertical distribution. This can be overcome by the use of airborne research platforms such as balloons or aircraft, which can be equipped with *in situ* measurement instruments and perform kilometer-scale flights up deep into the stratosphere (Ouchi et al., 2019; Mahnke et al., 2021). However, the lower boundary layer in particular is only limitedly accessible by these means. Unmanned aircraft systems (UAS), with their ability to ascend from the ground to the upper troposphere, have filled this gap in recent years and can complement networks of ground-based measurement stations for a three-dimensional view of the lower boundary layer (Falco et al., 2021; Rabins et al., 2023). In addition to their affordability, an advantage of UAS is their precise maneuverability, which allows them to perform vertical profiling with minimal horizontal deviation or defined mapping of targeted areas or volumes.

Depending on the scientific objective, fixed- or rotary-wing UAS are used. Fixed-wing UAS can be used to probe larger areas with flight distances and altitudes of up to several kilometers for several hours, but require runways or landing nets and experienced pilots (Roberts et al., 2008; Reuder et al., 2012). In contrast, rotary-wing UAS are more limited in-flight duration, but can be controlled by less experienced personnel and allow for even more flight patterns, such as hovering. Because of these advantages, hexacopter and other rotary-wing UAS have recently found many applications in PBL research and are gradually becoming established in tropospheric research (Sziroczak et al., 2022; Hervo et al., 2023).

Applications include the investigation of turbulent fluxes, boundary layer stability, or condensation phenomena (Adkins, 2020; Hamilton et al., 2022), but also wind field measurements at wind turbines (Adkins and Sescu, 2017; Li et al., 2022), or the investigation of wind turbine propeller efficiency degradation due to icing (Gao et al., 2021). Aerosol particle and trace gas sensors are commonly deployed on UAS for the investigation of particle transport, photochemical processes, or tropospheric dynamics (Roberts et al., 2008; Miller et al., 2024). In addition to such studies in typically unpolluted environments, local emission sources are also often investigated, whether natural sources such as coastal wave breaking or volcanic activity (Brady et al., 2016; Galle et al., 2021; Lappin et al., 2023; Radtke et al., 2023) or anthropogenic sources such as landfills, refinery platforms, agricultural farms, or other industrial sites (Golston et al., 2018; Allen et al., 2019; Castro Gamez et al., 2019; Gålfalk et al., 2021; Andersen et al., 2023; Bonne et al., 2024).

A critical limitation for such studies, however, is the limited payload of the UAS, which allows either very limited information with a single or few high quality instruments (Womack et al., 2022), or the use of multiple lightweight but lower quality sensors, which can provide data of low and frequently questionable quality and often require complex correction procedures (Schuldt et al., 2023). Offline analyses of aerosol filter samples or, for the gas phase, desorption tubes, Tedlar bags, or Aircore tubes have also been applied (Andersen et al., 2023; Liang and Shen, 2023; Niedek et al., 2023; Zhu et al., 2024), but all have the disadvantage of being both time consuming and limited to the investigation of only a few variables, typically at a very limited number of locations during a single flight. A first approach to overcome this limitation was presented by Brus et al. (2021a) and Pohorsky et al. (2024), who developed different modular systems for aerosol particle and gas phase analysis which were mounted on a rotary-wing UAS or a tethered helikite, respectively. While this is a step towards a more comprehensive investigation of the troposphere, the simultaneous measurement of a variety of aerosol, trace gas, and meteorological variables is crucial for understanding microphysical processes, especially in the PBL. However, to our knowledge, no UAS capable of providing such a broad overview has been presented in the literature due to the aforementioned obstacles.

Here we present the development and application of the hexacopter-based Flying Laboratory (FLab), which can be used to study aerosol particles, trace gases, and meteorological variables simultaneously and in real time in the lower boundary layer. The instrumentation was selected to cover relevant variables commonly used for air pollution studies in semi-urban and urban environments, especially in the vicinity of aerosol sources, and to mirror key variables simultaneously measured on-board the ground-based research platform MoLa (Mobile Laboratory, Drewnick et al. (2012)).

Section 5.3 describes the technical and instrumental setup of FLab, with emphasis on the arrangement of the instruments for undisturbed measurements and the electronic setup. In Section 5.4, we analyze and discuss the uncertainty of the measured variables on board FLab and possible measurement biases due to the flight motion. Finally, Section 5.5 presents some exemplary research applications that illustrate the benefits of hourly vertical profiling measurements and demonstrate how UAS-based measurements can bridge the gap between ground-based and airborne measurements.

5.3 The Flying Laboratory FLab

5.3.1 Description of the FLab platform

The Flying Laboratory is based on a commercial DJI M600 hexacopter, which has a base weight of 9.1 kg (including batteries) and is designed to carry a payload of up to 6 kg. In its current configuration, FLab has a diameter of 1.58 m and a height of 1.86 m. The maximum flight velocity is 18 m s^{-1} with a maximum ascent and descent rate of 5 m s^{-1} and 3 m s^{-1} , respectively. FLab is capable of operating at altitudes up to 2500 m AMSL (above mean sea level; higher with an optional high-altitude propeller set) and at distances up to 5 km; however, in our measurements legal limitations restrict its operation to altitudes of up to 500 m AGL (above ground level) and horizontally up to distances where the aircraft is still visible with the bare eye.

The payload consists of instruments for the measurement of aerosol particles, trace gases, and meteorological variables, as well as of electronic infrastructure for power supply and data management. Most of the payload is installed in an aluminum rack mounted under the UAS to keep the center of gravity of the entire system below the UAS body (Fig. 5.1a). In addition, an anemometer and an optical particle counter (see Section 5.3.2 for details), two instruments for which undisturbed advection of ambient air is critical, are located at a distance of 110 cm and 100 cm above the rotor plane, respectively. They are mounted on a frame consisting of two vertical carbon fiber tubes with custom 3D-printed organic polymer cross connectors to minimize vibration during operation at the lowest possible weight. In addition to these two instruments, a FLARM transponder (ATOM UAV, FLARM Technology AG), which is a traffic awareness and collision avoidance system for airborne objects and is quasi-mandatory in the European Union for the authorization of flights above 120 m AGL (European Parliament and Council, 2019), is also mounted at an elevated position on the frame. This position was chosen to allow unobstructed radio emission from the device. For nighttime measurements, the frame can be equipped with an LED band for better visibility of the UAS.

The FLab power supply is divided into two completely independent units (Fig. 5.1b). The UAS, including propulsion, UAS electronics and FLARM, is powered by six intelligent flight batteries (DJI TB47S, LiPo 6S, 99.9 Wh). The FLab payload, including instruments and data acquisition electronics, is powered by an on-board battery (type: GBA 2.0 Ah, Robert Bosch Power Tools GmbH), or alternatively, between flights, by the custom-built 18 V ground power unit, to which it can be switched without interruption. This allows uninterrupted operation of the payload electronics when the on-board battery is changed.

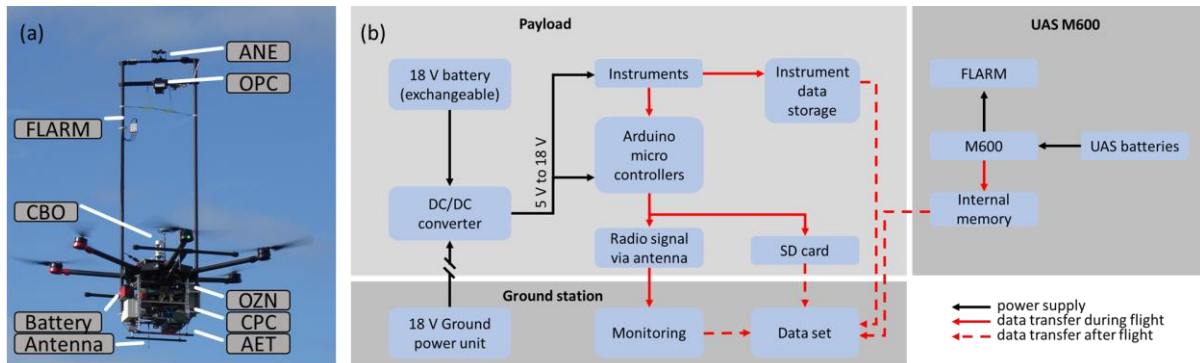


Fig. 5.1: Photo of FLab with the positions of the measurement instruments and the components of the electronic infrastructure indicated; see Table 5.1 for an explanation of the acronyms (a). Schematic layout of the FLab electronics, showing the power supply infrastructure (black arrows) and data management (red arrows) for different parts of FLab (b).

Both power supplies provide 18 V power to multiple DC/DC converters that generate voltages from 5 V to 18 V to supply all instruments as required.

The complete FLab dataset of an aerial mission includes instrument data and system data from the M600 UAS (Fig. 5.1b). The ozone monitor and the aethalometer store their data in independent internal memories. In addition, both instruments as well as all the other instruments transmit measurement data in real-time to Arduino Mega microcontrollers (ATmega 2560). Due to the low processing power of the Arduino Mega, three microcontrollers are required in the FLab to receive raw data and to process the partially large output strings to compact data packages. An Arduino Uno (ATmega, 328P) is used to store the processed instrument data on a common SD card for all instruments. The data stored on the on-board SD card are simultaneously transmitted to the ground station via a serial transceiver module (HM-TRP-RS232 series 100 mW, Shenzhen Hope Microelectronics Co., Ltd., China) and an antenna (DeLOCK ISM 433 MHz, type 88877, Tragant GmbH, Germany) located under the payload rack. At the ground station, the data is recorded along with the current ground station time. The transmitted data can be evaluated in real time by a crew member who can alert the pilot about any unexpected weather conditions or plumes. The M600 UAS stores various technical variables such as orientation, velocity, GPS location, propeller rotation rate, etc. on an internal storage device. However, this data is not accessible to the crew during operation and must be downloaded after the flight for further processing (Fig. 5.1b).

This results in four data sets: the M600 UAS data set, two instrument data sets (stored individually and on the common SD card), and the data received from the ground station. All of these are merged into a single common data set by aligning them to the reference time stamps, namely those of the ground station. To do this, they are correlated with varying time shifts to the corresponding ground reference time series until the Pearson correlation coefficient is at its maximum (typically very close to 1). To align the M600 UAS data, the altitude data from the M600 UAS are correlated with the pressure data recorded by the FLab anemometer to correct for any time shift between the data sets.

5.3.2 Instrumentation

The instruments installed on board FLab were selected to cover the most relevant measurable quantities for a robust investigation of anthropogenic emission plumes and boundary layer dynamics. Therefore, we chose instruments for the following variables: particle number concentration (particle

diameter $d_p > 10$ nm), particle size distribution (optical diameter: $0.35 \mu\text{m} < d_{\text{opt}} < 40 \mu\text{m}$; also used to determine particulate mass concentrations up to $1 \mu\text{m}$ and $2.5 \mu\text{m}$ particle diameter, i.e., PM_{10} and $\text{PM}_{2.5}$), black carbon mass concentration, O_3 and CO_2 volume mixing ratios, and meteorological variables (wind direction and speed, temperature, pressure, relative humidity). The DJI M600 can carry a maximum payload of 6 kg, which must include the instruments, but also the power supply, data acquisition electronics, and mechanical installation. Considering this limitation, the instruments had to combine aspects such as low weight and compact size with high data quality and robustness as well as high time resolution of the measurements, resulting in the FLab setup as presented in Table 5.1.

Several instruments have been modified to meet the requirements of on-board FLab operation. All instruments with RS232 interface (CO_2 monitor (CBO), condensation particle counter (CPC), O_3 monitor (OZN)) and instruments with various serial interfaces (anemometer (ANE), aethalometer (AET) and optical particle counter (OPC)) required modifications to convert the output to 5V TTL (Transistor-Transistor Logic) level, which is read by the microcontroller. From the CBO, CPC, and OZN, the housing was removed from the factory version of the instrument to reduce weight, while the AET and OPC have increased weight due to modifications to their inlet system (see Table 5.1). On the bottom side of the ANE, 1 cm^2 of the housing and a membrane (which protects the ANE electronics from condensation during extreme humidity changes) were removed to reduce the humidity sensor measurement delay. The downward-facing opening in the housing allows for rapid air exchange at the humidity sensor while the sensor is shielded from direct solar radiation, minimizing the effect of solar heating on the humidity measurement. The temperature is determined from relative humidity and speed of sound and consequently not strongly affected by solar heating. Without the membrane, the ANE relative humidity and temperature data were in best agreement with the reference instrument; therefore, we relied on the ANE rather than the CBO or OPC (see Table 5.1) for both variables in all further analyses. The CBO required additional adjustments for in-flight operation: a filter cage was removed from the optics to allow faster adjustment of the measurement volume to ambient CO_2 levels, and the in-flight data from this instrument is pressure and temperature corrected using formulae provided by the manufacturer. The CPC and OZN did not require adjustments for in-flight operation other than calibration. This is because concentrations of small particles (which dominate the CPC measurements) and gases quickly equilibrate around the FLab instrument cage due to the turbulent air motion, induced by the downwash. Since sampling and transport losses (other than diffusion) are negligible for both variables, short inlet lines to the side of the instrument cage provide representative sampling and reliable sample transport to the instruments. A short sampling delay of 2 s (derived theoretically for the design of the inlet system and experimentally validated) was found for the CPC and corrected accordingly in the data analysis. For the AET, a laminar inlet flow of $170 \text{ cm}^3 \text{ min}^{-1}$ is passed through a 30 mm long inlet tube with an inner diameter of 3.3 mm. The AET measures in dual-spot or single-spot mode (referring to the number of spots analyzed simultaneously). The dual-spot mode compensates for mass loading effects on the filter on which black carbon is collected, while the single-spot mode has a 30% higher sample flow rate and therefore reduced noise (Drinovec et al., 2015).

We tested both modes for our application (see Section 5.5). Transport losses and sampling delays can be neglected for all instruments as no long sampling tubes were used and all corresponding sampling delays are well below the 1 s temporal resolution of the data acquisition.

The installation positions of the instruments were based on the individual requirements of the respective measurements. For the anemometer and the OPC (which also measures particles with $d_{\text{opt}} > 1 \mu\text{m}$), a mounting position was chosen that is as little affected as possible by the downwash from the UAS

Table 5.1: FLab instrumentation.

Acronym	Instrument	Measured quantity	Time resolution	Installation weight (previous if modified)
AET ^a	Aethalometer	Black carbon mass concentration	2 s	425 g (420 g)
ANE ^b	Anemometer	Horizontal wind speed and direction; temperature; relative humidity; pressure	1 s*	60 g
CBO ^c	Carbon dioxide monitor	Mixing ratio of CO ₂ ; temperature	2 s**	320 g (360 g)
CPC ^d	Condensation particle counter	particle number concentration	1 s	810 g (1.7 kg)
OPC ^e	Optical particle counter	particle size distribution based on optical diameter; temperature; relative humidity	1 s	240 g*** (105 g)
OZN ^f	Ozone monitor	Mixing ratio of O ₃	2 s	1.16 kg (2.6 kg)
DJI ^g	UAS: DJI Matrice 600 (M600)	3D orientation; 3D flight velocity; GPS position; wind speed and direction; altitude based on pressure level and GPS; propeller rotation rate; various internal data	≤1 s	9.1 kg (with battery set)

^a microAeth[®] MA200, AethLabs, USA. ^b TriSonica[™] Mini, Anemoment LLC, USA. ^c CARBOCAP[®] Carbon Dioxide Probe GMP343, Vaisala Oyj, Finland. ^d Condensation Particle Counter Model 3007, TSI, Inc., USA. ^e OPC-N3, Alphasense AMETEK[®], United Kingdom. ^f Model 205 Dual Beam Ozone Monitor, 2B Technologies, Inc., USA. ^g Matrice 600, SZ DJI Technology Co., Ltd., China. *internal sampling frequency of 40 Hz, but output frequency of 1 Hz. **data output is at 1 Hz, but new data points are measured with 0.5 Hz.

***final installation weight including external pump.

propellers (see Sections 5.3.2.1 and 5.3.2.2). The measurements with the gas sensors and of the sub-micron particles (CPC and AET) are not strongly affected by the wind from the propellers. Therefore, these instruments, as well as the power supply and data acquisition electronics, were installed below the body of the UAS (the CBO directly on top of the body) to counterbalance the anemometer/OPC frame and to keep the center of gravity of the FLab as low and centered as possible.

5.3.2.1 Wind measurements on board FLab

Wind speed and direction measurements aboard a UAS are always a measurement of the wind relative to the platform. To obtain absolute values, this data must be combined with GPS velocity data from the UAS. There are several ways to determine the relative wind on board a multicopter, including installing anemometers on the UAS for a direct measurement, or estimating wind speed based on the pitch angle and power consumption of the UAS propellers. The pitch angle method is accurate, but it requires extensive study of the flight behavior of the UAS used, which can change with changes in its weight or center of mass (Wildmann and Wetz, 2022). Thus, while the M600 UAS control software provides absolute wind velocity and direction data based on this method (Mathes, 2023), these values

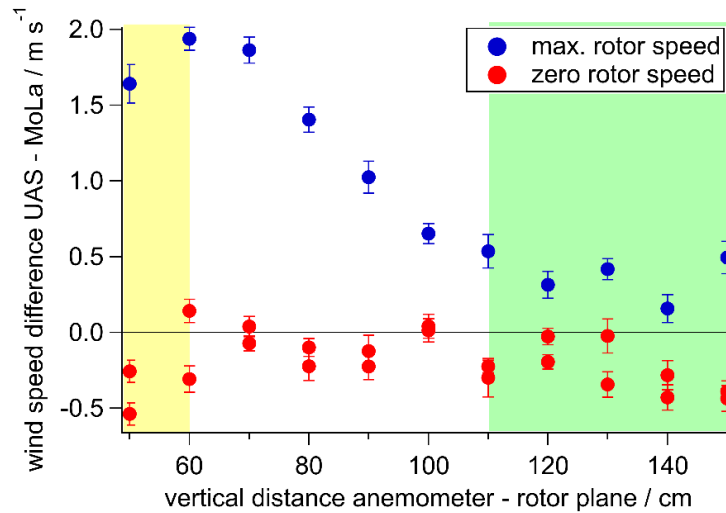


Fig. 5.2: Difference in wind velocities measured by MoLa and UAS anemometers at maximum (blue) and zero rotor speed (red), for different UAS anemometer mounting positions. The downwash-related bias was constant when the anemometer was mounted at least 110 cm above the rotor plane (green); the data are consistent with a dead volume below 60 cm (yellow). Error bars are calculated from the standard errors of the MoLa-/UAS-based measurements using Gaussian error propagation.

must be used with caution, as the flight behavior of the UAS may have changed due to the attachment of the payload, resulting in potentially biased calculations. Therefore, an anemometer was installed to directly measure the relative wind.

Multicopters perturb the surrounding wind field by aspiration of air from above and sidelong the rotors, creating a strong downwash below the UAS. External anemometers are typically installed on the aspiration side at some distance from the rotors to minimize the air perturbations produced by the propellers (Adkins, 2020; Thielicke et al., 2021). The intensity and extent of the perturbed wind field varies with the distance from the rotors and the number and size of the rotors. Therefore, the perturbed wind field needs to be investigated individually for each UAS (Abichandani et al., 2020).

In order to investigate the influence of the UAS propeller operation on the measured ambient wind speed at different mounting positions of the anemometer above the UAS propeller plane, experiments with a fixed UAS were performed. For this, it had to be taken into account that the near-ground operation of a multicopter results in a highly disturbed wind field around the aircraft. For a JF01-10 crop protection UAS of comparable size, it was found that the wind field perturbation was no longer disturbed by the ground when operating at an altitude of at least 3 m above the ground (Zheng et al., 2018). Therefore, we mounted the M600 UAS on a forklift at a height of about 5 m above ground and placed it 5 m away from a reference 2D ultrasonic anemometer (WTX520, Vaisala Ojy) mounted on the Mobile Laboratory (MoLa, Drownick et al., 2012) at the same height. The UAS anemometer was installed at heights ranging from 50 cm to 150 cm above the UAS propeller plane and was always kept at the same height as the reference anemometer. Three measurements were performed under ambient conditions for 2 minutes each: twice with the propellers turned off and once at the maximum rotation rate. During the measurement period, the absolute wind speed measured with the reference anemometer ranged from 1.4 m s^{-1} to 4.0 m s^{-1} , and the wind direction varied within a range of 132° . No disturbance of the wind measured by the reference anemometer was found when the UAS was turned on.

For each anemometer position, the difference between the averaged wind speeds measured on the UAS and on MoLa was calculated for both measurement situations, i.e., with the propellers operating

and with the propellers turned off. If there is no difference in wind speeds, it indicates 100% agreement between the FLab and MoLa anemometers. In this experiment, the propellers were operated at full speed to determine the maximum spatial extent and maximum influence of the downwash, which depends on the propeller's load and therefore may be smaller in-flight depending on the respective flight maneuver and wind conditions. The results without rotating propellers were used to ensure the comparability of the measurements with the respective instruments when the wind field was not disturbed by the UAS. Fig. 5.2 shows that without rotating propellers there is reasonable agreement between the UAS anemometer and the MoLa instrument for all anemometer positions (red markers). Under normal flight conditions, i.e., with the propellers rotating at full speed (blue markers), the largest difference between the UAS and the reference anemometers is found for the mounting position 60 cm above the propeller plane. At lower mounting heights of the anemometer, a decreasing perturbation of the wind field is observed, consistent with a dead volume close to the rotor plane, which has been proposed as a possible mounting position for hover flights (Li et al., 2023b). Since horizontal movement of the UAS would drag the dead volume into an already disturbed regime, this mounting position is not suitable for general flight operations. For mounting positions more than 60 cm above the propeller plane, the wind difference between the FLab and MoLa decreases with increasing distance from the rotor plane and stabilizes at a distance of about 110 cm. Since the position of the anemometer should be as close as possible to the UAS body in order to minimize the weight of the tube for the mounting frame and the leverage in case of strong gusts, the ideal height for mounting the anemometer is 110 cm above the rotor plane. The anemometer mount has a vibration frequency of 10 ± 1 Hz with a maximum amplitude of 2 cm, as determined during the flights using video graphical analysis. Therefore, for the 1-second anemometer data, the effects of the setup vibration on the wind measurement largely cancel out, resulting in a potential bias of less than 0.02 m s^{-1} , well within the instrument's uncertainty of 0.1 m s^{-1} given by the manufacturer (Anemoment, 2021). According to the manufacturer, the anemometer is capable of measuring 3D wind up to angles of incidence of 15° , and in our characterization measurements (Section 5.4.2), we do not observe any significant influence of the horizontal flight velocity (up to 15 m s^{-1} , which relates to a maximum tilt angle of 11°) on determined wind speed. However, it cannot be ruled out that the anemometer may still be affected by wind distortion caused by the UAS in situations with a very high pitch angle, such as when the UAS is flying into strong winds. The anemometer wind data were transformed from the body-fixed reference system via yaw, pitch, and roll angles to the terrestrial reference system using 3D rotation matrices and converted to absolute (above ground) velocities using the flight velocity recorded by the UAS (Thielicke et al., 2021).

5.3.2.2 OPC sampling inlet optimization

The optical particle counter (OPC) measures particles larger than 350 nm in optical diameter. To minimize sampling bias of aerosol particles into the instrument due to the strong airflow caused by the propellers, we mounted the OPC approximately 100 cm above the rotor plane with the inlet pointing upwards and no inlet tube attached. In this mounting position, directly below the anemometer (see Section 5.3.2.1), the perturbation of the ambient wind field by the UAS propellers is very small, resulting in a minimal influence on the sampling efficiency. Since no inlet tube is used, transport losses to the instrument can be neglected in the very short and vertically oriented inlet of the OPC.

In the original configuration of the instrument, the sample flow of the OPC is generated by a low-power fan and is determined by the particle time-of-flight through the measurement volume (Alphasense, 2019). During the first test flights of FLab, we observed a strong dependence of the OPC sample flow rate on the UAS vertical velocity (Fig. S9.16a, red markers). To reduce the influence of the vertical

velocity of the UAS on the OPC sample flow, we installed plates above the inlet and below the outlet of the OPC to shield the sample flow from the vertical motion of the ambient air (Fig. S9.16b). The effect of the plates was evaluated for different plate distances from the OPC between 3 mm and 25 mm with test flights at different vertical velocities (Fig. S9.16a, blue markers).

The most stable setup in terms of flow dependence on vertical UAS velocity was found for the configuration with a distance of 10 mm from the front plate to the inlet and 9.5 mm from the outlet of the OPC to the outlet plate (Fig. S9.16a), but some dependence of the sample flow on the flight velocity remained. Other groups have demonstrated for a similar OPC setup that an external pump stabilizes the flow and allows for a more constant particle throughput without compromising instrument performance (Bezantakos and Biskos, 2022). To further stabilize the sample flow, we replaced the low-power fan with an external pump (G 6/02 EB rotary vane pump, Metzger Technik GmbH) and sealed leaks in the OPC housing near the data output cables that would otherwise reduce the sample flow (Fig. S9.16c). Fig. S9.16a (black markers) confirms that the sample flow in this setup appears to be independent of vertical velocity, but is slightly reduced compared to the fan-driven setup.

Previous studies for the similarly constructed OPC-N2 (Alphasense AMETEK[®]) found no dependence of the measurement results on temperature > 5 °C and pressure > 700 mbar (Bezantakos et al., 2018), where our measurements also took place. Therefore, no temperature or pressure correction was applied to the data, while hygroscopic particle growth was corrected according to the Köhler theory using the meteorological data from the anemometer and an assumed Köhler κ of 0.3 for particles in continental regions (Andreae and Rosenfeld, 2008).

5.4 Characterization of FLab Performance

A series of dedicated experiments were performed with FLab to evaluate its performance in terms of time resolution and under vertical and horizontal motion.

Ground-based measurements over an extended time interval (several days) were performed at the Max Planck Institute for Chemistry in Mainz (semi-urban environment) to determine the uncertainty of the data from each instrument for different averaging intervals and thus the achievable temporal and spatial resolution (Section 5.4.1).

In-flight experiments were performed at a rural site in a wine-growing area near Ockenheim, Rhineland-Palatinate, Germany (Sections 5.4.2 and 5.4.3). At this site, a rather homogeneously mixed aerosol is expected due to the distance to the residential areas of Ockenheim (550 m to the east) and Kempten (1.1 km to the north) and to major roads, especially a highway at a distance of 900 m in the northwest-west direction (Fig. S9.17). Horizontal-only and vertical-only characterization flights were performed on 26 March and 10 April 2024, respectively, under sunny and cloudy conditions (Table 5.2). During the experiments, the weather station and corresponding MoLa trace gas and aerosol measurements (Table S9.7) with a sampling height of 6 m AGL served as reference for the FLab data.

As mentioned above, the measurement site for the in-flight characterization was chosen to be far enough away from any local sources to allow experiments to be conducted under homogeneous conditions. Since the AET was designed specifically for black carbon plume detection, this had the disadvantage that the measured black carbon mass concentrations were close to the detection limit during all flights. AET determines the black carbon mass concentration from the attenuation at five different wavelengths, with the lowest wavelength (370 nm) having the lowest noise level. Therefore,

Table 5.2: Flight patterns of the characterization flights.

Flight number	Date and local take-off time, weather condition	Flight duration	Flight pattern	Flight velocities*
F1	26 March 2024 at 15:34, sunny	14 min 56 s	Horizontal (20 legs at 6 m AGL, ± 100 m from take-off site towards north/south)	0 m s ⁻¹ , 2 m s ⁻¹ , 4 m s ⁻¹ , 6 m s ⁻¹ , 8 m s ⁻¹ , 10 m s ⁻¹
F2	26 March 2024 at 16:21, sunny	14 min 18 s	Horizontal (19 legs at 6 m AGL, ± 100 m from take-off site towards north/south)	0 m s ⁻¹ , 2 m s ⁻¹ , 4 m s ⁻¹ , 6 m s ⁻¹ , 8 m s ⁻¹ , 10 m s ⁻¹ , 15 m s ⁻¹
F3	26 March 2024 at 16:45, sunny	14 min 37 s	Horizontal (19 legs at 6 m AGL, ± 100 m from take-off site towards north/south)	0 m s ⁻¹ , 2 m s ⁻¹ , 4 m s ⁻¹ , 6 m s ⁻¹ , 8 m s ⁻¹ , 10 m s ⁻¹ , 15 m s ⁻¹
F4**	10 April 2024 at 13:20, cloudy	14 min 31 s	Vertical (7 legs from 6 m to 120 m AGL and back, hovering for 5 s in 6 m and 120 m AGL)	0 m s ⁻¹ , 1 m s ⁻¹ , 2 m s ⁻¹ , 3 m s ⁻¹
F5	10 April 2024 at 13:42, cloudy	14 min 18 s	Vertical (6 legs from 6 m to 120 m AGL and back, hovering for 5 s in 6 m and 120 m AGL)	0 m s ⁻¹ , 1 m s ⁻¹ , 2 m s ⁻¹ , 3 m s ⁻¹
F6	10 April 2024 at 14:02, cloudy	13 min 55 s	Vertical (6 legs from 6 m to 120 m AGL and back, hovering for 5 s in 6 m and 120 m AGL)	0 m s ⁻¹ , 1 m s ⁻¹ , 2 m s ⁻¹ , 3 m s ⁻¹

*0 m s⁻¹ correspond to hover flights at the turning points between the horizontal/vertical legs.

**the last ascent was performed up to 60 m AGL due to low battery capacity.

in the analysis (Sections 5.4 and 5.5), we only considered the concentration of light-absorbing species determined from the 370 nm measurement, noting that black carbon concentrations are typically determined with wavelengths from the infrared spectrum (Pikridas et al., 2019).

wavelengths, with the lowest wavelength (370 nm) having the lowest noise level. Therefore, in the analysis (Sections 5.4 and 5.5), we only considered the concentration of light-absorbing species determined from the 370 nm measurement, noting that black carbon concentrations are typically determined with wavelengths from the infrared spectrum (Pikridas et al., 2019).

Two different types of wind data were collected with FLab: in addition to the anemometer (ANE), the on-board computer of the UAS collects wind data determined from the pitch angle and rotor speed (DJI; see also Sections 5.3.2.1).

5.4.1 Instrumental time resolution and uncertainty

The operation of instruments onboard mobile platforms always requires a trade-off between extending the averaging times of the instruments to minimize the uncertainty of the data and reducing the averaging times to improve the temporal resolution and hence the spatial resolution of the data. This problem is aggravated in UAS measurements because the total sampling time during a single UAS flight is typically very limited by battery capacity (12-16 minutes in our case), and at the same time measurements over extended spatial distances with good spatial resolution are desired. In order to find a compromise that meets our measurement needs, we determined the dependence of the individual

instrumental uncertainties on the duration of the averaging intervals in dedicated laboratory experiments.

In order to quantify the uncertainty for each variable as a function of sampling and averaging time, ground-based measurements of ambient air were performed with the FLab instruments for several hours up to several days (see description at beginning of Section 5.4). During this period, local emissions and diurnal cycles caused a changing intensity of the measured variables. To separate the statistical noise in the time series from the influence of the signal's trends over time, we calculated the Allan variance. The Allan variance is the statistical variance of the differences between adjacent data points as a function of the averaging time. When plotting the Allan variance versus the corresponding averaging times (Allan variance plot, e.g., Fig. S9.18), typically a decrease of the Allan variance with increasing averaging time is observed due to decreasing influence of statistical noise. At some point, the Allan variance reaches a minimum and thereafter starts to increase again. This is when the influence of temporal trends becomes more important than statistical differences between adjacent data points. The minimum in the Allan plot separates averaging times where statistical noise dominates from those where temporal trends dominate the variability in adjacent data points (Werle et al., 1993). Depending on the observed variable, we found the minimum Allan variance between 80 s and 100 s averaging time for our instruments (Fig. S9.18). Therefore, to estimate the statistical uncertainty of the measured variables, strictly speaking, only periods up to 100 s can be considered trendless. The raw data (with temporal resolution according to Table 5.1) were averaged in increments according to the respective sampling times of interest (ranging from 2 s to 100 s). The relative standard deviations (RSD) of the data averaged in this way were calculated using a sliding window approach for a window size of 600 s. The window size was extended beyond the 100 s range (the maximum trendless averaging time according to the Allan variance analysis) in order to be able to calculate relative uncertainties for averaging intervals up to 100 s with at least 6 values in each RSD calculation. Calculations with window sizes of 100 s and 600 s showed for averaging times up to 20 s that this increase in window size leads to small relative increases (0.1% to 13% of the respective values for the shorter window size) in the RSD obtained for most variables and instruments, with the exception of CPC (+40%) and pressure measurement (+95%), two variables that have low to extremely low relative uncertainties (see Fig. 5.3). Finally, from these RSDs, the median was calculated for each target averaging time to eliminate outliers due to short-term events in the data and to minimize the influence of trends in the concentration time series.

Fig. 5.3 shows that the RSD decreases with increasing averaging time for all instruments. The magnitude of the RSD is strongly dependent on the measured quantity and the individual instrument. If purely statistical effects cause the RSD, it should decrease with increasing averaging time t with $t^{-0.5}$ (slope of the dotted line in Fig. 5.3).

Instruments that measure particle mass concentrations, such as the AET and the OPC, where the output is based on the measurement of a relatively small number of particles per unit time, should follow this $t^{-0.5}$ statistical dependence. While this is approximately the case for the OPC, a steeper decrease in RSD was found for the AET for averaging times between 10 s and 100 s. We suspect that this is due to the internal processing of the raw data by this instrument and possibly to the fact that condensation and evaporation effects on the filters increasingly cancel each other out with longer averaging times. For instruments where counting statistics are not critical to instrument performance, such as the CPC (where large numbers of particles are measured in short time intervals), the O₃ or CO₂ monitor (which

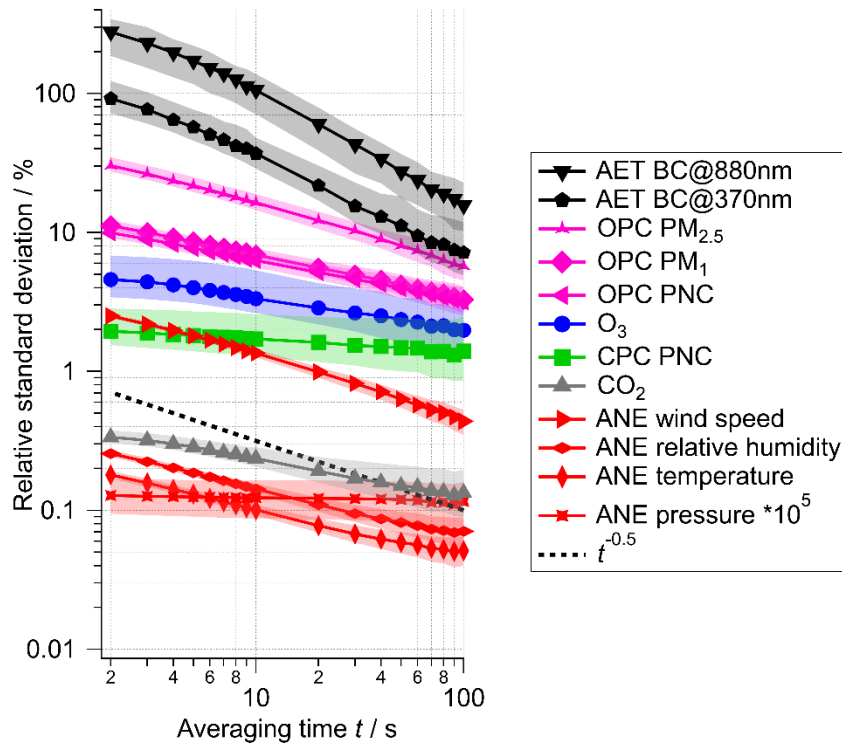


Fig. 5.3: Statistical uncertainty (relative standard deviation) of the measured quantities onboard FLab as a function of averaging time. Same colors correspond to the same instruments that recorded the data. The markers show the median over the time series and the shaded area shows the corresponding interquartile range.

measure a quasi-continuum of molecules), a smaller slope in the RSD- t dependence is observed. This is due to the fact that for these instruments the precision is determined by a combination of other influences such as electronic noise or measurement cycles. For the CO_2 instrument and the CPC, averaging times above 40 s and 80 s, respectively, do not lead to a further reduction in uncertainty.

To calculate the statistical uncertainty as a function of the selected averaging time, we found that Hill equations were best suited to parameterize the results of our measurements. The Hill equations were fitted to the RSD of all studied variables for averaging times between 2 s and 100 s. The coefficients of the corresponding Hill equations are listed in Table S9.8.

Since the most suitable averaging time depends on the scientific goal and which levels of uncertainties are acceptable, as well as on desired flight pattern and atmospheric conditions, no general recommendation can be given. Nevertheless, this study can help to estimate expected uncertainties and herewith support mission planning. From Fig. 5.3 we found that averaging times of more than 10 s correspond to a statistical uncertainty of 0.1% to 20% for most variables and up to 100% for black carbon, while for 30 s averaging times 0.07% to 10% and 50%, respectively, were determined. This means that for vertical profile measurements, a resolution of height bins in the order of a few tenths of meters can be achieved with reasonable measurement uncertainty, depending on the vertical flight velocity.

5.4.2 Influence of horizontal motion

In order to determine whether the horizontal motion of the UAS affects the measurement on board FLab, we performed three dedicated experiments with horizontal flights (F1 to F3, Table 5.2), all at 6 m AGL. Each flight consisted of several round trips from the start position to 100 m north, back past

the start position until the UAS was 100 m south of the start point, and finally back to the initial start position. Each of these flight patterns was executed at a pre-programmed horizontal velocity, which was kept constant over the entire distance. During each flight, several patterns were completed at different velocities, as listed in Table 5.2.

As shown in Fig. S9.19, during flight F1 at 15:44 LT (local time) a 40° change in wind direction occurred, which was associated with a change in several variables such as CO₂ volume mixing ratio, CPC PNC (particle number concentration), relative humidity and temperature. In contrast, conditions were stable during F2 and F3. Nevertheless, all flights are used to assess the effect of horizontal motion on instrument performance.

For each flight, the collected data from all instruments were binned in two different ways, after verifying that the flight direction did not affect the measured quantities. By binning the data for all horizontal velocities in 20-m increments as a function of the horizontal flight distance from the start position it is possible to investigate potential small scale inhomogeneities at the measurement site. For this purpose, the mean and standard error of all data were calculated for the respective bins and demonstrate that within a range of 200 m gradients and structures of, e.g., temperature, wind speed and CPC PNC (Fig. S9.20) can be resolved. These structures may be due to the sloping topography or to local emission sources such as the MoLa exhaust, which polluted the flight path from -30 to 0 m in the case of easterly winds. Fig. S9.20h and Fig. S9.21 highlight the Flab's capability of resolving such small-scale inhomogeneities like the MoLa exhaust plume on a 1-second-time scale within a few tens of meters and independent of horizontal flight velocity, resulting in enhanced CPC PNC in the averaged horizontal flight tracks in this example.

In order to investigate potential effects of flight velocity on the measurements, the acquired FLab data need to be corrected for variations that do not originate from flight velocity influences but from temporal and spatial trends in the probed air. First, the time series of each variable of the FLab data were corrected for temporal variations in the reference data (measured by MoLa; these data were smoothed by calculating the 15 s rolling mean in order to minimize noise). The temporal correction is done by multiplication of each FLab data point with the ratio of the respective data point in the 15 s rolling mean time series of the MoLa data to the first data point in this time series. For this we assume that temporal variations are the same at all measurement locations due to the (assumed) homogeneous atmospheric distribution over this range. Second, a correction for the average spatial structure (i.e., average horizontal trend or, as in Section 5.4.3, vertical profile) was applied to the FLab data for each variable. For this purpose, average horizontal or vertical profiles (20 m, respectively 10 m bin size) were calculated from the FLab time series after correcting them for the temporal trends (see Fig. S9.22b). Then, the data in the FLab time series were corrected for this average spatial distribution by multiplication of each data point with the ratio of the value in the average profile for the respective position to that for the reference position (i.e., the 0 m mark; Fig. S9.22c). Finally, the thusly corrected FLab data were rebinned according to flight velocity by calculating for each variable the mean over all flights and all positions at a given velocity (Fig. S9.22f). Combined uncertainties from temporal and spatial correction, individual instruments, and flight-to-flight variability were estimated and are shown as error ranges in the respective figures. Fig. 5.4 and Fig. S9.23 show the resulting dependence of different variables on flight velocity and apparent wind speed, respectively. The apparent wind speed is calculated by adding the vectors of flight velocity and ambient (horizontal) wind. Most variables are either not affected by high flight velocities, such as black carbon mass concentration, CO₂, O₃, and relative humidity, or, like the CPC, show an insignificant deviation of 1%, well within its uncertainty. However,

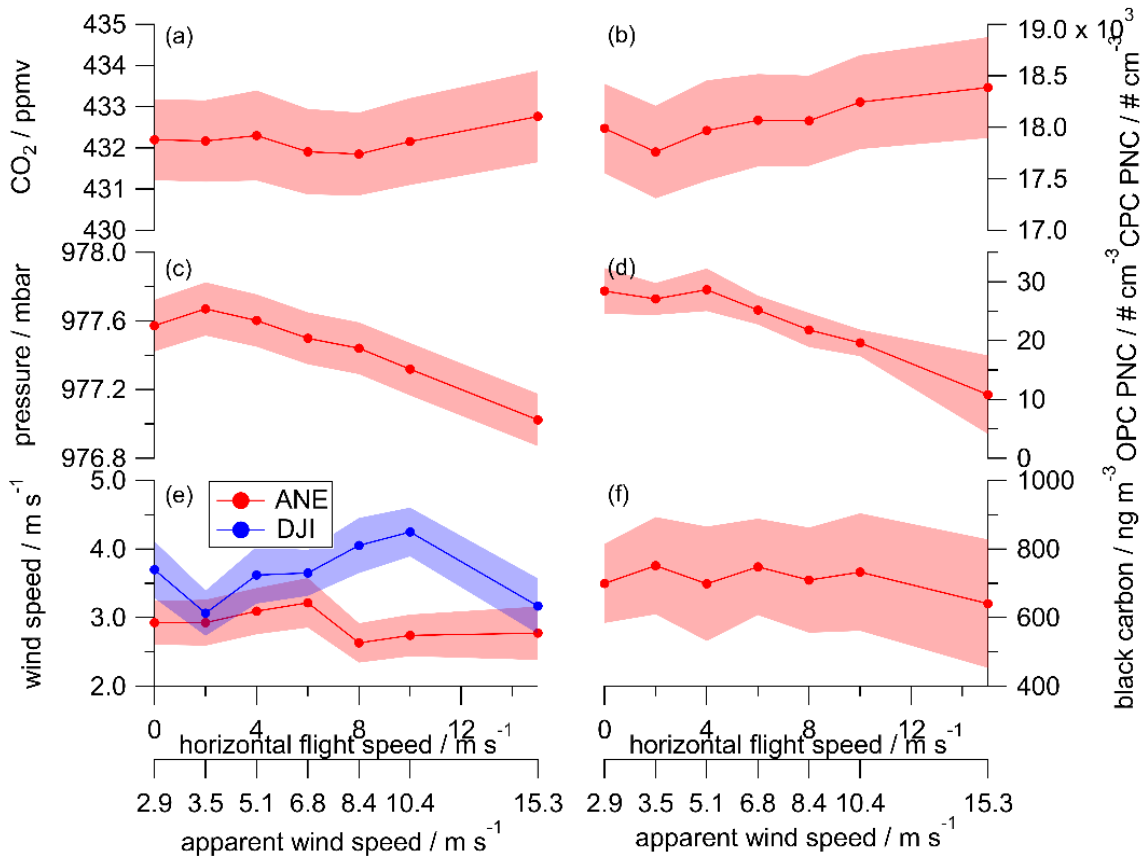


Fig. 5.4: The variables CO₂ (a) and particle number concentration (PNC) measured with the CPC (b) show no significant dependence on horizontal flight velocity, while pressure (c) and OPC PNC (d) decrease with increasing flight velocity. The ANE wind speed (e, red) and black carbon (f) appear to be completely unaffected, while the wind speed measured by the M600 UAS itself (e, blue) shows an irregular but significant trend. The shaded areas represent the errors calculated as described in Section 5.4.2. The lines between the markers are for orientation only and are not intended to indicate a relationship.

the particle number concentration measured with the OPC decreases significantly at flight velocities $> 6 \text{ m s}^{-1}$, consistent with apparent, though insignificant, trends in PM₁ and PM_{2.5}. Here, the vertical inlet may lead to inefficient sampling at high horizontal aspiration velocities, which could potentially be corrected if necessary, e.g., under very windy conditions (Brockmann, 2011), which is possible due to small trend uncertainties. Also, the measured pressure decreases with increasing flight velocity, probably due to the Bernoulli effect; the measurement at (nominally) 0 m s^{-1} may be slightly affected by the apparent wind from the UAS rotation at the end of each flight lag, causing the slight pressure drop. The temperature in the ANE is calculated from the speed of sound and therefore relies on the measured pressure, causing a similar trend (Fig. S9.23e); however, both trends are negligible compared to the measurement uncertainties provided by the manufacturer. The ambient wind speed derived from the ANE does not appear to be significantly affected by relative winds up to 15 m s^{-1} . In contrast, the wind speed received from the M600 UAS, which is based on the GPS position and the rotors thrust force, overestimates the wind speed and appears less reliable (Fig. 5.4e). The attached payload could cause a miscalculation of the wind speed by the M600 on-board computer, which bases its calculations on the nominal flight behavior of the (payload-free) M600.

The results show that horizontal flight (or relative wind) velocities up to 15 m s^{-1} do not relevantly affect most variables, except for those of the OPC, whose sampling efficiency is apparently reduced at

wind speeds $> 6 \text{ m s}^{-1}$; the internal wind measurement of the M600 seems unreliable with the payload attached. Uncertainties may be due to binning, acceleration and deceleration effects, but also to the normalization to the MoLa time series, which is measured at a distance of up to 130 m and may differ from the FLab data due to spatial inhomogeneity.

5.4.3 Influence of vertical motion

The effect of the vertical velocity of the UAS on the measurements was investigated analogously to the horizontal flights. For this purpose, we performed three flights, F4 to F6, consisting of several vertical profiles up to 120 m AGL with pre-programmed velocities (Table 5.2). All flights were performed under similar meteorological conditions with no apparent change in air mass (Fig. S9.24), except that the wind direction changed from east to north before flight F5 and back again after F5, but was stable during F5. Due to the change in wind direction, plumes of CO_2 and small particles were detected at ground level and with MoLa during this flight because the MoLa exhaust was partially sampled.

Following the approach for the horizontal flights, the FLab data of all instruments for each flight were binned in two different ways: with respect to altitude and with respect to vertical velocity, respectively. Binning with respect to altitude results in vertical profiles that contain the average of all measured data, independent of vertical velocity, for each 10 m increment (Fig. 5.5 and Fig. S9.25; with standard errors shown as uncertainty range). For the analysis of the dependence of the measured variables on the vertical velocity, the measured data were first normalized by the MoLa time series and then by the vertical profiles before being averaged over the entire altitude range covered for each vertical velocity setting individually, analogous to Section 5.4.2 (Fig. 5.6 and Fig. S9.26). The total uncertainty includes the uncertainty from the temporal and spatial normalization, from the averaging of the three flights, and from the statistical uncertainty (Section 5.4.1) for the respective averaging time. Here we assume that the MoLa measurements are comparable to the FLab measurements independent of the spatial distance, while the actual uncertainty of this correction increases with increasing vertical distance. A positive vertical velocity indicates ascending motion and a negative velocity indicates descending motion.

Analogous to the analysis in Section 5.4.2, the horizontal wind speed and direction data collected by the anemometer (ANE in Fig. 5.5 and Fig. 5.6e) were compared with the data recorded by the UAS (DJI). The horizontal wind speed determined by the UAS is almost constant within $\pm 0.1 \text{ m s}^{-1}$ for all altitude levels within each flight (Fig. 5.5 and Fig. 5.6e). In contrast, the wind speed measured by the anemometer is generally larger and varies with altitude (Fig. 5.5a), as expected. From this comparison and the one in Section 5.4.2, we conclude that the UAS-derived wind speed is unreliable with the payload attached and should not be used for analysis.

From the same figure it can be seen that there are strong differences between the wind speed measurements during ascent and descent, especially for flights F4 and F6: the ascent-related wind velocities (diamond markers) are greater than those of the descent (circular markers), measured at the same altitude (Fig. 5.5a), a behavior observed at all ascent rates (Fig. 5.6e). This effect is not only observed for the wind speed measurements, but also for the wind direction measured by the anemometer (Fig. 5.5b). There is an average shift of 27° in wind direction measured during descent compared to ascent. This probably indicates a bias in the wind direction measurement during descent due to the movement into the turbulent downwash volume, which may contain a general circulation of air caused by the rotation of the propellers (Zheng et al., 2018), while during ascent the UAS moves into unperturbed

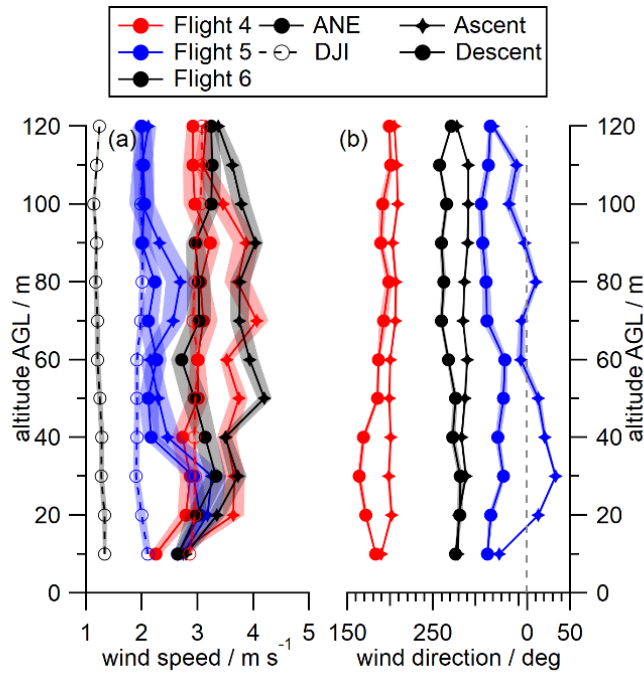


Fig. 5.5: Vertical profiles of wind speed (a) and wind direction (b) of flights F4, F5 and F6 show the differences between ascent and descent in the ANE data (diamonds and circles on solid lines). Vertical profiles of wind speed obtained from the M600 UAS (DJI, dashed lines) show no altitude dependence. The shaded areas represent the standard error within the 10 m increments.

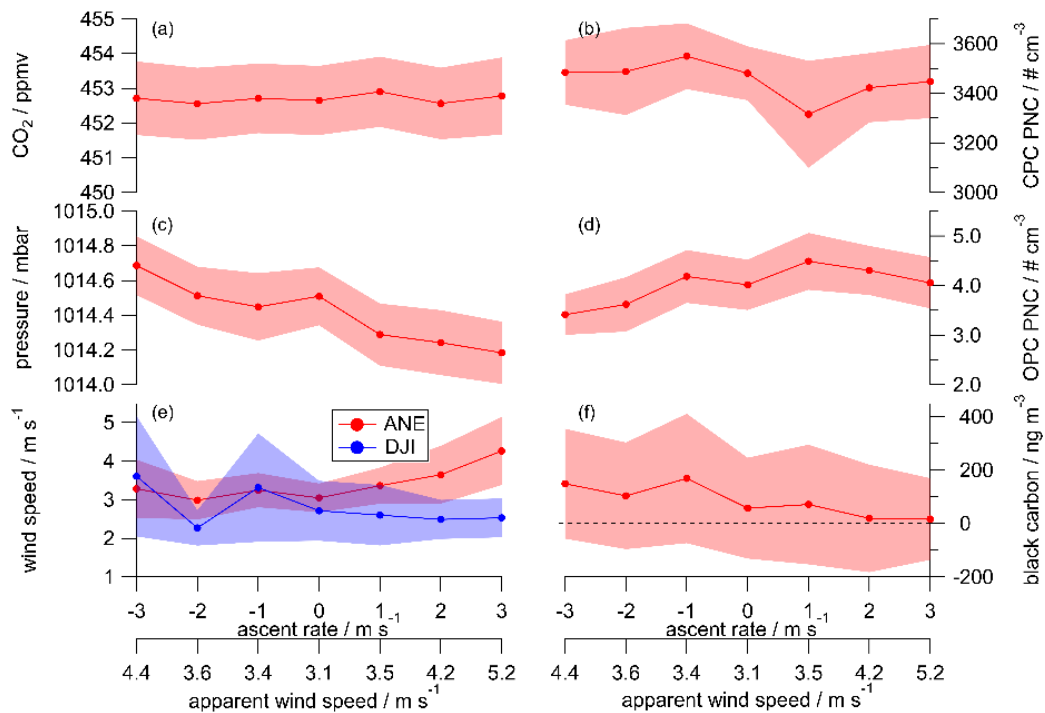


Fig. 5.6: The variables CO_2 (a) and particle number concentration (PNC) measured with the CPC (b) appear to be unaffected by vertical velocity, while pressure (c) and OPC PNC (d) reveal a slight dependence. ANE wind speed (e, red) and black carbon (f) show an apparent trend within the uncertainty range, while the wind speed measured by the M600 UAS itself (e, blue) is not affected by vertical motion. Ascent and descent rates are given as positive and negative ascent rates, respectively. The shaded areas represent the errors as described in the text. The lines between the markers are for orientation only and are not intended to indicate a relationship.

air. In our case, the downwash seems to generate a wind field that counteracts the atmospheric wind in terms of speed and also influences the wind direction. Therefore, the anemometer provides unbiased wind data only during ascent, and ANE wind data measured during descent should be used with caution.

Most of the other variables do not show a significant relationship with ascent rate (Fig. 5.6 and Fig. S9.26). No influence of vertical velocity is found for CO_2 , O_3 and CPC particle number concentration. Patterns within the uncertainty range are found for OPC (PNC, $\text{PM}_{2.5}$ and PM_{10}) and for temperature, but are negligible within the given uncertainties. Spatio-temporal overcorrection seems to cause the non-intuitive but insignificant pattern found for relative humidity (Fig. Fig. S9.26b). In contrast to the relationship found for horizontal motion (Fig. 5.4c), the measured pressure decreases with increased ascent rate, but increases with descent rate. Here, the dynamic pressure dominates over the Bernoulli effect because the pressure sensor is open to the bottom and is directly exposed to aspirated air masses from below. This small potential bias must be considered when calculating flight altitude from recorded pressure levels during ascent or descent, although it is within the manufacturer's stated uncertainty.

The measured black carbon mass concentration decreases substantially with increasing vertical velocity during ascent down to 10% of the descent data. During ascent, the filter with the sampled material is lifted into lower pressure air, presumably causing evaporation of volatile compounds from the filter and consequently changing the relative amount of light scattering, which is assumed to be constant for the internal correction. Descending may cause the opposite effect, i.e., condensation of semi-volatile compounds on the filter, which is colder due to previous measurements at higher altitude. Thus, filter sampling can be significantly biased when semi-volatile compounds are involved and filters are subjected to changing pressures. Nevertheless, the black carbon trend is within the extremely large uncertainties of these measurements, which are due to the low black carbon levels on this day rather than evaporation of the sampled compounds. Therefore, we conclude that the AET data are not useful for continuous vertical profiling flights in uncontaminated areas, and we do not further consider black carbon concentrations in absolute terms in this study. Flight patterns that include hovering at the same altitude for several minutes would be more suitable for filter-based *in situ* measurements.

In summary, the vertical motion of the UAS with velocities in the range of -3 to 3 m s^{-1} does not significantly affect the data quality of the measured variables, except for AET. Using the same flight pattern for successive profiling flights would result in better comparability of data between flights. In contrast to previous work investigating vertical velocities $\geq 5 \text{ m s}^{-1}$ (Brus et al., 2021b), no hysteresis was found between ascent and descent for the temperature and humidity sensors, indicating that the instrument sensors can equilibrate sufficiently quickly for the vertical velocity of $\pm 3 \text{ m s}^{-1}$ used in the given setup.

5.4.4 Development of an optimized vertical profiling flight pattern

Depending on the desired measurement application, very different flight patterns have been used with UAS in the past. In the literature, circular or systematic mapping horizontal flights are frequently found, which do not include any vertical variation (Grimaccia et al., 2015; Burgués et al., 2021). In contrast, purely vertical flights allow the measurement of vertical profiles with separate data for ascent and descent (Andersen et al., 2023; Quinn et al., 2024). In both cases, when large areas need to be covered, capturing temporal changes can be challenging due to the typically short flight durations. For smaller mapping areas, such temporal changes can be assessed by repeated flight operations, as shown in flight F1 in Section 5.4.2. Hover flights at a fixed location, on the other hand, focus purely on the analysis of temporal variations at high temporal resolution, without providing information on spatial

variations. Hovering also allows slow sensors to equilibrate to ambient conditions and allows longer sampling times to achieve sufficiently low detection limits of the quantities under study (Barbieri et al., 2019; Brus et al., 2021a; Niedek et al., 2023).

Here, we focus on the investigation of vertical profiles with repeated flights over the day to determine the temporal evolution of the stratification of the lower boundary layer. Based on the results in Section 5.4.3, a significant influence of the vertical motion of the UAS on the measurement results is not expected for most variables. Wind speed and direction data from the anemometer should only be used when measured during ascent or during hovering. Hover phases near a reference station are highly recommended for all measurement flights to allow frequent comparison of UAS-based measurements with higher-quality instruments. Comparison of data from both platforms helps to detect and correct temporal drifts of UAS-based instruments exposed to rapidly changing environmental conditions. Low-cost chemical sensors and instruments without sophisticated compensation methods would also benefit from such cross-platform comparisons.

In order to find the optimal flight pattern for vertical profiling, test flights were conducted with a consistent ascent and descent rate of 3 m s^{-1} as a compromise between the statistical uncertainty of the observed variables and the spatio-temporal resolution. A vertical velocity of 3 m s^{-1} allows, for example, four ascents from the ground to 300 m AGL or two ascents to 500 m AGL within the available flight time of FLab. Furthermore, by combining data recorded during ascent and descent, a total measurement time of 26.4 s per 10 m height bin was obtained for the flight pattern described in Section 5.5.1. Statistical uncertainties are expected to range from 0.08% to 10% depending on the instrument (Table S9.8). Depending on the research question, the binning can be adjusted, e.g., to improve the measurement statistics.

Occasionally, we observed strong rolling motion of the FLab during descent at low horizontal wind speeds $\leq 3 \text{ m s}^{-1}$, resulting from the UAS entering its own downwash regime. This uncontrolled flight behavior can be avoided by adding a horizontal velocity component of up to 2 m s^{-1} (see Section 5.4.2), directed into the wind to the vertical motion. This causes the UAS to tilt and shifts the downwash regime from below to the side opposite to the direction of flight. As a result, this diagonal rather than straight vertical flight pattern reduces the UAS oscillation without affecting data quality.

This results in a flight pattern that is adapted to the wind speed: straight vertical ascending for wind speeds $> 3 \text{ m s}^{-1}$ and ascending with a horizontal component for lower wind speeds. To follow this suggested flight pattern, the pilot must take into account possible changes in wind direction with altitude when planning the flight.

5.5 Applications of FLab

5.5.1 Evolution of the stratification of the lower troposphere

To evaluate and demonstrate the FLab's ability to capture changes in the vertical distribution of aerosols and trace gases during the day, eight hours of hourly vertical profiling flights were performed. For this experiment, we chose the same measurement site near Ockenheim as described in Section 5.4, and measured in combination with MoLa (serving as a ground-based reference) on 5 June 2023, between 8:00 and 17:00 (all times are local time). We launched the FLab eight times (once per hour) for vertical flights up to 300 m AGL with a vertical velocity of $\pm 3 \text{ m s}^{-1}$ without a horizontal component (see Section 5.4.4). The battery capacity of the UAS limited the flight duration to 15 minutes. Each flight consisted of four ascent/descent cycles and a hover period of 10 s each time the FLab reached

the altitude of the MoLa inlet (6 m AGL). The third ascent of the flight at 15:15 was aborted at 100 m AGL due to sudden gusts; a fourth ascent to 300 m AGL was performed. Between the flights, the CBO's measurement cell was covered with a protective cover while the FLab was parked on the landing site without ventilation or shade, in contrast to more recent field deployments.

The meteorological conditions at the measurement site for each day are summarized in Fig. S9.27; conditions were sunny with moderate winds.

The recorded FLab instrument data were binned into 10 m increments for all ascents and descents of each flight, and the mean and standard error for the entire flight were calculated for each altitude bin (top panels in the subfigures of Fig. 5.7 and S9.28). If the standard error was smaller than the statistically expected uncertainty from Section 5.4.1, the statistical uncertainty was used instead. FLab and MoLa data can be compared when FLab was hovering near the MoLa inlet below 10 m AGL (bottom panels in the subfigures of Fig. 5.7 and S9.28 with 1-min averages of the MoLa data).

Over the day, the values of relative humidity and ambient temperature in the vertical profiles mainly follow the typical daily trends with increasing temperature until mid-afternoon and correspondingly decreasing relative humidity, analogous to the observations with MoLa (Fig. S9.27 and Fig. S9.28). While the relative humidity values are rather constant over the whole altitude range covered, the ambient temperatures show a clear decrease with altitude. Wind speed and direction remain constant over the day at ground level, but show a complex behavior in the profiles, with a general increase in wind speed with altitude, especially in the lowermost fraction of the altitude range (Fig. S9.28d). In addition, the variation in wind direction is most pronounced in the lower part of the profiles (Fig. S9.28e).

At ground level, the mixing ratio of O_3 increases continuously until 15:00 as a consequence of photochemical processes. CO_2 peaks at 9:00 before decreasing by 7.7 ppmv by early afternoon due to increased dilution in the developing mixing layer and does not indicate any specific emission sources in the vicinity (Oliveira et al., 2007). Both, O_3 and CO_2 mixing ratios, increase slightly with altitude during the first flight in the morning, but for both trace gases the vertical gradient and the vertical inhomogeneity decrease thereafter as the entrainment zone breaks up and the convective mixing layer develops (Kotthaus et al., 2023). O_3 appears to be well mixed up to 300 m AGL from 10:30 and develops according to its diurnal cycle (Neu et al., 1994; Law et al., 2008), however, CO_2 mixing ratios measured above 100 m decrease by 2 ppmv compared to the ground, which could be due to polluted air masses from regional sources that were not transported above 100 m AGL in the short time.

At ground level, we measured enhanced PM_{10} and $PM_{2.5}$ levels by up to 50% between 9:00 and 12:15 with the OPC in MoLa, and a further increase around 16:00; the development of the time series of the FLab OPC particle number concentration (i.e., for $d_{opt} > 350$ nm) and the corresponding $PM_{2.5}$ were very similar (Fig. S9.28g). The total particle number concentration measured with the CPC doubled during the day and had two broad maxima between 10:00 and 11:00 and 13:00 and 15:00, in addition to short-term variations. Advection from different nearby aerosol emission sources is an unlikely reason for this behavior, since the wind direction and speed at the ground remained rather constant throughout the day and did not show any changes in parallel with these trends. In general, the particle-related quantities determined with FLab while hovering near the ground are in agreement with the corresponding values measured with MoLa. However, the vertical profiles of the particle number concentrations measured with the CPC and OPC show strong differences between the two variables due to the different particle size ranges measured with the two instruments.

OPC PNC generally decrease with altitude (Fig. 5.7c), although the gradient varies throughout the day. The strongest gradients are found at 13:30 and 16:30, when the highest concentrations were measured near the ground. In contrast, an almost constant background concentration of 7 \# cm^{-3} was observed $> 200 \text{ m}$ AGL during all flights of the day. The observed gradients are consistent with the assumption that particles in the OPC size range are generated at or near the ground and successively transported to higher altitudes.

In contrast, the vertical distribution of the PNC of small aerosol particles (measured with the CPC) shows several different gradients and the variation of PNC is rather dominated by the different concentrations measured at ground level with no consistent vertical profile (Fig. 5.7d). However, the CPC PNC increases by an average of $380 \pm 240 \text{ \# cm}^{-3}$ in the lowest 50 m AGL. This gradient could be due to inhomogeneous source distributions, similar to those for CO_2 , and to particle deposition at ground level. For flights at 9:30, 13:30, and 14:30, strong structures are observed around 150 m AGL, which may indicate stratification not detected by any other instrument. This underscores the importance of measuring different types of variables simultaneously, from meteorological to gas and aerosol particle ones.

During this field experiment, black carbon mass concentrations did not show any variation with altitude above the noise level, however, the results did reveal some instrumental characteristics that are important for future field operations. The aethalometer measured in single-spot mode for the first few hours and then automatically switched to dual-spot mode (see Section 5.3.2), apparently when the

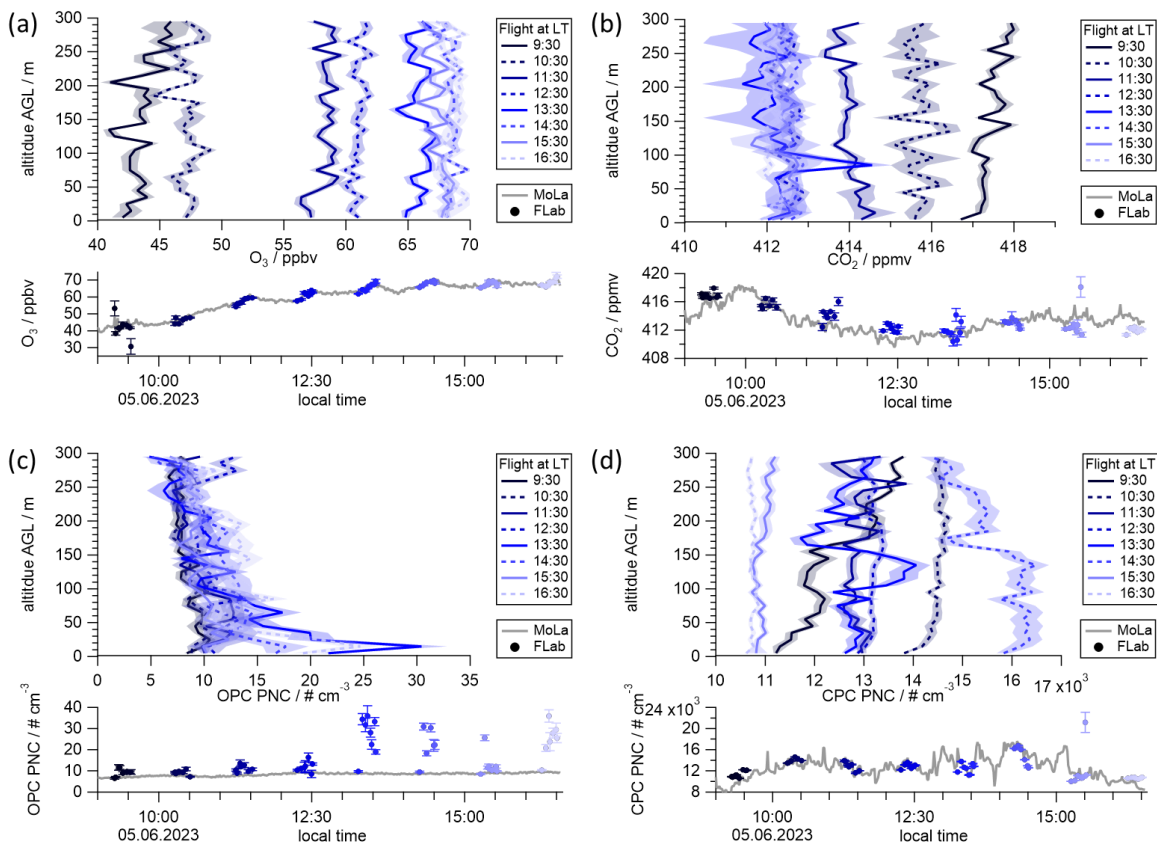


Fig. 5.7: Vertical profiles of O_3 (a) and CO_2 (b) mixing ratios are dominated by the diurnal cycle of the mixing layer and the incoming radiation and show the strongest changes until 12:30. Vertical profiles of the OPC PNC (c) show a successive vertical uplift of particles ($d_{\text{opt}} > 350 \text{ nm}$) around noon and in the afternoon. Vertical profiles of the CPC PNC (d) appear to be strongly influenced by the ground level

PNC, but show inhomogeneous vertical distributions depending on the individual flight. The shaded areas represent the standard error or the statistical uncertainty from Section 5.4.1, whichever is greater. The bottom panel of each sub-figure shows the direct comparison of the FLab (blue) and MoLa (gray) data while FLab was hovering near the MoLa inlet.

filter loading reached a certain level (Fig. S9.29). This switch was associated with a sharp increase in the noise level of the measurements (Fig. S9.29) due to the reduction in sample flow per spot. In addition, for both measurement modes, there were striking differences between the flight and no-flight concentration levels reported by the instrument, with much lower, sometimes negative, concentrations during the no-flight periods. We hypothesize that the instrument heated up during periods of static sun exposure between flights, which may have caused evaporation of particulate material from the filter, resulting in negative mass concentration values. For unknown reasons, these differences were more pronounced in the dual-spot mode. Since the standard deviations were also greatly increased in this mode compared to the single-spot mode, we decided to use only the single-spot mode in future applications.

5.5.2 Bridging the gap between ground-based and aircraft-based measurements

Co-located measurements on four different platforms were used to further evaluate the performance and usefulness of the FLab measurements in the lower troposphere. As part of the BISTUM23 measurement campaign in the Swabian Jura in August 2023, we operated MoLa as a ground-based reference station and FLab for vertical profiling up to 500 m AGL. On 10 August 2023, the research aircraft HALO (High Altitude Long range) orbited the measurement site at 500 m AGL and subsequently ascended to several thousand meters on its way to another research target (Fig. S9.30). The on-board HALO instruments collected, among others, meteorological, O₃, and PM_{2.5} data (Dragoneas et al., 2022; Giez et al., 2022). Following the flyby, a balloon-borne Vaisala RS41-SG radiosonde was launched, reaching 2000 m AGL within 7 min and providing meteorological data from ground level to the stratosphere.

Fig. 5.8 shows a comparison of variables collected on board the different measurement platforms during and shortly after this flyby. To allow direct comparison of variables from different platforms, the data are not normalized for temperature or pressure at each measurement location. This comparison shows generally good agreement for all variables across all platforms. Below 500 m AGL vertical profiles were obtained with the radiosonde and FLab. For most variables the trends in this altitude range are consistent; however, for relative humidity an offset of ~10% and for wind speed reduced values of a few meters per second were measured with the radiosonde. These discrepancies between FLab and radiosonde data are discussed in detail in Text S9.6 of the Supplement.

Comparison of the radiosonde and HALO data reveals reasonable discrepancies for all available variables, which may be due to the unavoidable temporal and spatial separation of the measurements on the two platforms in the respective altitudes. Similar variability for measurements with similar temporal distance was observed with the MoLa ceilometer, which detected slight shifts in the backscatter signal profiles (e.g., in the location of the maxima around 1000 m and 1300 m AGL) between the time of the HALO flyby and that of the radiosonde launch (light and dark green traces in Fig. 5.8, respectively).

Although a direct comparison of HALO and FLab data is not possible due to the lack of overlap in the altitude ranges covered, a reasonable agreement of all variables in the link between the respective profiles at 500 m AGL is observed between the two platforms. This example shows that FLab is able to reliably bridge observations from ground level to 500 m AGL, an altitude range that is typically not accessible with research aircrafts.

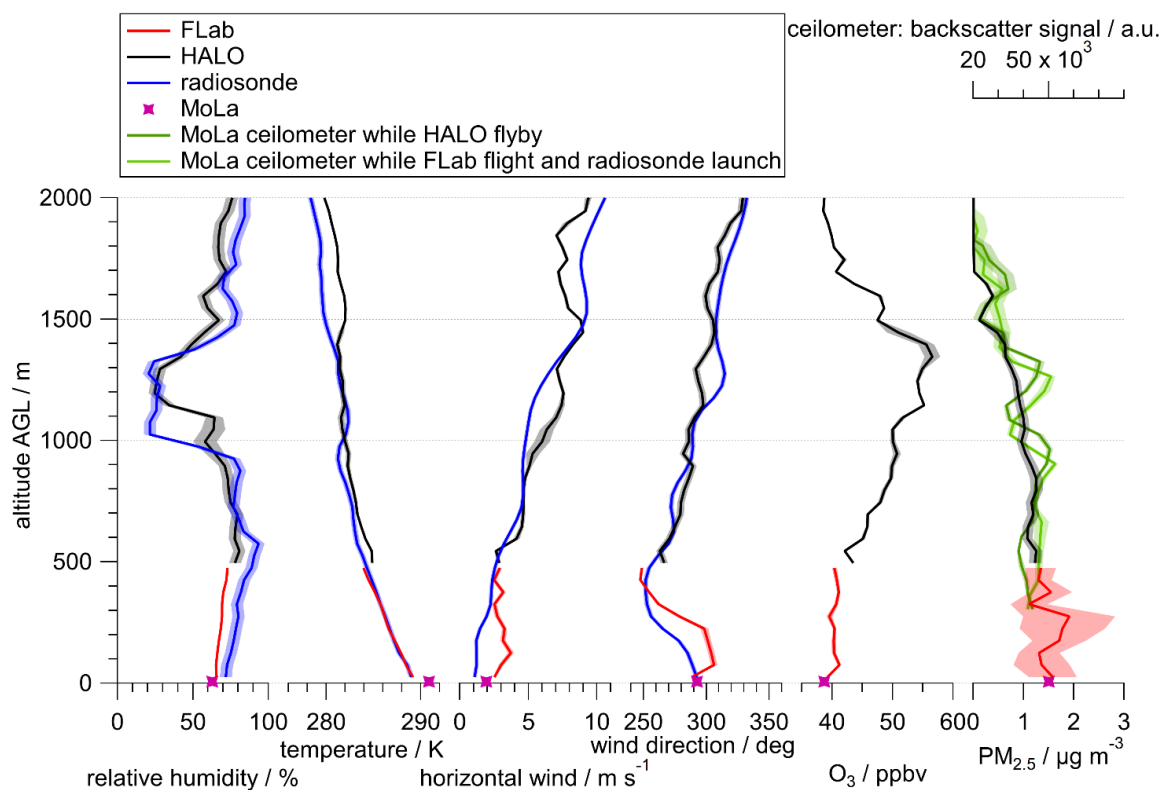


Fig. 5.8: Vertical profiles of meteorological variables, O_3 and $PM_{2.5}$ show good agreement between different platforms: MoLa (pink and green), FLab (red), radiosonde (blue) and HALO (black). The shaded areas show the respective uncertainty ranges and are derived from the instrumental uncertainty and the standard error of each variable within the 50 m increments.

5.6 Summary

We have developed and characterized a research UAS (unmanned aircraft system) for atmospheric composition measurements based on a commercial hexacopter (Matrice 600, DJI Ltd.): the Flying Laboratory FLab. FLab was designed as a flexible platform to simultaneously measure aerosol particles, trace gases, and meteorological variables to study the vertical structure of the lowermost atmosphere and the distribution of pollutants in the lower troposphere.

The research UAS was equipped with lightweight and high-quality instruments to measure a wide range of relevant variables characteristic of many types of anthropogenic and natural emissions, such as particle number and black carbon mass concentrations, particle size distributions (from which PM_1 and $PM_{2.5}$ concentrations can be calculated), CO_2 and O_3 mixing ratios, and relevant meteorological variables: air pressure, temperature, relative humidity, and wind direction and speed. An elevated mounting position for the anemometer was identified to measure the ambient wind largely unaffected by rotor downwash. In addition, we developed a dedicated infrastructure for power and data management for the instruments, as well as hardware and software for real-time ground-based monitoring of the in-situ measurements aboard FLab. In the field, this software can help detect plumes or dangerous flight conditions such as sudden gusts or precipitation.

The research UAS was characterized both on the ground and in flight to evaluate different vertical flight patterns. In laboratory experiments, the measurement uncertainty as a function of the averaging interval was determined for all measured variables, and an optimal averaging time of at least 30 s was determined for our applications to achieve uncertainties of $< 10\%$. Furthermore, we investigated the

influence of horizontal and vertical motion with different flight velocities ranging from 0 m s^{-1} to 15 m s^{-1} and 0 m s^{-1} to 3 m s^{-1} , respectively, on the measurement results. From the horizontal flights, it was found that the horizontal motion slightly affected the temperature and pressure measurements (for velocities $> 2 \text{ m s}^{-1}$); however, this deviation was still within the uncertainties given by the manufacturer of the respective instrument. These experiments also showed a significant decrease in the sampling efficiency of the OPC for wind speeds $> 6 \text{ m s}^{-1}$. Vertical motion of the FLab was found to affect the optical particle counter results in the original setup, which was then modified with an external pump to stabilize the sample flow and a modified inlet to reduce the impact of vertical air advection on the inlet and outlet. Black carbon measurements turned out to be impractical for continuous vertical profiling flights under unpolluted conditions.

We found that straight vertical ascents/descents in windy conditions and diagonal vertical ascents/descents in calm conditions were the safest flight patterns for vertical profiling.

The application of FLab in hourly profiling measurements demonstrated that this approach provides valuable information on the vertical structure of the lower boundary layer and its evolution during the day. Comparison of data measured on board different platforms revealed that FLab is able to reliably bridge the altitude range between ground-based measurements and low-flying research aircrafts. Co-located measurements with FLab and the mobile aerosol laboratory MoLa show that continuous ground-based measurements can be successfully complemented by the UAS to add information about the vertical distribution of the measured variables. While MoLa is able to measure the temporal evolution, diurnal cycles or plumes of pollutants at ground level, it cannot analyze vertical inhomogeneity or transport processes up to higher altitudes. In combination with the FLab, we were able to detect vertical inhomogeneities that can occur with the development of the turbulent boundary layer. Thus, the combination of MoLa and FLab provides high quality ground-based measurements while allowing an assessment of their representativeness for the lower boundary layer.

Author contributions: LM analyzed the data and drafted the manuscript. TB and PS built the research UAS in close collaboration with FD, FF and LM. LM programmed the monitoring software and performed the flights together with TB and PS, while FD and FF performed the measurements with MoLa. LV provided and analyzed the radiosonde data. LM, FF and FD discussed the data processing and the presented results. All co-authors commented on the manuscript.

Acknowledgements: This work was supported by internal funding from the Max Planck Society. LM, LV and PS are funded by the Deutsche Forschungsgemeinschaft (DFG, German Research Foundation) – TRR 301 “TPChange” – Project-ID 428312742. The authors thank the following participants of the PHILEAS project for providing data from the HALO flight: Andreas Zahn (Karlsruhe Institute of Technology) for the FAIRO O_3 data, Andreas Giez (German Aerospace Center) for the BAHAMAS meteorological data, and Franziska Köllner (Johannes Gutenberg University Mainz/Max Planck Institute for Chemistry) and Philipp Brauner (Max Planck Institute for Chemistry) for the sky-OPC data.

Financial support: This work was supported by internal funding from the Max Planck Society. Lasse Moormann, Luis Valero, and Philipp Schuhmann are funded by the Deutsche Forschungsgemeinschaft (DFG, German Research Foundation) – TRR 301 “TPChange” (Project-ID 428312742). The article processing charges for this open-access publication were covered by the Max Planck Society.

6 Vertically-resolved Diurnal Variation of Organic Aerosol Particles

This chapter contains a paper that has been published as

Borchers, C., Moormann, L., Geil, B., Karbach, N., Wasserzier, D., Hoffmann, T.: *Development and use of a lightweight sampling system for height-selective drone-based measurements of organic aerosol particles*, EGU sphere [preprint], <https://doi.org/10.5194/egusphere-2024-4015>, 2025

The preprint was peer-reviewed and accepted for publication in Atmospheric Measurement Techniques. It is currently in print.

Contribution to this manuscript by Lasse Moormann:

I am the second author of this work. Following the development of the aerosol sampler, I coordinated the fieldwork and contributed to the conceptual comparison of organic aerosols sampled at several heights. While the sampler was being operated during the BISTUM23 campaign, I conducted vertical profiling using FLab and analyzed the data. Using this data, I contributed actively to discussions and interpretations of the vertical profiles of the composition of aerosol particles and their diurnal changes. I revised the manuscript from its initial version onwards. Finally, I contributed to the characterization measurements of the sampler that were required during the review process.

6.1 Abstract

Organic aerosols (OA) are introduced into the atmosphere from a variety of natural and anthropogenic sources. Especially in the sub micrometer range, the organic fraction contributes to a large proportion of the particle mass and thus has an impact on climate and air quality. To gain insights into sources and sinks and the significance of dispersion, mixing and ageing processes for OA, vertical profiling of the concentration of organic aerosols is particularly helpful. Therefore, the aim of this study is to present an aerosol particle sampler that is suitable to be used onboard uncrewed aerial vehicles (UAVs). The sampler consists of a three-dimensionally printed filter holder connected to a lightweight high-performance pump that can generate a flow rate of up to 103 SLPM for up to 30 minutes. The sampler was characterized and applied on a proof-of-concept study during the BISTUM23 campaign in August 2023 in Southern Germany. Vertical profiles were measured with three samplers mounted on ground and UAVs and collected aerosol particles in an altitude of 1.5 m, 120 m and 500 m above ground level simultaneously. The filters were analyzed with UHPLC-HRMS, and a targeted approach was used to determine vertical profiles and diurnal trends of biogenic, anthropogenic and biomass burning marker compounds. A non-targeted analysis revealed a high number of CHO-containing compounds, which were oxidized to a greater extent during the course of the day and at increasing altitudes. The system presented here provides a comparatively simple and cost-effective way to sample OA at different altitudes and at different locations and thus obtain vertical concentration profiles of the organic aerosol composition.

6.2 Introduction

Organic aerosol particles (OA) are accountable for a large proportion (20–90%) of the sub-micron particle mass in the lower troposphere. They affect air quality, climate and human health (Kanakidou et al., 2005; Jimenez et al., 2009; Benoit et al., 2023). Primary organic aerosols (POA) are emitted directly, for example from biogenic sources such as plant debris or in the form of spores, bacteria or viruses, or from sources that are mostly anthropogenic such as combustion processes. Secondary organic aerosols (SOA) are formed by oxidation of volatile organic precursors and subsequent condensation of the products (gas-to-particle conversion) (Kerminen et al., 2005; Kroll and Seinfeld, 2008; Reddington et al., 2011). The chemical composition of OA provides information on the individual sources and source processes (De Gouw and Jimenez, 2009). Nitroaromatic compounds, for example, are released during the combustion of coal or wood, and are contained in vehicle exhaust gases. They can also be formed as secondary products from the reaction of phenols or cresols with NO_x (Harrison et al., 2005; Lu et al., 2019; Wang et al., 2020). The combustion of lignocellulose, the most abundant biomass resource on Earth, leads to the production of phenolic compounds with aldehyde functionalities, including 4-hydroxybenzaldehyde, vanillin and syringaldehyde. Phenol aldehydes can be oxidized in the atmosphere by OH radicals, NO_3 radicals or ozone, leading to the production of carboxylic acids (Net et al., 2011; Cao et al., 2022; Rana and Guzman, 2022). Vegetation on Earth emits large amounts of volatile organic compounds (VOCs) such as isoprene and various monoterpenes (MTs), with the most important MT, α -pinene, accounting for about one third of global MT emissions (Sindelarova et al., 2014). In the atmosphere, oxidation by OH radicals, NO_3 radicals or ozone leads to various products that differ in their volatility by several orders of magnitude. Products such as 2-methyl tetrols, terpenylic acid, terebic acid, and pinonic acid are described as the main oxidation products (Hoffmann et al., 1997; Claeys et al., 2004; Kroll and Seinfeld, 2008; Müller et al., 2012; Nozière et al., 2015; Bianchi et al., 2019;

Kołodziejczyk et al., 2020). It can be concluded that the elucidation of the chemical composition of OA can provide valuable information about the sources, source strengths and processing of organic aerosol components, such as the contribution of biogenic sources in terrestrial ecosystems or the role of anthropogenic contributions to organic aerosols.

The implementation of atmospheric concentration measurements in the form of vertical gradient measurements offers several advantages: firstly, measurements at multiple heights allow the identification of sources and sinks, as they can distinguish between local plumes and emission sources at ground level and atmospheric background concentrations. The latter are particularly characterized by aging in the case of OA (Li et al., 2024). Vertical profiling can also be used to investigate the transport and distribution of OA. Therefore, many monitoring stations also perform atmosphere-related observations from tall towers, as they enable measurements at several heights within the planetary boundary layer or even beyond, and can thus reflect both local processes at lower altitudes and regional influences at higher altitudes (Williams et al., 2011; Andreae et al., 2015; Mikhailov et al., 2017; Li et al., 2024). This is where UAVs can also be used without the need for a suitable tower infrastructure. In addition to acquiring vertical profiles, the utilization of UAVs enables measurements to be taken in difficult-to-access areas, such as volcanic plumes, or over larger areas at the same height, helping to characterize emission sources (Kuantama et al., 2019; Karbach et al., 2022). The use of miniaturized sampling systems in conjunction with UAVs has attracted considerable attention in recent years (Böhmländer et al., 2025). Compared to conventional sampling methods that use towers, balloons or aircraft, these systems offer the advantages of smaller size, environmental friendliness and the ability to collect samples in remote locations that are difficult to access (Bieber et al., 2020; Lan et al., 2020; Thivet et al., 2025).

The aim of this proof-of-concept study was therefore to develop a new low-cost and lightweight aerosol sampling system for UAVs. To do this, a filter holder was designed and produced using 3D printing and connected to a lightweight high-performance pump. The sampled filters were then extracted and analyzed using UHPLC-MS. The system was characterized and vertical concentration profiles of OA compounds at different times of the day were determined as part of the BISTUM23 campaign in August in the Swabian Jura, Southern Germany.

6.3 Experimental Procedures

6.3.1 Sampling system

For aerosol sampling, a home-made 3D-printed filter holder (polylactic acid) was connected to an electric fan motor with an impeller (CDS-R540-QA012; DC 7.2 V; 70 W; inlet diameter 20 mm, SIP Cinderson Motor CO., LTD), which enables high gas flow rates. The electric fan motor is directly plugged into the outlet ports of the battery. The inlet diameter of the filter holder was 20 mm. The filters with a diameter of 70 mm were placed on a stainless-steel mesh to prevent the filter from tearing even at high flow rates (see Fig. 6.1). The sampling unit was powered by a lithium polymer battery (LiPO 7.4 V; 5000 mAh; Conrad Energy), which allows an operating time of about 30 minutes, which is slightly above the approximate maximum flight time of the UAVs on which the sampler is mounted on. The total weight of the filter holder and electric blade motor is 280 grams, which corresponds to the weight of the battery.

To check the stability of the flow rate through the sampling unit, a filter holder (equipped with Pallflex™ Emfab™ filters TX40HI20WW, 70 mm) was connected to a flow meter (model 4043, TSI GmbH, USA) and the flow rate was recorded at 30-second intervals over a total period of 30 minutes.

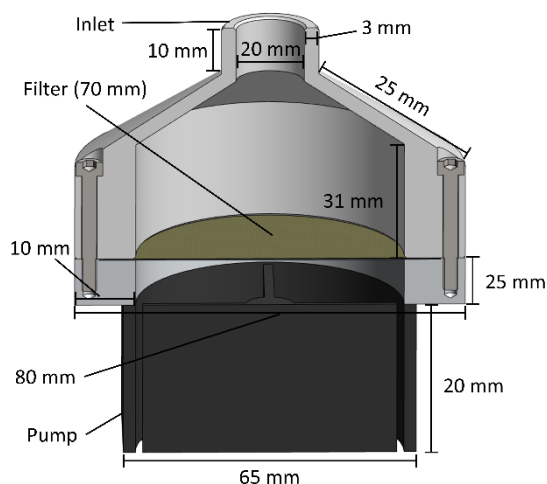


Fig. 6.1: Schematic representation of the filter holder. The air containing aerosol particles is sucked through the filter, which is positioned on a stainless-steel mesh.

6.3.2 Sampling procedure

The filter holders were attached below the UAVs with the filter opening facing to the side (Fig. S9.32). During a deployment near the village of Essenheim near Mainz (49° 55' N, 8° 10' E), the UAVs (model Matrice 200 and Matrice 300, both DJI) and the third filter holder were operated at the same height, approx. 5 m above the ground, and with a horizontal distance of approx. 5 m. Borosilicate glass microfibers, reinforced with glass cloth and bonded with PTFE (Pallflex™ Emfab™ Filters TX40HI20WW, 70 mm), were used for aerosol sampling. Sampling time was between 20 and 30 minutes depending on the battery power of the UAVs. To conduct the vertical profile measurements, the system was operated near the village of Albstadt, in the Swabian Jura (48° 15' N, 8° 59' N). The pump of the collector was activated on the ground, and the UAV was subsequently flown directly to the designated collection height. This process typically required between one and two minutes to complete. The two UAVs were simultaneously operated at 120 m and 500 m (one above the other with a horizontal offset of about 10 m), while the third filter holder was attached to a wooden frame at a height of about 1.5 m above the ground, with again a vertical offset of about 10 m (Fig. S9.33). A third measurement UAV, FLab, (Moormann et al., 2025b) was used to simultaneously quantify gas tracers and meteorological data in hourly vertical profiles over the course of a day at the same measurement location. In particular, height-resolved monitoring the O₃ mixing ratio and wind conditions within 500 m range above ground show oxidative potential of air and supports attribution of air mass origin.

6.3.3 Analysis

The filters were stored at -25 °C until analysis. The filters were extracted according to the following protocol. They were cut into small pieces and placed in a vial that had been previously baked at 450 °C for at least 8 hours. They were then extracted with 3 mL and twice 1.5 mL of a 9:1 (v/v) mixture of LC/MS grade methanol (Carl Roth) and LC/MS grade water (Thermo Fisher Scientific) for 30 minutes on a shaking plate. The supernatant was successively transferred to a 1.5 mL HPLC vial and concentrated to approximately 50 µL at 30 °C under a gentle N₂ stream. The residue was then filtered with a PTFE filter (pore size: 0.20 µm; Altmann Analytik). Since the volume of the solution is not known, a camphor sulfonic acid standard was added to obtain a correction factor for potential volume discrepancies (see Text S9.7).

Analysis was performed in triplicate using a Dionex UltiMate 3000 ultra-high-performance liquid chromatography system coupled to a heated electrospray ionization source (HESI) and a high-resolution Q-Exactive Orbitrap mass spectrometer (HRMS) (all Thermo Fisher Scientific). An Acquity UPLC CSH Fluoro Phenyl (PFP) column, 100 mm×2.1 mm with 1.7 μm particle size (Waters) was used for chromatography. The eluent A was 98% LC/MS grade water (Thermo Fisher Scientific) with 0.04% formic acid and acetonitrile (VWR Chemicals), the eluent B was 98% acetonitrile and water, and the injection volume was 5 μL . An $\text{H}_2\text{O}/\text{ACN}$ gradient was used for the analysis. A flow rate of 0.5 mL min^{-1} and a gradient as described below was used: Starting with 10% B, increasing to 99% B in 11 min, after which B was held at 99% for 1 min, decreased to 10% in 0.5 min, and held again for 0.5 min. The HESI source was used in negative mode, resulting in the formation of deprotonated molecular ions. The sheath gas and auxiliary gas pressures were 40 and 20 a. u. (arbitrary unit) respectively. The auxiliary gas heater temperature was 150 $^\circ\text{C}$ and the capillary temperature was 350 $^\circ\text{C}$. The sprayer voltage was set to -4.00 kV. Further details on the additional chemicals used, including their respective purities, can be found in Table S9.9.

6.4 Results and Discussion

6.4.1 Sampler characteristics

Fig. 6.2 shows the airflow through the filter holder as a function of time. During the measurement, the recorded airflow decreases from 103.4 SLPM to 92.1 SLPM. This may be due to the fact that no voltage regulator was installed between the battery and the motor, so the voltage in the battery decreases over time, and thus the power of the motor also decreases. A statistically significant (significance level $\alpha = 0.05$) linear relationship was obtained between flow rate and time. A linear fit ($y = mx + b$) was performed, with $m = (-0.41 \pm 0.01) \text{ SLPM min}^{-1}$ and $b = (102.9 \pm 0.2) \text{ SLPM}$ as fit parameters. This function can then be used to determine the volume of air collected within the sampling time (see Text S9.7).

Fig. 6.2b shows the dependence of flow the flow rate on the pressure. This relationship is used to calculate the flow rate at different altitudes, as detailed in the Supplementary Material (Text S9.7). Most aerosol particle collectors operate at flow rates between 10 and 500 L min^{-1} to collect aerosol particles over periods of several hours or days (Ma et al., 2022; Leppla et al., 2023). Since the presented system is designed for use onboard UAVs, a lightweight configuration is crucial. These constraints result in an operational time of 20 to 30 minutes and a flow rate of approximately 100 L min^{-1} . However, sample preparation is essential to be able to detect individual components despite these restrictions. Due to the extraction method and the reduction of the sample volume to only 50 μL of liquid, it is possible to detect a wide range of biogenic and anthropogenic substances. Fig. 6.3 shows an excerpt of an extracted ion chromatogram (EIC) of a LC-MS run for m/z 185.0819 (red line) and m/z 157.0506 (blue line), which originate from a loaded and a blank filter (red and blue dashed lines). The mass traces refer to biogenic marker substances. As the mass spectrometer was operated with a HESI ion source in negative mode, the EICs demonstrate the deprotonated compounds. The signal observed at a retention time of approximately 2 min in the EIC at m/z 157.0506 can be attributed to terebic acid, which is an oxidation product of α -pinene (Kołodziejczyk et al., 2020). The second mass trace (m/z 185.0819) shows several signals. The occurrence of these signals can be attributed to several constitutional isomers of pinic acid, an oxidation product of α -pinene, which exhibit identical mass-to-charge ratios. However, not only α -pinene is emitted in the atmosphere, but also various other terpenes such as 3-carene, sabinene or limonene. These terpenes oxidize and form compounds such as 3-careic acid,

sabincic acid, or limonic acid, which have the same sum formula as pinic acid. This results in the occurrence of different compounds at a single mass trace (Glasius et al., 2000).

It is evident that the signals of the loaded filters differ by an order of magnitude from those of the blank filter and that a high signal-to-noise ratio is achieved for both mass traces. This demonstrates that with the light aerosol sampling system presented here, in conjunction with the extraction method described, it is possible to detect and quantify various marker substances despite the relatively short sampling time. As a result, the presented system is ideally suited for use onboard UAVs.

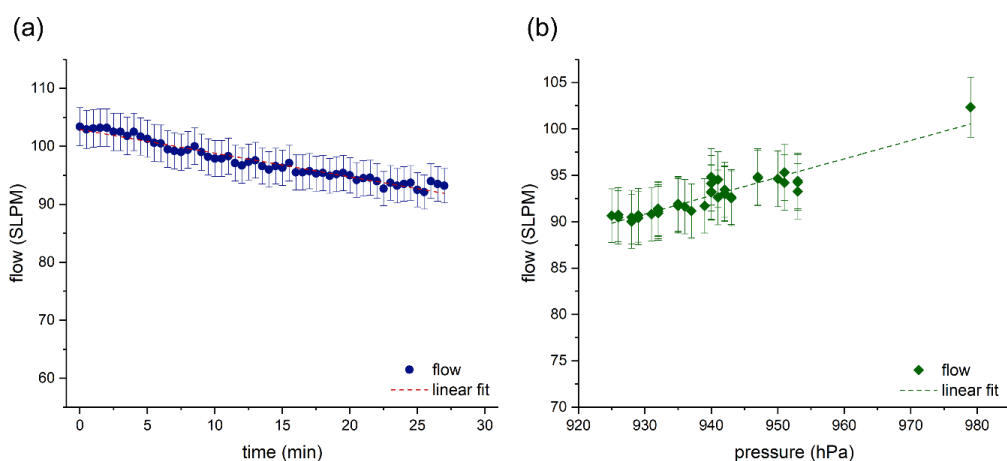


Fig. 6.2: (a) Flow through the filter holder as a function of time (at 980 hPa) (blue dots), the dashed line represents a linear fit of the data. The errors correspond to 2% of the measured value, which represents the measurement uncertainty of the flow meter (b) Flow through the filter holder as a function of pressure (green diamonds), the dashed line represents a linear fit of the data. The errors correspond to 2% of the measured value, which represents the measurement uncertainty of the flow meter.

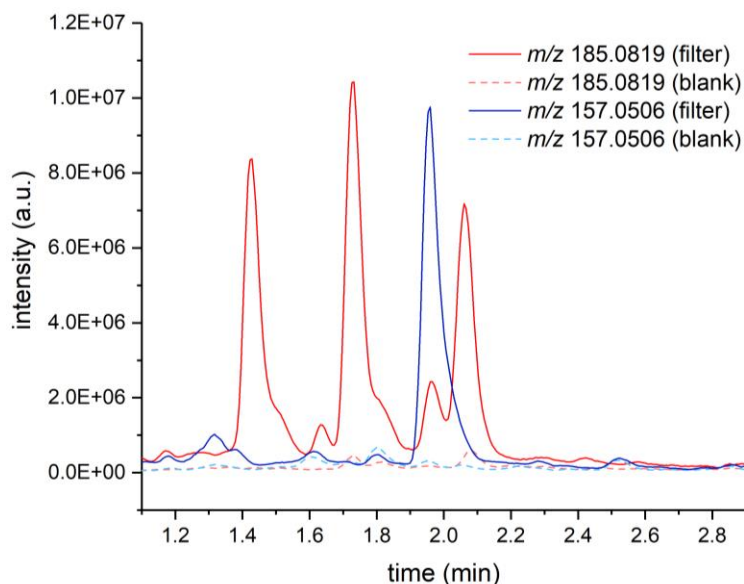


Fig. 6.3: Extracted ion chromatogram for m/z 185.0819 (red line) and m/z 157.0506 (blue line) for a loaded filter and the corresponding EIC for a blank filter (red and blue dashed line). This EIC is representative of biogenic marker compounds like pinic acid, limonic acid, sabincic acid, 3-caric acid (red line), or terebic acid (blue line).

6.4.2 Influence of the sampling UAV on the measured concentrations

To evaluate whether differences in the UAV models or sample device mounting positions (see Fig. S9.32) impact analysis results (e.g., due to aspiration flow variations), two samplers onboard UAVs and one at a metal framework were operated simultaneously at ~5 m height near Essenheim during a test flight. Fig. 6.4 compares the concentrations of a few selected exemplary compounds (pinic acid, 4-nitrophenol, terebic acid and 2,6-dimethyl-4-nitrophenol) at different sampling times for the respective systems. The results of these replicate measurements at the three different sampling periods are shown in brown, blue and green. According to these results, the concentrations of the individual compounds fluctuate noticeably between the different sampling periods, which is plausible due to the approximately one-hour delay between the three sampling periods. The differences between these measurement flights can be attributed to the different time of the flights and the resulting changes in the composition of the collected aerosol particles. The discrepancy between the second and third measurements is particularly evident for the anthropogenic markers 4-nitrophenol and 2,6-dimethyl-4-nitrophenol. Such fluctuations can be attributed, for example, to a change in wind direction and thus to a different origin of the sampled air mass. However, it is crucial that the differences between the different sampling systems within a measurement flight are comparatively low for the analytes.

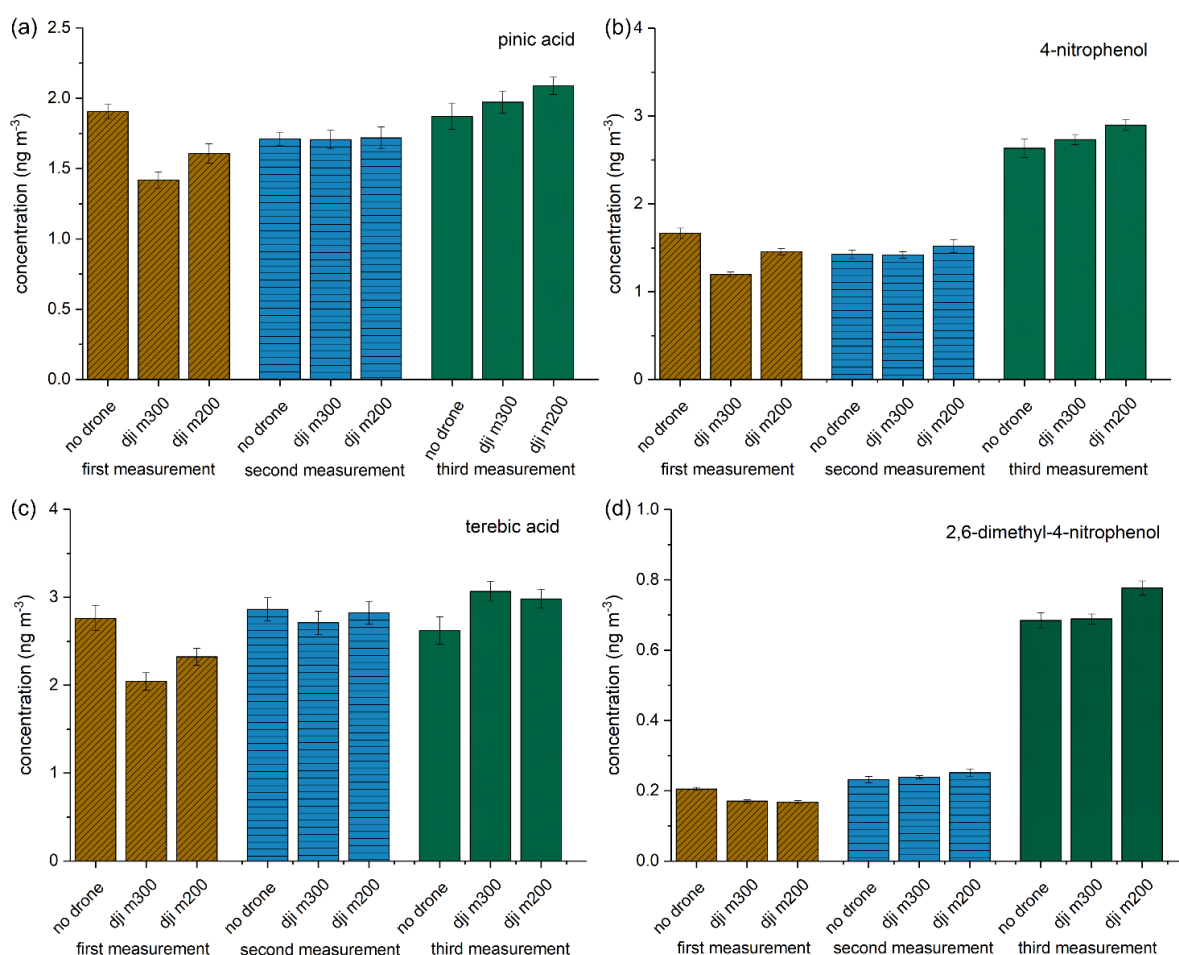


Fig. 6.4: Mean concentration of pinic acid, 4-nitrophenol, terebic acid and 2,6-dimethyl-4-nitrophenol, for the three measurement setups (no UAV; dji m300; dji m200) during three measurement flights (brown, blue and green). The error bar is the result of two error sources: the standard deviation derived

from the triple determination made by the LC-MS measurement; and the error associated with the flow measurement of the filter holder.

It can be concluded that the type of UAV used, or minor differences in the mounting position of the sampler on the UAV and the resulting differences in air turbulence around the filter holder, have no significant influence on the analytical results. A study by Crazzolaro et al. (2019) investigated the air-flow around a larger UAV than the one used in this study, using a colored smoke test. Their findings indicated that the air mass within a radius of up to two meters above the UAV can be affected by the downwash from the UAV. This phenomenon is therefore presumed to exert only a negligible influence on the measured concentrations in a mixed atmospheric boundary layer, as is the case with our results.

6.4.3 Vertical profiles of biogenic, biomass burning and anthropogenic marker compounds

The characterized filter sampler was used to sample aerosol particles simultaneously to measurements of a third measurement UAV, FLab (Moormann et al., 2025b) during the BISTUM23 campaign in August 2023 in Albstadt, Germany. This approach allowed for the acquisition of daily and height trends for OA at a measurement site, which is surrounded in all directions by a mixture of grassland, forest, agricultural land, and urban infrastructure (see Fig. S9.33).

Fig. 6.5 shows three height profiles at 10:35 am, 1:35 pm and 4:30 pm local time (UTC+2) for concentrations of the three biogenic marker components pinic acid (black square), terpenylic acid (blue triangle) and terebic acid (green diamond) in 1.5 m, 120 m and 500 m.

It can be seen that the concentrations at a height of 120 m are higher than at ground level (1.5 m). This observation can have multiple causes, for example the different footprint areas attributable to the various heights or also dry deposition of corresponding aerosol-borne components on the ground (Bamberger et al., 2011; Spielmann et al., 2017). Actually, this trend between 1.5 m and 120 m also coincides with the measured ozone concentration (Fig. S9.34). The ozone concentration is slightly lower at ground level than in the higher region. However, the concentrations of the selected oxidation products decrease up to a height of 500 m. This finding could be attributed to the higher average

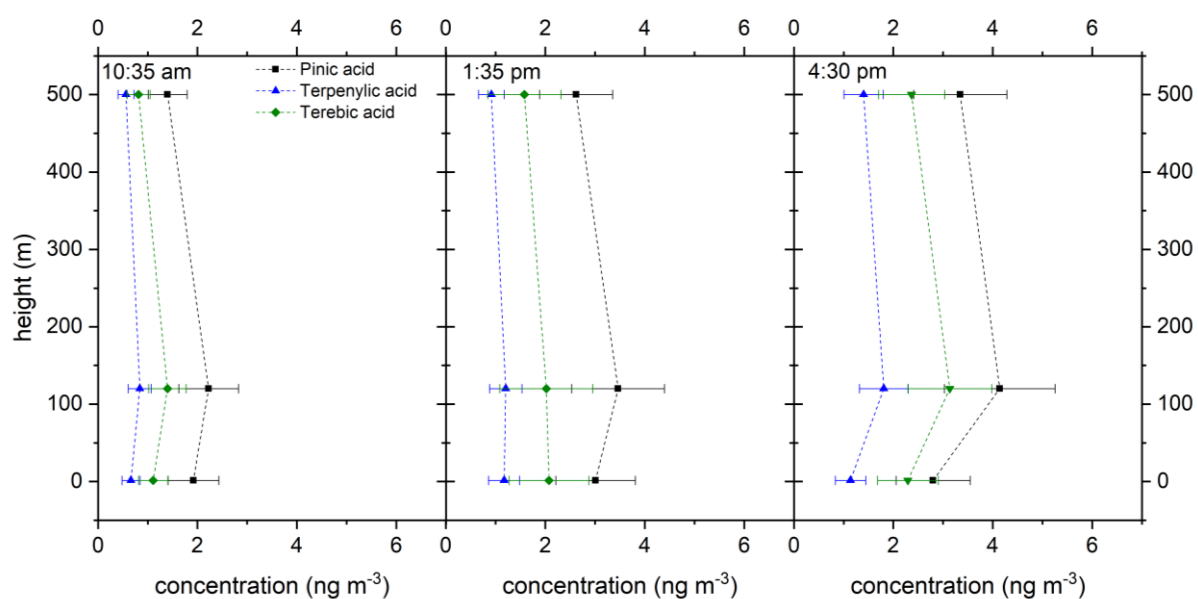


Fig. 6.5: Vertical profiles of the biogenic marker compounds pinic acid (black square), terpenylic acid (blue triangle) and terebic acid (green diamond) at the different times (all times are in UTC+2). For better clarity, these points are connected by dashed lines. The error bar is the result of two error

sources: the standard deviation derived from the triple determination made by the LC-MS measurement; and the error associated with the flow measurement of the filter holder.

residence time of the corresponding aerosol populations. One potential explanation for the concentration decrease is, among others, the further oxidation of the compounds measured here, which could lead to the formation of more highly oxidized compounds. In addition to the altitude trend, a distinct daytime trend can also be seen. From morning to afternoon, the concentrations of all three compounds increase at all altitude levels, although the relative increase depends on the individual compound. This is also in good agreement with the measured ozone concentration. The ozone concentration increases during the day at all altitudes.

Fig. 6.6 shows the altitude profile of some marker compounds for anthropogenic sources of OA and biomass burning, salicylic acid (purple circle), 4-hydroxybenzaldehyde (pink hexagon), 4-nitrophenol (turquoise pentagon), 2,6-dimethyl-4-nitrophenol (light blue half-filled circle), and 2,4-dinitrophenol (brown star). The actually measured concentrations are shown as symbols. For these marker substances, no clear trend can be seen in terms of altitude or time of day. It can be observed that the trend in terms of altitude or time of day is comparable for salicylic acid and 4-hydroxybenzaldehyde, as well as for 4-nitrophenol and 2,4-dinitrophenol. The differences between the trends are probably due to different sources of the marker substances. For example, salicylic acid and 4-hydroxybenzaldehyde are formed during the combustion of lignin (Fleming et al., 2020; Cao et al., 2022; Rana and Guzman, 2022). In addition, salicylic acid has been detected in vehicle exhausts, making it both an anthropogenic and a biomass-burning marker compound (Li et al., 2020a). The nitroaromatic compounds may originate from the combustion of biomass and the nitration of phenols or vehicle exhaust gases (Lu et al., 2019; Kulakova et al., 2020; Zhang et al., 2022). Consequently, they can also be considered as marker substances for biomass burning and anthropogenic substances. The highest concentrations of salicylic acid, 4-nitrophenol, 2,6-dimethyl-4-nitrophenol and 2,4-dinitrophenol were observed in the morning at a height of 120 m. This indicates that the air mass sampled at 10:35 am had crossed an area where biomass had been burned or where there was heavy traffic. The wind direction determined by FLab is southwest with a wind speed of 2 to 3 m s⁻¹ (Fig. S9.35 and Fig. S9.36).

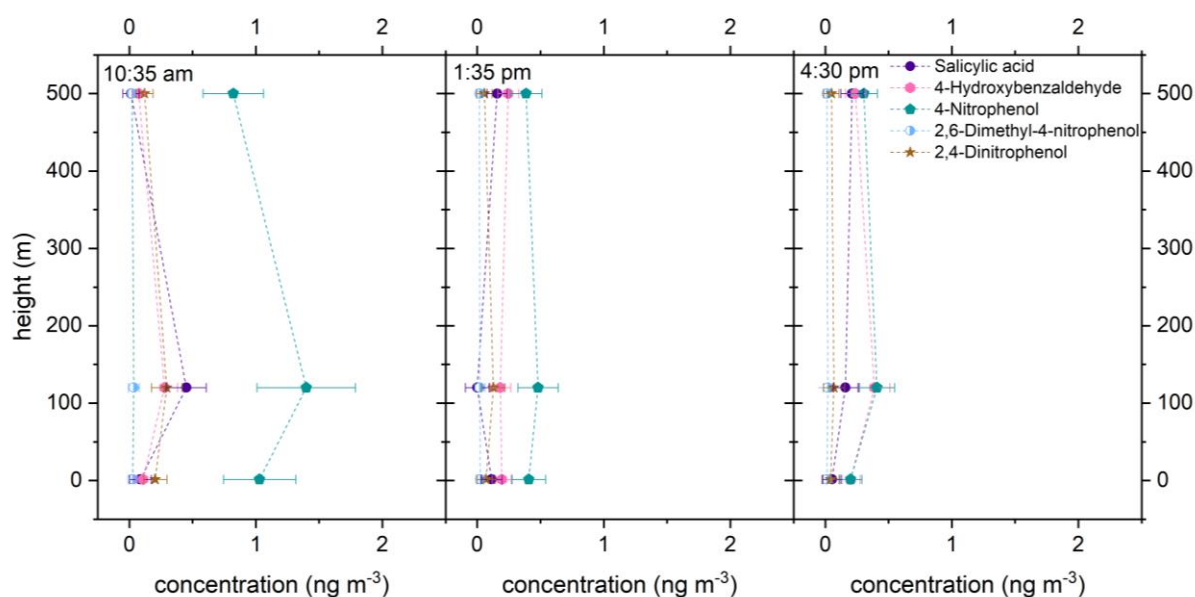


Fig. 6.6: Vertical profiles of the anthropogenic marker compounds salicylic acid (purple circle), 4-hydroxybenzaldehyde (pink hexagon), 4-nitrophenol (turquoise pentagon), 2,6-dimethyl-4-nitrophenol (light blue half-filled circle), and 2,4-dinitrophenol (brown star). The actually measured concentrations

are shown as symbols. For better clarity, these are connected with dashed lines. The error bar is the result of two error sources: the standard deviation derived from the triple determination made by the LC-MS measurement; and the error associated with the flow measurement of the filter holder.

A federal highway is also located in this direction. The backward trajectory for the 120 m sample created with the NOAA HYSPLIT model (Stein et al., 2015; Rolph et al., 2017) indicates that the sampled air masses crossed the federal highway at around 8 am (Fig. S9.37). Higher concentrations of anthropogenic markers can be attributed to rush-hour traffic. At ground level, the plume is less extended due to the surface layer (Stull, 2015), while at 500 m, it is diluted by dynamic air mixing or different origin of the air masses (Fig. S9.37). Thus, compound concentrations from the federal road, especially in the morning, are lower at 1.5 m and 500 m.

The measured concentrations of the anthropogenic markers are lower than those of the biogenic ones. The lower concentrations can be explained by the fact that the sampling site was in a rural area where anthropogenic influences are possibly less significant than biogenic ones.

6.4.4 Height dependent van Krevelen diagrams

In addition to the targeted analysis of individual marker compounds described above, a non-target analysis was also carried out. The results are shown in a series of Van Krevelen diagrams in Fig. 6.7. The underlying molecular formulas of the compounds shown can be unambiguously assigned due to the use of a high-resolution mass spectrometer with accurate mass determination and were determined using MZmine 2.53 software (Pluskal et al., 2010). These were used to determine the H/C and O/C ratios, which were then plotted against each other. The compounds were assigned to the four substance classes CHO (blue), CHON (green), CHOS (orange) and CHONS (pink), with CHO being the most abundant class. The size of the dots is defined by the measured peak intensity of the respective LC-MS measurement. All signals were normalized to the duration of the sampling. Since a HESI source was used as the ion source, it is important to consider the potentially different ionization efficiencies of the compounds. The ionization efficiency can differ by several orders of magnitude for differently functionalized compounds (Oss et al., 2010; Liigand et al., 2021). Therefore, the dot size essentially provides an overview of the concentration changes of the respective compounds as a function of time or height. However, it does not provide any information about the relative amounts between different compounds. The Van Krevelen diagrams are divided into five sections for better clarity. These are based on the maximum carbonyl ratio (MCR) of the compounds. This describes the maximum contribution of the carbonyl/epoxy functionalities of the components and thus provides an indication of their degree of oxidation. The five groups are *V*: highly unsaturated (combustion related), *IV*: oxidized unsaturated (primary organic carbon, oxidation products from aromatic VOC), *III*: intermediately oxidized (monoterpene first generation oxidation products), *II*: highly oxidized (monoterpene oxidation products, oxidative aging), and *I*: very highly oxidized (isoprene oxidation products) (Zhang et al., 2021). The composition of the aerosols should not differ significantly regardless of the origin of the air mass due to the remote location. At first glance, however, it can be seen that the Van Krevelen diagram at a height of 120 m in the morning (Fig. 6.7d) differs significantly from all the others. This sample shows a strikingly high number of CHO-containing compounds with high peak areas in the region between areas *III* and *IV* and in area *V*, likely originating from combustion processes. Studies link these regions of the Van Krevelen diagram to biomass combustion (Tang et al., 2020). Compounds in this area ($C_{20}H_{26}O_3$, $C_{20}H_{28}O_2$, $C_{20}H_{28}O_3$, $C_{20}H_{30}O_2$, $C_{20}H_{30}O_4$) are identified as biomass combustion markers in previous research (Smith et al., 2009; Ramteke et al., 2025). The intense biomass burning and anthropogenic tracers in the 120 m morning sample (section 6.4.3) may result from vehicle exhaust

and biomass burning, as discussed for the vertical profiles of anthropogenic substances in Fig. 6.6 and section 6.4.3. However, the change in the surface layer and atmospheric boundary layer heights in the morning hours is likely related to these observations. To examine general trends over height and time of day, the Van Krevelen diagram for a height of 120 m in the morning is not considered in the discussion below.

The vertical profiles at 1:35 pm and 4:30 pm are very similar. At a height of 1.5 m, there are several substances in area *IV* that are no longer present at heights of 120 m and 500 m, or are present in significantly lower concentrations. This can be attributed to the oxidation of the substances to more highly oxidized compounds. In addition, a shift of the points to higher O/C and H/C ratios is observed between 120 m and 500 m, which leads to an increased number of substances in section *II*. This also indicates that the observed compounds at higher altitudes are evolving into more highly oxidized substances. The observed tendency towards higher concentrations of higher-oxidized compounds at higher altitudes can be explained by the longer residence time in the atmosphere before reaching these altitudes. Consequently, terpenes, isoprene and their oxidation products are exposed to

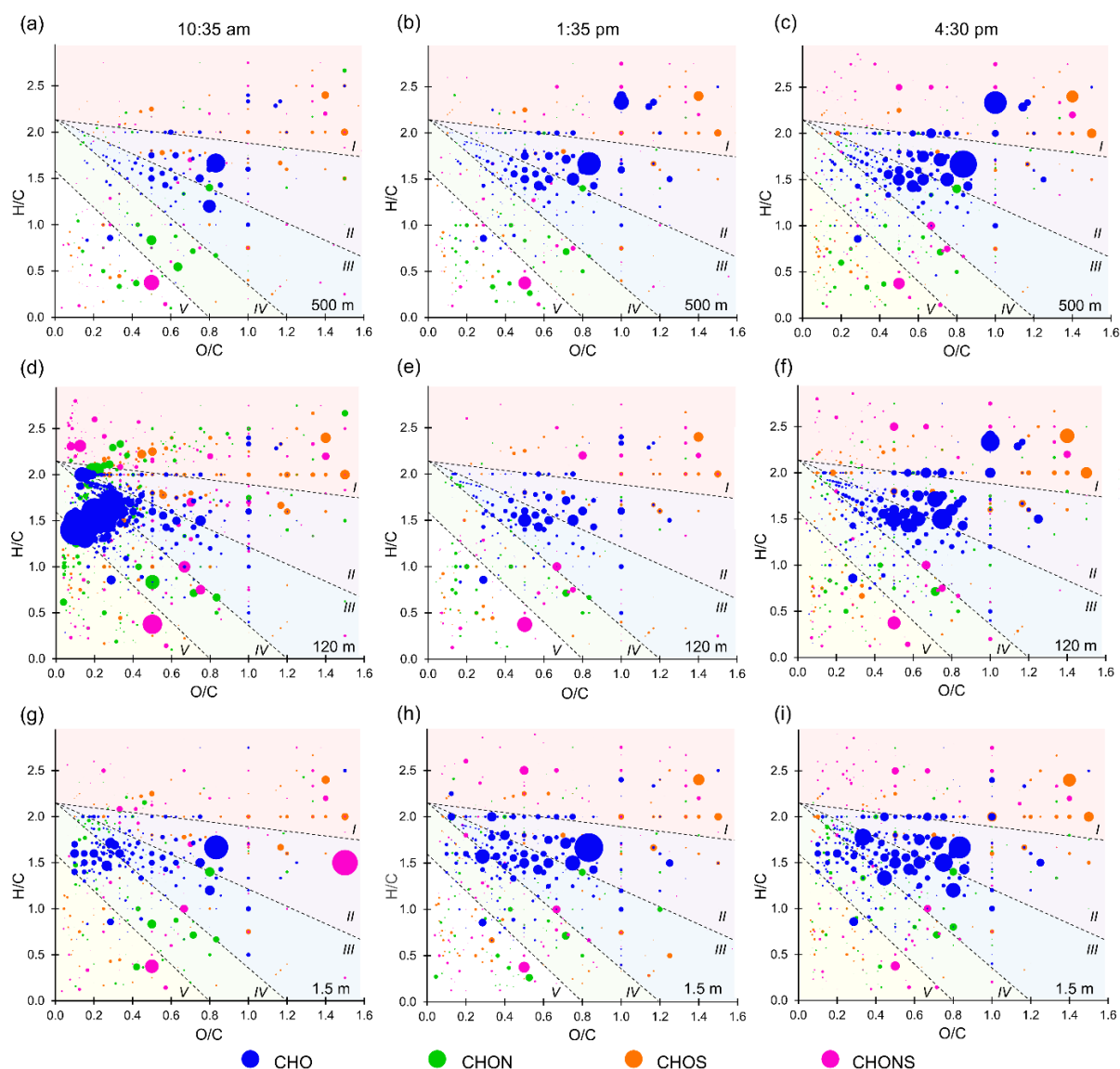


Fig. 6.7: Van Krevelen diagrams in the late morning (left), in the early afternoon (middle) and in the late afternoon (right). The different substance classes are represented by different colors (CHO blue; CHON

green; CHOS orange; CHONS pink) The size of the dots correlate with the measured peak area of the compounds. The Van Krevelen diagrams are divided into 5 areas depending on the MCR, which are separated by dashed lines (Zhang et al., 2021).

oxidizing species for a longer period of time, resulting in the formation of more highly oxidized compounds.

For the variation during the day, the diagrams at the same altitudes can be compared with each other. It is noticeable that the size of the points and thus the associated measured concentration increases during the course of the day, particularly for the CHO-containing compounds. This finding is also consistent with the targeted approach, which detects an increase in the concentrations of biogenic SOA compounds (in this case CHO compounds) during the course of the day. The higher concentration of CHO-containing compounds can be attributed to the rising temperature and the accumulating oxidation product concentrations over the course of the day. As the temperature rises, more biogenic substances such as terpenes are emitted by the trees, which are then oxidized to CHO-containing compounds over the course of the day (Niinemets et al., 2004; Vettikkat et al., 2023).

6.5 Conclusions

This study demonstrates that UAVs can also be used as a sampling platform for detailed chemical characterization of organic aerosol components using UHPLC-MS. The developed aerosol sampling unit allows the collection of sufficient aerosol mass for both targeted and non-targeted analysis of primary and secondary organic aerosol components within the maximum flight time of the UAVs used. The newly developed, very light aerosol sampling system with a weight of approx. 560 g was successfully tested at two locations in Germany. Comparative measurements with three identical aerosol samplers on different UAVs (Matrice 200 and Matrice 300 models, both DJI) showed that the UAVs themselves and slight differences of the mounting position on the UAVs had no significant influence on the results. During a measurement campaign (BISTUM23), a series of filters were sampled in parallel using two UAVs and a ground-based framework, supported by another measurement UAV that measured the gas phase and meteorological conditions throughout the day. The aim was to perform vertical concentration measurements to investigate the variations in aerosol composition during the course of a day. For this purpose, aerosol samples were collected simultaneously at ground level, 120 m above ground and 500 m above ground.

The primary aim of the measurements shown above is a proof-of-concept, as the amount of data alone is of course not sufficient to make general statements about vertical concentration profiles of organic aerosol components. Nevertheless, some initial conclusions can be drawn about the measured analytes. The biogenic SOA markers pinic acid, terebic acid, and terpenylic acid show increasing concentrations from the morning hours to the afternoon hours. This result is consistent with the observed increase in ozone concentrations during the day. Both the rising temperatures during the day and thus the increasing release of precursor VOCs during the day and the increasing importance of oxidation reactions can explain this concentration trend (Niinemets et al., 2004; Vettikkat et al., 2023). Interestingly, the vertical concentration measurement showed that the maximum concentration of these compounds was often observed at a height of 120 m, an observation that may be attributed to different footprint regions, dry deposition and chemical ageing (Bamberger et al., 2011; Spielmann et al., 2017). The highest concentrations of anthropogenic markers were observed in the morning hours. The wind data (Fig. S9.35 and Fig. S9.36) and HYSPLIT back trajectories (Fig. S9.37) indicate that this phenomenon may be due to the main road during rush hour. In general, the concentration of anthropogenic marker compounds is lower than that of biogenic compounds, which can be explained by the

remote location of the sampling site, where biogenic processes can have a greater influence than anthropogenic activities.

The results of the non-targeted analysis of the filter samples are consistent with the trends identified in the targeted analysis and show an increase of oxidized compounds throughout the day and with increasing altitude. Consistent with the targeted approach, compounds associated with automobile exhaust and biomass combustion products are particularly present in the morning samples. In summary, this study highlights the use of UAVs as an innovative platform for the sampling and chemical characterization of organic aerosols using UHPLC-MS. The developed sampling unit collects sufficient aerosol mass within the UAVs' flight time, enabling both targeted and non-targeted analysis of primary and secondary organic aerosols. A voltage regulator could be integrated in the future to ensure a constant flow through the aerosol sampler. This approach facilitates cost-effective, height-selective sampling, allowing the measurement of vertical concentration profiles and access to otherwise challenging or inaccessible locations for aerosol sampling.

Author contribution: CB and TH developed the filter holder and planned the measurements; CB performed the analytical measurement of the OA samples, analyzed the data and wrote the manuscript draft; BG, NK and TH performed the UAV flights; LM performed the flights of FLab and analyzed the ozone and wind data; TH, LM, BG and NK reviewed and edited the paper.

Financial support: This work was funded by the Deutsche Forschungsgemeinschaft (DFG, German Research Foundation) – TRR 301 – Project-ID 428312742 and HO 1748/24-1 (Project-ID 541033130).

7 Influence of Irradiance and Mixing Layers on the Representativity of Ground-based Measurements

This chapter contains a first complete manuscript draft. After further coauthor exchange and optimization, it will be submitted to a peer-review journal as

Moormann, L., Fachinger, F., Drewnick, F.: *In-situ measurements of boundary layer structures: influence of irradiance and mixing layers on the representativity of ground-based measurements*

Contribution to this manuscript by Lasse Moormann:

As the first author of this work, I conducted all measurements with FLab during the BISTUM23 and BISTUM24 campaigns, after successfully applying for permission for aerial deployment. I conducted night-time vertical profiling, including developing the measurement strategy and maintaining the instruments. I analyzed the FLab data from both campaigns and developed data evaluation methods to investigate the representativeness of ground-based measurements. Finally, I prepared all figures and wrote the manuscript, which was then revised with input from all co-authors.

7.1 Abstract

Ground-based atmospheric measurement stations are typically treated as horizontally representative, yet their vertical representativity is often assumed rather than evaluated. To assess this critically, we conducted drone-based in situ vertical profiling during two 2.5-week summer field campaigns in rural Central Germany during which we also examined the effectiveness of pollutant and meteorological tracers for detecting mixing layer heights (MLHs). Using a gradient-based approach, we evaluated how irradiance, MLHs, and location of a measurement site influence ground-based station representativity. Nighttime vertical profiling of temperature, humidity, wind speeds, and trace substances (CO₂, O₃, particle mass and number concentrations) in the lowest 120 m revealed a multiple-layer fine-scale stratification with trace substances showing enhanced sensitivity for MLH detection than traditionally used meteorological variables. Among all variables, O₃ and potential temperature were the most effective MLH markers, highlighting the benefits of combining pollutant and meteorological measurements to understand stratification processes.

Daytime profiles up to 500 m in slightly unstable conditions showed that under low irradiation, MLHs closely reflected atmospheric instability and constrained aerosol distributions, whereas strong irradiance produced well-mixed conditions that weakened the dependence of pollutant distributions on MLHs. This suggests that distinguishing between high- and low-irradiation conditions in the planetary boundary layer could improve parameterization for vertical mixing. The investigation of ground-based representativity within the mixing layer suggests that MLHs and radiatively driven mixing should be considered when interpreting ground-based station data. Meteorological variables tend to remain more robust across radiative regimes, while pollutant measurements additionally require accounting for local sinks and entrainment.

7.2 Introduction

Ground-based measurements have been the primary method for ambient atmospheric research and monitoring, evolving from single-point observations to monitoring networks for various pollutants (EPA, 2025; UBA, 2025) and reference stations (Hoerger et al., 2015; Pastorello et al., 2020). It is typically assumed that measurements from a single station are representative for a broader area. The representativity of a measurement site is a vaguely defined quantity for how well a measurement station provides data that are not influenced by local anomalies (Hakuba et al., 2013; Merlone et al., 2024). Horizontally, representativity may range from only a few tens of meters in urban stations, but may reach over several hundreds of kilometers in flat, homogenous terrain (Ho et al., 2020; Yang et al., 2020). Vertical representativity is less critically reflected and is constrained by two considerations:

- a) It varies with horizontal location in complex terrain or heterogeneous emission areas, where the vertical structure of air masses differs over short distances (Peters et al., 2022), and
- b) even over homogeneous terrain, the lower troposphere exhibits a pronounced diel stratification with diel turbulence, limiting how well a single near-surface measurement represents the full layer (Dandou et al., 2009).

Although these limitations are recognized—and (a) is typically considered during site selection, (b) is often neglected in ground-based studies, where the planetary boundary layer (PBL) is implicitly treated as uniformly “mixed.”

During daytime, the PBL often grows to about 1–2 km above ground as a consequence of surface heating and buoyancy-driven turbulence, which reduces vertical gradients of surface-emitted pollutants. After sunset, radiative cooling stabilizes the surface layer (SL) and the PBL collapses into a shallow nocturnal boundary layer (NBL), typically a few tens to a few hundreds of meters deep, capped by an inversion separating it from the residual layer (RL) aloft. The RL is a remnant of the daytime PBL and is largely decoupled from the surface (Stull, 1988). In addition to irregular stratification within the NBL, low-level jets (LLJ) can be generated after the formation of the RL in the early night, when the RL is already separated from the surface layer. This results in less surface friction, which can contribute to a stronger laminar geotropically-influenced flow that can transport air masses for up to a few hours over long distances (Blackadar, 1957; Luiz and Fiedler, 2024). During sunrise, intensifying radiation-driven turbulence dissipates the NBL top and mixing of the NBL with the RL forms a new PBL, closing the diel cycle of the PBL.

Mixing layer heights (MLHs) are quantifiable measures that describe the upper boundaries of the well-mixed lowermost layer, where chemically or dynamically different air masses adjoin. Reliably distinguishing such layers supports the interpretation of microphysical and dynamical processes. As MLHs have different altitudes at different times of day, and are affected by various mechanisms (see above), definitions and diagnostic criteria that describe a MLH are manifold and case dependent. Definitions range from stability measures like the Richardson number and the gradient of the potential temperature (Monin and Obukhov, 1954; Busch et al., 1976; Wyngaard and LeMone, 1980; Troen and Mahrt, 1986) to pollutant concentration changes of, e.g., aerosol particles, O₃, or CO₂ (Collis and Ligda, 1964; Okada et al., 2012; Perrone and Romano, 2018; He et al., 2023). Some definitions are based on threshold values, other approaches consider gradient changes or inflection points in vertical profiles. Thus, a universal definition of the MLH does not exist (Mercer et al., 2018).

Available technologies for studying boundary layer meteorology include model approaches, experimental data, and hybrid methods. Regional-scale and re-analysis models provide insights into processes in the vertical structure of the PBL (Nieuwstadt, 1984; Debolskiy et al., 2023), but model idealization may not suit complex terrains like valleys or hills with complex dynamics and fail at predicting unusual stratification (Moeng and Sullivan, 1994; Emanuel and Živković-Rothman, 1999). Ground-based measurements are often extrapolated to model vertical profiles (Monin and Obukhov, 1954; Troen and Mahrt, 1986). Remote-sensing tools like satellites, Lidars and radars provide low maintenance-intensive observations to support ground-based observations or to correct model data (Collaud Coen et al., 2014; Duncan Jr et al., 2022; Kotthaus et al., 2023; Wang et al., 2025), though remote-sensing tools have an enhanced risk of misinterpretation due to the limited number of measurable variables. In situ platforms like radiosondes (Seidel et al., 2010; Guo et al., 2016), aircraft (Moores et al., 1979; Dai et al., 2014), tall towers (Andreae et al., 2015; He et al., 2023), and UAS (uncrewed aerial systems) can be used to record multiple variables for a comprehensive analysis (Reuder et al., 2012; McWilliams et al., 2023; Moormann et al., 2025b), reducing uncertainty in boundary layer analysis. However, these methods are costly and labour-intensive (in construction and operation) and require extensive validation of the respective platforms. Radiosondes and aircraft focus on large-scale phenomena, while towers and UAS typically operate within the lower few hundred meters. Towers require extensive installation, while UAS are flexible and manoeuvrable and, hence, are optimal for boundary layer observations.

This study uses drone-based in-situ measurements at two similar hilly sites in Central and Southern Germany during summer to evaluate

- a) the applicability and sensitivity of various meteorological variables and trace gases and matter (CO_2 , O_3 , and aerosol particles concentrations) for detecting vertical structures using gradient-based methods (up to 120 m with 2 m resolution) during nighttime, featuring a fog event and a low-level jet and
- b) the representativity of ground-based measurements with respect to the mixing layer (from vertical 500 m-profiling measurements) for meteorological variables and trace matter, focusing on influences from irradiation, the PBL height (PBLH) and adiabatic effects.

7.3 Methodology

Two field measurement campaigns (BISTUM23, August 2023 and BISTUM24, June 2024) were conducted at rural sites in Central and Southern Germany in summertime to investigate the dynamics of stratification on the trace matter distribution in the lowermost troposphere. For 2.5 weeks each, co-located UAS-based and ground-based measurements were performed.

7.3.1 Measurement sites

Both campaigns, BISTUM23 and BISTUM24, were conducted in rural areas on the grassy-forested slopes of German low-mountain ranges, with no nearby emission sources.

BISTUM23 took place near Albstadt, Swabian Alb ($48^\circ 15' \text{ N}$, $8^\circ 59' \text{ E}$, Fig. S9.40), with the ground station at 886 m above sea level. The site was chosen due to the absence of large habituated or industrialized regions upwind of the location.

BISTUM24 was performed near Spielberg, Vogelsberg region ($50^\circ 19' \text{ N}$, $9^\circ 15' \text{ E}$) with a ground station at 391 m above sea level (Fig. S9.40). Air masses reaching the BISTUM24 site showed an anthropogenic influence indicated by enhanced pollution levels when they had passed the Frankfurt Rhine-Main metropolitan area (FRM, ~ 30 km upwind with 5.9 million inhabitants). To investigate whether air masses were well mixed, 24 h-backward trajectories (Sect. 7.3.3) with starting points in 50 m-altitude increments were used to differentiate between air masses that had passed FRM and air masses that had passed only rural regions prior to arriving at the BISTUM24 site. Using this classification, average vertical profiles of the trace substance variables O_3 , CO_2 and the particle number concentration were calculated for both aspiration cases. Fig. S9.41 shows that, although pollutant levels were higher when air masses had passed FRM, plumes in both cases were well-mixed in the lowermost 500 m. Therefore, we consider the BISTUM24 site as sufficiently distant from major emission sources to be able to assume that anthropogenic plumes have already been vertically mixed.

Hence, we assume that the variability of trace matter concentrations in the lowermost 500 m for both campaigns are due to natural atmospheric processes.

7.3.2 Experimental data

During both campaigns, atmospheric data were collected using ground-based and UAS-based measurement platforms. The ground-based research van “MoLa” (Mobile Laboratory; Drewnick et al., 2012) operated continuously with inlets for aerosol and gases positioned 6 m above ground level. It was used

for on-line measurement of various variables, including CO₂ and O₃ mixing ratios, particle number concentrations (PNC), particle mass concentrations across different size ranges, and meteorological data such as wind speed and direction, relative humidity, temperature, precipitation, and irradiance (Table S9.13). An ultrasonic anemometer, positioned 5 m above ground near MoLa, was used to measure latent heat flux (Table S9.13; exclusively during BISTUM24).

The UAS-based measurement platform, known as the Flying Laboratory (FLab; Moormann et al., 2025b), monitored a wide set of variables similar to several of those measured by MoLa. These included CO₂ and O₃ mixing ratios, PNC for particles larger than 10 nm (PNC_{> 10 nm}, low measurement uncertainty) and 350 nm (PNC_{> 350 nm}, high statistical uncertainty), particulate matter PM₁ and PM_{2.5}, as well as meteorological data like horizontal wind speed and direction, temperature, and relative humidity (Table S9.13).

While in MoLa, high-grade instrumentation was used for precise ground-based measurements, FLab utilized mid-grade sensors to minimize payload and enable aerial operation. FLab was typically operated hourly for vertical profiling up to 500 m during the day, if rain or stormy gusts ($> 16 \text{ m s}^{-1}$) did not threaten safe operation. In addition, a full-night operation for profiling the lowest 120 m during BISTUM24 was conducted. Each flight lasted ~ 15 min and began with hovering at 6 m above ground level near the MoLa inlet, followed by two ascents and descents with a vertical speed of 3 m s^{-1} . Between these ascents and after the final descent, additional hovering near the MoLa inlet was performed for comparison of the high-grade ground sensors with the UAS sensors.

7.3.3 Data evaluation

Instrumentation of MoLa and FLab were calibrated prior to the campaign. Regular inter-platform comparisons between MoLa and FLab (Sect. 7.3.2) were used to correct for sensitivity drifts of UAS-borne instruments as suggested in Moormann et al. (2025b). The influences of rapid changes in humidity, temperature and pressure on the instruments during vertical motion were corrected with formulae provided by the manufacturers.

In order to investigate vertical profiles within the 15 min-time frames of the individual flights, the FLab data need to be corrected for temporal variation of probed air mass properties. This is necessary because air masses have not been probed in different altitudes simultaneously. Therefore, the 1 s-time series of each variable of the FLab data were corrected for temporal variations in the reference data (measured by MoLa; these data were previously smoothed by calculating the 15 s rolling mean in order to reduce the influence of noise). This temporal correction was done by multiplication of each FLab data point with the ratio of the respective data point in the smoothed time series of the MoLa data to a representative data point in the MoLa time series (at the beginning of each campaign). For this correction we assume that temporal variations are the same at all measurement locations due to an (assumed) homogeneous atmospheric distribution over this range. Throughout the following, only such temporally corrected data was used, with exceptions for wind speed due to fast fluctuation and R_i , which cannot be estimated by MoLa; all data are given in local time (UTC +2).

Data from UAS-borne measurements were averaged for vertical increments of 2 m and 25 m for further investigation. Error calculations account for the standard error of the averages and the instrument's uncertainty for the respective averaging time (Moormann et al., 2025b).

The PBLHs for both campaigns were estimated based on the definition by Wang and Wang (2014) using the ICON-D2 model (Crueger et al., 2018; DWD, 2025b), methodically described in Moormann et al. (2025a).

7.4 Nocturnal Boundary Layer: Height Criteria and Fine-scale Structure

In the evening, the PBL transitions from convectively mixed daytime conditions to stable, stratified nocturnal conditions. This change results in a complex, time-dependent vertical structure with several distinct layers (Nieuwstadt, 1984; Kotthaus et al., 2023). Various methods and modelling approaches are employed to determine nocturnal MLHs, similar to how MLHs are determined during the day. However, MLH detection methods that are based on a single atmospheric marker often fail unpredictably due to changes in air mass dynamics or composition around the MLH or due to the lack of vertical resolution (Kotthaus et al., 2023). While many MLH estimations rely on ground-based data, remote sensing and modeling approaches, methods based on frequent high-resolution in-situ measurements are considered the most accurate. These latter methods can estimate MLHs with accuracies of a few meters (Cava et al., 2019; Mahrt and Acevedo, 2023).

To explore which are the most sensitive and most accurate atmospheric variables for determining MLHs during nighttime, we operated the FLab hourly throughout the night from June 20 to 21, 2024. Vertical profiling commenced after the passing of a cold front (with associated heavy rain) at 15:00 on June 20. During the night, the vertical profiling was limited to 120 m above ground, which was anticipated to be sufficiently high to surpass the NBL and eventually reach an LLJ. While this limitation restricted the profiling flights to lower altitudes, it allowed to ascent slower and more often. Longer sampling time in the 120 m range improved data reliability of the spatially highly-resolved 2 m-increments of the vertical profiles (Fig. S9.42). MLHs were manually identified for a variety of FLab-measured trace substance concentrations (Fig. 7.1a) and meteorological variables (Fig. 7.1b) based on the observation of strong gradient changes and inflection points. To account for subjectivity of this definition, we estimated a conservative uncertainty based on the respective vertical profile (i.e., we estimated the range of justifiable MLHs for each case). Additionally to the gradient-based criteria, we use the bulk Richardson number (Ri) as a fixed criterion to identify the MLH due to its widespread use in boundary layer studies (Stull, 1988). $Ri > 0.25$ indicates stable atmospheric conditions (as expected above the NBL), while $Ri < 0.25$ describes unstable conditions (i.e., within the NBL).

Fig. 7.1 depicts all 1 h-MLHs and shows that a nocturnal cycle is discernible in MLHs determined both from trace gases and matter and from atmospheric variables. Even before sunset at 22:00, several variables' vertical profiles suggest stratification in different heights across the 120 m altitude range. After sunset until 02:00, a layer top was observed at ~50 m with a strong spread between variables, which slightly ascended to ~80 m while narrowing the spread. After 05:00, this uppermost (within the probed altitude range) detected MLH was slightly lifted from 70 m to 100 m and then disappeared after 10:00 in good agreement especially for MLHs determined with meteorological variables. Based on this general analysis, the lower layer can be attributed to the NBL and the upper layer to the RL as they are the most prominent nocturnal layers.

In addition to the identification of the NBL height, the highly time-resolved profiles of various variables allow an identification of three fine-structured layers: a descending layer between 23:00 and 01:00 down to 100 m, a shallow layer between 02:00 and 04:00 below 10 m and an additional layer in the NBL reaching from the ground up to 50 m from 05:00 to 08:00, while the NBL height was ~90 m.

The descending mixing layer top (from 23:00 to 01:00) is primarily detected by abrupt changes of the trace gas and matter gradients (O_3 , CO_2 , and PM_{10}) and wind-related variables (Ri and wind speed). The layer situated above the NBL is likely the RL that remained from the previous day, while the descending layer above this layer could be the lower part of an LLJ. The assumption that an LLJ was formed is

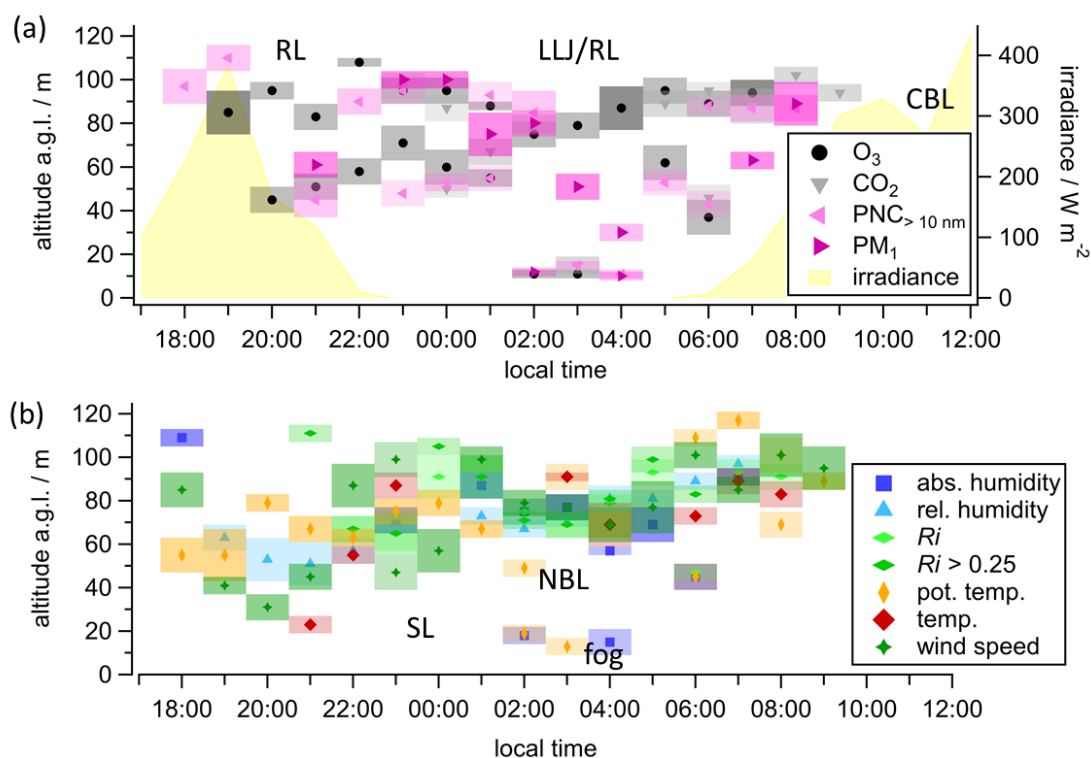


Fig. 7.1: Estimated boundary layer heights (with uncertainty ranges depicted as shaded areas) during the night of June 20 to 21, 2024. The boundary layer heights were derived from strongest gradient changes of the respective trace gas and matter variables (a) and meteorological variables (b) and when $Ri > 0.25$ was fulfilled.

supported by the observation of more laminar and faster winds in this altitude range that led to enhanced vertical gradients. Additionally, a different chemical composition of the uppermost layer is reflected by sudden gradients and concentrations changes in O_3 , CO_2 , and PM_{10} which indicate that the respective air may originate from more distant regions. Starting at 01:00, the separation between the RL and the LLJ-affected layer becomes indistinct, which indicates a weakening of the LLJ after at least 3 h.

Furthermore, independent of the establishment of a strong NBL, the absolute humidity- and potential temperature (θ)-profiles indicate the formation of a shallow layer up to 10 m above ground level (a.g.l.) at 02:00, 1 h before the ground-based measurement station recorded a fog event. While the fog thickened and the ground-based station observed enhanced PNC and reduced O_3 (Fig. S9.43), MLHs derived from vertical gradients of PNC and O_3 (MLH = 10-12 m a.g.l.) agree with those from absolute humidity- and θ -profiles.

A third fine-structure in the stratification was identified at 05:00 in 50 ± 10 m and lasted for 4 h until its dissipation before 09:00. Apparently, the preceding fog event initiated the formation of a cold pool during night (Chachere and Pu, 2016), which converts turbulent energy into an upwards directed latent heat flux and forms a shallow inversion layer above the ground (Wilson and Fovell, 2016). In this case trace gas and matter variables (CO_2 , O_3 and PM_{10}) were more sensitive for the identification of this feature than meteorological variables (except for 07:00 in 45 m). Thermodynamic stability indicators like θ or Ri were not able to detect this layer, likely due to relatively small changes of the already low nocturnal energy budget, while the distribution of CO_2 , O_3 and PM_{10} from ground is limited by the available turbulent energy for mixing. As radiative heating starts warming the ground, this lowermost layer dissipates 2 h prior to the NBL, which emphasises the sensitivity of this stratification. This third example

of the fine-structure analysis shows that the spatially highly-resolved vertical profiles are not only capable of identifying synoptic-scale phenomena such as LLJs, but also of revealing favourable local conditions for fog and of characterizing the vertical extent of fog events. As shown in this example, especially trace gas and matter variables can be helpful to differentiate layers under dynamically weak conditions, where meteorological indicators might fail.

These analyses of the NBL fine-structure using hourly vertical profiles of multiple variables show that there is a strong difference between the power of different variables to detect details in atmospheric stratification. Throughout the night from 18:00 to 10:00, the profiles of O_3 and the potential temperature θ provide useful MLH information 23 times and 19 times, respectively. In contrast, the air temperature and the $Ri = 0.25$ -criteria were the least sensitive variables for MLH-detection, each indicating the MLH 8 times. O_3 - and θ -profiles even provide information on multiple layers 10 and 7 times during the night, respectively, whereas the other variables typically reveal information on double layers only once or not at all. O_3 and θ appear therefore to be the most sensitive indicators for MLH detection. Hence, they are recommended for nocturnal MLH detection. Nevertheless, as a best-practice, we suggest to validate the MLH determined by any indicator using multiple variables, also to understand its formation background and the underlying dynamics that often cannot be interpreted with a sole variable.

This analysis demonstrates that:

- a) Highly spatially and time-resolved vertical profiles are essential for detecting shallow layers.
- b) While meteorological variables are necessary for characterizing air masses, trace gas and matter variables may offer higher sensitivity and accuracy for NBLH detection.
- c) Trace substance variables can provide information about stratification even when dynamic influences are minimal.

However, there remains a need for objective stratification detection algorithms, as manual estimations of MLH can be subjective and may lead to misinterpretation.

7.5 Influence of Solar Irradiance on Trace Matter Distribution

After sunrise, radiative heating leads to mixing of the RL into the NBL and affects the maximum extent of the convective boundary layer. Although this relationship is widely recognized, the impact of solar irradiance on the distribution of trace matter in the lowermost troposphere remains an active area of research. Here, we investigate the influence of solar irradiance on the distribution of trace matter, their gradients and to which extent ground-based measurements describe the conditions in the PBL accurately, particularly under convective conditions.

7.5.1 Classification of “clear-sky” and “cloudy” days

All measurement days during BISTUM23 and BISTUM24 could be categorized as “B/C” (moderately/slightly unstable) according to the Pasquill-Gifford stability categories (Gifford, 1961). This scheme has been traditionally used to classify the atmosphere according to its stability, based on wind speed and solar irradiation. Since wind speeds depend strongly on local topography and Pasquill-Gifford methods often fail to identify daytime instability at many sites (Kahl and Chapman, 2018), especially in the “B/C” regime, further classification is necessary.

For simplicity, we categorize measurement days throughout the campaigns into "clear-sky" and "cloudy" depending on the integrated daily solar irradiance that has reached the measurement site. A strong correlation (Pearson's $r^2 = 0.74$, Fig. S9.44) between latent heat flux measured in 5 m above ground and irradiance during BISTUM24 (30-min averages) suggests that irradiance can be used as a proxy for solar radiation-driven mixing, especially in the lower part of the PBL (Behrendt et al., 2020), although there are additional drivers for latent heat flux apart from irradiance which we do not regard in this study. For BISTUM23 and BISTUM24, the unimpeded average hourly solar irradiance was calculated from local photometer measurements under perfectly cloudless conditions taking into account the sun's zenith angle. We then compared the observed daily total irradiance (integration over the whole day) to this theoretical daily maximum: days with a fraction > 75% were classified as "clear-sky," otherwise as "cloudy." Days with heavy rainfall were also classified as "cloudy" to account for evaporation-driven gradients (Fig. S9.45). For comparisons between the two field campaigns, which both were conducted in a hilly terrain in summer, we keep the classified days of the two campaigns separated, resulting in a total number of 10 "cloudy" and 4 "clear-sky" days for BISTUM23 and 10 "cloudy" and 5 "clear-sky" days for BISTUM24.

Hourly drone-based 500 m-vertical profiles were calculated for all measured variables from both campaigns. Hours of the day represented by only a single available profile within a campaign and cloudiness-class were excluded from further analysis. The classification resulted in 42 vertical 500 m-profiles under "clear-sky"-conditions during BISTUM23 and 70 profiles during BISTUM24. In contrast, 42 and 59 vertical 500 m-profiles were probed during "cloudy" days during BISTUM23 and BISTUM24, respectively. The number of profiles with respect to the number of measurement days is comparatively fewer for both campaigns for the "cloudy" days due to the often less favorable flight conditions compared to "clear-sky" days. The daily mean differences in irradiance between "clear-sky" and "cloudy" days were: 170 W m^{-2} for BISTUM23 and 178 W m^{-2} for BISTUM24 (for 13 h of irradiance $> 50 \text{ W m}^{-2}$); the daily mean differences in precipitation were: 3.0 mm (BISTUM23) and 3.5 mm (BISTUM24). These results from the campaigns suggest comparability, although measurement site-specific influences (sources, sinks, heat reservoir, etc.) and different weather events, especially on "cloudy" days, can significantly affect the lower tropospheric structure due to cold pool formation, additional stratifications and air mass entrainment (Moormann et al., 2025a). In contrast, "clear-sky" days are expected to be more similar due to the dominance of irradiance-driven convective mixing.

7.5.2 Representativity of diurnal ground-based measurements

Site selection for ground-based measurements typically favors horizontal representativity, whereas vertical representativity within the mixing layer – where stations are often located – is commonly assumed to be "sufficient". It is rarely considered that this assumption is idealized. In practice, the PBL is frequently treated as a single, well-mixed layer once its height is diagnosed, neglecting vertical gradients, fine-scale stratification, dynamical processes and temporal variability of MLHs.

In this section we discuss how the diurnal stratification and irradiance-driven turbulent mixing in the PBL influence the representativity of various variables measured at ground-based stations.

7.5.2.1 Metrics for representativity of ground-based measurements

As a quantitative measure of the vertical representativity of ground-based measurements, we define the ratio R of the average of the vertical 500 m-column mean divided by the value in the lowermost altitude bin (0 - 25 m a.g.l., for 25 m vertical resolution) above ground.

The mean sampling height in the lowest altitude bin is at ~9 m above ground, considering the longer hover periods in 6 m altitude in between vertical profiling flights. This mean height is suitable for comparison with ground-based measurements, because most ground-based stations probe air in 3 - 10 m altitude (Savijärvi, 2006), while sampling in 10 m is common for meteorological stations to reduce surface influences (Pastorello et al., 2020). Perfect representativity is given for $R = 1$, whereas our “ground-based” measurements overestimate mixing layer quantities with respect to the 500 m column for $R < 1$ and underestimate them for $R > 1$.

In addition, we computed vertical gradients (dX/dz , X being the variable of consideration) within the 0 - 500 m column as a second metric; non-zero gradients indicate an inhomogeneous distribution of a variable, that can be due to natural dilution, local sources and sinks, or vertical stratification (i.e., an incompletely mixed layer). Absolute magnitudes of the gradients could be used for inter-study comparisons, which are beyond the scope of this manuscript.

7.5.2.2 Diurnal variation in pollutant distribution

Meteorological variables and trace gases show similar diurnal trends in representativity of ground-based measurements for the mixing layer for both campaigns. Exemplarily for BISTUM24, Fig. 7.2 illustrates the average diurnal variation of representativity for various trace gas and matter variables, including CO_2 , O_3 , and the particle number concentration of particles larger than 10 nm ($\text{PNC}_{>10\text{ nm}}$), which are often measured ground-based in atmospheric studies. These variables cover a range of different behaviors, as CO_2 is a chemically inert anthropogenic tracer, originating from sources like industrial production or vehicle exhaust, whereas O_3 is more reactive and is depleted via reactions with NO and unsaturated VOCs as well as by photolysis (Atkinson et al., 1992; Olszyna et al., 1994). $\text{PNC}_{>10\text{ nm}}$ reflects processes in the particle phase and is strongly influenced by anthropogenic emission sources, noting that particle formation also happens naturally under radiative influence.

In the morning and the evening, all three variables show strong gradients and a significant over- or underestimation of ground-based measurements with respect to the 500 m-column, while the deviation from complete representativity (dotted line in Fig. 7.2) is minimal between 12:00 and 20:00. The reason for these differences over the day is the development of stratification due to the diel structure of the PBL. Formation and dissipation of the NBL were already discussed in Sect. 7.4 and are the reason for low representativity of ground-based measurements as the probed vertical-range (0 – 500 m altitude) exceeds the NBL and results in partial sampling of air masses in the RL, which has, e.g., higher O_3 mixing ratios, but lower levels of CO_2 and $\text{PNC}_{>10\text{ nm}}$, compared to the NBL. Probing these two chemically different layers consequentially results in an underestimation of O_3 and an overestimation of CO_2 and $\text{PNC}_{>10\text{ nm}}$ by ground-based measurements. This emphasizes that good representativity of ground-based measurements is generally only valid for the range up to the upper boundary of the lowermost layer.

Between 12:00 and 20:00 the MLH is larger than 500 m and vertical profiling within a single well-mixed layer results in the absence of gradients and in tight representativity over this period. While CO_2 and O_3 show insignificant gradients during this period, indicating a well-mixed layer, the measurements in the lowermost 25 m slightly underestimate the CO_2 and O_3 levels in the mixing layer by 4 ppmv and 0.4 ppbv (1% and 3% of the absolute levels), respectively. O_3 depletion near ground occurs frequently due to an enhanced concentration of reaction partners at this location, while O_3 mixing ratios generally increase in the troposphere with height (Roelofs and Lelieveld, 1997). Although CO_2 is generally emitted at ground level, reduced mixing ratios might be measured near ground as photosynthesis could be a significant sink in this biogenic environment.

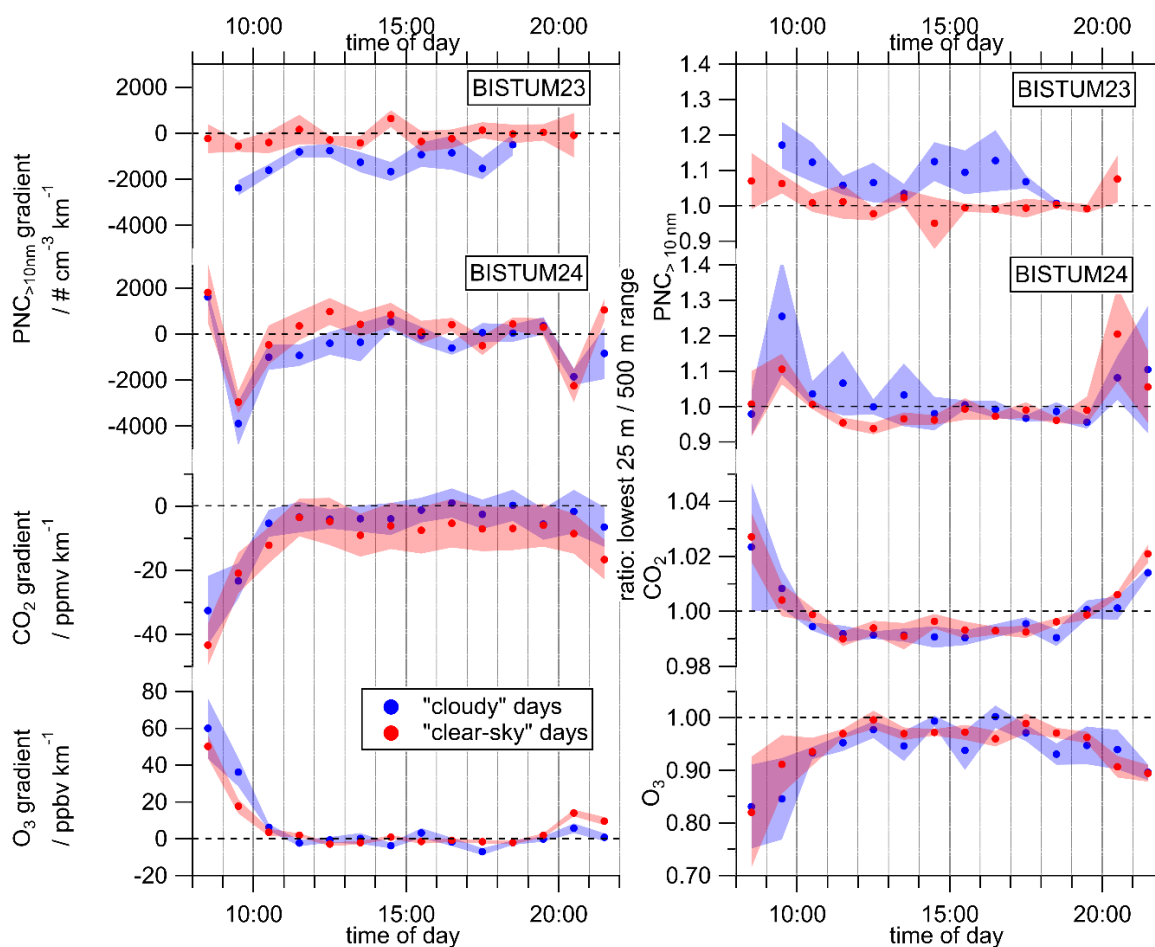


Fig. 7.2: Average gradients of $\text{PNC}_{>10\text{nm}}$ (a), CO_2 (b) and O_3 (c) in the lowermost 500 m above ground (left) show a diurnal variation for “clear-sky” (red) and “cloudy” days (blue), which is reflected in the representativity of ground-based measurements for the 500 m-column above (right). Interquartile ranges are presented as shaded areas.

Observations on “clear-sky” and “cloudy” days show similar diurnal trends, revealing little influence of the irradiance on the distribution of both gases. In absence of mixing layers, the variability of the underestimation of the chemically inert CO_2 is negligible, and for O_3 it is $\sim 1\%$ on “clear-sky” days. However, on “cloudy” days, the underestimation of O_3 varies significantly, from 0% to 8%, throughout the day. Rainfall could enhance the variability on “cloudy” days by triggering more primary biogenic emissions that deplete O_3 near the surface, while unstable stratification can cause downdrafts that entrain O_3 -rich air from the free troposphere down to below 500 m (Moormann et al., 2025a).

While the distributions of trace gases are little affected by irradiance, the influence of irradiance-driven mixing is stronger for the PNC. Between 12:00 and 20:00, when the MLH exceeds 500 m (the altitude range of our measurements), an insignificant gradient is observed on “clear-sky” days for BISTUM23 and BISTUM24 (see Section 7.5.2.3). Strong vertical mixing allows representative ground-based measurements for the lowermost 500 m during BISTUM23, in contrast to BISTUM24, when measurements in the lowest 25 m-increment underestimate the $\text{PNC}_{>10\text{nm}}$ until 15:00 (Fig. 7.2). $\text{PNC}_{>10\text{nm}}$ is potentially underestimated because oxidants can react with near ground emitted substances, while the ground itself could act as a particle diffusion sink. Simultaneously, enhanced oxidant entrainment from the RL or the free troposphere can promote new particle formation above the surface layer (Curtius et al., 2024; Borchers et al., 2025) and result in the temporary positive gradient of PNC. This observation might be limited to “clear-sky” days because mixing ratios of low-volatile gases, which are required for

new particle formation, are higher under radiation-intensive conditions (Kamens et al., 1982; Cox et al., 2020). On “cloudy” days when convective turbulence is expected to be lower, negative gradients of $\text{PNC}_{>10\text{ nm}}$ due to low vertical transport into higher altitudes are apparent until 15:00.

Diurnal profiles of CO_2 , O_3 , and PNC show that independent of the chemical reactivity of the gas or particle phase, stratification strongly influences the range of vertical representativity by ground-based measurements due to the dynamic diel cycle of the PBLH, while sources or sinks at ground, i.e., in proximity to a ground-based measurement site, influence the vertical profile of these trace matter variables, too.

7.5.2.3 Influence of solar irradiance on aerosol gradients in the PBL

The results from the previous section show that gradients of aerosol particles depend on stratification, the PBLH and that irradiance drives vertical mixing of aerosol particles. The vertical distribution of meteorological and trace matter variables in the PBL is often described with models which parameterize the PBL structure based on factors as the surface roughness, heat flux or the PBLH. Within a well-mixed PBL, meteorological variables such as the potential temperature θ , absolute humidity, or wind speed show a linear dependency on the logarithm of the altitude (Stull, 1988). A shallow PBL compresses this vertical profile, increasing the absolute gradient of the variable, whereas a deep PBL stretches the profile, decreasing the absolute gradient.

Solar irradiance enhances convective turbulence, increasing the PBLH during the day. Consequently, irradiance is expected to indirectly weaken the gradients of vertical profiles until complete mixing occurs, resulting in negligible gradients. Hence, due to this relationship, the PBLH was generally used as marker for the amount of turbulence in the PBL. However, even under strong insolation and strong convective conditions, the further lifting of the PBLH can be limited by a capping inversion above the PBL, despite maximized vertical mixing in the PBL.

To investigate the influence of the PBLH and irradiance on the vertical gradients of variables, we separate “clear-sky” and “cloudy” days and test for a linear relationship between the gradients and natural logarithm of the PBLH ($\ln(\text{PBLH})$), with PBLH derived from the ICON-D2 model as described in Sect. 7.3.3. As a proof-of-concept of this analysis, we use the vertical potential-temperature gradient $d\theta/dz$ as a proxy for static stability and turbulent mixing, where more negative $d\theta/dz$ indicates greater instability and larger positive values indicate increased stability.

In Fig. 7.3, hourly $d\theta/dz$ -data from both campaigns were combined assuming that differences in the gradients originate from different PBLHs rather than from measurement site’s influences, noting that the local topography can influence the PBLH. To exclude samples from above the capping inversion and focus on the analysis of a single mixed layer, only vertical profiles with a PBLH above 500 m were used.

On all investigated “clear-sky” and “cloudy” days, $d\theta/dz$ is negative and generally decreases with increasing PBLH, which indicates enhanced atmospheric instability, consistent with enhanced convective turbulence in deeper PBLs. Despite similar trends for both cases, this dependency of $d\theta/dz$ on the $\ln(\text{PBLH}$ [in m]) is more pronounced on “cloudy” days (slopes for “clear-sky” days: $-0.6 \pm 0.3 \text{ K km}^{-1}$, $r = -0.24$ and “cloudy” days: $-1.3 \pm 0.4 \text{ K km}^{-1}$, $r = -0.40$), when the atmosphere is expected to be more stable in general. In contrast, under “clear-sky” conditions intense irradiance already promotes strong turbulence independent of the vertical extension of the PBL, so a strong $d\theta/dz$ - $\ln(\text{PBLH})$ -relationship is not expected.

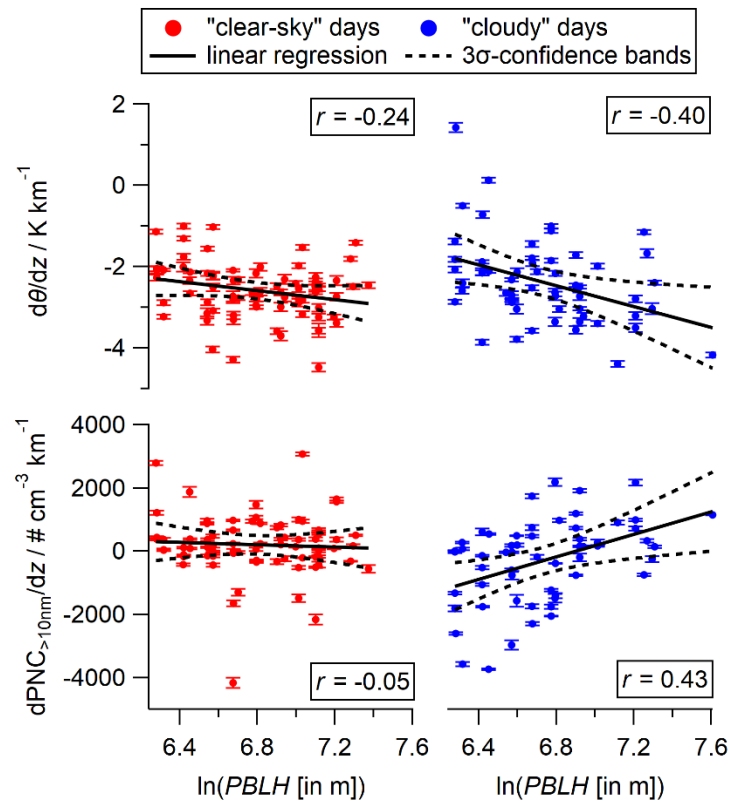


Fig. 7.3: Gradients for the potential temperature $d\theta/dz$ (top) and the particle number concentration $PNC_{>10nm}/dz$ (bottom) in the lowermost 500 m in a mixed PBL from both campaigns. Linear regression and its 3 σ -confidence bands are depicted in solid and dotted lines.

Recent studies have examined vertical pollutant distributions in highly polluted areas, where aerosol particles in the PBL absorb and scatter radiation, causing surface cooling and atmospheric heating, which affects PBL development from sunrise onwards (Petäjä et al., 2016; Ma et al., 2020). In contrast, experimental characterization of vertical particle distributions under clean PBL conditions is scarce because Lidar has limited sensitivity to small particles, and profiles typically require in situ CPC measurements. Lagrangian modelling tools are commonly used to study vertical pollutant dynamics: FLEXPART represents turbulent vertical dispersion but shows lower agreement with observations near the surface under slightly unstable conditions (Hanna, 1984; Bakels et al., 2024), while LAGRANTO computes air-parcel trajectories without considering particle growth (Sprenger and Wernli, 2015). These convective transport schemes assume that strong irradiance is synonymous to an increased PBLH and enhanced turbulence, however this is not the case as shown in this section. The influence of strong and low radiative conditions on the vertical pollutant distribution in dependence of the PBLH has not been studied, yet.

The influence of irradiance on the vertical mixing of small particles was already discussed in Sect. 7.5.2.2. Here, we further investigate the relationship between irradiance, the PBLH and vertical gradients of the $PNC_{>10nm}$ ($dPNC_{>10nm}/dz$), which is a reliable pollutant tracer with low measurement uncertainty ($\sim 1\%$). In a perfectly mixed layer that is capped by a strong inversion layer, neither a vertical gradient nor an influence of the PBLH on the distribution of $PNC_{>10nm}$ are expected. This is observed on "clear-sky" days (Fig. 7.3, $r = -0.05$), whereas on "cloudy" days, $dPNC_{>10nm}/dz$ is negative for small PBLHs and increases as PBLH increases, approaching well-mixed conditions for a PBLH of ~ 1340 m ($\ln(PBLH)$ [in m]) = 7.2 with, $r = -0.43$). This observation shows that on "cloudy" days, the PBLH is a

useful measure for the mixing state, whereas on “clear-sky” days irradiance appears sufficient to homogenize $PNC_{>10\text{ nm}}$ largely independent of PBLH.

Normalizing $dPNC_{>10\text{ nm}}/dz$ by the $PNC_{>10\text{ nm}}$ measured at ground yields relative gradients. The relative mean decrease of the $PNC_{>10\text{ nm}}$ with $\ln(PBLH [\text{in m}])$ is $(-0.4 \pm 0.1) \% \text{ km}^{-1}$ under “cloudy” conditions and $(-0.02 \pm 0.08) \% \text{ km}^{-1}$ on “clear-sky” days (“%” refers to the amount of $PNC_{>10\text{ nm}}$ at ground, Fig. S9.46). However, the spread of the data points in Fig. 7.3 and S9.46 indicates substantial uncertainty regarding individual vertical profiles.

Summarizing, irradiance plays a crucial role in controlling mixing in this grassy, hilly terrain. To finally understand irradiance-driven convective transport processes, similar studies spanning a wider range of irradiance levels and PBL depths in regions with distinct surface energy budgets and turbulence regimes (e.g., rainforests, polar areas) would be valuable.

7.5.3 Representativity of Ground-based Measurements in a Mixed PBL

The analysis of nocturnal MLHs (Sect. 7.4) and the diurnal variability of trace matter in the lowermost 500 m (Sect. 7.5.2.1) highlight that stratification significantly affects vertical gradients of meteorological and trace matter variables. In Sect. 7.5.2.2, the analysis of gradients in a single probed mixing layer further shows that atmospheric instability and vertical mixing are mainly driven by irradiance and that assuming turbulence solely from the PBLH might result in significant biases (especially for strong radiative conditions). To evaluate how well ground-based measurement stations can quantify and represent conditions in a mixing layer, gradients of the vertical profiles (Fig. 7.4) and ratios of the lowermost 25 m-increments to the vertical 500 m-column (Fig. 7.5) were calculated for the daily periods from 12:00 to 20:00 according to the absence of a NBL in this period (Sect. 7.5.1).

Table 7.1 presents a summary of the representativity of ground-based measurements for within a mixing layer, considering local and radiative influences, based on the results in Fig. 7.4 and Fig. 7.5. These results are discussed separately for meteorological and trace gas and matter variables in the following.

7.5.3.1 Meteorological variables

Meteorological variables provide insights into atmospheric conditions by indicating dynamic mixing and thermodynamical processes. Vertical gradients of variables from both campaigns show significant influence in higher altitudes from air mass dilution from aloft (with dry air) that reduces the absolute

Table 7.1: Representativity of ground-based measurements for various variables in a mixing layer: green (very representative), yellow (mostly representative) and red (not representative). The effects of adiabatic cooling, strong radiative and measurement location-specific influences (sinks, sources, etc.) on the representativity are additionally indicated as either significant (XX) or very likely (X).

Representativity	PM _{2.5}	PM ₁	PNC _{>350nm}	PNC _{>10nm}	CO ₂	O ₃	Ri	wind speed	θ_{eq}	θ	T	RH	abs. hum.
Influenced by													
Adiabatic cooling	X*	X*	X*	X*							XX	XX	
Irradiance				XX		X		XX					
Location	X	X	X	X	X				X	X	XX		XX

*if not given in standardized volumetric units

humidity that is fed by water evaporated from ground. Reduced ambient pressure in higher altitudes causes adiabatic cooling, which forms the vertical gradient of temperature (T) and, together with moisture dilution, shapes the gradient of relative humidity (RH). The potential temperature (θ), equivalent potential temperature (θ_{eq}) and bulk Richardson number (Ri) are markers for atmospheric stability: θ accounts for dry-adiabatic effects, θ_{eq} also incorporates water-vapor variability, and Ri combines thermal stratification and wind shear. The gradients of potential temperature ($d\theta/dz$) and equivalent potential temperature ($d\theta_{eq}/dz$), along with that of Ri , are all negative throughout the campaigns and indicate atmospheric instability.

When not considering the hourly PBLH like in Fig. 7.4, negative gradients on “clear-sky” and “cloudy” days are similar. This implies that irradiance is an important factor for describing the turbulence in a specific mixing layer when PBLHs are available (see Sect. 7.5.2.3), however in bulk description the influence is less relevant.

Well defined gradients, and only minimal overestimation of θ in the lowermost 25 m-increment, for the 500 m-column indicates that θ , T , and absolute humidity can representatively be measured with ground-stations. This can be achieved with measurements in different heights slightly above ground to estimate the locally-influenced dilution and adiabatic cooling rate. The adiabatic cooling likely reflects buoyant updrafts initiated by ground heating and depends on local heat reservoirs and ambient pressure. In contrast, RH and θ_{eq} show a significant unregular variability in their gradients, which is likely due to a combination of locally and temporally varying evaporation or advection of moist air masses.

Ri and wind speed were not representatively measured by ground-based stations. Although vertical wind profiles are well described in ideal model setups and depend mainly on the surface roughness, here, a combination of synoptic scale conditions and inhomogeneous hilly terrain may reduce the representativity of near-ground measurements. Additionally, we found that the wind speed gradients are larger for lower than for stronger radiative conditions. This correlation is expected as strong gusts above the SL occur due to, e.g., frontal events, which imply cloudiness. As the Ri depends on temperature, humidity and horizontal wind speed, representative measurements with ground-based stations for this variable are also hard to achieve.

7.5.3.2 Trace matter variables

The distribution of pollutants and trace matter is affected by the horizontal advection of clean or polluted air masses and vertical mixing, which reduces vertical inhomogeneities and distributes surface-influenced air in the mixing layer. Unlike meteorological variables, trace gas and matter exhibit stronger day-to-day variability as the air mass composition varies with different source regions, leading to an increased uncertainty when gradients are calculated from absolute values.

An ideally mixed layer would have a negligible vertical gradient for trace gas and matter mixing ratios. Consistent with this, under clear-sky daytime conditions reduced vertical gradients of the O_3 mixing ratio were observed, making ground-based measurements slightly more representative for the lower troposphere than under cloudy conditions. In contrast, on “cloudy” days reduced photochemical O_3 production and reduced turbulence limit in-situ O_3 production and vertical mixing, respectively, so entrainment from air aloft (RL/free troposphere) largely controls the vertical O_3 profile. Similarly, CO_2 is dispersed within the mixing layer and can occasionally be well represented by ground-based measurements. Consistent with Sect. 7.5.2.2, both gases experience sinks (chemical depletion of O_3 and biosphere-driven uptake (photosynthesis) for CO_2) at the surface, which bias surface concentrations

and lead to an underestimation of the 500 m-column with ground-based measurements. Taking into account the bias caused by these sinks would enable more representative measurements. While gases are frequently reported as mixing ratios (which are independent of the pressure decrease with altitude), ground-based aerosol measurements are commonly reported as volumetric concentrations that are rarely standardized. Consequently, if vertical changes in air density are not accounted for, using ground-level volumetric concentrations to represent a well-mixed 500 m column will overestimate the column-mean aerosol load by $\sim 2.7\%$. This bias is not considered in Fig. 7.5 due to its marginal effect and the convention of reporting particulate matter in volumetric units. As a best practice, ground-based measurement stations should report volumetric variables in standardized units. Low concentrations of aerosol particles with diameters larger than 350 nm were measured with an optical particle counter and led to poor counting statistics and consequently high uncertainty. As a result, these measurements were not used for gradient analysis. The number and mass fractions of these particles ($\text{PNC}_{>350\text{ nm}}$, PM_1 , $\text{PM}_{2.5}$) inferred from near-ground measurements tend to overestimate the corresponding 500 m-column averages by $\sim 25\%$, albeit with large uncertainties (interquartile ranges corresponding to roughly 10–80% overestimation; Fig. 7.5). This ratio appears to be site-dependent, although not significant due to the wide interquartile ranges. Irradiance does not appear to affect the representativity of ground-based measurements for larger particles. In contrast, the representativity of ground-based measurements for the 500 m column and the vertical gradients of $\text{PNC}_{>10\text{ nm}}$ is significantly influenced by irradiance and measurement-site location. Good representativity is achievable on “clear-sky” days (see Sect. 7.5.2.3). The systematic overestimation of larger particles ($\text{PNC}_{>350\text{ nm}}$, PM_1 and $\text{PM}_{2.5}$) compared to $\text{PNC}_{>10\text{ nm}}$ in the lowermost 25 m-increment with respect to the vertical 500 m profiles might be due to ground-level particle sources and entrainment

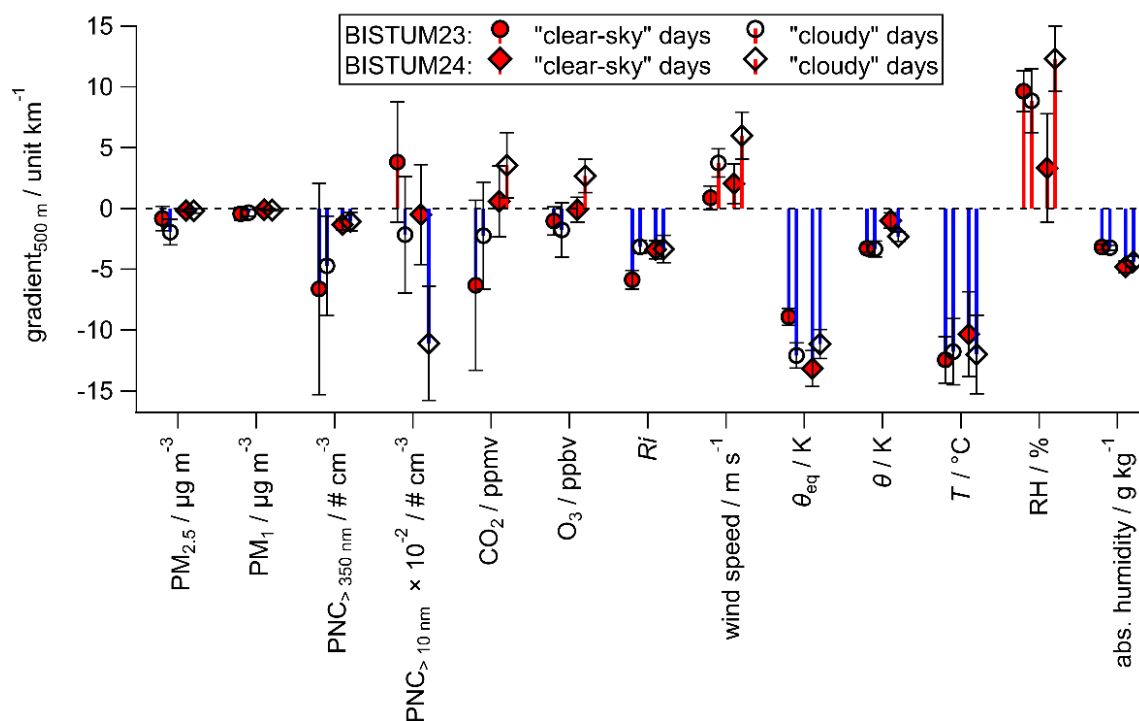


Fig. 7.4: Gradients in the lowermost 500 m in a mixed PBL are presented for meteorological and trace gas and matter variables during two campaigns (circles and diamonds) for “clear-sky” and “cloudy” days (red and white markers, respectively). Blue bars show negative, red bars positive gradients, and error bars represent the overall uncertainty, mainly due to day-to-day variability.

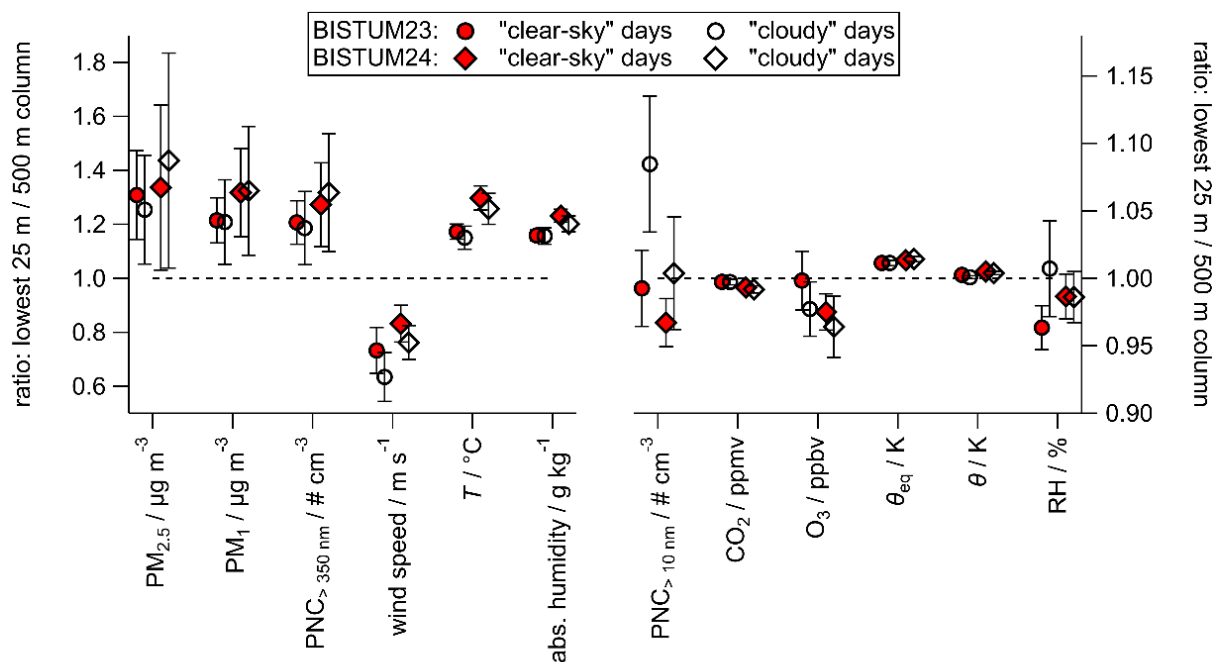


Fig. 7.5: Representativity of ground-based measurements with regard to the lowermost 500 m in a mixed PBL are presented for meteorological and trace gas and matter variables during two campaigns (circles and diamonds) for “clear-sky” and “cloudy” days (red and white, respectively). The x-axis is split to enhance visibility of variables with better representativity (note the different y-axis scalings). Error bars represent the overall uncertainty, mainly due to day-to-day variability.

of particle-poor air from above the surface layer. More efficient physical deposition of large particles in PM_1 compared to smaller particles in $PNC_{>10\text{ nm}}$ is unlikely, since particles with diameters of $\sim 1\ \mu\text{m}$ have a similar lifetime compared to particles contributing to $PNC_{>10\text{ nm}}$. Within the atmosphere, particles in the size range from 10 nm to $1\ \mu\text{m}$ area similarly mixed by eddies, hence no difference is expected for PM_1 and $PNC_{>10\text{ nm}}$ (Hinds, 1999). Differences between the sites plausibly explain the small discrepancy between BISTUM23 and BISTUM24.

While meteorological indicators show relatively similar gradients and representativity of ground-based measurements with respect to the mixing layer for “cloudy” and “clear-sky” days, pollutant indicators exhibit stronger variability and differences. This is mainly due to complex chemical production and loss processes or plumes, which cause significant variations in gradients driven by irradiance-induced mixing processes.

7.6 Summary

Drone-based in situ measurements were conducted during two 2.5-week summer field campaigns in rural Central and Southern Germany to study dynamics and stratification in the lowermost troposphere. Nighttime vertical profiles of temperature, humidity, wind speed, and trace gas and matter (CO_2 , O_3 , particle concentrations) in the lowermost 120 m were used to detect fine-scale nocturnal stratification. Due to the complex terrain, the definition “strong gradient change” was applied to each variable as a criterion to detect mixing layer heights (MLH) on an hourly time scale. Although subjective and applied on only a single night, this method showed that trace gas and matter variables were mostly more sensitive in detecting MLHs than traditionally used meteorological variables. Among all variables,

O₃ and potential temperature identified MLH most often, suggesting that combined pollutant and meteorological measurements are beneficial to investigate stratification processes, even under conditions when dynamic influences are minimal.

Diurnal vertical profiles up to 500 m above ground are used to study the influence of irradiance intensity on the distribution of trace matter and on dynamics within the convective boundary layer, as well as the representativity of ground-based measurement stations for this layer. All days during the campaigns were considered “atmospherically slightly unstable”, a stability regime in which vertical mixing is described with a high uncertainty. To investigate influence of irradiance in this regime, days were classified by the daily integrated measured irradiance at ground.

Independent of irradiance, ground-based measurements are not vertically representative of the column up to the MLH during morning/evening transitions when a NBL is present. Under low irradiance, MLH reflects not only the degree of atmospheric instability but also the vertical distribution of aerosol particles. Under high irradiance, strong turbulence produces well-mixed conditions; vertical pollutant gradients are weak and their dependence on MLH diminishes. Accordingly, distinguishing between low- and high-irradiance conditions in the PBL could enhance model parameterizations and improve the description of vertical mixing under slightly unstable conditions.

The major goal of this study is to point out that ground-based measurements, which are used worldwide in networks or during individual field campaigns, are generally taken as representative and rarely consider vertical limitation by MLHs or gradient dependencies of radiative-driven mixing. Representativity of meteorological variables for the mixing layer is generally not affected by irradiance and can be enhanced by estimating local vertical gradients with ground-based measurements in multiple heights. In contrast, representative measurements of trace gas and matter must account for local sinks at ground, entrainment from clean air aloft and a stronger influence of irradiance.

Acknowledgements: This work was supported by internal funds of the Max Planck Society. LM was funded by the Deutsche Forschungsgemeinschaft (DFG, German Research Foundation) – TRR 301 “TPChange” – Project-ID 428312742. The authors thank Thomas Böttger and Philipp Schuhmann (both Max Planck Institute for Chemistry) for support during BISTUM23 and BISTUM24 and Holger Tost (Johannes Gutenberg University Mainz) for providing the modeled mixing layer heights.

Author contribution: LM conducted the measurements with Flab, analyzed the data and wrote the manuscript, while FD and FF conducted the measurements with MoLa and the flux tower and analyzed the data. LM, FF, and FD discussed the data processing and the presented results. All co-authors commented on the manuscript.

Financial support: This work was supported by internal funding from the Max Planck Society. LM is funded by the Deutsche Forschungsgemeinschaft (DFG, German Research Foundation) – TRR 301 “TPChange” (Project-ID 428312742).

8 Influence of Synoptic Rain Fronts on the Local Boundary Layer Dynamics

This chapter contains a paper that has been published as

Moormann, L., Fachinger, F., Drewnick, F., Tost, H.: *Boundary Layer Dynamics after Rain Fronts: High-Resolution Reconstruction and Model Validation using ground- and drone-based Measurements*, EGU sphere [preprint], <https://doi.org/10.5194/egusphere-2025-3862>

The preprint is in the peer-reviewed phase for publication in Atmospheric Chemistry and Physics.

Contribution to this manuscript by Lasse Moormann:

As the first author of this work, I conducted all measurements with FLab during the BISTUM23 and BISTUM24 campaigns, after successfully applying for permission for aerial deployment. I maintained the instruments throughout the campaigns. I analyzed the FLab data from both campaigns and developed methods to investigate the influence of rain events for several hours after they occurred. Finally, I prepared all figures and wrote the manuscript, which was then revised with input from all the co-authors.

8.1 Abstract

Understanding atmospheric processes enables enhancing weather forecasts and models. Research in polluted areas showed that severe rain fronts influence pollutant distribution and chemical processes in the planetary boundary layer, while studies at continental rural mid-latitude sites emphasized stratification's impact on pollutants, but neglected the influence of rain fronts. This study connects meteorological and chemical boundary layer processes during summer rain in Central and Southern rural Germany, focusing on two events: a warm front in a high-pressure system and a cold front following a convergence line.

By combining near-hourly drone-based vertical profiles of the lowest 500 m, continuous ground-based observations, and ICON forecast model data, a detailed assessment of tropospheric dynamics for both events was achieved. Findings reveal that delayed nocturnal boundary layer breakup and poor vertical mixing result in weakly oxidized organic aerosol and reduced secondary aerosol formation near ground. Suppressed vertical mixing in the morning delays daytime chemical processes. A temporary reduction of O₃ after rain was observed, likely due to depletion from reactions with surface emissions, until mixing restored vertical homogeneity.

The ICON model accurately predicted the mixing layer height under stable conditions, but underestimated it during cold pool formation with rain showers and thunderstorms. In-situ measurements indicate that cold pool dynamics enhance subsequent convective development. These findings enhance the understanding of air mass exchange and precipitation's effects on the lower rural troposphere as well as frontal weather scenarios and atmospheric composition changes, linking local experimental and model forecast observations to larger-scale synoptic situations.

8.2 Introduction

Understanding the details of atmospheric processes during different weather events is crucial for improving weather prediction, climate modelling, and environmental risk assessments (Chen et al., 2008; Wei et al., 2011; Szirczak et al., 2022). Fronts, particularly warm and cold fronts, play a fundamental role in shaping local and regional weather conditions in the mid latitudes, influencing temperature gradients, wind patterns, and precipitation, as well as the chemical composition of the atmosphere. While synoptic-scale models provide valuable insights into these phenomena, accurately capturing the fine-scale interactions within the atmospheric boundary layer remains a significant challenge (Steenefeld, 2014; Qian et al., 2016; Golzio et al., 2021; Szirczak et al., 2022). Ground-based and aerial measurement approaches offer the potential to bridge this gap by providing spatial and temporal high-resolution data on key atmospheric variables (McWilliams et al., 2023; Moormann et al., 2025b).

The formation of near-surface air mass layers is a critical factor in atmospheric dynamics, as these layers control energy exchange, moisture fluxes, and pollutant dispersion. The structure of these layers is influenced by surface heating, turbulence, and synoptic-scale forcing, leading to variations in stability and mixing. During the night, radiative cooling at the surface leads to stable stratification referred to as nocturnal boundary layer (NBL), reducing vertical mixing and fostering the formation of temperature inversions. The evolution of the NBL during frontal passages is particularly complex, as stability transitions and wind shear interactions can enhance turbulence intermittency and alter mixing processes, which can have significant implications for local weather phenomena, distribution of trace species, and air quality (Stull, 1988). A thorough understanding of these dynamics is essential for improving numerical weather prediction and refining models of boundary layer processes.

Measurement towers, equipped with sonic anemometers and radiometers, offer continuous, wind profiles, high-frequency turbulence, and thermodynamic data at fixed locations but are limited by their inability to capture spatial variability and typically cover a very limited vertical range (Oliveira et al., 2020). Radiosondes provide detailed vertical atmospheric profiles deep into the stratosphere, yet they only offer snapshots or incur high costs when frequently launched (Helbig et al., 2021). The Monin–Obukhov Similarity Theory is capable of extrapolating near-surface measurements to different heights under quasi-stationary conditions, though it struggles with rapidly changing stability regimes and complex terrains (Monin and Obukhov, 1954; Markowski et al., 2019). Meanwhile, remote sensing techniques like lidar, sodar, and radar deliver high-resolution spatial and temporal profiles of wind, turbulence, and aerosol distributions without physical contact, but they are constrained by limitations in resolving fine-scale turbulence, signal penetration issues, and reduced precision near the surface, especially under challenging atmospheric conditions (Kotthaus et al., 2023).

Recent advancements in atmospheric science have led to the integration of drone-based observations and large-scale numerical weather models to enhance the understanding of boundary layer dynamics. Drones provide flexible, spatially highly resolved measurements of temperature, humidity, and wind as well as trace gases and aerosol particles at multiple altitudes, offering a valuable complement to ground-based instruments (Bonne et al., 2024; Radtke et al., 2024; Moormann et al., 2025b). When combined with numerical weather prediction models, these measurements can improve the representation of sub-grid scale processes and help validate model simulations (Szintai et al., 2010; Zum Berge et al., 2023). However, challenges remain, including limited flight durations, regulatory constraints, and the need for robust data assimilation techniques (Elston et al., 2015; Villa et al., 2016; Moormann et al., 2025b).

Previous studies have investigated frontal events with large scale model data or use large data sets of local data at ground level or measurement towers. While model data lack the high spatial resolution in the planetary boundary layer (PBL), in-situ measurements are usually limited to specific variables. Large data sets of local data cover underlying dynamics of different rain fronts, however, they often do not cover a sufficient vertical range (Bopape et al., 2021; Helbig et al., 2021; Wang et al., 2021; Machado et al., 2024b; Machado et al., 2024a).

This study investigates and aims to reconstruct atmospheric processes during two distinct, but common weather events – a warm front in a stable high-pressure system (Sect. 8.4) and a cold front in a convergence zone (Sect. 8.5) – by integrating ground-based measurements, drone-based observations, and synoptic local-scale model data (Sect. 8.3). While the measurements provide a large comprehensive data set of the local meteorology as well as gas and aerosol trace matter characteristics with high temporal resolution, the model contributes the greater regional-scale picture. A detailed analysis of various variables derived from these complementary data sources leads to a complex overview of processes, providing a more comprehensive understanding of frontal dynamics, short and longer-term impacts of rain, and the limitations of existing observational and modelling approaches.

8.3 Methodology

Data from two measurement campaigns (BISTUM23, August 2023 and BISTUM24, June 2024) were analyzed to understand the influence of rain events on stratification and dynamical processes in the lowermost troposphere. A warm front in a stable high-pressure system (case 1, Sect. 8.4) and a cold front in a convergence zone (case 2, Sect. 8.5) were selected as examples of two kinds of rain events, which originate from different large-scale meteorological conditions and allow the analysis of various

post-rain processes depending on the front type. The analysis of each case follows the same approach using a) local measurements at a ground station for continuous measurements and on-board a drone for quasi-hourly vertical profiling and b) large-scale assessment of the meteorological conditions using a radiosonde and ICON model data.

8.3.1 Measurement sites

For the two campaigns BISTUM23 and BISTUM24, two rural sites in German low-mountain ranges were selected. BISTUM23 took place near the city of Albstadt in the Swabian Alb (48° 15' N, 8° 59' E) with the ground station at 886 m above mean sea level (a.s.l.). BISTUM24 was performed near the village of Spielberg in the Vogelsberg area with the ground station at 391 m a.s.l. (50° 19' N, 9° 15' E). Both sites were chosen because they are in rural areas, which lowers the risk of contamination from local anthropogenic sources. The ground stations were located at the top of a hill, close to the flank of the mountain range where the aspiration usually occurs (Fig. S9.47). Therefore, the topographical conditions favor orographic lifting of air masses, which can facilitate deep convective events (Barros and Lettenmaier, 1994; Liu and Kirshbaum, 2025).

8.3.2 Experimental data

Measurements were performed on the same three platforms for each campaign and are listed in Table S9.13. Continuous ground-based measurements on-board the Mobile Laboratory (MoLa, Drewnick et al. (2012)) include the O/C ratio of the organic fraction of the submicron aerosol particles, measured with an aerosol mass spectrometer, particle size distribution (merged data of a fast mobility particle sizer and an optical particle counter), particle number concentration (PNC), O₃ mixing ratio, and wind data as well as temperature, humidity, and pressure. The MoLa inlet was 6 m above ground level (a.g.l.). A ceilometer monitored the aerosol backscatter signal above the site up to 10 km a.g.l. Additionally, during BISTUM24, 3D wind measurements at 5 m a.g.l. provided sensible heat flux (Q_H) and turbulent kinetic energy (TKE) data at 30 min-averaging intervals, as recommended for fair weather and pre-storm weather (Markowski et al., 2019).

Drone-based measurements were performed with the Flying Laboratory research drone (FLab, Moormann et al. (2025b)), which provides a wide particle and gas phase dataset including O₃, PNC, and meteorological data. This allows the estimation of these variables' gradients in the lowest 500 m a.g.l. as well as the calculation of the bulk Richardson number Ri Eq. (8.1) calculated from the acceleration of gravity g , the flight height above ground level $h_{a.g.l.}$, the virtual potential temperature θ_v , and the horizontal wind speeds u and v at ground at the respective air level:

$$Ri = \frac{g(\theta_{v,air} - \theta_{v,ground})h_{a.g.l.}}{\theta_{v,air} \left((u_{air} - u_{ground})^2 + (v_{air} - v_{ground})^2 \right)} \quad (8.1)$$

Data from radiosondes, launched from the same site, help to verify the model data analysis of the meteorological conditions on a larger scale and provide the convective available potential energy ($CAPE$) as an indicator of the vertical uplift forcing before and after the weather events as well as the elevated boundary layer heights (Stull, 1988).

8.3.3 Model data

Large-scale synoptical information such as 24 h-backward trajectories, the mixing layer height and radar information for the respective measurement site were derived as described in the following. The trajectories in Fig. S9.50 were calculated for 24 h-backwards with the HySplit analysis tool to detect source regions outside Germany and were started from 0 m, 120 m and 500 m above ground level (Stein et al., 2015). Besides the HySplit trajectories driven by 0.25°-GFS analysis data, ICON-D2 analysis and hourly forecast data for the gaps between the analysis time events (3 hourly) were utilised to calculate corresponding mixing layer heights and backward trajectories within the German domain (Fig. S9.53 and Fig. S9.58). ICON-D2 is the operational weather forecasting model of the German Weather Service (DWD) and provides detailed weather information on a horizontal grid width of approximately 2 km. ICON-D2 is a non-hydrostatic model, with parameterisations for shallow convection and a sophisticated boundary layer and surface exchange scheme. Even though ICON-D2 itself operates on a triangular grid, the data has been re-gridded to a regular longitude-latitude grid with a similar grid width to ICON-D2. A detailed description of the ICON model has been provided by (Zängl et al., 2015; Crueger et al., 2018) and further descriptions are available at (DWD, 2025b).

ICON-D2 uses terrain-following Gal-Chen coordinates, according to (Klemp, 2011), with 60 vertical levels in total. The lowest kilometer above ground for the Albstadt site is described with 16 vertical levels, whereas for Spielberg 15 levels cover the lowest kilometer with corresponding layer thicknesses between 30 m close to the surface and 100 m in 1 km altitude above ground. Turbulence and surface exchange processes are parameterised with a second-order scheme following (Raschendorfer, 2001). To obtain a higher temporal resolution than the 3 hourly analysis data, forecasts for the respective two hours in between the analysis time spots have been merged with the analysis data set, i.e., forecasts with up to 2 h lead time. The forecast data was obtained from the PAMORE data archive (DWD, 2025a) for the duration of the campaign.

The backward trajectories in Fig. S9.53 and Fig. S9.58 have been calculated using a tailored trajectory program, which regrids the model data to a regular latitude-longitude-altitude grid, including the respective grid elevation of the orography. The trajectories themselves were calculated based on a 1 min-timestep, and were finalised when the trajectory left the domain of ICON-D2 or after 24 hours. The MLH is selected as the lowest altitude where all the following criteria in the ICON-D2 data are fulfilled: Brunt–Väisälä frequency $> 5 \times 10^{-5} \text{ s}^{-1}$, vertical gradient of potential virtual temperature $> 0.3 \text{ K km}^{-1}$, and vertical gradient of absolute humidity must be curved (Wang and Wang, 2014). Additional synoptic scale information, displayed in Fig. S9.48 and Fig. S9.49 (surface pressure, geopotential in 500 hPa), for the selected events has been obtained from ERA5 reanalysis data (Hersbach et al., 2020) as well as from radar data (WN data set) from the radar network of the DWD (e.g., Kreklow et al. (2019)). The radar and trajectory data were obtained from the DWD data server (DWD, 2025c) during the campaigns. The respective satellite images are obtained from EUMETSAT from the MSG SEVIRI (Schmetz et al., 2002) instrument. Frontal lines in Fig. S9.48 and Fig. S9.49 were manually added to highlight strong pressure gradients.

8.4 Case study I: Delayed Breakup of NBL during Warm Front Rain in High-pressure System

Our first case study focuses on the basic characterization of different air masses and investigates how strong stratification can suppress turbulence and delay the breakup of the NBL until the afternoon. This situation took place at 20 June 2024 at the Spielberg site.

8.4.1 Synoptic situation and local meteorology

The synoptic map in Fig. S9.48 shows that the measurement site was centrally located in a large high-pressure system that covered substantial parts of western and central Europe with an indicated warm front crossing the measurement site. Two rain events with different intensities can be attributed to the warm front: first rain: ~20 min duration, 0.5 mm accumulated rainfall starting at 11:00; second rain: ~10 min duration, 0.1 mm precipitation starting at 15:20. FLab measured three vertical profiles before and five after the major rain event (Fig. 8.1), allowing investigation of hour-scale influences of the rain event on the atmosphere in the lowermost 500 m a.g.l. After the second rain event, no profiling flights were possible due to temporary airspace restrictions. Note, the following height ranges describe the height above ground level and time is given in local time (LT = UTC + 2 h), unless otherwise noted.

At 500 hPa a stable ridge was located above central Europe, leading to large-scale subsidence. Radio soundings before and after the rain event show no change in tropopause height or *CAPE* (Fig. S9.51), suggesting no significant change due to the front. The high-pressure system appears to be stable, and the backward trajectories show no uplift as would be expected for warm fronts, i.e., the uplift at the warm front is compensated or suppressed by the large-scale subsidence. However, from the ceilometer data a cloud uplift from 3 km to 5 km (or a trailing higher midlevel cloud) can be deduced immediately after the first rain (Fig. S9.52). The immediate but short-lived dynamical stabilization above the residual layer (RL) after the rain event and the hardly changed conditions below the RL lead to the assumption that the trajectories may not show any uplift due to a strong RL and that the rain event can indeed be described as a warm front (see Sections 8.4.2 and 8.4.3.1). A follow-up rain event like the one at 15:20 is typical for warm fronts.

8.4.2 Driving forces of air mass mixing

Stratification, such as the NBL that forms near the ground during the night, usually dissipates by mid-day due to convective forcing. Irradiance is the driving heat source that provides the necessary energy for the buoyancy of the near ground-level NBL. Typically, irradiance heats the ground, which conserves energy during cloud cover or darkness, and creates turbulences in the air, which release energy by dissipating eddies (Stull, 1988).

The strong correlation between irradiance and sensible heat flux throughout the day (Pearson correlation coefficient $r = 0.87$) indicates that sensible heat flux is generated mainly by direct irradiance and is not driven by stored energy from the ground (Fig. 8.1). During the 11:00 rain event, irradiance and hence the sensible heat flux reach a minimum, while *TKE* is available independently – most likely due to advected air masses. The existing *TKE* and the small amount of sensible heat flux are not sufficient to elevate the NBL prior to rainfall. During the first two hours after rainfall, the thermal energy in the NBL must still accumulate before mixing of the low-level residual layer with the free tropospheric air can occur between 13:00 and 14:00, as the model predicts. To provide evidence for this suggested

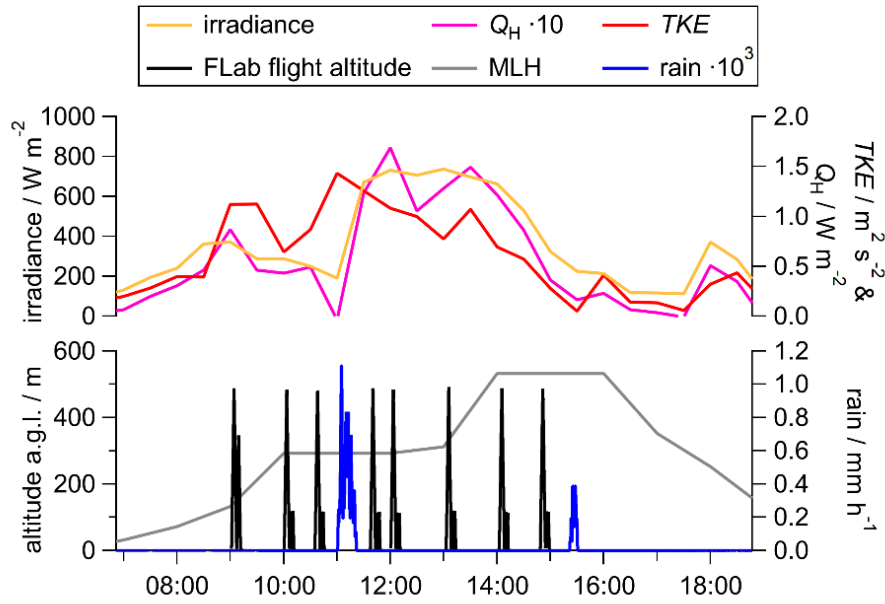


Fig. 8.1: The turbulence kinetic energy (TKE , red) increases in the morning, without being reduced prior to and during the first rain event, in contrast to the time series of irradiance (orange) and sensible heat flux (Q_H , pink, all 30 min averages). The strong correlation between irradiance and Q_H during the rain period indicates that there is no energy conservation at the ground. The hourly mixing layer height (ICON model MLH, gray) reflects stratification in 300 m a.g.l. in the morning, so FLab (drone flight altitude, black, 1 s data) measures inside and above the NBL before and directly after the main rain event (blue, 1s data).

development and a more holistic understanding, the air masses in the lowest 500 m need to be characterized with in-situ data.

8.4.3 Characterization of different air masses

The air masses are characterized in reference to the 11:00 rain event primarily with FLab measurement data, which provide information on air mass stability and history. To reduce statistical and measurement uncertainty, the presented FLab-related data have been binned in 100 m increments for the height ranges from 0 to 500 m (see Fig. 8.2 and Fig. 8.3). Note that strong gradients which are often measured within a few tens of meters above the ground are averaged out in the 0 to 100 m bins. To account for concentration changes over time, the O_3 and PNC data measured on-board FLab were corrected for temporal trends using the analogous continuous ground-based data measured by MoLa. The identification of different air masses (I, IIa, and IIb) and the underlying processes discussed in the following subsections lead to a schematic description of the lowermost troposphere after rainfall which is presented in Fig. 8.4.

8.4.3.1 Air mass stability

Stability indicators for vertical stratification like the bulk Richardson number Ri and the gradient of the equivalent potential temperature $d\theta_{eq}/dz$ are derived from FLab measurements. Air masses are considered statically unstable for negative Ri , dynamically unstable for positive $Ri < 0.25$, and dynamically stable, i.e., laminar, for $Ri > 0.25$, whereas a negative $d\theta_{eq}/dz$ implies instability and positive $d\theta_{eq}/dz$

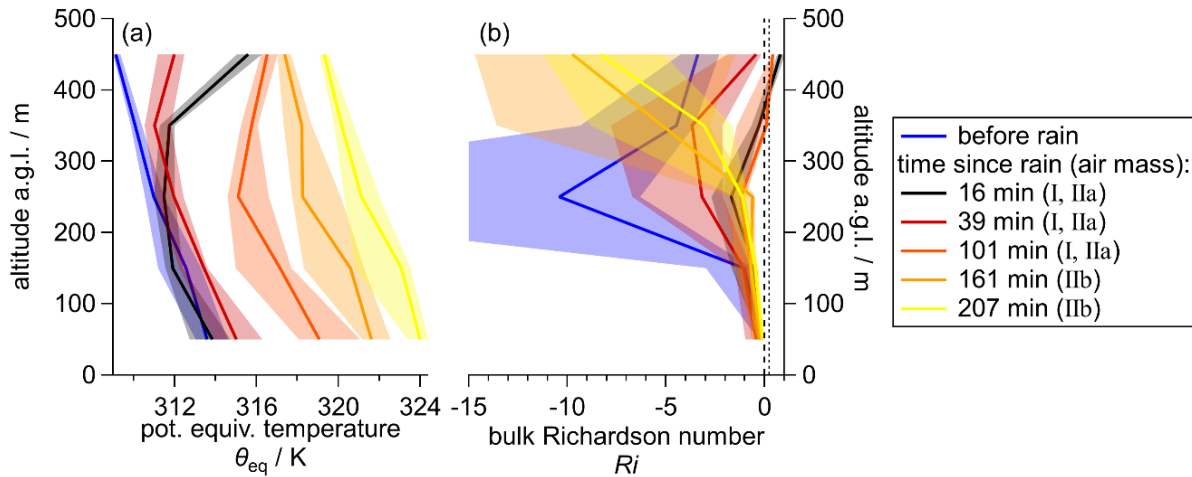


Fig. 8.2: The gradient of the equivalent potential temperature $d\theta_{eq}/dz$ (a) indicates unstable conditions throughout the day below 300 m, while the air mass above 300 m is stabilized after the rain at 11:00. The bulk Richardson number Ri (right) is consistent with a successive destabilization after the rain and indicates a stratification between 200 m and 300 m before the rain. The solid traces show the median and the shaded area is the interquartile range of the binned data. Dashed lines indicate $Ri = 0$ and $Ri = 0.25$.

stable conditions (Stull, 1988). The TKE data, derived from the ground-based wind measurements (Fig. 8.1) show consistent turbulent conditions in the lowermost 200 m in agreement with $Ri = 0.5 \pm 0.1$ and $d\theta_{eq}/dz < 0$ for all flights after the rain event (Fig. 8.2). A sharp increase of the Ri , but still negative Ri and $d\theta_{eq}/dz$ at 250 m altitude indicates the boundary between the two stratified statical unstable layers before the rain (Fig. 8.2b). However, above 300 m, 15 min after the rain, air masses are suddenly stabilized, indicated by $d\theta_{eq}/dz = 38.5 \text{ K km}^{-1}$ and contain a dynamically stable flow (Fig. 8.2a). The positive $d\theta_{eq}/dz$ persists at least until completion of the flight 100 minutes after the rain event and then becomes progressively negative, simultaneously with the Ri ; i.e., $d\theta_{eq}/dz$ and Ri drift into a more turbulent regime in the lowermost 500 m (Fig. 8.2).

The upper layer can be classified as downdrafted free tropospheric air (air mass I in Fig. 8.4), while the lower layer is probably a remnant of the NBL which is still present after the rain (air mass IIa in Fig. 8.4). The final breakup of the RL between the 3rd and fourth flight after the rain (between 100 min and 160 min after rainfall) is induced by increasing turbulence-driven instability above 300 m as indicated by a consistent negative $d\theta_{eq}/dz$ and a decreasing Ri . Probably, increased convective forcing turns air mass IIa into air mass IIb (Fig. 8.4, see Sect. 8.4.3). Here, the continuous increase in instability with height shows that stratification is reduced such that turbulence may increase due to larger eddies at higher altitudes.

8.4.3.2 Air mass composition and history

The air mass history like, e.g., travelled areas can be determined by 24 h-backward trajectories for different altitudes. Fig. S9.53 shows that the trajectories reaching the measurement site in the lowermost 100 m a.g.l. never travelled higher than 1000 m a.s.l. during the last six hours before rainfall, while trajectories arriving above 100 m a.g.l. at the measurement site show a strong downdraft of free tropospheric air close to the ground. According to Fig. 8.4, the new air mass (I) above 300 m is dynamically stable and differs strongly from the statically unstable air mass below 300 m before mixing (IIa and IIb in Fig. 8.4). In comparison to the in-situ measurements and the model MLH, backward trajectory tracks provide useful insight into air mass movement but lack accuracy at the vertical 100 m scale.

As shown in Fig. 8.3, at altitudes above 300 m, O₃ levels are increased by up to 30%, compared to those before the rainfall, and PNC decreased by up to 70% after rain for at least 100 min. Contrary, concentrations in the lowest 300 m remain within a range of 10% for O₃ and 20% for PNC. High O₃ levels and low PNC can be attributed to a freshly ingested, clean air mass with a high-altitude origin (Neuman et al., 2012; Tsamalis et al., 2014), confirming the free tropospheric history of air mass (I) before convective mixing. The influence of the rain on O₃ and PNC in the near-ground layer will be discussed in Sect. 8.5.3 in detail. After 100 min after the rain event no systematic gradient is observable for O₃ and PNC anymore. Consistent with the findings in Sect. 8.4.3.1, the stratification, observed directly after the rain event, has disappeared 2 h after the rain, and no significant differences of O₃ and PNC from the 100 m measurement increments can be observed in the lowermost 500 m, confirming a well-mixed layer. In addition to the photochemical production of O₃, mixing with free tropospheric air also causes a rapid increase of O₃ at ground level (Neuman et al., 2012), potentially causing photochemical aging of the aerosol, as suggested by the strong correlation ($r = 0.94$) for the time series of O₃ levels and the O/C ratio of organic particulate aerosol measured with the ground-based MoLa (Fig. S9.54). Aspiration of already-aged aerosols as a reason for enhanced O/C ratios is unlikely due to the stability of the PM₁ concentration measured in the afternoon. This strong correlation shows that a delayed breakup of the NBL can also lead to a delay in the onset of diurnal chemistry.

Taken these results in combination with the results shown in Fig. 8.2, the freshly ingested air mass can be attributed to the laminar and dynamically stable free tropospheric air mass I; initially, the lower-level statically unstable air mass IIa below 300 m does not show indication of mixing of air mass I with IIa. From 100 minutes after the rain, almost no gradients of O₃ and PNC are observed, indicating that the layering has dissipated and air masses I and IIa have mixed to form air mass IIb across the entire 500 m range (compare Fig. 8.4).

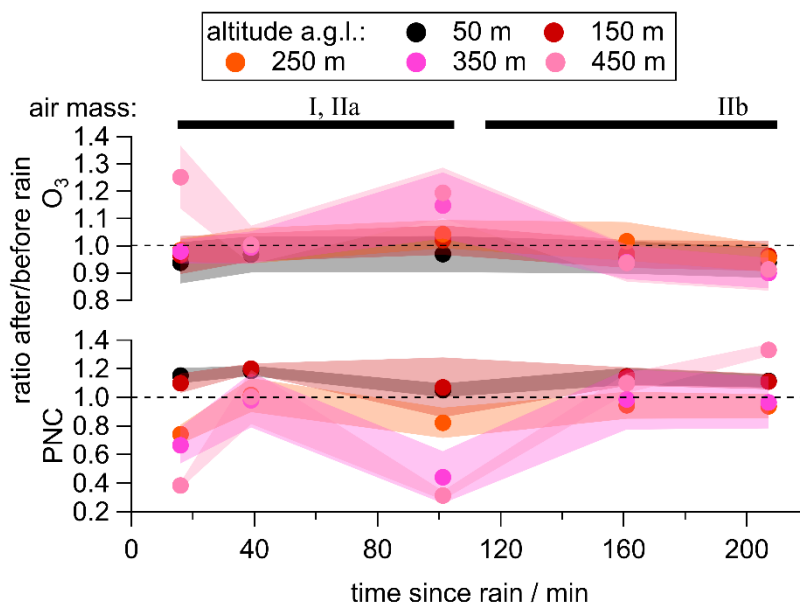


Fig. 8.3: The ratios of the O₃ mixing ratio (top) and the particle number concentrations PNC (bottom) after to before the rainfall (at 11:00) were calculated for different altitude increments (color-scale) for five vertical profiles measured at different times after the rain. Error bars represent the combined standard error of flights before and after the rain. Attributed air masses that are identified within a flight are indicated at the top of the graph.

8.4.3.3 Delayed NBL breakup

Boundary layer lifting can be limited or suppressed by overlying inversion layers and insufficient convective forcing. In addition to the low convective forcing due to low irradiance caused by the cloud cover, stratification is supported by the subsidence of air mass I, which is drier and warmer than the underlying NBL. Strong wind shear drives the turbulent mixing dynamically until the temperature has increased, i.e., the energy has accumulated within the NBL and convection-driven turbulence mixes air mass I with air mass IIa 100 min after the rain. Dissipation of the boundary between the dynamically different air masses I and IIa forms the mixed air mass IIb, as shown in Fig. 8.4. Comparison of the observed stratification height from the in-situ data and the MLH derived from ICON data agrees within the model height resolution (± 70 m in 300 m, Fig. 8.4). This demonstrates that the ICON model can forecast the MLH with high accuracy at least under relatively stable large-scale conditions.

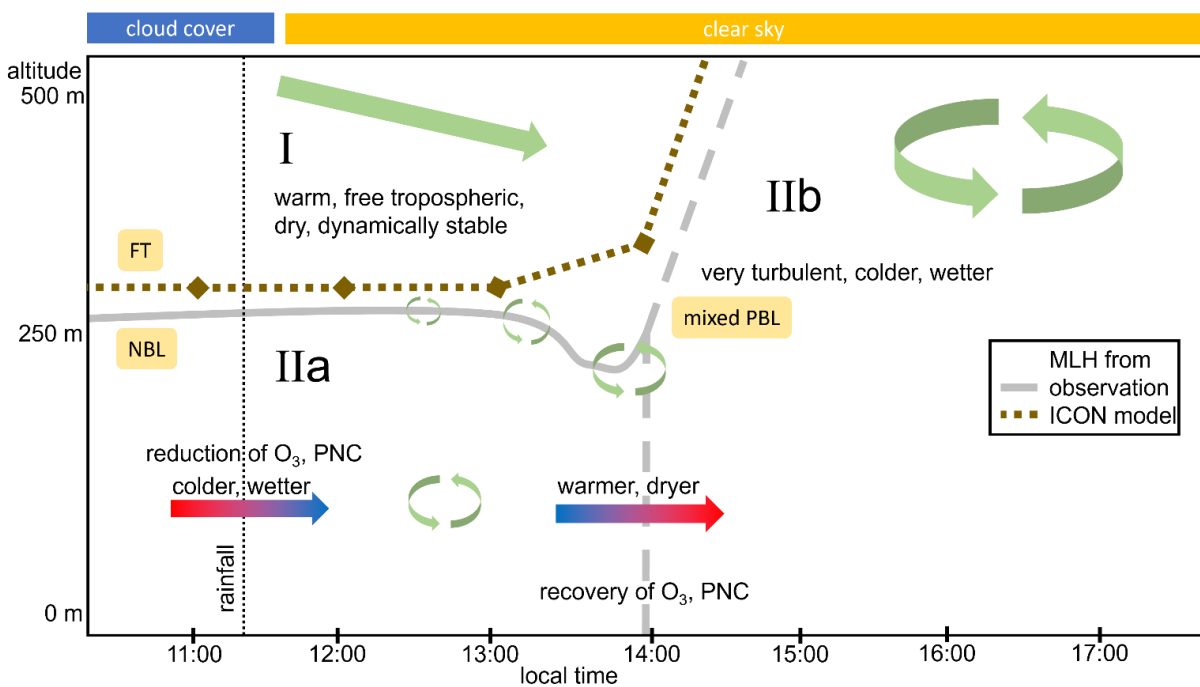


Fig. 8.4: A reconstruction of different characteristics and dynamics of the air masses (I, IIa and IIb, separated by grey lines) observed before and after the rainfall event. The estimated MLH from the ICON model is presented in olive with markers indicating hourly time stamps and lines between the data points to guide the eyes. Greenish arrows represent dynamic processes, multi-colored arrows thermal processes.

8.5 Case Study II: Impact of a Cold Front and a Convergence Line on the Lowermost Troposphere

To investigate how thunderstorms affect pollutant distribution and air mass dynamics in the lower troposphere, throughout a day when a thunderstorm occurred eleven FLab-based vertical profiling measurements were conducted hourly, as long as weather conditions allowed for safe operation.

8.5.1 Synoptic situation and local meteorology

During the 12 August 2023, four precipitation events were observed at ground level at the Albstadt site, while the ceilometer recorded seven, including three that did not reach the ground due to evaporation of rain droplets at higher altitudes (Fig. S9.55 and Fig. S9.56, Fig. S9.55 and Fig. 8.5). Even after the last rain event with a strong thunderstorm at 15:00, clouds were still present and the irradiance did not reach the levels of cloudless days, although the conditions became mild and the temperature rose by up to 10 °C.

For this day, synoptic maps show a convergence line and a cold front crossing the site from 14:40 to 15:20 (Fig. S9.50 and Fig. S9.56). A severe thunderstorm may have been caused by the combination of substantial lability and *CAPE* in addition to orographic lifting of warm air in conjunction with the convergent flow between 14:30 to 15:00. Radiosondes launched from the site recorded *CAPE* of 1400 J kg⁻¹ at 14:00, while it decreased to less than 10% of this value, i.e., 130 J kg⁻¹, after the thunderstorm (radiosonde at 16:40, Fig. S9.57) during mild, sunny conditions. 24 h-backward trajectories (calculated with Hysplit, Stein et al. (2015)) indicate aspiration of air masses, amongst other across the mountain ranges of the Black Forest and the Swabian Alb, during the 100 km long track before they reached the measurement site (Fig. S9.50 and Fig. S9.58).

8.5.2 Reconstruction of air mass exchange by cold fronts and a convergence line

In this subsection, similar to the approach for Fig. 8.4 (Sect. 8.4) we develop an overview schematic that describes the details of the boundary layer processes around the investigated event (Fig. 8.6). The schematic contains air masses characterized by dynamical and chemical properties, which are tagged with roman letters (I, IIa, IIb, III, and IV) and should not be confused with the air masses mentioned in the previous Sect. 8.4.

The meteorological situation on 12 August 2023, can be separated into a dynamically unstable pre-thunderstorm period and a stable post-thunderstorm period. In contrast to the situation described in Sect. 8.4, no ground-based flux measurement data are available. A consistent $Ri = 0$ at the 50 m mark during all times when the Flab was operating indicates unstable conditions, i.e., small-scale turbulence at the ground, which are not significantly influenced by processes above 100 meters (Fig. 8.5a). Before the first rain event at 08:30, a layer boundary at the 250 m mark was identified by sign changes of the weak gradients for Ri , potential temperature, absolute humidity, O_3 , and PNC (Fig. S9.59 or orange dots in Fig. 8.5). While positive gradients of potential temperature and Ri indicate increasing dynamic stability with altitude, the upper air mass above 200 m is classified as laminar with $Ri = 0.6$ with enhanced moisture and O_3 levels (O_3 increased by 6 ppbv), and reduced particulate pollution (PNC decreased by > 1000 particles cm⁻³). Here, free tropospheric air (I in Fig. 8.6) overlays a weak NBL (IIa in Fig. 8.6) above 200 m, similar to the case in Sect. 8.4.

After the first rainfall event (0.5 mm in 15 min), the NBL remains present, reaching heights of up to 200 m as predicted by ICON. However, the air mass I above the NBL becomes more stable (increasing

Ri and $d\theta_{eq}/dz$) after the rainfall event. Before 10:00, it rises to a height of 1100 m, where the ceilometer detects the upper boundary of an aerosol layer (see Fig. S9.56).

After a light second rainfall of 0.1 mm at 10:00, no RL and uniform gradients are observed over the whole 500 m-altitude range for all FLab-measured variables until 13:00. In air mass IIb mixing has eliminated the gradients. Since the first two rain events at 08:30 and 10:00, potential temperature near ground has increased by only 2-3 K, suggesting that diurnal heating primarily contributes to latent heat rather than driving vertical mixing (Fig. 8.5c). This observation is in agreement with very slow evaporation from moist soil that might explain the unusually stable equivalent potential temperature at the 50 m mark between 10:00 and 13:00 (Fig. 8.5b), while the difference to the potential temperature decreases (Fig. 8.5c). A similar pattern is observed for the last rain event, although here evaporation is accelerated by strong irradiance and turbulence-driven mixing.

At 13:30, a cold front delivered 2.4 mm of rain in 10 minutes leading to a 2.2 °C decrease in air temperature and 2.1 g kg⁻¹ increase in humidity at ground, while equivalent potential temperature remains constant at ground, as measured with MoLa (Fig. S9.60). However, at 50 m altitude and above no change in temperature, humidity, and the vertical gradient of equivalent potential temperature is observed. The slow evaporation of moisture from previous rainfall forms a localized moist patch, which, on a regional scale, might develop into a cold pool. Cold pools create a positive feedback loop: They generate broader clouds that are less affected by entrainment, leading to increased precipitation, larger moist patches, and further expansion of cold pools – ultimately fostering larger clouds with enhanced convective mass fluxes (Schlemmer and Hohenegger, 2014). Tompkins (2001) shows that along an already recovered cold pool, the increased equivalent potential temperature (here increased by 6 K at ground and by 2.1 K at the 50 m altitude bin, Fig. 8.5b and Fig. S9.60) and water vapor trigger new convective cells, like the upcoming rain front in this case study. Due to increased latent heat flux, thermal convection is suppressed initially, leading to a homogeneously laminar air mass III with $Ri = 0.28$ above 100 m, while air in the lowest 100 m is dynamically stable due to surface roughness. The downdraft of air mass III is likely enhanced by the cold pool, as penetrative downdrafts from the mid-troposphere commonly occur after rainfall exceeding 2 mm h⁻¹ (Barnes and Garstang, 1982), in agreement with model results under convergence zone conditions (Schlemmer and Hohenegger, 2014).

At 14:30 the last rain event of the day with 5.4 mm precipitation in 40 min was associated with a severe thunderstorm under a convergence line as described in Sect. 8.5.1. Despite the reduced *CAPE* after the storm, the new air mass IV remains unstable. Unlike the unstable air mass III, which might be unstable due to deep-convective vertical forcing (*CAPE*), this air mass IV is likely unstable due to small-scale turbulence indicated by a suddenly negative Ri above 100 m altitude and a remaining negative $d\theta_{eq}/dz$ from 15:30 on (Fig. 8.5a, b). Additionally, the convection did not take place in a frontal system, thus the existing air mass was not replaced by a colder, more stable air mass. Instead, only a part of the *CAPE* was consumed by the convective event which was initiated and substantially driven by the convergence. After the rain event, the post-convective subsidence led to cloud free conditions and thus growing instability caused by irradiance and enhanced ground temperatures (Fig. S9.60). Higher temperatures and thermally driven convection at the ground allow for drying of the moist near-ground layer, and for recovery of the lowermost troposphere from the thunderstorm as thermal mixing removes the vertical gradients of potential temperature, absolute humidity, PNC and O₃ after the last rain event (Fig. 8.5c-f). A summary of the temporal exchange of air masses and the accompanying processes is shown in Fig. 8.6.

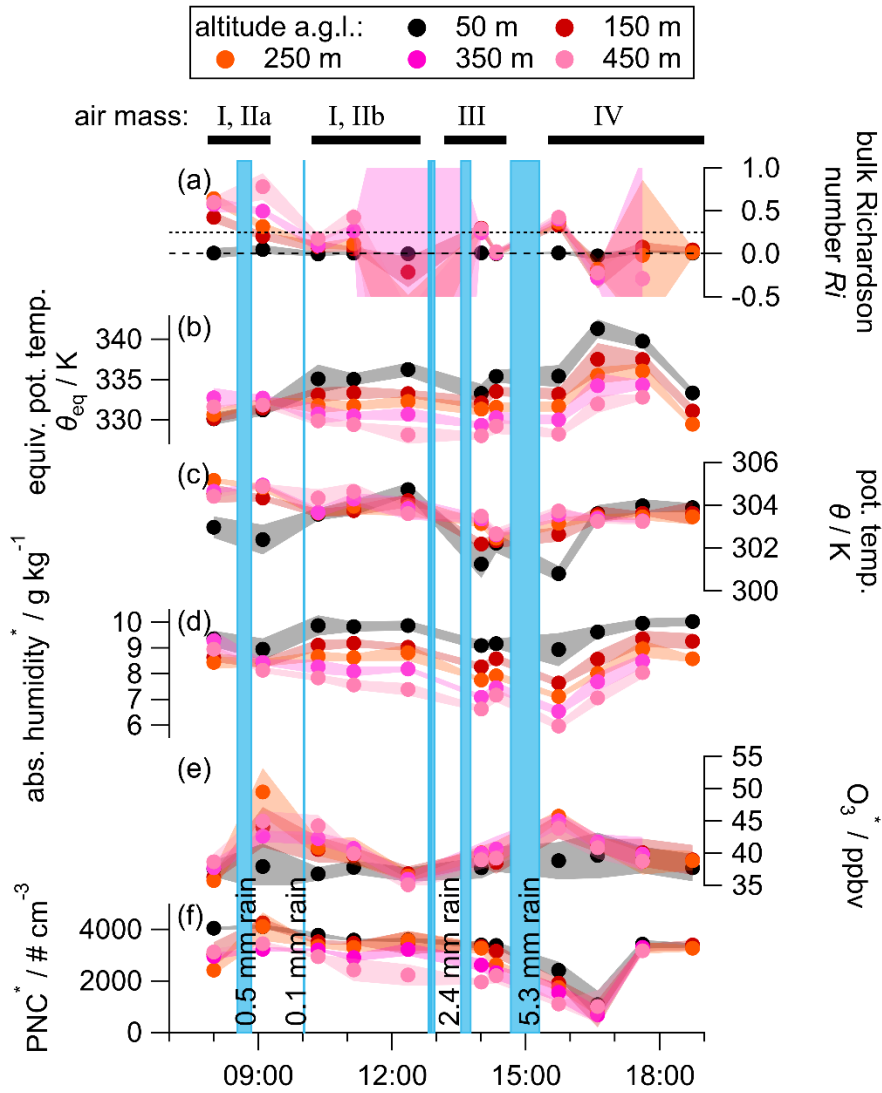


Fig. 8.5: Development of medians of 100 m altitude increments of the bulk Richardson number Ri (a), equivalent potential temperature θ_{eq} (b), potential temperature θ (c), absolute humidity (d), O_3 mixing ratio (e), and the particle number concentration (PNC, f) with time on 12 August 2023. Variables marked with * are corrected for temporal variation using the corresponding MoLa data. Error bars are derived from interquartile ranges. Dotted lines indicate $Ri = 0$ and $Ri = 0.25$. Rainfall periods are marked in blue with the amount of rain noted (precipitation at 13:00 and 14:00 were summed).

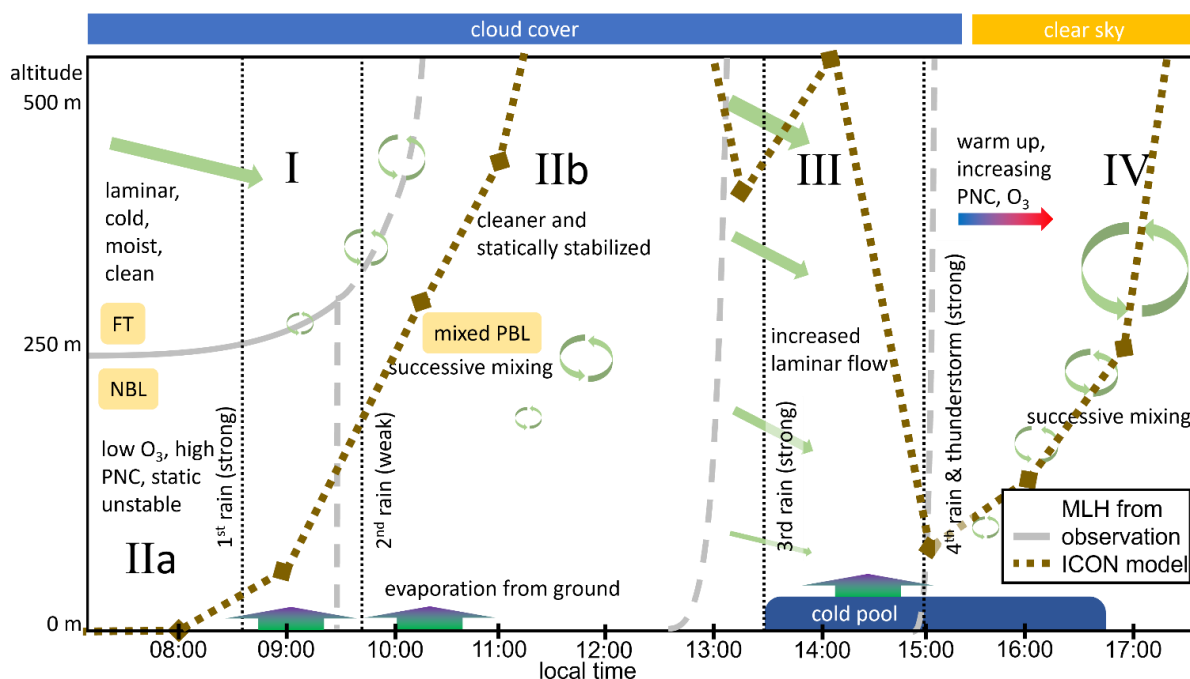


Fig. 8.6: A reconstruction of different characteristics and dynamics of the air masses (I, IIa, IIb, III, and IV, separated by grey lines; solid line illustrates stratification, dashed lines transition periods) on 12 August 2023. The estimated MLH from the ICON model (1-h resolution) is presented in olive with dashed lines between the data points to guide the eye. Greenish arrows display dynamic processes, multi-colored arrows thermal processes.

8.5.3 Impact of rain events on pollutant distribution

During the day, four rain events with different amounts of precipitation occurred, leading to different changes in the trace matter distribution. Contrary to the morning precipitation events, when there was no lifting of air masses before they reached the measurement site, for the rainfall events at 13:30 and 14:30 the 24 h-backward trajectories show a lifting up to above 2000 m a.s.l. and a sudden downdraft due to the cold pool, 7 h and 1 h before arrival of the air masses at the measurement site, respectively (Fig. S9.58). This downdraft dynamic was also observed by the ceilometer, which measured cloud layers subsiding from 2500 m down to 700 m a.g.l prior to the thunderstorm (Fig. S9.56). This downdraft results in the injection of clean, O₃-rich air with low particle load into the lowermost troposphere and represents the transition to air mass III (Fig. 8.5e, f, and Fig. 8.6).

After each rain event, O₃ mixing ratios are increased at altitudes above 200 m (due to the air mass downdraft from higher altitudes, Fig. 8.5e), but decreased near the ground by 3.0 ± 1.3 ppbv, excluding the 10:00 rainfall, as shown in Fig. S9.61. As a consequence, O₃ gradients are enhanced by 7 ppbv km^{-1} for each rain event and subsequently disappear within a few hours due to convective mixing within the PBL. Reduced ground-level O₃ concentrations following rainfall may result from deposition or enhanced O₃ depletion, whereas outwash seems unlikely due to the poor solubility of O₃ in water. Depletion could be driven by the increased release of primary biogenic volatile organic compounds (BVOCs) from vegetation or by peroxide-scavenging after rainfall (Bela et al., 2018; Rossabi et al., 2018; Miyama et al., 2020; Machado et al., 2024a). BVOCs have been identified as an O₃ sink in natural and anthropogenic conditions (Fitzky et al., 2019; Machado et al., 2024a). However, this emission-driven O₃ removal mechanism cannot be verified due to the lack of BVOC data.

Fig. 8.5f highlights that for the same rain events, when O₃-rich air was injected into the lowest 500 m, the CPC PNC was consistently reduced by 25% (except when the NBL was still present, because air mass I is already in the free troposphere). The PNC gradient remained unchanged during and after the regeneration period, and the PM₁ levels measured at ground remained constant immediately after rain (Fig. S9.60), indicating that washout was minimal under these conditions. This is likely due to the size of the measured aerosol particles that are in the Greenfield gap and consequentially inefficiently removed by outwash (Cherrier et al., 2017).

These observations show that rain itself does not necessarily significantly influence the distribution of pollutants such as O₃, PM₁, and PNC. However, post-rain air masses determine the composition and gradients at higher levels, while rain-induced emissions from the ground may act as a sink for reactive substances as O₃.

8.5.4 Influence of cold pool formation on model MLH

In Section 8.4 we showed that the determination of the MLH using 1-h forecast data from the ICON model is feasible with high accuracy under stable conditions during a weak warm front (Fig. 8.4). The MLH estimation criteria in the model include the Brunt–Väisälä frequency, humidity, and potential virtual temperature gradients. Until this point of the study the MLH is used as a synonym for the height of the planetary boundary layer (PBLH), which is considered the most relevant measure separating the free troposphere and the ground-influenced layer with different dynamical characteristics and composition (Stull, 1988; Tignat-Perrier et al., 2020; Kotthaus et al., 2023). Note that other kinds of stratification occur regularly in the troposphere and are often not predictable, due to local topography, emissions, and heat reservoirs.

For the convergence line / cold front case analyzed in this section, the modelled MLH, shown in Fig. S9.55 and also included in Fig. 8.6, increases from 0 m at 08:30 to 200 m at 10:00 and 300 m at 11:00. This observation is consistent with the NBL identified from in-situ FLab data and demonstrates additionally to Fig. 8.4 that the MLH algorithm predicts the height of the NBL (in this case the PBL) accurately. However, between 12:00 and 18:00, the modelled MLH drops below 500 m before returning to levels above 600 m at 18:00, where it continues following its diurnal cycle (Fig. S9.55). The average predicted diurnal cycle of the MLH at the measurement site from Sect. 8.5 shows maxima of the PBL between 800 to 1000 m at 14:00 to 15:00 on clear-sky days, while being < 20 m during night (Fig. S9.55). The difference between the modelled MLH in the cold front case, compared to the average diurnal cycle of the PBLH, may be explained by reduced irradiance (average of 100 W m⁻² during this period). The formation of a cold pool at ground leads to an increase of latent heat flux and consequentially to less turbulent mixing. Therefore, the cold pool acts as an energy sink and suppresses energy consumption for further turbulent mixing. Although convection has driven the PBLH up to the free troposphere before the rain, the cold pool contributes to layering of the convective-driven RL above a shallow turbulent mixing layer. This stratification disappears as the cold pool dissolves.

These dynamic processes drastically alter the vertical gradients, and may have influenced the MLH model output, which relies solely on gradients. The ICON 1-h forecast models that the MLH exceeds 500 m after 11:45 and thus differs strongly from our in-situ observations. After irradiance decreased, MLH criteria were met even below 400 m due to rapidly changing gradients caused by vertical dynamics within the convergence zone. ICON data predict a MLH of 600 m at 18:00 that can be assigned as a realistic PBLH 2.5 h after the last rain, in agreement with the mean life time of a cold pool (Tompkins, 2001). Interpolating the MLH between 12:00 and 18:00 may lead to an inaccurate estimate, because

the PBLHs maximum is expected in between. In agreement, radio soundings at 14:10 and 16:40 indicate a boundary layer up to slightly above 800 hPa, i.e., 1.400 m and 1.300 m based on changing lapse rates and temperature gradients (Fig. S9.57, Seidel et al. (2010)). The PBLH derived from the radio soundings is 100 m to 200 m higher than the estimated average MLH for the measurement site (Fig. S9.55), indicating that the PBLH has lifted due to convective forcing by the thunderstorm. A more robust parameterization of the MLH estimation for the PBLH for cold pool scenarios may consider two MLHs: a lower MLH separating an additional shallow cold pool-driven layer at ground from the previously well-mixed PBL and a second MLH separating the PBL from the free troposphere in the altitude range close to the PBL before rain events.

8.5.5 Convergence zone advection and measurement limitations

Due to unsafe flight conditions, vertical profiling during the thunderstorm was not possible; instead, ground-based MoLa data were used to analyze meteorological processes during this time (Fig. S9.60). Between 14:30 and 15:30, a strong cloud layer largely suppressed irradiance and minimized thermal convection, leading to dynamically deep convective inflow-driven air masses with surface wind speeds peaking at 8 m s^{-1} . As the rainfall starts, strong downward movement of air is implied by a descending cloud layer height, a high wind speed period, and a 40% reduction in PM_{10} due to mixing in of unpolluted free tropospheric air (Fig. S9.56 and Fig. S9.60). Although it is known for cold pool-induced deep convective events that the horizontal wind speed is maximal before rainfall starts (Tompkins, 2001), a strong downdraft from the start of rainfall until the maximum of the precipitation rate was not described, yet, probably because observational studies describe longer-lasting rainfalls only (Young et al., 1995; Tompkins, 2001).

As the rain band advanced, heavy rain ceased and wind direction turned by 180° , an effect attributed to a moving convergence zone (Crook and Klemp, 2000), which changed the air track from passing a rural forest (western) to the town of Albstadt (eastern, Fig. S9.47a). This resulted in increased NO_x and PNC with lower aerosol oxidation levels, indicated by the reduced particulate organics O/C ratio (Fig. S9.60). After rainfall, near-surface O_3 was reduced (possibly due to depletion by enhanced anthropogenic or natural emissions as NO_x or BVOCs, see Sect. 8.5.3), though it slowly recovered as the wind direction turned back from east to west after 40 min. When irradiance exceeded 400 W m^{-2} at 15:35, photochemical activity led to enhanced PM_{10} and PNC; simultaneously, temperature and absolute humidity increased as the grassland dried.

These rapid shifts in air mass history and wind dynamics behind the convergence line highlight the need of in-situ 3D turbulence observations, e.g., with wind LIDAR (Bélair et al., 2025) to fully capture local upwelling and advection processes within the PBL; measurements at a less polluted site (independent of wind direction) would be helpful to identify compositional changes due to the thunderstorm itself or thunderstorm-related effects like BVOC emissions from the ground.

8.6 Summary

By integrating hourly in-situ vertical profiles of the lowest 500 m with continuous ground-based observations, synoptic situation, and modelled PBLH, we can thoroughly analyze dynamical mixing, stratification, and thermal and chemical processes in two typical rain front scenarios in the continental mid-latitudes. Previous studies have often used remote sensing methods and focused separately on

dynamical (Ryan et al., 2000; Oliveira et al., 2020; Helbig et al., 2021; Luiz and Fiedler, 2024) or chemical processes in various terrains (Knote et al., 2015; Miyama et al., 2020).

Our highly-resolved in situ measurements showed a significant influence of the atmospheric stratification on pollutant distribution for a stable continental PBL (Platis et al., 2016; Pohorsky et al., 2025). However, the influence of rain fronts in the mid-latitudes has not been studied so far. We fill the research gap by providing a combined analysis with highly-resolved in-situ measurements in the PBL for physical and chemical processes under frontal conditions, even including a cold pool.

In the first case study, a weak warm front associated with a large-scale high-pressure system approaches the measurement site in the morning. A warm, stable, descending air mass suppresses the vertical expansion of the NBL, while shear winds suppress turbulent mixing between the free troposphere and the NBL. Precipitation further cools the surface, converting ground thermal energy into latent heat. Although irradiance gradually increases turbulent instability, it takes about 2 h after the passage of the front for the accumulated energy to lift the NBL and to form a convectively mixed boundary layer. This delayed breakup of the NBL postpones the entrainment of free tropospheric, O₃-rich air and the cloud cover delays the onset of daytime photochemistry into the afternoon. The ICON forecast model accurately estimates the MLH under these conditions.

In contrast, the second case study examines a synoptic cold front trailing behind a convergence line, accompanied by several rain showers and a severe summertime thunderstorm. The ICON model underestimates the MLH after the passage of the convergence line during these unstable conditions. In order to understand the reason for the failure of MLH determination and improve weather prediction models, it is essential to reconstruct air mass exchange in the lowermost troposphere and to identify the tropospheric processes. During this cold front event, five air masses are identified, characterized by their dynamical, thermodynamical, and chemical properties. These observations reveal that a moist patch forms at ground after the morning rain; as it dries slowly, it promotes the development of a deep convective thunderstorm and triggers a positive feedback loop that leads to the formation of a cold pool. The recovery of vertical gradients and the dissipation of the cold pool in the lowest 500 m occurs over approximately 2.5 hours after the rain event, consistent with recovery processes observed in the tropics (Tompkins, 2001).

After precipitation events with more than 0.5 mm rain, we observed a decrease of ground-level O₃ mixing ratios, possibly due to depletion by fresh biogenic emissions; additionally, unpolluted, O₃-rich free tropospheric air is injected into the lowest 500 m. The gradients resulting from evaporation, O₃ depletion, and injection of free tropospheric air disappear within two hours after rain, driven by thermal convective mixing as temperatures and irradiance increase.

In-situ analysis and reconstructions of the lowermost troposphere reveal that air mass exchange, turbulent mixing, irradiance, and physicochemical processes each play distinct roles in defining air mass characteristics. The overview figures (Fig. 8.4 and Fig. 8.6) illustrate the post-frontal regeneration processes. These processes occur not only in rural rain events but also in other frontal situations under common meteorological conditions in the mid-latitudes. Thus, these results have broader implications on how to consider atmospheric chemical processes and compositional change in the PBL in pollutant modeling associated with rain fronts (and cold pools) due to dynamical changes. Despite being limited to two cases with hourly resolution and no in-rain flights, the study shows that combined model- and ground-based analysis can conceptually identify complex boundary layer phenomena like pollutant sinks and local stratification. This emphasizes that high-resolution vertical data are crucial for assessing individual weather events, avoid misinterpretation, and enhance forecasting and model calculations.

Acknowledgements: The authors thank Thomas Böttger and Philipp Schuhmann (both Max Planck Institute for Chemistry) for support during the BISTUM23 and BISTUM24 campaign and Luis Valero (Johannes Gutenberg-University, Mainz) for providing the skew- T diagrams and corresponding $CAPE$ values from radiosonde measurements.

Author contributions: LM performed drone-based measurements, analyzed the data and drafted the manuscript. FF and FD performed ground-based measurements and related data post-processing. HT provided synoptic maps and mixing layer height calculations. All authors discussed the data and the presented results. All co-authors commented on the manuscript.

Financial support: This work was supported by internal funding from the Max Planck Society. LM is funded by the Deutsche Forschungsgemeinschaft (DFG, German Research Foundation) – TRR 301 “TPChange” (Project-ID 428312742); similarly, HT acknowledges funding from the same project ID (subproject Z03).

9 Conclusion and Outlook

In this work, the influence of air mass transport in the planetary boundary layer (PBL) on the distribution of trace substances, and associated chemical processes was investigated using two measurement approaches: stationary ground-based measurements and in situ vertical profiling within the PBL. The work comprises six studies in total: three technical studies, that describe the development and validation of measurement devices, and three studies in which the meteorological influences as air mass transport and boundary layer dynamics on the local pollutant distribution in continental Germany is investigated.

Offline aerosol analysis can be biased when advected air masses from different emission sources or the background are mixed during sampling, complicating source-background separation. The AERTRACC (AERosol and TRACe gas Collector) was used to separately collect aerosol particles (with cut-offs for PM_1 and PM_{10}) on filters and gases on thermal desorption tubes. Incorporating AERTRACC into the research van MoLa (“Mobile Laboratory”) allowed individual sampling under up to four pre-defined conditions. An offline-analysis method was developed for molecular characterization of individual samples collected on filters and thermal desorption tubes. For both substrates and individual inlet systems, a heated carrier gas vaporizes molecules according to a dedicated temperature program and separates them depending on their vapor pressure.

For a proof-of-concept study, the AERTRACC sampler was deployed in MoLa in ambient air near a pizza oven under varying wind conditions. Filter and thermal desorption tube samples were analyzed offline with thermal desorption iodide CIMS (chemical ionization mass spectrometry) and the molecular composition of emissions from the wood-fired pizza oven and the background were separately determined. Molecules identified with the CIMS could be attributed to biomass burning and cooking emissions, traffic and aged aerosol or mixed sources. Significantly enhanced concentrations of biomass burning and cooking-related markers were measured on the substrates that were loaded with emissions from the pizza oven, while markers for traffic and aged air were similar in all samples. This study shows that a combination of well-chosen sampling conditions allows effective and efficient separation of source-related aerosols.

The incorporation of AERTRACC into the MoLa system highlights its portability and enables the provision of source-resolved particle and trace gas samples from mobile applications. As the substrate is interchangeable, future studies can analyze the aerosol samples obtained with AERTRACC using other offline methods, such as gas chromatography, liquid chromatography after filter extraction, or microscopy. This makes aerosol samples accessible to inorganic analysis methods. Additionally, the definable sampling conditions allow unsupervised field deployment in regions with rapidly changing winds, which usually lead to indistinguishable air masses. Examples are non-frequent emissions from ship traffic or heavy industry processes near populated sites.

While drone-based platforms are gradually establishing for in situ measurements in the troposphere, most measurement drones are limited to observing only a few variables due to the low available payload. A completely new drone-based measurement platform FLab (“Flying Laboratory”) was developed that is capable to investigate meteorological conditions and microphysical processes in the lowermost troposphere. FLab was equipped with mid-grade instruments that provide data for most relevant variables to serve as an independent measurement platform. Dedicated experiments regarding the influence of the drone’s downwash on measured wind speed showed that an additional framework

was required to mount the wind sensor distant to the rotors. A user interface, as well as a data logging and processing tool, were developed for the online-monitoring of data measured with FLab, and for further data usage. The variables monitored with FLab, were also measured at ground with MoLa and allow extrapolation of MoLa measurements into the vertical dimension. FLab carries six instruments to measure aerosol particles (particle number concentration and size distribution; particulate matter and black carbon mass concentrations), trace gases (CO_2 , O_3) and meteorological conditions (wind, temperature, humidity, pressure).

FLab was characterized in detail, regarding horizontal and vertical motion of the drone, showing that vertical profiling can lead to severe artefacts of filter-based measurements (e.g., with an aethalometer), while other measurements are not affected. Optimal flight patterns for vertical profiling were evaluated and applied in a first field employment for hourly profiling up to 300 m for 8 h. This demonstrated the capability of FLab to capture the evolution of the structure of the lower PBL and to detect elevated stratification patterns during the day. FLab also proved to a useful platform to bridge the gap between ground- and aircraft-based measurements in the lowermost 500 m with vertically highly-resolved data.

For future vertical profiling, it would be beneficial to exchange the aethalometer with another instrument, as the filter-based black carbon measurements under unpolluted ambient conditions were not compatible with vertical profiling and did not provide useful data. Alternative instruments could include gas sensors for the selective detection of CO, for example, as this indicates incomplete combustion of anthropogenic emissions and is more sensitive than CO_2 while not being sensitive to biogenic exchange (Graven et al., 2009). Another option would be a multimetric nanoparticle detector that can measure the size of ultra-fine particles (Asbach et al., 2024). Such a device would bridge the gap between the CPC and the occasionally inaccurate OPC in the drone setup, allowing a stronger focus on aerosol particle analysis. Switching to a waterproof drone framework and sealing electronic interfaces would enable operation in moist conditions without having to consider potential precipitation as a safety risk.

While FLab is capable to quantify aerosol particle number concentrations and the size distributions, the chemical composition of organic aerosols (OA) remains unknown. Since the chemical composition provides valuable information about aerosol sources, mixing and aging processes, FLab investigation was augmented with a novel externally developed low-cost aerosol samplers for drone-borne deployment.

MoLa, FLab and the OA sampler, were taken to two field campaigns that were an integral source of data presented in this work. Both campaigns aimed at investigating land-atmosphere interaction and transport of trace matter into the upper troposphere. The first campaign, BISTUM23, took place in the unpolluted Swabian Alp in August 2023 and the second campaign BISTUM24 was conducted in June 2024 in the Vogelsberg region downwind of Frankfurt metropolitan area. During both campaigns, FLab was operated hourly up to 500 m above ground for vertical profiling while MoLa served as a continuously measuring ground-based station.

During BISTUM23, the OA sampler was mounted on a framework in 1.5 m, and on two additional drones. Both drones ascended to 120 m and 500 m above ground, respectively, and sampled OA for ~30 h each, three times a day, while hovering at these altitude levels. The OA sampling was complemented with vertical profiling with FLab. Analyzing sampled OA with electrospray-ionization mass spectrometry with a targeted approach for biogenic and anthropogenic markers revealed diurnal

trends of vertical profiles. A non-target analysis revealed overall higher levels of CHO-containing molecules and increased oxidation throughout the day independent on the altitude, in agreement with vertical profiles of O_3 and PBL height observations from FLab. This multi-drone approach demonstrates the capability of the on-board aerosol sampling device.

In the future, more frequent altitude-resolved aerosol sampling throughout the day and nighttime would provide a more detailed analysis of oxidation processes, vertical transport and lifetime of the targeted markers.

During nighttime, vertical profiling with FLab up to 120 m above ground allowed detection of multiple shallow layers and measurements above the nocturnal boundary layer. By combining pollutant and meteorological variables it was not only possible to determine the nocturnal boundary layer height, but also to identify fine-scale layers and to explain their formation by a low-level jet, a fog event and subsequent stratification under low-turbulent conditions. A comparison between various directly measured and derived variables showed that on average pollutant markers (particle number concentration, PM_{10} , CO_2 and O_3) were more sensitive and precise in detecting stratification than many traditional meteorological variables (bulk Richardson number or absolute humidity). Overall, O_3 and the potential temperature were the most effective markers for stratification detection, suggesting being weighted higher in mixing layer height detection schemes.

In total 383 vertical profiles up to 500 m altitude were conducted during BISTUM23 (186 profiles in 95 flights) and BISTUM24 (197 profiles in 113 flights), adding up to ~400 km vertically probed air. Additional flights were performed, when FLab could not reach the 500 m mark due to air space restrictions, or unsafe flight conditions due to limited visibility range, a high chance of precipitation, clouds and stormy gusts. The high number of vertical profiles with a high temporal resolution of 1-2 s allowed statistical analysis of lower tropospheric data, i.e., the PBL.

One research objective of these field campaigns was to investigate the representativity of ground-based measurements with respect to the overall situation in the PBL, which is often assumed to be well-mixed. The PBL is a dynamic system with varying height, weak short-term mixing layers, and a composition driven by land-atmosphere interactions, making it challenging for ground-based measurements to accurately represent a mixing layer's composition. This work highlights the limitations of the representativity of ground-based measurements, which is due to the varying altitude of the lowermost mixing layer (especially the nocturnal boundary layer height in the lowermost 500 m in the morning and evening). Besides varying mixing layer heights, the variability of meteorological variables complicates representative measurements of conditions in the mixing layer by ground-based stations is mainly impacted by local conditions due to different local adiabatic cooling rates; varying irradiance does not seem to influence gradients of meteorological tracers. Although irradiance is the main driver of turbulence, and hence vertical mixing, radiative-driven vertical mixing has not been considered explicitly in theoretical descriptions of vertical distribution of pollutants. As mixing layer heights and solar irradiance distort vertical profiles, the influence of solar irradiance and the PBL height under "slightly unstable" atmospheric conditions was investigated by PBL height-dependent gradient analysis, distinguishing between strong- and weak-radiative conditions. It was shown that the PBL height should not be used as a sole proxy for the intensity of turbulent mixing (as commonly used in model parameterization). Additionally, a differentiation between low- and high-radiative conditions is proposed to describe pollutant gradients in the PBL more accurately: strong radiation results in well-mixed conditions independent of the PBL height, while under low-radiative conditions the PBL height provides a

well estimate for the vertical distribution of pollutants. Consequently, achieving good representativity of ground-based measurements for pollutants in a mixing layer requires consideration of radiative conditions that can alter the vertical pollutant distribution, as well as local sinks and sources which can severely influence ground-based measurements.

The here developed methods would be useful in future studies to investigate the influence of radiation-driven vertical mixing of pollutants in other regions with different local heat reservoirs and sinks, such as rainforest or arctic regions. This could help to better understand the required amount of radiative input for well-mixed conditions and would help to improve the knowledge of the representativity of the large number of ground-based measurements under different environmental conditions.

Synoptic scale weather events such as rain fronts or thunderstorms influence local meteorological conditions and atmospheric composition by “cleaning the atmosphere” and formation of atmospheric layers. The impact of stratification on pollutant distribution in the PBL is well-known (Pohorsky et al., 2025), however the influence of rain fronts was neglected in previous studies. In this work, the influence of common synoptic mid-latitude rain fronts on the physical and chemical processes in the boundary layer was investigated. It was shown, that an early morning rain front can delay the nocturnal boundary layer dissipation by hours, reducing vertical mixing and slowing down formation and oxidation of organic aerosol, while near the surface, biogenic emissions due to rain might cause a temporary O₃ depletion.

Vertical profiling with FLab was also used to validate synoptic scale model-based mixing layer height predictions for relatively stable atmospheric conditions. In contrast to stable conditions, in situ measurements showed high uncertainty in model-based PBL height predictions during an abundant cold pool subsequent to a thunderstorm and heavy precipitation. Despite the fact that only two rain events were analyzed, linking model observation with local experimental studies of continuous ground-based measurements and vertical profiling show the potential to enhance the understanding of the influence of synoptic scale meteorology on chemical processes in the local boundary layer.

Further vertical profiling after rain events, assisted by ground-based measurements of biogenic volatile organic compounds, could help validate the hypothesis that ground-level O₃ is depleted by biogenic emissions in response to grass- or soil-based organisms. Additionally, a richer dataset would be useful for optimizing model-based MLH estimations.

CIMS measurements of chlorine-containing trace gases during BISTUM24 showed that synoptic scale air mass transport influences the local atmospheric chlorine chemistry in Central Germany, when air masses have passed marine-anthropogenic dominated regions at ~400 km distance. This was not the case for unpolluted-continental air mass history. ClONO₂ in the troposphere was reported for the first time and its daily variation was presented along with diel cycles of Cl₂, ClNO₂ and HOCl. ClO and Cl radical production rates were estimated from ClONO₂ mixing during night. High Cl and ClO production rates imply an unknown source of ClONO₂ or its pre-cursors Cl or ClO in the night. In the morning, enhanced ClNO₂ mixing ratios at ground indicate residual layer air entrainment into the nocturnal boundary layer. Daytime photolysis of chlorine compounds resulted in Cl radical production rates of $1.0 \times 10^6 \text{ Cl cm}^{-3} \text{ s}^{-1}$, exceeding previously reported ones even from polluted areas. The high Cl production rate is probably caused by HOCl, which contributes up to 80% to the Cl production and has been neglected in previous studies. Its contribution of up to 40% to total primary formed OH in the morning and evening is emphasized, being significant for estimating local oxidation processes. Comparing the Cl and OH production rates, indicate a substantial Cl influence of up to 20% on the methane lifetime.

In future, sensitivity studies based on chemistry models will be required to evaluate the global influence of this work's findings regarding abundance and lifetime of chlorine-containing species and their oxidation potential on hydrocarbons.

Overall, this work connects model-based observations with in situ measurements from multiple novel measurement platforms and devices in various situations and settings. It enhances atmospheric understanding by combining synoptic scale weather events and air mass transport with local meteorological events in the PBL, emphasizing the synoptical meteorological influence on the local pollutant distribution and chemical processes that finally affect local climate and human's health.

References

- Abdullahi, K. L., Delgado-Saborit, J. M., and Harrison, R. M.: Emissions and indoor concentrations of particulate matter and its specific chemical components from cooking: A review, *Atmospheric Environment*, 71, 260-294, <https://doi.org/10.1016/j.atmosenv.2013.01.061>, 2013.
- Abichandani, P., Lobo, D., Ford, G., Bucci, D., and Kam, M.: Wind Measurement and Simulation Techniques in Multi-Rotor Small Unmanned Aerial Vehicles, *IEEE Access*, 8, 54910-54927, <https://doi.org/10.1109/access.2020.2977693>, 2020.
- ACTRIS: ACTRIS Data Centre, <https://dc.actris.nilu.no/>, Access Date, 2025
- Adkins, K. A. and Sescu, A.: Observations of relative humidity in the near-wake of a wind turbine using an instrumented unmanned aerial system, *International Journal of Green Energy*, 14, 845-860, <https://doi.org/10.1080/15435075.2017.1334661>, 2017.
- Adkins, K. A., Swinford, C. J., Wambolt, P. D., & Bease, G.: Development of a sensor suite for atmospheric boundary layer measurement with a small multirotor unmanned aerial system, *International Journal of Aviation, Aeronautics, and Aerospace*, 7, <https://doi.org/10.15394/ijaaa.2020.1433>, 2020.
- Aggarwal, S., Bansal, P., Wang, Y., Jorga, S., Macgregor, G., Rohner, U., Bannan, T., Salter, M., Zieger, P., Mohr, C., and Lopez-Hilfiker, F.: Identifying key parameters that affect sensitivity of flow tube chemical ionization mass spectrometers, *Atmospheric Measurement Techniques*, 18, 4227-4247, <https://doi.org/10.5194/amt-18-4227-2025>, 2025.
- Aljawhary, D., Lee, A. K. Y., and Abbatt, J. P. D.: High-resolution chemical ionization mass spectrometry (ToF-CIMS): application to study SOA composition and processing, *Atmos. Meas. Tech.*, 6, 3211-3224, <https://doi.org/10.5194/amt-6-3211-2013>, 2013.
- Allen, G., Hollingsworth, P., Kabbabe, K., Pitt, J. R., Mead, M. I., Illingworth, S., Roberts, G., Bourn, M., Shallcross, D. E., and Percival, C. J.: The development and trial of an unmanned aerial system for the measurement of methane flux from landfill and greenhouse gas emission hotspots, *Waste Manag*, 87, 883-892, <https://doi.org/10.1016/j.wasman.2017.12.024>, 2019.
- Alphasense: Alphasense User Manual OPC-N3 Optical Particle Counter, <https://www.alphasense.com/downloads/software>, 2019.
- Altstädter, B., Platis, A., Jähn, M., Baars, H., Lücknerath, J., Held, A., Lampert, A., Bange, J., Hermann, M., and Wehner, B.: Airborne observations of newly formed boundary layer aerosol particles under cloudy conditions, *Atmospheric Chemistry and Physics*, 18, 8249-8264, <https://doi.org/10.5194/acp-18-8249-2018>, 2018.
- Alves, C. A., Gonçalves, C., Mirante, F., Nunes, T., Evtuyugina, M., Sánchez de la Campa, A., Rocha, A. C., and Marques, M. C.: Organic speciation of atmospheric particles in Alvão Natural Park (Portugal), *Environmental Monitoring and Assessment*, 168, 321-337, <https://doi.org/10.1007/s10661-009-1116-1>, 2010.
- Andersen, T., Zhao, Z., de Vries, M., Necki, J., Swolkien, J., Menoud, M., Röckmann, T., Roiger, A., Fix, A., Peters, W., and Chen, H.: Local-to-regional methane emissions from the Upper Silesian Coal Basin (USCB) quantified using UAV-based atmospheric measurements, *Atmos. Chem. Phys.*, 23, 5191-5216, <https://doi.org/10.5194/acp-23-5191-2023>, 2023.
- Andreae, M. O. and Rosenfeld, D.: Aerosol–cloud–precipitation interactions. Part 1. The nature and sources of cloud-active aerosols, *Earth-Science Reviews*, 89, 13-41, <https://doi.org/10.1016/j.earscirev.2008.03.001>, 2008.
- Andreae, M. O., Artaxo, P., Fischer, H., Freitas, S. R., Grégoire, J. M., Hansel, A., Hoor, P., Kormann, R., Krejci, R., Lange, L., Lelieveld, J., Lindinger, W., Longo, K., Peters, W., De Reus, M., Scheeren, B., Silva Dias, M. A. F., Ström, J., Van Velthoven, P. F. J., and Williams, J.: Transport of biomass burning smoke to the upper troposphere by deep convection in the equatorial region, *Geophysical Research Letters*, 28, 951-954, <https://doi.org/10.1029/2000gl012391>, 2001.
- Andreae, M. O., Acevedo, O. C., Araùjo, A., Artaxo, P., Barbosa, C. G. G., Barbosa, H. M. J., Brito, J., Carbone, S., Chi, X., Cintra, B. B. L., da Silva, N. F., Dias, N. L., Dias-Júnior, C. Q., Ditas, F., Ditz, R., Godoi,

- A. F. L., Godoi, R. H. M., Heimann, M., Hoffmann, T., Kesselmeier, J., Könemann, T., Krüger, M. L., Lavric, J. V., Manzi, A. O., Lopes, A. P., Martins, D. L., Mikhailov, E. F., Moran-Zuloaga, D., Nelson, B. W., Nölscher, A. C., Santos Nogueira, D., Piedade, M. T. F., Pöhlker, C., Pöschl, U., Quesada, C. A., Rizzo, L. V., Ro, C. U., Ruckteschler, N., Sá, L. D. A., de Oliveira Sá, M., Sales, C. B., dos Santos, R. M. N., Saturno, J., Schöngart, J., Sörgel, M., de Souza, C. M., de Souza, R. A. F., Su, H., Targhetta, N., Tóta, J., Trebs, I., Trumbore, S., van Eijck, A., Walter, D., Wang, Z., Weber, B., Williams, J., Winderlich, J., Wittmann, F., Wolff, S., and Yáñez-Serrano, A. M.: The Amazon Tall Tower Observatory (ATTO): overview of pilot measurements on ecosystem ecology, meteorology, trace gases, and aerosols, *Atmos. Chem. Phys.*, 15, 10723-10776, <https://doi.org/10.5194/acp-15-10723-2015>, 2015.
- Anemoment: TriSonica Mini Sensors: User Manual, 2021.
- Angelucci, A. A., Furlani, T. C., Wang, X., Jacob, D. J., Vandenboer, T. C., and Young, C. J.: Understanding Sources of Atmospheric Hydrogen Chloride in Coastal Spring and Continental Winter, *ACS Earth and Space Chemistry*, 5, 2507-2516, <https://doi.org/10.1021/acsearthspacechem.1c00193>, 2021.
- Asbach, C., Todea, A. M., and Kaminski, H.: Evaluation of a Partector Pro for atmospheric particle number size distribution and number concentration measurements at an urban background site, *Aerosol Research*, 2, 1-12, <https://doi.org/10.5194/ar-2-1-2024>, 2024.
- Atkinson, R., Aschmann, S. M., Arey, J., and Shorees, B.: Formation of OH radicals in the gas phase reactions of O₃ with a series of terpenes, *Journal of Geophysical Research: Atmospheres*, 97, 6065-6073, <https://doi.org/10.1029/92JD00062>, 1992.
- Atkinson, R., Baulch, D. L., Cox, R. A., Crowley, J. N., Hampson, R. F., Hynes, R. G., Jenkin, M. E., Rossi, M. J., and Troe, J.: Evaluated kinetic and photochemical data for atmospheric chemistry: Volume III – gas phase reactions of inorganic halogens, *Atmospheric Chemistry and Physics*, 7, 981-1191, <https://doi.org/10.5194/acp-7-981-2007>, 2007.
- Bai, Z., Ji, Y., Pi, Y., Yang, K., Wang, L., Zhang, Y., Zhai, Y., Yan, Z., and Han, X.: Hygroscopic analysis of individual Beijing haze aerosol particles by environmental scanning electron microscopy, *Atmospheric Environment*, 172, 149-156, <https://doi.org/10.1016/j.atmosenv.2017.10.031>, 2018.
- Bakels, L., Tatsii, D., Tipka, A., Thompson, R., Dütsch, M., Blaschek, M., Seibert, P., Baier, K., Bucci, S., Cassiani, M., Eckhardt, S., Groot Zwaafink, C., Henne, S., Kaufmann, P., Lechner, V., Maurer, C., Mulder, M. D., Pisso, I., Plach, A., Subramanian, R., Vojta, M., and Stohl, A.: FLEXPART version 11: improved accuracy, efficiency, and flexibility, *Geoscientific Model Development*, 17, 7595-7627, <https://doi.org/10.5194/gmd-17-7595-2024>, 2024.
- Bamberger, I., Hörtnagl, L., Ruuskanen, T. M., Schnitzhofer, R., Müller, M., Graus, M., Karl, T., Wohlfahrt, G., and Hansel, A.: Deposition fluxes of terpenes over grassland, *Journal of Geophysical Research*, 116, <https://doi.org/10.1029/2010jd015457>, 2011.
- Bannan, T. J., Khan, M. A. H., Le Breton, M., Priestley, M., Worrall, S. D., Bacak, A., Marsden, N. A., Lowe, D., Pitt, J., Allen, G., Topping, D., Coe, H., McFiggans, G., Shallcross, D. E., and Percival, C. J.: A Large Source of Atomic Chlorine From ClNO₂ Photolysis at a U.K. Landfill Site, *Geophysical Research Letters*, 46, 8508-8516, <https://doi.org/10.1029/2019gl083764>, 2019.
- Bannan, T. J., Booth, A. M., Bacak, A., Muller, J. B. A., Leather, K. E., Le Breton, M., Jones, B., Young, D., Coe, H., Allan, J., Visser, S., Slowik, J. G., Furger, M., Prévôt, A. S. H., Lee, J., Dunmore, R. E., Hopkins, J. R., Hamilton, J. F., Lewis, A. C., Whalley, L. K., Sharp, T., Stone, D., Heard, D. E., Fleming, Z. L., Leigh, R., Shallcross, D. E., and Percival, C. J.: The first UK measurements of nitryl chloride using a chemical ionization mass spectrometer in central London in the summer of 2012, and an investigation of the role of Cl atom oxidation, *Journal of Geophysical Research: Atmospheres*, 120, 5638-5657, <https://doi.org/10.1002/2014jd022629>, 2015.
- Barbieri, L., Kral, S. T., Bailey, S. C. C., Frazier, A. E., Jacob, J. D., Reuder, J., Brus, D., Chilson, P. B., Crick, C., Detweiler, C., Doddi, A., Elston, J., Foroutan, H., González-Rocha, J., Greene, B. R., Guzman, M. I., Houston, A. L., Islam, A., Kemppinen, O., Lawrence, D., Pillar-Little, E. A., Ross, S. D., Sama, M. P., Schmale, D. G., Schuyler, T. J., Shankar, A., Smith, S. W., Waugh, S., Dixon, C., Borenstein, S., and de Boer, G.: Intercomparison of Small Unmanned Aircraft System (sUAS) Measurements for Atmospheric Science during the LAPSE-RATE Campaign, <https://doi.org/10.3390/s19092179>, 2019.

- Barnes, G. M. and Garstang, M.: Subcloud Layer Energetics of Precipitating Convection, *Monthly Weather Review*, 110, 102-117, [https://doi.org/10.1175/1520-0493\(1982\)110<0102:SLEOPC>2.0.CO;2](https://doi.org/10.1175/1520-0493(1982)110<0102:SLEOPC>2.0.CO;2), 1982.
- Barros, A. P. and Lettenmaier, D. P.: Dynamic modeling of orographically induced precipitation, *Reviews of Geophysics*, 32, 265-284, <https://doi.org/10.1029/94rg00625>, 1994.
- Behrendt, A., Wulfmeyer, V., Senff, C., Muppa, S. K., Späth, F., Lange, D., Kalthoff, N., and Wieser, A.: Observation of sensible and latent heat flux profiles with lidar, *Atmospheric Measurement Techniques*, 13, 3221-3233, <https://doi.org/10.5194/amt-13-3221-2020>, 2020.
- Bela, M. M., Barth, M. C., Toon, O. B., Fried, A., Ziegler, C., Cummings, K. A., Li, Y., Pickering, K. E., Homeyer, C. R., Morrison, H., Yang, Q., Mecikalski, R. M., Carey, L., Biggerstaff, M. I., Betten, D. P., and Alford, A. A.: Effects of Scavenging, Entrainment, and Aqueous Chemistry on Peroxides and Formaldehyde in Deep Convective Outflow Over the Central and Southeast United States, *Journal of Geophysical Research: Atmospheres*, 123, 7594-7614, <https://doi.org/10.1029/2018jd028271>, 2018.
- Bélair, F., Dyer-Hawes, Q., and Romanic, D.: The Dynamics of the Urban Boundary Layer Before and During a Severe Thunderstorm Outflow Over Downtown Montréal, *Boundary-Layer Meteorology*, 191, <https://doi.org/10.1007/s10546-024-00896-4>, 2025.
- Benoit, R., Vernier, H., Vernier, J.-P., Joly, L., Dumelié, N., Wienhold, F. G., Crevoisier, C., Delpoux, S., Bernard, F., Dagaut, P., and Berthet, G.: The first balloon-borne sample analysis of atmospheric carbonaceous components reveals new insights into formation processes, *Chemosphere*, 326, 138421, <https://doi.org/10.1016/j.chemosphere.2023.138421>, 2023.
- Bertram, T. H. and Thornton, J. A.: Toward a general parameterization of N₂O₅ reactivity on aqueous particles: the competing effects of particle liquid water, nitrate and chloride, *Atmospheric Chemistry and Physics*, 9, 8351-8363, <https://doi.org/10.5194/acp-9-8351-2009>, 2009.
- Bertram, T. H., Thornton, J. A., Riedel, T. P., Middlebrook, A. M., Bahreini, R., Bates, T. S., Quinn, P. K., and Coffman, D. J.: Direct observations of N₂O₅ reactivity on ambient aerosol particles, *Geophysical Research Letters*, 36, <https://doi.org/10.1029/2009gl040248>, 2009.
- Bey, I., Aumont, B., and Toupance, G.: The nighttime production of OH radicals in the continental troposphere, *Geophysical Research Letters*, 24, 1067-1070, <https://doi.org/10.1029/97gl00889>, 1997.
- Bezantakos, S. and Biskos, G.: Temperature and pressure effects on the performance of the portable TSI 3007 condensation particle counter: Implications on ground and aerial observations, *Journal of Aerosol Science*, 159, 105877, <https://doi.org/10.1016/j.jaerosci.2021.105877>, 2022.
- Bezantakos, S., Schmidt-Ott, F., and Biskos, G.: Performance evaluation of the cost-effective and lightweight Alphasense optical particle counter for use onboard unmanned aerial vehicles, *Aerosol Science and Technology*, 52, 385-392, <https://doi.org/10.1080/02786826.2017.1412394>, 2018.
- Bezantakos, S., Costi, M., Barmounis, K., Antoniou, P., Vouterakos, P., Keleshis, C., Sciare, J., and Biskos, G.: Qualification of the Alphasense optical particle counter for inline air quality monitoring, *Aerosol Science and Technology*, 55, 361-370, <https://doi.org/10.1080/02786826.2020.1864276>, 2021.
- Bhattacharyya, N., Modi, M., Jahn, L. G., and Hildebrandt Ruiz, L.: Different chlorine and hydroxyl radical environments impact m-xylene oxidation products, *Environmental Science: Atmospheres*, 3, 1174-1185, <https://doi.org/10.1039/d3ea00024a>, 2023.
- Bhowmik, H. S., Shukla, A., Lalchandani, V., Dave, J., Rastogi, N., Kumar, M., Singh, V., and Tripathi, S. N.: Inter-comparison of online and offline methods for measuring ambient heavy and trace elements and water-soluble inorganic ions (NO₃⁻, SO₄²⁻, NH₄⁺, and Cl⁻) in PM_{2.5} over a heavily polluted megacity, Delhi, *Atmos. Meas. Tech.*, 15, 2667-2684, <https://doi.org/10.5194/amt-15-2667-2022>, 2022.
- Bi, J., Li, Y., Lin, Z., Yang, Z., Chen, F., Liu, S., and Li, C.: Effect of different cooking methods on flavor compounds of Chinese traditional condiment Wuxiang powder, *Journal of Food Processing and Preservation*, 46, <https://doi.org/10.1111/jfpp.16358>, 2022.
- Bianchi, F., Kurtén, T., Riva, M., Mohr, C., Rissanen, M. P., Roldin, P., Berndt, T., Crouse, J. D., Wennberg, P. O., Mentel, T. F., Wildt, J., Junninen, H., Jokinen, T., Kulmala, M., Worsnop, D. R., Thornton, J. A., Donahue, N., Kjaergaard, H. G., and Ehn, M.: Highly Oxygenated Organic Molecules

- (HOM) from Gas-Phase Autoxidation Involving Peroxy Radicals: A Key Contributor to Atmospheric Aerosol, *Chemical Reviews*, 119, 3472-3509, <https://doi.org/10.1021/acs.chemrev.8b00395>, 2019.
- Bieber, P., Seifried, T. M., Burkart, J., Gratzl, J., Kasper-Giebl, A., Schmale, D. G., and Grothe, H.: A Drone-Based Bioaerosol Sampling System to Monitor Ice Nucleation Particles in the Lower Atmosphere, *Remote Sensing*, 12, 552, <https://doi.org/10.3390/rs12030552>, 2020.
- Blackadar, A. K.: Boundary Layer Wind Maxima and Their Significance for the Growth of Nocturnal Inversions, *Bulletin of the American Meteorological Society*, 38, 283-290, <https://doi.org/10.1175/1520-0477-38.5.283>, 1957.
- Böhländer, A., Lacher, L., Brus, D., Douglgeris, K. M., Brasseur, Z., Boyer, M., Kuula, J., Leisner, T., and Möhler, O.: A novel aerosol filter sampler for measuring the vertical distribution of ice-nucleating particles via fixed-wing uncrewed aerial vehicles, *Atmos. Meas. Tech.*, 18, 3959-3971, <https://doi.org/10.5194/amt-18-3959-2025>, 2025.
- Bonne, J.-L., Donnat, L., Albora, G., Burgalat, J., Chauvin, N., Combaz, D., Cousin, J., Decarpenterie, T., Duclaux, O., Dumelié, N., Galas, N., Juery, C., Parent, F., Pineau, F., Maunoury, A., Ventre, O., Bénassy, M.-F., and Joly, L.: A measurement system for CO₂ and CH₄ emissions quantification of industrial sites using a new in situ concentration sensor operated on board uncrewed aircraft vehicles, *Atmospheric Measurement Techniques*, 17, 4471-4491, <https://doi.org/10.5194/amt-17-4471-2024>, 2024.
- Bopape, M.-J. M., Waitolo, D., Plant, R. S., Phaduli, E., Nkonde, E., Simfukwe, H., Mkandawire, S., Rakate, E., and Maisha, R.: Sensitivity of Simulations of Zambian Heavy Rainfall Events to the Atmospheric Boundary Layer Schemes, *Climate*, 9, 38, <https://doi.org/10.3390/cli9020038>, 2021.
- Borchers, C., Moormann, L., Geil, B., Karbach, N., and Hoffmann, T.: Development and use of a lightweight sampling system for height-selective drone-based measurements of organic aerosol particles, <https://doi.org/10.5194/egusphere-2024-4015>, 2025.
- Boris, A. J., Lee, T., Park, T., Choi, J., Seo, S. J., and Collett Jr, J. L.: Fog composition at Baengnyeong Island in the eastern Yellow Sea: detecting markers of aqueous atmospheric oxidations, *Atmos. Chem. Phys.*, 16, 437-453, <https://doi.org/10.5194/acp-16-437-2016>, 2016.
- Brady, J. M., Stokes, M. D., Bonnardel, J., and Bertram, T. H.: Characterization of a Quadrotor Unmanned Aircraft System for Aerosol-Particle-Concentration Measurements, *Environ Sci Technol*, 50, 1376-1383, <https://doi.org/10.1021/acs.est.5b05320>, 2016.
- Brockmann, J. E.: Aerosol Transport in Sampling Lines and Inlets, in: *Aerosol Measurement*, 68-105, <https://doi.org/10.1002/9781118001684.ch6>, 2011.
- Brown, S. S. and Stutz, J.: Nighttime radical observations and chemistry, *Chemical Society Reviews*, 41, 6405, <https://doi.org/10.1039/c2cs35181a>, 2012.
- Brus, D., Gustafsson, J., Kemppinen, O., De Boer, G., and Hirsikko, A.: Atmospheric aerosol, gases, and meteorological parameters measured during the LAPSE-RATE campaign by the Finnish Meteorological Institute and Kansas State University, *Earth System Science Data*, 13, 2909-2922, <https://doi.org/10.5194/essd-13-2909-2021>, 2021a.
- Brus, D., Gustafsson, J., Vakkari, V., Kemppinen, O., De Boer, G., and Hirsikko, A.: Measurement report: Properties of aerosol and gases in the vertical profile during the LAPSE-RATE campaign, *Atmospheric Chemistry and Physics*, 21, 517-533, <https://doi.org/10.5194/acp-21-517-2021>, 2021b.
- Burgués, J., Esclapez, M. D., Doñate, S., Pastor, L., and Marco, S.: Aerial Mapping of Odorous Gases in a Wastewater Treatment Plant Using a Small Drone, *Remote Sensing*, 13, <https://doi.org/10.3390/rs13091757>, 2021.
- Burkholder, J., Sander, S., Abbatt, J., Barker, J., Cappa, C., Crouse, J., Dibble, T., Huie, R., Kolb, C., and Kurylo, M.: Chemical kinetics and photochemical data for use in atmospheric studies; evaluation number 19, Pasadena, CA: Jet Propulsion Laboratory, National Aeronautics and Space ..., <https://jpldataeval.jpl.nasa.gov/index.html>, 2020.
- Burkholder, J. B., Talukdar, R. K., and Ravishankara, A. R.: Temperature dependence of the ClONO₂ UV absorption spectrum, *Geophysical Research Letters*, 21, 585-588, <https://doi.org/10.1029/93gl03303>, 1994.

- Busch, N. E., Chang, S. W., and Anthes, R. A.: A Multi-Level Model of the Planetary Boundary Layer Suitable for Use with Mesoscale Dynamic Models, *Journal of Applied Meteorology and Climatology*, 15, 909-919, [https://doi.org/10.1175/1520-0450\(1976\)015<0909:AMLMOT>2.0.CO;2](https://doi.org/10.1175/1520-0450(1976)015<0909:AMLMOT>2.0.CO;2), 1976.
- Cahill, T. A., Wilkinson, K., and Schnell, R.: Composition analyses of size-resolved aerosol samples taken from aircraft downwind of Kuwait, spring 1991, *Journal of Geophysical Research: Atmospheres*, 97, <https://doi.org/10.1029/92JD01373>, 1992.
- Caldwell, T. E., Foster, K. L., Benter, T., Langer, S., Hemminger, J. C., and Finlayson-Pitts, B. J.: Characterization of HOCl Using Atmospheric Pressure Ionization Mass Spectrometry, *The Journal of Physical Chemistry A*, 103, 8231-8238, <https://doi.org/10.1021/jp9906841>, 1999.
- Canagaratna, M. R., Jimenez, J. L., Kroll, J. H., Chen, Q., Kessler, S. H., Massoli, P., Hildebrandt Ruiz, L., Fortner, E., Williams, L. R., Wilson, K. R., Surratt, J. D., Donahue, N. M., Jayne, J. T., and Worsnop, D. R.: Elemental ratio measurements of organic compounds using aerosol mass spectrometry: characterization, improved calibration, and implications, *Atmos. Chem. Phys.*, 15, 253-272, <https://doi.org/10.5194/acp-15-253-2015>, 2015.
- Canagaratna, M. R., Jayne, J. T., Jimenez, J. L., Allan, J. D., Alfarra, M. R., Zhang, Q., Onasch, T. B., Drewnick, F., Coe, H., Middlebrook, A., Delia, A., Williams, L. R., Trimborn, A. M., Northway, M. J., Decarlo, P. F., Kolb, C. E., Davidovits, P., and Worsnop, D. R.: Chemical and microphysical characterization of ambient aerosols with the aerodyne aerosol mass spectrometer, *Mass Spectrometry Reviews*, 26, 185-222, <https://doi.org/10.1002/mas.20115>, 2007.
- Cao, M., Li, W., Ge, P., Chen, M., and Wang, J.: Seasonal variations and potential sources of biomass burning tracers in particulate matter in Nanjing aerosols during 2017–2018, *Chemosphere*, 303, 135015, <https://doi.org/10.1016/j.chemosphere.2022.135015>, 2022.
- Caravan, R. L., Vansco, M. F., and Lester, M. I.: Open questions on the reactivity of Criegee intermediates, *Communications Chemistry*, 4, <https://doi.org/10.1038/s42004-021-00483-5>, 2021.
- Castro Gamez, A. F., Rodriguez Maroto, J. M., and Vellido Perez, I.: Quantification of methane emissions in a Mediterranean landfill (Southern Spain). A combination of flux chambers and geostatistical methods, *Waste Manag*, 87, 937-946, <https://doi.org/10.1016/j.wasman.2018.12.015>, 2019.
- Cava, D., Mortarini, L., Giostra, U., Acevedo, O., and Katul, G.: Submeso Motions and Intermittent Turbulence Across a Nocturnal Low-Level Jet: A Self-Organized Criticality Analogy, *Boundary-Layer Meteorology*, 172, 17-43, <https://doi.org/10.1007/s10546-019-00441-8>, 2019.
- Celik, S., Drewnick, F., Fachinger, F., Brooks, J., Darbyshire, E., Coe, H., Paris, J. D., Eger, P. G., Schuladen, J., Tadic, I., Friedrich, N., Dienhart, D., Hottmann, B., Fischer, H., Crowley, J. N., Harder, H., and Borrmann, S.: Influence of vessel characteristics and atmospheric processes on the gas and particle phase of ship emission plumes: in situ measurements in the Mediterranean Sea and around the Arabian Peninsula, *Atmos. Chem. Phys.*, 20, 4713-4734, <https://doi.org/10.5194/acp-20-4713-2020>, 2020.
- Chachere, C. N. and Pu, Z.: Connections Between Cold Air Pools and Mountain Valley Fog Events in Salt Lake City, *Pure and Applied Geophysics*, 173, 3187-3196, <https://doi.org/10.1007/s00024-016-1316-x>, 2016.
- Chataut, G., Bhatta, B., Joshi, D., Subedi, K., and Kafle, K.: Greenhouse gases emission from agricultural soil: A review, *Journal of Agriculture and Food Research*, 11, 100533, <https://doi.org/10.1016/j.jafr.2023.100533>, 2023.
- Chen, G., Fan, X., Yu, S., Tham, Y. J., Lin, Z., Ji, X., Xu, L., and Chen, J.: HOCl Formation Driven by Photochemical Processes Enhanced Atmospheric Oxidation Capacity in a Coastal Atmosphere, *Environmental Science & Technology*, 59, <https://doi.org/10.1021/acs.est.5c01363>, 2025a.
- Chen, G., Fan, X., Wang, H., Tham, Y. J., Lin, Z., Ji, X., Xu, L., Hu, B., and Chen, J.: Formation drivers and photochemical effects of ClNO₂ in a coastal city of Southeast China, *Atmospheric Chemistry and Physics*, 25, 7815-7828, <https://doi.org/10.5194/acp-25-7815-2025>, 2025b.
- Chen, G., Xu, L., Yu, S., Xue, L., Lin, Z., Yang, C., Ji, X., Fan, X., Tham, Y. J., Wang, H., Hong, Y., Li, M., Seinfeld, J. H., and Chen, J.: Increasing Contribution of Chlorine Chemistry to Wintertime Ozone Formation Promoted by Enhanced Nitrogen Chemistry, *Environmental Science & Technology*, 58, 22714-22721, <https://doi.org/10.1021/acs.est.4c09523>, 2024.

- Chen, G., Canonaco, F., Tobler, A., Aas, W., Alastuey, A., Allan, J., Atabakhsh, S., Aurela, M., Baltensperger, U., Bougiatioti, A., De Brito, J. F., Ceburnis, D., Chazeau, B., Chebaicheb, H., Daellenbach, K. R., Ehn, M., El Haddad, I., Eleftheriadis, K., Favez, O., Flentje, H., Font, A., Fossun, K., Freney, E., Gini, M., Green, D. C., Heikkinen, L., Herrmann, H., Kalogridis, A.-C., Keernik, H., Lhotka, R., Lin, C., Lunder, C., Maasikmets, M., Manousakas, M. I., Marchand, N., Marin, C., Marmureanu, L., Mihalopoulos, N., Močnik, G., Nečki, J., O'Dowd, C., Ovadnevaite, J., Peter, T., Petit, J.-E., Pikridas, M., Matthew Platt, S., Pokorná, P., Poulain, L., Priestman, M., Riffault, V., Rinaldi, M., Rózański, K., Schwarz, J., Sciare, J., Simon, L., Skiba, A., Slowik, J. G., Sosedova, Y., Stavroulas, I., Styszko, K., Teinmaa, E., Timonen, H., Tremper, A., Vasilescu, J., Via, M., Vodička, P., Wiedensohler, A., Zografou, O., Cruz Minguillón, M., and Prévôt, A. S. H.: European aerosol phenomenology – 8: Harmonised source apportionment of organic aerosol using 22 Year-long ACSM/AMS datasets, *Environment International*, 166, 107325, <https://doi.org/10.1016/j.envint.2022.107325>, 2022.
- Chen, Y., Takeuchi, M., Nah, T., Xu, L., Canagaratna, M. R., Stark, H., Baumann, K., Canonaco, F., Prévôt, A. S. H., Huey, L. G., Weber, R. J., and Ng, N. L.: Chemical characterization of secondary organic aerosol at a rural site in the southeastern US: insights from simultaneous high-resolution time-of-flight aerosol mass spectrometer (HR-ToF-AMS) and FIGAERO chemical ionization mass spectrometer (CIMS) measurements, *Atmos. Chem. Phys.*, 20, 8421-8440, <https://doi.org/10.5194/acp-20-8421-2020>, 2020.
- Chen, Z. H., Cheng, S. Y., Li, J. B., Guo, X. R., Wang, W. H., and Chen, D. S.: Relationship between atmospheric pollution processes and synoptic pressure patterns in northern China, *Atmospheric Environment*, 42, 6078-6087, <https://doi.org/10.1016/j.atmosenv.2008.03.043>, 2008.
- Cherrier, G., Belut, E., Gerardin, F., Tanière, A., and Rimbart, N.: Aerosol particles scavenging by a droplet: Microphysical modeling in the Greenfield gap, *Atmospheric Environment*, 166, 519-530, <https://doi.org/10.1016/j.atmosenv.2017.07.052>, 2017.
- Chow, J. C., Fujita, E. M., Watson, J. G., Lu, Z., Lawson, D. R., and Ashbaugh, L. L.: Evaluation of filter-based aerosol measurements during the 1987 Southern California Air Quality Study, *Environmental Monitoring and Assessment*, 30, 49-80, <https://doi.org/10.1007/bf00546199>, 1994.
- Chua, G., Naik, V., and Horowitz, L. W.: Exploring the drivers of tropospheric hydroxyl radical trends in the Geophysical Fluid Dynamics Laboratory AM4.1 atmospheric chemistry–climate model, *Atmospheric Chemistry and Physics*, 23, <https://doi.org/10.5194/acp-23-4955-2023>, 2023.
- Cicerone, R. J.: Halogens in the atmosphere, *Reviews of Geophysics*, 19, 123-139, <https://doi.org/10.1029/rg019i001p00123>, 1981.
- Claeys, M., Graham, B., Vas, G., Wang, W., Vermeylen, R., Pashynska, V., Cafmeyer, J., Guyon, P., Andreae, M. O., Artaxo, P., and Maenhaut, W.: Formation of Secondary Organic Aerosols Through Photooxidation of Isoprene, *Science*, 303, 1173-1176, <https://doi.org/10.1126/science.1092805>, 2004.
- Clement, R. E. and Karasek, F. W.: Sample Composition Changes in Sampling and Analysis of Organic Compounds in Aerosols, *International Journal of Environmental Analytical Chemistry*, 7, 109-120, <https://doi.org/10.1080/03067317908071482>, 1979.
- Coggon, M. M., Lim, C. Y., Koss, A. R., Sekimoto, K., Yuan, B., Gilman, J. B., Hagan, D. H., Selimovic, V., Zarzana, K. J., Brown, S. S., Roberts, J. M., Müller, M., Yokelson, R., Wisthaler, A., Krechmer, J. E., Jimenez, J. L., Cappa, C., Kroll, J. H., de Gouw, J., and Warneke, C.: OH chemistry of non-methane organic gases (NMOGs) emitted from laboratory and ambient biomass burning smoke: evaluating the influence of furans and oxygenated aromatics on ozone and secondary NMOG formation, *Atmos. Chem. Phys.*, 19, 14875-14899, <https://doi.org/10.5194/acp-19-14875-2019>, 2019.
- Collaud Coen, M., Praz, C., Haeefe, A., Ruffieux, D., Kaufmann, P., and Calpini, B.: Determination and climatology of the planetary boundary layer height above the Swiss plateau by in situ and remote sensing measurements as well as by the COSMO-2 model, *Atmos. Chem. Phys.*, 14, 13205-13221, <https://doi.org/10.5194/acp-14-13205-2014>, 2014.
- Collis, R. T. H. and Ligda, M. G. H.: Laser Radar Echoes from the Clear Atmosphere, *Nature*, 203, 508-508, <https://doi.org/10.1038/203508a0>, 1964.
- Commodore, A., Wilson, S., Muhammad, O., Svendsen, E., and Pearce, J.: Community-based participatory research for the study of air pollution: a review of motivations, approaches, and

- outcomes, *Environmental Monitoring and Assessment*, 189, 378, <https://doi.org/10.1007/s10661-017-6063-7>, 2017.
- Cox, R. A., Ammann, M., Crowley, J. N., Herrmann, H., Jenkin, M. E., McNeill, V. F., Mellouki, A., Troe, J., and Wallington, T. J.: Evaluated kinetic and photochemical data for atmospheric chemistry: Volume VII – Criegee intermediates, *Atmospheric Chemistry and Physics*, 20, 13497-13519, <https://doi.org/10.5194/acp-20-13497-2020>, 2020.
- Craven, J. S., Yee, L. D., Ng, N. L., Canagaratna, M. R., Loza, C. L., Schilling, K. A., Yatavelli, R. L. N., Thornton, J. A., Ziemann, P. J., Flagan, R. C., and Seinfeld, J. H.: Analysis of secondary organic aerosol formation and aging using positive matrix factorization of high-resolution aerosol mass spectra: application to the dodecane low-NO_x system, *Atmos. Chem. Phys.*, 12, 11795-11817, <https://doi.org/10.5194/acp-12-11795-2012>, 2012.
- Crazzolaro, C., Ebner, M., Platis, A., Miranda, T., Bange, J., and Junginger, A.: A new multicopter-based unmanned aerial system for pollen and spores collection in the atmospheric boundary layer, *Atmos. Meas. Tech.*, 12, 1581-1598, <https://doi.org/10.5194/amt-12-1581-2019>, 2019.
- Crenn, V., Sciare, J., Croteau, P. L., Verlhac, S., Fröhlich, R., Belis, C. A., Aas, W., Äijälä, M., Alastuey, A., Artiñano, B., Baisnée, D., Bonnaire, N., Bressi, M., Canagaratna, M., Canonaco, F., Carbone, C., Cavalli, F., Coz, E., Cubison, M. J., Esser-Gietl, J. K., Green, D. C., Gros, V., Heikkinen, L., Herrmann, H., Lunder, C., Minguillón, M. C., Močnik, G., O'Dowd, C. D., Ovadnevaite, J., Petit, J. E., Petralia, E., Poulain, L., Priestman, M., Riffault, V., Ripoll, A., Sarda-Estève, R., Slowik, J. G., Setyan, A., Wiedensohler, A., Baltensperger, U., Prévôt, A. S. H., Jayne, J. T., and Favez, O.: ACTRIS ACSM intercomparison – Part 1: Reproducibility of concentration and fragment results from 13 individual Quadrupole Aerosol Chemical Speciation Monitors (Q-ACSM) and consistency with co-located instruments, *Atmos. Meas. Tech.*, 8, 5063-5087, <https://doi.org/10.5194/amt-8-5063-2015>, 2015.
- Crook, N. A. and Klemp, J. B.: Lifting by Convergence Lines, *Journal of the Atmospheric Sciences*, 57, 873-890, [https://doi.org/10.1175/1520-0469\(2000\)057<0873:LBCL>2.0.CO;2](https://doi.org/10.1175/1520-0469(2000)057<0873:LBCL>2.0.CO;2), 2000.
- Crowley, J. N., Schuster, G., Pouvesle, N., Parchatka, U., Fischer, H., Bonn, B., Bingemer, H., and Lelieveld, J.: Nocturnal nitrogen oxides at a rural mountain-site in south-western Germany, *Atmospheric Chemistry and Physics*, 10, 2795-2812, <https://doi.org/10.5194/acp-10-2795-2010>, 2010.
- Crueger, T., Giorgetta, M. A., Brokopf, R., Esch, M., Fiedler, S., Hohenegger, C., Kornbluh, L., Mauritsen, T., Nam, C., Naumann, A. K., Peters, K., Rast, S., Roeckner, E., Sakradzija, M., Schmidt, H., Vial, J., Vogel, R., and Stevens, B.: ICON-A, The Atmosphere Component of the ICON Earth System Model: II. Model Evaluation, *Journal of Advances in Modeling Earth Systems*, 10, 1638-1662, <https://doi.org/10.1029/2017ms001233>, 2018.
- Cubison, M. J., Ortega, A. M., Hayes, P. L., Farmer, D. K., Day, D., Lechner, M. J., Brune, W. H., Apel, E., Diskin, G. S., Fisher, J. A., Fuelberg, H. E., Hecobian, A., Knapp, D. J., Mikoviny, T., Riemer, D., Sachse, G. W., Sessions, W., Weber, R. J., Weinheimer, A. J., Wisthaler, A., and Jimenez, J. L.: Effects of aging on organic aerosol from open biomass burning smoke in aircraft and laboratory studies, *Atmos. Chem. Phys.*, 11, 12049-12064, <https://doi.org/10.5194/acp-11-12049-2011>, 2011.
- Curtius, J., Heinritzi, M., Beck, L. J., Pöhlker, M. L., Tripathi, N., Krumm, B. E., Holzbeck, P., Nussbaumer, C. M., Hernández Pardo, L., Klimach, T., Barmounis, K., Andersen, S. T., Bardakov, R., Bohn, B., Cecchini, M. A., Chaboureau, J.-P., Dauhut, T., Dienhart, D., Dörich, R., Edtbauer, A., Giez, A., Hartmann, A., Holanda, B. A., Joppe, P., Kaiser, K., Keber, T., Klebach, H., Krüger, O. O., Kürten, A., Mallaun, C., Marno, D., Martinez, M., Monteiro, C., Nelson, C., Ort, L., Raj, S. S., Richter, S., Ringsdorf, A., Rocha, F., Simon, M., Sreekumar, S., Tsokankunku, A., Unfer, G. R., Valenti, I. D., Wang, N., Zahn, A., Zauner-Wieczorek, M., Albrecht, R. I., Andreae, M. O., Artaxo, P., Crowley, J. N., Fischer, H., Harder, H., Herdies, D. L., Machado, L. A. T., Pöhlker, C., Pöschl, U., Possner, A., Pozzer, A., Schneider, J., Williams, J., and Lelieveld, J.: Isoprene nitrates drive new particle formation in Amazon's upper troposphere, *Nature*, 636, 124-130, <https://doi.org/10.1038/s41586-024-08192-4>, 2024.
- Dai, C., Wang, Q., Kalogiros, J. A., Lenschow, D. H., Gao, Z., and Zhou, M.: Determining Boundary-Layer Height from Aircraft Measurements, *Boundary-Layer Meteorology*, 152, 277-302, <https://doi.org/10.1007/s10546-014-9929-z>, 2014.

- Dai, J., Wang, T., Shen, H., Xia, M., Sun, W., and Brasseur, G. P.: Significant Impact of a Daytime Halogen Oxidant on Coastal Air Quality, *Environmental Science & Technology*, 59, 2169-2180, <https://doi.org/10.1021/acs.est.4c08360>, 2025.
- Dalton, E. Z., Hoffmann, E. H., Schaefer, T., Tilgner, A., Herrmann, H., and Raff, J. D.: Daytime Atmospheric Halogen Cycling through Aqueous-Phase Oxygen Atom Chemistry, *Journal of the American Chemical Society*, 145, 15652-15657, <https://doi.org/10.1021/jacs.3c03112>, 2023.
- Dandou, A., Tombrou, M., Schäfer, K., Emeis, S., Protonotariou, A. P., Bossioli, E., Soulakellis, N., and Suppan, P.: A Comparison Between Modelled and Measured Mixing-Layer Height Over Munich, *Boundary-Layer Meteorology*, 131, 425-440, <https://doi.org/10.1007/s10546-009-9373-7>, 2009.
- Davidson, J. A., Cantrell, C. A., Shetter, R. E., McDaniel, A. H., and Calvert, J. G.: Absolute infrared absorption cross sections for ClONO₂ at 296 and 223 K, *Journal of Geophysical Research: Atmospheres*, 92, 10921-10925, <https://doi.org/10.1029/jd092id09p10921>, 1987.
- Davidson, J. A., Viggiano, A. A., Howard, C. J., Dotan, I., Fehsenfeld, F. C., Albritton, D. L., and Ferguson, E. E.: Rate constants for the reactions of O₂⁺, NO₂⁺, NO⁺, H₃O⁺, CO₃⁻, NO₂⁻, and halide ions with N₂O₅ at 300 K, *The Journal of Chemical Physics*, 68, 2085-2087, <https://doi.org/10.1063/1.436032>, 1978.
- De Gouw, J. and Jimenez, J. L.: Organic Aerosols in the Earth's Atmosphere, *Environmental Science & Technology*, 43, 7614-7618, <https://doi.org/10.1021/es9006004>, 2009.
- De Haan, D. O. and Birks, J. W.: Heterogeneous Reactions of Chlorine Peroxide with Halide Ions, *The Journal of Physical Chemistry A*, 101, 8026-8034, <https://doi.org/10.1021/jp970948o>, 1997.
- Debolskiy, A. V., Mortikov, E. V., Glazunov, A. V., and Lüpkes, C.: Evaluation of Surface Layer Stability Functions and Their Extension to First Order Turbulent Closures for Weakly and Strongly Stratified Stable Boundary Layer, *Boundary-Layer Meteorology*, 187, 73-93, <https://doi.org/10.1007/s10546-023-00784-3>, 2023.
- Decarlo, P. F., Kimmel, J. R., Trimborn, A., Northway, M. J., Jayne, J. T., Aiken, A. C., Gonin, M., Fuhrer, K., Horvath, T., Docherty, K. S., Worsnop, D. R., and Jimenez, J. L.: Field-Deployable, High-Resolution, Time-of-Flight Aerosol Mass Spectrometer, *Analytical Chemistry*, 78, 8281-8289, <https://doi.org/10.1021/ac061249n>, 2006.
- Deiber, G., George, C., Le Calvé, S., Schweitzer, F., and Mirabel, P.: Uptake study of ClONO₂ and BrONO₂ by Halide containing droplets, *Atmos. Chem. Phys.*, 4, 1291-1299, <https://doi.org/10.5194/acp-4-1291-2004>, 2004.
- Després, V. R., Huffman, J. A., Burrows, S. M., Hoose, C., Safatov, A. S., Buryak, G., Fröhlich-Nowoisky, J., Elbert, W., Andreae, M. O., Pöschl, U., and Jaenicke, R.: Primary biological aerosol particles in the atmosphere: a review, *Tellus B: Chemical and Physical Meteorology*, 64, 15598, <https://doi.org/10.3402/tellusb.v64i0.15598>, 2012.
- Dettmer, K. and Engewald, W.: Adsorbent materials commonly used in air analysis for adsorptive enrichment and thermal desorption of volatile organic compounds, *Analytical and Bioanalytical Chemistry*, 373, 490-500, <https://doi.org/10.1007/s00216-002-1352-5>, 2002.
- Dettmer, K. and Engewald, W.: Ambient air analysis of volatile organic compounds using adsorptive enrichment, *Chromatographia*, 57, S339-S347, <https://doi.org/10.1007/bf02492126>, 2003.
- Dewald, P., Seubert, T., Andersen, S. T., Türk, G. N. T. E., Schuladen, J., McGillen, M. R., Denjean, C., Etienne, J.-C., Garrouste, O., Jamar, M., Harb, S., Cirtog, M., Michoud, V., Cazaunau, M., Bergé, A., Cantrell, C., Dusanter, S., Picquet-Varrault, B., Kukui, A., Xue, C., Mellouki, A., Lelieveld, J., and Crowley, J. N.: NO₃ reactivity during a summer period in a temperate forest below and above the canopy, *Atmospheric Chemistry and Physics*, 24, 8983-8997, <https://doi.org/10.5194/acp-24-8983-2024>, 2024.
- Diesch, J.-M., Drewnick, F., Klimach, T., and Borrmann, S.: Investigation of gaseous and particulate emissions from various marine vessel types measured on the banks of the Elbe in Northern Germany, *Atmospheric Chemistry and Physics*, 13, 3603-3618, <https://doi.org/10.5194/acp-13-3603-2013>, 2013.
- Dörich, R., Eger, P., Lelieveld, J., and Crowley, J. N.: Iodide CIMS and m/z 62: the detection of HNO₃ as NO₃⁻ in the presence of PAN, peroxyacetic acid and ozone, *Atmospheric Measurement Techniques*, 14, 5319-5332, <https://doi.org/10.5194/amt-14-5319-2021>, 2021.

- Dragoneas, A., Molleker, S., Appel, O., Hünig, A., Böttger, T., Hermann, M., Drewnick, F., Schneider, J., Weigel, R., and Borrmann, S.: The realization of autonomous, aircraft-based, real-time aerosol mass spectrometry in the upper troposphere and lower stratosphere, *Atmospheric Measurement Techniques*, 15, 5719-5742, <https://doi.org/10.5194/amt-15-5719-2022>, 2022.
- Drewnick, F., Pikkmann, J., Fachinger, F., Moormann, L., Sprang, F., and Borrmann, S.: Aerosol filtration efficiency of household materials for homemade face masks: Influence of material properties, particle size, particle electrical charge, face velocity, and leaks, *Aerosol Science and Technology*, 55, 63-79, <https://doi.org/10.1080/02786826.2020.1817846>, 2021.
- Drewnick, F., Böttger, T., von der Weiden-Reinmüller, S. L., Zorn, S. R., Klimach, T., Schneider, J., and Borrmann, S.: Design of a mobile aerosol research laboratory and data processing tools for effective stationary and mobile field measurements, *Atmospheric Measurement Techniques*, 5, 1443-1457, <https://doi.org/10.5194/amt-5-1443-2012>, 2012.
- Drewnick, F., Schneider, J., Hings, S. S., Hock, N., Noone, K., Targino, A., Weimer, S., and Borrmann, S.: Measurement of Ambient, Interstitial, and Residual Aerosol Particles on a Mountaintop Site in Central Sweden using an Aerosol Mass Spectrometer and a CVI, *Journal of Atmospheric Chemistry*, 56, 1-20, <https://doi.org/10.1007/s10874-006-9036-8>, 2007.
- Drewnick, F., Hings, S. S., Decarlo, P., Jayne, J. T., Gonin, M., Fuhrer, K., Weimer, S., Jimenez, J. L., Demerjian, K. L., Borrmann, S., and Worsnop, D. R.: A New Time-of-Flight Aerosol Mass Spectrometer (TOF-AMS)—Instrument Description and First Field Deployment, *Aerosol Science and Technology*, 39, 637-658, <https://doi.org/10.1080/02786820500182040>, 2005.
- Drinovec, L., Močnik, G., Zotter, P., Prévôt, A. S. H., Ruckstuhl, C., Coz, E., Rupakheti, M., Sciare, J., Müller, T., Wiedensohler, A., and Hansen, A. D. A.: The "dual-spot" Aethalometer: an improved measurement of aerosol black carbon with real-time loading compensation, *Atmospheric Measurement Techniques*, 8, 1965-1979, <https://doi.org/10.5194/amt-8-1965-2015>, 2015.
- Droege, A. T. and Tully, F. P.: Hydrogen-atom abstraction from alkanes by hydroxyl radical. 6. Cyclopentane and cyclohexane, *Journal of Physical Chemistry*, 91, 1222-1225, <https://doi.org/10.1021/j100289a037>, 1987.
- Du, M., Voliotis, A., Shao, Y., Wang, Y., Bannan, T. J., Pereira, K. L., Hamilton, J. F., Percival, C. J., Alfarra, M. R., and McFiggans, G.: Combined application of online FIGAERO-CIMS and offline LC-Orbitrap mass spectrometry (MS) to characterize the chemical composition of secondary organic aerosol (SOA) in smog chamber studies, *Atmos. Meas. Tech.*, 15, 4385-4406, <https://doi.org/10.5194/amt-15-4385-2022>, 2022.
- Duncan Jr, J. B., Bianco, L., Adler, B., Bell, T., Djalalova, I. V., Riihimäki, L., Sedlar, J., Smith, E. N., Turner, D. D., Wagner, T. J., and Wilczak, J. M.: Evaluating convective planetary boundary layer height estimations resolved by both active and passive remote sensing instruments during the CHEESEHEAD19 field campaign, *Atmospheric Measurement Techniques*, 15, 2479-2502, <https://doi.org/10.5194/amt-15-2479-2022>, 2022.
- Duncan, S. M., Tomaz, S., Morrison, G., Webb, M., Atkin, J., Surratt, J. D., and Turpin, B. J.: Dynamics of Residential Water-Soluble Organic Gases: Insights into Sources and Sinks, *Environmental Science & Technology*, 53, 1812-1821, <https://doi.org/10.1021/acs.est.8b05852>, 2019.
- DWD: Pamore - Retrieving archived forecast model data, German Meteorological Service, <https://www.dwd.de/EN/ourservices/pamore/pamore.html>, Access Date, 2025a
- DWD: Model documentation ICON-D2 (Regional model Germany), German Meteorological Service, https://www.dwd.de/DE/leistungen/nwv_icon_d2_modelldokumentation/nwv_icon_d2_modelldokumentation.html, 2025b
- DWD: Open Data Server of the German Meteorological Service, German Meteorological Service, <https://opendata.dwd.de>, Access Date, 2025c
- Ebert, M., Weigel, R., Kandler, K., Günther, G., Molleker, S., Groß, J. U., Vogel, B., Weinbruch, S., and Borrmann, S.: Chemical analysis of refractory stratospheric aerosol particles collected within the arctic vortex and inside polar stratospheric clouds, *Atmos. Chem. Phys.*, 16, 8405-8421, <https://doi.org/10.5194/acp-16-8405-2016>, 2016.

- Eichler, P., Müller, M., D'Anna, B., and Wisthaler, A.: A novel inlet system for online chemical analysis of semi-volatile submicron particulate matter, *Atmos. Meas. Tech.*, **8**, 1353-1360, <https://doi.org/10.5194/amt-8-1353-2015>, 2015.
- Eigen, M. and Kustin, K.: The kinetics of halogen hydrolysis, *Journal of the American Chemical Society*, **84**, 1355-1361, <https://doi.org/10.1021/ja00867a005>, 1962.
- Ekman, V. W.: On the influence of the earth's rotation on ocean-currents, *Arch. Math. Astron. Phys.*, **2**, 1-52, <https://empslocal.ex.ac.uk/people/staff/gv219/classics.d/Ekman05.pdf>, 1905.
- Elkins, J. W., Thompson, T. M., Swanson, T. H., Butler, J. H., Hall, B. D., Cummings, S. O., Fishers, D. A., and Raffo, A. G.: Decrease in the growth rates of atmospheric chlorofluorocarbons 11 and 12, *Nature*, **364**, 780-783, <https://doi.org/10.1038/364780a0>, 1993.
- Elser, M., Huang, R. J., Wolf, R., Slowik, J. G., Wang, Q., Canonaco, F., Li, G., Bozzetti, C., Daellenbach, K. R., Huang, Y., Zhang, R., Li, Z., Cao, J., Baltensperger, U., El-Haddad, I., and Prévôt, A. S. H.: New insights into PM_{2.5} chemical composition and sources in two major cities in China during extreme haze events using aerosol mass spectrometry, *Atmos. Chem. Phys.*, **16**, 3207-3225, <https://doi.org/10.5194/acp-16-3207-2016>, 2016.
- Elston, J., Argrow, B., Stachura, M., Weibel, D., Lawrence, D., and Pope, D.: Overview of Small Fixed-Wing Unmanned Aircraft for Meteorological Sampling, *Journal of Atmospheric and Oceanic Technology*, **32**, 97-115, <https://doi.org/10.1175/jtech-d-13-00236.1>, 2015.
- Emanuel, K. A. and Živković-Rothman, M.: Development and Evaluation of a Convection Scheme for Use in Climate Models, *Journal of the Atmospheric Sciences*, **56**, 1766-1782, [https://doi.org/10.1175/1520-0469\(1999\)056<1766:DAEOAC>2.0.CO;2](https://doi.org/10.1175/1520-0469(1999)056<1766:DAEOAC>2.0.CO;2), 1999.
- Engel, A., Schmidt, U., and McKenna, D.: Stratospheric trends of CFC-12 over the past two decades: Recent observational evidence of declining growth rates, *Geophysical Research Letters*, **25**, 3319-3322, <https://doi.org/10.1029/98gl02520>, 1998.
- Engel, A., Strunk, M., Müller, M., Haase, H.-P., Poss, C., Levin, I., and Schmidt, U.: Temporal development of total chlorine in the high-latitude stratosphere based on reference distributions of mean age derived from CO₂ and SF₆, *Journal of Geophysical Research: Atmospheres*, **107**, <https://doi.org/10.1029/2001JD000584>, 2002.
- EPA: Air Data: Air Quality Data Collected at Outdoor Monitors Across the US, United States Environmental Protection Agency, <https://www.epa.gov/outdoor-air-quality-data>, Access Date, 2025
- European Parliament and Council: Commission Implementing Regulation (EU) 2019/947 of 24 May 2019 on the rules and procedures for the operation of unmanned aircraft, *Official Journal of the European Union*, <https://eur-lex.europa.eu/legal-content/EN/TXT/?uri=CELEX%3A02019R0947-20220404>, 2019
- Faber, P., Drewnick, F., and Borrmann, S.: Aerosol particle and trace gas emissions from earthworks, road construction, and asphalt paving in Germany: Emission factors and influence on local air quality, *Atmospheric Environment*, **122**, 662-671, <https://doi.org/10.1016/j.atmosenv.2015.10.036>, 2015.
- Faber, P., Drewnick, F., Bierl, R., and Borrmann, S.: Complementary online aerosol mass spectrometry and offline FT-IR spectroscopy measurements: Prospects and challenges for the analysis of anthropogenic aerosol particle emissions, *Atmospheric Environment*, **166**, 92-98, <https://doi.org/10.1016/j.atmosenv.2017.07.014>, 2017.
- Fachinger, F. and Moormann, L.: (The ultimate) PANEL for Data Analysis (37), Max-Planck-Institute for Chemistry [code], 2025.
- Fachinger, F., Drewnick, F., and Borrmann, S.: How villages contribute to their local air quality – The influence of traffic- and biomass combustion-related emissions assessed by mobile mappings of PM and its components, *Atmospheric Environment*, **263**, 118648, <https://doi.org/10.1016/j.atmosenv.2021.118648>, 2021.
- Fachinger, F., Drewnick, F., Gieré, R., and Borrmann, S.: How the user can influence particulate emissions from residential wood and pellet stoves: Emission factors for different fuels and burning conditions, *Atmospheric Environment*, **158**, 216-226, <https://doi.org/10.1016/j.atmosenv.2017.03.027>, 2017.

- Falco, N., Wainwright, H. M., Dafflon, B., Ulrich, C., Soom, F., Peterson, J. E., Brown, J. B., Schaettle, K. B., Williamson, M., Cothren, J. D., Ham, R. G., McEntire, J. A., and Hubbard, S. S.: Influence of soil heterogeneity on soybean plant development and crop yield evaluated using time-series of UAV and ground-based geophysical imagery, *Scientific Reports*, **11**, <https://doi.org/10.1038/s41598-021-86480-z>, 2021.
- Faloon, I., Tan, D., Brune, W., Hurst, J., Barkot, D., Couch, T. L., Shepson, P., Apel, E., Riemer, D., Thornberry, T., Carroll, M. A., Sillman, S., Keeler, G. J., Sagady, J., Hooper, D., and Paterson, K.: Nighttime observations of anomalously high levels of hydroxyl radicals above a deciduous forest canopy, *Journal of Geophysical Research: Atmospheres*, **106**, 24315-24333, <https://doi.org/10.1029/2000jd900691>, 2001.
- Farley, R. N., Collier, S., Cappa, C. D., Williams, L. R., Onasch, T. B., Russell, L. M., Kim, H., and Zhang, Q.: Source apportionment of soot particles and aqueous-phase processing of black carbon coatings in an urban environment, *Atmos. Chem. Phys.*, **23**, 15039-15056, <https://doi.org/10.5194/acp-23-15039-2023>, 2023.
- Faxon, C., Bean, J., and Ruiz, L.: Inland Concentrations of Cl₂ and ClNO₂ in Southeast Texas Suggest Chlorine Chemistry Significantly Contributes to Atmospheric Reactivity, *Atmosphere*, **6**, 1487-1506, <https://doi.org/10.3390/atmos6101487>, 2015.
- Finlayson-Pitts, B. J., Ezell, M. J., and Pitts, J. N.: Formation of chemically active chlorine compounds by reactions of atmospheric NaCl particles with gaseous N₂O₅ and ClONO₂, *Nature*, **337**, 241-244, <https://doi.org/10.1038/337241a0>, 1989.
- Finley, B. D. and Saltzman, E. S.: Measurement of Cl₂ in coastal urban air, *Geophysical Research Letters*, **33**, <https://doi.org/10.1029/2006gl025799>, 2006.
- Fitzky, A. C., Sandén, H., Karl, T., Fares, S., Calfapietra, C., Grote, R., Saunier, A., and Rewald, B.: The Interplay Between Ozone and Urban Vegetation—BVOC Emissions, Ozone Deposition, and Tree Ecophysiology, *Frontiers in Forests and Global Change*, **2**, <https://doi.org/10.3389/ffgc.2019.00050>, 2019.
- Fleming, L. T., Lin, P., Roberts, J. M., Selimovic, V., Yokelson, R., Laskin, J., Laskin, A., and Nizkorodov, S. A.: Molecular composition and photochemical lifetimes of brown carbon chromophores in biomass burning organic aerosol, *Atmos. Chem. Phys.*, **20**, 1105-1129, <https://doi.org/10.5194/acp-20-1105-2020>, 2020.
- Forbes, P.: Atmospheric Chemistry Analysis: A Review, *Analytical Chemistry*, **92**, 455-472, <https://doi.org/10.1021/acs.analchem.9b04623>, 2020.
- Fry, J. L., Kiendler-Scharr, A., Rollins, A. W., Brauers, T., Brown, S. S., Dorn, H. P., Dubé, W. P., Fuchs, H., Mensah, A., Rohrer, F., Tillmann, R., Wahner, A., Wooldridge, P. J., and Cohen, R. C.: SOA from limonene: role of NO₃ in its generation and degradation, *Atmospheric Chemistry and Physics*, **11**, 3879-3894, <https://doi.org/10.5194/acp-11-3879-2011>, 2011.
- Fuzzi, S., Baltensperger, U., Carslaw, K., Decesari, S., Denier van der Gon, H., Facchini, M. C., Fowler, D., Koren, I., Langford, B., Lohmann, U., Nemitz, E., Pandis, S., Riipinen, I., Rudich, Y., Schaap, M., Slowik, J. G., Spracklen, D. V., Vignati, E., Wild, M., Williams, M., and Gilardoni, S.: Particulate matter, air quality and climate: lessons learned and future needs, *Atmos. Chem. Phys.*, **15**, 8217-8299, <https://doi.org/10.5194/acp-15-8217-2015>, 2015.
- Gålfalk, M., Nilsson Pålédal, S., and Bastviken, D.: Sensitive Drone Mapping of Methane Emissions without the Need for Supplementary Ground-Based Measurements, *ACS Earth and Space Chemistry*, **5**, 2668-2676, <https://doi.org/10.1021/acsearthspacechem.1c00106>, 2021.
- Galle, B., Arellano, S., Bobrowski, N., Conde, V., Fischer, T. P., Gerdes, G., Gutmann, A., Hoffmann, T., Itikarai, I., Krejci, T., Liu, E. J., Mulina, K., Nowicki, S., Richardson, T., Rüdiger, J., Wood, K., and Xu, J.: A multi-purpose, multi-rotor drone system for long-range and high-altitude volcanic gas plume measurements, *Atmospheric Measurement Techniques*, **14**, 4255-4277, <https://doi.org/10.5194/amt-14-4255-2021>, 2021.
- Ganske, J. A., Ezell, M. J., Berko, H. N., and Finlayson-Pitts, B. J.: The reaction of OH with ClNO₂ at 298 K: kinetics and mechanisms, *Chemical Physics Letters*, **179**, 204-210, [https://doi.org/10.1016/0009-2614\(91\)90317-3](https://doi.org/10.1016/0009-2614(91)90317-3), 1991.

- Gao, L., Tao, T., Liu, Y., and Hu, H.: A field study of ice accretion and its effects on the power production of utility-scale wind turbines, *Renewable Energy*, 167, 917-928, <https://doi.org/10.1016/j.renene.2020.12.014>, 2021.
- Gao, L., Song, J., Mohr, C., Huang, W., Vallon, M., Jiang, F., Leisner, T., and Saathoff, H.: Kinetics, SOA yields and chemical composition of secondary organic aerosol from β -caryophyllene ozonolysis with and without nitrogen oxides between 213 and 313 K, <https://doi.org/10.35097/1314>, 2023.
- Gaston, C. J., Lopez-Hilfiker, F. D., Whybrew, L. E., Hadley, O., McNair, F., Gao, H., Jaffe, D. A., and Thornton, J. A.: Online molecular characterization of fine particulate matter in Port Angeles, WA: Evidence for a major impact from residential wood smoke, *Atmospheric Environment*, 138, 99-107, <https://doi.org/10.1016/j.atmosenv.2016.05.013>, 2016.
- Ge, Y., Solberg, S., Heal, M. R., Reimann, S., Van Caspel, W., Hellack, B., Salameh, T., and Simpson, D.: Evaluation of modelled versus observed non-methane volatile organic compounds at European Monitoring and Evaluation Programme sites in Europe, *Atmospheric Chemistry and Physics*, 24, 7699-7729, <https://doi.org/10.5194/acp-24-7699-2024>, 2024.
- Ghosh, B., Papanastasiou, D. K., Talukdar, R. K., Roberts, J. M., and Burkholder, J. B.: Nitryl Chloride (ClNO₂): UV/Vis Absorption Spectrum between 210 and 296 K and O(3P) Quantum Yield at 193 and 248 nm, *The Journal of Physical Chemistry A*, 116, 5796-5805, <https://doi.org/10.1021/jp207389y>, 2012.
- Giez, A., Zöger, M., Mallaun, C., Nenakhov, V., Schimpf, M., Grad, C., Numberger, A., and Raynor, K.: Determination of the Measurement Errors for the HALO Basic Data System BAHAMAS by Means of Error Propagation, *Deutsches Zentrum für Luft- und Raumfahrt, Oberpfaffenhofen*, <https://doi.org/10.57676/5rdc-q708>, 2022.
- Gifford, F. A.: Use of routine meteorological observations for estimating atmospheric dispersion, *Nucl. Safety*, 2, 47-51, 1961.
- Gilardoni, S.: Advances in Organic Aerosol Characterization: From Complex to Simple, *Aerosol and Air Quality Research*, 17, 1447-1451, <https://doi.org/10.4209/aaqr.2017.01.0007>, 2017.
- Glasius, M., Lahaniati, M., Calogirou, A., Di Bella, D., Jensen, N. R., Hjorth, J., Kotzias, D., and Larsen, B. R.: Carboxylic Acids in Secondary Aerosols from Oxidation of Cyclic Monoterpenes by Ozone, *Environmental Science & Technology*, 34, 1001-1010, <https://doi.org/10.1021/es990445r>, 2000.
- Golston, L., Aubut, N., Frish, M., Yang, S., Talbot, R., Gretencord, C., McSpurr, J., and Zondlo, M.: Natural Gas Fugitive Leak Detection Using an Unmanned Aerial Vehicle: Localization and Quantification of Emission Rate, *Atmosphere*, 9, <https://doi.org/10.3390/atmos9090333>, 2018.
- Golzio, A., Ferrarese, S., Cassardo, C., Diolaiuti, G. A., and Pelfini, M.: Land-Use Improvements in the Weather Research and Forecasting Model over Complex Mountainous Terrain and Comparison of Different Grid Sizes, *Boundary-Layer Meteorology*, 180, 319-351, <https://doi.org/10.1007/s10546-021-00617-1>, 2021.
- Gordon, H., Kirkby, J., Baltensperger, U., Bianchi, F., Breitenlechner, M., Curtius, J., Dias, A., Dommen, J., Donahue, N. M., Dunne, E. M., Duplissy, J., Ehrhart, S., Flagan, R. C., Frege, C., Fuchs, C., Hansel, A., Hoyle, C. R., Kulmala, M., Kürten, A., Lehtipalo, K., Makhmutov, V., Molteni, U., Rissanen, M. P., Stozhkov, Y., Tröstl, J., Tsagkogeorgas, G., Wagner, R., Williamson, C., Wimmer, D., Winkler, P. M., Yan, C., and Carslaw, K. S.: Causes and importance of new particle formation in the present-day and preindustrial atmospheres, *Journal of Geophysical Research: Atmospheres*, 122, 8739-8760, <https://doi.org/10.1002/2017jd026844>, 2017.
- Graven, H. D., Stephens, B. B., Guilderson, T. P., Campos, T. L., Schimel, D. S., Campbell, J. E., and Keeling, R. F.: Vertical profiles of biospheric and fossil fuel-derived CO₂ and fossil fuel CO₂:CO ratios from airborne measurements of $\Delta^{14}\text{C}$, *Tellus B: Chemical and Physical Meteorology*, 61, 536, <https://doi.org/10.1111/j.1600-0889.2009.00421.x>, 2009.
- Grayson, J. W., Evoy, E., Song, M., Chu, Y., Maclean, A., Nguyen, A., Upshur, M. A., Ebrahimi, M., Chan, C. K., Geiger, F. M., Thomson, R. J., and Bertram, A. K.: The effect of hydroxyl functional groups and molar mass on the viscosity of non-crystalline organic and organic-water particles, *Atmos. Chem. Phys.*, 17, 8509-8524, <https://doi.org/10.5194/acp-17-8509-2017>, 2017.

- Grimaccia, F., Aghaei, M., Mussetta, M., Leva, S., and Quater, P. B.: Planning for PV plant performance monitoring by means of unmanned aerial systems (UAS), *International Journal of Energy and Environmental Engineering*, 6, 47-54, <https://doi.org/10.1007/s40095-014-0149-6>, 2015.
- Grooß, J.-U., Müller, R., Crowley, J. N., and Hegglin, M. I.: Chlorine peroxide reaction explains observed wintertime hydrogen chloride in the Antarctic vortex, *Communications Earth & Environment*, 6, <https://doi.org/10.1038/s43247-025-02499-4>, 2025.
- Gross, J. H.: *Massenspektrometrie*, Springer, Berlin Heidelberg, <https://doi.org/10.1007/978-3-8274-2981-0>, 2012.
- Guo, H., Xu, M., and Hu, Q.: Changes in near-surface wind speed in China: 1969–2005, *International Journal of Climatology*, 31, 349-358, <https://doi.org/10.1002/joc.2091>, 2011.
- Guo, J., Miao, Y., Zhang, Y., Liu, H., Li, Z., Zhang, W., He, J., Lou, M., Yan, Y., and Bian, L.: The climatology of planetary boundary layer height in China derived from radiosonde and reanalysis data, *Atmospheric Chemistry and Physics*, 16, 13309-13319, <https://doi.org/10.5194/acp-16-13309-2016>, 2016.
- Hakuba, M. Z., Folini, D., Sanchez-Lorenzo, A., and Wild, M.: Spatial representativeness of ground-based solar radiation measurements, *Journal of Geophysical Research: Atmospheres*, 118, 8585-8597, <https://doi.org/10.1002/jgrd.50673>, 2013.
- Hallquist, M., Wenger, J. C., Baltensperger, U., Rudich, Y., Simpson, D., Claeys, M., Dommen, J., Donahue, N. M., George, C., Goldstein, A. H., Hamilton, J. F., Herrmann, H., Hoffmann, T., Iinuma, Y., Jang, M., Jenkin, M. E., Jimenez, J. L., Kiendler-Scharr, A., Maenhaut, W., McFiggans, G., Mentel, T. F., Monod, A., Prévôt, A. S. H., Seinfeld, J. H., Surratt, J. D., Szmigielski, R., and Wildt, J.: The formation, properties and impact of secondary organic aerosol: current and emerging issues, *Atmos. Chem. Phys.*, 9, 5155-5236, <https://doi.org/10.5194/acp-9-5155-2009>, 2009.
- Hamilton, J., de Boer, G., Doddi, A., and Lawrence, D. A.: The DataHawk2 uncrewed aircraft system for atmospheric research, *Atmos. Meas. Tech.*, 15, 6789-6806, <https://doi.org/10.5194/amt-15-6789-2022>, 2022.
- Hamilton, J. F., Rami Alfarra, M., Wyche, K. P., Ward, M. W., Lewis, A. C., McFiggans, G. B., Good, N., Monks, P. S., Carr, T., White, I. R., and Purvis, R. M.: Investigating the use of secondary organic aerosol as seed particles in simulation chamber experiments, *Atmos. Chem. Phys.*, 11, 5917-5929, <https://doi.org/10.5194/acp-11-5917-2011>, 2011.
- Hammes, J., Lutz, A., Mentel, T., Faxon, C., and Hallquist, M.: Carboxylic acids from limonene oxidation by ozone and hydroxyl radicals: insights into mechanisms derived using a FIGAERO-CIMS, *Atmos. Chem. Phys.*, 19, 13037-13052, <https://doi.org/10.5194/acp-19-13037-2019>, 2019.
- Hanna, S. R.: *Applications in Air Pollution Modeling*, in, Springer Netherlands, 275-310, https://doi.org/10.1007/978-94-010-9112-1_7, 1984.
- Harper, M.: Sorbent trapping of volatile organic compounds from air, *Journal of Chromatography A*, 885, 129-151, [https://doi.org/10.1016/S0021-9673\(00\)00363-0](https://doi.org/10.1016/S0021-9673(00)00363-0), 2000.
- Harrison, M. A. J., Barra, S., Borghesi, D., Vione, D., Arsene, C., and Iulian Olariu, R.: Nitrated phenols in the atmosphere: a review, *Atmospheric Environment*, 39, 231-248, <https://doi.org/10.1016/j.atmosenv.2004.09.044>, 2005.
- Haskins, J. D., Lee, B. H., Lopez-Hilfiker, F. D., Peng, Q., Jaeglé, L., Reeves, J. M., Schroder, J. C., Campuzano-Jost, P., Fibiger, D., McDuffie, E. E., Jiménez, J. L., Brown, S. S., and Thornton, J. A.: Observational Constraints on the Formation of Cl₂ From the Reactive Uptake of ClNO₂ on Aerosols in the Polluted Marine Boundary Layer, *Journal of Geophysical Research: Atmospheres*, 124, 8851-8869, <https://doi.org/10.1029/2019jd030627>, 2019.
- Haskins, J. D., Jaeglé, L., Shah, V., Lee, B. H., Lopez-Hilfiker, F. D., Campuzano-Jost, P., Schroder, J. C., Day, D. A., Guo, H., Sullivan, A. P., Weber, R., Dibb, J., Campos, T., Jimenez, J. L., Brown, S. S., and Thornton, J. A.: Wintertime Gas-Particle Partitioning and Speciation of Inorganic Chlorine in the Lower Troposphere Over the Northeast United States and Coastal Ocean, *Journal of Geophysical Research: Atmospheres*, 123, <https://doi.org/10.1029/2018jd028786>, 2018.
- He, G., He, C., Wang, H., Lu, X., Pei, C., Qiu, X., Liu, C., Wang, Y., Liu, N., Zhang, J., Lei, L., Liu, Y., Wang, H., Deng, T., Fan, Q., and Fan, S.: Nighttime ozone in the lower boundary layer: insights from 3-year

- tower-based measurements in South China and regional air quality modeling, *Atmospheric Chemistry and Physics*, 23, 13107-13124, <https://doi.org/10.5194/acp-23-13107-2023>, 2023.
- Heard, D. E.: *Analytical Techniques for Atmospheric Measurement*, Blackwell Publishing Ltd., Ames, Iowa 2006.
- Hegg, D. A., Radke, L. F., Hobbs, P. V., Rasmussen, R. A., and Riggan, P. J.: Emissions of some trace gases from biomass fires, *Journal of Geophysical Research: Atmospheres*, 95, 5669-5675, <https://doi.org/10.1029/JD095iD05p05669>, 1990.
- Helbig, M., Gerken, T., Beamesderfer, E. R., Baldocchi, D. D., Banerjee, T., Biraud, S. C., Brown, W. O. J., Brunzell, N. A., Burakowski, E. A., Burns, S. P., Butterworth, B. J., Chan, W. S., Davis, K. J., Desai, A. R., Fuentes, J. D., Hollinger, D. Y., Kljun, N., Mauder, M., Novick, K. A., Perkins, J. M., Rahn, D. A., Rey-Sanchez, C., Santanello, J. A., Scott, R. L., Seyednasrollah, B., Stoy, P. C., Sullivan, R. C., de Arellano, J. V.-G., Wharton, S., Yi, C., and Richardson, A. D.: Integrating continuous atmospheric boundary layer and tower-based flux measurements to advance understanding of land-atmosphere interactions, *Agricultural and Forest Meteorology*, 307, 108509, <https://doi.org/10.1016/j.agrformet.2021.108509>, 2021.
- Hersbach, H., Bell, B., Berrisford, P., Hirahara, S., Horányi, A., Muñoz-Sabater, J., Nicolas, J., Peubey, C., Radu, R., Schepers, D., Simmons, A., Soci, C., Abdalla, S., Abellan, X., Balsamo, G., Bechtold, P., Biavati, G., Bidlot, J., Bonavita, M., De Chiara, G., Dahlgren, P., Dee, D., Diamantakis, M., Dragani, R., Flemming, J., Forbes, R., Fuentes, M., Geer, A., Haimberger, L., Healy, S., Hogan, R. J., Hólm, E., Janisková, M., Keeley, S., Laloyaux, P., Lopez, P., Lupu, C., Radnoti, G., De Rosnay, P., Rozum, I., Vamborg, F., Villaume, S., and Thépaut, J. N.: The ERA5 global reanalysis, *Quarterly Journal of the Royal Meteorological Society*, 146, 1999-2049, <https://doi.org/10.1002/qj.3803>, 2020.
- Hervo, M., Romanens, G., Martucci, G., Weusthoff, T., and Haeefe, A.: Evaluation of an Automatic Meteorological Drone Based on a 6-Month Measurement Campaign, *Atmosphere*, 14, 1382, <https://doi.org/10.3390/atmos14091382>, 2023.
- Hindman, E. E., Durkee, P. A., Sinclair, P. C., and Haar, T. H. V.: Detection of marine aerosol particles in coastal zones using satellite imagery, *International Journal of Remote Sensing*, 5, 577-586, <https://doi.org/10.1080/01431168408948838>, 1984.
- Hinds, W. C.: *Aerosol technology : properties, behavior, and measurement of airborne particles*, 2nd, Wiley, New York 1999.
- Ho, C.-C., Chen, L.-J., and Hwang, J.-S.: Estimating ground-level PM_{2.5} levels in Taiwan using data from air quality monitoring stations and high coverage of microsensors, *Environmental Pollution*, 264, 114810, <https://doi.org/10.1016/j.envpol.2020.114810>, 2020.
- Hoerger, C. C., Claude, A., Plass-Duelmer, C., Reimann, S., Eckart, E., Steinbrecher, R., Aalto, J., Arduini, J., Bonnaire, N., and Cape, J. N.: ACTRIS non-methane hydrocarbon intercomparison experiment in Europe to support WMO GAW and EMEP observation networks, *Atmospheric Measurement Techniques*, 8, 2715-2736, <https://doi.org/10.5194/amt-8-2715-2015>, 2015.
- Hoffmann, T., Odum, J. R., Bowman, F., Collins, D., Klockow, D., Flagan, R. C., and Seinfeld, J. H.: Formation of Organic Aerosols from the Oxidation of Biogenic Hydrocarbons, *Journal of Atmospheric Chemistry*, 26, 189-222, <https://doi.org/10.1023/A:1005734301837>, 1997.
- Hoffmann, T., R. Bandur, U. Marggraf, and M. Linscheid: Molecular composition of organic aerosols formed in the α -pinene/O₃ reaction: Implications for new particle formation processes, *Journal of Geophysical Research: Atmospheres*, 103, 25569-25578, <https://doi.org/10.1029/98JD01816>, 1998.
- Hu, D. and Yu, J. Z.: Secondary organic aerosol tracers and malic acid in Hong Kong: seasonal trends and origins, *Environmental Chemistry*, 10, <https://doi.org/10.1071/en13104>, 2013.
- Huang, X. F. and Yu, J. Z.: Is vehicle exhaust a significant primary source of oxalic acid in ambient aerosols?, *Geophysical Research Letters*, 34, <https://doi.org/10.1029/2006GL028457>, 2007.
- Huang, Y., Ho, S. S. H., Ho, K. F., Lee, S. C., Yu, J. Z., and Louie, P. K.: Characteristics and health impacts of VOCs and carbonyls associated with residential cooking activities in Hong Kong, *Journal of hazardous materials*, 186, 344-351, <https://doi.org/10.1016/j.jhazmat.2010.11.003>, 2011.
- ICL: Londonair, Imperial College London, <https://www.londonair.org.uk/london/asp/datadownload.asp>, Access Date, 2025

- IPCC: Climate Change 2021 – The Physical Science Basis: Working Group I Contribution to the Sixth Assessment Report of the Intergovernmental Panel on Climate Change, Cambridge University Press, Cambridge, <https://doi.org/10.1017/9781009157896>, 2023.
- IUPAC: Database of Evaluated kinetic data, IUPAC Task Group on Atmospheric Chemical Kinetic Data Evaluation, <http://iupac.pole-ether.fr>, Access Date, 2025
- Jacob, J. D., Chilson, P. B., Houston, A. L., and Smith, S. W.: Considerations for Atmospheric Measurements with Small Unmanned Aircraft Systems, *Atmosphere*, 9, 252, <https://doi.org/10.3390/atmos9070252>, 2018.
- Jayne, J. T., Leard, D. C., Zhang, X., Davidovits, P., Smith, K. A., Kolb, C. E., and Worsnop, D. R.: Development of an aerosol mass spectrometer for size and composition analysis of submicron particles, *Aerosol Science & Technology*, 33, 49-70, <https://doi.org/10.1080/027868200410840>, 2000.
- Ji, Y., Huey, L. G., Tanner, D. J., Lee, Y. R., Veres, P. R., Neuman, J. A., Wang, Y., and Wang, X.: A vacuum ultraviolet ion source (VUV-IS) for iodide–chemical ionization mass spectrometry: a substitute for radioactive ion sources, *Atmospheric Measurement Techniques*, 13, 3683-3696, <https://doi.org/10.5194/amt-13-3683-2020>, 2020.
- Jia, L. and Xu, Y.: Different roles of water in secondary organic aerosol formation from toluene and isoprene, *Atmos. Chem. Phys.*, 18, 8137-8154, <https://doi.org/10.5194/acp-18-8137-2018>, 2018.
- Jimenez, J. L., Canagaratna, M. R., Donahue, N. M., Prevot, A. S. H., Zhang, Q., Kroll, J. H., DeCarlo, P. F., Allan, J. D., Coe, H., Ng, N. L., Aiken, A. C., Docherty, K. S., Ulbrich, I. M., Grieshop, A. P., Robinson, A. L., Duplissy, J., Smith, J. D., Wilson, K. R., Lanz, V. A., Hueglin, C., Sun, Y. L., Tian, J., Laaksonen, A., Raatikainen, T., Rautiainen, J., Vaattovaara, P., Ehn, M., Kulmala, M., Tomlinson, J. M., Collins, D. R., Cubison, M. J., E., Dunlea, J., Huffman, J. A., Onasch, T. B., Alfarra, M. R., Williams, P. I., Bower, K., Kondo, Y., Schneider, J., Drewnick, F., Borrmann, S., Weimer, S., Demerjian, K., Salcedo, D., Cottrell, L., Griffin, R., Takami, A., Miyoshi, T., Hatakeyama, S., Shimono, A., Sun, J. Y., Zhang, Y. M., Dzepina, K., Kimmel, J. R., Sueper, D., Jayne, J. T., Herndon, S. C., Trimborn, A. M., Williams, L. R., Wood, E. C., Middlebrook, A. M., Kolb, C. E., Baltensperger, U., and Worsnop, D. R.: Evolution of Organic Aerosols in the Atmosphere, *Science*, 326, 1525-1529, <https://doi.org/10.1126/science.1180353>, 2009.
- Johnston, M. V. and Kerecman, D. E.: Molecular characterization of atmospheric organic aerosol by mass spectrometry, *Annual Review of Analytical Chemistry*, 12, 247-274, <https://doi.org/10.1146/annurev-anchem-061516-045135>, 2019.
- Kahl, J. D. W. and Chapman, H. L.: Atmospheric stability characterization using the Pasquill method: A critical evaluation, *Atmospheric Environment*, 187, 196-209, <https://doi.org/10.1016/j.atmosenv.2018.05.058>, 2018.
- Kamens, R. M., Gery, M. W., Jeffries, H. E., Jackson, M., and Cole, E. I.: Ozone–isoprene reactions: Product formation and aerosol potential, *International Journal of Chemical Kinetics*, 14, 955-975, <https://doi.org/10.1002/kin.550140902>, 1982.
- Kanakidou, M., Seinfeld, J. H., Pandis, S. N., Barnes, I., Dentener, F. J., Facchini, M. C., Van Dingenen, R., Ervens, B., Nenes, A., Nielsen, C. J., Swietlicki, E., Putaud, J. P., Balkanski, Y., Fuzzi, S., Horth, J., Moortgat, G. K., Winterhalter, R., Myhre, C. E. L., Tsigaridis, K., Vignati, E., Stephanou, E. G., and Wilson, J.: Organic aerosol and global climate modelling: a review, *Atmos. Chem. Phys.*, 5, 1053-1123, <https://doi.org/10.5194/acp-5-1053-2005>, 2005.
- Karbach, N., Bobrowski, N., and Hoffmann, T.: Observing volcanoes with drones: studies of volcanic plume chemistry with ultralight sensor systems, *Scientific Reports*, 12, 17890, <https://doi.org/10.1038/s41598-022-21935-5>, 2022.
- Keene, W. C., Sander, R., Pszenny, A. A. P., Vogt, R., Crutzen, P. J., and Galloway, J. N.: Aerosol pH in the marine boundary layer: A review and model evaluation, *Journal of Aerosol Science*, 29, 339-356, [https://doi.org/10.1016/S0021-8502\(97\)10011-8](https://doi.org/10.1016/S0021-8502(97)10011-8), 1998.
- Keene, W. C., Pszenny, A. A. P., Jacob, D. J., Duce, R. A., Galloway, J. N., Schultz-Tokos, J. J., Sievering, H., and Boatman, J. F.: The geochemical cycling of reactive chlorine through the marine troposphere, *Global Biogeochemical Cycles*, 4, 407-430, <https://doi.org/10.1029/gb004i004p00407>, 1990.

- Keller-Rudek, H., Moortgat, G. K., Sander, R., and Sørensen, R.: The MPI-Mainz UV/VIS Spectral Atlas of Gaseous Molecules of Atmospheric Interest, *Earth Syst. Sci. Data*, 5, 365-373, <https://doi.org/10.5194/essd-5-365-2013>, 2013.
- Kellner, R., Mermet, J.-M., Otto, M., Valcárcel, M., and Widmer, H. M.: Analytical Chemistry. A Modern Approach to Analytical Science, *Analytical and Bioanalytical Chemistry*, Wiley-VCH Verlag GmbH & Co. KGaA, Weinheim 2006.
- Kercher, J. P., Riedel, T. P., and Thornton, J. A.: Chlorine activation by N₂O₅: simultaneous, in situ detection of ClNO₂ and N₂O₅ by chemical ionization mass spectrometry, *Atmos. Meas. Tech.*, 2, 193-204, <https://doi.org/10.5194/amt-2-193-2009>, 2009.
- Kerminen, V. M., Lihavainen, H., Komppula, M., Viisanen, Y., and Kulmala, M.: Direct observational evidence linking atmospheric aerosol formation and cloud droplet activation, *Geophysical Research Letters*, 32, n/a-n/a, <https://doi.org/10.1029/2005gl023130>, 2005.
- Khan, M. A. H., Ashfold, M. J., Nickless, G., Martin, D., Watson, L. A., Hamer, P. D., Wayne, R. P., Canosa-Mas, C. E., and Shallcross, D. E.: Night-time NO₃ and OH radical concentrations in the United Kingdom inferred from hydrocarbon measurements, *Atmospheric Science Letters*, 9, 140-146, <https://doi.org/10.1002/asl.175>, 2008.
- Kirkby, J. and Cloud, C.: Atmospheric nucleation and growth in the CLOUD experiment at CERN, 2013, <https://doi.org/10.1063/1.4803258>, 2013.
- Klein, F., Pieber, S. M., Ni, H., Stefanelli, G., Bertrand, A., Kilic, D., Pospisilova, V., Temime-Roussel, B., Marchand, N., El Haddad, I., Slowik, J. G., Baltensperger, U., Cao, J., Huang, R.-j., and Prévôt, A. S. H.: Characterization of Gas-Phase Organics Using Proton Transfer Reaction Time-of-Flight Mass Spectrometry: Residential Coal Combustion, *Environmental Science & Technology*, 52, 2612-2617, <https://doi.org/10.1021/acs.est.7b03960>, 2018.
- Klemp, J. B.: A terrain-following coordinate with smoothed coordinate surfaces, *Monthly weather review*, 139, 2163-2169, <https://doi.org/10.1175/MWR-D-10-05046.1>, 2011.
- Knote, C., Hodzic, A., and Jimenez, J. L.: The effect of dry and wet deposition of condensable vapors on secondary organic aerosols concentrations over the continental US, *Atmospheric Chemistry and Physics*, 15, 1-18, <https://doi.org/10.5194/acp-15-1-2015>, 2015.
- Ko, M. K. W. and Sze, N. D.: Diurnal variation of ClO: Implications for the stratospheric chemistries of ClONO₂, HOCl, and HCl, *Journal of Geophysical Research: Atmospheres*, 89, 11619-11632, <https://doi.org/10.1029/jd089id07p11619>, 1984.
- Kołodziejczyk, A., Pyczk, P., Błaziak, K., Pobudkowska, A., Sarang, K., and Szmigielski, R.: Physicochemical Properties of Terebic Acid, MBTCA, Diaterpenylic Acid Acetate, and Pinanediol as Relevant α -Pinene Oxidation Products, *ACS Omega*, 5, 7919-7927, <https://doi.org/10.1021/acsomega.9b04231>, 2020.
- Kong, X., Salvador, C. M., Carlsson, S., Pathak, R., Davidsson, K. O., Le Breton, M., Gaita, S. M., Mitra, K., Hallquist, Å. M., Hallquist, M., and Pettersson, J. B. C.: Molecular characterization and optical properties of primary emissions from a residential wood burning boiler, *Science of The Total Environment*, 754, 142143, <https://doi.org/10.1016/j.scitotenv.2020.142143>, 2021.
- Koppmann, R., von Czapiewski, K., and Reid, J. S.: A review of biomass burning emissions, part I: gaseous emissions of carbon monoxide, methane, volatile organic compounds, and nitrogen containing compounds, *Atmos. Chem. Phys. Discuss.*, 2005, 10455-10516, <https://doi.org/10.5194/acpd-5-10455-2005>, 2005.
- Kotthaus, S., Bravo-Aranda, J. A., Collaud Coen, M., Guerrero-Rascado, J. L., Costa, M. J., Cimini, D., O'Connor, E. J., Hervo, M., Alados-Arboledas, L., Jiménez-Portaz, M., Mona, L., Ruffieux, D., Illingworth, A., and Haeffelin, M.: Atmospheric boundary layer height from ground-based remote sensing: a review of capabilities and limitations, *Atmospheric Measurement Techniques*, 16, 433-479, <https://doi.org/10.5194/amt-16-433-2023>, 2023.
- Koulouri, E., Saarikoski, S., Theodosi, C., Markaki, Z., Gerasopoulos, E., Kouvarakis, G., Mäkelä, T., Hillamo, R., and Mihalopoulos, N.: Chemical composition and sources of fine and coarse aerosol particles in the Eastern Mediterranean, *Atmospheric Environment*, 42, 6542-6550, <https://doi.org/10.1016/j.atmosenv.2008.04.010>, 2008.

- Kourtchev, I., Fuller, S., Aalto, J., Ruuskanen, T. M., McLeod, M. W., Maenhaut, W., Jones, R., Kulmala, M., and Kalberer, M.: Molecular Composition of Boreal Forest Aerosol from Hyytiälä, Finland, Using Ultrahigh Resolution Mass Spectrometry, *Environmental Science & Technology*, 47, 4069-4079, <https://doi.org/10.1021/es3051636>, 2013.
- Kreklow, J., Tetzlaff, B., Kuhnt, G., and Burkhard, B.: A Rainfall Data Intercomparison Dataset of RADKLIM, RADOLAN, and Rain Gauge Data for Germany, *Data*, 4, 118, <https://doi.org/10.3390/data4030118>, 2019.
- Kroll, J. H. and Seinfeld, J. H.: Chemistry of secondary organic aerosol: Formation and evolution of low-volatility organics in the atmosphere, *Atmospheric Environment*, 42, 3593-3624, <https://doi.org/10.1016/j.atmosenv.2008.01.003>, 2008.
- Křůmal, K., Mikuška, P., Horák, J., Hopan, F., and Krpec, K.: Comparison of emissions of gaseous and particulate pollutants from the combustion of biomass and coal in modern and old-type boilers used for residential heating in the Czech Republic, Central Europe, *Chemosphere*, 229, 51-59, <https://doi.org/10.1016/j.chemosphere.2019.04.137>, 2019.
- Krzyzanowski, M., Apte, J. S., Bonjour, S. P., Brauer, M., Cohen, A. J., and Prüss-Ustun, A. M.: Air Pollution in the Mega-cities, *Current Environmental Health Reports*, 1, 185-191, <https://doi.org/10.1007/s40572-014-0019-7>, 2014.
- Kuantama, E., Tarca, R., Dzitac, S., Dzitac, I., Vesselenyi, T., and Tarca, I.: The Design and Experimental Development of Air Scanning Using a Sniffer Quadcopter, *Sensors*, 19, 3849, <https://doi.org/10.3390/s19183849>, 2019.
- Kulakova, E. S., Safarov, A. M., Safarova, V. I., Malkova, M. A., and Kantor, E. A.: Phenol monitoring in the air of the city residential part, *IOP Conference Series: Earth and Environmental Science*, 579, 012102, <https://doi.org/10.1088/1755-1315/579/1/012102>, 2020.
- Kurtén, T., Hyttinen, N., D'Ambro, E. L., Thornton, J., and Prisle, N. L.: Estimating the saturation vapor pressures of isoprene oxidation products C₅H₁₂O₆ and C₅H₁₀O₆ using COSMO-RS, *Atmos. Chem. Phys.*, 18, 17589-17600, <https://doi.org/10.5194/acp-18-17589-2018>, 2018.
- Kuwata, M., Zorn, S. R., and Martin, S. T.: Using Elemental Ratios to Predict the Density of Organic Material Composed of Carbon, Hydrogen, and Oxygen, *Environmental Science & Technology*, 46, 787-794, <https://doi.org/10.1021/es202525q>, 2012.
- Lan, H., Hartonen, K., and Riekkola, M.-L.: Miniaturised air sampling techniques for analysis of volatile organic compounds in air, *TrAC Trends in Analytical Chemistry*, 126, 115873, <https://doi.org/10.1016/j.trac.2020.115873>, 2020.
- Lappin, F., De Boer, G., Klein, P., Hamilton, J., Spencer, M., Calmer, R., Segales, A. R., Rhodes, M., Bell, T. M., Buchli, J., Britt, K., Asher, E., Medina, I., Butterworth, B., Otterstatter, L., Ritsch, M., Puxley, B., Miller, A., Jordan, A., Gomez-Faulk, C., Smith, E., Borenstein, S., Thornberry, T., Argrow, B., and Pillar-Little, E.: Data collected using small uncrewed aircraft system during the TRacking Aerosol Convection Interactions Experiment (TRACER), <https://doi.org/10.5194/essd-2023-371>, 2023.
- Laskin, J., Laskin, A., and Nizkorodov, S. A.: Mass Spectrometry Analysis in Atmospheric Chemistry, *Analytical Chemistry*, 90, 166-189, <https://doi.org/10.1021/acs.analchem.7b04249>, 2018.
- Lauraguais, A., Coeur-Tourneur, C., Cassez, A., Deboudt, K., Fourmentin, M., and Choël, M.: Atmospheric reactivity of hydroxyl radicals with guaiacol (2-methoxyphenol), a biomass burning emitted compound: Secondary organic aerosol formation and gas-phase oxidation products, *Atmospheric Environment*, 86, 155-163, <https://doi.org/10.1016/j.atmosenv.2013.11.074>, 2014.
- Law, R. M., Peters, W., Rödenbeck, C., Aulagnier, C., Baker, I., Bergmann, D. J., Bousquet, P., Brandt, J., Bruhwiler, L., Cameron-Smith, P. J., Christensen, J. H., Delage, F., Denning, A. S., Fan, S., Geels, C., Houweling, S., Imasu, R., Karstens, U., Kawa, S. R., Kleist, J., Krol, M. C., Lin, S. J., Lokupitiya, R., Maki, T., Maksyutov, S., Niwa, Y., Onishi, R., Parazoo, N., Patra, P. K., Pieterse, G., Rivier, L., Satoh, M., Serrar, S., Taguchi, S., Takigawa, M., Vautard, R., Vermeulen, A. T., and Zhu, Z.: TransCom model simulations of hourly atmospheric CO₂: Experimental overview and diurnal cycle results for 2002, *Global Biogeochemical Cycles*, 22, <https://doi.org/10.1029/2007gb003050>, 2008.

- Lawler, M. J., Sander, R., Carpenter, L. J., Lee, J. D., Von Glasow, R., Sommariva, R., and Saltzman, E. S.: HOCl and Cl₂ observations in marine air, *Atmospheric Chemistry and Physics*, **11**, 7617-7628, <https://doi.org/10.5194/acp-11-7617-2011>, 2011.
- Le Breton, M., Hallquist, Å. M., Pathak, R. K., Simpson, D., Wang, Y., Johansson, J., Zheng, J., Yang, Y., Shang, D., Wang, H., Liu, Q., Chan, C., Wang, T., Bannan, T. J., Priestley, M., Percival, C. J., Shallcross, D. E., Lu, K., Guo, S., Hu, M., and Hallquist, M.: Chlorine oxidation of VOCs at a semi-rural site in Beijing: significant chlorine liberation from ClNO₂ and subsequent gas- and particle-phase Cl-VOC production, *Atmospheric Chemistry and Physics*, **18**, 13013-13030, <https://doi.org/10.5194/acp-18-13013-2018>, 2018.
- Lee, B. H., Lopez-Hilfiker, F. D., Mohr, C., Kurtén, T., Worsnop, D. R., and Thornton, J. A.: An Iodide-Adduct High-Resolution Time-of-Flight Chemical-Ionization Mass Spectrometer: Application to Atmospheric Inorganic and Organic Compounds, *Environmental Science & Technology*, **48**, 6309-6317, <https://doi.org/10.1021/es500362a>, 2014.
- Lee, T. J. and Rendell, A. P.: Ab initio characterization of peroxyhypochlorous acid: implications for atmospheric chemistry, *The Journal of Physical Chemistry*, **97**, 6999-7002, <https://doi.org/10.1021/j100129a014>, 1993.
- Lelieveld, J., Dentener, F. J., Peters, W., and Krol, M. C.: On the role of hydroxyl radicals in the self-cleansing capacity of the troposphere, *Atmospheric Chemistry and Physics*, **4**, <https://doi.org/10.5194/acp-4-2337-2004>, 2004.
- Leppla, D., Zannoni, N., Kremper, L., Williams, J., Pöhlker, C., Sá, M., Solci, M. C., and Hoffmann, T.: Varying chiral ratio of pinic acid enantiomers above the Amazon rainforest, *Atmos. Chem. Phys.*, **23**, 809-820, <https://doi.org/10.5194/acp-23-809-2023>, 2023.
- Leu, M.-T., Timonen, R. S., Keyser, L. F., and Yung, Y. L.: Heterogeneous Reactions of HNO₃(g) + NaCl(s) .fwdarw. HCl(g) + NaNO₃(s) and N₂O₅(g) + NaCl(s) .fwdarw. ClNO₂(g) + NaNO₃(s), *The Journal of Physical Chemistry*, **99**, 13203-13212, <https://doi.org/10.1021/j100035a026>, 1995.
- Li, M., Wang, X., Lu, C., Li, R., Zhang, J., Dong, S., Yang, L., Xue, L., Chen, J., and Wang, W.: Nitrated phenols and the phenolic precursors in the atmosphere in urban Jinan, China, *Science of The Total Environment*, **714**, 136760, <https://doi.org/10.1016/j.scitotenv.2020.136760>, 2020a.
- Li, Q., Meidan, D., Hess, P., Añel, J. A., Cuevas, C. A., Doney, S., Fernandez, R. P., van Herpen, M., Höglund-Isaksson, L., Johnson, M. S., Kinnison, D. E., Lamarque, J.-F., Röckmann, T., Mahowald, N. M., Saiz-Lopez, A., Li, Q., Meidan, D., Hess, P., Añel, J. A., Cuevas, C. A., Doney, S., Fernandez, R. P., van Herpen, M., Höglund-Isaksson, L., Johnson, M. S., Kinnison, D. E., Lamarque, J.-F., Röckmann, T., Mahowald, N. M., and Saiz-Lopez, A.: Global environmental implications of atmospheric methane removal through chlorine-mediated chemistry-climate interactions, *Nature Communications* **2023** **14**:1, 14, <https://doi.org/10.1038/s41467-023-39794-7>, 2023a.
- Li, Y., Ren, H., Zhou, S., Pei, C., Gao, M., Liang, Y., Ye, D., Sun, X., Li, F., Zhao, J., Hang, J., Fan, S., and Fu, P.: Tower-based profiles of wintertime secondary organic aerosols in the urban boundary layer over Guangzhou, *Science of The Total Environment*, **950**, 175326, <https://doi.org/10.1016/j.scitotenv.2024.175326>, 2024.
- Li, Y., Nie, W., Liu, Y., Huang, D., Xu, Z., Peng, X., George, C., Yan, C., Tham, Y. J., Yu, C., Xia, M., Fu, X., Wang, X., Xue, L., Wang, Z., Xu, Z., Chi, X., Wang, T., and Ding, A.: Photoinduced Production of Chlorine Molecules from Titanium Dioxide Surfaces Containing Chloride, *Environmental Science & Technology Letters*, **7**, 70-75, <https://doi.org/10.1021/acs.estlett.9b00704>, 2020b.
- Li, Y. J., Chen, Q., Guzman, M. I., Chan, C. K., and Martin, S. T.: Second-generation products contribute substantially to the particle-phase organic material produced by & beta-caryophyllene ozonolysis, *Atmos. Chem. Phys.*, **11**, 121-132, <https://doi.org/10.5194/acp-11-121-2011>, 2011.
- Li, Z., Pu, O., Pan, Y., Huang, B., Zhao, Z., and Wu, H.: A study on measuring wind turbine wake based on UAV anemometry system, *Sustainable Energy Technologies and Assessments*, **53**, 102537, <https://doi.org/10.1016/j.seta.2022.102537>, 2022.
- Li, Z., Pu, O., Pan, Y., Huang, B., Zhao, Z., and Wu, H.: A Study on Measuring the Wind Field in the Air Using a Multi-rotor UAV Mounted with an Anemometer, *Boundary-Layer Meteorology*, <https://doi.org/10.1007/s10546-023-00798-x>, 2023b.

- Li, Z., Guo, J., Ding, A., Liao, H., Liu, J., Sun, Y., Wang, T., Xue, H., Zhang, H., and Zhu, B.: Aerosol and boundary-layer interactions and impact on air quality, *National Science Review*, 4, 810-833, <https://doi.org/10.1093/nsr/nwx117>, 2017.
- Liang, C. W. and Shen, C. H.: Integrated unmanned aerial vehicle platform with sensing and sampling systems for the measurement of air pollutant concentrations, *Atmos. Meas. Tech. Discuss.*, 2023, 1-21, <https://doi.org/10.5194/amt-2023-162>, 2023.
- Liebmann, J., Karu, E., Sobanski, N., Schuladen, J., Ehn, M., Schallhart, S., Quéléver, L., Hellen, H., Hakola, H., Hoffmann, T., Williams, J., Fischer, H., Lelieveld, J., and Crowley, J. N.: Direct measurement of NO₃ radical reactivity in a boreal forest, *Atmospheric Chemistry and Physics*, 18, 3799-3815, <https://doi.org/10.5194/acp-18-3799-2018>, 2018.
- Liggio, J., Moussa, S. G., Wentzell, J., Darlington, A., Liu, P., Leithead, A., Hayden, K., O'Brien, J., Mittermeier, R. L., Staebler, R., Wolde, M., and Li, S. M.: Understanding the primary emissions and secondary formation of gaseous organic acids in the oil sands region of Alberta, Canada, *Atmos. Chem. Phys.*, 17, 8411-8427, <https://doi.org/10.5194/acp-17-8411-2017>, 2017.
- Liigand, P., Liigand, J., Kaupmees, K., and Kruve, A.: 30 Years of research on ESI/MS response: Trends, contradictions and applications, *Analytica Chimica Acta*, 1152, 238117, <https://doi.org/10.1016/j.aca.2020.11.049>, 2021.
- Lim, H.-J., Carlton, A. G., and Turpin, B. J.: Isoprene Forms Secondary Organic Aerosol through Cloud Processing: Model Simulations, *Environmental Science & Technology*, 39, 4441-4446, <https://doi.org/10.1021/es048039h>, 2005.
- Link, M. F.: Air quality implications from oxidation of anthropogenic and biogenic precursors in the troposphere, Colorado State University, <https://api.mountainscholar.org/server/api/core/bitstreams/2392473d-5e9b-48b6-8f74-494de11e3ff7/content>, 2019.
- Liu, J. and Kirshbaum, D. J.: Environmental Conditions Controlling the Morphology of Shallow Orographic Convection, *Journal of the Atmospheric Sciences*, 82, 483-500, <https://doi.org/10.1175/jas-d-24-0113.1>, 2025.
- Lobert, J. M., Keene, W. C., Logan, J. A., and Yevich, R.: Global chlorine emissions from biomass burning: Reactive Chlorine Emissions Inventory, *Journal of Geophysical Research: Atmospheres*, 104, 8373-8389, <https://doi.org/10.1029/1998jd100077>, 1999.
- Lopez-Hilfiker, F. D., Pospisilova, V., Huang, W., Kalberer, M., Mohr, C., Stefenelli, G., Thornton, J. A., Baltensperger, U., Prevot, A. S. H., and Slowik, J. G.: An extractive electrospray ionization time-of-flight mass spectrometer (EESI-TOF) for online measurement of atmospheric aerosol particles, *Atmos. Meas. Tech.*, 12, 4867-4886, <https://doi.org/10.5194/amt-12-4867-2019>, 2019.
- Lopez-Hilfiker, F. D., Mohr, C., Ehn, M., Rubach, F., Kleist, E., Wildt, J., Mentel, T. F., Lutz, A., Hallquist, M., Worsnop, D., and Thornton, J. A.: A novel method for online analysis of gas and particle composition: description and evaluation of a Filter Inlet for Gases and AEROSols (FIGAERO), *Atmos. Meas. Tech.*, 7, 983-1001, <https://doi.org/10.5194/amt-7-983-2014>, 2014.
- Lopez-Hilfiker, F. D., Mohr, C., Ehn, M., Rubach, F., Kleist, E., Wildt, J., Mentel, T. F., Carrasquillo, A. J., Daumit, K. E., Hunter, J. F., Kroll, J. H., Worsnop, D. R., and Thornton, J. A.: Phase partitioning and volatility of secondary organic aerosol components formed from α -pinene ozonolysis and OH oxidation: the importance of accretion products and other low volatility compounds, *Atmos. Chem. Phys.*, 15, 7765-7776, <https://doi.org/10.5194/acp-15-7765-2015>, 2015.
- Lu, C., Wang, X., Dong, S., Zhang, J., Li, J., Zhao, Y., Liang, Y., Xue, L., Xie, H., Zhang, Q., and Wang, W.: Emissions of fine particulate nitrated phenols from various on-road vehicles in China, *Environmental Research*, 179, 108709, <https://doi.org/10.1016/j.envres.2019.108709>, 2019.
- Luiz, E. W. and Fiedler, S.: Global Climatology of Low-Level-Jets: Occurrence, Characteristics, and Meteorological Drivers, *Journal of Geophysical Research: Atmospheres*, 129, <https://doi.org/10.1029/2023jd040262>, 2024.
- Ma, J., Ungeheuer, F., Zheng, F., Du, W., Wang, Y., Cai, J., Zhou, Y., Yan, C., Liu, Y., Kulmala, M., Daellenbach, K. R., and Vogel, A. L.: Nontarget Screening Exhibits a Seasonal Cycle of PM_{2.5} Organic

- Aerosol Composition in Beijing, *Environmental Science & Technology*, 56, 7017-7028, 10.1021/acs.est.1c06905, 2022.
- Ma, Y., Ye, J., Xin, J., Zhang, W., Vilà-Guerau De Arellano, J., Wang, S., Zhao, D., Dai, L., Ma, Y., Wu, X., Xia, X., Tang, G., Wang, Y., Shen, P., Lei, Y., and Martin, S. T.: The Stove, Dome, and Umbrella Effects of Atmospheric Aerosol on the Development of the Planetary Boundary Layer in Hazy Regions, *Geophysical Research Letters*, 47, <https://doi.org/10.1029/2020gl087373>, 2020.
- Machado, L. A. T., Unfer, G. R., Brill, S., Hildmann, S., Pöhlker, C., Cheng, Y., Williams, J., Hartwig, H., Andreae, M. O., Artaxo, P., Curtius, J., Franco, M. A., Cecchini, M. A., Edtbauer, A., Hoffmann, T., Holanda, B., Khadir, T., Krejci, R., Kremper, L. A., Liu, Y., Meller, B. B., Pöhlker, M. L., Quesada, C. A., Ringsdorf, A., Riipinen, I., Trumbore, S., Wolff, S., Lelieveld, J., and Pöschl, U.: Frequent rainfall-induced new particle formation within the canopy in the Amazon rainforest, *Nature Geoscience*, <https://doi.org/10.1038/s41561-024-01585-0>, 2024a.
- Machado, L. A. T., Kesselmeier, J., Botía, S., Van Asperen, H., O. Andreae, M., De Araújo, A. C., Artaxo, P., Edtbauer, A., R. Ferreira, R., Franco, M. A., Harder, H., Jones, S. P., Dias-Júnior, C. Q., Haytzmann, G. G., Quesada, C. A., Komiya, S., Lavric, J., Lelieveld, J., Levin, I., Nölscher, A., Pfannerstill, E., Pöhlker, M. L., Pöschl, U., Ringsdorf, A., Rizzo, L., Yáñez-Serrano, A. M., Trumbore, S., Valenti, W. I. D., Vila-Guerau De Arellano, J., Walter, D., Williams, J., Wolff, S., and Pöhlker, C.: How rainfall events modify trace gas mixing ratios in central Amazonia, *Atmospheric Chemistry and Physics*, 24, 8893-8910, <https://doi.org/10.5194/acp-24-8893-2024>, 2024b.
- Mackenzie-Rae, F. A., Wallis, H. J., Rickard, A. R., Pereira, K. L., Saunders, S. M., Wang, X., and Hamilton, J. F.: Ozonolysis of α -phellandrene – Part 2: Compositional analysis of secondary organic aerosol highlights the role of stabilised Criegee intermediates, *Atmos. Chem. Phys.*, 18, 4673-4693, <https://doi.org/10.5194/acp-18-4673-2018>, 2018.
- Mahnke, C., Weigel, R., Cairo, F., Vernier, J.-P., Afchine, A., Krämer, M., Mitev, V., Matthey, R., Viciani, S., D'Amato, F., Ploeger, F., Deshler, T., and Borrmann, S.: The Asian tropopause aerosol layer within the 2017 monsoon anticyclone: microphysical properties derived from aircraft-borne in situ measurements, *Atmospheric Chemistry and Physics*, 21, 15259-15282, <https://doi.org/10.5194/acp-21-15259-2021>, 2021.
- Mahrt, L. and Acevedo, O.: Types of Vertical Structure of the Nocturnal Boundary Layer, *Boundary-Layer Meteorology*, 187, 141-161, <https://doi.org/10.1007/s10546-022-00716-7>, 2023.
- Marcy, T. P., Gao, R. S., Northway, M. J., Popp, P. J., Stark, H., and Fahey, D. W.: Using chemical ionization mass spectrometry for detection of HNO₃, HCl, and ClONO₂ in the atmosphere, *International Journal of Mass Spectrometry*, 243, 63-70, <https://doi.org/10.1016/j.ijms.2004.11.012>, 2005.
- Maric, D., Burrows, J. P., Meller, R., and Moortgat, G. K.: A study of the UV-visible absorption spectrum of molecular chlorine, *Journal of Photochemistry and Photobiology A: Chemistry*, 70, 205-214, [https://doi.org/10.1016/1010-6030\(93\)85045-A](https://doi.org/10.1016/1010-6030(93)85045-A), 1993.
- Markowski, P. M., Lis, N. T., Turner, D. D., Lee, T. R., and Buban, M. S.: Observations of Near-Surface Vertical Wind Profiles and Vertical Momentum Fluxes from VORTEX-SE 2017: Comparisons to Monin–Obukhov Similarity Theory, *Monthly Weather Review*, 147, 3811-3824, <https://doi.org/10.1175/mwr-d-19-0091.1>, 2019.
- Masoud, C. G., Modi, M., Bhattacharyya, N., Jahn, L. G., McPherson, K. N., Abue, P., Patel, K., Allen, D. T., and Hildebrandt Ruiz, L.: High Chlorine Concentrations in an Unconventional Oil and Gas Development Region and Impacts on Atmospheric Chemistry, *Environmental Science & Technology*, 57, 15454-15464, <https://doi.org/10.1021/acs.est.3c04005>, 2023.
- Mathes, W.: DatCon Version 4.3.0 (4.3.0), bug@flylog.info [code], <https://datfile.net/DatCon/intro.html>, 2023.
- McWilliams, J. C., Meneveau, C., Patton, E. G., and Sullivan, P. P.: Stable Boundary Layers and Subfilter-Scale Motions, *Atmosphere*, 14, 1107, <https://doi.org/10.3390/atmos14071107>, 2023.
- Mehra, A., Wang, Y., Krechmer, J. E., Lambe, A., Majluf, F., Morris, M. A., Priestley, M., Bannan, T. J., Bryant, D. J., Pereira, K. L., Hamilton, J. F., Rickard, A. R., Newland, M. J., Stark, H., Croteau, P., Jayne, J. T., Worsnop, D. R., Canagaratna, M. R., Wang, L., and Coe, H.: Evaluation of the chemical composition

- of gas- and particle-phase products of aromatic oxidation, *Atmos. Chem. Phys.*, 20, 9783-9803, <https://doi.org/10.5194/acp-20-9783-2020>, 2020.
- Mercer, A., Chang, R., and Folkens, I.: Nocturnal Relative Humidity Maxima above the Boundary Layer in the U.S. Midwest: A Diagnostic for the Mountain–Plains Solenoidal Circulation, *Monthly Weather Review*, 146, 641-658, <https://doi.org/10.1175/MWR-D-17-0189.1>, 2018.
- Mercier, F., Gloennec, P., Blanchard, O., and Le Bot, B.: Analysis of semi-volatile organic compounds in indoor suspended particulate matter by thermal desorption coupled with gas chromatography/mass spectrometry, *Journal of Chromatography A*, 1254, 107-114, <https://doi.org/10.1016/j.chroma.2012.07.025>, 2012.
- Merlone, A., Beges, G., Bottacin, A., Brunet, M., Gilabert, A., Groselj, D., Harper, A., Hechler, P., Ivanov, M., Musacchio, C., Trewin, B., and Wright, W.: Climatological reference stations: Definitions and requirements, *International Journal of Climatology*, 44, 1710-1724, <https://doi.org/10.1002/joc.8406>, 2024.
- Mielke, L. H., Furgeson, A., and Osthoff, H. D.: Observation of ClNO₂ in a Mid-Continental Urban Environment, *Environmental Science & Technology*, 45, 8889-8896, <https://doi.org/10.1021/es201955u>, 2011.
- Mikhailov, E. F., Mironova, S., Mironov, G., Vlasenko, S., Panov, A., Chi, X., Walter, D., Carbone, S., Artaxo, P., Heimann, M., Lavric, J., Pöschl, U., and Andreae, M. O.: Long-term measurements (2010–2014) of carbonaceous aerosol and carbon monoxide at the Zotino Tall Tower Observatory (ZOTTO) in central Siberia, *Atmos. Chem. Phys.*, 17, 14365-14392, <https://doi.org/10.5194/acp-17-14365-2017>, 2017.
- Miller, A. J., Ramelli, F., Fuchs, C., Omanovic, N., Spirig, R., Zhang, H., Lohmann, U., Kanji, Z. A., and Henneberger, J.: Two new multirotor uncrewed aerial vehicles (UAVs) for glaciogenic cloud seeding and aerosol measurements within the CLOUDLAB project, *Atmospheric Measurement Techniques*, 17, 601-625, <https://doi.org/10.5194/amt-17-601-2024>, 2024.
- Mirza, A. K., Ballard, S. P., Dance, S. L., Maisey, P., Rooney, G. G., and Stone, E. K.: Comparison of aircraft-derived observations with in situ research aircraft measurements, *Quarterly Journal of the Royal Meteorological Society*, 142, 2949-2967, <https://doi.org/10.1002/qj.2864>, 2016.
- Miyama, T., Morishita, T., Kominami, Y., Noguchi, H., Yasuda, Y., Yoshifuji, N., Okano, M., Yamanoi, K., Mizoguchi, Y., Takanashi, S., Kitamura, K., and Matsumoto, K.: Increases in Biogenic Volatile Organic Compound Concentrations Observed after Rains at Six Forest Sites in Non-Summer Periods, *Atmosphere*, 11, 1381, <https://doi.org/10.3390/atmos11121381>, 2020.
- Moeng, C.-H. and Sullivan, P. P.: A Comparison of Shear- and Buoyancy-Driven Planetary Boundary Layer Flows, *Journal of Atmospheric Sciences*, 51, 999-1022, [https://doi.org/10.1175/1520-0469\(1994\)051<0999:ACOSAB>2.0.CO;2](https://doi.org/10.1175/1520-0469(1994)051<0999:ACOSAB>2.0.CO;2), 1994.
- Mohr, C., Huffman, J. A., Cubison, M. J., Aiken, A. C., Docherty, K. S., Kimmel, J. R., Ulbrich, I. M., Hannigan, M., and Jimenez, J. L.: Characterization of Primary Organic Aerosol Emissions from Meat Cooking, Trash Burning, and Motor Vehicles with High-Resolution Aerosol Mass Spectrometry and Comparison with Ambient and Chamber Observations, *Environmental Science & Technology*, 43, 2443-2449, <https://doi.org/10.1021/es8011518>, 2009.
- Molina, L. T. and Molina, M. J.: Absolute absorption cross sections of ozone in the 185- to 350-nm wavelength range, *Journal of Geophysical Research: Atmospheres*, 91, 14501-14508, <https://doi.org/10.1029/jd091id13p14501>, 1986.
- Molina, M. J. and Rowland, F. S.: Stratospheric sink for chlorofluoromethanes: chlorine atom-catalysed destruction of ozone, *Nature*, 249, 810-812, <https://doi.org/10.1038/249810a0>, 1974.
- Monin, A. S. and Obukhov, A. M.: Basic laws of turbulent mixing in the surface layer of the atmosphere, *Tr. Akad. Nauk. SSSR Geophys. Inst.*, 24, 163-187, https://gibbs.science/efd/handouts/monin_obukhov_1954.pdf, 1954.
- Moomaw, W. R.: Industrial emissions of greenhouse gases, *Energy Policy*, 24, 951-968, [https://doi.org/10.1016/S0301-4215\(96\)80360-0](https://doi.org/10.1016/S0301-4215(96)80360-0), 1996.
- Moores, W. H., Caughey, S. J., Readings, C. J., Milford, J. R., Mansfield, D. A., Abdulla, S., Guymer, T. H., and Johnston, W. B.: Measurements of boundary layer structure and development over SE England

- using aircraft and tethered balloon instrumentation, *Quarterly Journal of the Royal Meteorological Society*, 105, 397-421, <https://doi.org/10.1002/qj.49710544406>, 1979.
- Moormann, L.: Analyse von Emissionen aus Kochprozessen mittels offline-Iodid-CIMS - Methodenentwicklung und Anwendung -, Chemistry Department, Johannes Gutenberg University Mainz, Mainz, 2021.
- Moormann, L., Fachinger, F., Drewnick, F., and Tost, H.: Boundary Layer Dynamics after Rain Fronts: High-Resolution Reconstruction and Model Validation using ground- and drone-based Measurements, *EGUsphere*, 2025, 1-23, 10.5194/egusphere-2025-3862, 2025a.
- Moormann, L., Böttger, T., Schuhmann, P., Valero, L., Fachinger, F., and Drewnick, F.: The Flying Laboratory FLab: development and application of a UAS to measure aerosol particles and trace gases in the lower troposphere, *Atmos. Meas. Tech.*, 18, 1441-1459, <https://doi.org/10.5194/amt-18-1441-2025>, 2025b.
- Müller, K., Unice, K., Panko, J., and Wagner, S.: Tire emissions during the use phase of tires – current and future trends, *Environmental Science: Advances*, 4, 1344-1363, <https://doi.org/10.1039/d4va00407h>, 2025.
- Müller, L., Reinnig, M. C., Naumann, K. H., Saathoff, H., Mentel, T. F., Donahue, N. M., and Hoffmann, T.: Formation of 3-methyl-1,2,3-butanetricarboxylic acid via gas phase oxidation of pinonic acid – a mass spectrometric study of SOA aging, *Atmos. Chem. Phys.*, 12, 1483-1496, <https://doi.org/10.5194/acp-12-1483-2012>, 2012.
- Mutzel, A., Zhang, Y., Böge, O., Rodigast, M., Kolodziejczyk, A., Wang, X., and Herrmann, H.: Importance of secondary organic aerosol formation of α -pinene, limonene, and m-cresol comparing day- and nighttime radical chemistry, *Atmos. Chem. Phys.*, 21, 8479-8498, <https://doi.org/10.5194/acp-21-8479-2021>, 2021.
- Net, S., Alvarez, E. G., Gligorovski, S., and Wortham, H.: Heterogeneous reactions of ozone with methoxyphenols, in presence and absence of light, *Atmospheric Environment*, 45, 3007-3014, <https://doi.org/10.1016/j.atmosenv.2011.03.026>, 2011.
- Neu, U., Künzle, T., and Wanner, H.: On the relation between ozone storage in the residual layer and daily variation in near-surface ozone concentration — A case study, *Boundary-Layer Meteorology*, 69, 221-247, <https://doi.org/10.1007/BF00708857>, 1994.
- Neuman, J. A., Trainer, M., Aikin, K. C., Angevine, W. M., Brioude, J., Brown, S. S., de Gouw, J. A., Dube, W. P., Flynn, J. H., Graus, M., Holloway, J. S., Lefer, B. L., Nedelec, P., Nowak, J. B., Parrish, D. D., Pollack, I. B., Roberts, J. M., Ryerson, T. B., Smit, H., Thouret, V., and Wagner, N. L.: Observations of ozone transport from the free troposphere to the Los Angeles basin, *Journal of Geophysical Research: Atmospheres*, 117, <https://doi.org/10.1029/2011JD016919>, 2012.
- Ng, N. L., Canagaratna, M. R., Zhang, Q., Jimenez, J. L., Tian, J., Ulbrich, I. M., Kroll, J. H., Docherty, K. S., Chhabra, P. S., Bahreini, R., Murphy, S. M., Seinfeld, J. H., Hildebrandt, L., Donahue, N. M., DeCarlo, P. F., Lanz, V. A., Prévôt, A. S. H., Dinar, E., Rudich, Y., and Worsnop, D. R.: Organic aerosol components observed in Northern Hemispheric datasets from Aerosol Mass Spectrometry, *Atmos. Chem. Phys.*, 10, 4625-4641, <https://doi.org/10.5194/acp-10-4625-2010>, 2010.
- Nguyen, T. B., Roach, P. J., Laskin, J., Laskin, A., and Nizkorodov, S. A.: Effect of humidity on the composition of isoprene photooxidation secondary organic aerosol, *Atmos. Chem. Phys.*, 11, 6931-6944, <https://doi.org/10.5194/acp-11-6931-2011>, 2011.
- Niedek, C. R., Mei, F., Zawadowicz, M. A., Zhu, Z., Schmid, B., and Zhang, Q.: Quantitative chemical assay of nanogram-level particulate matter using aerosol mass spectrometry: characterization of particles collected from uncrewed atmospheric measurement platforms, *Atmos. Meas. Tech.*, 16, 955-968, <https://doi.org/10.5194/amt-16-955-2023>, 2023.
- Nieuwstadt, F. T. M.: The Turbulent Structure of the Stable, Nocturnal Boundary Layer, *Journal of Atmospheric Sciences*, 41, 2202-2216, [https://doi.org/10.1175/1520-0469\(1984\)041<2202:TTSOTS>2.0.CO;2](https://doi.org/10.1175/1520-0469(1984)041<2202:TTSOTS>2.0.CO;2), 1984.
- Niinemets, Ü., Loreto, F., and Reichstein, M.: Physiological and physicochemical controls on foliar volatile organic compound emissions, *Trends in Plant Science*, 9, 180-186, <https://doi.org/10.1016/j.tplants.2004.02.006>, 2004.

- Nozière, B., Kalberer, M., Claeys, M., Allan, J., D'Anna, B., Decesari, S., Finessi, E., Glasius, M., Grgić, I., Hamilton, J. F., Hoffmann, T., Iinuma, Y., Jaoui, M., Kahnt, A., Kampf, C. J., Kourtchev, I., Maenhaut, W., Marsden, N., Saarikoski, S., Schnelle-Kreis, J., Surratt, J. D., Szidat, S., Szmigielski, R., and Wisthaler, A.: The Molecular Identification of Organic Compounds in the Atmosphere: State of the Art and Challenges, *Chemical Reviews*, 115, 3919-3983, <https://doi.org/10.1021/cr5003485>, 2015.
- Oberto, L., Bisi, M., Kazemipour, A., Steiger, A., Kleine-Ostmann, T., and Schrader, T.: Measurement comparison among time-domain, FTIR and VNA-based spectrometers in the THz frequency range, *Metrologia*, 54, 77-84, <https://doi.org/10.1088/1681-7575/aa54c2>, 2017.
- Okada, K., Okada, N., Takagi, K., Urano, S.-I., Nishida, Y., Aguilos, M., and Kobayashi, T.: CO₂ flux estimation for a valley terrain using the atmospheric boundary layer method, *Journal of Agricultural Meteorology*, 68, 165-174, <https://doi.org/10.2480/agrmet.68.3.1>, 2012.
- Oliveira, M. I., Acevedo, O. C., Sörgel, M., Nascimento, E. L., Manzi, A. O., Oliveira, P. E. S., Brondani, D. V., Tsokankunku, A., and Andreae, M. O.: Planetary boundary layer evolution over the Amazon rainforest in episodes of deep moist convection at the Amazon Tall Tower Observatory, *Atmos. Chem. Phys.*, 20, 15-27, <https://doi.org/10.5194/acp-20-15-2020>, 2020.
- Oliveira, P. H. F., Artaxo, P., Pires, C., De Lucca, S., ProcÓpio, A., Holben, B., Schafer, J., Cardoso, L. F., Wofsy, S. C., and Rocha, H. R.: The effects of biomass burning aerosols and clouds on the CO₂ flux in Amazonia, *Tellus B*, 59, 338-349, <https://doi.org/10.1111/j.1600-0889.2007.00270.x>, 2007.
- Olszyna, K. J., Bailey, E. M., Simonaitis, R., and Meagher, J. F.: O₃ and NO_y relationships at a rural site, *Journal of Geophysical Research: Atmospheres*, 99, 14557-14563, <https://doi.org/10.1029/94jd00739>, 1994.
- Oss, M., Krueve, A., Herodes, K., and Leito, I.: Electrospray Ionization Efficiency Scale of Organic Compounds, *Analytical Chemistry*, 82, 2865-2872, <https://doi.org/10.1021/ac902856t>, 2010.
- Osthoff, H. D., Roberts, J. M., Ravishankara, A. R., Williams, E. J., Lerner, B. M., Sommariva, R., Bates, T. S., Coffman, D., Quinn, P. K., Dibb, J. E., Stark, H., Burkholder, J. B., Talukdar, R. K., Meagher, J., Fehsenfeld, F. C., and Brown, S. S.: High levels of nitryl chloride in the polluted subtropical marine boundary layer, *Nature Geoscience*, 1, 324-328, <https://doi.org/10.1038/ngeo177>, 2008.
- Ouchi, M., Matsumi, Y., Nakayama, T., Shimizu, K., Sawada, T., Machida, T., Matsueda, H., Sawa, Y., Morino, I., Uchino, O., Tanaka, T., and Imasu, R.: Development of a balloon-borne instrument for CO₂ vertical profile observations in the troposphere, *Atmospheric Measurement Techniques*, 12, 5639-5653, <https://doi.org/10.5194/amt-12-5639-2019>, 2019.
- Oum, K. W., Lakin, M. J., DeHaan, D. O., Brauers, T., and Finlayson-Pitts, B. J.: Formation of Molecular Chlorine from the Photolysis of Ozone and Aqueous Sea-Salt Particles, *Science*, 279, <https://doi.org/10.1126/science.279.5347.74>, 1998.
- Paatero, P. and Tapper, U.: Positive matrix factorization: A non-negative factor model with optimal utilization of error estimates of data values, *Environmetrics*, 5, 111-126, <https://doi.org/10.1002/env.3170050203>, 1994.
- Pagonis, D., Campuzano-Jost, P., Guo, H., Day, D. A., Schueneman, M. K., Brown, W. L., Nault, B. A., Stark, H., Siemens, K., Laskin, A., Piel, F., Tomsche, L., Wisthaler, A., Coggon, M. M., Gkatzelis, G. I., Halliday, H. S., Krechmer, J. E., Moore, R. H., Thomson, D. S., Warneke, C., Wiggins, E. B., and Jimenez, J. L.: Airborne extractive electrospray mass spectrometry measurements of the chemical composition of organic aerosol, *Atmos. Meas. Tech.*, 14, 1545-1559, <https://doi.org/10.5194/amt-14-1545-2021>, 2021.
- Pandis, S. N., Wexler, A. S., and Seinfeld, J. H.: Dynamics of tropospheric aerosols, *The Journal of Physical Chemistry*, 99, 9646-9659, <https://doi.org/10.1021/j100024a003>, 1995.
- Pandis, S. N., Harley, R. A., Cass, G. R., and Seinfeld, J. H.: Secondary organic aerosol formation and transport, *Atmospheric Environment. Part A. General Topics*, 26, 2269-2282, [https://doi.org/10.1016/0960-1686\(92\)90358-R](https://doi.org/10.1016/0960-1686(92)90358-R), 1992.
- Parshintsev, J. and Hyötyläinen, T.: Methods for characterization of organic compounds in atmospheric aerosol particles, *Analytical and Bioanalytical Chemistry*, 407, 5877-5897, <https://doi.org/10.1007/s00216-014-8394-3>, 2015.

- Pastorello, G., Trotta, C., Canfora, E., Chu, H., Christianson, D., Cheah, Y.-W., Poindexter, C., Chen, J., Elbashandy, A., Humphrey, M., Isaac, P., Polidori, D., Reichstein, M., Ribeca, A., Van Ingen, C., Vuichard, N., Zhang, L., Amiro, B., Ammann, C., Arain, M. A., Ardö, J., Arkebauer, T., Arndt, S. K., Arriga, N., Aubinet, M., Aurela, M., Baldocchi, D., Barr, A., Beamesderfer, E., Marchesini, L. B., Bergeron, O., Beringer, J., Bernhofer, C., Berveiller, D., Billesbach, D., Black, T. A., Blanken, P. D., Bohrer, G., Boike, J., Bolstad, P. V., Bonal, D., Bonnefond, J.-M., Bowling, D. R., Bracho, R., Brodeur, J., Brümmer, C., Buchmann, N., Burban, B., Burns, S. P., Buysse, P., Cale, P., Cavagna, M., Cellier, P., Chen, S., Chini, I., Christensen, T. R., Cleverly, J., Collalti, A., Consalvo, C., Cook, B. D., Cook, D., Coursolle, C., Cremonese, E., Curtis, P. S., D'Andrea, E., Da Rocha, H., Dai, X., Davis, K. J., Cinti, B. D., Grandcourt, A. D., Ligne, A. D., De Oliveira, R. C., Delpierre, N., Desai, A. R., Di Bella, C. M., Tommasi, P. D., Dolman, H., Domingo, F., Dong, G., Dore, S., Duce, P., Dufrêne, E., Dunn, A., Dušek, J., Eamus, D., Eichelmann, U., Elkhidir, H. A. M., Eugster, W., Ewenz, C. M., Ewers, B., Famulari, D., Fares, S., Feigenwinter, I., Feitz, A., Fensholt, R., Filippa, G., Fischer, M., Frank, J., Galvagno, M., Gharun, M., Gianelle, D., Gielen, B., Gioli, B., Gitelson, A., Goded, I., Goeckede, M., Goldstein, A. H., Gough, C. M., Goulden, M. L., Graf, A., Griebel, A., Gruening, C., Grünwald, T., Hammerle, A., Han, S., Han, X., Hansen, B. U., Hanson, C., Hatakka, J., He, Y., Hehn, M., Heinesch, B., Hinko-Najera, N., Hörtnagl, L., Hutley, L., Ibrom, A., Ikawa, H., Jackowicz-Korczynski, M., Janouš, D., Jans, W., Jassal, R., Jiang, S., Kato, T., Khomik, M., Klatt, J., Knohl, A., Knox, S., Kobayashi, H., Koerber, G., Kolle, O., Kosugi, Y., Kotani, A., Kowalski, A., Kruijt, B., Kurbatova, J., Kutsch, W. L., Kwon, H., Launiainen, S., Laurila, T., Law, B., Leuning, R., Li, Y., Liddell, M., Limousin, J.-M., Lion, M., Liska, A. J., Lohila, A., López-Ballesteros, A., López-Blanco, E., Loubet, B., Loustau, D., Lucas-Moffat, A., Lüers, J., Ma, S., Macfarlane, C., Magliulo, V., Maier, R., Mammarella, I., Manca, G., Marcolla, B., Margolis, H. A., Marras, S., Massman, W., Mastepanov, M., Matamala, R., Matthes, J. H., Mazzenga, F., McCaughey, H., McHugh, I., McMillan, A. M. S., Merbold, L., Meyer, W., Meyers, T., Miller, S. D., Minerbi, S., Moderow, U., Monson, R. K., Montagnani, L., Moore, C. E., Moors, E., Moreaux, V., Moureaux, C., Munger, J. W., Nakai, T., Neiryneck, J., Nestic, Z., Nicolini, G., Noormets, A., Northwood, M., Noretto, M., Nouvellon, Y., Novick, K., Oechel, W., Olesen, J. E., Ourcival, J.-M., Papuga, S. A., Parmentier, F.-J., Paul-Limoges, E., Pavelka, M., Peichl, M., Pendall, E., Phillips, R. P., Pilegaard, K., Pirk, N., Posse, G., Powell, T., Prasse, H., Prober, S. M., Rambal, S., Rannik, Ü., Raz-Yaseef, N., Rebmann, C., Reed, D., Dios, V. R. D., Restrepo-Coupe, N., Reverter, B. R., Roland, M., Sabbatini, S., Sachs, T., Saleska, S. R., Sánchez-Cañete, E. P., Sanchez-Mejia, Z. M., Schmid, H. P., Schmidt, M., Schneider, K., Schrader, F., Schroder, I., Scott, R. L., Sedlák, P., Serrano-Ortiz, P., Shao, C., Shi, P., Shironya, I., Siebicke, L., Šigut, L., Silberstein, R., Sirca, C., Spano, D., Steinbrecher, R., Stevens, R. M., Sturtevant, C., Suyker, A., Tagesson, T., Takanashi, S., Tang, Y., Tapper, N., Thom, J., Tomassucci, M., Tuovinen, J.-P., Urbanski, S., Valentini, R., Van Der Molen, M., Van Gorsel, E., Van Huissteden, K., Varlagin, A., Verfaillie, J., Vesala, T., Vincke, C., Vitale, D., Vygodskaya, N., Walker, J. P., Walter-Shea, E., Wang, H., Weber, R., Westermann, S., Wille, C., Wofsy, S., Wohlfahrt, G., Wolf, S., Woodgate, W., Li, Y., Zampedri, R., Zhang, J., Zhou, G., Zona, D., Agarwal, D., Biraud, S., Torn, M., and Papale, D.: The FLUXNET2015 dataset and the ONEFlux processing pipeline for eddy covariance data, *Scientific Data*, 7, <https://doi.org/10.1038/s41597-020-0534-3>, 2020.
- Peng, X., Wang, T., Wang, W., Ravishankara, A. R., George, C., Xia, M., Cai, M., Li, Q., Salvador, C. M., Lau, C., Lyu, X., Poon, C. N., Mellouki, A., Mu, Y., Hallquist, M., Saiz-Lopez, A., Guo, H., Herrmann, H., Yu, C., Dai, J., Wang, Y., Wang, X., Yu, A., Leung, K., Lee, S., and Chen, J.: Photodissociation of particulate nitrate as a source of daytime tropospheric Cl₂, *Nature Communications*, 13, <https://doi.org/10.1038/s41467-022-28383-9>, 2022.
- Permar, W., Wang, Q., Selimovic, V., Wielgasz, C., Yokelson, R. J., Hornbrook, R. S., Hills, A. J., Apel, E. C., Ku, I. T., Zhou, Y., Sive, B. C., Sullivan, A. P., Collett, J. L., Campos, T. L., Palm, B. B., Peng, Q., Thornton, J. A., Garofalo, L. A., Farmer, D. K., Kreidenweis, S. M., Levin, E. J. T., Demott, P. J., Flocke, F., Fischer, E. V., and Hu, L.: Emissions of Trace Organic Gases From Western U.S. Wildfires Based on WE-CAN Aircraft Measurements, *Journal of Geophysical Research: Atmospheres*, 126, <https://doi.org/10.1029/2020jd033838>, 2021.
- Perraud, V., Horne, J. R., Martinez, A. S., Kalinowski, J., Meinardi, S., Dawson, M. L., Wingen, L. M., Dabdub, D., Blake, D. R., Gerber, R. B., and Finlayson-Pitts, B. J.: The future of airborne sulfur-containing

- particles in the absence of fossil fuel sulfur dioxide emissions, *Proceedings of the National Academy of Sciences*, 112, 13514-13519, <https://doi.org/10.1073/pnas.1510743112>, 2015.
- Perrone, M. R. and Romano, S.: Relationship between the planetary boundary layer height and the particle scattering coefficient at the surface, *Atmospheric Research*, 213, 57-69, <https://doi.org/10.1016/j.atmosres.2018.04.017>, 2018.
- Petäjä, T., Järvi, L., Kerminen, V. M., Ding, A. J., Sun, J. N., Nie, W., Kujansuu, J., Virkkula, A., Yang, X., Fu, C. B., Zilitinkevich, S., and Kulmala, M.: Enhanced air pollution via aerosol-boundary layer feedback in China, *Scientific Reports*, 6, 18998, <https://doi.org/10.1038/srep18998>, 2016.
- Peters, D. R., Popoola, O. A. M., Jones, R. L., Martin, N. A., Mills, J., Fonseca, E. R., Stidworthy, A., Forsyth, E., Carruthers, D., Dupuy-Todd, M., Douglas, F., Moore, K., Shah, R. U., Padilla, L. E., and Alvarez, R. A.: Evaluating uncertainty in sensor networks for urban air pollution insights, *Atmospheric Measurement Techniques*, 15, 321-334, <https://doi.org/10.5194/amt-15-321-2022>, 2022.
- Phillips, G. J., Tang, M. J., Thieser, J., Brickwedde, B., Schuster, G., Bohn, B., Lelieveld, J., and Crowley, J. N.: Significant concentrations of nitryl chloride observed in rural continental Europe associated with the influence of sea salt chloride and anthropogenic emissions, *Geophysical Research Letters*, 39, n/a-n/a, <https://doi.org/10.1029/2012gl051912>, 2012.
- Phillips, G. J., Thieser, J., Tang, M., Sobanski, N., Schuster, G., Fachinger, J., Drewnick, F., Borrmann, S., Bingemer, H., Lelieveld, J., and Crowley, J. N.: Estimating N₂O₅ uptake coefficients using ambient measurements of NO₃, N₂O₅, ClNO₂ and particle-phase nitrate, *Atmospheric Chemistry and Physics*, 16, 13231-13249, <https://doi.org/10.5194/acp-16-13231-2016>, 2016.
- Piel, F., Müller, M., Mikoviny, T., Pusede, S. E., and Wisthaler, A.: Airborne measurements of particulate organic matter by proton-transfer-reaction mass spectrometry (PTR-MS): a pilot study, *Atmos. Meas. Tech.*, 12, 5947-5958, <https://doi.org/10.5194/amt-12-5947-2019>, 2019.
- Pikmann, J.: Untersuchung gesundheitsrelevanter Aerosole mit Schwerpunkt auf Emissionen aus Kochaktivitäten, Johannes Gutenberg-Universität Mainz, Mainz, <http://doi.org/10.25358/openscience-9028>, 2023.
- Pikmann, J., Drewnick, F., Fachinger, F., and Borrmann, S.: Particulate emissions from cooking: emission factors, emission dynamics, and mass spectrometric analysis for different cooking methods, *Atmos. Chem. Phys.*, 24, 12295-12321, <https://doi.org/10.5194/acp-24-12295-2024>, 2024.
- Pikridas, M., Bezantakos, S., Močnik, G., Keleşhis, C., Brechtel, F., Stavroulas, I., Demetriades, G., Antoniou, P., Vouterakos, P., Argyrides, M., Liakakou, E., Drinovec, L., Marinou, E., Amiridis, V., Vrekoussis, M., Mihalopoulos, N., and Sciare, J.: On-flight intercomparison of three miniature aerosol absorption sensors using unmanned aerial systems (UASs), *Atmospheric Measurement Techniques*, 12, 6425-6447, <https://doi.org/10.5194/amt-12-6425-2019>, 2019.
- Platis, A., Altstädter, B., Wehner, B., Wildmann, N., Lampert, A., Hermann, M., Birmili, W., and Bange, J.: An Observational Case Study on the Influence of Atmospheric Boundary-Layer Dynamics on New Particle Formation, *Boundary-Layer Meteorology*, 158, 67-92, <https://doi.org/10.1007/s10546-015-0084-y>, 2016.
- Pluskal, T., Castillo, S., Villar-Briones, A., and Orešič, M.: MZmine 2: Modular framework for processing, visualizing, and analyzing mass spectrometry-based molecular profile data, *BMC Bioinformatics*, 11, 395, <https://doi.org/10.1186/1471-2105-11-395>, 2010.
- Pohorsky, R., Baccarini, A., Tolu, J., Winkel, L. H. E., and Schmale, J.: Modular Multiplatform Compatible Air Measurement System (MoMuCAMS): a new modular platform for boundary layer aerosol and trace gas vertical measurements in extreme environments, *Atmos. Meas. Tech.*, 17, 731-754, <https://doi.org/10.5194/amt-17-731-2024>, 2024.
- Pohorsky, R., Baccarini, A., Brett, N., Barret, B., Bekki, S., Pappaccogli, G., Dieudonné, E., Temime-Roussel, B., D'Anna, B., Cesler-Maloney, M., Donato, A., Decesari, S., Law, K. S., Simpson, W. R., Fochesatto, J., Arnold, S. R., and Schmale, J.: In situ vertical observations of the layered structure of air pollution in a continental high-latitude urban boundary layer during winter, *Atmos. Chem. Phys.*, 25, 3687-3715, <https://doi.org/10.5194/acp-25-3687-2025>, 2025.
- Poraicu, C., Müller, J. F., Stavroukou, T., Amelynck, C., Verreyken, B. W. D., Schoon, N., Vigouroux, C., Kumps, N., Brioude, J., Tulet, P., and Mouchel-Vallon, C.: Constraining the budget of NO_x and volatile

- organic compounds at a remote tropical island using multi-platform observations and WRF-Chem model simulations, *Atmos. Chem. Phys.*, 25, 6903–6941, <https://doi.org/10.5194/acp-25-6903-2025>, 2025.
- Priestley, M., Le Breton, M., Bannan, T. J., Worrall, S. D., Bacak, A., Smedley, A. R. D., Reyes-Villegas, E., Mehra, A., Allan, J., Webb, A. R., Shallcross, D. E., Coe, H., and Percival, C. J.: Observations of organic and inorganic chlorinated compounds and their contribution to chlorine radical concentrations in an urban environment in northern Europe during the wintertime, *Atmospheric Chemistry and Physics*, 18, 13481–13493, <https://doi.org/10.5194/acp-18-13481-2018>, 2018.
- Priestley, M., Bannan, T. J., Le Breton, M., Worrall, S. D., Kang, S., Pullinen, I., Schmitt, S., Tillmann, R., Kleist, E., Zhao, D., Wildt, J., Garmash, O., Mehra, A., Bacak, A., Shallcross, D. E., Kiendler-Scharr, A., Hallquist, Å. M., Ehn, M., Coe, H., Percival, C. J., Hallquist, M., Mentel, T. F., and McFiggans, G.: Chemical characterisation of benzene oxidation products under high- and low-NO_x conditions using chemical ionisation mass spectrometry, *Atmos. Chem. Phys.*, 21, 3473–3490, <https://doi.org/10.5194/acp-21-3473-2021>, 2021.
- Prinn, R. G., Weiss, R. F., Fraser, P. J., Simmonds, P. G., Cunnold, D. M., Alyea, F. N., O'Doherty, S., Salameh, P., Miller, B. R., Huang, J., Wang, R. H. J., Hartley, D. E., Harth, C., Steele, L. P., Sturrock, G., Midgley, P. M., and McCulloch, A.: A history of chemically and radiatively important gases in air deduced from ALE/GAGE/AGAGE, *Journal of Geophysical Research: Atmospheres*, 105, 17751–17792, <https://doi.org/10.1029/2000jd900141>, 2000.
- Pszenny, A. A. P., Keene, W. C., Jacob, D. J., Fan, S., Maben, J. R., Zetwo, M. P., Springer-Young, M., and Galloway, J. N.: Evidence of inorganic chlorine gases other than hydrogen chloride in marine surface air, *Geophysical Research Letters*, 20, 699–702, <https://doi.org/10.1029/93gl00047>, 1993.
- Qi, L., Vogel, A. L., Esmailirad, S., Cao, L., Zheng, J., Jaffrezo, J. L., Fermo, P., Kasper-Giebl, A., Daellenbach, K. R., Chen, M., Ge, X., Baltensperger, U., Prévôt, A. S. H., and Slowik, J. G.: A 1-year characterization of organic aerosol composition and sources using an extractive electrospray ionization time-of-flight mass spectrometer (EESI-TOF), *Atmos. Chem. Phys.*, 20, 7875–7893, <https://doi.org/10.5194/acp-20-7875-2020>, 2020.
- Qian, Y., Yan, H., Berg, L. K., Hagos, S., Feng, Z., Yang, B., and Huang, M.: Assessing Impacts of PBL and Surface Layer Schemes in Simulating the Surface–Atmosphere Interactions and Precipitation over the Tropical Ocean Using Observations from AMIE/DYNAMO, *Journal of Climate*, 29, 8191–8210, <https://doi.org/10.1175/jcli-d-16-0040.1>, 2016.
- Quinn, P. K., Bates, T. S., Coffman, D. J., Johnson, J. E., and Upchurch, L. M.: Use of an uncrewed aerial system to investigate aerosol direct and indirect radiative forcing effects in the marine atmosphere, *Atmospheric Measurement Techniques*, 17, 3157–3170, <https://doi.org/10.5194/amt-17-3157-2024>, 2024.
- Rabins, L. F., Theuerkauf, E. J., and Bunting, E. L.: Using existing infrastructure as ground control points to support citizen science coastal UAS monitoring programs, *Frontiers in Environmental Science*, 11, <https://doi.org/10.3389/fenvs.2023.1101458>, 2023.
- Radtke, J. K., Kies, B. N., Mottishaw, W. A., Zeuli, S. M., Voon, A. T. H., Koerber, K. L., Petty, G. W., Vermeuel, M., Bertram, T. H., Desai, A. R., Hupy, J. P., Pierce, R. B., Wagner, T. J., and Cleary, P. A.: Observing Low Altitude Features in Ozone Concentrations in a Shoreline Environment via Unmanned Aerial Systems, <https://doi.org/10.5194/amt-2023-143>, 2023.
- Radtke, J. K., Kies, B. N., Mottishaw, W. A., Zeuli, S. M., Voon, A. T. H., Koerber, K. L., Petty, G. W., Vermeuel, M. P., Bertram, T. H., Desai, A. R., Hupy, J. P., Pierce, R. B., Wagner, T. J., and Cleary, P. A.: Observing low-altitude features in ozone concentrations in a shoreline environment via uncrewed aerial systems, *Atmos. Meas. Tech.*, 17, 2833–2847, <https://doi.org/10.5194/amt-17-2833-2024>, 2024.
- Ragains, M. and Finlayson-Pitts, B.: Kinetics and mechanism of the reaction of Cl atoms with 2-methyl-1, 3-butadiene (isoprene) at 298 K, *The Journal of Physical Chemistry A*, 101, 1509–1517, <https://doi.org/10.1021/jp962786m>, 1997.
- Ramteke, S., Sahu, B. L., Patel, K. S., Pandey, P. K., Yurdakul, S., Martín-Ramos, P., Ren, H., and Fu, P.: Characterization of Organic Aerosols in the Ambient Air of Raipur, Central India: Distribution, Seasonal

- Variations, and Source Apportionment, *Aerosol Science and Engineering*, 9, 89-103, <https://doi.org/10.1007/s41810-024-00246-4>, 2025.
- Rana, M. S. and Guzman, M. I.: Oxidation of Phenolic Aldehydes by Ozone and Hydroxyl Radicals at the Air–Solid Interface, *ACS Earth and Space Chemistry*, 6, 2900-2909, <https://doi.org/10.1021/acsearthspacechem.2c00206>, 2022.
- Raschendorfer, M.: The new turbulence parameterization of LM, <http://www.cosmo-model.org>, 2001.
- Reddington, C. L., Carslaw, K. S., Spracklen, D. V., Frontoso, M. G., Collins, L., Merikanto, J., Minikin, A., Hamburger, T., Coe, H., Kulmala, M., Aalto, P., Flentje, H., Plass-Dülmer, C., Birmili, W., Wiedensohler, A., Wehner, B., Tuch, T., Sonntag, A., O'Dowd, C. D., Jennings, S. G., Dupuy, R., Baltensperger, U., Weingartner, E., Hansson, H. C., Tunved, P., Laj, P., Sellegri, K., Boulon, J., Putaud, J. P., Gruening, C., Swietlicki, E., Roldin, P., Henzing, J. S., Moerman, M., Mihalopoulos, N., Kouvarakis, G., Ždímal, V., Zíková, N., Marinoni, A., Bonasoni, P., and Duchi, R.: Primary versus secondary contributions to particle number concentrations in the European boundary layer, *Atmos. Chem. Phys.*, 11, 12007-12036, <https://doi.org/10.5194/acp-11-12007-2011>, 2011.
- Ren, X., Harder, H., Martinez, M., Leshner, R. L., Oligier, A., Simpas, J. B., Brune, W. H., Schwab, J. J., Demerjian, K. L., He, Y., Zhou, X., and Gao, H.: OH and HO₂ Chemistry in the urban atmosphere of New York City, *Atmospheric Environment*, 37, 3639-3651, [https://doi.org/10.1016/S1352-2310\(03\)00459-X](https://doi.org/10.1016/S1352-2310(03)00459-X), 2003.
- Reuder, J., Jonassen, M. O., and Ólafsson, H.: The Small Unmanned Meteorological Observer SUMO: Recent developments and applications of a micro-UAS for atmospheric boundary layer research, *Acta Geophysica*, 60, 1454-1473, <https://doi.org/10.2478/s11600-012-0042-8>, 2012.
- Reyes-Villegas, E., Bannan, T., Le Breton, M., Mehra, A., Priestley, M., Percival, C., Coe, H., and Allan, J. D.: Online Chemical Characterization of Food-Cooking Organic Aerosols: Implications for Source Apportionment, *Environmental Science & Technology*, 52, 5308-5318, <https://doi.org/10.1021/acs.est.7b06278>, 2018.
- Riedel, T. P., Bertram, T. H., Crisp, T. A., Williams, E. J., Lerner, B. M., Vlasenko, A., Li, S.-M., Gilman, J., de Gouw, J., Bon, D. M., Wagner, N. L., Brown, S. S., and Thornton, J. A.: Nitryl Chloride and Molecular Chlorine in the Coastal Marine Boundary Layer, *Environmental Science & Technology*, 46, 10463-10470, <https://doi.org/10.1021/es204632r>, 2012.
- Riedel, T. P., Wolfe, G. M., Danas, K. T., Gilman, J. B., Kuster, W. C., Bon, D. M., Vlasenko, A., Li, S. M., Williams, E. J., Lerner, B. M., Veres, P. R., Roberts, J. M., Holloway, J. S., Lefer, B., Brown, S. S., and Thornton, J. A.: An MCM modeling study of nitryl chloride (ClNO₂) impacts on oxidation, ozone production and nitrogen oxide partitioning in polluted continental outflow, *Atmospheric Chemistry and Physics*, 14, 3789-3800, <https://doi.org/10.5194/acp-14-3789-2014>, 2014.
- Rissanen, M. P., Mikkilä, J., Iyer, S., and Hakala, J.: Multi-scheme chemical ionization inlet (MION) for fast switching of reagent ion chemistry in atmospheric pressure chemical ionization mass spectrometry (CIMS) applications, *Atmospheric Measurement Techniques*, 12, 6635-6646, <https://doi.org/10.5194/amt-12-6635-2019>, 2019.
- Riva, M., Rantala, P., Krechmer, J. E., Peräkylä, O., Zhang, Y., Heikkinen, L., Garmash, O., Yan, C., Kulmala, M., Worsnop, D., and Ehn, M.: Evaluating the performance of five different chemical ionization techniques for detecting gaseous oxygenated organic species, *Atmos. Meas. Tech.*, 12, 2403-2421, <https://doi.org/10.5194/amt-12-2403-2019>, 2019.
- Roberts, G. C., Ramana, M. V., Corrigan, C., Kim, D., and Ramanathan, V.: Simultaneous observations of aerosol–cloud–albedo interactions with three stacked unmanned aerial vehicles, *Proceedings of the National Academy of Sciences*, 105, 7370-7375, <https://doi.org/10.1073/pnas.0710308105>, 2008.
- Roberts, J. M., Osthoff, H. D., Brown, S. S., Ravishankara, A. R., Coffman, D., Quinn, P., and Bates, T.: Laboratory studies of products of N₂O₅ uptake on Cl-containing substrates, *Geophysical Research Letters*, 36, <https://doi.org/10.1029/2009gl040448>, 2009.
- Röder, L. L., Ort, L. M., Lelieveld, J., and Fischer, H.: Determination of Temporal Stability and Instrument Performance of an airborne QCLAS via Allan-Werle-plots, <https://doi.org/10.21203/rs.3.rs-3619758/v1>, 2023.

- Roelofs, G.-J. and Lelieveld, J.: Model study of the influence of cross-tropopause O₃ transports on tropospheric O₃ levels, *Tellus B: Chemical and Physical Meteorology*, 49, 38, <https://doi.org/10.3402/tellusb.v49i1.15949>, 1997.
- Röhrl, A. and Lammel, G.: Determination of malic acid and other C₄ dicarboxylic acids in atmospheric aerosol samples, *Chemosphere*, 46, 1195-1199, [https://doi.org/10.1016/S0045-6535\(01\)00243-0](https://doi.org/10.1016/S0045-6535(01)00243-0), 2002.
- Rolph, G., Stein, A., and Stunder, B.: Real-time Environmental Applications and Display sYstem: READY, *Environmental Modelling & Software*, 95, 210-228, <https://doi.org/10.1016/j.envsoft.2017.06.025>, 2017.
- Rondo, L., Kürten, A., Ehrhart, S., Schobesberger, S., Franchin, A., Junninen, H., Petäjä, T., Sipilä, M., Worsnop, D. R., and Curtius, J.: Effect of ions on the measurement of sulfuric acid in the CLOUD experiment at CERN, *Atmos. Meas. Tech.*, 7, 3849-3859, <https://doi.org/10.5194/amt-7-3849-2014>, 2014.
- Rossabi, S., Choudoir, M., Helmig, D., Hueber, J., and Fierer, N.: Volatile Organic Compound Emissions From Soil Following Wetting Events, *Journal of Geophysical Research: Biogeosciences*, 123, 1988-2001, <https://doi.org/10.1029/2018jg004514>, 2018.
- Roth, A., Schneider, J., Klimach, T., Mertes, S., van Pinxteren, D., Herrmann, H., and Borrmann, S.: Aerosol properties, source identification, and cloud processing in orographic clouds measured by single particle mass spectrometry on a central European mountain site during HCCT-2010, *Atmos. Chem. Phys.*, 16, 505-524, <https://doi.org/10.5194/acp-16-505-2016>, 2016.
- Rowland, F. S.: Chlorofluorocarbons, Stratospheric Ozone, and the Antarctic 'Ozone Hole', *Environmental Conservation*, 15, 101-115, <https://doi.org/10.1017/S0376892900028897>, 1988.
- Ryan, B. F., Katzfey, J. J., Abbs, D. J., Jakob, C., Lohmann, U., Rockel, B., Rotstayn, L. D., Stewart, R. E., Szeto, K. K., Tselioudis, G., and Yau, M. K.: Simulations of a Cold Front by Cloud-Resolving, Limited-Area, and Large-Scale Models, and a Model Evaluation Using In Situ and Satellite Observations, *Monthly Weather Review*, 128, 3218-3235, [https://doi.org/10.1175/1520-0493\(2000\)128<3218:SOACFB>2.0.CO;2](https://doi.org/10.1175/1520-0493(2000)128<3218:SOACFB>2.0.CO;2), 2000.
- Saarikoski, S., Carbone, S., Decesari, S., Giulianelli, L., Angelini, F., Canagaratna, M., Ng, N. L., Trimborn, A., Facchini, M. C., Fuzzi, S., Hillamo, R., and Worsnop, D.: Chemical characterization of springtime submicrometer aerosol in Po Valley, Italy, *Atmos. Chem. Phys.*, 12, 8401-8421, [10.5194/acp-12-8401-2012](https://doi.org/10.5194/acp-12-8401-2012), 2012.
- Salcedo, D., Onasch, T. B., Dzepina, K., Canagaratna, M. R., Zhang, Q., Huffman, J. A., DeCarlo, P. F., Jayne, J. T., Mortimer, P., Worsnop, D. R., Kolb, C. E., Johnson, K. S., Zuberi, B., Marr, L. C., Volkamer, R., Molina, L. T., Molina, M. J., Cardenas, B., Bernabé, R. M., Márquez, C., Gaffney, J. S., Marley, N. A., Laskin, A., Shutthanandan, V., Xie, Y., Brune, W., Leshner, R., Shirley, T., and Jimenez, J. L.: Characterization of ambient aerosols in Mexico City during the MCMA-2003 campaign with Aerosol Mass Spectrometry: results from the CENICA Supersite, *Atmos. Chem. Phys.*, 6, 925-946, <https://doi.org/10.5194/acp-6-925-2006>, 2006.
- Savijärvi, H.: Radiative and turbulent heating rates in the clear-air boundary layer, *Quarterly Journal of the Royal Meteorological Society*, 132, 147-161, <https://doi.org/10.1256/qj.05.61>, 2006.
- Sawyer, V. and Li, Z.: Detection, variations and intercomparison of the planetary boundary layer depth from radiosonde, lidar and infrared spectrometer, *Atmospheric environment*, 79, 518-528, <https://doi.org/10.1016/j.atmosenv.2013.07.019>, 2013.
- Schauer, J. J., Kleeman, M. J., Cass, G. R., and Simoneit, B. R. T.: Measurement of Emissions from Air Pollution Sources. 2. C₁ through C₃₀ Organic Compounds from Medium Duty Diesel Trucks, *Environmental Science & Technology*, 33, 1578-1587, <https://doi.org/10.1021/es980081n>, 1999.
- Schauer, J. J., Kleeman, M. J., Cass, G. R., and Simoneit, B. R. T.: Measurement of Emissions from Air Pollution Sources. 5. C₁-C₃₂ Organic Compounds from Gasoline-Powered Motor Vehicles, *Environmental Science & Technology*, 36, 1169-1180, <https://doi.org/10.1021/es0108077>, 2002a.
- Schauer, J. J., Kleeman, M. J., Cass, G. R., and Simoneit, B. R. T.: Measurement of Emissions from Air Pollution Sources. 4. C₁-C₂₇ Organic Compounds from Cooking with Seed Oils, *Environmental Science & Technology*, 36, 567-575, <https://doi.org/10.1021/es002053m>, 2002b.

- Schlemmer, L. and Hohenegger, C.: The Formation of Wider and Deeper Clouds as a Result of Cold-Pool Dynamics, *Journal of the Atmospheric Sciences*, 71, 2842-2858, <https://doi.org/10.1175/jas-d-13-0170.1>, 2014.
- Schmetz, J., Pili, P., Tjemkes, S., Just, D., Kerkmann, J., Rota, S., and Ratier, A.: An introduction to Meteosat second generation (MSG), *Bulletin of the American Meteorological Society*, 83, 977-992, 2002.
- Schneider, J., Weimer, S., Drewnick, F., Borrmann, S., Helas, G., Gwaze, P., Schmid, O., Andreae, M. O., and Kirchner, U.: Mass spectrometric analysis and aerodynamic properties of various types of combustion-related aerosol particles, *International Journal of Mass Spectrometry*, 258, 37-49, <https://doi.org/10.1016/j.ijms.2006.07.008>, 2006.
- Schrod, J., Thomson, E. S., Weber, D., Kossmann, J., Pöhlker, C., Saturno, J., Ditas, F., Artaxo, P., Clouard, V., Saurel, J.-M., Ebert, M., Curtius, J., and Bingemer, H. G.: Long-term deposition and condensation ice-nucleating particle measurements from four stations across the globe, *Atmospheric Chemistry and Physics*, 20, 15983-16006, <https://doi.org/10.5194/acp-20-15983-2020>, 2020.
- Schröder, B., Fulem, M., and Martins, M. A. R.: Vapor pressure predictions of multi-functional oxygen-containing organic compounds with COSMO-RS, *Atmospheric Environment*, 133, 135-144, <https://doi.org/10.1016/j.atmosenv.2016.03.036>, 2016.
- Schuldt, T., Gkatzelis, G. I., Wesolek, C., Rohrer, F., Winter, B., Kuhlbusch, T. A. J., Kiendler-Scharr, A., and Tillmann, R.: Electrochemical sensors on board a Zeppelin NT: in-flight evaluation of low-cost trace gas measurements, *Atmos. Meas. Tech.*, 16, 373-386, <https://doi.org/10.5194/amt-16-373-2023>, 2023.
- Schulten, H. R. and Schurath, U.: Analysis of aerosols from the ozonolysis of 1-butene by high-resolution field desorption mass spectrometry, *The Journal of Physical Chemistry*, 79, 51-57, <https://doi.org/10.1021/j100568a012>, 1975.
- Schwantes, R. H., Charan, S. M., Bates, K. H., Huang, Y., Nguyen, T. B., Mai, H., Kong, W., Flagan, R. C., and Seinfeld, J. H.: Low-volatility compounds contribute significantly to isoprene secondary organic aerosol (SOA) under high-NO_x conditions, *Atmos. Chem. Phys.*, 19, 7255-7278, <https://doi.org/10.5194/acp-19-7255-2019>, 2019.
- Schweitzer, F., Mirabel, P., and George, C.: Multiphase Chemistry of N₂O₅, ClNO₂, and BrNO₂, *The Journal of Physical Chemistry A*, 102, 3942-3952, <https://doi.org/10.1021/jp980748s>, 1998.
- Seidel, D. J., Ao, C. O., and Li, K.: Estimating climatological planetary boundary layer heights from radiosonde observations: Comparison of methods and uncertainty analysis, *Journal of Geophysical Research: Atmospheres*, 115, <https://doi.org/10.1029/2009JD013680>, 2010.
- Shao, Y., Voliotis, A., Du, M., Wang, Y., Pereira, K., Hamilton, J., Alfarra, M. R., and McFiggans, G.: Chemical composition of secondary organic aerosol particles formed from mixtures of anthropogenic and biogenic precursors, *Atmos. Chem. Phys.*, 22, 9799-9826, <https://doi.org/10.5194/acp-22-9799-2022>, 2022.
- Shrivastava, M., Cappa, C. D., Fan, J., Goldstein, A. H., Guenther, A. B., Jimenez, J. L., Kuang, C., Laskin, A., Martin, S. T., Ng, N. L., Petaja, T., Pierce, J. R., Rasch, P. J., Roldin, P., Seinfeld, J. H., Shilling, J., Smith, J. N., Thornton, J. A., Volkamer, R., Wang, J., Worsnop, D. R., Zaveri, R. A., Zelenyuk, A., and Zhang, Q.: Recent advances in understanding secondary organic aerosol: Implications for global climate forcing, *Reviews of Geophysics*, 55, 509-559, <https://doi.org/10.1002/2016rg000540>, 2017.
- Si, Y., Lu, Q., Zhang, X., Hu, X., Wang, F., Li, L., and Gu, S.: A review of advances in the retrieval of aerosol properties by remote sensing multi-angle technology, *Atmospheric Environment*, 244, 117928, <https://doi.org/10.1016/j.atmosenv.2020.117928>, 2021.
- Simoneit, B. R. T., Rogge, W. F., Lang, Q., and Jaffé, R.: Molecular characterization of smoke from campfire burning of pine wood (*Pinus elliotii*), *Chemosphere - Global Change Science*, 2, 107-122, [https://doi.org/10.1016/S1465-9972\(99\)00048-3](https://doi.org/10.1016/S1465-9972(99)00048-3), 2000.
- Sindelarova, K., Granier, C., Bouarar, I., Guenther, A., Tilmes, S., Stavrou, T., Müller, J. F., Kuhn, U., Stefani, P., and Knorr, W.: Global data set of biogenic VOC emissions calculated by the MEGAN model over the last 30 years, *Atmos. Chem. Phys.*, 14, 9317-9341, <https://doi.org/10.5194/acp-14-9317-2014>, 2014.

- Smith, D. M., Cui, T., Fiddler, M. N., Pokhrel, R. P., Surratt, J. D., and Bililign, S.: Laboratory studies of fresh and aged biomass burning aerosol emitted from east African biomass fuels – Part 2: Chemical properties and characterization, *Atmos. Chem. Phys.*, 20, 10169-10191, <https://doi.org/10.5194/acp-20-10169-2020>, 2020.
- Smith, J. S., Laskin, A., and Laskin, J.: Molecular Characterization of Biomass Burning Aerosols Using High-Resolution Mass Spectrometry, *Analytical Chemistry*, 81, 1512-1521, <https://doi.org/10.1021/ac8020664>, 2009.
- Sobanski, N., Schuladen, J., Schuster, G., Lelieveld, J., and Crowley, J. N.: A five-channel cavity ring-down spectrometer for the detection of NO₂, NO₃, N₂O₅, total peroxy nitrates and total alkyl nitrates, *Atmospheric Measurement Techniques*, 9, 5103-5118, <https://doi.org/10.5194/amt-9-5103-2016>, 2016.
- Solomon, S.: Stratospheric ozone depletion: A review of concepts and history, *Reviews of Geophysics*, 37, 275-316, <https://doi.org/10.1029/1999rg900008>, 1999.
- Spicer, C. W., Chapman, E. G., Finlayson-Pitts, B. J., Plastridge, R. A., Hubbe, J. M., Fast, J. D., and Berkowitz, C. M.: Unexpectedly high concentrations of molecular chlorine in coastal air, *Nature*, 394, 353-356, <https://doi.org/10.1038/28584>, 1998.
- Spielmann, F. M., Langebner, S., Ghirardo, A., Hansel, A., Schnitzler, J.-P., and Wohlfahrt, G.: Isoprene and α -pinene deposition to grassland mesocosms, *Plant and Soil*, 410, 313-322, <https://doi.org/10.1007/s11104-016-3009-8>, 2017.
- Sprenger, M. and Wernli, H.: The LAGRANTO Lagrangian analysis tool – version 2.0, *Geoscientific Model Development*, 8, 2569-2586, <https://doi.org/10.5194/gmd-8-2569-2015>, 2015.
- Stavroulas, I., Bougiatioti, A., Grivas, G., Paraskevopoulou, D., Tsagkaraki, M., Zampas, P., Liakakou, E., Gerasopoulos, E., and Mihalopoulos, N.: Sources and processes that control the submicron organic aerosol composition in an urban Mediterranean environment (Athens): a high temporal-resolution chemical composition measurement study, *Atmos. Chem. Phys.*, 19, 901-919, <https://doi.org/10.5194/acp-19-901-2019>, 2019.
- Steenefeld, G.-J.: Current challenges in understanding and forecasting stable boundary layers over land and ice, *Frontiers in Environmental Science*, 2, <https://doi.org/10.3389/fenvs.2014.00041>, 2014.
- Stein, A. F., Draxler, R. R., Rolph, G. D., Stunder, B. J. B., Cohen, M. D., and Ngan, F.: NOAA's HYSPLIT Atmospheric Transport and Dispersion Modeling System, *Bulletin of the American Meteorological Society*, 96, 2059-2077, <https://doi.org/10.1175/bams-d-14-00110.1>, 2015.
- Struckmeier, C., Drewnick, F., Fachinger, F., Gobbi, G. P., and Borrmann, S.: Atmospheric aerosols in Rome, Italy: sources, dynamics and spatial variations during two seasons, *Atmos. Chem. Phys.*, 16, 15277-15299, <https://doi.org/10.5194/acp-16-15277-2016>, 2016.
- Stull, R. B.: An Introduction to Boundary Layer Meteorology, *Atmospheric and Oceanographic Sciences Library*, <https://doi.org/10.1007/978-94-009-3027-8>, 1988.
- Stull, R. B.: *Practical Meteorology : An Algebra-based Survey of Atmospheric Science*, 10.14288/1.0300441, 2015.
- Sun, Y. L., Zhang, Q., Schwab, J. J., Demerjian, K. L., Chen, W. N., Bae, M. S., Hung, H. M., Hogrefe, O., Frank, B., Rattigan, O. V., and Lin, Y. C.: Characterization of the sources and processes of organic and inorganic aerosols in New York city with a high-resolution time-of-flight aerosol mass spectrometer, *Atmos. Chem. Phys.*, 11, 1581-1602, <https://doi.org/10.5194/acp-11-1581-2011>, 2011.
- Sutapa, I. W., Kasmanto, D. A., Rosmawaty, and Maahury, M. F.: Biodiesel cracking process from beef tallow using catalyst bentonite intercalated NiCl₂, 2021, <https://dx.doi.org/10.1063/5.0059518>, 2021.
- Szintai, B., Kaufmann, P., and Rotach, M. W.: Simulation of Pollutant Transport in Complex Terrain with a Numerical Weather Prediction–Particle Dispersion Model Combination, *Boundary-Layer Meteorology*, 137, 373-396, <https://doi.org/10.1007/s10546-010-9541-9>, 2010.
- Sziroczak, D., Rohacs, D., and Rohacs, J.: Review of using small UAV based meteorological measurements for road weather management, *Progress in Aerospace Sciences*, 134, 100859, <https://doi.org/10.1016/j.paerosci.2022.100859>, 2022.

- Szmigielski, R., Surratt, J. D., Vermeylen, R., Szmigielska, K., Kroll, J. H., Ng, N. L., Murphy, S. M., Sorooshian, A., Seinfeld, J. H., and Claeys, M.: Characterization of 2-methylglyceric acid oligomers in secondary organic aerosol formed from the photooxidation of isoprene using trimethylsilylation and gas chromatography/ion trap mass spectrometry, *Journal of Mass Spectrometry*, 42, 101-116, <https://doi.org/10.1002/jms.1146>, 2007.
- Tang, J., Li, J., Su, T., Han, Y., Mo, Y., Jiang, H., Cui, M., Jiang, B., Chen, Y., Tang, J., Song, J., Peng, P., and Zhang, G.: Molecular compositions and optical properties of dissolved brown carbon in biomass burning, coal combustion, and vehicle emission aerosols illuminated by excitation–emission matrix spectroscopy and Fourier transform ion cyclotron resonance mass spectrometry analysis, *Atmos. Chem. Phys.*, 20, 2513-2532, <https://doi.org/10.5194/acp-20-2513-2020>, 2020.
- Teiwes, R., Elm, J., Bilde, M., and Pedersen, H. B.: The reaction of hydrated iodide I(H₂O)_n- with ozone: a new route to IO₂-products, *Physical Chemistry Chemical Physics*, 21, 17546-17554, <https://doi.org/10.1039/c9cp01734h>, 2019.
- Tham, Y. J., Yan, C., Xue, L., Zha, Q., Wang, X., and Wang, T.: Presence of high nitryl chloride in Asian coastal environment and its impact on atmospheric photochemistry, *Chinese Science Bulletin*, 59, 356-359, <https://doi.org/10.1007/s11434-013-0063-y>, 2014.
- Thielicke, W., Hübert, W., Müller, U., Eggert, M., and Wilhelm, P.: Towards accurate and practical drone-based wind measurements with an ultrasonic anemometer, *Atmospheric Measurement Techniques*, 14, 1303-1318, <https://doi.org/10.5194/amt-14-1303-2021>, 2021.
- Thieser, J., Schuster, G., Schuladen, J., Phillips, G. J., Reiffs, A., Parchatka, U., Pöhler, D., Lelieveld, J., and Crowley, J. N.: A two-channel thermal dissociation cavity ring-down spectrometer for the detection of ambient NO₂, RO₂NO₂ and RONO₂, *Atmos. Meas. Tech.*, 9, 553-576, <https://doi.org/10.5194/amt-9-553-2016>, 2016.
- Thivet, S., Bagheri, G., Kornatowski, P. M., Fries, A., Lemus, J., Simionato, R., Díaz-Vecino, C., Rossi, E., Yamada, T., Scollo, S., and Bonadonna, C.: In situ volcanic ash sampling and aerosol–gas analysis based on UAS technologies (AeroVolc), *Atmos. Meas. Tech.*, 18, 2803-2824, <https://doi.org/10.5194/amt-18-2803-2025>, 2025.
- Thornton, J. A., Kercher, J. P., Riedel, T. P., Wagner, N. L., Cozic, J., Holloway, J. S., Dubé, W. P., Wolfe, G. M., Quinn, P. K., Middlebrook, A. M., Alexander, B., and Brown, S. S.: A large atomic chlorine source inferred from mid-continental reactive nitrogen chemistry, *Nature*, 464, 271-274, <https://doi.org/10.1038/nature08905>, 2010.
- Tignat-Perrier, R., Dommergue, A., Vogel, T. M., and Larose, C.: Microbial Ecology of the Planetary Boundary Layer, *Atmosphere*, 11, 1296, <https://doi.org/10.3390/atmos11121296>, 2020.
- Tolbert, M. A., Rossi, M. J., Malhotra, R., and Golden, D. M.: Reaction of Chlorine Nitrate with Hydrogen Chloride and Water at Antarctic Stratospheric Temperatures, *Science*, 238, 1258-1260, <https://doi.org/10.1126/science.238.4831.1258>, 1987.
- Tompkins, A. M.: Organization of Tropical Convection in Low Vertical Wind Shears: The Role of Cold Pools, *Journal of the Atmospheric Sciences*, 58, 1650-1672, [https://doi.org/10.1175/1520-0469\(2001\)058<1650:OOTCIL>2.0.CO;2](https://doi.org/10.1175/1520-0469(2001)058<1650:OOTCIL>2.0.CO;2), 2001.
- Tong, Y., Qi, L., Stefanelli, G., Wang, D. S., Canonaco, F., Baltensperger, U., Prévôt, A. S. H., and Slowik, J. G.: Quantification of primary and secondary organic aerosol sources by combined factor analysis of extractive electrospray ionisation and aerosol mass spectrometer measurements (EESI-TOF and AMS), *Atmos. Meas. Tech.*, 15, 7265-7291, <https://doi.org/10.5194/amt-15-7265-2022>, 2022.
- Troen, I. B. and Mahrt, L.: A simple model of the atmospheric boundary layer; sensitivity to surface evaporation, *Boundary-Layer Meteorology*, 37, 129-148, <https://doi.org/10.1007/bf00122760>, 1986.
- Tsamalis, C., Ravetta, F., Gheusi, F., Delbarre, H., and Augustin, P.: Mixing of free-tropospheric air with the lowland boundary layer during anabatic transport to a high altitude station, *Atmospheric Research*, 143, 425-437, <https://doi.org/10.1016/j.atmosres.2014.03.011>, 2014.
- UBA: Station Database of the Environmental Agency, German Environmental Agency, <https://www.env-it.de/stationen/public/language.do;jsessionid=301985B5B53A47A60F18CE16DCEDC92E?language=en>, Access Date, 2025

- TUV Calculator: https://www.acom.ucar.edu/Models/TUV/Interactive_TUV/, last access: 15.06.2025.
- Ulbrich, I., Canagaratna, M., Zhang, Q., Worsnop, D., and Jimenez, J.: Interpretation of organic components from Positive Matrix Factorization of aerosol mass spectrometric data, *Atmospheric Chemistry and Physics*, 9, 2891-2918, <https://doi.org/10.5194/acp-9-2891-2009>, 2009.
- Ulbrich, I. M., Handschy, A., Lechner, M., and Jimenez, J. L.: High-Resolution AMS Spectral Database, University of Colorado [dataset], <http://cires.colorado.edu/jimenez-group/HRAMSsd/>, 2022.
- Vaisala: User's Guide: Vaisala CARBOCAP Carbon Dioxide Probe GMP343, 2013.
- Van Brussel, S. and Huyse, H.: Citizen science on speed? Realising the triple objective of scientific rigour, policy influence and deep citizen engagement in a large-scale citizen science project on ambient air quality in Antwerp, *Journal of Environmental Planning and Management*, 62, 534-551, <https://doi.org/10.1080/09640568.2018.1428183>, 2019.
- Vettikkat, L., Miettinen, P., Buchholz, A., Rantala, P., Yu, H., Schallhart, S., Petäjä, T., Seco, R., Männistö, E., Kulmala, M., Tuittila, E. S., Guenther, A. B., and Schobesberger, S.: High emission rates and strong temperature response make boreal wetlands a large source of isoprene and terpenes, *Atmos. Chem. Phys.*, 23, 2683-2698, <https://doi.org/10.5194/acp-23-2683-2023>, 2023.
- Vickers, D. and Mahrt, L.: Observations of non-dimensional wind shear in the coastal zone, *Quarterly Journal of the Royal Meteorological Society*, 125, 2685-2702, <https://doi.org/10.1002/qj.49712555917>, 1999.
- Villa, T. F., Gonzalez, F., Miljevic, B., Ristovski, Z. D., and Morawska, L.: An Overview of Small Unmanned Aerial Vehicles for Air Quality Measurements: Present Applications and Future Perspectives, *Sensors (Basel)*, 16, <https://doi.org/10.3390/s16071072>, 2016.
- Volpe, C., Wahlen, M., Pszenny, A. A. P., and Spivack, A. J.: Chlorine isotopic composition of marine aerosols: Implications for the release of reactive chlorine and HCl cycling rates, *Geophysical Research Letters*, 25, 3831-3834, <https://doi.org/10.1029/1998gl900038>, 1998.
- Von Clarmann, T. and Johansson, S.: Chlorine nitrate in the atmosphere, *Atmospheric Chemistry and Physics*, 18, 15363-15386, <https://doi.org/10.5194/acp-18-15363-2018>, 2018.
- von der Weiden-Reinmüller, S. L., Drewnick, F., Crippa, M., Prévôt, A. S. H., Meleux, F., Baltensperger, U., Beekmann, M., and Borrmann, S.: Application of mobile aerosol and trace gas measurements for the investigation of megacity air pollution emissions: the Paris metropolitan area, *Atmos. Meas. Tech.*, 7, 279-299, <https://doi.org/10.5194/amt-7-279-2014>, 2014.
- Von Hobe, M., Groöß, J. U., Müller, R., Hrechanyy, S., Winkler, U., and Stroh, F.: A re-evaluation of the ClO/Cl₂O₂ equilibrium constant based on stratospheric in-situ observations, *Atmospheric Chemistry and Physics*, 5, 693-702, <https://doi.org/10.5194/acp-5-693-2005>, 2005.
- Wang, H. and Lee, Y.-P.: Infrared Spectrum of the Adduct 2-Chloro-2-hydroperoxybut-3-ene [(C₂H₃)CCl(CH₃)OOH] of the Reaction between the Criegee Intermediate Methyl Vinyl Ketone Oxide [C₂H₃C(CH₃)OO] and HCl, *The Journal of Physical Chemistry A*, 128, 8690-8698, <https://doi.org/10.1021/acs.jpca.4c04936>, 2024.
- Wang, H., Kawamura, K., Ho, K. F., and Lee, S. C.: Low Molecular Weight Dicarboxylic Acids, Ketoacids, and Dicarbonyls in the Fine Particles from a Roadway Tunnel: Possible Secondary Production from the Precursors, *Environmental Science & Technology*, 40, 6255-6260, <https://doi.org/10.1021/es060732c>, 2006.
- Wang, H., Gao, Y., Wang, S., Wu, X., Liu, Y., Li, X., Huang, D., Lou, S., Wu, Z., Guo, S., Jing, S., Li, Y., Huang, C., Tyndall, G. S., Orlando, J. J., and Zhang, X.: Atmospheric Processing of Nitrophenols and Nitrocresols From Biomass Burning Emissions, *Journal of Geophysical Research: Atmospheres*, 125, <https://doi.org/10.1029/2020jd033401>, 2020.
- Wang, P. K., Shih-Hao, S., Charvát, Z., Štástka, J., and Hsin-Mu, L.: Cross tropopause transport of water by mid-latitude deep convective storms: A review, *TAO: Terrestrial, Atmospheric and Oceanic Sciences*, 22, 4, [https://doi.org/10.3319/TAO.2011.06.13.01\(A\)](https://doi.org/10.3319/TAO.2011.06.13.01(A)), 2011.
- Wang, R., Zhu, Y., Qiao, F., Liang, X.-Z., Zhang, H., and Ding, Y.: High-resolution Simulation of an Extreme Heavy Rainfall Event in Shanghai Using the Weather Research and Forecasting Model: Sensitivity to Planetary Boundary Layer Parameterization, *Advances in Atmospheric Sciences*, 38, 98-115, <https://doi.org/10.1007/s00376-020-9255-y>, 2021.

- Wang, X., Xu, J., Wu, S., Wang, Q., Dai, G., Zhu, P., Su, Z., Chen, S., Shi, X., and Fan, M.: Evolution of wind field in the atmospheric boundary layer using multiple-source observations during the passage of Super Typhoon Doksuri (2305), *Atmospheric Measurement Techniques*, 18, 3305-3320, <https://doi.org/10.5194/amt-18-3305-2025>, 2025.
- Wang, X., Wang, H., Xue, L., Wang, T., Wang, L., Gu, R., Wang, W., Tham, Y. J., Wang, Z., Yang, L., Chen, J., and Wang, W.: Observations of N₂O₅ and ClNO₂ at a polluted urban surface site in North China: High N₂O₅ uptake coefficients and low ClNO₂ product yields, *Atmospheric Environment*, 156, 125-134, <https://doi.org/10.1016/j.atmosenv.2017.02.035>, 2017.
- Wang, X., Jacob, D. J., Eastham, S. D., Sulprizio, M. P., Zhu, L., Chen, Q., Alexander, B., Sherwen, T., Evans, M. J., Lee, B. H., Haskins, J. D., Lopez-Hilfiker, F. D., Thornton, J. A., Huey, G. L., and Liao, H.: The role of chlorine in global tropospheric chemistry, *Atmospheric Chemistry and Physics*, 19, 3981-4003, <https://doi.org/10.5194/acp-19-3981-2019>, 2019.
- Wang, X. Y. and Wang, K. C.: Estimation of atmospheric mixing layer height from radiosonde data, *Atmospheric Measurement Techniques*, 7, 1701-1709, <https://doi.org/10.5194/amt-7-1701-2014>, 2014.
- Wayne, R. P., Poulet, G., Biggs, P., Burrows, J. P., Cox, R. A., Crutzen, P. J., Hayman, G. D., Jenkin, M. E., Le Bras, G., Moortgat, G. K., Platt, U., and Schindler, R. N.: Halogen oxides: Radicals, sources and reservoirs in the laboratory and in the atmosphere, *Atmospheric Environment*, 29, 2677-2881, [https://doi.org/10.1016/1352-2310\(95\)98124-Q](https://doi.org/10.1016/1352-2310(95)98124-Q), 1995.
- Wei, P., Cheng, S., Li, J., and Su, F.: Impact of boundary-layer anticyclonic weather system on regional air quality, *Atmospheric Environment*, 45, 2453-2463, <https://doi.org/10.1016/j.atmosenv.2011.01.045>, 2011.
- Werle, P., Mücke, R., and Slemr, F.: The limits of signal averaging in atmospheric trace-gas monitoring by tunable diode-laser absorption spectroscopy (TDLAS), *Applied Physics B Photophysics and Laser Chemistry*, 57, 131-139, <https://doi.org/10.1007/bf00425997>, 1993.
- Whitehead, K. and Hugenholtz, C. H.: Remote sensing of the environment with small unmanned aircraft systems (UASs), part 1: a review of progress and challenges, *Journal of Unmanned Vehicle Systems*, 02, 69-85, <https://doi.org/10.1139/juvs-2014-0006>, 2014.
- WHO: WHO global air quality guidelines. Particulate matter (PM_{2.5} and PM₁₀), ozone, nitrogen dioxide, sulfur dioxide and carbon monoxide., World Health Organization 2021.
- Wildmann, N. and Wetz, T.: Towards vertical wind and turbulent flux estimation with multicopter uncrewed aircraft systems, *Atmospheric Measurement Techniques*, 15, 5465-5477, <https://doi.org/10.5194/amt-15-5465-2022>, 2022.
- Williams, B., Goldstein, A., Kreisberg, N., Hering, S., Worsnop, D., Ulbrich, I., Docherty, K., and Jimenez, J.: Major components of atmospheric organic aerosol in southern California as determined by hourly measurements of source marker compounds, *Atmospheric Chemistry and Physics*, 10, 11577-11603, <https://doi.org/10.5194/acp-10-11577-2010>, 2010.
- Williams, B. J., Goldstein, A. H., Kreisberg, N. M., and Hering, S. V.: An In-Situ Instrument for Speciated Organic Composition of Atmospheric Aerosols: Thermal Desorption Aerosol GC/MS-FID (TAG), *Aerosol Science and Technology*, 40, 627-638, <https://doi.org/10.1080/02786820600754631>, 2006.
- Williams, J., Crowley, J., Fischer, H., Harder, H., Martinez, M., Petäjä, T., Rinne, J., Bäck, J., Boy, M., Dal Maso, M., Hakala, J., Kajos, M., Keronen, P., Rantala, P., Aalto, J., Aaltonen, H., Paatero, J., Vesala, T., Hakola, H., Levula, J., Pohja, T., Herrmann, F., Auld, J., Mesarchaki, E., Song, W., Yassaa, N., Nölscher, A., Johnson, A. M., Custer, T., Sinha, V., Thieser, J., Pouvesle, N., Taraborrelli, D., Tang, M. J., Bozem, H., Hosaynali-Beygi, Z., Axinte, R., Oswald, R., Novelli, A., Kubistin, D., Hens, K., Javed, U., Trawny, K., Breitenberger, C., Hidalgo, P. J., Ebben, C. J., Geiger, F. M., Corrigan, A. L., Russell, L. M., Ouwersloot, H. G., Vilà-Guerau de Arellano, J., Ganzeveld, L., Vogel, A., Beck, M., Bayerle, A., Kampf, C. J., Bertelmann, M., Köllner, F., Hoffmann, T., Valverde, J., González, D., Riekkola, M. L., Kulmala, M., and Lelieveld, J.: The summertime Boreal forest field measurement intensive (HUMPPA-COPEC-2010): an overview of meteorological and chemical influences, *Atmos. Chem. Phys.*, 11, 10599-10618, <https://doi.org/10.5194/acp-11-10599-2011>, 2011.

- Wilson, T. H. and Fovell, R. G.: Modeling the Evolution and Life Cycle of Stable Cold Pools, *Weather and Forecasting*, 31, 1753-1769, <https://doi.org/10.1175/WAF-D-16-0108.1>, 2016.
- Womack, C. C., Brown, S. S., Ciciora, S. J., Gao, R. S., McLaughlin, R. J., Robinson, M. A., Rudich, Y., and Washenfelder, R. A.: A lightweight broadband cavity-enhanced spectrometer for NO₂ measurement on uncrewed aerial vehicles, *Atmos. Meas. Tech.*, 15, 6643-6652, <https://doi.org/10.5194/amt-15-6643-2022>, 2022.
- Woolfenden, E.: Sorbent-based sampling methods for volatile and semi-volatile organic compounds in air. Part 2. Sorbent selection and other aspects of optimizing air monitoring methods, *Journal of Chromatography A*, 1217, 2685-2694, <https://doi.org/10.1016/j.chroma.2010.01.015>, 2010.
- Wyngaard, J. C. and LeMone, M. A.: Behavior of the Refractive Index Structure Parameter in the Entraining Convective Boundary Layer, *Journal of Atmospheric Sciences*, 37, 1573-1585, [https://doi.org/10.1175/1520-0469\(1980\)037<1573:BOTRIS>2.0.CO;2](https://doi.org/10.1175/1520-0469(1980)037<1573:BOTRIS>2.0.CO;2), 1980.
- Xia, M., Peng, X., Wang, W., Yu, C., Sun, P., Li, Y., Liu, Y., Xu, Z., Wang, Z., Xu, Z., Nie, W., Ding, A., and Wang, T.: Significant production of ClNO₂ and possible source of Cl₂ from N₂O₅ uptake at a suburban site in eastern China, *Atmospheric Chemistry and Physics*, 20, 6147-6158, <https://doi.org/10.5194/acp-20-6147-2020>, 2020.
- Xu, W., He, Y., Qiu, Y., Chen, C., Xie, C., Lei, L., Li, Z., Sun, J., Li, J., Fu, P., Wang, Z., Worsnop, D. R., and Sun, Y.: Mass spectral characterization of primary emissions and implications in source apportionment of organic aerosol, *Atmos. Meas. Tech.*, 13, 3205-3219, <https://doi.org/10.5194/amt-13-3205-2020>, 2020.
- Yang, F., He, Q., Huang, J., Mamtimin, A., Yang, X., Huo, W., Zhou, C., Liu, X., Wei, W., Cui, C., Wang, M., Li, H., Yang, L., Zhang, H., Liu, Y., Zheng, X., Pan, H., Jin, L., Zou, H., Zhou, L., Liu, Y., Zhang, J., Meng, L., Wang, Y., Qin, X., Yao, Y., Liu, H., Xue, F., and Zheng, W.: Desert Environment and Climate Observation Network over the Taklimakan Desert, *Bulletin of the American Meteorological Society*, 102, E1172-E1191, <https://doi.org/10.1175/BAMS-D-20-0236.1>, 2020.
- Yang, L. H., Takeuchi, M., Chen, Y., and Ng, N. L.: Characterization of thermal decomposition of oxygenated organic compounds in FIGAERO-CIMS, *Aerosol Science and Technology*, 55, 1321-1342, <https://doi.org/10.1080/02786826.2021.1945529>, 2021.
- Yatavelli, R., Stark, H., Thompson, S., Kimmel, J., Cubison, M., Day, D., Campuzano-Jost, P., Palm, B., Hodzic, A., and Thornton, J.: Semicontinuous measurements of gas-particle partitioning of organic acids in a ponderosa pine forest using a MOVI-HRToF-CIMS, *Atmospheric Chemistry and Physics*, 14, 1527-1546, <https://doi.org/10.5194/acp-14-1527-2014>, 2014.
- Yatavelli, R. L. N., Lopez-Hilfiker, F., Wargo, J. D., Kimmel, J. R., Cubison, M. J., Bertram, T. H., Jimenez, J. L., Gonin, M., Worsnop, D. R., and Thornton, J. A.: A Chemical Ionization High-Resolution Time-of-Flight Mass Spectrometer Coupled to a Micro Orifice Volatilization Impactor (MOVI-HRToF-CIMS) for Analysis of Gas and Particle-Phase Organic Species, *Aerosol Science and Technology*, 46, 1313-1327, <https://doi.org/10.1080/02786826.2012.712236>, 2012.
- Ye, C., Yuan, B., Lin, Y., Wang, Z., Hu, W., Li, T., Chen, W., Wu, C., Wang, C., Huang, S., Qi, J., Wang, B., Wang, C., Song, W., Wang, X., Zheng, E., Krechmer, J. E., Ye, P., Zhang, Z., Wang, X., Worsnop, D. R., and Shao, M.: Chemical characterization of oxygenated organic compounds in the gas phase and particle phase using iodide CIMS with FIGAERO in urban air, *Atmos. Chem. Phys.*, 21, 8455-8478, <https://doi.org/10.5194/acp-21-8455-2021>, 2021.
- Yee, L. D., Kautzman, K. E., Loza, C. L., Schilling, K. A., Coggon, M. M., Chhabra, P. S., Chan, M. N., Chan, A. W. H., Hersey, S. P., Crouse, J. D., Wennberg, P. O., Flagan, R. C., and Seinfeld, J. H.: Secondary organic aerosol formation from biomass burning intermediates: phenol and methoxyphenols, *Atmos. Chem. Phys.*, 13, 8019-8043, <https://doi.org/10.5194/acp-13-8019-2013>, 2013.
- Young, C. J., Joudan, S., Tao, Y., Wentzell, J. J. B., and Liggio, J.: High Time Resolution Ambient Observations of Gas-Phase Perfluoroalkyl Carboxylic Acids: Implications for Atmospheric Sources, *Environmental Science & Technology Letters*, 11, 1348-1354, <https://doi.org/10.1021/acs.estlett.4c00897>, 2024.
- Young, C. J., Washenfelder, R. A., Roberts, J. M., Mielke, L. H., Osthoff, H. D., Tsai, C., Pikelnaya, O., Stutz, J., Veres, P. R., and Cochran, A. K.: Vertically resolved measurements of nighttime radical

- reservoirs in Los Angeles and their contribution to the urban radical budget, *Environmental science & technology*, 46, 10965-10973, <https://doi.org/10.1021/es302206a>, 2012.
- Young, G. S., Perugini, S. M., and Fairall, C. W.: Convective Wakes in the Equatorial Western Pacific during TOGA, *Monthly Weather Review*, 123, 110-123, [https://doi.org/10.1175/1520-0493\(1995\)123<0110:CWITEW>2.0.CO;2](https://doi.org/10.1175/1520-0493(1995)123<0110:CWITEW>2.0.CO;2), 1995.
- Zängl, G., Reinert, D., Rípodas, P., and Baldauf, M.: The ICON (ICOsahedral Non-hydrostatic) modelling framework of DWD and MPI-M: Description of the non-hydrostatic dynamical core, *Quarterly Journal of the Royal Meteorological Society*, 141, 563-579, <https://doi.org/10.1002/qj.2378>, 2015.
- Zhang, L., Hu, B., Liu, X., Luo, Z., Xing, R., Li, Y., Xiong, R., Li, G., Cheng, H., Lu, Q., Shen, G., and Tao, S.: Variabilities in Primary N-Containing Aromatic Compound Emissions from Residential Solid Fuel Combustion and Implications for Source Tracers, *Environmental Science & Technology*, 56, 13622-13633, <https://doi.org/10.1021/acs.est.2c03000>, 2022.
- Zhang, W. and Zhang, H.: Secondary Ion Chemistry Mediated by Ozone and Acidic Organic Molecules in Iodide-Adduct Chemical Ionization Mass Spectrometry, *Analytical Chemistry*, 93, 8595-8602, <https://doi.org/10.1021/acs.analchem.1c01486>, 2021.
- Zhang, Y., Wang, K., Tong, H., Huang, R. J., and Hoffmann, T.: The maximum carbonyl ratio (MCR) as a new index for the structural classification of secondary organic aerosol components, *Rapid Communications in Mass Spectrometry*, 35, <https://doi.org/10.1002/rcm.9113>, 2021.
- Zhao, D., Pullinen, I., Fuchs, H., Schrade, S., Wu, R., Acir, I. H., Tillmann, R., Rohrer, F., Wildt, J., Guo, Y., Kiendler-Scharr, A., Wahner, A., Kang, S., Vereecken, L., and Mentel, T. F.: Highly oxygenated organic molecule (HOM) formation in the isoprene oxidation by NO₃ radical, *Atmos. Chem. Phys.*, 21, 9681-9704, <https://doi.org/10.5194/acp-21-9681-2021>, 2021.
- Zhao, J., Mickwitz, V., Luo, Y., Häkkinen, E., Graeffe, F., Zhang, J., Timonen, H., Canagaratna, M., Krechmer, J. E., Zhang, Q., Kulmala, M., Kangasluoma, J., Worsnop, D., and Ehn, M.: Characterization of the Vaporization Inlet for Aerosols (VIA) for online measurements of particulate highly oxygenated organic molecules (HOMs), *Atmospheric Measurement Techniques*, 17, 1527-1543, <https://doi.org/10.5194/amt-17-1527-2024>, 2024.
- Zhao, R., Mungall, E. L., Lee, A. K. Y., Aljawhary, D., and Abbatt, J. P. D.: Aqueous-phase photooxidation of levoglucosan – a mechanistic study using aerosol time-of-flight chemical ionization mass spectrometry (Aerosol ToF-CIMS), *Atmos. Chem. Phys.*, 14, 9695-9706, <https://doi.org/10.5194/acp-14-9695-2014>, 2014.
- Zheng, M., Yan, C., and Zhu, T.: Understanding sources of fine particulate matter in China, *Philosophical Transactions of the Royal Society A: Mathematical, Physical and Engineering Sciences*, 378, 20190325, <https://doi.org/10.1098/rsta.2019.0325>, 2020.
- Zheng, Y., Yang, S., Liu, X., Wang, J., Norton, T., Chen, J., and Tan, Y.: The computational fluid dynamic modeling of downwash flow field for a six-rotor UAV, *Frontiers of Agricultural Science and Engineering*, 0, 0, <https://doi.org/10.15302/j-fase-2018216>, 2018.
- Zhou, W., Xu, W., Kim, H., Zhang, Q., Fu, P., Worsnop, D. R., and Sun, Y.: A review of aerosol chemistry in Asia: insights from aerosol mass spectrometer measurements, *Environmental Science: Processes & Impacts*, 22, 1616-1653, <https://doi.org/10.1039/d0em00212g>, 2020.
- Zhou, Y., Huang, X. H., Bian, Q., Griffith, S. M., Louie, P. K. K., and Yu, J. Z.: Sources and atmospheric processes impacting oxalate at a suburban coastal site in Hong Kong: Insights inferred from 1 year hourly measurements, *Journal of Geophysical Research: Atmospheres*, 120, 9772-9788, <https://doi.org/10.1002/2015JD023531>, 2015.
- Zhu, Y., Hinds, W. C., Kim, S., Shen, S., and Sioutas, C.: Study of ultrafine particles near a major highway with heavy-duty diesel traffic, *Atmospheric Environment*, 36, 4323-4335, [https://doi.org/10.1016/S1352-2310\(02\)00354-0](https://doi.org/10.1016/S1352-2310(02)00354-0), 2002.
- Zhu, Z., González-Rocha, J., Ding, Y., Frausto-Vicencio, I., Heerah, S., Venkatram, A., Dubey, M., Collins, D., and Hopkins, F. M.: Toward on-demand measurements of greenhouse gas emissions using an uncrewed aircraft AirCore system, *Atmospheric Measurement Techniques*, 17, 3883-3895, <https://doi.org/10.5194/amt-17-3883-2024>, 2024.

Zorn, S. R., Drewnick, F., Schott, M., Hoffmann, T., and Borrmann, S.: Characterization of the South Atlantic marine boundary layer aerosol using an aerodyne aerosol mass spectrometer, *Atmos. Chem. Phys.*, 8, 4711-4728, <https://doi.org/10.5194/acp-8-4711-2008>, 2008.

Zum Berge, K., Gaiser, A., Knaus, H., Platis, A., and Bange, J.: Seasonal Changes in Boundary-Layer Flow Over a Forested Escarpment Measured by an Uncrewed Aircraft System, *Boundary-Layer Meteorology*, 186, 69-91, <https://doi.org/10.1007/s10546-022-00743-4>, 2023.

Appendix

Acronyms

ACS	AERTRACC control software
AERTRACC	Aerosol and trace gas collector
AET	Aethalometer
AGL or a.g.l.	Above ground level
a.s.l.	Above sea level
AMS	Aerosol mass spectrometer
ANE	Anemometer
BBOA	Biomass burning organic aerosol
BC	Black carbon
BISTUM	Bridging surface emissions, transport and UTLS matter
CBL	Convective boundary layer
CBO	CO ₂ monitor
CHARON	Chemical analysis of aerosol online
CIMS	Chemical ionization mass spectrometry
COA	Cooking organic aerosol
CPC	Condensation particle counter
CRDS	Cavity ring-down spectroscopy
DJI	Drone model: Matrice600 by DJI
DWD	German Weather Service
EC	Elemental carbon
EESI	Electrospray ionization
e.g.	<i>Exempli gratia</i> (for example)
EIC	Extracted ion chromatogram
et al.	<i>Et alia</i> (and others)
FLab	Flying laboratory
Fig.	Figure
FIGAERO	Filter inlet for gas and aerosols
FRM	Frankfurt Rhine-Main metropolitan area
FT	Free troposphere
FTIR	Fourier-transform infrared spectroscopy
HALO	High altitude-long range

HESI	Heated electrospray ionization
HR	High resolution
ICON	Icosahedral non-hydrostatic model
ICP	Inductively coupled plasma
i.e.	<i>Id est</i> (that is)
IMR	Ion molecular reactor
IUPAC	International Union for Physical and Applied Chemistry
LLJ	Low-level jet
LoD	Detection limit
MCR	Maximum carbonyl ratio
MARGA	Monitor for aerosols and gases in ambient air
MLH	Mixing layer height
MoLa	Mobile laboratory
MPIC	Max Planck Institute for Chemistry
MS	Mass spectrometer
MT	Monoterpenes
NBL	Nocturnal boundary layer
NBLH	Nocturnal boundary layer height
NMR	Nuclear magnetic resonance spectroscopy
OA	Organic aerosol
OC	Organic carbon
OPC	Optical particle counter
OOA	Oxygenated organic aerosol
OPS	Optical particle spectrometer
OZN	O ₃ monitor
PAH	Polycyclic aromatic hydrocarbons
PBL	Planetary boundary layer
PBLH	Planetary boundary layer height
PILS	Particle-into-liquid-sampler
PNC	Particle number concentrations
PMF	Positive matrix factorization
POA	Primary organic aerosols
RL	Residual layer
RSD	Relative standard deviation
Sect.	Section

SEM	Scanning electron microscope
SIMS	Secondary ion mass spectrometry
SL	Surface layer
SOA	Secondary organic aerosols
TAG	Thermal desorption aerosol gas chromatography
TD	Thermal desorption
TDT	Thermal desorption tubes
ToF	Time-of-Flight
TTL	Transistor-transistor logic
UAS	Unmanned aircraft systems
UAV	Uncrewed aerial vehicles
UHPLC	Ultra high-pressure liquid chromatography
VOC	Volatile organic compounds
VUV	Vacuum ultraviolet lamp
XRF	X-ray fluorescence

Symbols

α	Significance level or conversion rate
A	Aerosol particle surface
γ	Uptake coefficient
c	Mean molecular velocity (chapter 4) or concentration (chapter 6)
C_p	Specific heat
$CAPE$	Convective available potential energy
d_p	Particle diameter
d_{opt}	Optical particle diameter
e	Elemental particle charge
E_{el}	Electric field strength
E_{kin}	Kinetic Energy
f_{55}	fractions of the organic signals at single m/z , e.g., m/z 55
g	Acceleration of gravity
J	Photolysis rate
k	Reaction rate
k_{het}	Heterogenous loss rate coefficient
m	Mass
Δm	Mass difference

m/z	Mass-to-charge ratio
Q	Volumetric flow
Q_H	(Sensible) heat flux
P	Molecule or atom production rate
$PBLH$	Planetary boundary layer height
ρ	Air density
R	Representativity of the lowermost 25 m above ground compared to the lowermost 500 m column
r, r^2	Pearson's correlation coefficient
RH	Relative humidity
Ri	Bulk Richardson number
Ri_c	Critical bulk Richardson number
θ	Potential temperature
θ_{eq}	Equivalent potential temperature
θ_v	Virtual potential temperature
T	Temperature
T_v	Virtual temperature
t	Averaging time
TKE	Turbulent kinetic energy
U	Voltage
u, v	Horizontal wind velocities
v_i	Ion velocity
w	Vertical wind velocity
z	Ion charge or altitude

Use of AI Tools

Table 9.1: Used AI tools throughout the work.

AI tool	Used for	Why	When
ChatGPT – gpt-4o/5o	Improvement of written language	Better readability	Throughout the entire work
DeepL Write	Improvement of written language	Better readability	Throughout the entire work
Perplexity.ai	Finding my way into the topic	Overview of current research questions	First literature research for chapter 4 and 8

Supplementary Information for Chapter 3

Text S9.1: Calculation of PM₁ mass concentrations

The PM₁ mass concentrations were calculated from the combined particle number size distributions of FMPS ($d_p = 5.6 - 560$ nm) and OPC ($d_p = 0.25 - 32$ μm) assuming spherical particles with a density calculated based on the AMS and black carbon data using the equation of Kuwata et al. (2012) for organic density and Salcedo et al. (2006) for overall density. Since we found that the FMPS undermeasures the concentrations in the uppermost size channels these were corrected using the lower OPC size channels. Details on OPC data treatment like the conversion from optical diameter to geometric diameter are provided in Drewnick et al. (2021). The uncertainty for the calculated PM₁ mass concentration is 25%. It was calculated by error propagation from the uncertainty of the density (15%) and the uncertainty of the FMPS and OPC data merging (20%).

Text S9.2: AMS and PMF data analysis

For the AMS data analysis all standard analysis procedure steps were performed with SQUIRREL 1.63I and PIKA 1.23I. A collection efficiency of 0.5 (Canagaratna et al., 2007) was applied and ionization efficiency (IE) and relative ionization efficiency (RIE) were determined in calibrations before the measurements. Elemental ratios were calculated based on the improved calibration method (Canagaratna et al., 2015).

For PMF analysis of the organic aerosol, the high-resolution data with error matrix were prepared with PIKA 1.23I. Ions with signal-to-noise ratio (SNR) < 2 were downweighted through increase of the corresponding error by a factor of 2, while ions with SNR < 0.2 were discarded from the data. The CO₂⁺ ion and related ions (m/z 16, 17, 18 and 28) were downweighted by a factor of SQRT(5) as they all contain the same information. Additionally, “noisy” ions without contribution to the total measured signal were discarded. To find a robust solution the analysis was run for 1 to 7 factor solutions, with $f_{\text{peak}} -1$ to 1 (steps of 0.1) and seed 0 to 50 (steps of 1). For further analysis, the three-factor solution was chosen with $f_{\text{peak}}=0$ and seed=0. The solution was chosen based on comparison of the time series (Fig. S1a) with those of other instrument data and of the mass spectra (Fig. S9.1) with literature references (Fig. S9.2). The residual mass is smaller than 1 %.

Text S9.3: CIMS data analysis

For the CIMS data analysis, the software Tofware 3.2.3 (Aerodyne Inc., USA) and custom data procedures were used. All standard analysis procedure steps were performed including m/z calibration (with I(H₂O)⁻, I(CH₂O₂)⁻, I(HNO₃)⁻, I₂⁻ and I₃⁻, deviation < 3 ppm), background correction using the field blanks and normalization to the iodide signal.

Text S9.4: Error calculation for Fig. 3.5.

To determine the reproducibility, several samples were prepared with equal sample amounts by simultaneously sampling the same aerosol onto multiple filters and TDTs. For the overall reproducibility, the standard deviation over all samples for all individual compounds, which were identified in this study (Sect. 3.5), was calculated and then these standard deviations were averaged over all compounds.

As error for the signal intensity of individual compounds the uncertainty, derived from the reproducibility determination, and the error from a Gaussian error propagation of the standard deviation of the blanks and the samples were compared and the larger one was chosen. The signal intensity from compounds found on blank filters was negligible in contrast to source and background samples. The error for the ratios was calculated using Gaussian error propagation from the errors of signal intensity of source and background samples. Error bars of the overall source ratios represent the standard error of the ratios of all ions assigned to the respective sources.

Table S9.2: List of identified compounds from filter analysis with acronyms used in the main text, molecular formula of the respective detected ion, and assigned sources based on the quoted references.

<i>m/z</i>	Detected ion	Assigned compound	Acronym	Assigned sources	Reference
202.921	IC ₂ H ₄ O ₃ ⁻	glycolic acid	GCOA	biomass burning, cooking emissions	(Lim et al., 2005; Reyes-Villegas et al., 2018; Coggon et al., 2019)
212.905	IC ₃ H ₂ O ₃ ⁻	oxopropanedial, oxoacrylic acid	OPDA	biomass burning	(Alves et al., 2010; Zhao et al., 2014)
214.921	IC ₃ H ₄ O ₃ ⁻	pyruvic acid	PYA	biomass burning, cooking emissions	(Lim et al., 2005; Wang et al., 2006; Abdullahi et al., 2013; Reyes-Villegas et al., 2018; Coggon et al., 2019; Permar et al., 2021)
216.900	IC ₂ H ₂ O ₄ ⁻	oxalic acid	OXA	biomass burning, vehicle emissions	(Lim et al., 2005; Wang et al., 2006; Huang and Yu, 2007; Zhou et al., 2015)
222.893	ICH ₄ O ₃ S ⁻	methanesulfonic acid	MSA	aged aerosol	(Perraud et al., 2015)
224.872	IH ₂ O ₄ S ⁻	sulfuric acid	SA	oxidation of SO ₂	(Perraud et al., 2015)
232.932	IC ₃ H ₆ O ₄ ⁻	glyceric acid	GCEA	cooking emissions	(Reyes-Villegas et al., 2018)
238.921	IC ₅ H ₄ O ₃ ⁻	hydroxy furfural, furoic acid	HF/FA	biomass burning	(Permar et al., 2021)
242.916	IC ₄ H ₄ O ₄ ⁻	butenedioic acid	BDA	biomass burning	(Röhrl and Lammel, 2002; Hu and Yu, 2013; Ye et al., 2021)
246.947	IC ₄ H ₈ O ₄ ⁻	methylglyceric acid	MGCEA	aged aerosol, cooking emission	(Szmigielski et al., 2007; Reyes-Villegas et al., 2018)
252.937	IC ₆ H ₆ O ₃ ⁻	hydroxymethyl furfural	HMF	biomass burning	(Yee et al., 2013; Permar et al., 2021)
255.948	IC ₅ H ₇ NO ₃ ⁻	pyroglutamic acid	PGA	cooking emissions	(Reyes-Villegas et al., 2018)
256.932	IC ₅ H ₆ O ₄ ⁻	methylbutendioic acid	MBDA	biomass burning	(Coggon et al., 2019; Ye et al., 2021)
258.947	IC ₅ H ₈ O ₄ ⁻	glutaric acid	GA	biomass burning, cooking emissions	(Wang et al., 2006; Reyes-Villegas et al., 2018; Coggon et al., 2019)
260.927	IC ₄ H ₆ O ₅ ⁻	malic acid	MLA	biomass burning, vehicle emissions	(Röhrl and Lammel, 2002; Wang et al., 2006)
268.932	IC ₆ H ₆ O ₄ ⁻	oxidized aromats	OAR2	aged aerosol, biomass burning	(Yee et al., 2013)
276.958	IC ₅ H ₁₀ O ₅ ⁻	pyranose	PY	biomass burning, cooking emissions	(Simoneit et al., 2000; Reyes-Villegas et al., 2018; Chen et al., 2020)
288.958	IC ₆ H ₁₀ O ₅ ⁻	levoglucosan, galactosan, mannosan	LG	biomass burning, cooking emissions	(Abdullahi et al., 2013; Gaston et al., 2016; Reyes-Villegas et al., 2018; Křůmal et al., 2019)
295.943	IC ₇ H ₇ NO ₄ ⁻	nitroguaiacol	NG	biomass burning	(Lauraguais et al., 2014; Coggon et al., 2019)
300.958	IC ₇ H ₁₀ O ₅ ⁻	oxidized aromats, 3-acetylpentane-dioic acid	OAR1	aged aerosol, biomass burning	(Yee et al., 2013; Chen et al., 2020)
302.937	IC ₆ H ₈ O ₆ ⁻	ascorbic acid, hydroxy-furans	AS	biomass burning, vehicle emissions	(Priestley et al., 2021)
303.932	IC ₅ H ₇ NO ₆ ⁻	oxidized isoprene nitrate	IPN1	aged aerosol	(Zhao et al., 2021)
305.948	IC ₅ H ₉ NO ₆ ⁻	oxidized isoprene nitrate	IPN2	aged aerosol	(Zhao et al., 2021)
306.968	IC ₆ H ₁₂ O ₆ ⁻	monosaccharide	MS	biomass burning, cooking emissions	(Gaston et al., 2016; Ye et al., 2021)

Table S9.3: List of identified compounds from TDT analysis with acronyms used in the main text, molecular formula of the respective detected ion, and assigned sources based on the quoted references.

<i>m/z</i>	Detected ion	Assigned compound	Acronym	Assigned sources	Reference
171.926	ICH ₃ NO ⁻	formamide	FM	biomass burning, aged aerosol	(Priestley et al., 2018; Schwantes et al., 2019; Permar et al., 2021; Ye et al., 2021)
186.926	IC ₂ H ₄ O ₂ ⁻	acetic acid	AA	biomass burning, aged aerosol, traffic	(Lim et al., 2005; Liggio et al., 2017; Kong et al., 2021; Permar et al., 2021; Ye et al., 2021)
188.942	IC ₂ H ₆ O ₂ ⁻	ethylene glycol	EG	aged aerosol, biomass burning	(Schulten and Schurath, 1975; Reyes-Villegas et al., 2018; Duncan et al., 2019; Kong et al., 2021)
199.921	IC ₂ H ₃ NO ₂ ⁻	N-formylformamide, nitroethen	FFM	biomass burning	(Priestley et al., 2018; Permar et al., 2021)
200.942	IC ₃ H ₆ O ₂ ⁻	propanoic acid	PA	biomass burning, cooking, aged aerosol	(Jia and Xu, 2018; Priestley et al., 2018; Reyes-Villegas et al., 2018; Bi et al., 2022)
202.957	IC ₃ H ₈ O ₂ ⁻	propandiol, hydroxyacetone	PDO	aged aerosol	(Schulten and Schurath, 1975; Mehra et al., 2020)
212.905	IC ₃ H ₂ O ₃ ⁻	oxopropanedial, oxoacrylic acid	OPDA	biomass burning	(Alves et al., 2010; Craven et al., 2012; Zhao et al., 2014; Du et al., 2022)
214.921	IC ₃ H ₄ O ₃ ⁻	pyruvic acid	PYA	biomass burning, cooking emission, traffic	(Lim et al., 2005; Wang et al., 2006; Abdullahi et al., 2013; Reyes-Villegas et al., 2018; Coggon et al., 2019; Permar et al., 2021)
214.957	IC ₄ H ₈ O ₂ ⁻	butyric acid, methyl propanoate	BA	biomass burning, traffic	(Liggio et al., 2017; Priestley et al., 2018; Duncan et al., 2019; Permar et al., 2021)
224.942	IC ₅ H ₆ O ₂ ⁻	furfuryl alcohol, 2-furanmethanol	FFA	biomass burning, aged aerosol	(Nguyen et al., 2011; Priestley et al., 2018; Kong et al., 2021; Permar et al., 2021)
230.989	IC ₅ H ₁₂ O ₂ ⁻	alkyldiole	OAL3	traffic	(Schröder et al., 2016; Grayson et al., 2017; Sutapa et al.)
234.963	IC ₇ H ₈ O ⁻	cresol	CRES	biomass burning, cooking, aged aerosol	(Klein et al., 2018; Mutzel et al., 2021; Permar et al., 2021)
240.973	IC ₆ H ₁₀ O ₂ ⁻	hexanoic acid, cyclopentanoic acid	HA	biomass burning, traffic	(Abdullahi et al., 2013; Liggio et al., 2017; Reyes-Villegas et al., 2018)
252.973	IC ₇ H ₁₀ O ₂ ⁻	Cyclohexene- carboxylic acid	CHCA	traffic, aged aerosol	(Liggio et al., 2017; Hammes et al., 2019; Smith et al., 2020)
256.968	IC ₆ H ₁₀ O ₃ ⁻	oxohexanoic acid, ethyl acetoacetate, methyl oxopentanoic acid	OHA	biomass burning, cooking, aged aerosol	(Boris et al., 2016; Duncan et al., 2019; Kong et al., 2021)
269.004	IC ₈ H ₁₄ O ₂ ⁻	oxidized alkane	OAL4	aged aerosol	(Craven et al., 2012; Shao et al., 2022)
270.984	IC ₇ H ₁₂ O ₃ ⁻	oxidized alkane	OAL2	aged aerosol	(Mackenzie-Rae et al., 2018; Hammes et al., 2019)
271.020	IC ₈ H ₁₆ O ₂ ⁻	octanoic acid	OA	traffic, cooking	(Schauer et al., 1999, 2002a, b; Abdullahi et al., 2013)
275.974	IC ₅ H ₁₁ NO ₄ ⁻	oxidized alkane	OAL1	aged aerosol	(Link, 2019)
283.020	IC ₉ H ₁₆ O ₂ ⁻	nonenoic acid	NA	aged aerosol	(Hamilton et al., 2011; Qi et al., 2020)
292.953	IC ₅ H ₁₀ O ₆ ⁻	sugar acid	SUGA	cooking	(Kurtén et al., 2018; Reyes-Villegas et al., 2018)
296.999	IC ₉ H ₁₄ O ₃ ⁻	pinalic-3-acid, limonic acid	PINA	cooking, aged aerosol	(Reyes-Villegas et al., 2018; Hammes et al., 2019)

297.036	IC ₁₀ H ₁₈ O ₂ ⁻	decenoic acid, pinanediol, linalool oxide	DCA	aged aerosol	(Kirkby and Cloud; Rondo et al., 2014; Bi et al., 2022)
299.051	IC ₁₀ H ₂₀ O ₂ ⁻	decanoic acid	DA	traffic	(Schauer et al., 1999, 2002a, b; Sutapa et al.)
311.015	IC ₁₀ H ₁₆ O ₃ ⁻	oxocarboxylic acid	OCA	aged aerosol, traffic, cooking	(Liggio et al., 2017; Hammes et al., 2019; Reyes-Villegas et al., 2018; Kong et al., 2021; Ye et al., 2021)
327.083	IC ₁₂ H ₂₄ O ₂ ⁻	dodecanoic acid, methylundecanoic acid	DDA	traffic, cooking	(Schauer et al., 1999, 2002b; Sutapa et al.)
363.083	IC ₁₅ H ₂₄ O ₂ ⁻	β-caryophyllene-aldehyde	CPA	aged aerosol	(Li et al., 2011; Gao et al., 2023)

Table S9.4: Average concentrations of potentially source-related aerosol components and total source-related sampling time for the three-divided wind sectors in comparison to the undivided wind sector and the combined wind sector + OPC sampling condition.

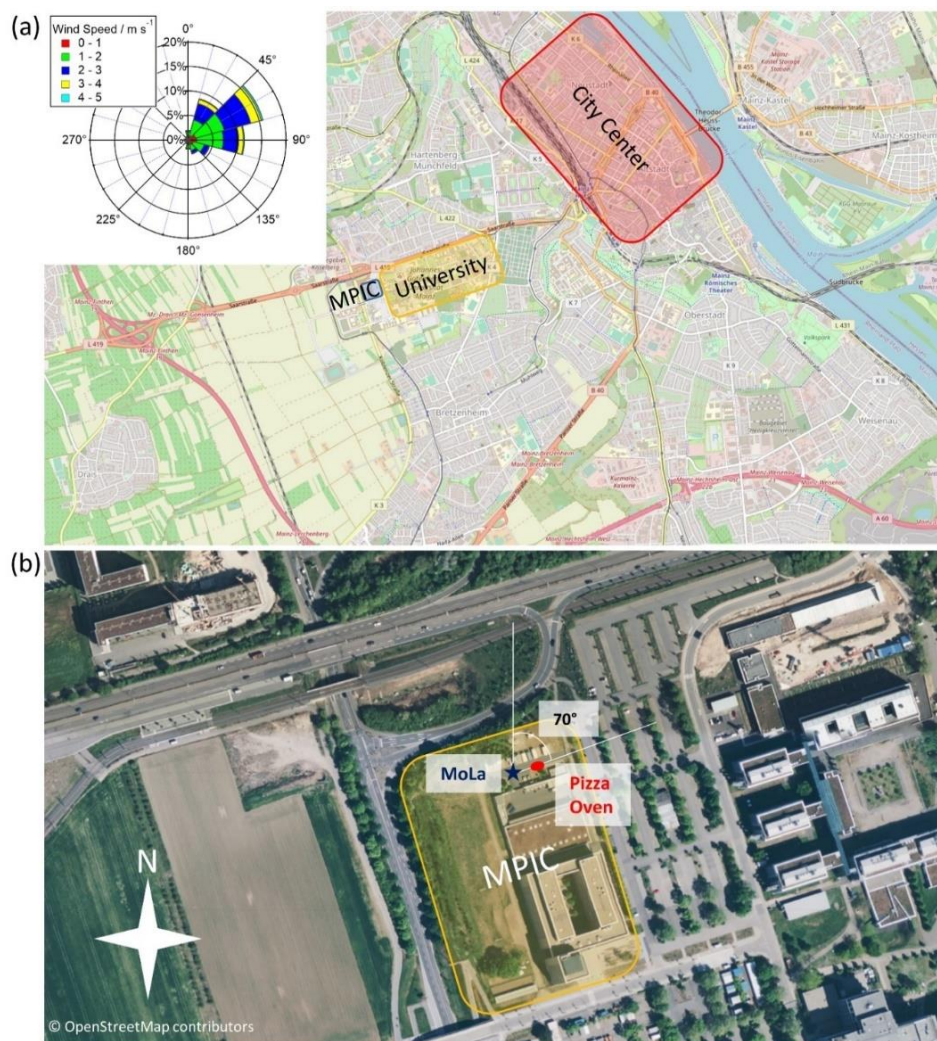
	45-60°	60-75°	75-90°	Wind (45-90°)	Wind+OPC
Black Carbon (ng m ⁻³)	2.7	3.3	3.1	3.1	22.0
CPC (# cm ⁻³)	1.5	1.9	1.8	1.7	2.8
PAH (ng m ⁻³)	2.1	2.6	2.9	2.5	13.4
PM1 (μg m ⁻³)	2.3	2.9	2.4	2.5	5.2
Organics (μg m ⁻³)	1.7	2.0	2.0	1.9	3.5
OPC (# cm ⁻³)	1.6	1.8	1.8	1.7	22.0
BBOA (μg m ⁻³)	3.6	5.6	5.6	4.9	1.3
OOA (μg m ⁻³)	3.5	3.5	3.5	3.5	3.7
COA (μg m ⁻³)	1.2	1.7	1.9	1.6	1.0
Sampling Time (s)	1198	1273	1087	3779	979

Table S9.5: Average concentrations of potentially source-related aerosol components and total source-related sampling time for the five-divided wind sectors in comparison to the undivided wind sector and the combined wind sector + OPC sampling condition.

	45-54°	54-63°	63-72°	72-81°	81-90°	Wind (45-90°)	Wind+OPC
Black Carbon (ng m ⁻³)	2.7	2.8	3.5	3.1	3.1	3.1	22.0
CPC (# cm ⁻³)	1.4	1.7	1.9	1.9	1.7	1.7	2.8
PAH (ng m ⁻³)	2.1	2.4	2.6	2.9	2.6	2.5	13.4
PM1 (μg m ⁻³)	2.4	2.3	3.0	2.6	2.2	1.7	5.2
Organics (μg m ⁻³)	1.7	1.8	2.0	2.2	1.7	1.9	3.5
OPC (# cm ⁻³)	1.6	1.6	1.9	2.0	1.4	1.7	22.0
BBOA (μg m ⁻³)	3.3	4.1	6.0	6.5	4.5	4.9	1.3
OOA (μg m ⁻³)	3.5	3.5	3.5	3.5	3.6	3.5	3.7
COA (μg m ⁻³)	1.2	1.5	1.6	2.0	1.8	1.6	1.0
Sampling Time (s)	700	757	759	733	609	3779	979

Table S9.6: Average concentrations of potentially source-related aerosol components and total source-related sampling time for the seven-divided wind sectors in comparison to the undivided wind sector and the combined wind sector + OPC sampling condition.

	45- 51°	51- 58°	58- 64°	64- 71°	71- 77°	77- 84°	84- 90°	Wind (45-90°)	Wind+OPC
Black Carbon (ng m^{-3})	2.8	2.4	3.1	3.7	3.0	2.8	3.5	3.1	22.0
CPC ($\# \text{cm}^{-3}$)	1.4	1.6	1.8	1.9	1.9	1.8	1.7	1.7	2.8
PAH (ng m^{-3})	2.1	2.1	2.4	2.9	2.7	2.6	3.0	2.5	13.4
PM1 ($\mu\text{g m}^{-3}$)	2.3	2.3	2.9	2.8	2.8	2.3	2.2	1.7	5.2
Organics ($\mu\text{g m}^{-3}$)	1.7	1.5	2.0	2.0	2.2	1.8	1.8	1.9	3.5
OPC ($\# \text{cm}^{-3}$)	1.6	1.5	1.7	1.8	2.0	1.7	1.4	1.7	22.0
BBOA ($\mu\text{g m}^{-3}$)	3.2	3.1	5.8	5.3	6.9	5.1	4.7	4.9	1.3
OOA ($\mu\text{g m}^{-3}$)	3.5	3.5	3.5	3.6	3.5	3.6	3.5	3.5	3.7
COA ($\mu\text{g m}^{-3}$)	1.1	1.2	1.9	1.5	2.0	1.8	1.9	1.6	1.0
Sampling Time (s)	527	497	607	511	555	466	395	3779	979

**Fig. S9.1:** Site map with the location of the institute (MPIC) within the city and a wind rose plot (a) and a magnification to show the location of MoLa and the pizza oven on the premises of the institute (Source: ©OpenStreetMap contributors).

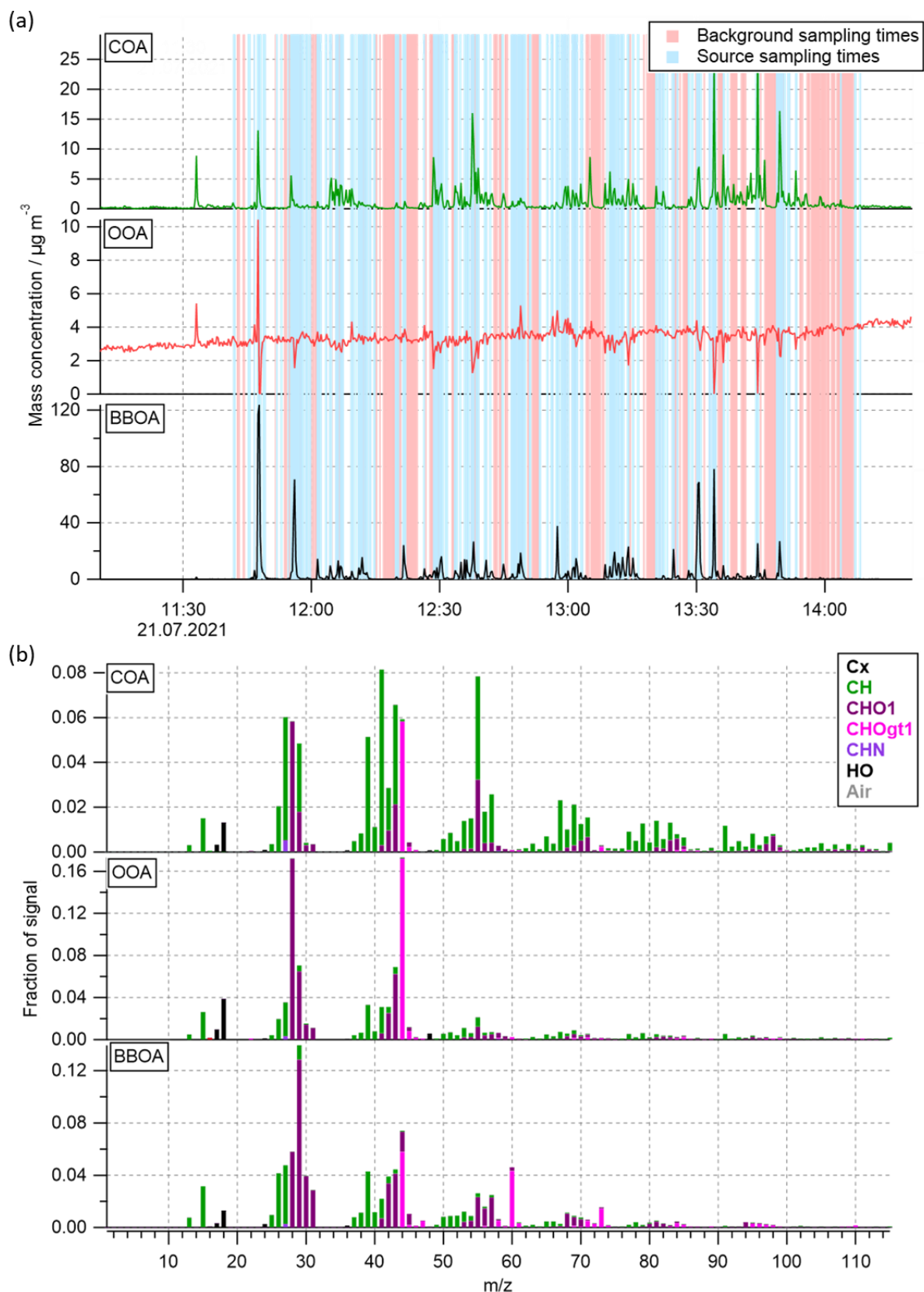


Fig. S9.2: Time series (a) and mass spectra with the source and background aerosol sampling times highlighted in blue and red (b) of the chosen 3-factor solution of the PMF analysis representing the three different aerosol types, observed during the field-validation measurement.

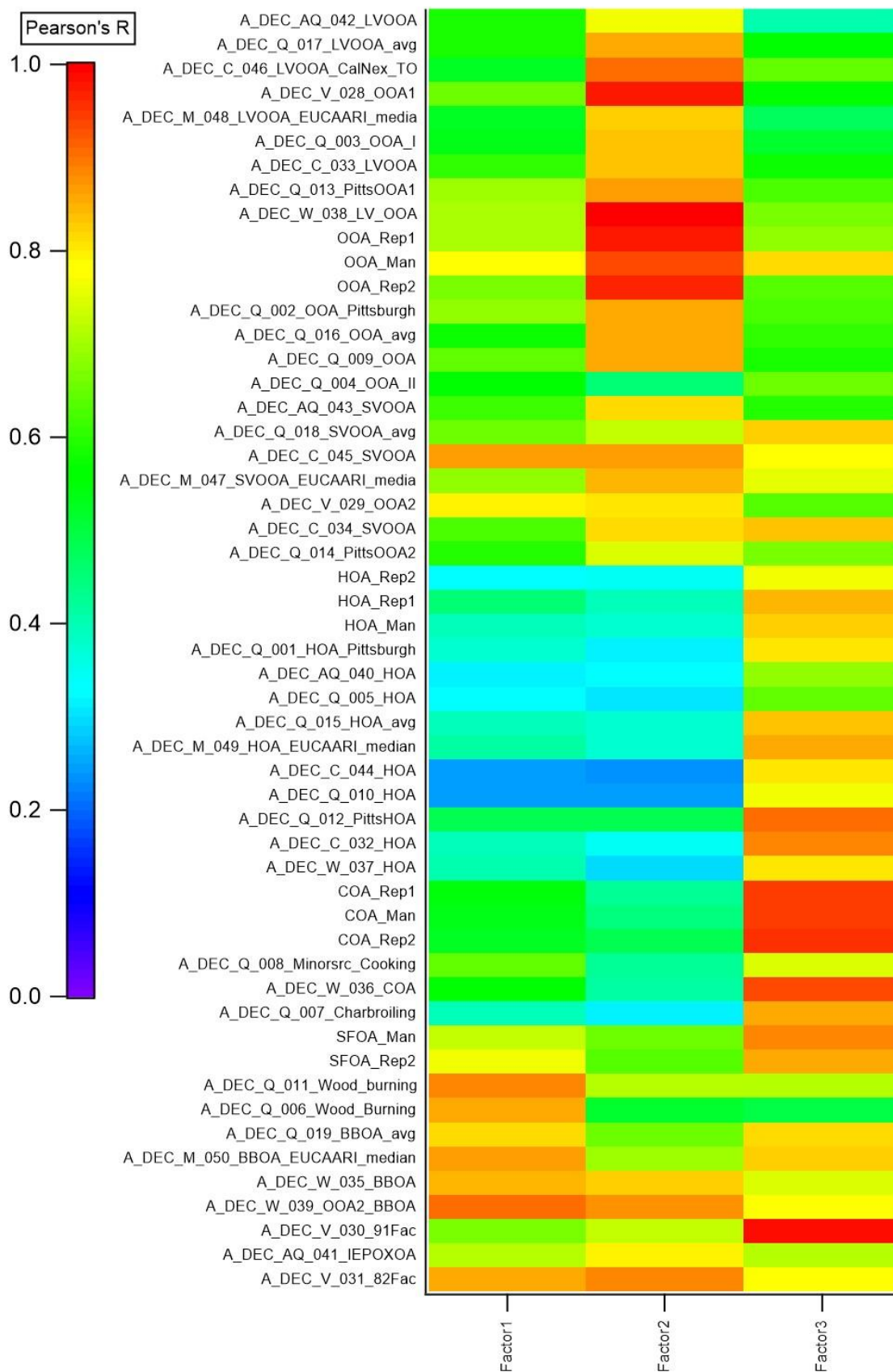


Fig. S9.3: Comparison of the three PMF factor mass spectra with reference spectra. Shown are Pearson R values from correlation of the PMF factor mass spectra with different reference mass spectra from the AMS Spectral Database (Ulbrich, 2022) as color-coded boxes.

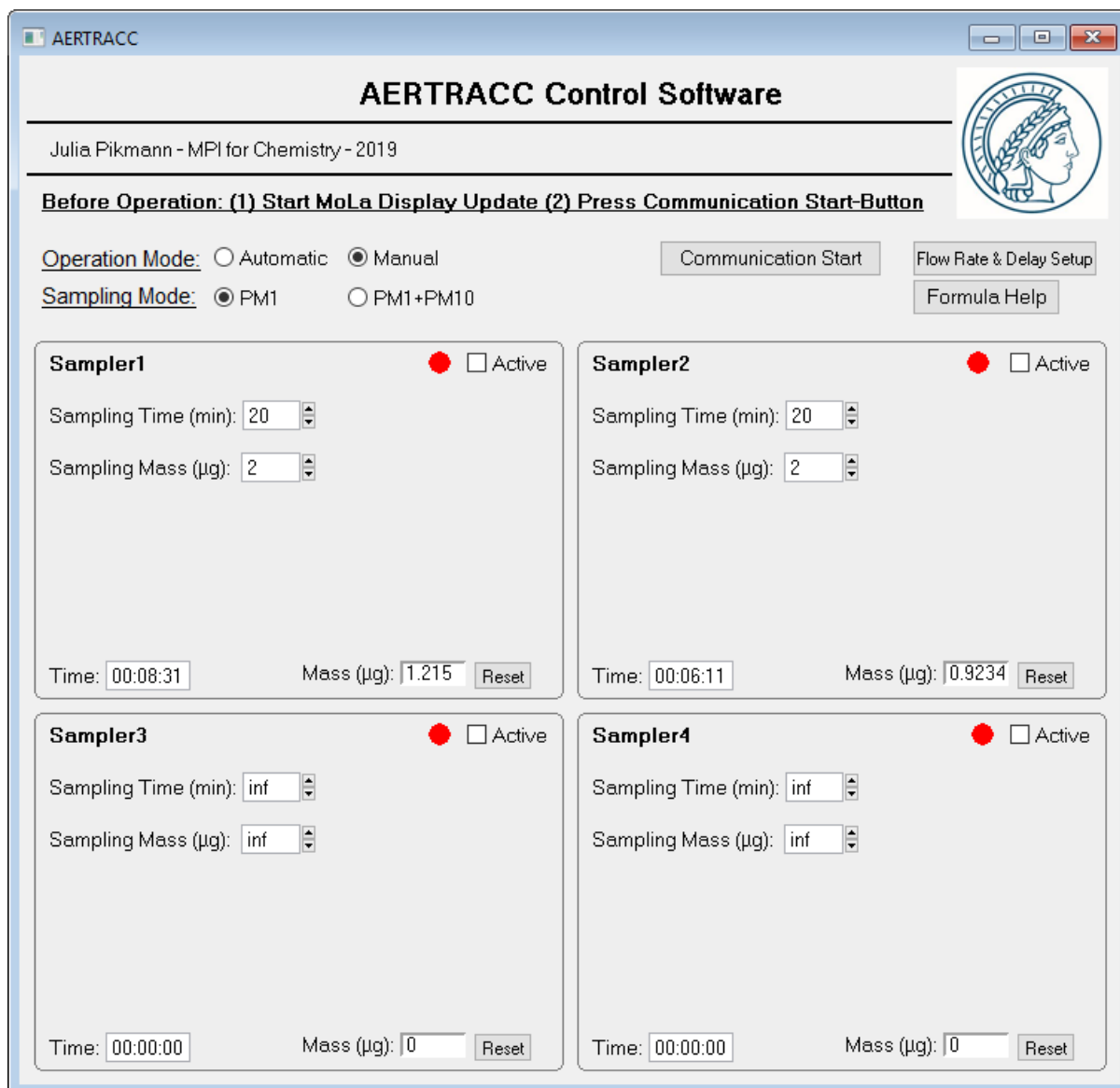


Fig. S9.4: User interface of the AERTRACC software in manual sampling mode. For each sampling path, a sampling time and mass limit can be set. To sample, the “Active” checkbox needs to be checked; then the red indicator for “non-sampling” turns green for “sampling”. For each sampling path, two displays show the current accumulated collection time and accumulated aerosol mass. The panel for automatic sampling mode is shown in the main text.

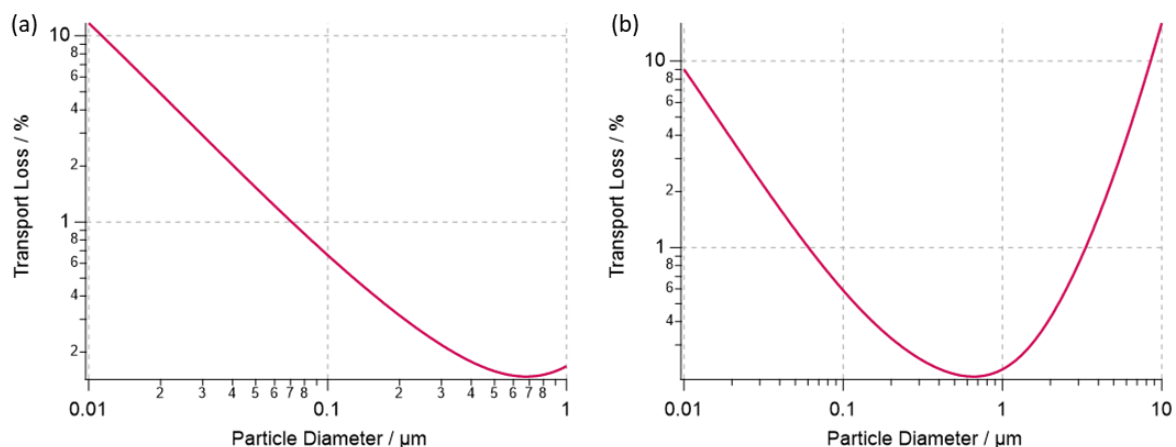


Fig. S9.5: Size-dependent transport losses for the (a) PM₁-only and (b) PM₁/PM₁₀ sampling mode. For the calculations, it was assumed that the particles are spherical with a density of 1 g cm⁻³. The considered particle loss mechanisms are diffusion, sedimentation, and inertial deposition.

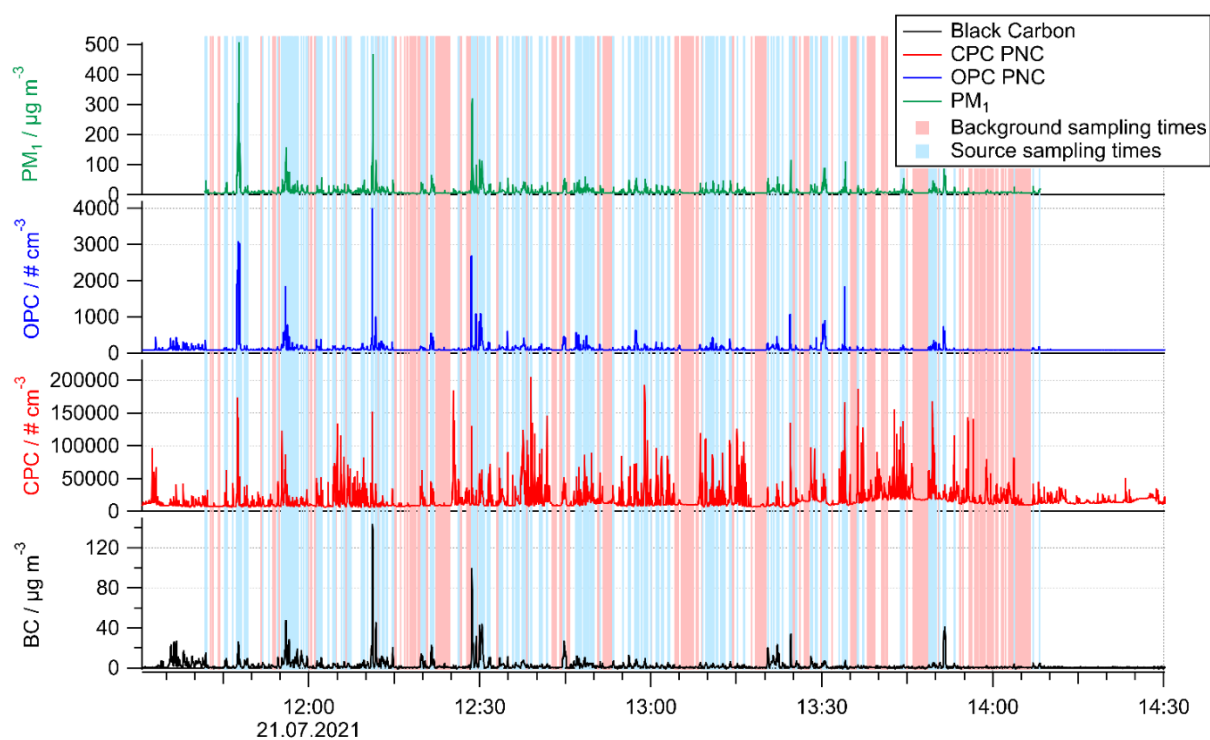


Fig. S9.6: Time series for the relevant parameters black carbon and PM₁ mass concentration as well as CPC and OPC particle number concentration. The source and background aerosol sampling times are highlighted in blue and red.

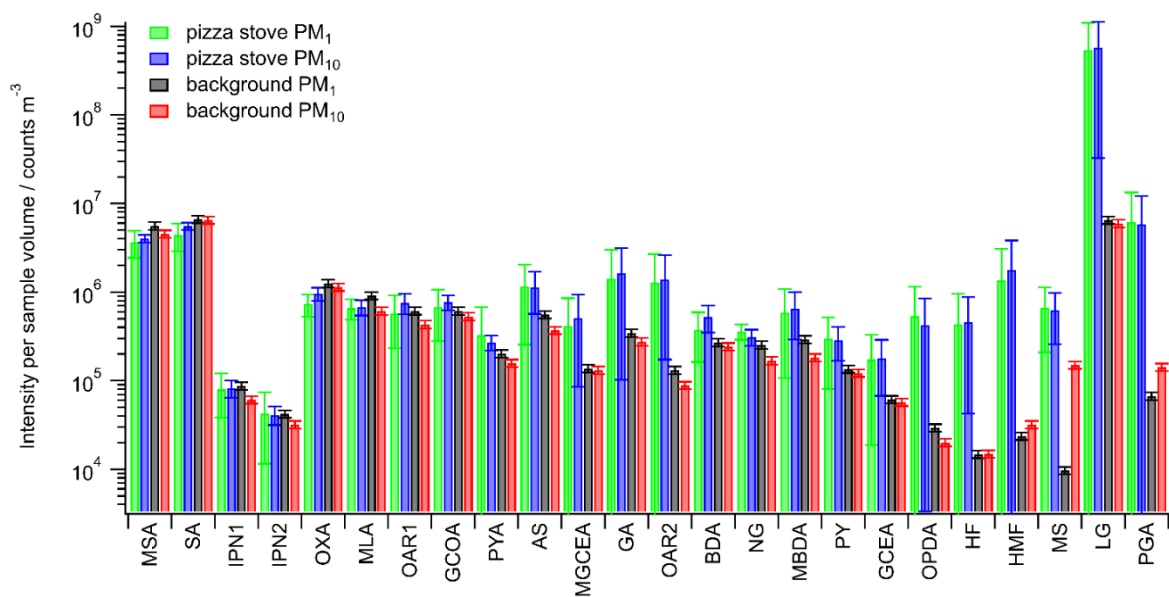


Fig. S9.7: Ion signal intensities normalized to the respective sampled volume for the PM₁ and PM₁₀ filters from pizza oven and background sampling. Error Bars show the larger uncertainty, either the reproducibility or the uncertainty estimated by error propagation from the standard deviation of the blank and the ambient measurements.

Supplementary Information for Chapter 4

Text S9.5: Formation of chlorine-containing species from secondary ion chemistry

ICINO₃⁻

Due to the high correlation of $r^2 = 0.86$ between ClONO₂ and ClNO₂ throughout the campaign, we initially suspected that the reaction of ClNO₂ with IO_x⁻ ions in the IMR of the CIMS instrument was responsible for the observed ICINO₃⁻ signal. IO_x⁻ ($x = 1$ to 3) is formed from the reaction of the reagent ions I⁻ and IH₂O⁻ with O₃ inside the IMR and is known to be involved in (unwanted) secondary ion reactions when using iodide as primary ions (Teiwes et al., 2019; Zhang and Zhang, 2021; Dörich et al., 2021; Young et al., 2024). In order to investigate whether the ICINO₃⁻ measurements were an artefact of secondary ion-chemistry, we conducted a series of laboratory experiments with elevated levels of O₃ to study the formation of ICINO₃⁻ via reactions R17a and R17b under humidified and dry conditions in the IMR. In these experiments, a constant amount of ClNO₂ (~1 ppbv) was added to the CIMS inlet with addition of O₃ between 0 and 170 ppbv, thereby varying the amount of IO_x⁻ in the IMR.



We found that neither the ClNO₂ mixing ratio (measured as ICINO₂⁻) nor that of ICINO₃⁻ had changed significantly when O₃ was added with mixing ratios up to 170 ppbv under both dry and wet conditions. The IO_x⁻ signal increased linearly (Fig. S7a) over this range of O₃ mixing ratios, which exceeds those encountered during the BISTUM24 campaign (8 to 67 ppbv). We therefore conclude that the measurement of ClONO₂ is not a measurement artefact and that ClONO₂ was indeed present at the mixing ratios reported.

IHCIO₂⁻

In addition to IHClO⁻ (the detected ion cluster of HOCl in the CIMS), IHCIO₂⁻ was detected at a signal intensity of 25% that of IHClO⁻. A potential source of this ion is the reaction between atmospheric peroxyhypochlorous acid (HOOCI) and iodide in the IMR of the CIMS instrument. A recent study has highlighted the potential contribution of HOOCI to chlorine chemistry in the Antarctic vortex (Groß et al., 2025), where its source is the heterogeneous reaction between dichlorine dioxide (Cl₂O₂) and HCl (De Haan and Birks, 1997). While this may be possible in the cold polar vortex, where Cl₂O₂ is stable, this process will certainly be insignificant in the troposphere due to thermolability (Von Hobe et al., 2005). Theoretical studies (Lee and Rendell, 1993) propose the existence of HOOCI under tropospheric conditions though it has never been detected experimentally there. Thus, we consider the formation of IHCIO₂⁻ as being due to secondary ion chemistry of HOCl or HCl with IO_x⁻ in the IMR as more likely than detection of atmospheric HOOCI.

We investigated the possible involvement of IO_x⁻ due to enhanced O₃ levels (i.e., IO_x⁻) in the formation of IHCIO₂⁻ by mixing a flow of HOCl with O₃ (0 to 200 ppbv) under humid and dry IMR conditions and found that both IHCIO₂⁻ and IHClO⁻ were detected. The IHClO⁻ signal increased with added O₃, while the IHCIO₂⁻ signal remained constant (Fig. S7c). In a further experiment in the absence of HOCl, but with high amounts of HCl (not quantified, but significantly above the detection limit), both IHClO⁻ and IHCIO₂⁻ signals increased with added O₃ (and thus with higher IO_x⁻ counts, Fig. S7d). This indicates the

direct oxidation and cluster formation of HCl to IHClO^- and IHClO_2^- (R18), in contrast to a successive oxidation scheme (like for IHNO_3^- ; Dörich et al., 2021).



It appears very likely that atmospheric HCl and O_3 are the main source of IHClO^- and IHClO_2^- in the IMR. However, the relatively low O_3 levels from the ambient measurements in this work are not expected to influence the IHClO^- signal significantly, hence, a correction was not applied.

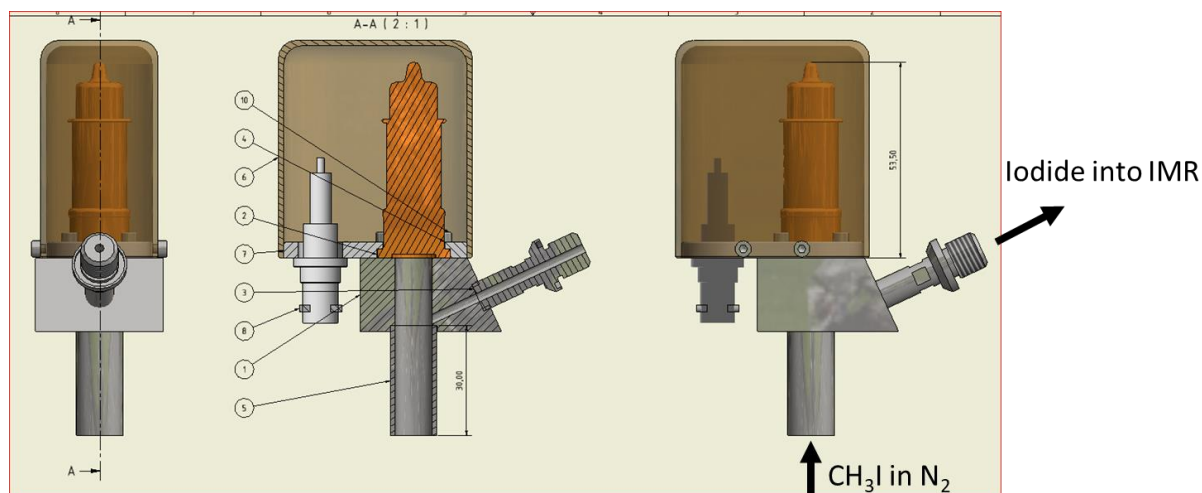


Fig. S9.8: The VUV lamp (orange striped) is capsulated by a 3D-printed plastic (brownish box). The capsulating plastics has a hole to observe ignition of the lamp. The lamp radiates downwards into the grey tube contrary to the reagent gas flow.

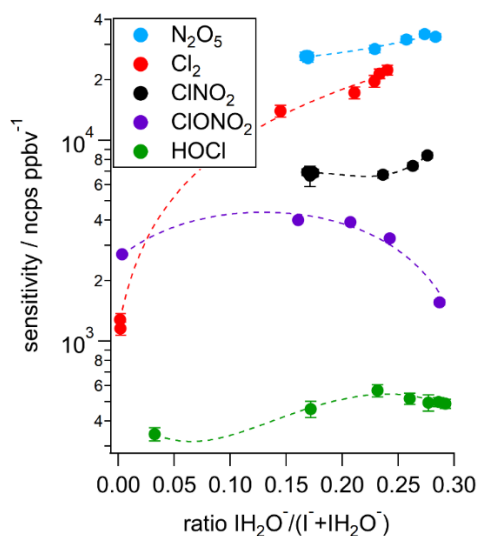


Fig. S9.9: Sensitivity dependency on the $\text{IH}_2\text{O}^- / (\text{I}^- + \text{IH}_2\text{O}^-)$ ratio in the IMR for IClONO_2^- (black), IN_2O_5^- (light blue), ICl_2^- (red), IClONO_2^- (dark blue) and IHOCI^- (green).

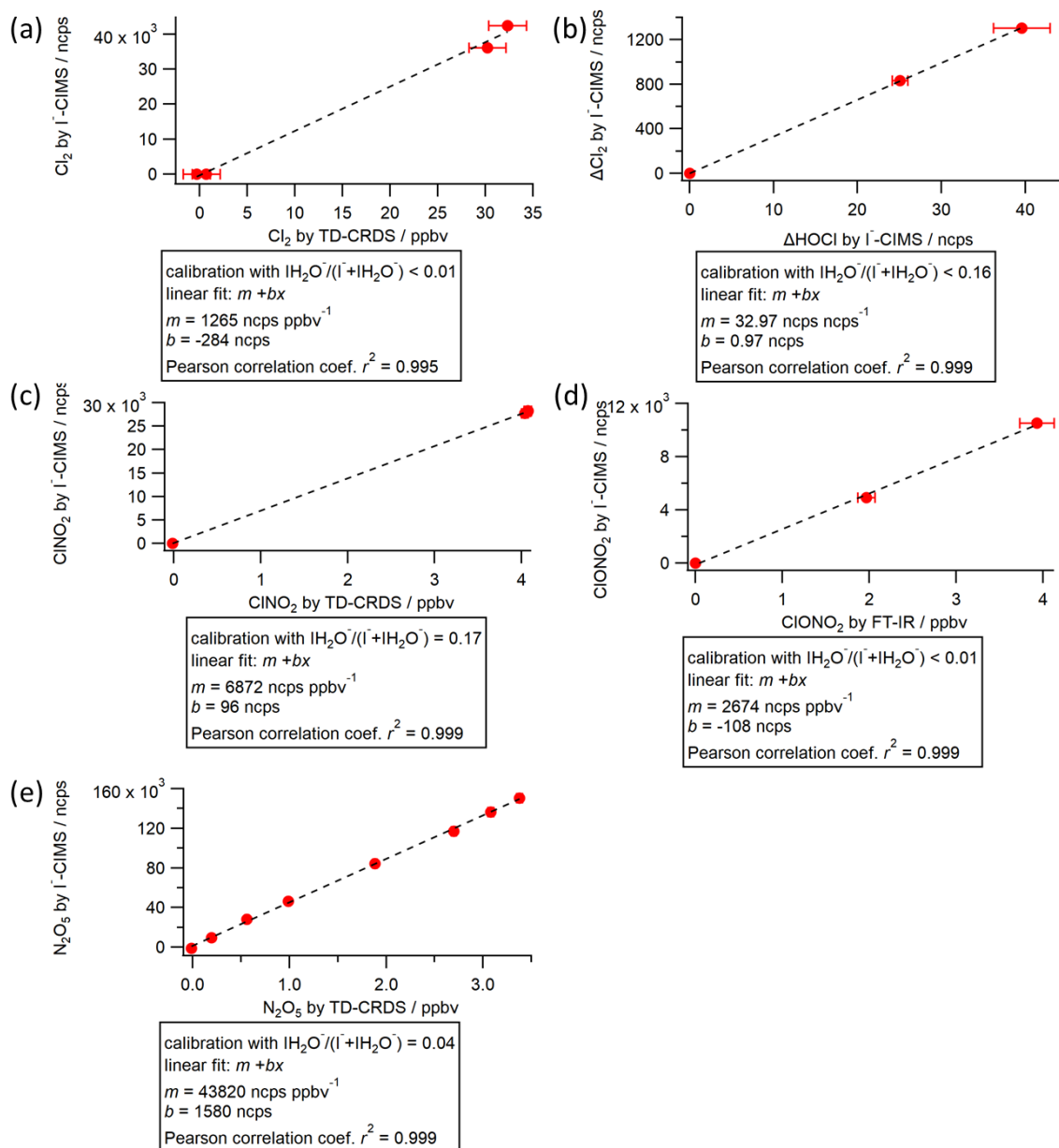


Fig. S9.10: Calibration curves (red) for Cl_2 (a), HOCl (b), ClONO_2 (c), ClONO_2 (d) and N_2O_5 (e) with linear regressions (black dashed lines). Error bars represent the standard deviation of data points.

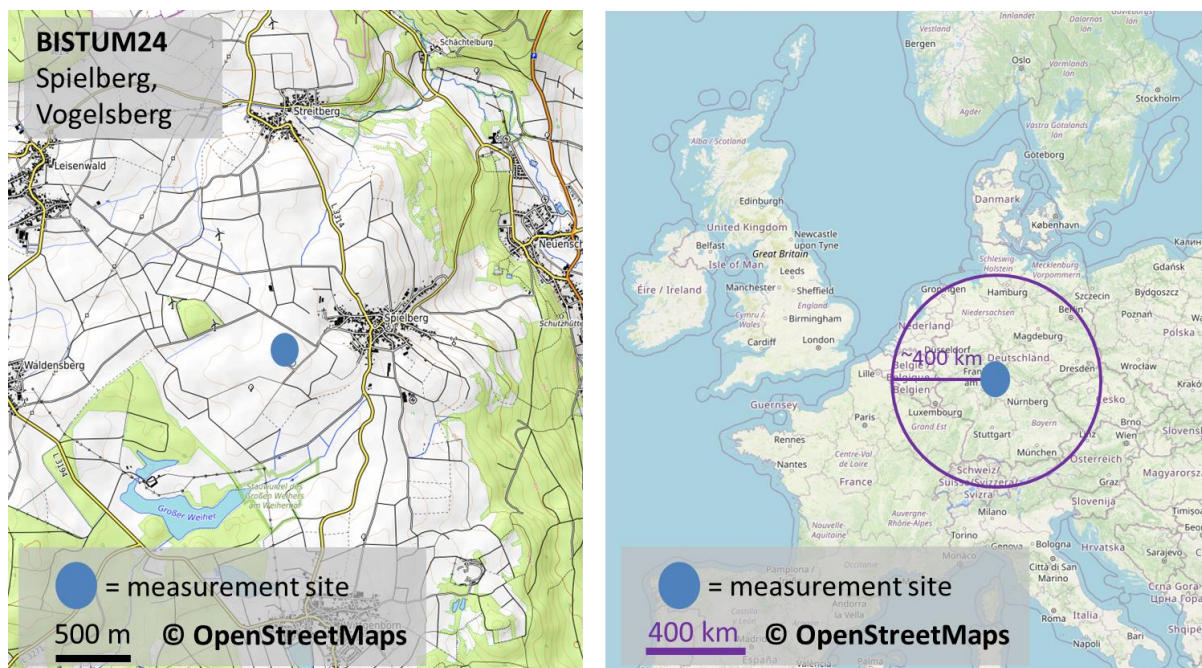


Fig. S9.11: The field measurements took place in rural Spielberg, Hessen, Germany from June 6 to 22, 2024. Maps were publicly available from ©OpenStreetMaps via its Creative Commons licence.

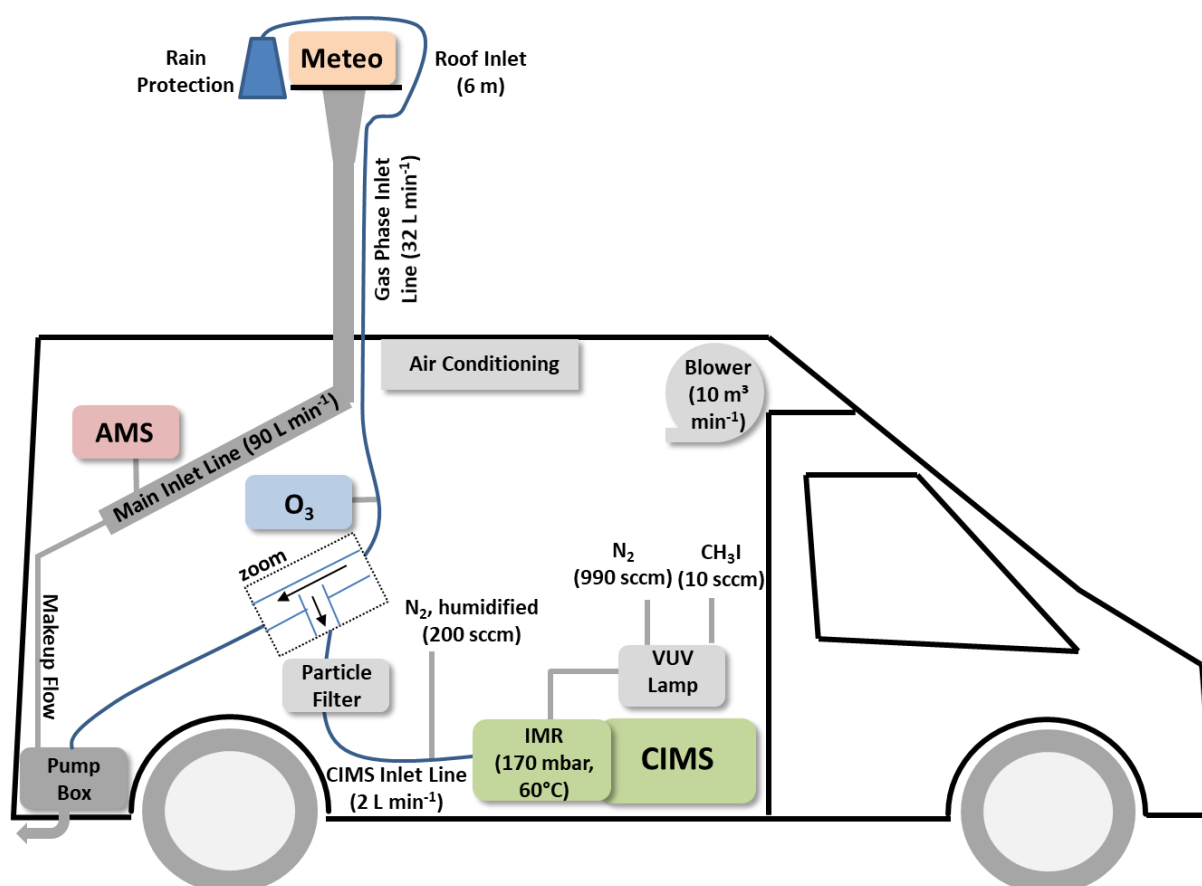


Fig. S9.12: Schematic representation of MoLa with relevant instruments: AMS (red), O₃ monitor (blue), weather station for meteorological data (yellow) and CIMS (green) and separate tubing for aerosol and gas samples: stainless steel (grey), PTFE (blue). The figure was adapted from Drewnick et al. (2012).

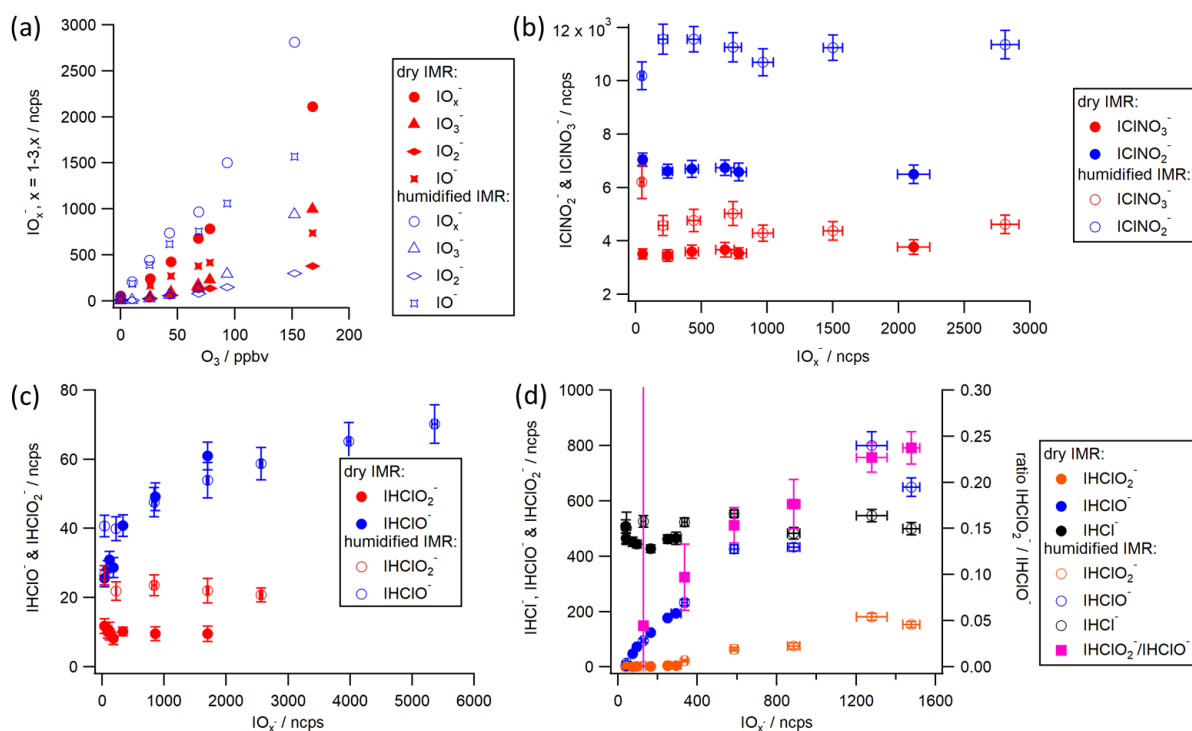


Fig. S9.14: Overview of experiments to investigate secondary ion chemistry due to O_3 inside the IMR (ion molecule reactor) of the CIMS. The relationship between O_3 and IO_x^- is linear for a dry and humidified IMR, although the contribution to IO_x^- (x=1-3) changes with the amount of O_3 (a). (b) shows that no secondary ion chemistry formation of ICINO_3^- is expected over a broad range of O_3 mixing ratios, neither for the humidified nor for the dry IMR case. In contrast, (c) indicates a significant increase of IHClO^- with higher IO_x^- levels in the IMR, which is not the case for IHClO_2^- as long as the HCl concentration in the IMR is below the detection limit. The same experiment with enhanced HCl levels is shown in (d), where the $\text{IHClO}_2^- / \text{IHClO}^-$ ratio increases with IO_x^- levels.

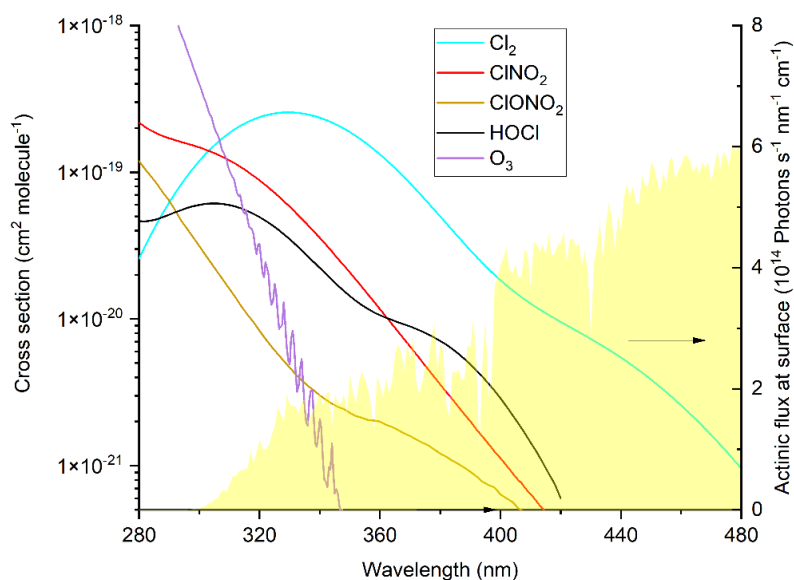


Fig. S9.15: UV absorption spectra of the chlorine trace-gases detected in this study (Cl_2 (blue, Maric et al. (1993)), ClNO_2 (red, Ghosh et al. (2012)), ClONO_2 (bright green, Burkholder et al. (1994)) and HOCl (black, IUPAC (2025)) and of O_3 (violet, Molina and Molina (1986)). The actinic flux is shown for local noon (cloud free sky) on June 10th 2024 at the location of the BISTUM24 campaign (UCAR, 2025).

Supplementary Information for Chapter 5

Text S9.6: Comparison of radiosonde and FLab data in the lowest 500 m AGL

To assess the comparability of radiosonde and FLab data, three additional measurements with quasi-simultaneous radiosonde launches and FLab flights are presented in Fig. S9.31 in addition to the radiosonde data shown in Fig. 5.8. The radiosondes were launched from the site described in Sect. 5.5.2 on different days after noon. All radiosondes carried a brand new, freshly unpacked RS41-sensor (Vaisala Oyj, Finland). The radiosondes provide data such as relative humidity, temperature, horizontal wind speed and direction, and position, which was used to calculate the distance to the reference station MoLa (Jost et al., in preparation for AMT). Shaded areas show the uncertainty resulting from the instrument uncertainty and the variation within the 50 m altitude increments.

In contrast to Fig. 5.8, the difference in relative humidity between the FLab and radiosonde measurements varies widely, but is usually within the uncertainty range, with no systematic positive or negative offset between the two. Together with the observation of almost cloud-free conditions on 10 August 2023, but a relative humidity measured with the radiosonde of about 90% at 500 m AGL (Fig. 5.8), this suggests that the sensor used in the flyby scenario shown in Fig. 5.8 may have malfunctioned. Temperature measurements at altitudes > 50 m AGL are in good agreement for all measurements, whereas the respective preparation ground before launch may influence the temperature measurement in lowest altitudes (radiosondes prepared on a tarpaulin, FLab on wooden planks on grassland).

The agreement of wind speed and direction measurements between the two platforms is highly dependent on weather conditions. In low wind conditions (wind speed < 5 m s⁻¹), the radiosonde ascends almost vertically. The sensor mounted 50 m below the balloon swings loosely horizontally after the abrupt launch, as indicated by the oscillating distance to MoLa (Fig. S9.31a and c). Furthermore, the wind has a direct influence on the motion of the balloon, which is transmitted to the payload (where the position measurement takes place) via the 50 m long tether. This results in a motion of the payload which is driven by the wind conditions almost 50 m above its own position. Both effects cause a difference in the radiosonde wind measurement compared to that of the FLab. Under windy conditions (wind speed > 5 m s⁻¹), FLab and the radiosonde are in much better agreement at low altitudes (Fig. S9.31b), however, a slight difference in the horizontal wind speed measured on both platforms is observed above 300 m AGL. At this altitude, the difference is probably due to the increasing distance between the radiosonde and FLab, while the 10° wind direction difference is not affected by the increasing distance. A more detailed analysis of these differences is not possible due to the lack of detailed information on the processing of the radiosonde data.

In summary, the quality of the radiosonde humidity data is highly dependent on the individual sensor, while ground preparation conditions can also slightly affect humidity and temperature measurements, however, differences above 50 m AGL are typically negligible. Windy launch conditions allow a better estimation of wind speed with the radiosonde just above ground, but may cause a greater difference between the balloon-borne and FLab measurements at higher altitudes due to the increasing horizontal distance between the two platforms. Since wind speed during the launch on 10 August 2023 was rather low (Fig. 5.8), this explains the discrepancy between FLab and radiosonde measurements during this flight.

Table S9.7: MoLa instruments used for characterization of the FLab.

Instrument	Measured variables	Time resolution
Aethalometer ^a	Black and brown carbon mass concentration	1 s
CPC ^b	Particle number concentration	1 s
OPC ^c	Particle size distribution based on optical diameter	6 s
O ₃ ^d	Mixing ratio of O ₃	2 s
LICOR ^e	Mixing ratio of CO ₂ , H ₂ O	1 s
Meteorological station ^f	Wind direction, wind speed, relative humidity, temperature, rain intensity, pressure	1 s
Ceilmeter ^g	Altitude-dependent backscatter signal intensity	30 s
FMPS ^h	Particle size distribution based on electrical mobility	6 s

^aMagee Scientific Aethalometer[®] Model AE33, Magee Scientific, USA. ^bCondensation Particle Counter Model 3786, TSI, Inc., USA. ^cOptical Particle Counter Model 1.109, Grimm Aerosoltechnik GmbH, Germany. ^dMonitor 205 Dual Beam Ozone Monitor, 2B Technologies, Inc., USA. ^eLI840, LI-COR, Inc., USA. ^fWXT520, Vaisala Oyj, Finland. ^gCHM 15k, Luftt Mess- und Regeltechnik GmbH, Germany. ^hFast Mobility Particle Sizer Model 3091, TSI, Inc., USA.

Table S9.8: Coefficients for the Hill equations for each variable to calculate the statistical uncertainty of the measured variables from the respective averaging time (in seconds).

$$\text{Hill equation: } \textit{uncertainty} / \% = \left(\textit{base} + \frac{\textit{max} - \textit{base}}{1 + \left(\frac{\textit{xhalf}}{\textit{averaging time}} \right)^{\textit{rate}}} \right) * 100\% \quad (\text{S9.1})$$

Instrument: variable	<i>base</i>	<i>max</i>	<i>xhalf</i>	<i>rate</i>
AET: black carbon@880nm	4.6664	0.032179	2.8866	1.0122
AET: black carbon@370nm	1.7017	0.019704	2.3234	0.93295
ANE: relative humidity	0.0044786	0.00050038	2.1736	0.78583
ANE: temperature	0.0031714	0.00037684	2.0814	0.79232
ANE: wind speed	0.056469	0.00020911	1.3282	0.58095
CBO: CO ₂ mixing ratio	0.0039588	0.0010941	7.9264	0.98681
CPC: particle number conc.	0.02681	0.0033615	37.358	0.26378
OPC: particle number conc.	0.17411	0.019143	2.188	0.61314
OPC: PM ₁	0.19538	0.018385	2.3192	0.62145
OPC: PM _{2.5}	0.83355	0.0014132	0.67953	0.52631
OZN: O ₃ mixing ratio	0.060544	0.013247	7.0617	0.67567

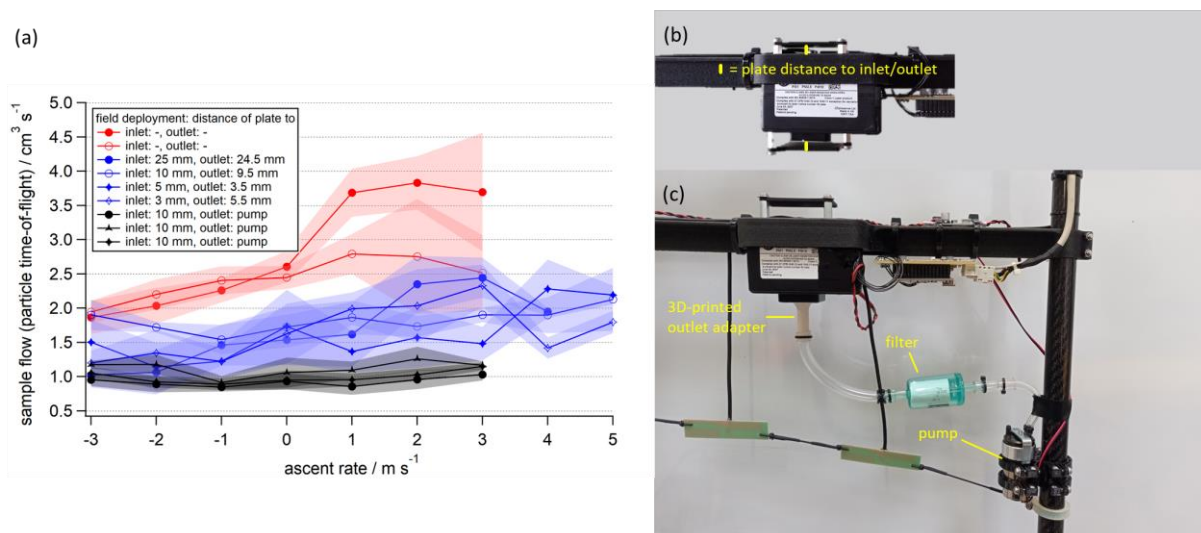


Fig. S9.16: The distance between the plate and the inlet/outlet of the OPC affects the sample flow differently with changing vertical velocity of the FLab (a). Setup of the plates in front of the inlet and behind the outlet of the OPC (b) and setup with an external pump (c) replacing the fan (Bezantakos et al., 2021). Lines between markers are for orientation and are not intended to indicate a relationship.

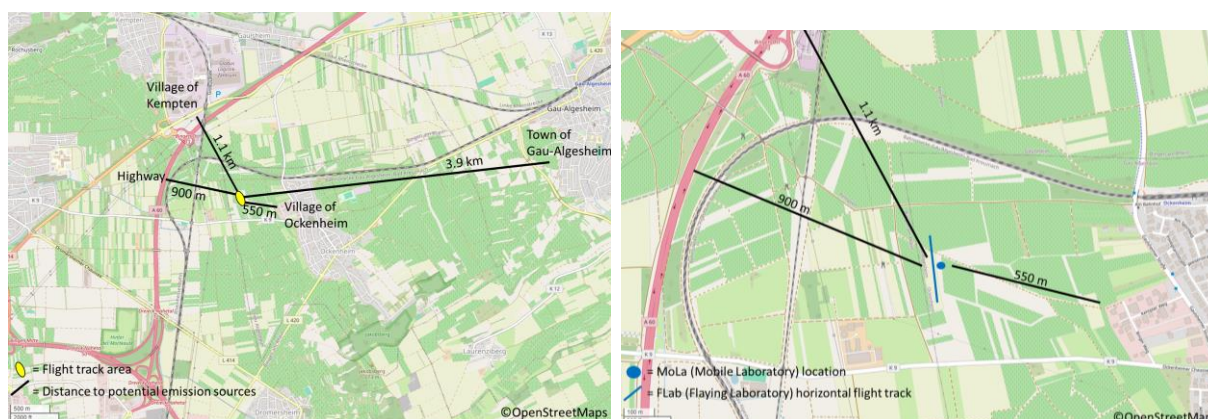


Fig. S9.17: Measurement site near Ockenheim used for the horizontal and vertical characterization flights in Sections 5.4.2 and 5.4.3 as well as for the field experiment in Section 5.5.1. © OpenStreetMap contributors 2024. Distributed under the Open Data Commons Open Database License (ODbL) v1.0.

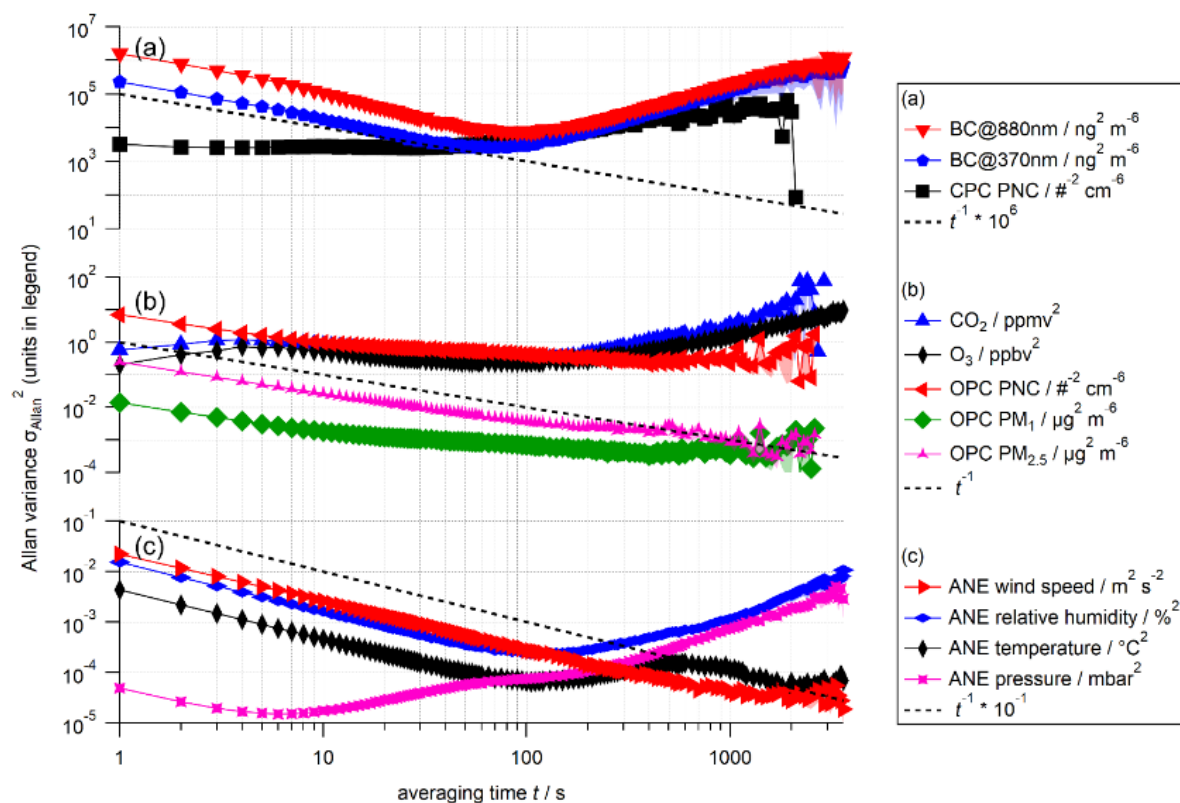


Fig. S9.18: Allan variance of the measured quantities of the FLab instruments as a function of averaging time, presented in three sub-panels (a-c) for clarity. Markers show the mean over the time series, while the standard error is shown as a shaded area (Röder et al., 2023). t^{-1} represents the slope of the statistically expected Allan variance.

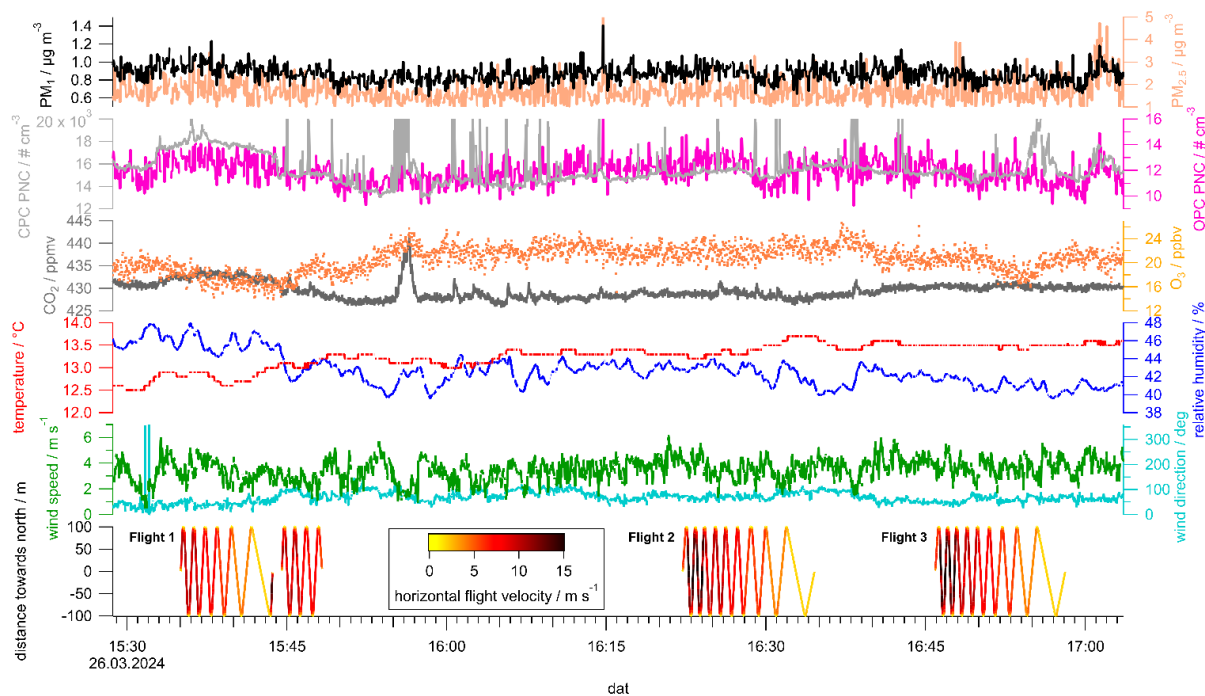


Fig. S9.19: Time series of various quantities measured by MoLa (top five panels) on 26 March 2024, showing a change in air masses and pollutants during flight F1 and stable conditions during flights F2 and F3 (bottom panel).

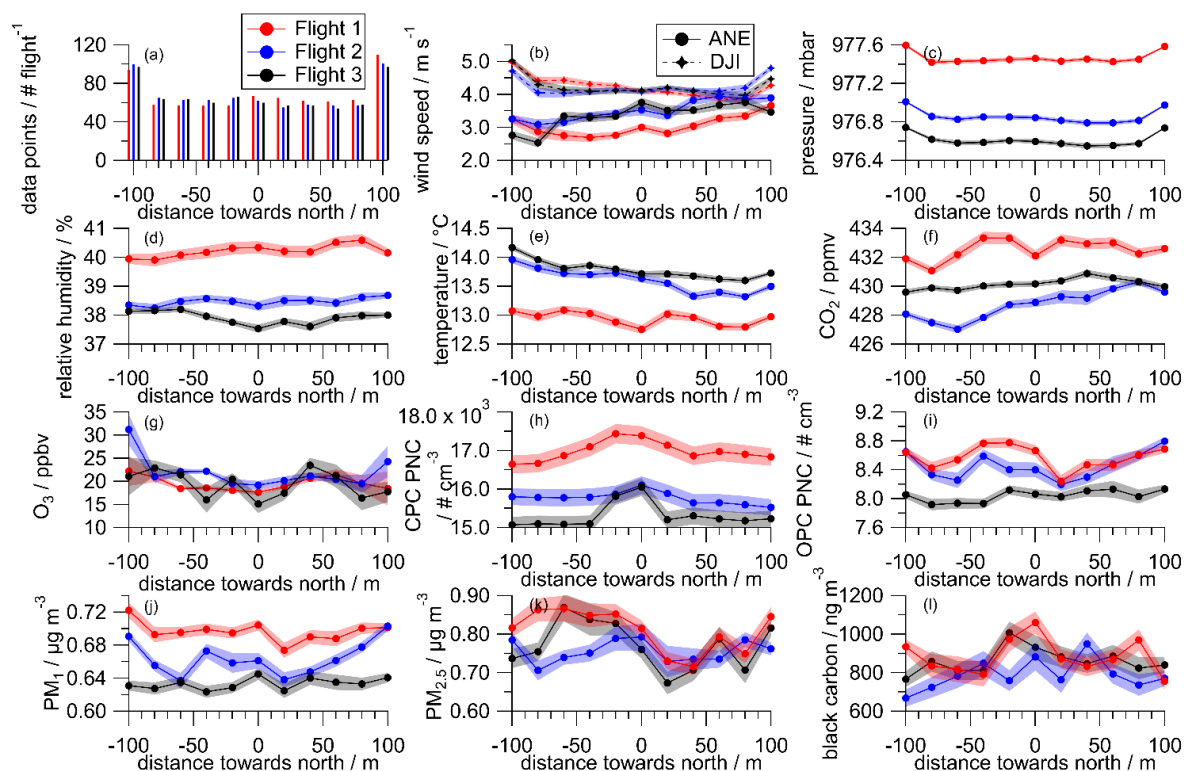


Fig. S9.20: Number of data points collected by FLab (a) for horizontal flight 1 (red), flight 2 (blue) and flight 3 (black) with: wind speed determined by ANE (b, dots) and DJI (b, diamonds), pressure (c), relative humidity (d), temperature (e), CO₂ (f) and O₃ mixing ratios (g), CPC and OPC particle number concentrations (h and i), particulate matter PM₁ (j) and PM_{2.5} (k) determined from the OPC data, and black carbon mass concentrations (l). The shaded areas indicate the standard error.

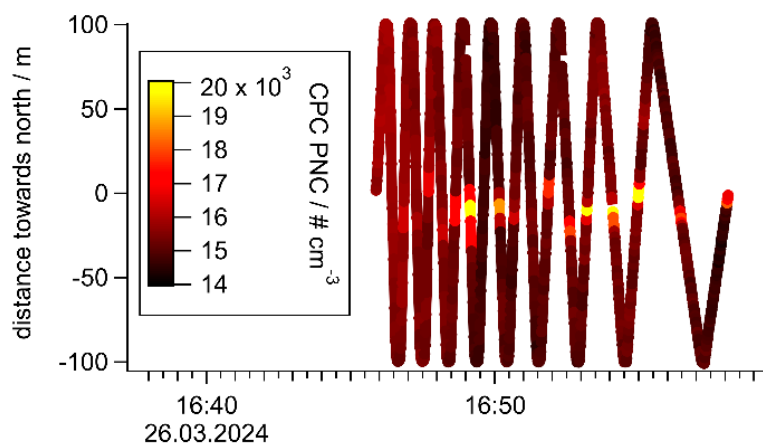


Fig. S9.21: 1-second data of the CPC particle number concentration highlights the polluted flight track between 0 m and -30 m.

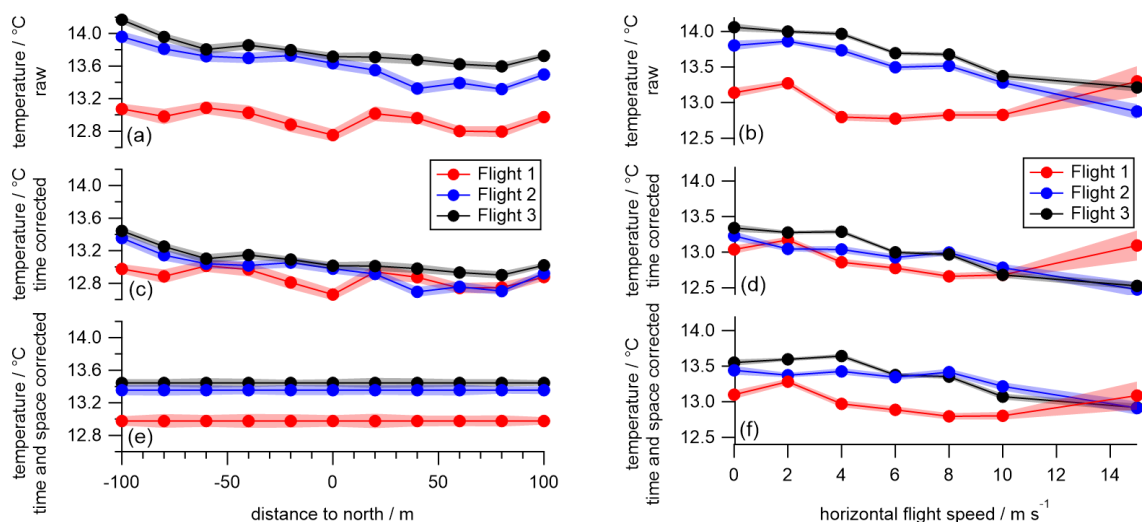


Fig. S9.22: The average temperature profile (20 m bins) is calculated from the uncorrected data from the horizontal flights from Section 5.4.2 (shown in panel a). The underlying temperature data from (a) are plotted depending on the horizontal flight velocity for each flight in (b), i.e., (b) shows the temperature dependence on flight speed if temporal and spatial variations are not regarded. (c, d) shows the same, using data corrected for temporal variation in ambient temperature; while in (e, f) the data were additionally corrected for spatial variability (see Section 5.4.2); (f) is the final corrected dataset.

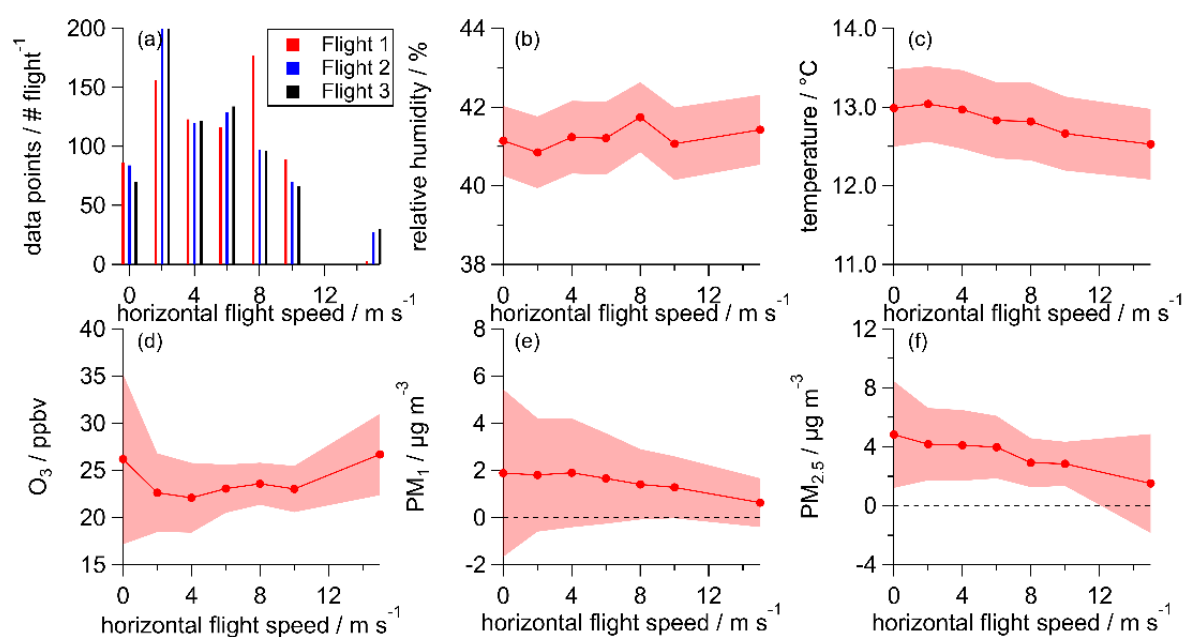


Fig. S9.23: Effect of horizontal flight velocity on measured variables. Number of data points per velocity setting (a) during Flight 1 (red), Flight 2 (blue) or Flight 3 (black) and average flight speed dependence for relative humidity (b), temperature (c), O_3 mixing ratio (d), and particulate matter PM_{10} (e) and $\text{PM}_{2.5}$ (f) determined from the OPC. The shaded areas show the uncertainty determined as described in Section 5.4.2.

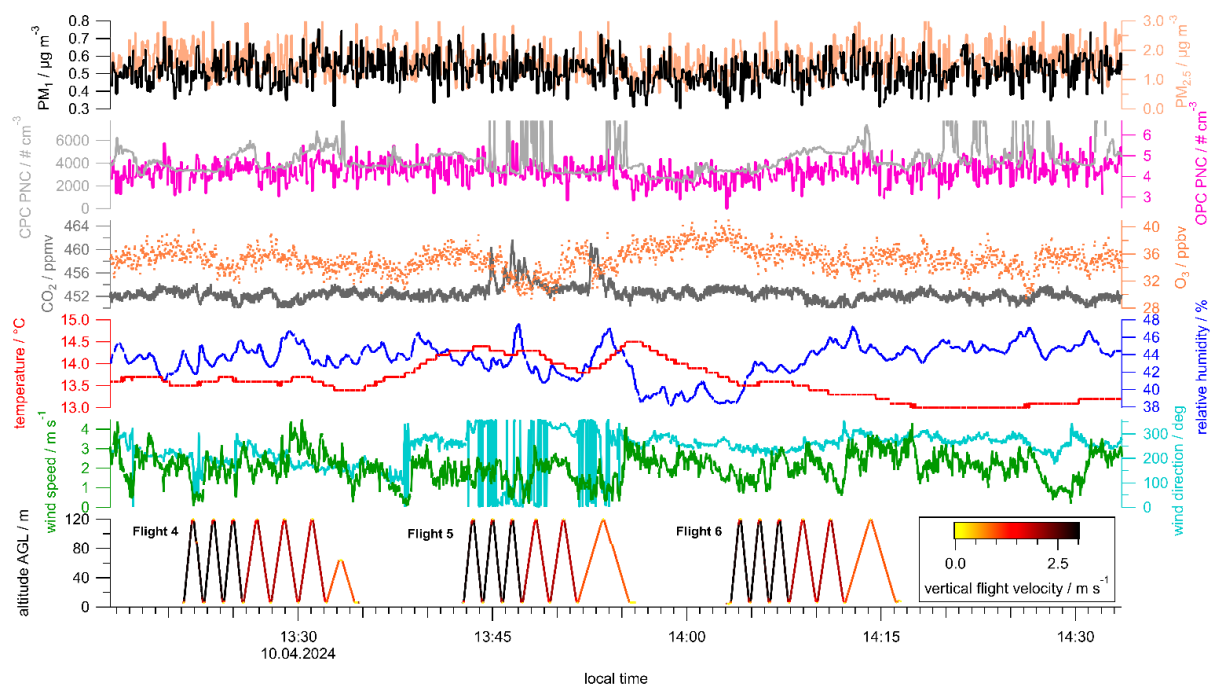


Fig. S9.24: Time series of various quantities measured by MoLa (top five panels) on 10 April 2024, showing stable environmental conditions during flights F4 and F6 and peaks in small particle concentrations and CO_2 during flight F5 (altitude derived from FLab measurements, bottom panel).

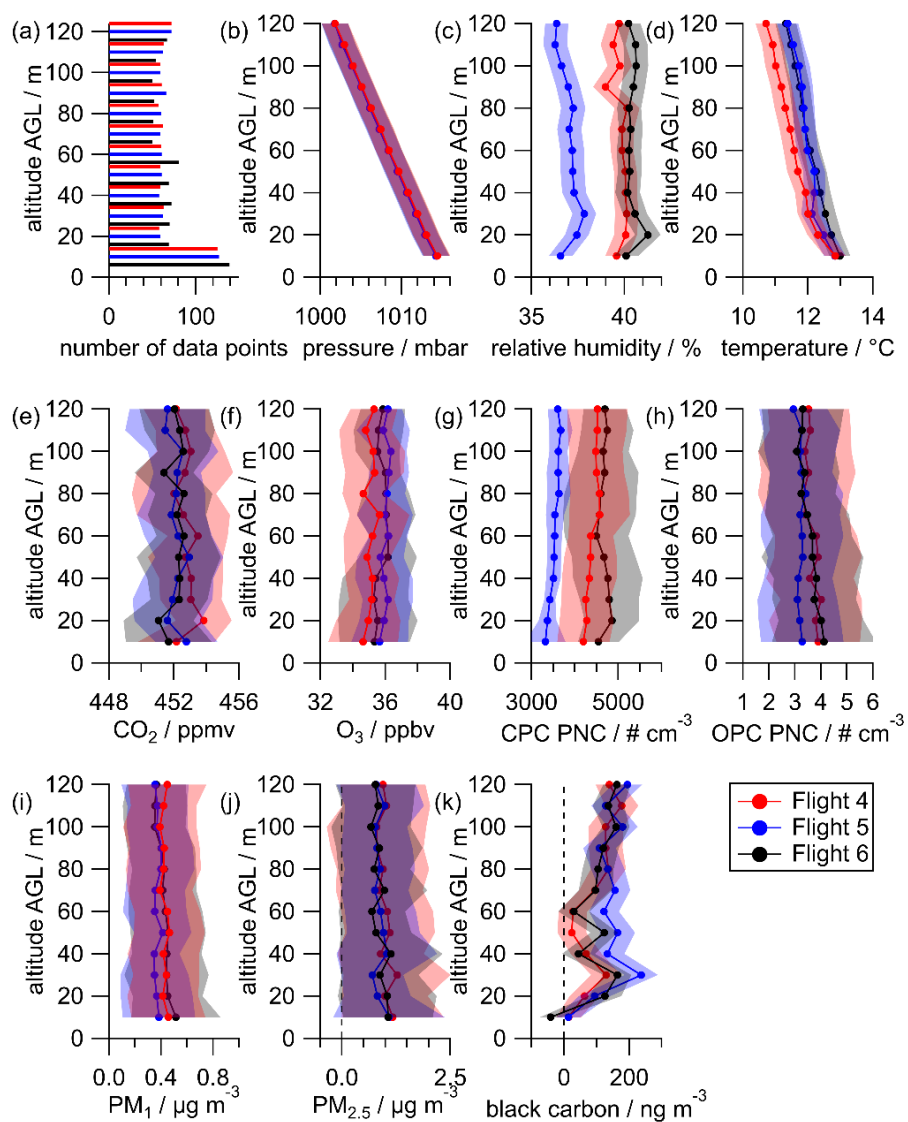


Fig. S9.25: Vertical profiles were measured with FLab during flights F4 (red), F5 (blue) and F6 (black). Averages for 10 m increments were calculated from the number of data points presented in (a) and are shown for the following variables: pressure (b), relative humidity (c), temperature (d), CO_2 (e) and O_3 mixing ratios (f), particle number concentration measured with CPC (g) and OPC (h), particulate matter PM_{10} (i) and $\text{PM}_{2.5}$ (j), and black carbon concentration (k). The shaded areas show the combined standard error and instrumental uncertainty within the 10 m altitude AGL increments.

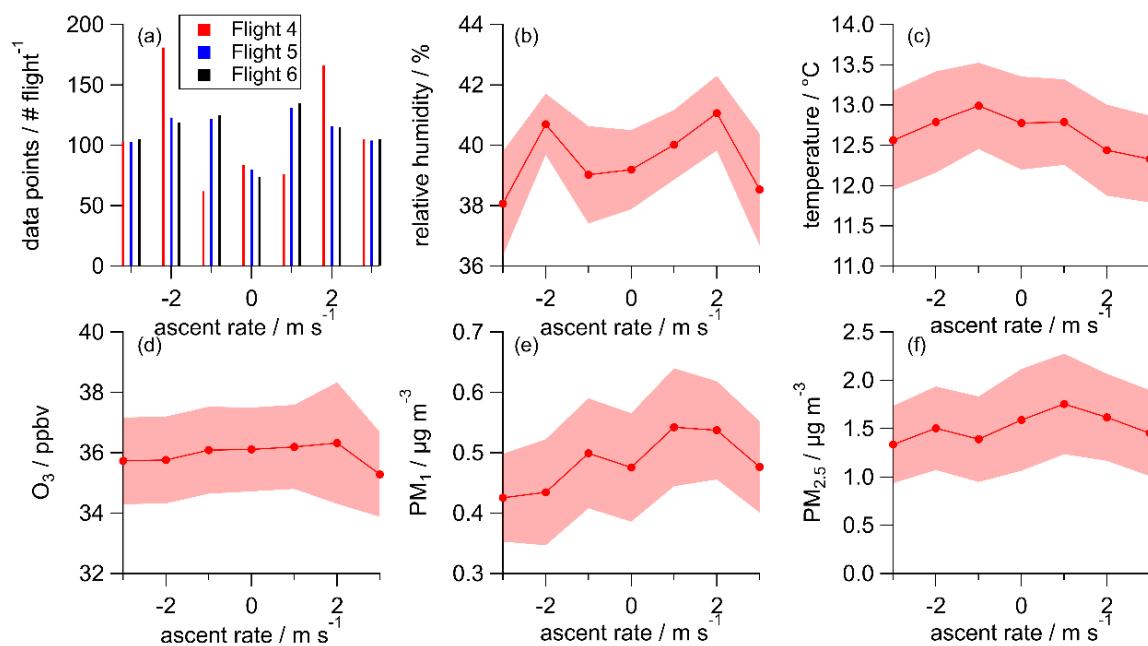


Fig. S9.26: During flight 4 (red), flight 5 (blue) and flight 6 (black) the number of data points (a) of the following atmospheric variables measured with FLab seem to be largely unaffected by its ascent/descent rate: relative humidity (b), temperature (c), O_3 mixing ratio (d) and particle mass concentrations PM_1 (e) and $PM_{2.5}$ (f) measured with OPC. Error bars show the uncertainty (determined as described in Sect. 5.4.2) within the 1 m s^{-1} increments. The lines between the markers are for orientation only and are not intended to indicate a relationship.

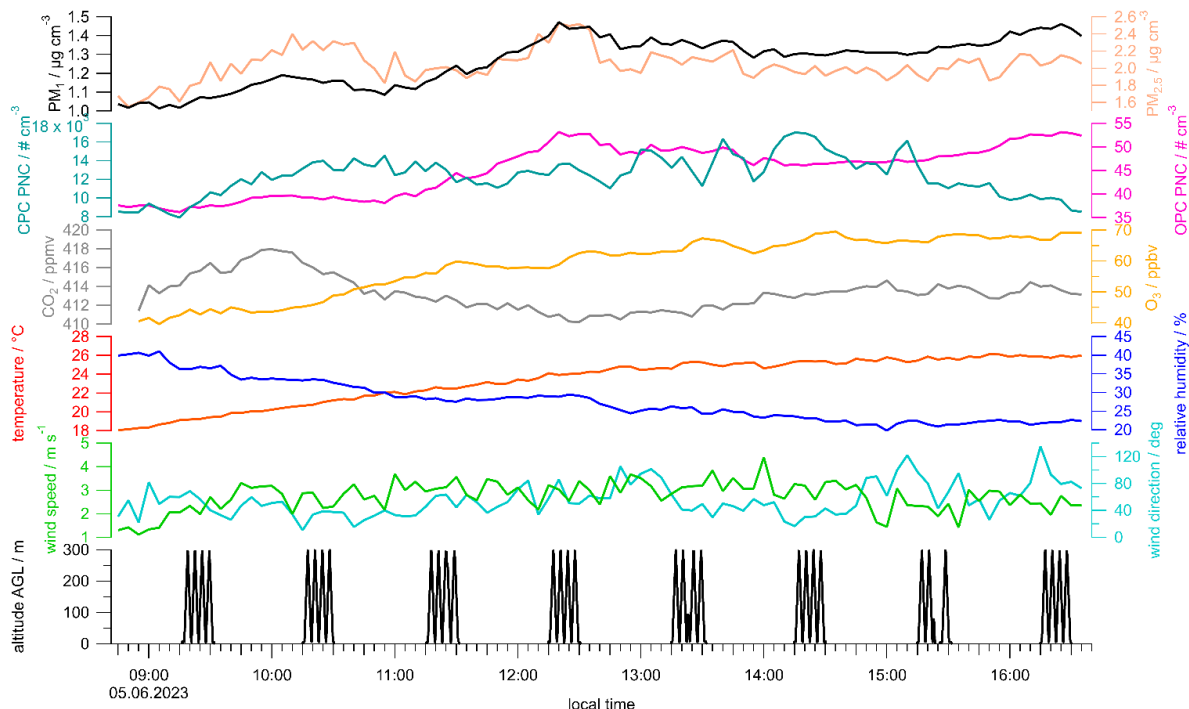


Fig. S9.27: Time series of variables measured with MoLa on 5 June 2023 at a rural site in Ockenheim show an increase in particle occurrence at 9:15 and in the afternoon, while O_3 and air temperature increase and CO_2 and relative humidity decrease during the day. No air mass changes due to changes in wind direction or emission sources were observed at MoLa. Time series of measured variables were averaged to 5 minutes.

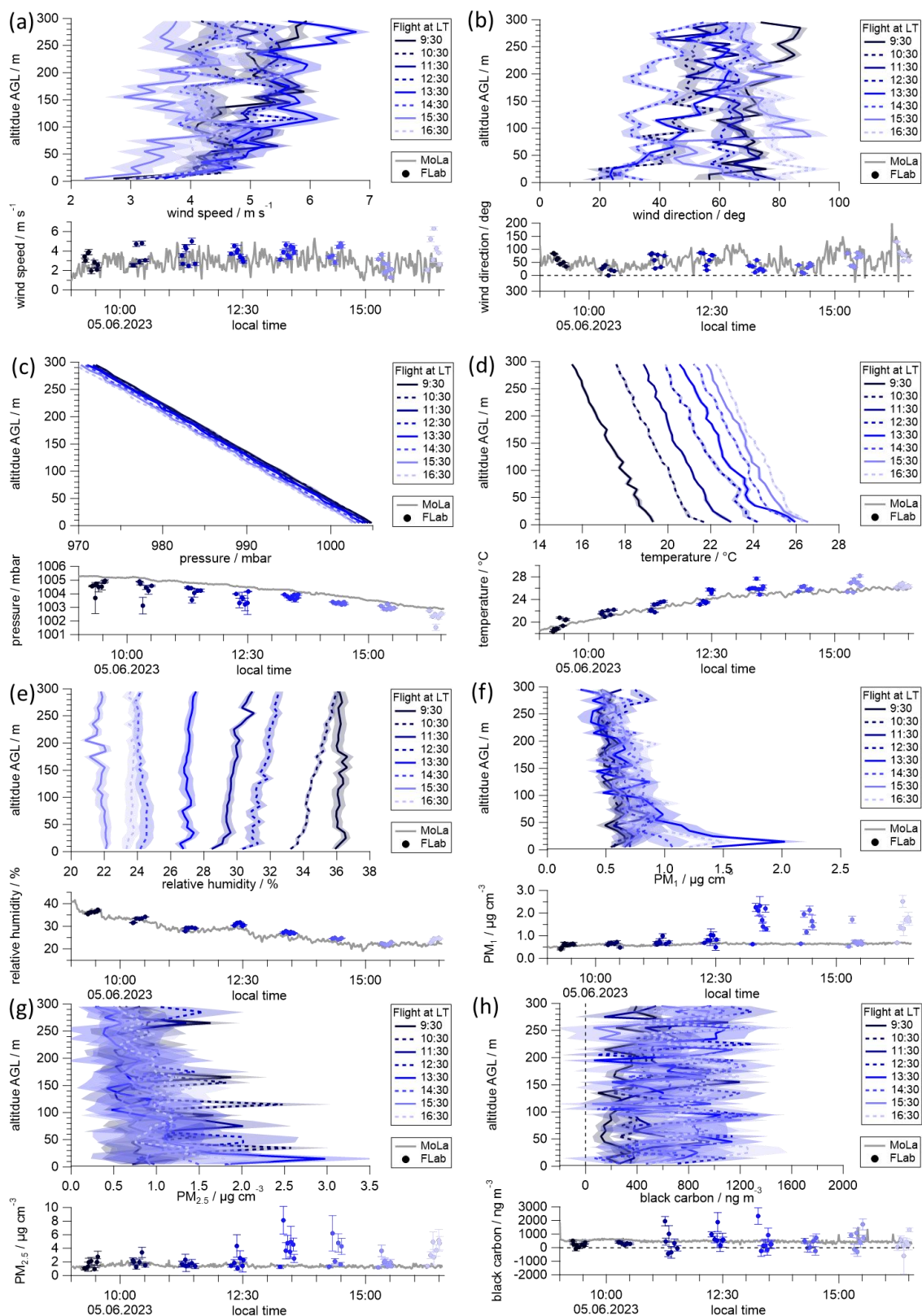


Fig. S9.28: Vertical profiles measured with FLab on 5 June 2023 (upper panels of the subfigures) showing trends of pressure (a), temperature (b), relative humidity (c), wind direction (d) and wind speed (e),

and particle mass concentrations for PM_{10} (f), $\text{PM}_{2.5}$ (g), and black carbon (h). Comparison measurements between MoLa (gray) and FLab (blueish) are performed when FLab was hovering below 10 m AGL next to MoLa (lower panels of subfigures).

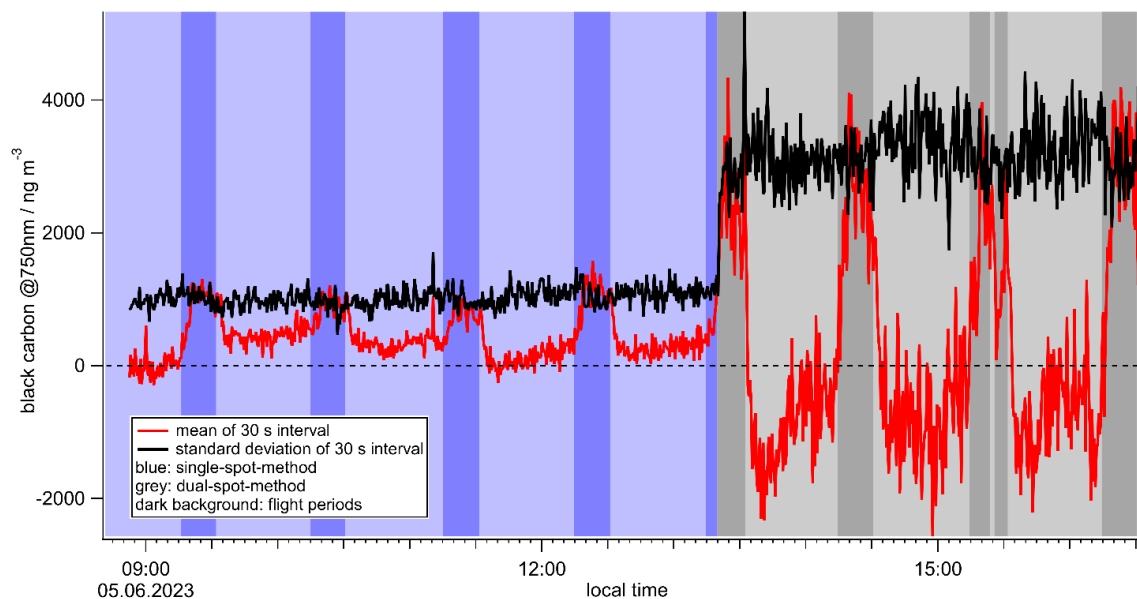


Fig. S9.29: Time series of the black carbon concentration measured with the MA200 Aethalometer showing differences between single-spot (blue) and dual-spot (gray) modes as well as between flight (dark) and nonflight (light) periods.

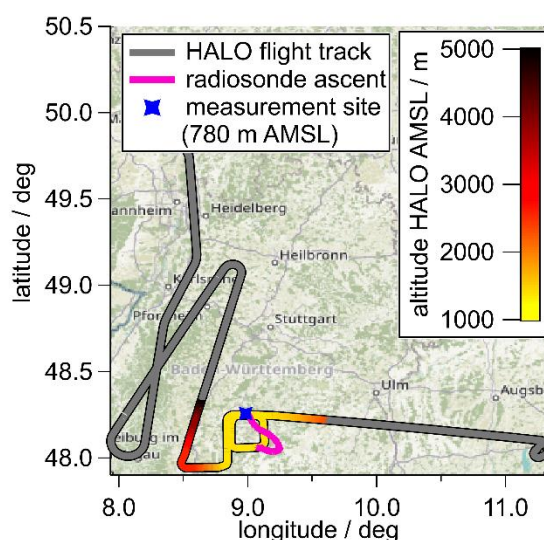


Fig. S9.30: Flight tracks of the radiosonde (pink) and the HALO aircraft (yellow to red below 5000 m and gray > 5000 m above mean sea level, AMSL) during the overflight of the BISTUM23 site at 778 m AMSL (blue), which was the base for the MoLa and FLab measurements and the launch site of the radiosonde. ©OpenStreetMap contributors 2024. Distributed under the Open Data Commons Open Database License (ODbL) v1.0.

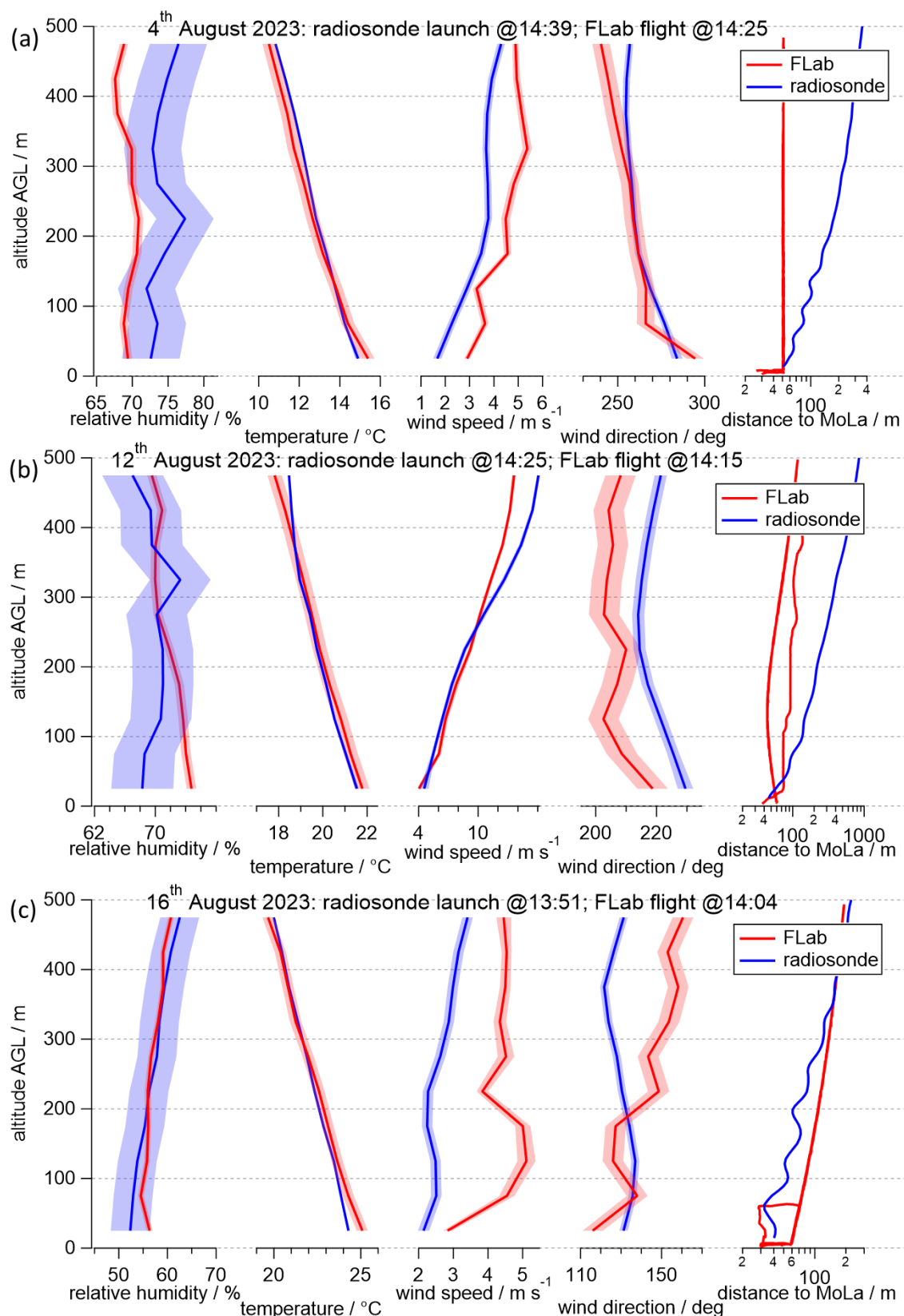


Fig. S9.31: Meteorological data (relative humidity, temperature, and horizontal wind speed and direction) were measured with radiosondes (blue) and FLab (red) up to 500 m AGL during the BISTUM23 campaign. The distance between the platforms and the stationary MoLa ground station reflects the oscillating flight behavior of the radiosonde (hanging about 50 m below the balloon) after launch.

Supplementary Information for Chapter 6

Text S9.7: Determination of the concentration

The extraction solution was not concentrated to dryness to prevent loss of semi-volatile compounds, so the volume prior to HPLC-MS analysis is unknown. To overcome this issue, a known amount of camphor sulfonic acid was added to both the calibration solutions and the samples as internal standard. This ensured that the concentration of all solutions would correspond to 35 ng/mL of the internal standard if the samples had the targeted 50 μL volume. In order to perform the volume correction, the mean value of the signal area of the camphor sulfonic acid of all calibration solutions is calculated. Following this, the ratio of the signal area for the respective sample to this mean value is multiplied by the concentration of the analytes determined by the calibration. This allows the concentration of the analytes to be obtained as if they were dissolved in 50 μL .

As the HPLC-MS analysis only determines the concentration of the sample in the extraction solution it is necessary to determine the concentration in the aerosol ($c(\text{compound})$). This is achieved by first calculating the mass $m(\text{compound})$ on the filter according to the following Eq. (S9.2), with V_{solution} representing the Volume and $c_{\text{solution}}(\text{compound})$ symbolizing the blank-corrected concentration of the compound in the extraction solution prior to the HPLC-MS measurement.

$$m(\text{compound}) = c_{\text{solution}}(\text{compound}) \cdot V_{\text{solution}} \quad (\text{S9.2})$$

The collected air volume (V_{air}) is then determined by integrating the linear equation of the fit for the flow (Q) (Eq. (S9.3)) through the filter holder, which leads to Eq. (S9.4). In the following equations t is the sampling time.

$$Q = (-0.41 \pm 0.01) \text{ SLPM min}^{-1} \cdot t + (102.8 \pm 0.2) \text{ SLPM} \quad (\text{S9.3})$$

$$V_{\text{air}} = \frac{(-0.027 \pm 0.002)}{2} \text{ SLPM min}^{-1} \cdot t^2 + (18.97 \pm 0.04) \text{ SLPM} \cdot t \quad (\text{S9.4})$$

Since the flow through the collector is pressure dependent, it must be corrected for the different pressures at different heights (1.5 m: 920 hPa; 120 m: 907 mbar; 500 m: 870 mbar; measured by FLab). The linear fit for the dependence of flow on pressure ($Q(p)$) is used for the correction (Eq. (S9.5)).

$$Q(p) = (0.20 \pm 0.01) \text{ SLPM hPa}^{-1} \cdot p + (-93 \pm 12) \quad (\text{S9.5})$$

The collected air volume $V_{\text{air}}(p)$ is subsequently corrected according to Eq. (S9.6). The flow at 980 hPa is utilized as a reference because the time dependence was determined at this air pressure.

$$V_{\text{air}}(p) = V_{\text{air}} \cdot \frac{Q(p)}{Q(980 \text{ hPa})} \quad (\text{S9.6})$$

The concentration of the compound of interest can then be calculated as shown in Eq. (S9.7).

$$c(\text{compound}) = \frac{m(\text{compound})}{V_{\text{air}}(p)} \quad (\text{S9.7})$$

Table S9.9: Chemical compounds used in this study, including their respective purities.

Compound	Label	Purity
cis-pinic acid	Synthesized	N/A
terpenylic acid	Synthesized	N/A
terebic acid	Sigma Aldrich	N/A
salicylic acid	Sigma Aldrich	99%
4-hydroxybenzaldehyde	Sigma Aldrich	>97.5%
4-nitrophenol	Alfa Aesar	99%
2,6-dimethyl-4-nitrophenol	Merck KGaA	N/A
2,4-dinitrophenol	Sigma Aldrich	>98%

Table S9.10: Measured concentration of pinic acid, 4-nitrophenol, terebic acid and 2,6-dimethyl-4-nitrophenol, of the three measurement setups (no UAV; dji m300; dji m200) during three measurement flights.

Flight	UAV	Pinic acid		Terebic acid		4-Nitrophenol		2,6-Dimethyl-4-nitrophenol	
		Concentration / ng m ⁻³	Error	Concentration / ng m ⁻³	Error	Concentration / ng m ⁻³	Error	Concentration / ng m ⁻³	Error
1	-	1.91	0.05	0.53	0.03	1.67	0.06	0.20	0.004
	Dji m300	1.42	0.06	0.39	0.02	1.20	0.03	0.17	0.004
	Dji m200	1.61	0.07	0.44	0.02	1.46	0.03	0.17	0.00
2	-	1.71	0.05	0.55	0.03	1.43	0.05	0.23	0.01
	Dji m300	1.71	0.07	0.52	0.03	1.42	0.04	0.24	0.005
	Dji m200	1.72	0.08	0.54	0.02	1.52	0.08	0.25	0.01
3	-	1.87	0.09	0.50	0.03	2.63	0.10	0.68	0.02
	Dji m300	1.97	0.08	0.58	0.02	2.73	0.06	0.69	0.01
	Dji m200	2.09	0.06	0.57	0.02	2.90	0.06	0.78	0.02

Table S9.11: Measured concentration of the biogenic marker compounds pinic acid, terpenylic acid and terebic acid at the different heights and times (all times are in UTC+2).

Time	Height / m	Pinic acid		Terpenylic acid		Terebic acid	
		Concentration / ng m ⁻³	Error	Concentration / ng m ⁻³	Error	Concentration / ng m ⁻³	Error
10:35 am	1.5	1.92	0.51	0.66	0.18	1.11	0.30
	120	2.22	0.60	0.84	0.23	1.40	0.38
	500	1.40	0.39	0.56	0.16	0.81	0.23
1:35 pm	1.5	3.01	0.80	1.17	0.31	2.07	0.55
	120	3.46	0.93	1.20	0.33	2.02	0.54
	500	2.62	0.73	0.91	0.26	1.58	0.44
4:30 pm	1.5	2.80	0.75	1.14	0.31	2.29	0.61
	120	4.14	1.11	1.81	0.49	3.13	0.84
	500	3.35	0.94	1.40	0.39	2.37	0.66

Table S9.12: Measured concentration of the biomass burning and anthropogenic marker compounds salicylic acid, 4-hydroxybenzaldehyde, 4-nitrophenol, 2,4-dinitrophenol at different heights and times (all times are in UTC+2).

Time	Height / m	Salicylic acid		4-Hydroxy-benzaldehyde		4-Nitrophenol		2,6-Dimethyl-4-nitrophenol		2,4-Dinitrophenol	
		Concentration / ng m ⁻³	Error	Concentration / ng m ⁻³	Error	Concentration / ng m ⁻³	Error	Concentration / ng m ⁻³	Error	Concentration / ng m ⁻³	Error
10:35 am	1.5	0.09	0.08	0.11	0.06	1.03	0.28	0.03	0.04	0.20	0.09
	120	0.45	0.16	0.28	0.10	1.40	0.39	0.04	0.04	0.30	0.12
	500	0.01	0.06	0.08	0.05	0.82	0.24	0.02	0.03	0.12	0.07
1:35 pm	1.5	0.11	0.08	0.19	0.07	0.41	0.13	0.02	0.03	0.07	0.07
	120	0.00	0.09	0.18	0.08	0.48	0.16	0.02	0.04	0.13	0.09
4:30 pm	500	0.16	0.08	0.24	0.08	0.39	0.12	0.02	0.03	0.06	0.06
	1.5	0.05	0.07	0.20	0.07	0.20	0.09	0.01	0.03	0.04	0.07
4:30 pm	120	0.16	0.10	0.39	0.12	0.41	0.14	0.02	0.04	0.07	0.08
	500	0.21	0.09	0.24	0.08	0.30	0.11	0.01	0.03	0.05	0.06

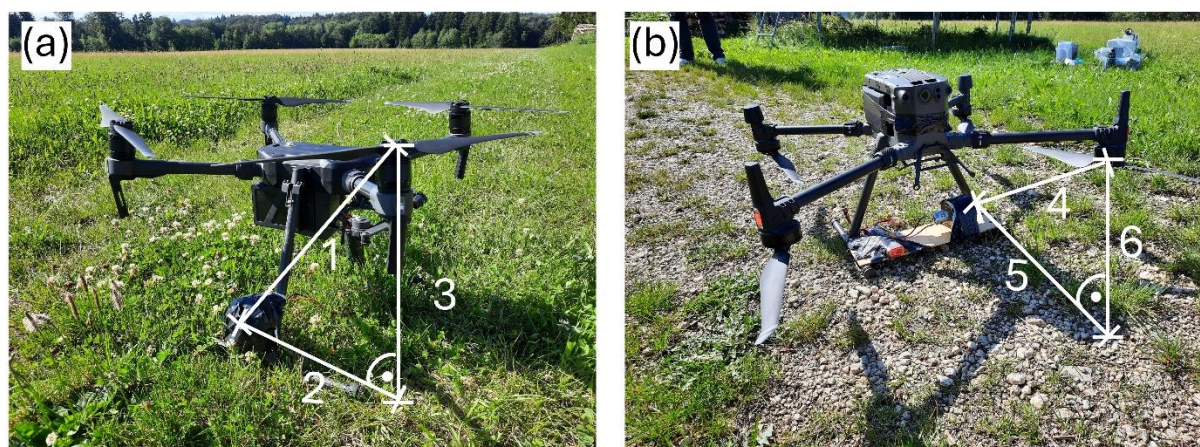


Fig. S9.32: Photo of the filter holder attached to the landing gear at the UAV dji m200 (a) and at plate between the landing gear of the dji m300 (b). The white lines indicate measured distances. Line 1 (51 cm) is the diagonal distance between the collector and the rotor of the UAV. Line 2 (26 cm) is the distance between the collector and the perpendicular to the rotor of the UAV, and line 3 (44 cm) is the height difference between the collector and the rotor for the UAV(dji m200). Line 4 (36 cm) is the diagonal distance between the collector and the rotor of the UAV. Line 5 (30 cm) is the distance between the collector and the perpendicular to the rotor of the UAV, and line 6 (19 cm) is the height difference between the collector and the rotor for the UAV(dji m300).

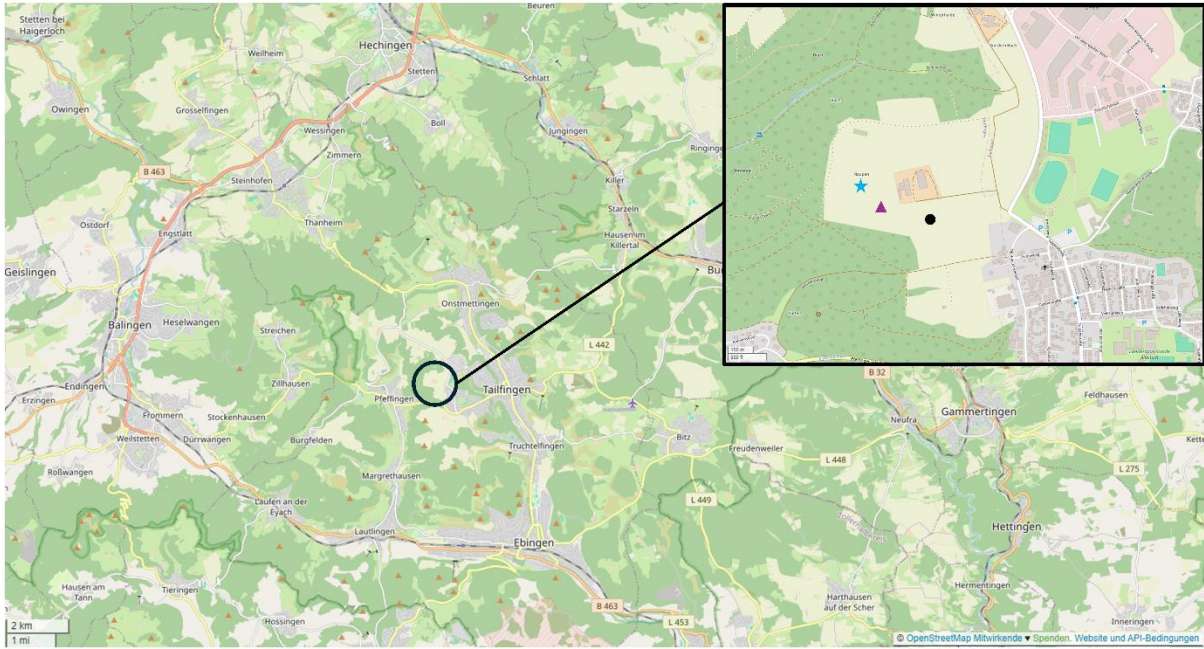


Fig. S9.33: Map (©OpenStreetMap contributors) showing the measurement site (close to Albstadt, southern Germany), which is surrounded in all directions by a mixture of forest, agricultural land, and urban infrastructure. The black circle represents the measurement site, which is shown in greater detail within the black box. The symbols indicate the approximate locations for the UAV measurements: a blue star (djim300), a purple triangle (dji m200), and a black dot (FLab).

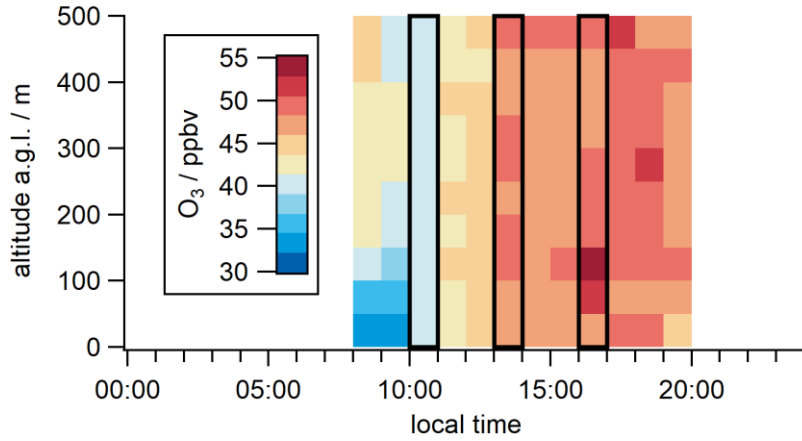


Fig. S9.34: Measured ozone concentration versus time of day. The measurements were carried out hourly in an altitude range from 0 to 500 m above ground level (AGL). The black boxes indicate the time intervals during when the parallel UAV flights were conducted.

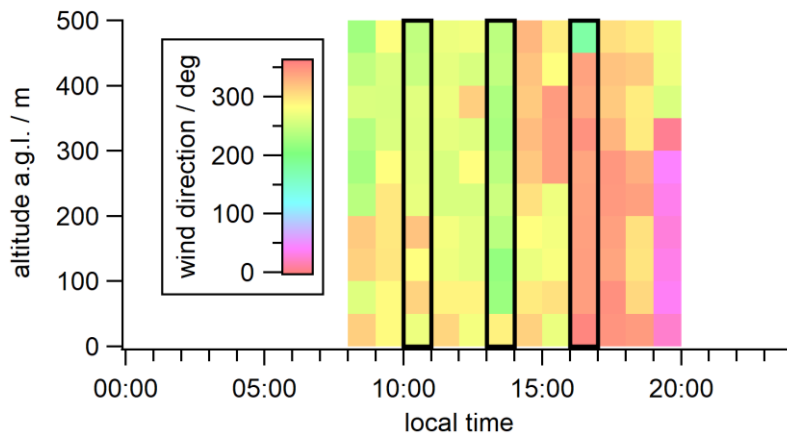


Fig. S9.35: Measured wind direction versus time of day. The measurements were carried out hourly in an altitude range from 0 to 500 m. The black boxes indicate the time intervals during when the parallel UAV flights were conducted.

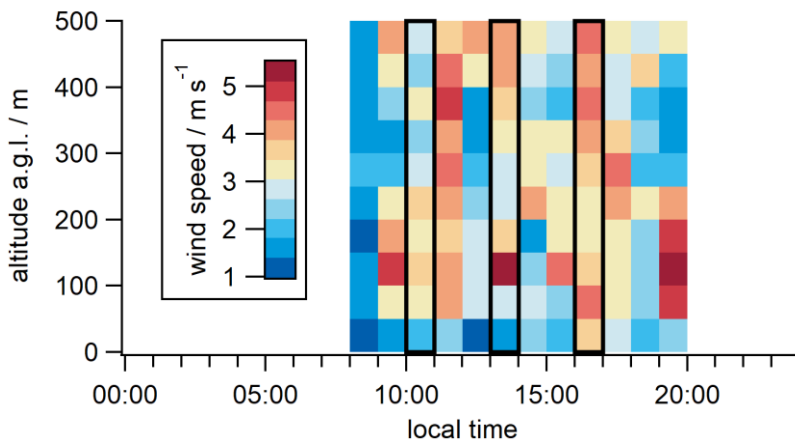


Fig. S9.36: Measured wind speed versus time of day. The measurements were carried out hourly in an altitude range from 0 to 500 m. The black boxes indicate the time intervals during when the parallel UAV flights were conducted.

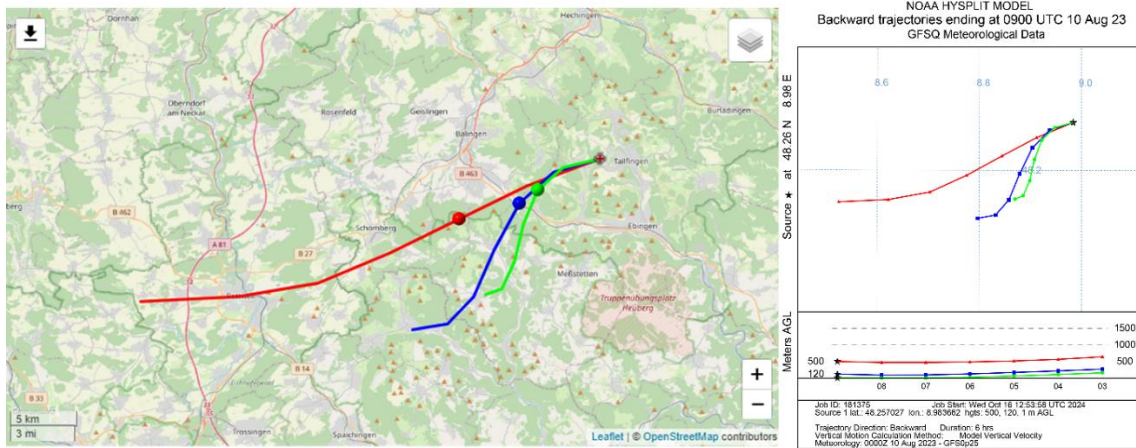


Fig. S9.37: Calculated 6 hour back trajectories with HYSPLIT (Stein et al., 2015; Rolph et al., 2017) for 1 m (green line), 120 m (blue line) and 500 m (red line) for the sampling on 10.08.2023 in the morning. The dots on the map (©OpenStreetMap contributors) indicate the time (8 am local time) at which the air mass at 120 m altitude crosses the main traffic road.

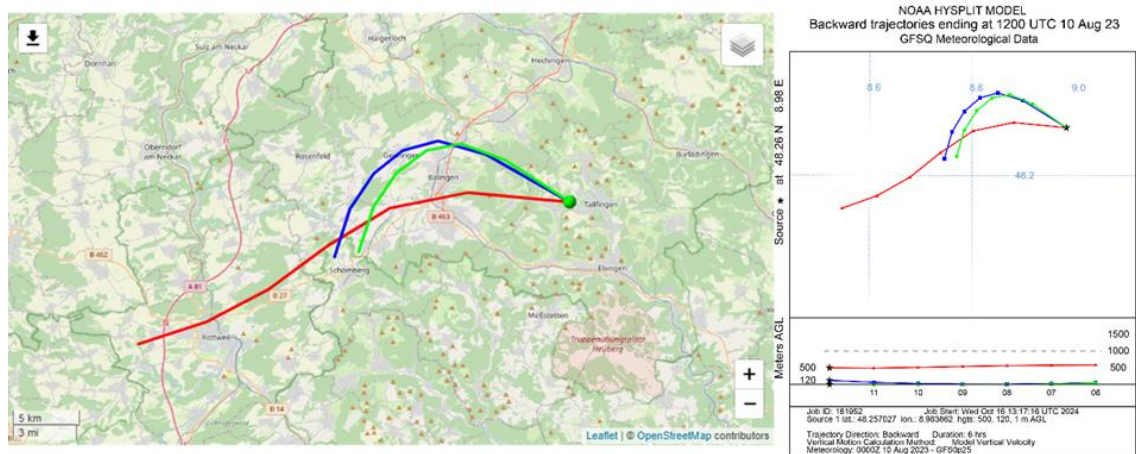


Fig. S9.38: Calculated 6 hour back trajectories with HYSPLIT (Stein et al., 2015; Rolph et al., 2017) for 1 m (green line), 120 m (blue line) and 500 m (red line) for the sampling on 10.08.2023 at noon (©OpenStreetMap contributors).

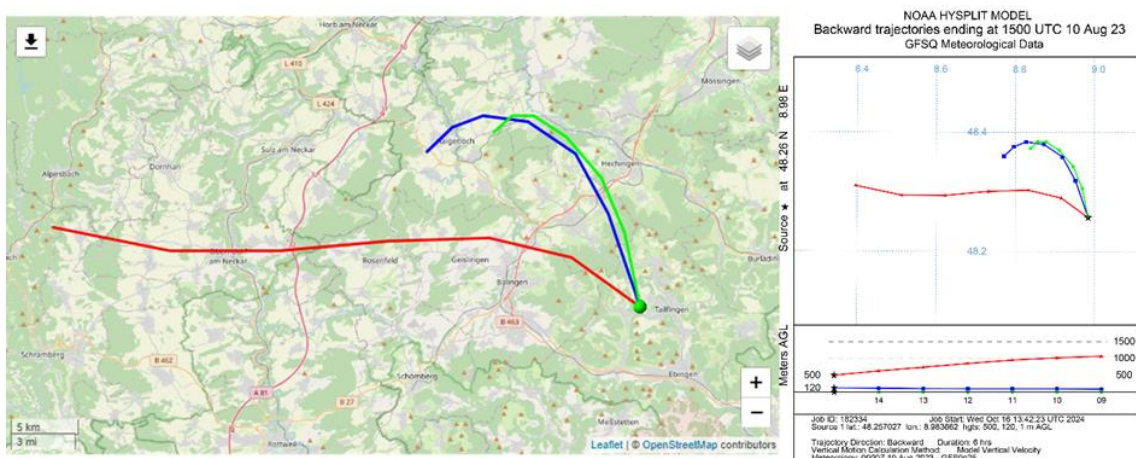


Fig. S9.39: Calculated 6 hour back trajectories with HYSPLIT (Stein et al., 2015; Rolph et al., 2017) for 1 m (green line), 120 m (blue line) and 500 m (red line) for the sampling on 10.08.2023 in the afternoon (©OpenStreetMap contributors).

Supplementary Information for Chapter 7

Table S9.13: Instruments used for characterization of the lower troposphere.

Instrument	Measured variables	Time resolution
MoLa (Drewnick et al., 2012)		
CPC ^a	Particle number concentration (> 2.5 nm)	1 s
EDM ^b	Particulate matter PM ₁	6 s
FMPS ^c	Particle size distribution (5.6 to 560 nm) based on electrical mobility diameter	1 s
Meteorological station ^d	Wind direction, wind speed, relative humidity, temperature, rain intensity, pressure	1 s
OPC ^e	Particle size distribution (0.25 to 35 µm) based on optical diameter	6 s
O ₃ -monitor ^f	Mixing ratio of O ₃	2 s
Pyranometer ^g	Solar irradiance	1s
^a Condensation Particle Counter Model 3786, TSI, Inc., USA. ^b Environmental Dust Monitor EDM180, Grimm Aerosoltechnik, Germany. ^c Fast Mobility Particle Sizer Model 3091, TSI, Inc., USA. ^d WXT520, Vaisala Oyj, Finland. ^e Optical Particle Counter Model 1.109, Grimm Aerosoltechnik GmbH, Germany. ^f Monitor 205 Dual Beam Ozone Monitor, 2B Technologies, Inc., USA. ^g CMP3 Pyranometer Sensor, Campbell Scientific Inc., UK.		
FLab (Moormann et al., 2025b)		
Anemometer ^h	Horizontal wind speed and direction; temperature; relative humidity; pressure	1 s
CPC ⁱ	Particle number concentration (> 10 nm)	1 s
CBO ^j	Mixing ratio of CO ₂	2 s
OPC ^k	Particle size distribution (350 nm to 35 µm) based on optical diameter; temperature; relative humidity	1 s
O ₃ -monitor ^l	Mixing ratio of O ₃	2 s
UAS: Matrice 600 ^m	3D orientation; 3D flight velocity; GPS position; wind speed and direction; altitude based on pressure level and GPS; propeller rotation rate; various internal data	≤1 s
^h TriSonica™ Mini, Anemoment LLC, USA. ⁱ Condensation Particle Counter Model 3007, TSI, Inc., USA. ^j CARBOCAP® Carbon Dioxide Probe GMP343, Vaisala Ojy, Finland. ^k OPC-N3, Alphasense AMETEK®, United Kingdom. ^l Model 205 Dual Beam Ozone Monitor, 2B Technologies, Inc., USA. ^m Matrice 600, SZ DJI Technology Co., Ltd., China.		
Flux tower		
Ultra-sonic anemometer ⁿ	3D wind direction, humidity, temperature	0.05 s
ⁿ CSAT3B 3-D Sonic Anemometer, Campbell Scientific, Inc., Logan, Utah, USA.		

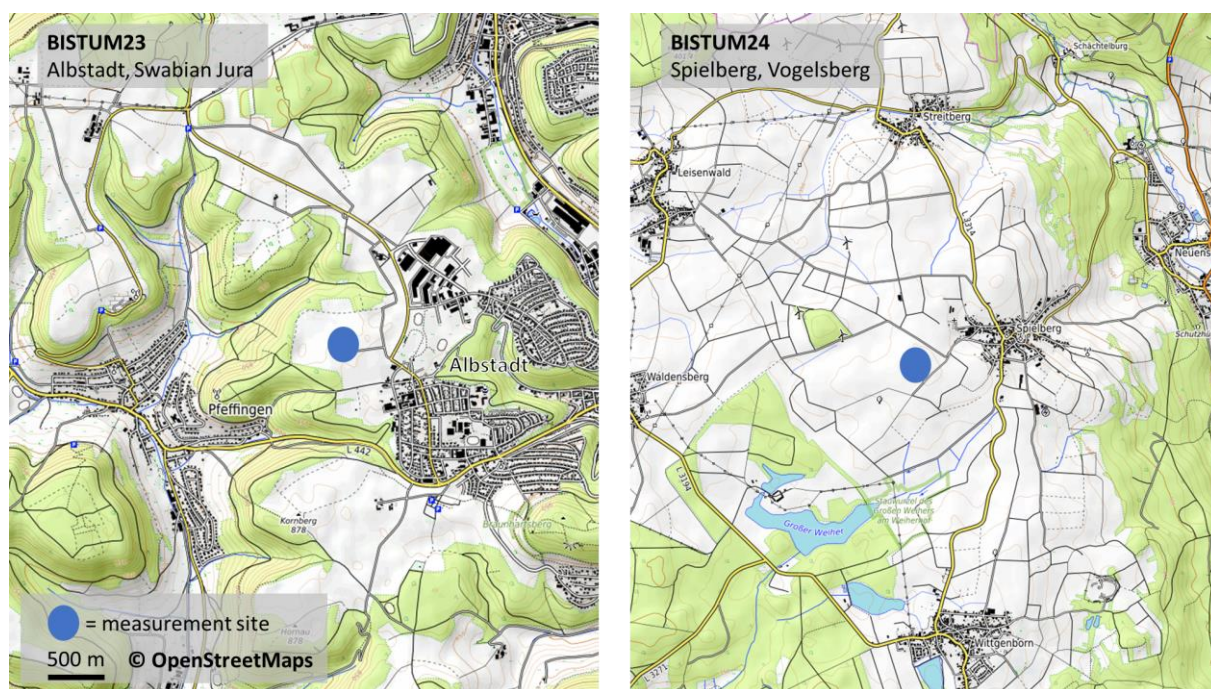


Fig. S9.40: Topographic maps of the rural measurement sites during BISTUM23 and BISTUM24.

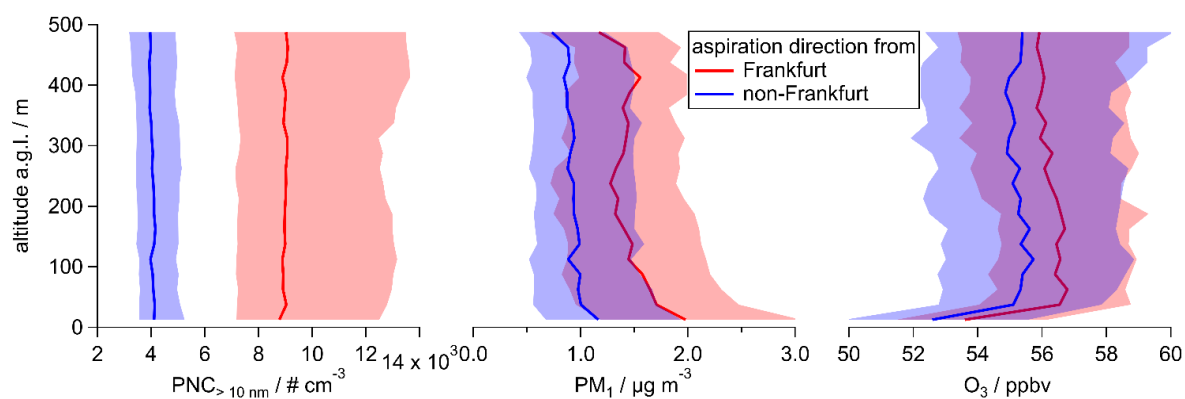


Fig. S9.41: Median vertical profiles of anthropogenic tracers for air masses passing the Frankfurt-Rhine-Main metropolitan area (red) and only rural areas (blue): the particle number concentration (a), the PM_{10} mass concentration (b) and O_3 mixing ratio (c). Shaded areas represent the respective interquartile ranges.

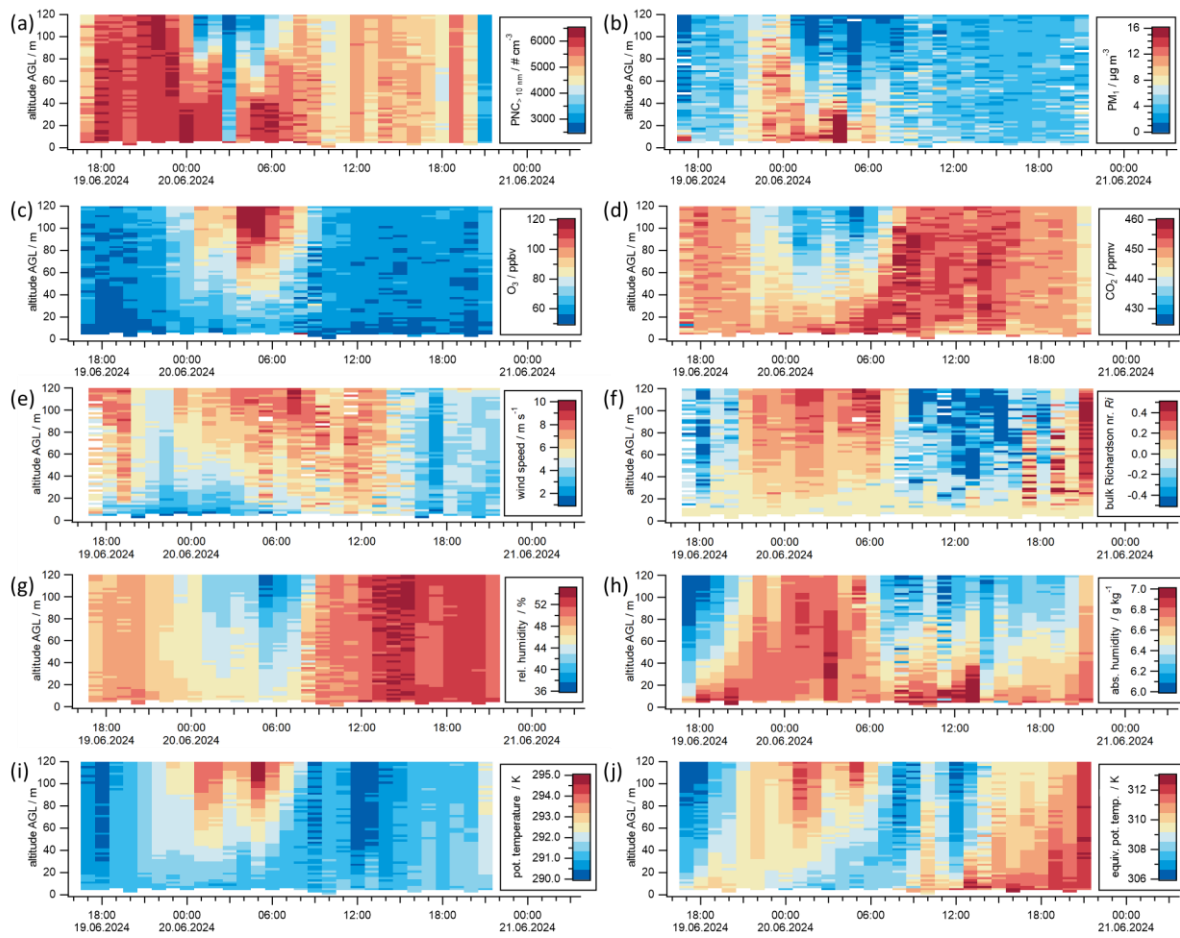


Fig. S9.42: Hourly high-resolution (2 m bins) vertical profiles throughout a full day and night during BISTUM24, including: the particle number concentration measured with the CPC ($\text{PNC}_{>10 \text{ nm}}$) (a), PM_{1} (b), O_3 (c), CO_2 (d), wind speed (e), bulk Richardson number (f), relative and absolute humidity (g and h), and potential and equivalent potential temperature (i and j).

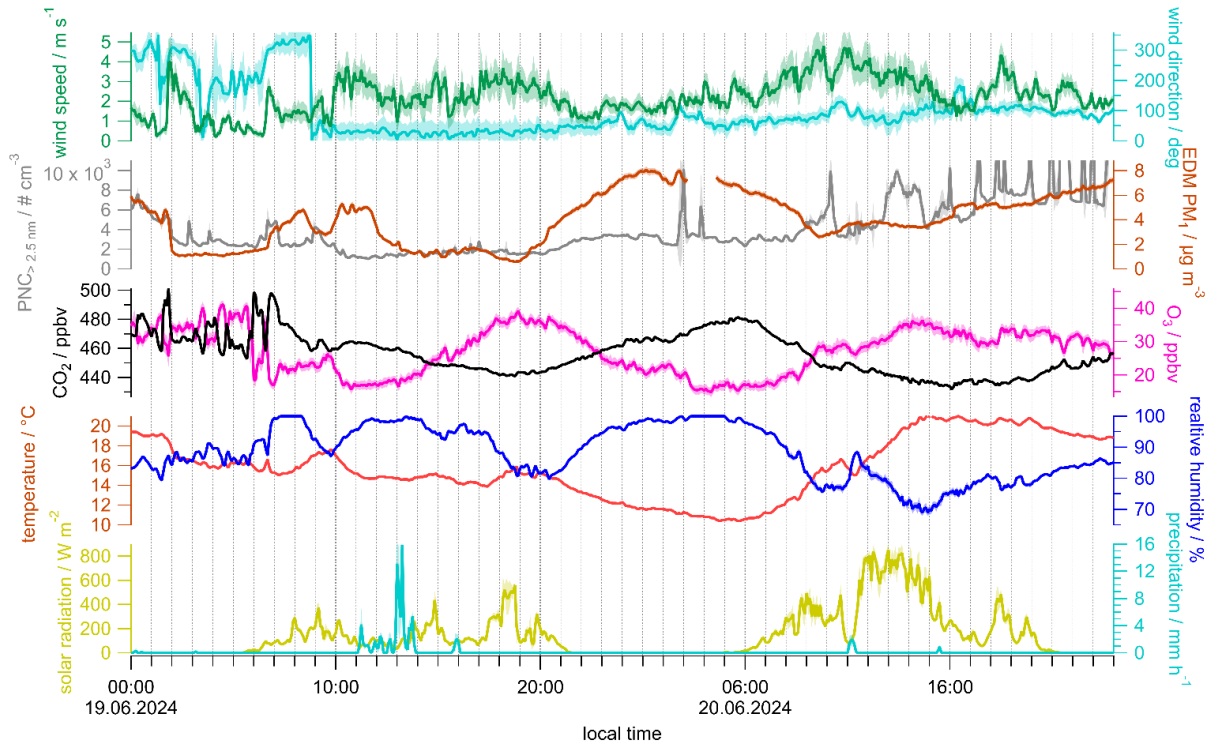


Fig. S9.43: Ground-based measurements on June 19 to June 21, 2024 show low radiative impact on June 19 and fog between 03:00 and 05:00 on June 20 that led to an increase of the PM₁ (orange) and the particle number concentration (grey), but a strong reduction of O₃ (pink), while air temperature (red), wind (green and turquoise) and CO₂ (black) appear unchanged.

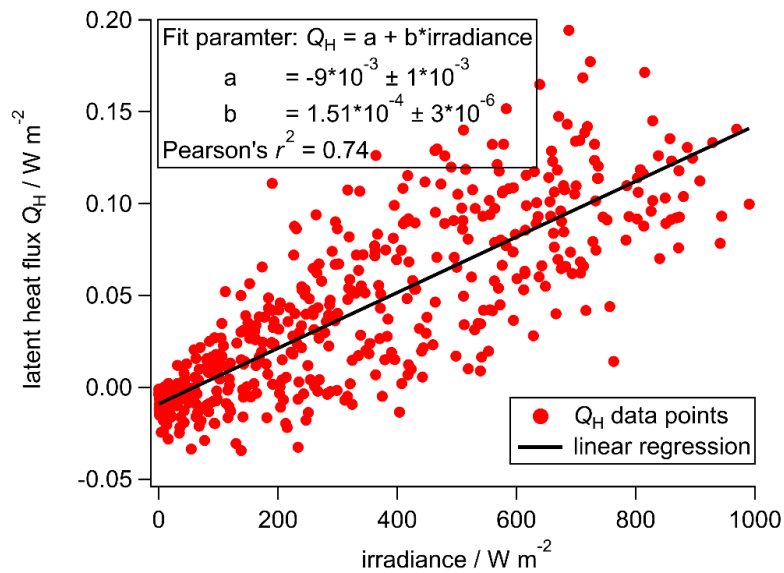


Fig. S9.44: The latent heat flux and the irradiance during BISTUM24 show a good correlation (Pearson's $r^2 = 0.74$).

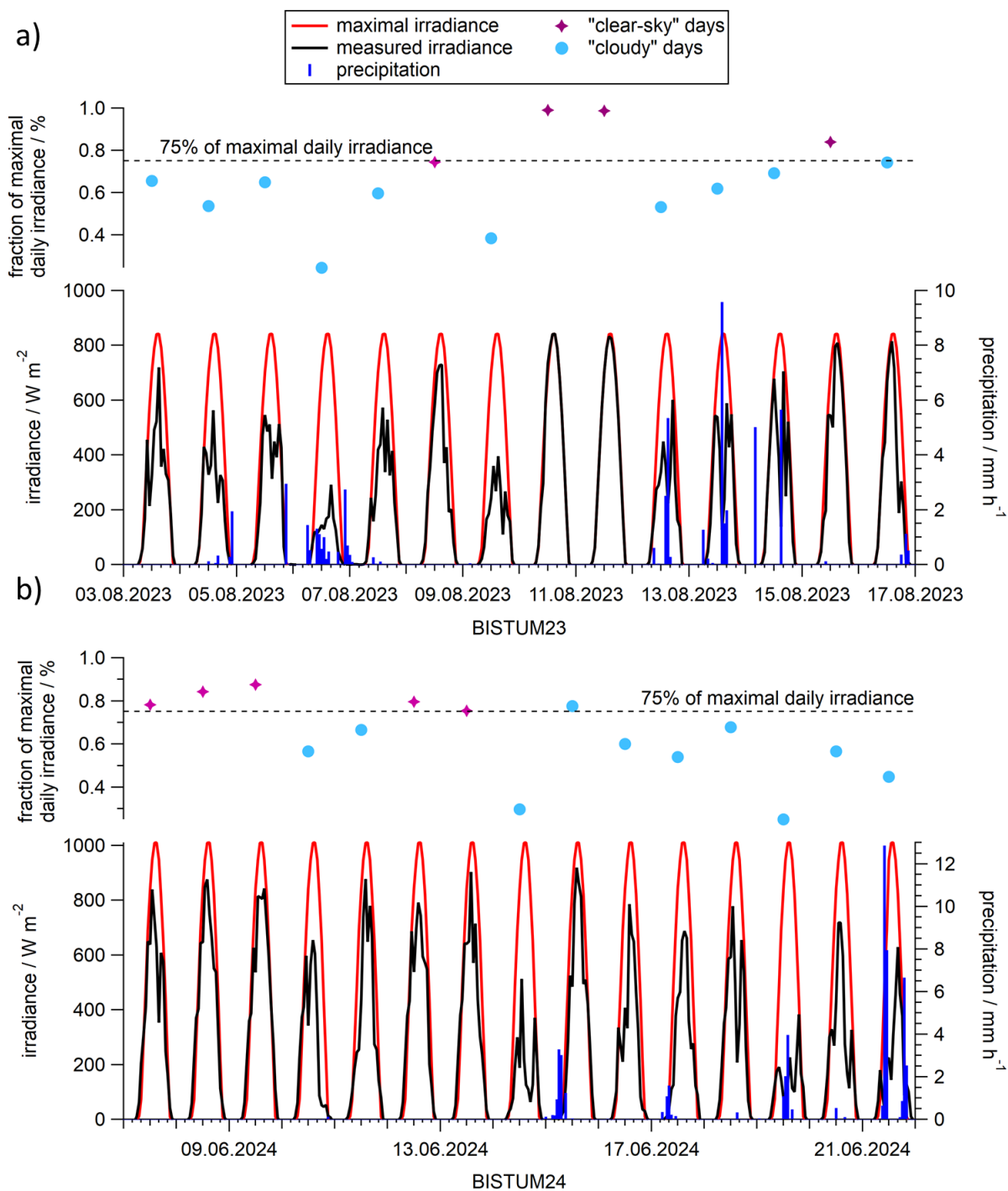


Fig. S9.45: “Clear-sky” days (violet markers) and “cloudy” days (bluish markers) were classified by the criteria that more or less than 75% of maximal daily possible irradiance (red and black lines) were measured throughout a day, respectively, and that no precipitation (blue) was measured. The classification of individual days is displayed for BISTUM23 (a) and BISTUM24 (b).

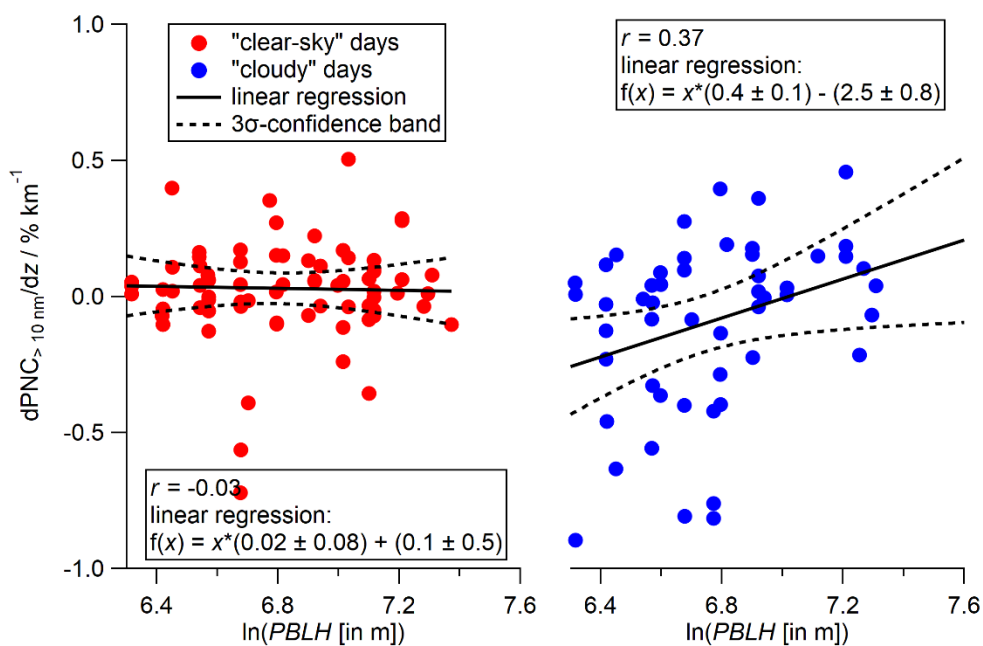


Fig. S9.46: Gradients of the particle number concentration of small particles $dPNC_{>10\text{ nm}}/dz$ normalized to a concentration value of "1" at ground level in the lowermost 500 m in a mixed PBL from both campaigns for "clear-sky" and "cloudy" days (red and blue markers, respectively). Linear regression and its 3σ -confidence bands are shown in straight and dotted lines. The uncertainty of the linear regression is given as 1σ .

Supplementary Information for Chapter 8

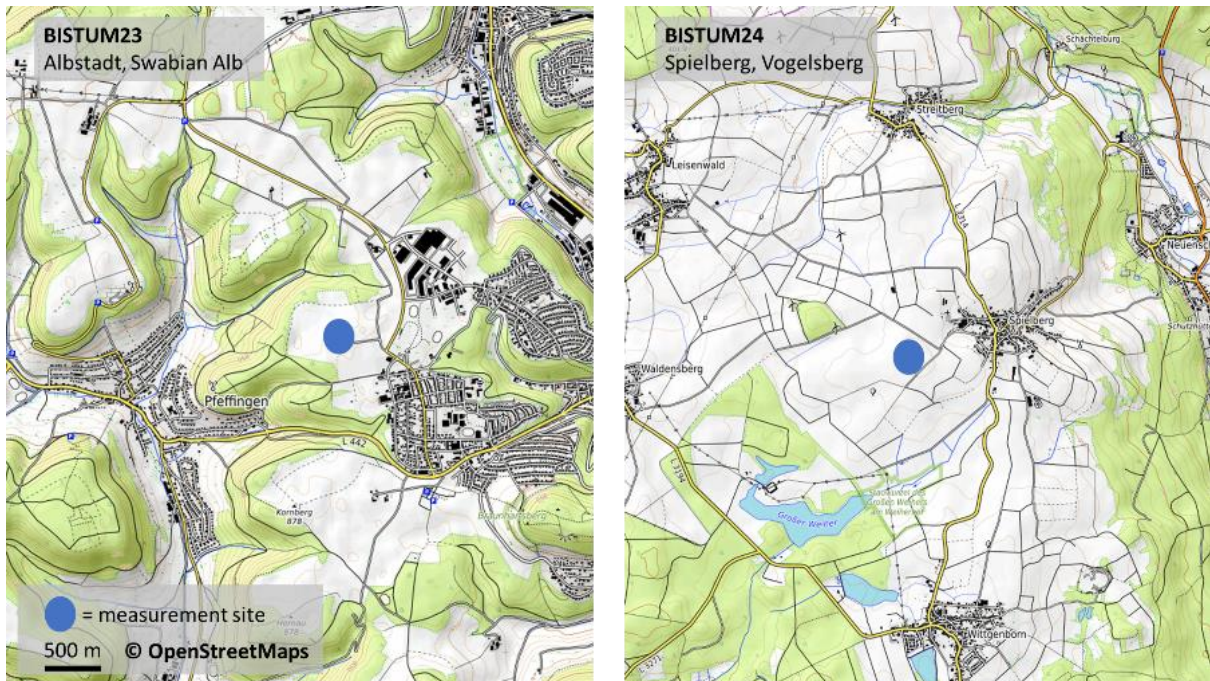


Fig. S9.47: Topographic map of the rural measurement sites during BISTUM23 (Sect. 8.5) and BISTUM24 (Sect. 8.4) ©OpenStreetMap contributors 2025. Distributed under the Open Data Commons Open Database License (ODbL) v1.0.

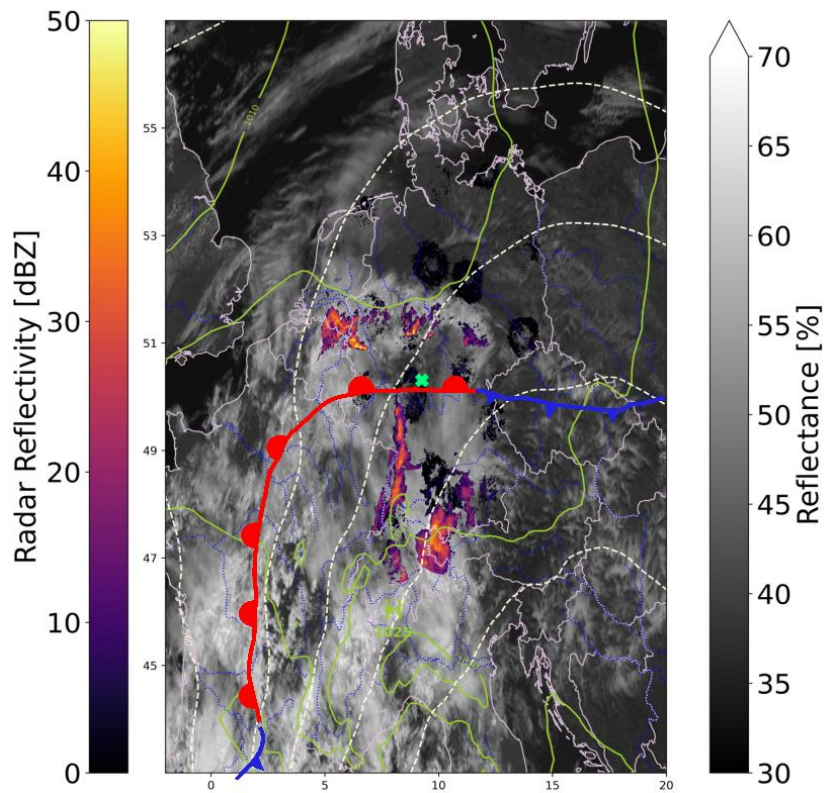


Fig. S9.48: Synoptic map for 12:00 on 20 June 2024 including the radar reflectivity shows the measurement site (green) in a large high-pressure system close to a warm front (in red).

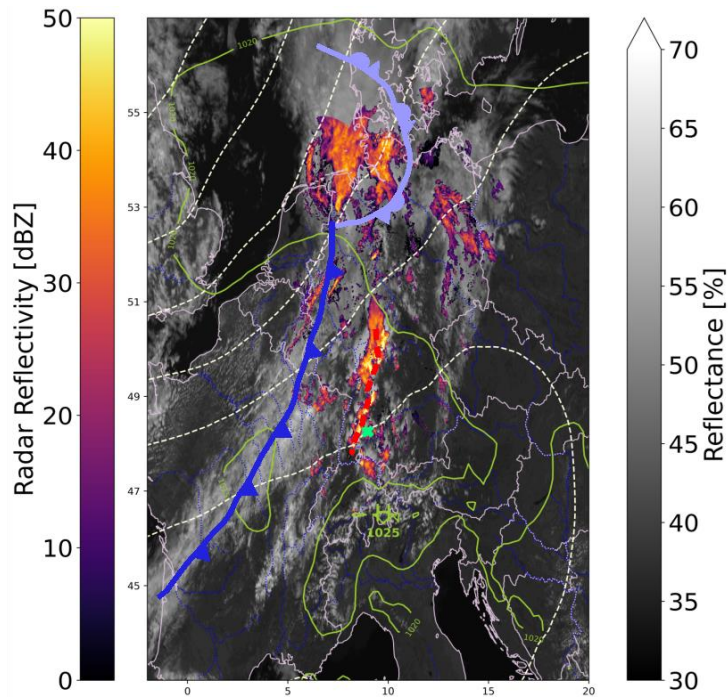


Fig. S9.49: Synoptic map from 12:00 on 12 August 2023 including the radar reflectivity shows a convergence line (red) at the measurement site (green) in vicinity to a large cold front (blue)

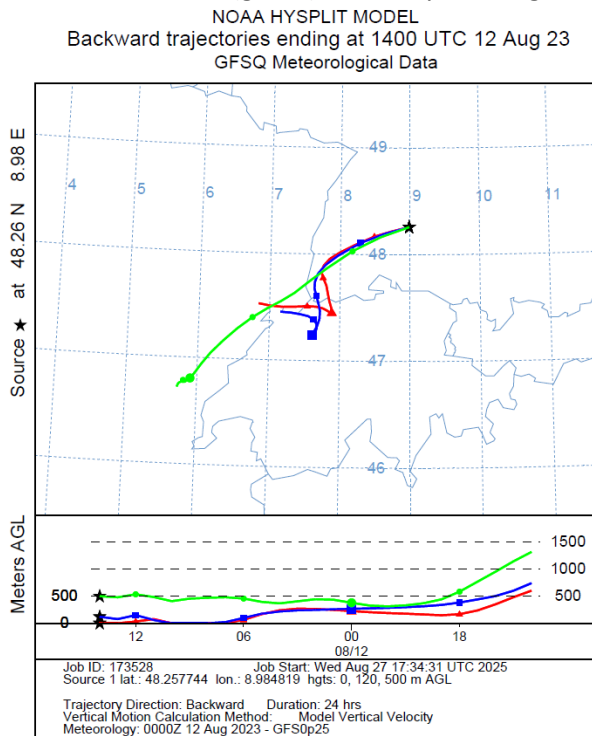


Fig. S9.50: 24 h-backward-trajectories reaching the measurement site at 12:00 local time on 12 August 2023 reveal south-westerly aspiration from rural areas. The trajectories were calculated with the HySplit analysis tool and were started from 0 m, 120 m and 500 m above ground level (Stein et al., 2015). The near surface trajectories are influenced stronger by the underlying surface, leading to a more westerly flow at the Northern flank of the high-pressure system ~18 h before arrival, but are then partially deflected by the Alps and additionally get further into the influence of the cyclonic system over the British islands. The trajectory at elevated altitude is able to follow the free tropospheric flow more closely, such that the eastward flow, which is more driven by the free tropospheric wave pattern is less dominant.

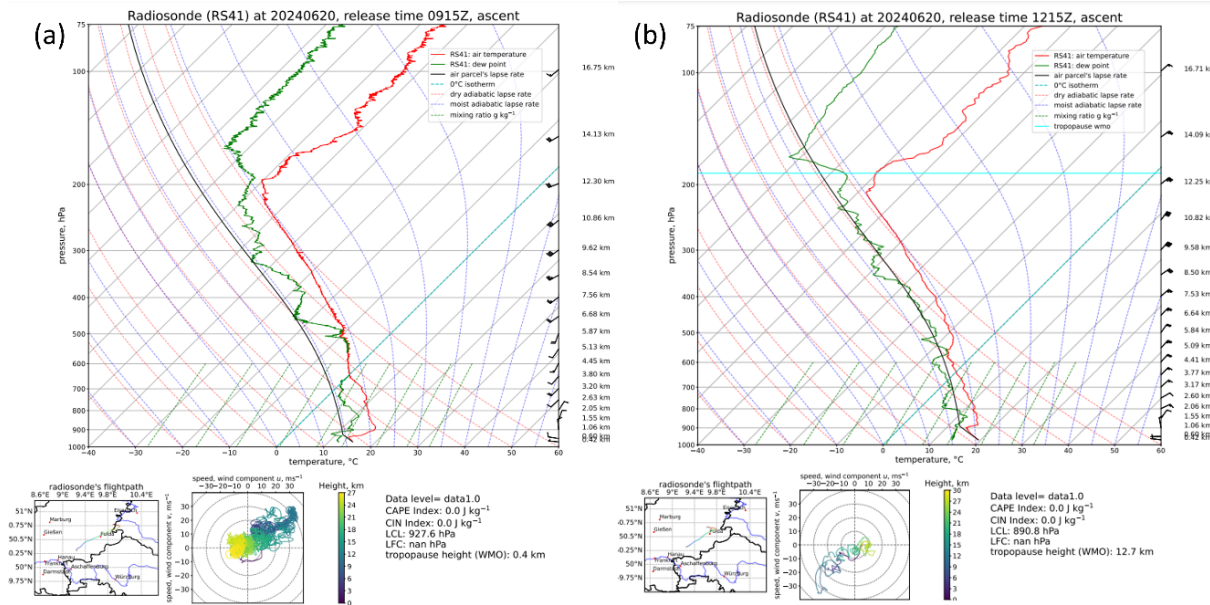


Fig. S9.51: Radiosonde ascents on 20 June 2024 indicate stable pre- and post-rain conditions ((a) at 09:15 and (b) at 12:15).

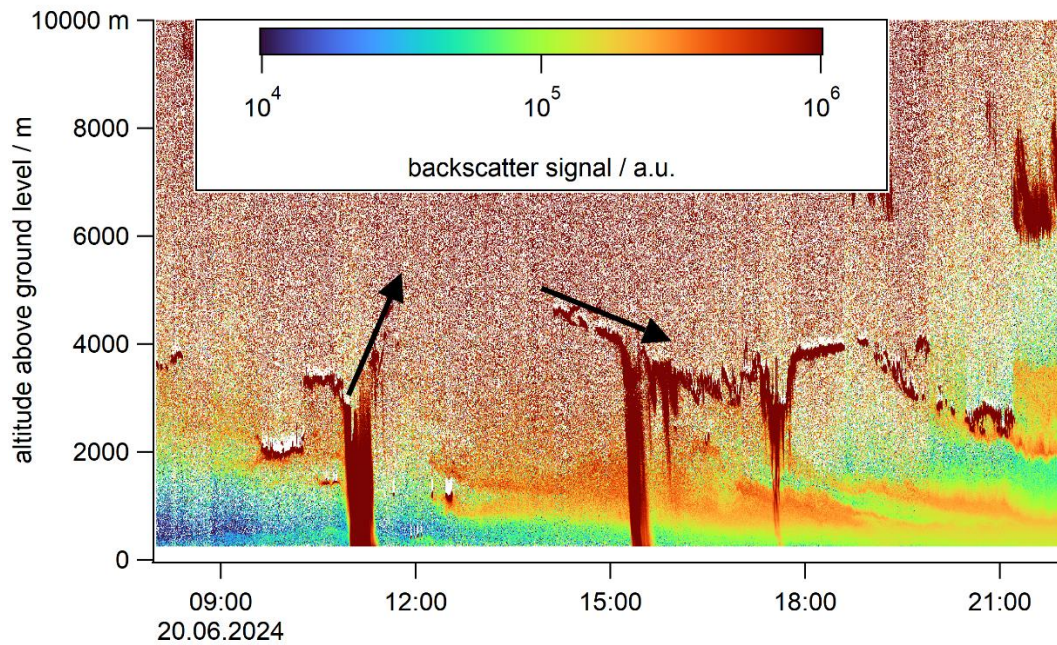


Fig. S9.52: The ceilometer in MoLa monitors an uplift of clouds (dark red) from 3 km to 5 km immediately after the rainfall at 11:00 and a later decrease of layers before the second rainfall (red color reaching ground level indicates precipitation). Data of the lowermost 200 m were removed due to high uncertainties.

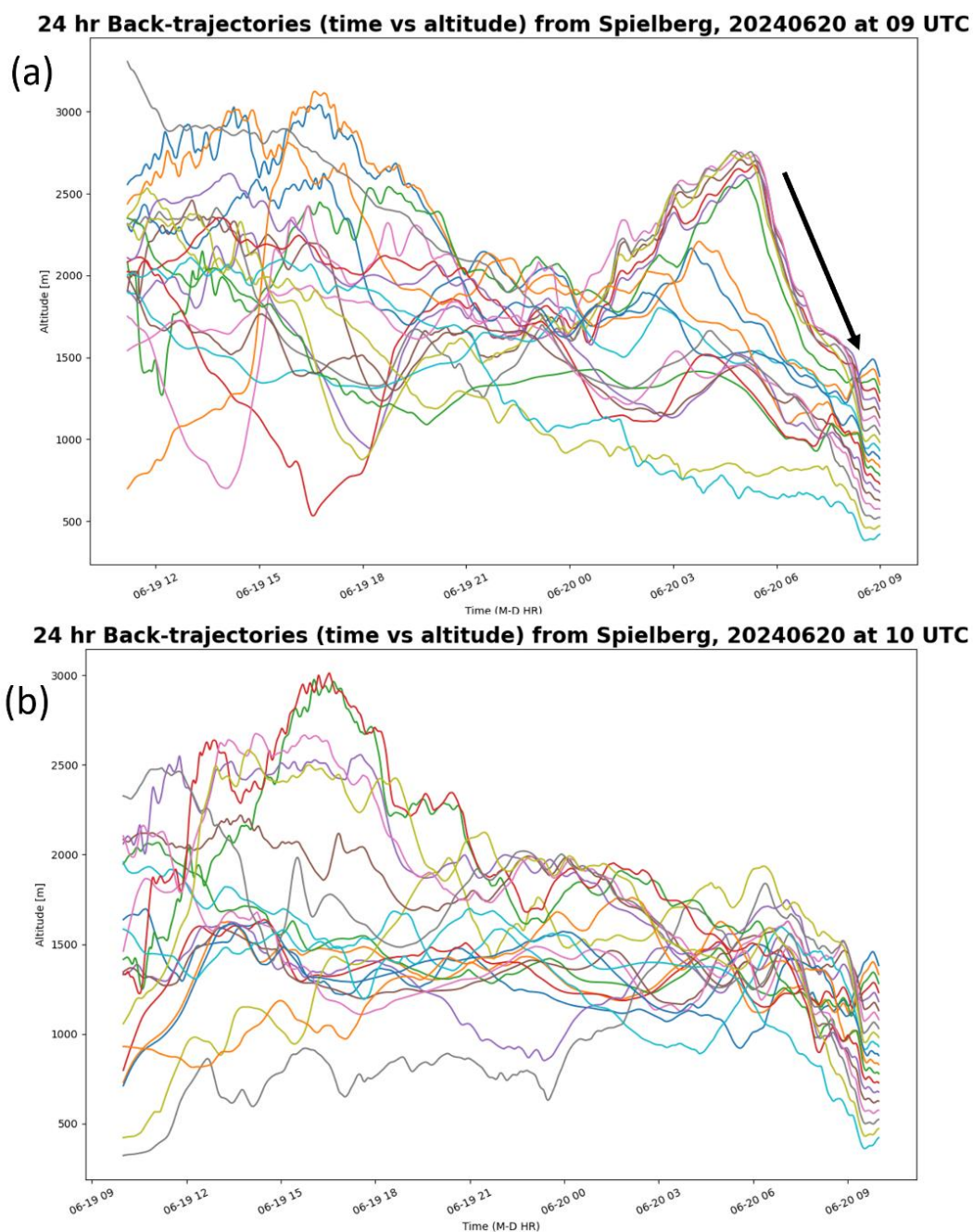


Fig. S9.53: During the rain event, 24-h backward trajectories show a strong downdraft from 3000 m a.s.l. from 6 h before reaching the measurement site for arrival altitude levels down to 150 m a.g.l., whereas the ground-near trajectories are isolated and do not reveal strong vertical movement (a). After the rain event, the aspiration level is more than 1000 m lower and trajectories are homogeneously distributed (b). Note that altitude levels are denoted as above mean sea level, and the measurement location is at 391 m a.s.l.

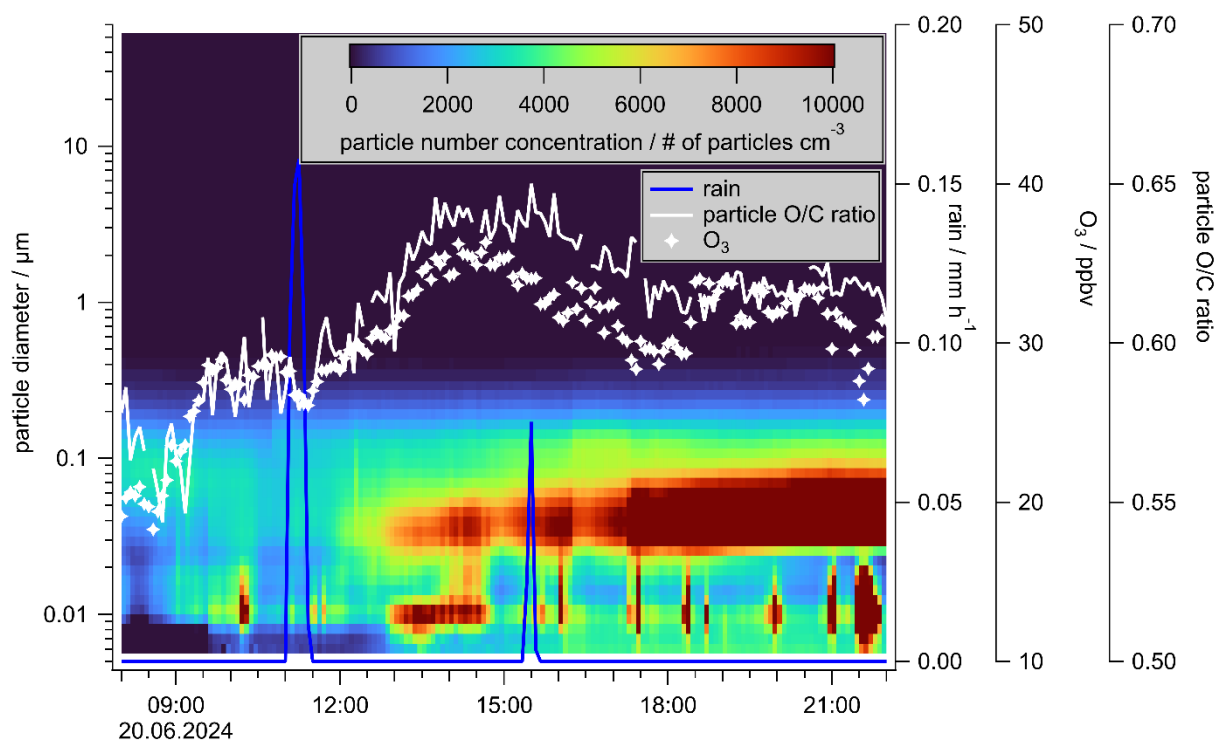


Fig. S9.54: The good agreement of time series of O_3 (white stars) and the O/C ratio of organic particle components (white trace) measured at ground level in MoLa show an increase of oxidized aerosol particles along with oxidizing reagent. Therefore, particles form and grow as indicated by increasing mode sizes of the particle number concentration for the nucleation and Aitken mode (image plot) after the rain at 11:00 (blue).

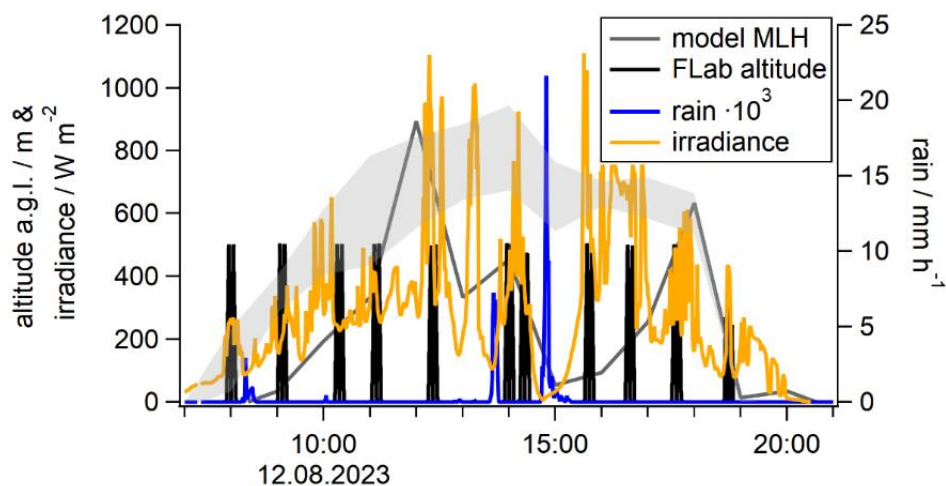


Fig. S9.55: Time series of irradiance (orange), precipitation (blue, both 1 min averages), and the modelled MLH (grey, hourly averages) on 12 August 2023. The flight altitude of FLab is displayed in black. The shaded area represents the typical diurnal cycle of the modelled MLH at the BISTUM23 measurement site for cloudless days.

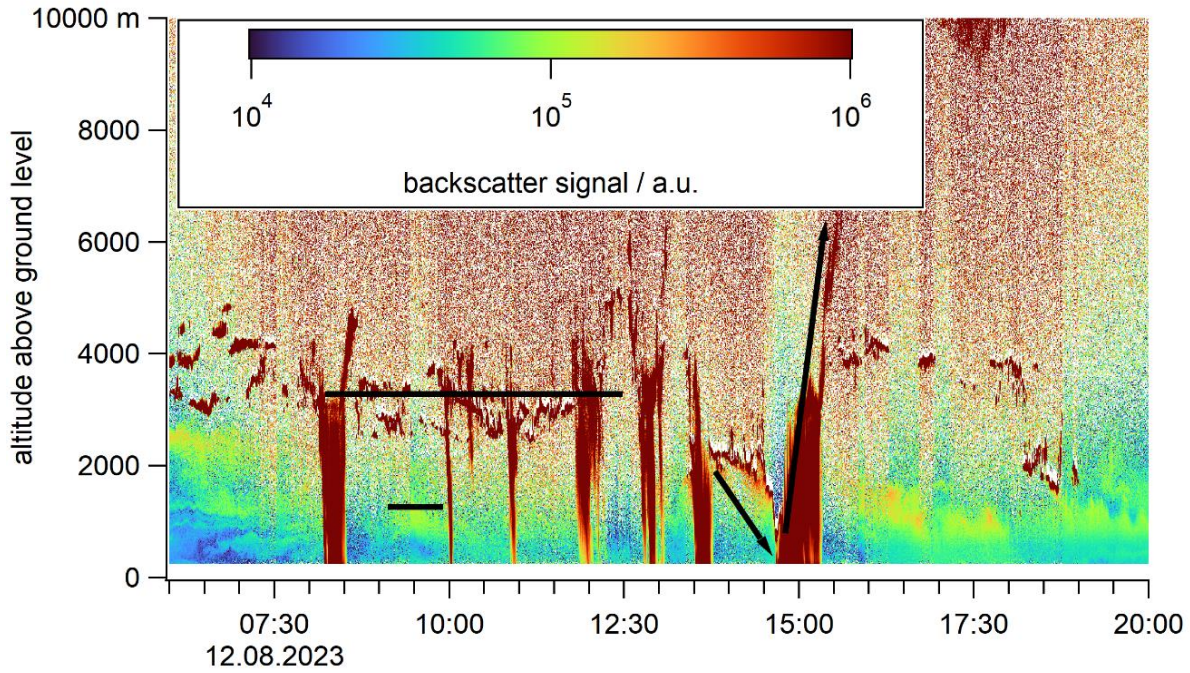


Fig. S9.56: The ceilometer in MoLa monitors a stable cloud layer between 3 to 4 km altitude a.g.l. and frequent rain events throughout the day (indicated by dark-red color). Before the thunderstorm at 14:30, a decreased cloud layer down to 1 km a.g.l. is observed, followed by a quick increase to 7 km. Data of the lowermost 200 m were removed due to high uncertainties.

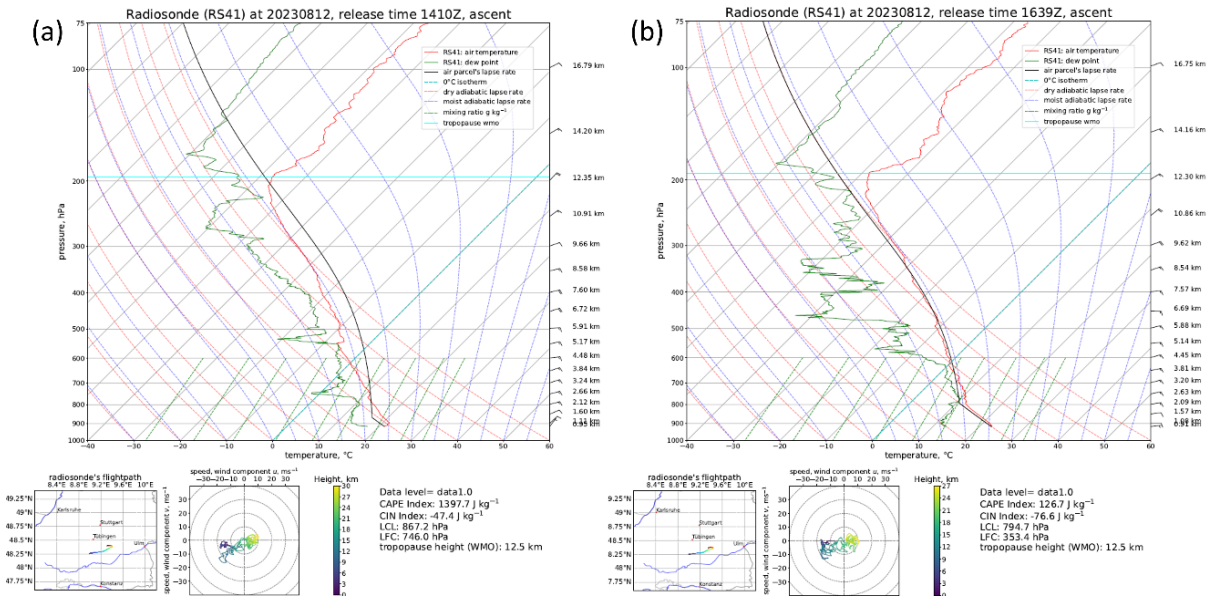


Fig. S9.57: Radiosonde ascents on 12 August 2023 show the unstable accumulation of CAPE before rain ((a), 14:10) and release of CAPE afterwards ((b), 16:39). Altitude is given in km a.s.l.

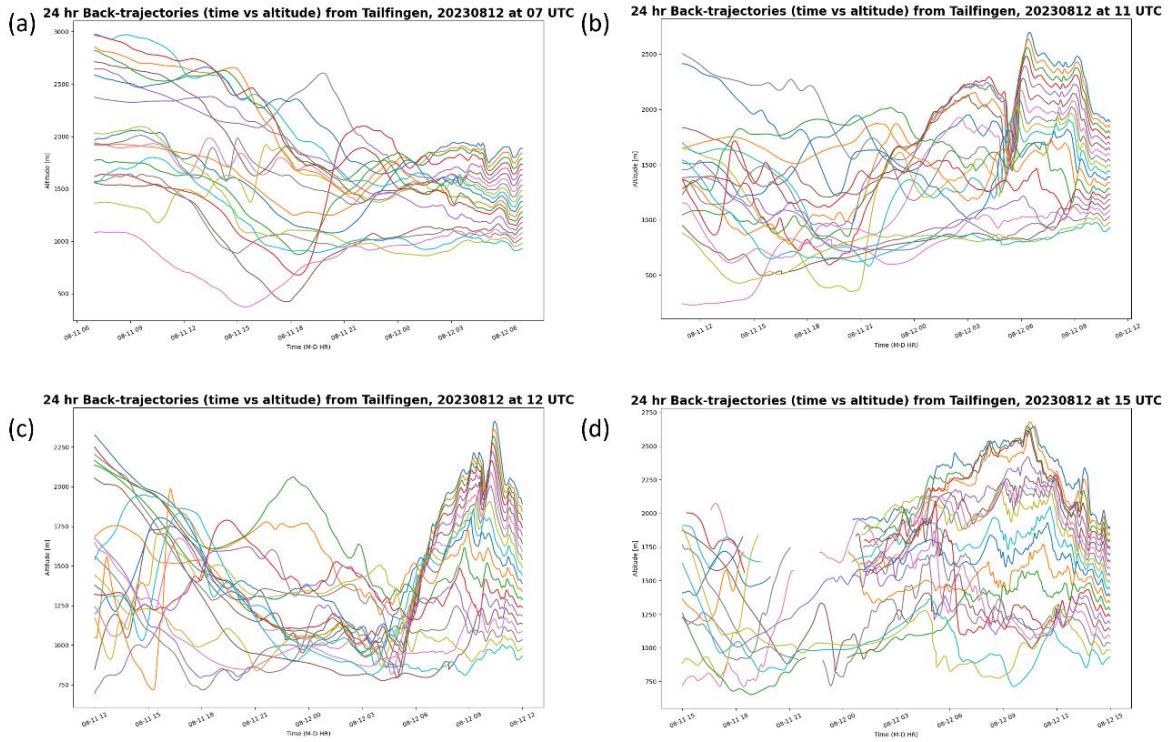


Fig. S9.58: 24-h backward trajectories for the BISTUM23 measurement site show a shallow aspiration height in (a) at 09:00 between the first and second rain event. A strong updraft, followed by a downdraft movement were found for 13:00 and 14:00 (before the third (b) and fourth rain event (c)), whereas after the thunderstorm trajectories at 17:00 show a low downdraft, with rather parallel trajectories (d). Note the different scaling of the y-axes; altitudes shown are in m a.s.l., the measurement site was located at 886 m a.s.l. LT (local time) is given in UTC + 2 h.

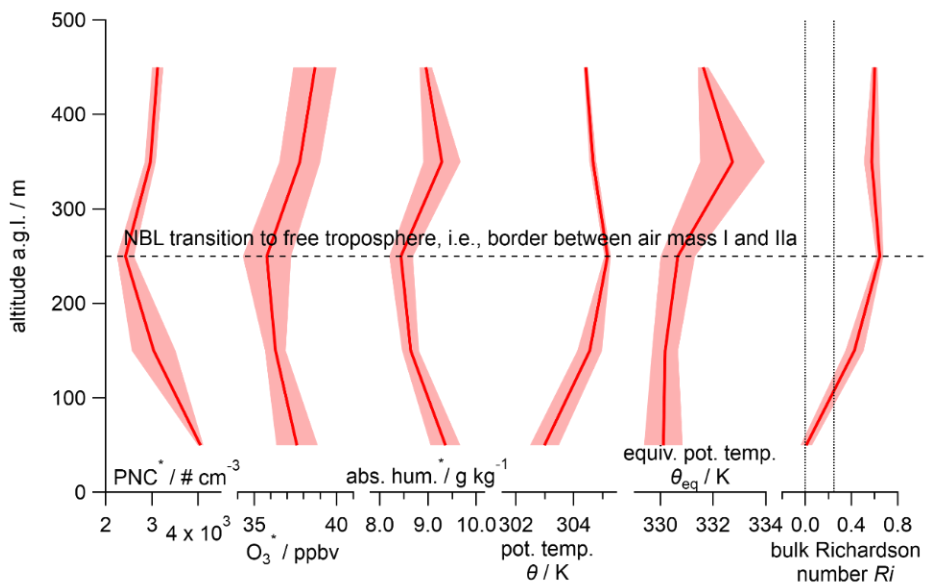


Fig. S9.59: Medians of vertical profiles (100 m altitude increments) of the particle number concentration (PNC), O_3 mixing ratio, absolute humidity, potential temperature θ , equivalent potential temperature θ_{eq} and the bulk Richardson number Ri on 12 August 2023 at 08:00. Variables marked

with * are corrected for temporal variation over the measurement period using the corresponding MoLa data. Error ranges represent the standard error. Dotted vertical lines indicate $Ri = 0$ and $Ri = 0.25$.

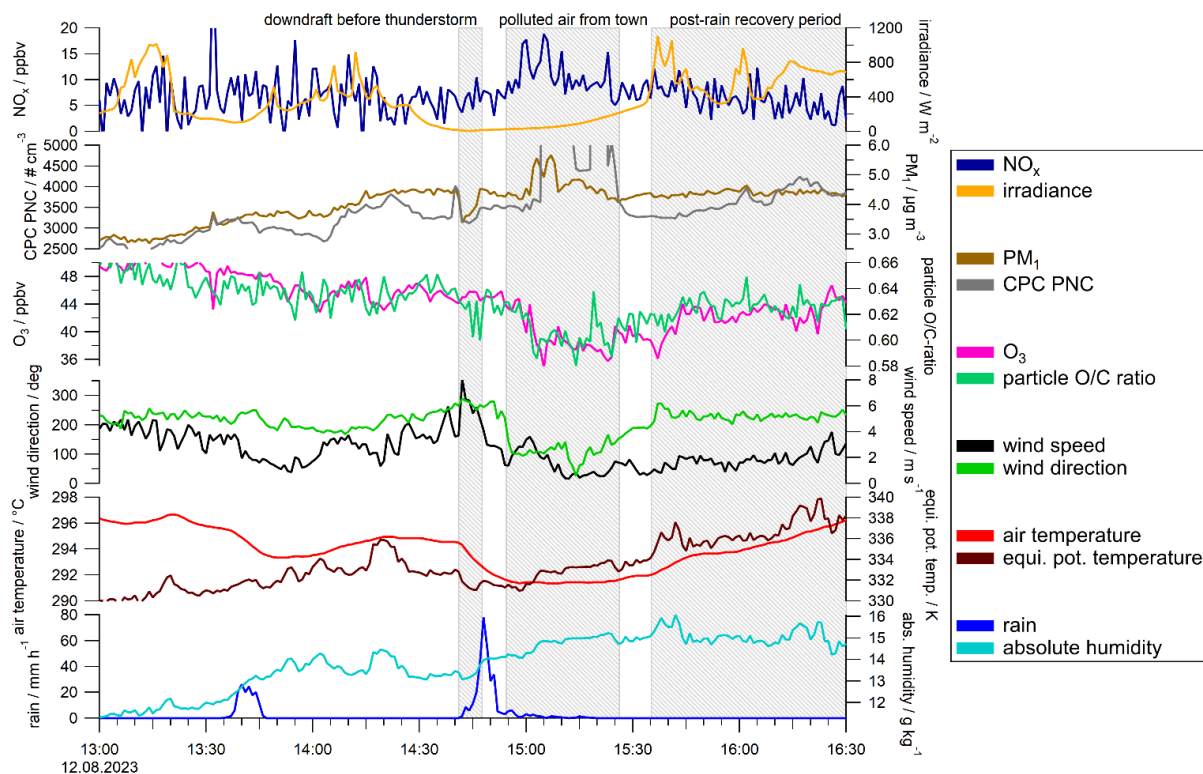


Fig. S9.60: 1 minute-time series of PM₁ (light brown), and wind speed (dark green), measured on-board MoLa, show clean air advection before rainfall (blue). After the thunderstorm, the wind direction changes (light green) affecting measured NO_x (dark blue), particle number concentration (PNC, grey), O₃ (pink) and the O/C ratio of PM₁ organics (green). As the irradiance (yellow) increases, the absolute humidity (turquoise) also increases due to evaporation of water from ground. Descriptions of various periods are given above the shaded areas.

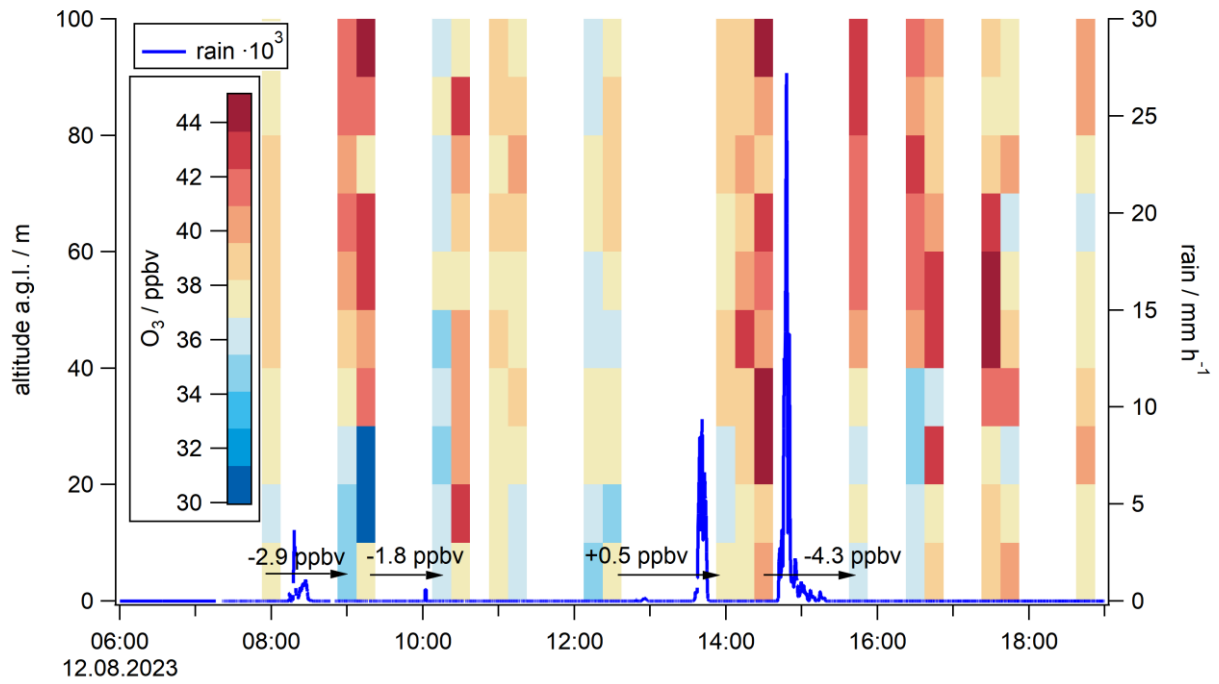


Fig. S9.61: A vertically resolved O₃-time series (15 minute-time increments with a 5 m altitude range, color-scaled, measured with FLab) show a decrease of 3.0 ± 1.3 ppbv O₃ at the lowest bin after rain (blue, 1 s data) and slow increase as O₃-rich air is injected from higher levels.

Acknowledgments

Personal List of Publications

Journal Publications (published)

Pikmann, J., **Moormann, L.**, Drewnick, F., Borrmann, S.: *The AERosol and TRACe gas Collector (AER-TRACC): an online-measurement-controlled sampler for source-resolved emission analysis*, Atmos. Meas. Tech., 16, 1323–1341, <https://doi.org/10.5194/amt-16-1323-2023>, 2023.

Moormann, L., Böttger, T., Schuhmann, P., Valero, L., Fachinger, F., Drewnick, F.: *The Flying Laboratory FLab: development and application of a UAS to measure aerosol particles and trace gases in the lower troposphere*, Atmos. Meas. Tech., 18, 1441–1459, <https://doi.org/10.5194/amt-18-1441-2025>, 2025.

Borchers, C., **Moormann, L.**, Geil, B., Karbach, N., Wasserzier, D., Hoffmann, T.: *Development and use of a lightweight sampling system for height-selective drone-based measurements of organic aerosol particles*, EGU sphere [preprint], <https://doi.org/10.5194/egusphere-2024-4015>, 2025.

Moormann, L., Fachinger, F., Drewnick, F., Tost, H.: *Boundary Layer Dynamics after Rain Fronts: High-Resolution Reconstruction and Model Validation using ground- and drone-based Measurements*, EGU sphere [preprint], <https://doi.org/10.5194/egusphere-2025-3862>.

Journal Publications (not published yet)

Moormann, L., Crowley, J. N., Fachinger, F., Drewnick, F.: *Quantification, Diel Variation and Photochemistry of Inorganic Chlorine Trace Gases in Continental Germany*, submitted to Environ. Sci.: Atmos.

Moormann, L., Fachinger, F., Drewnick, F.: *In-situ measurements of boundary layer structures: influence of irradiance and mixing layers on the representativity of ground-based measurements*, in prep.

Oral Presentations

Moormann, L., Drewnick F.: *Using CIMS with thermal desorption of particle and gas samples: Development of baseline correction and a split-flow sample inlet*, CIMS User Meeting, Frankfurt (Germany), May 2022.

Moormann, L., Valero L., Drewnick, F., Fachinger, F., Kandler, K., Weigel, R.: *Transport of aerosols and precursors from the planetary boundary layer into the UTLS - Bridging Surface emissions, Transport and UTLS Matter I*, 1st Research Area B-Meeting of SFB "TPChange", Frankfurt (Germany), October 2022.

Moormann, L.: *BISTUM: Setting up a drone for aerosol measurements*, Doktorandenseminar, Mainz, October 2022.

Moormann, L., Valero L., Drewnick, F., Fachinger, F., Kandler, K., Weigel, R.: *Transport of aerosols and precursors from the planetary boundary layer into the UTLS - Bridging Surface emissions, Transport and UTLS Matter II*, 2nd Research Area B-Meeting of SFB "TPChange", Frankfurt (Germany), October 2023.

Moormann, L., Fachinger, F., Drewnick, F., Borrmann, S.: *From conception to field campaign: Hexacopter-based on-line measurement of aerosol particles and trace gases complements ground-based analysis*, European Aerosol Conference, Tampere (Finland), August 2024.

Moormann, L., Valero L., Drewnick, F., Fachinger, F., Kandler, K., Weigel, R.: *Transport of aerosols and precursors from the planetary boundary layer into the UTLS - Bridging Surface emissions, Transport and UTLS Matter III*, 3rd Research Area B-Meeting of SFB "TPChange", Frankfurt (Germany), October 2024.

Moormann, L., Crowley, J. N., Fachinger, F., Drewnick, F.: *Observation of Reactive Chlorine Trace Gases in the Lowermost Troposphere in Rural Germany*, CIMS User Meeting, York (United Kingdom), May 2025.

Poster presentations

Fachinger, F., **Moormann, L.**, Junk, N., Weigel, R., Valero Tuya, L., Kandler, K., Drewnick, F.: *Transport of aerosols and precursors from the planetary boundary layer into the UTLS*, 1st TPChange Annual Meeting, Bad Kreuznach (Germany), March 2022.

Moormann, L.: *Development and operation of a measurement drone for investigation of the spatial distribution of pollutants in the lower troposphere*, CHESS Summer School, Elverum (Norway), September 2022.

Moormann, L., Drewnick, D., Fachinger, F., Böttger, T., Schuhmann, P.: *Spatial pollutant distribution in the lower troposphere*, 2nd TPChange Annual Meeting, Bad Kreuznach (Germany), March 2023.

Joppe, P., **Moormann, L.**, Büttner, M., Schneider, J., Kaiser, K., Köllner, F., Eppers, O., Borrmann, S.: *Small scale aerosol dynamics and gradients at the tropopause*, 2nd TPChange Annual Meeting, Bad Kreuznach (Germany), March 2023.

Moormann, L., Drewnick, D., Fachinger, F., Böttger, T., Schuhmann, P.: *Vertical pollutant distribution in the lower troposphere: first results and lessons learned from BISTUM 2023*, TPChallenges International Conference, Mainz (Germany), March 2024.

Schneiders, K., **Moormann, L.**, Dupont, S., Koenen, D., Rabe, J., Dagsson-Waldhauserová, P., Schepanski, K., Panta, A., Klose, M., Meyer, H., González-Flórez, C., González-Romero, A., Querol, X., Alastuey, A., Yus-Díez, J., Pérez García-Pando, C., Kandler, K.: *Long-term aerosol measurements of the Alphasense OPC-N3 in arctic regions: Sensor performance and corrections*, European Geosciences Union Conference, Vienna (Austria), April 2025.

Schneiders, K., **Moormann, L.**, Dupont, S., Koenen, D., Rabe, J., Dagsson-Waldhauserová, P., Schepanski, K., Panta, A., Klose, M., Meyer, H., González-Flórez, C., González-Romero, A., Querol, X., Alastuey, A., Yus-Díez, J., Pérez García-Pando, C., Kandler, K.: *Long-term aerosol measurements of the Alphasense OPC-N3 in arctic regions: Sensor performance and corrections*, European Aerosol Conference, Lecce (Italy), September 2025.

Valero, L., **Moormann, L.**, Weigel, R., Kandler, K., Fachinger, F., Drewnick, F.: *Cross-seasonal Investigation Regarding the Composition of atmospheric trace matter Up to UTLS heights (CIRCUS)*, TPChange Defense, Mainz (Germany), September 2025

Moormann, L., Crowley, J. N., Fachinger, F., Drewnick, F.: *Observation of Reactive Chlorine Trace Gases in the Lowermost Troposphere in Rural Germany*, IGAC-iCACGP ECR online Conference, online (international), September 2025.

Curriculum Vitae